ADVANCED COMPUTATIONAL METHODS FOR PREDICTING FRACTURE PHENOMENA IN ROCK-LIKE MATERIALS

PhD Thesis

Yousef Navidtehrani

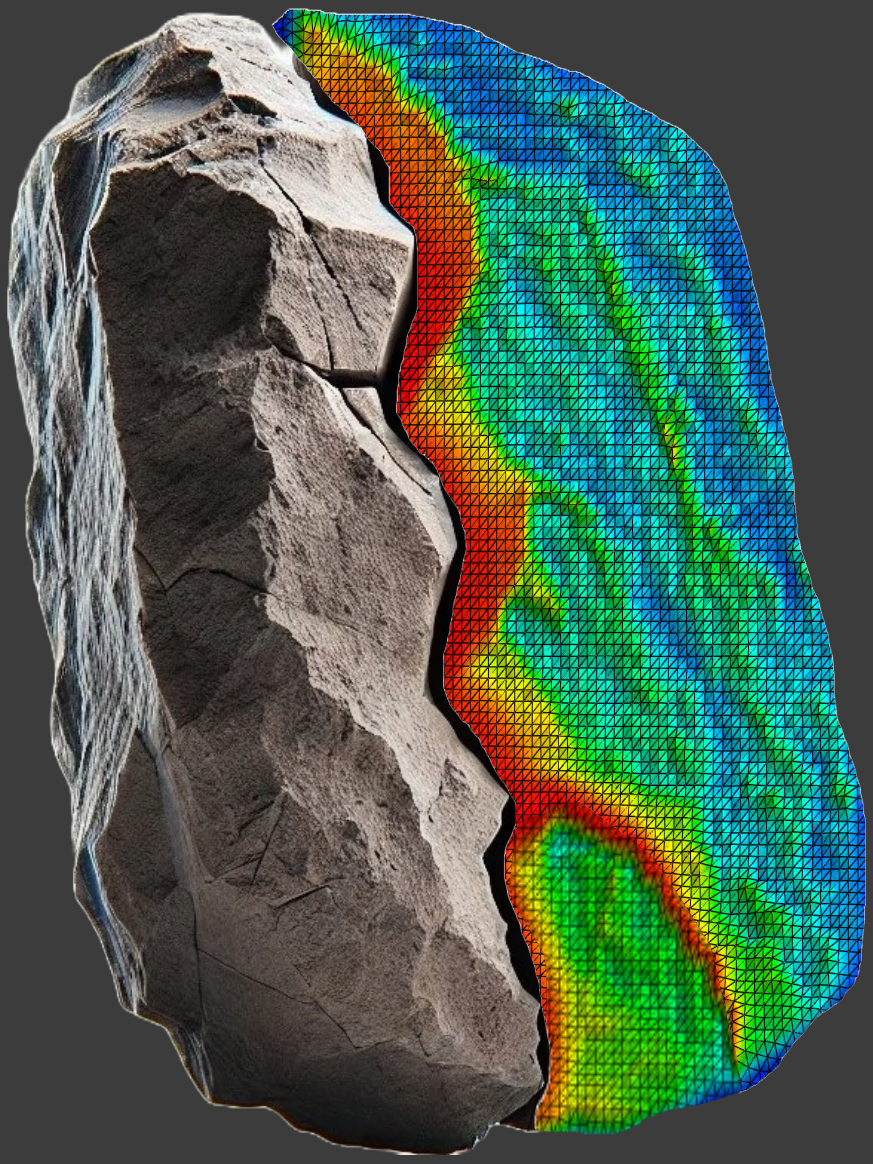

Universidad de Oviedo

Departamento de Construcción e Ingeniería de Fabricación

Programa de Doctorado en Materiales

TÍTULO DE LA TESIS DOCTORAL

MÉTODOS COMPUTACIONALES AVANZADOS PARA PREDECIR FENÓMENOS DE FRACTURA EN MATERIALES ROCOSOS

ADVANCED COMPUTATIONAL METHODS FOR PREDICTING FRACTURE PHENOMENA IN ROCK-LIKE MATERIALS

Doctorando:

Yousef Navidtehrani

Directores:

Dr. Covadonga Betegón Biempica

Dr. Emilio Martínez Pañeda

Gijón, Febrero 2025

I dedicate this work to my beloved parents and Karbalai Seyed Ahmad Najafi, who have been my guiding light; to my supportive siblings, who fill my life with joy; and to my wonderful wife, whose love inspires me each day.

The Book of Nature is written in the language of mathematics.

— Galileo Galilei

ACKNOWLEDGMENTS

I would like to express my deepest gratitude to my supervisors, Prof. Covadonga Betegón and Prof. Emilio Martínez Pañeda, for their unwavering support, guidance, and encouragement throughout my PhD journey. Their expertise and insights have been invaluable in shaping not only the direction of my research but also my approach to problem-solving and critical thinking. They have continually pushed me to achieve my best, challenging me to delve deeper into my subject and refine my skills as a researcher. Beyond their roles as mentors, they have extended friendship and personal support, helping me grow both academically and personally. Their kindness and genuine care have made an immeasurable difference, helping me navigate life in Spain, overcome challenges, and ultimately feel a true sense of belonging. I am profoundly grateful for their dedication, patience, and the many hours they invested in fostering my growth, both as a scholar and as an individual.

My sincere thanks go to the faculty, administrative staff, and laboratory technicians of the Continuum Mechanics and Structures section and DINROCK group at the University of Oviedo. I am especially grateful to Prof. Cristina Rodríguez, Prof. Antonio Argüelles Amado, Prof. Alfonso Fernández-Canteli, Prof. Javier Belzunce Varela, Prof. Celestino González Nicieza, Prof. Martina Inmaculada Álvarez Fernández, Prof. Jaime Aurelio Viña Olay, Dr. Pelayo Fernández, Dr. Miguel Muñiz, and Dr. Luis Borja Peral Martínez, whose support and guidance have been instrumental in my academic development. I also extend heartfelt thanks to my colleagues and friends from the SIMUMECAMAT group and those in the lab: Dr. Guillermo Álvarez Díaz, Lucas Castro García, Dr. Miguel Lozano Garcia, Roberto García García, Pejman Ebrahimzade, Dr. Diego-José Guerrero-Miguel, Guillermo Fernández Castro, Dr. Victor Arniella Guzmán, Sara Otero

Vega, Marcos Llera Prida, and Sofía Castaño Busón. Their camaraderie and collaboration have made my experience in Spain both fulfilling and memorable.

A special thanks is owed to Ricardo Lezcano Ruiz and his family, whose kindness and support provided a sense of family and belonging during my PhD. *Gracias a todos por hacer de España mi segundo hogar.*

I am profoundly grateful to Prof. Robert W. Zimmerman from Imperial College London for his invaluable advice and expertise, which were essential to a key part of my thesis. Working with him was an honor and deeply enriching. I also wish to thank Prof. Ravindra Duddu from Vanderbilt University for his crucial insights on another aspect of my work.

I would like to express my sincere gratitude to Prof. Peter Wriggers and Prof. Fadi Aldakheel at the Institute of Continuum Mechanics, Leibniz University Hannover, for their warm hospitality during my research stay. The insights and experiences I gained at Leibniz were invaluable, and I am thankful for their mentorship and the collaboration of the institute's members, which made my time there both productive and enjoyable.

Additionally, I extend my heartfelt thanks to Prof. Laura De Lorenzis and the Computational Mechanics Group at ETH Zürich for hosting me during another research stay. Her guidance and the opportunities provided for collaboration were integral to my research, and I am grateful to her team for their warmth and support, which made the experience both enriching and memorable.

Finally, I owe my deepest gratitude to my family, whose unwavering support made this journey possible. To my parents and sibling, thank you for your constant encouragement, understanding, and belief in me. To my beloved wife, thank you for your patience, sacrifices, and unwavering support. Your love has been my anchor, and I am deeply grateful to share this journey with you.

Abstract

Fracture modeling in rock-like materials presents significant challenges due to their inherent heterogeneity and anisotropy, leading to diverse behaviors under varying loading conditions. Conventional fracture modeling techniques often struggle to capture complex failure modes and face limitations in computational robustness. To address these challenges, this research adopts the phase field method, which represents fractures as continuous scalar fields, enabling the simulation of intricate fracture patterns—such as branching and coalescence—without the need for explicit crack tracking. This study introduces a generalized framework that combines strain energy decomposition with advanced failure criteria, such as the Drucker-Prager criterion, to enhance the phase field method's capacity for simulating compressive failure modes. Additionally, a novel strain energy formulation for materials containing voids and inclusions has been developed. The model's applicability is extended through multiphysics applications, including hydraulic fracturing, thermomechanical fracturing, and other complex interactions. Rigorous validation against experimental and benchmark datasets underscores the robustness of the proposed methods, offering a reliable computational tool for accurate fracture prediction in engineering applications. This research advances fracture mechanics by proposing innovative methodologies for tensile strength validation, notably through enhancements to the Brazilian Test for rock materials, thereby improving the precision of material parameter estimation in computational models. The developed framework represents a significant leap forward in predictive accuracy for rock fracture modeling, serving as a valuable resource for academic research and industrial applications that require dependable, high-precision fracture assessment under diverse loading and environmental conditions.

Resumen

La modelación de fracturas en materiales similares a rocas presenta desafíos significativos debido a su inherente heterogeneidad y anisotropía, lo que da lugar a comportamientos diversos bajo diferentes condiciones de carga. Las técnicas convencionales de modelación de fracturas a menudo tienen dificultades para capturar modos de falla complejos y enfrentan limitaciones en la robustez computacional. Para abordar estos desafíos, esta investigación adopta el método de campo de fases, que representa las fracturas como campos escalares continuos, permitiendo la simulación de patrones de fractura intrincados, como la ramificación y la coalescencia, sin la necesidad de rastrear explícitamente las grietas. Este estudio introduce un marco generalizado que combina la descomposición de la energía de deformación con criterios avanzados de falla, como el criterio de Drucker-Prager, para mejorar la capacidad del método de campo de fases en la simulación de modos de falla por compresión. Además, se ha desarrollado una nueva formulación de energía de deformación para materiales que contienen vacíos e inclusiones. La aplicabilidad del modelo se amplía a través de aplicaciones multifísicas, incluyendo fracturación hidráulica, fracturación termo-mecánica y otras interacciones complejas. La validación rigurosa contra conjuntos de datos experimentales y de referencia subraya la robustez de los métodos propuestos, ofreciendo una herramienta computacional confiable para la predicción precisa de fracturas en aplicaciones de ingeniería. Esta investigación avanza en la mecánica de fracturas al proponer metodologías innovadoras para la validación de la resistencia a la tracción, destacándose las mejoras en el ensayo brasileño para materiales de roca, mejorando así la precisión en la estimación de parámetros de material en modelos computacionales. El marco desarrollado representa un avance significativo en la precisión predictiva para la modelación de fracturas en rocas, sirviendo como un recurso valioso para la

investigación académica y aplicaciones industriales que requieren una evaluación de fracturas fiable y de alta precisión bajo diversas condiciones de carga y ambientales.

PUBLICATIONS

The following journal publications are included as part of this thesis:

Y. Navidtehrani, C. Betegón, J. Vallejos, E. Martínez-Pañeda. *A phase field model for hydraulic fracture: Drucker-Prager driving force and a hybrid coupling strategy*. Computer Methods In Applied Mechanics And Engineering 444, 118155 (2025).

Y. Navidtehrani, C. Betegón, E. Martínez-Pañeda. *A generalised framework for phase field-based modelling of coupled problems: application to thermo-mechanical fracture, hydraulic fracture, hydrogen embrittlement and corrosion*. Engineering Fracture Mechanics 326 ,111363 (2025).

Y. Navidtehrani, R. Duddu , E. Martínez-Pañeda. *Damage Mechanics Challenge: Predictions based on the phase field fracture model*. Engineering Fracture Mechanics 301, 110046 (2024).

Y. Navidtehrani, C. Betegón, R.W. Zimmerman, E. Martínez-Pañeda. *Griffith-based analysis of crack initiation location in a Brazilian test*. International Journal of Rock Mechanics and Mining Sciences 159, 105227 (2022).

Y. Navidtehrani, C. Betegón, E. Martínez-Pañeda. *A general framework for decomposing the phase field fracture driving force, particularised to a Drucker-Prager failure surface*. Theoretical and Applied Fracture Mechanics 121, 103555 (2022).

Y. Navidtehrani, C. Betegón, E. Martínez-Pañeda. *A unified Abaqus implementation of the phase field fracture method using only a user material subroutine*. Materials 14(8), 1913 (2021).

Y. Navidtehrani, C. Betegón, E. Martínez-Pañeda. *A simple and robust*

Abaqus implementation of the phase field fracture method. Applications in Engineering Science 6, 100050 (2021).

Table of Contents

1 INTRODUCTION **1**

1.1 Motivation 2

1.2 Aim and objectives 3

1.3 Thesis outline 4

2 METHODOLOGY **6**

2.1 Phase field method 9

2.1.1 Governing equations 10

2.1.2 Coupling with other fields 13

2.1.3 Applications of the phase field method 13

2.1.4 Advantages, challenges and limitations 14

2.2 Phase field fracture method 15

2.2.1 Variational derivative approaches 16

2.2.2 Ginzburg-Landau approach 20

2.2.3 Microforce-based approach 24

2.2.4 Irreversibility in phase field evolution for fracture mechanics 27

2.2.5 Particularising phase field fracture method 29

2.2.6 Strain energy decomposition as fracture driving force . . . 32

2.2.7 Phase field length scale as a material parameter 34

3 SUMMARY OF CONTRIBUTION AND DISCUSSION **37**

3.1 Griffith-based analysis of crack initiation location in a Brazilian test 40

3.1.1 Methodology 41

3.1.2 Key results and findings 42

3.1.3 Practical applications 45

3.1.4 Conclusion 45

3.2 Implementation and verification of phase field fracture method . . 46
3.2.1 Phase field implementation in Abaqus 47
3.2.2 Phase field fracture verification 49
3.3 Experimental validation of phase field fracture 53
3.3.1 Methodology 55
3.3.2 Key results and findings 55
3.3.3 Conclusion 57
3.4 Constitutive fracture behavior modeling of material for phase field method 58
3.4.1 Fracture driving force based on failure surface 58
3.4.2 General approach for additive decomposition of strain energy 66
3.4.3 Bresler–Pister based split 69
3.4.4 Strain energy split for material with voids and inclusions . 80
3.4.5 Conclusions 83
3.5 Multiphysics phase field fracture method 84
3.5.1 Thermal fracture modeling 85
3.5.2 Hydraulic fracture simulation 85
3.5.3 Implementation in Abaqus 86
3.5.4 Multiphysics phase field validation 87
3.6 Hydraulic phase field fracture modeling 89
3.6.1 Methodology 91
3.6.2 Key results and sindings 91
3.6.3 Practical applications 93
3.6.4 Conclusion 94

4 CONCLUSIONS **95**

4.1 Key Findings 95

4.2 Implications and contributions 99

5 FUTURE WORKS **101**

4 CONCLUSIONES **105**

4.1 Hallazgos Clave 105

4.2 Implicaciones y contribuciones 110

5 TRABAJO FUTURO **111**

Appendix A Paper 1 **131**

Appendix B Paper 2 **148**

Appendix C Paper 3 **161**

Appendix D Paper 4 **181**

Appendix E Paper 5 **197**

Appendix F Paper 6 **212**

Appendix G Paper 7 **244**

List of Figures

2.1 Phase field variable (ϕ) profile for a section of a domain containing cracks and voids. 16

3.1 Maps to assess if cracking nucleates at the center by comparing the range of material parameters showing in oval shape, application to: (a) granite, (b) sandstone, (c) limestone, and (d) marble. . 44

3.2 Phase field contour of: (a) Notched square plate under tension, (b) Notched square plate unde shear, (c) Screw tension tests, and (d) 3D Brazilian test. 51

3.3 Phase field contour of: (a) Three-Point Bending Test, (b) Mixed-Mode Fracture of a Single-Edge Notched Concrete Beam, (c) Notched Plate with an Eccentric Hole, and (d) 3D Analysis of Cracking Due to the Contact Interaction between Two Gears. 53

3.4 Geometry, dimensions, and boundary conditions of the challenge test. 54

3.5 Comparison between phase field fracture predictions and experimental data: crack trajectories (top) and force versus displacement plots (bottom) for (a) calibration test HC and (b) challenge test. . . 57

3.6 Phase field contour of Drucker-Prager based split, (a) direct shear test (DST) for different normal load, (b) compressive failure of concrete, unconfined sample, at the left and confined sample at the right, and (c) Localised failure of a soil slope. 63

3.7 Isolines of undamaged strain energy ψ_0, dissipated strain energy ψ_d, and stored strain energy ψ_s for Drucker-Prager strength surface in the space of invariants of strain invariants. 64

3.8 Elastic, frictional, frictionless and fracture regions of Drucker-Prager based model, (a) strain space $(I_1(\boldsymbol{\varepsilon}), \sqrt{J_2(\boldsymbol{\varepsilon})})$, and (b) stress space $(I_1(\boldsymbol{\sigma}), \sqrt{J_2(\boldsymbol{\sigma})})$. 72

3.9 Strength surface of Bresler-Pister failure criteria in the space of invariants of strain. The vector shows the decomposition of total tensor into elastic and damage parts. 73

3.10 Comparison of the stress paths of the undamaged stress $\boldsymbol{\sigma}_0$ and the elastic part of the stress $\boldsymbol{\sigma}_e$ in the invariant stress space $\left(I_1(\boldsymbol{\sigma}), \sqrt{J_2(\boldsymbol{\sigma})}\right)$ for a 3D single element with $\phi = 1$: (a) starting from the elastic region, transitioning into the frictional region, and finally entering the frictionless region; (b), (c) within the frictional region; and (d) within the fracture region. 75

3.11 Comparison of the stress paths of the total stress $\boldsymbol{\sigma}$, the undamaged stress $\boldsymbol{\sigma}_0$, and the elastic part of the stress $\boldsymbol{\sigma}_e$ in the invariant stress space $\left(I_1(\boldsymbol{\sigma}), \sqrt{J_2(\boldsymbol{\sigma})}\right)$ under loading-unloading conditions for a 3D single element: (a) starting in the elastic region, transitioning into the frictional region, and finally entering the frictionless region; (b), (c) within the frictional region; and (d) within the fracture region. The phase field values are represented by color. 77

3.12 Multi-axial compression test on concrete, (a) Boundary conditions and geometry, (b) phase field contour, and (c) comparison of load versus displacement for different case of multiaxial loading. . . . 79

3.13 Phase field contour of square domain with voids under compression. 80

3.14 Square domain with inclined crack at the center subjected under uniaxial compression, (a) geometry, dimensions and boundary conditions. phase field contour to show crack path for, (b) volumetric-deviatoric split $a = 0$, (c) $a = 0.45K$, and (d) no split of strain energy $a = 0.5K$. 82

3.15 Comparison of the force versus displacement of square domain with inclined crack at the center subjected under uniaxial compression for volumetric-deviatoric split $a = 0$, $a = 0.45K$, no split of strain energy $a = 0.5K$. 83

3.16 Phase field multiphysics: (a) comparison of phase field contour (at the left) and crack pattern from experiments (Jiang et al. Cui et al. (2021)) of quenching, and (b) phase field contours and pressure for a pressurized crack at Time=1200 sec, $p_{\text{center}} = 60$ MPa of pressurized crack. 89

3.17 Hydraulic fracture, (a) Crack-interaction, at the left: crack path for different fracture driving forces and at the right: fluid pressure p contour and fluid flux vector for the steady state of the case without strain energy decomposition, and (b) contour of phase field of s simultaneous injection into a axisymetric boundary with inital stress case study. 93

List of Tables

2.1 Degradation function $g(\phi)$, dissipation function $w(\phi)$, and scaling constant c_w for the AT2, AT1, and PF-CZM models. 30

3.1 Variable correspondence between heat transfer and phase field evolution equations. 48

List of Abbreviations

AM . . . . . Alternate Minimization

AMR . . . . . Adaptive Mesh Refinement

BEM . . . . . Boundary Element Method

CDEM . . . . . Continuum-Discontinuum Element Method

CZM . . . . . Cohesive Zone Model

DEM . . . . . Discrete Element Method

DoF . . . . . Degrees of Freedom

FDM . . . . . Finite Difference Method

FEM . . . . . Finite Element Method

PF-CZM . . . . . Phase Field-Cohesive Zone Models

PFM . . . . . Phase Field Method

PDE . . . . . Partial Differential Equation

RVE . . . . . Representative Volume Element

SDV . . . . . State variable

UST . . . . . Unified Strength Theory

XFEM . . . . . Extended Finite Element Method

1 | INTRODUCTION

Fracture modeling for rock-like materials is essential across a range of engineering fields, including geotechnics, mining, oil and gas extraction, geothermal energy production, tunneling, dam construction, seismic hazard analysis, earthquake engineering, nuclear waste disposal, landslide and rockfall prevention, carbon sequestration, and more. The complex behavior of rocks under diverse loading conditions—due to their inherent heterogeneity and anisotropy—necessitates precise modeling for accurate prediction and management of geological phenomena. Simulating crack initiation, propagation, and coalescence is critical for assessing the structural integrity of rock formations under various conditions.

Numerous computational techniques have been developed to model fractures in rock-like materials. Among these, the phase field fracture method represents a significant advancement, utilizing a continuous scalar field to represent cracks, thereby eliminating the need for explicit crack surface tracking. This approach is especially beneficial for handling complex fracture behaviors, such as branching and coalescence, without requiring detailed crack path tracking. Well-suited for complex geometries and loading scenarios typical in rock-like materials, the phase field method has gained considerable attention in recent years for its robust mathematical foundation and versatility in simulating a wide array of fracture phenomena.

Accurate fracture modeling of rock-like materials depends on the precise estimation of material parameters, a particularly challenging task due to the heterogeneous nature of these materials. This challenge is especially pronounced in the phase field method, where the selection of appropriate material parameters directly influences model accuracy. Specifically, tensile strength estimation is

crucial, informing key material parameters for phase field fracture modeling. In practice, tensile strength is frequently derived from the Brazilian Test, although the validity of this method remains debated within the rock mechanics community.

This thesis focuses on fracture modeling in rock-like materials, employing the phase field method with an emphasis on compressive failure modes—an area where conventional fracture models often fall short. By introducing a generalized framework for strain energy decomposition and incorporating failure criteria such as the Drucker-Prager model, this research extends the phase field method to a broader range of material behaviors, including multiphysics problems like hydraulic and thermomechanical fractures. Additionally, a novel approach is proposed to validate the tensile strength derived from the Brazilian Test, ensuring more accurate material parameter estimation.

1.1 Motivation

The motivation for this research stems from the increasing need to accurately predict fracture behavior in rock-like materials, particularly in industries where structural failure has substantial economic and environmental implications. Sectors such as mining, oil and gas extraction, and civil engineering rely heavily on precise fracture models to prevent failures in both natural and engineered rock formations. Beyond industrial applications, environmental concerns—such as groundwater contamination from industrial pollutants or fracking fluids and the secure long-term storage of CO_2 in subsurface geological formations—further underscore the necessity for robust and precise fracture modeling. Traditional models often struggle to fully capture complex rock behavior, especially under multiaxial stress or when multiple physical processes, such as thermal or hydraulic

effects, are involved in fracture evolution. Additionally, simulating compressive fractures, a common failure mode in rock-like materials, presents a further challenge, highlighting the need for advanced computational approaches like the phase field method.

1.2 Aim and objectives

This thesis primarily aims to develop an advanced phase field fracture model capable of accurately simulating the initiation, propagation, and interaction of fractures in rock-like materials under diverse loading conditions and multiphysics scenarios. The specific objectives of this research are:

- To assess the accuracy of tensile strength measurements from the Brazilian Test and propose a method for validating the results while minimizing geometrical constraints.
- To extend the phase field method by introducing a generalized framework for strain energy decomposition that addresses compressive failure in rock-like materials, using failure criteria, including the Drucker-Prager model.
- To develop and implement phase field models capable of simulating complex fracture phenomena, such as hydraulic fracturing and thermomechanical fractures.
- To validate the proposed models against experimental data and benchmark problems, ensuring robust and accurate predictions of real-world fracture behaviors.
- To provide a robust computational tool applicable to engineers and researchers, enabling the effective prediction and management of fractures in geotech-

nical and industrial applications.

1.3 Thesis outline

The structure of this thesis is as follows:

Chapter 2 (Methodology) discusses various numerical modeling techniques utilized for fracture modeling in rock-like materials. This chapter provides an in-depth explanation of the phase field method, including its governing equations and its coupling with other physical fields. Additionally, the advantages, limitations, and applications of the phase field method are thoroughly discussed. A comprehensive explanation of the phase field fracture method is also included, detailing the derivation of the phase field evolution equation through various approaches.

Chapter 3 (Discussion) presents the results and applications of seven key studies. These include the proposed method for validating the Brazilian Test, the unified implementation of phase field fracture with various constitutive models and fracture driving forces, and its verification through multiple case studies and experimental validations. This chapter also introduces a general framework for strain energy decomposition based on failure criteria such as Drucker-Prager and addresses the limitations of classical models in predicting compressive fracture. A new strain energy split for materials with voids and inclusions is presented to account for their effects on compressive failure. Additionally, an extension for multiphysics phenomena, such as hydraulic fracturing, is discussed, with a focus on coupling between the phase field and fluid equations. A novel mixed method is proposed, and the Drucker-Prager-based split is applied to hydraulic fracture models to simulate geotechnical phenomena, such as stick-slip behavior.

Chapter 4 (Conclusions) summarizes the key findings of this thesis and highlights

its contributions to the field of fracture mechanics.

Chapter 5 (Future Work) outlines potential extensions of this research, including further exploration of multiphysics couplings, improvements in computational efficiency, and broader applications of the phase field method to various materials and fracture processes.

2 | METHODOLOGY

Fracture modeling of rock-like materials involves simulating crack nucleation and propagation within inherently heterogeneous and anisotropic materials. Due to microstructural heterogeneity, nonlinear deformation, and anisotropy, these materials exhibit complex stress responses, making precise fracture mechanics modeling essential for various engineering applications. Broadly, fracture modeling approaches are categorized into three types: continuum-based, discontinuum-based, and hybrid approaches.

Continuum-based approaches treat rock as a continuous medium, integrating fractures into the material's constitutive behavior. Key methods in this category include the Finite Element Method (FEM) [1], Finite Difference Method (FDM) [2], and Boundary Element Method (BEM) [3].

In FEM, widely used in solid mechanics, the rock domain is discretized into small elements where stress and strain fields are calculated. Fracture propagation is commonly modeled using specialized techniques like the Cohesive Zone Model (CZM) [4], which simulates fractures by inserting cohesive elements between regular elements to control crack initiation and propagation. Another approach, the Extended Finite Element Method (XFEM) [5], enhances standard FEM formulations to represent discontinuities (e.g., cracks) without requiring the mesh to align with fracture surfaces. Although XFEM efficiently handles complex crack paths, it can be computationally intensive for high-dimensional problems. Additionally, the Phase Field Method (PFM) [6,7] represents cracks through a continuous scalar field, eliminating the need to explicitly track crack surfaces, which enables modeling of complex crack branching and merging patterns—particularly advantageous in brittle material studies.

The Peridynamics approach [8], a non-local continuum theory, models interactions between material points over finite distances and bypasses the need for spatial derivatives. This makes it suitable for problems involving discontinuities like fractures, as fractures emerge naturally as bonds break between material points. Peridynamics is particularly valuable for simulating fracture dynamics in rock-like materials under large deformations and dynamic loading conditions.

The Finite Difference Method (FDM) [2] solves differential equations for stress and displacement, with fractures represented by modifying grid points to indicate discontinuities or through explicit fracture propagation algorithms [9]. This method is often applied in large-scale geomechanical modeling but may face limitations in capturing complex fracture networks due to grid dependence.

The Boundary Element Method (BEM) [3, 10] reduces the problem's dimensionality by modeling only the boundaries of the rock domain, making it advantageous for semi-infinite or infinite domains, such as subsurface fractures. Fractures are included as boundary conditions, and fracture propagation is modeled by altering the boundary to represent crack growth [11]. This approach is particularly effective for subsurface fractures due to its reduction in computational complexity.

Discontinuum-Based Approaches explicitly model the discrete nature of rock fractures and joints. The primary methods here include the Discrete Element Method (DEM) [12] and Block Theory (Distinct Element Method) [13].

The DEM models rock as an assembly of discrete particles or blocks, with interaction laws governing their behavior. Fractures are represented as the separation or breakage of bonds between particles or blocks, forming naturally under stress [14]. DEM is particularly effective for simulating highly fractured or jointed rock masses, though it can be computationally intensive for large-scale systems.

Block Theory represents the rock mass as an assembly of discrete blocks rather

than particles. Each block can move, rotate, or deform independently, with contact mechanics governing the interactions between blocks. Pre-existing fractures and joints are explicitly represented, and new fractures may develop through block splitting or sliding [15]. Block Theory is particularly useful for highly jointed rock masses where individual block interactions significantly influence stability.

Hybrid Approaches combine elements of both continuum and discontinuum models to capture both the bulk behavior of the material and fracture dynamics. A notable example is the Continuum-Discontinuum Element Method (CDEM) [16], where the continuum approach is initially applied, transitioning to a discontinuum approach upon fracture initiation. This enables the model to evolve from an intact to a fractured state, with fractures represented by breaking elements or creating discontinuities between them as they propagate.

Lattice Models [17] represent the rock as a network of beams or springs forming a lattice structure. Deformation of the lattice mimics the rock's mechanical response, with fractures occurring as beams or springs break under stress. These models are particularly useful for simulating complex fracture networks and investigating the influence of microstructural heterogeneities on fracture behavior [18]. Lattice models can capture the effects of microstructural variations, making them valuable for multiscale modeling in rock fracture analysis.

In this thesis, the Phase field method (PFM) was selected due to its distinct advantages over traditional fracture modeling approaches. Extended Finite Element Method (XFEM), which require specialized techniques such as cohesive elements or mesh enrichment to capture fractures, PFM uses a continuous scalar field to represent cracks, eliminating the need to explicitly track crack surfaces. This approach inherently accommodates complex fracture patterns, including branching and merging, which can be challenging to model with FEM or XFEM. Addition-

ally, PFM overcomes some limitations of the Discrete Element Method (DEM) and Block Theory by avoiding the computationally expensive process of tracking and recalculating particle or block interactions. In contrast to Peridynamics, which relies on non-local interactions and can be computationally demanding for large domains, PFM maintains computational efficiency by using standard finite element frameworks while capturing discontinuities through a diffuse field representation. However, traditional PFM models face challenges in simulating complex cracking behavior under compression or multiaxial stress conditions, which are common in rock-like materials. To address this, a general framework based on strain energy split and failure criteria is introduced that allowing for more accurate constitutive fracture modeling of rock-like materials under various loading conditions.

In Section 2.1, the phase field method is introduced, detailing the governing equations and explaining its applications. Subsequently, Section 2.2 delves into the Phase Field Fracture Method, discussing the governing equations under various approaches and reviewing existing constitutive models.

2.1 Phase field method

The Phase field method (PFM) is a computational technique primarily used to model and simulate the evolution of complex interfaces and patterns in multiphase materials and physical processes, such as solidification and microstructural evolution. This method is employed across a variety of fields, including materials science, fluid dynamics, and biology.

The fundamental concept of the phase field method is to replace sharp interfaces between different phases with a continuous, smoothly varying field known as the

phase field. This phase field is represented by an order parameter, typically denoted by ϕ, which takes distinct values in different phases. For example, $\phi = 1$ may represent one phase (e.g., solid), $\phi = 0$ may represent another phase (e.g., liquid), and intermediate values of ϕ denote the interface between these phases. This smooth interface representation eliminates the need for explicit tracking of sharp boundaries, facilitating the modeling of interface dynamics, including complex phenomena such as merging and splitting.

2.1.1 Governing equations

The evolution of the phase field ϕ is governed by partial differential equations (PDEs) derived from thermodynamic principles. Key equations in phase field models include the Allen-Cahn equation [19], which describes the evolution of the phase field driven by interface dynamics and free energy minimization, and the Cahn-Hilliard equation [20], which models diffusive processes where mass conservation is crucial, such as phase separation. These equations are frequently coupled with additional physical equations (e.g., conservation of mass, momentum, and energy) to provide a comprehensive description of the system.

The phase field method typically originates from a free energy functional that represents the system's total energy as a function of the phase field ϕ and other variables, such as temperature or concentration. A standard free energy functional includes bulk energy, associated with the intrinsic energy of the individual phases; interfacial energy, representing the energy cost of creating an interface between phases; and gradient energy, which penalizes sharp spatial variations in the phase field to maintain smooth interfaces.

To begin, the free energy is calculated associated with the Allen-Cahn equation. The system's total free energy is expressed as a free energy functional, $\Psi^{\mathrm{AC}}(\phi)$,

which depends on the order parameter $\phi(\mathbf{x}, t)$. This order parameter typically denotes the local phase state within the system. The free energy functional is defined as follows:

$$\Psi^{\text{AC}}(\phi) = \int \left(\frac{\kappa}{2} |\nabla \phi|^2 + W(\phi) \right) dV, \tag{2.1}$$

where, $W(\phi)$ denotes the local free energy density, commonly modeled by a double-well potential. The parameter κ is a positive constant denoting the gradient energy coefficient, while $\nabla \phi$ is the gradient of the order parameter ϕ. The term $|\nabla \phi|^2$ accounts for the energy contribution arising from spatial inhomogeneities within the system.

The chemical potential $\mu(\phi)$ is defined as the functional derivative of the free energy with respect to the order parameter ϕ. It represents the thermodynamic driving force governing the evolution of the order parameter:

$$\mu(\phi) = \frac{\delta \Psi^{\text{AC}}(\phi)}{\delta \phi} = \frac{dW(\phi)}{d\phi} - \kappa \Delta \phi, \tag{2.2}$$

where Δ is Laplacian.

In non-conserved systems, the time evolution of the order parameter ϕ follows a gradient flow aimed at minimizing the free energy. Here, the rate of change of ϕ is directly proportional to the negative of the chemical potential:

$$\frac{\partial \phi}{\partial t} = -L \mu(\phi), \tag{2.3}$$

where L is a kinetic coefficient that characterizes the mobility of the order parameter. Substituting the expression for the chemical potential $\mu(\phi)$ yields:

$$\frac{\partial \phi}{\partial t} = -L\left(\frac{dW(\phi)}{d\phi} - \kappa\Delta\phi\right). \tag{2.4}$$

In a conserved system, the evolution of phase field is described by the Cahn-Hilliard equation. Here, phase field variable is considered as a concentration field. The concentration field $c(\mathbf{x}, t)$ remains conserved over time, which is expressed through a continuity equation:

$$\frac{\partial c}{\partial t} = -\nabla \cdot \mathbf{J}, \tag{2.5}$$

where $\mathbf{J}$ represents the concentration flux. According to Fick's law, this flux is proportional to the gradient of the chemical potential:

$$\mathbf{J} = -M\nabla\mu(c), \tag{2.6}$$

where M is the mobility coefficient.

By substituting the concentration flux from Equation (2.6) into the continuity equation (Equation (2.5)):

$$\frac{\partial c}{\partial t} = \nabla \cdot (M\nabla\mu(c)). \tag{2.7}$$

Substituting the expression for the chemical potential $\mu(c)$:

$$\frac{\partial c}{\partial t} = \nabla \cdot \left(M\nabla\left(\frac{dW(c)}{dc} - \kappa\Delta c\right)\right). \tag{2.8}$$

The final form of the Cahn-Hilliard equation is:

$$\frac{\partial c}{\partial t} = \nabla \cdot \left(M \nabla \left(\frac{dW(c)}{dc} \right) \right) - \nabla \cdot \left(M \kappa \nabla (\Delta c) \right). \tag{2.9}$$

This equation characterizes the time evolution of the concentration field, driven by variations in local free energy and interfacial energy.

2.1.2 Coupling with other fields

The phase field method is coupled with other physical fields, such as temperature, concentration, or mechanical deformation, to capture complex interactions. For example, in solidification, the phase field is coupled with heat diffusion and temperature. In fracture mechanics, phase field models integrate with displacement fields to simulate crack propagation. In microstructure evolution, the phase field may be coupled with stress or chemical diffusion fields to account for material behavior under varying conditions.

2.1.3 Applications of the phase field method

The phase field method is widely applied across numerous fields. In solidification and microstructure evolution, it is extensively used to simulate processes like solidification, crystal growth, and the evolution of microstructures within materials [21–23]. In fracture mechanics, the method enables modeling of crack propagation without explicit crack tracking, naturally accommodating complex crack paths [24–26]. For phase separation and diffusion, the phase field method effectively models phase separation in alloys and similar systems, managing diffuse interfaces between materials [20, 27]. In fluid dynamics, it is applied to multi-phase fluid flows, accurately capturing the interface between different fluids [28–30].

Additionally, in biology, the phase field method facilitates the modeling of complex phenomena such as pattern formation, tumor growth, and cellular structure development, providing valuable insights into various biological systems [31,32].

2.1.4 Advantages, challenges and limitations

The phase field method offers several key advantages:

- **Implicit interface representation**: By representing interfaces implicitly through the phase field, the method automatically manages interface dynamics without requiring explicit tracking. This is particularly beneficial for interfaces undergoing complex topological changes, such as merging or splitting.
- **Versatility**: The phase field method is highly adaptable, making it applicable to a wide range of physical problems, including phase transformations, grain growth, crack propagation, and biological pattern formation.
- **Suitability for complex geometries**: The method is especially effective for problems involving intricate geometries, multiple phases, and dynamic changes in interface topology.
- **Thermodynamically consistent**: Grounded in the minimization of a free energy functional, the phase field method is rooted in thermodynamic principles, promoting physically accurate and realistic simulations.

Despite its advantages, phase field modeling presents several limitations and challenges:

- **High computational demand**: A primary challenge of the phase field method is its high computational cost, especially when fine discretization is neces-

sary near interfaces or across extensive simulation domains.

- **Interface thickness sensitivity**: The selection of interface thickness, or the transition region where ϕ shifts between phases, affects both accuracy and computational efficiency. Narrower interfaces improve accuracy but significantly increase computational requirements.
- **Parameter sensitivity**: Accurate results rely on careful parameter selection, including mobility, interface width, and coupling coefficients, which can be complex and not always straightforward.
- **Numerical stability concerns**: The nonlinear nature of the governing PDEs can pose numerical stability challenges, often necessitating advanced numerical methods, such as implicit time-stepping, to maintain stable simulations.

2.2 Phase field fracture method

The phase field fracture method is an advanced computational technique for modeling crack initiation, propagation, and coalescence in materials. Grounded in principles of continuum and fracture mechanics, this method bypasses the complexities associated with explicit crack tracking, especially in intricate 3D simulations. Instead, it represents cracks as diffuse interfaces within a continuous domain, governed by a phase field variable.

Rooted in thermodynamic principles and variational calculus, the phase field fracture method is well-suited for simulating complex crack patterns, including branching, merging, and nucleation under varied loading conditions.

Fundamentally, phase field fracture is based on Griffith's theory of fracture me-

chanics [33] and foundational principles from materials science. In this framework, the material is defined by two distinct states: $\phi = 0$ represents the undamaged material, while $\phi = 1$ indicates a fully fractured state (Figure 2.1). The phase field variable, ϕ, transitions smoothly and continuously between these states, capturing the gradual development of damage. Various methodologies for deriving the phase field evolution equations are available and will be discussed in detail in the following sections.

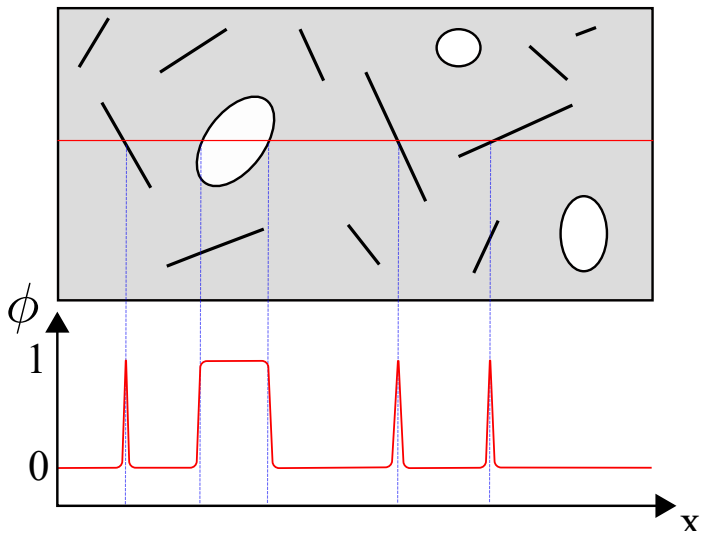

Figure 2.1: Phase field variable (ϕ) profile for a section of a domain containing cracks and voids.

2.2.1 Variational derivative approaches

Deriving thermodynamically consistent phase field formulations has become a widely adopted approach for modeling phase field evolution in continuum mechanics. Consider a body $\Omega \subset \mathbb{R}^n$ $(n \in [1, 2, 3])$, with an external boundary $\partial\Omega \subset \mathbb{R}^{n-1}$ and an outward unit normal vector $\mathbf{n}$, containing a crack surface $\Gamma \subset \mathbb{R}^{n-1}$.

According to Griffith's thermodynamic framework [33], crack initiation or propagation occurs when the total energy of the system decreases or remains constant. For an elastic solid, the variation in total energy $\mathcal{E}$ due to an infinitesimal crack growth dA is given by:

$$\frac{\mathrm{d}\mathcal{E}}{\mathrm{d}A} = \frac{\mathrm{d}\Pi}{\mathrm{d}A} + \frac{\mathrm{d}W_c}{\mathrm{d}A} = \frac{\mathrm{d}\Psi\left(\boldsymbol{\varepsilon}(\mathbf{u})\right)}{\mathrm{d}A} + \frac{\mathrm{d}W_e}{\mathrm{d}A} + \frac{\mathrm{d}W_c}{\mathrm{d}A}, \tag{2.10}$$

where W_c denotes the energy required to create new surfaces, and Π represents the total potential energy, consisting of the internal strain energy Ψ and the energy due to external forces W_e. The critical energy release rate $G_c = dW_c/dA$ is an intrinsic material property. The strain energy Ψ is determined by the strain field $\boldsymbol{\varepsilon}$, which is a function of the displacement field $\mathbf{u}$, given by $\boldsymbol{\varepsilon} = \left(\nabla\mathbf{u}^T + \nabla\mathbf{u}\right)/2$ in the case of infinitesimal strain. The total energy of the solid can be expressed as follows:

$$\mathcal{E}(\mathbf{u}) = \int_\Omega \psi\left(\boldsymbol{\varepsilon}(\mathbf{u})\right)\,\mathrm{d}V + \int_\Gamma G_c\,\mathrm{d}S - \int_\Omega \mathbf{b}\cdot\mathbf{u}\,\mathrm{d}V - \int_{\partial\Omega} \mathbf{T}\cdot\mathbf{u}\,\mathrm{d}S, \tag{2.11}$$

where $\mathbf{b}$ and $\mathbf{T}$ are the body force and traction vector, respectively. Crack evolution follows global energy minimization, but tracking the evolving fracture surface Γ poses computational challenges. This is addressed by introducing a scalar phase field variable ϕ, representing the damage field, transitioning from 0 (undamaged) to 1 (cracked). Using a degradation function $g(\phi)$, the regularized energy functional is:

$$\mathcal{E}_\ell\left(\mathbf{u},\phi\right)=\int_\Omega g(\phi)\psi_0\left(\boldsymbol{\varepsilon}\left(\mathbf{u}\right)\right)\,\mathrm{d}V+\int_\Omega G_c\gamma_\ell\left(\phi,\nabla\phi\right)\,\mathrm{d}V-\int_\Omega \mathbf{b}\cdot\mathbf{u}\,\mathrm{d}V-\int_{\partial\Omega}\mathbf{T}\cdot\mathbf{u}\,\mathrm{d}S, \tag{2.12}$$

where $\gamma_\ell(\phi,\nabla\phi)$ is the crack density function:

$$\gamma_\ell(\phi,\nabla\phi)=\frac{1}{4c_w\ell}\left(w(\phi)+\ell^2|\nabla\phi|^2\right), \tag{2.13}$$

where ℓ is the phase field length scale, $w(\phi)$ is the geometric crack function, and c_w is a scaling constant used to normalize the damage variable within the range [0, 1]. For linear elastic materials, the strain energy density of the undamaged configuration of material, denoted as $\psi_0\left(\boldsymbol{\varepsilon}\left(\mathbf{u}\right)\right)$, can be expressed as:

$$\psi_0\left(\boldsymbol{\varepsilon}\left(\mathbf{u}\right)\right)=\frac{1}{2}\boldsymbol{\varepsilon}\left(\mathbf{u}\right):\boldsymbol{C}_0:\boldsymbol{\varepsilon}\left(\mathbf{u}\right), \tag{2.14}$$

where $\boldsymbol{C}_0$ denotes the elastic stiffness tensor of the undamaged material. Consequently, the Cauchy stress tensor is defined as:

$$\boldsymbol{\sigma}=g(\phi)\boldsymbol{\sigma}_0=g(\phi)\frac{\partial\psi_0\left(\boldsymbol{\varepsilon}\right)}{\partial\boldsymbol{\varepsilon}}, \tag{2.15}$$

where the undamaged Cauchy stress is given by $\boldsymbol{\sigma}_0=\boldsymbol{C}_0:\varepsilon$.

Based on the constitutive choices outlined above, the first variation of the regularized energy functional $\mathcal{E}_\ell$ with respect to the primary kinematic variables $\mathbf{u}$ (displacement field) and ϕ (phase field) results in the following governing equations:

$$\int_{\Omega}\Big[g(\phi)\boldsymbol{\sigma}_0 : \mathrm{sym}\nabla\delta\mathbf{u} + \mathbf{b}\cdot\delta\mathbf{u} + g'(\phi)\,\psi_0\left(\boldsymbol{\varepsilon}\left(\mathbf{u}\right)\right)\delta\phi + \frac{G_c}{4c_w\ell}\left(w'(\phi)\delta\phi + \ell^2\nabla\phi\cdot\nabla\delta\phi\right)\Big]\,\mathrm{d}V - \int_{\partial\Omega}\mathbf{T}\cdot\delta\mathbf{u}\,\mathrm{d}S = 0. \tag{2.16}$$

Applying the necessary boundary conditions, $\mathbf{T} = \boldsymbol{\sigma}\cdot\mathbf{n}$ and $\nabla\phi\cdot\mathbf{n} = 0$ on $\partial\Omega$, and utilizing the Gauss divergence theorem on Equation (2.16), the linear momentum equation and the phase field evolution equation are derived as follows:

$$\begin{aligned} \nabla\cdot\left[g(\phi)\boldsymbol{\sigma}_0\right] + \mathbf{b} &= \mathbf{0} \quad \text{in} \quad \Omega \\ \frac{G_c}{4c_w\ell}\left(w'(\phi) - \ell^2\Delta\phi\right) + g'(\phi)\,\psi_0\left(\boldsymbol{\varepsilon}\left(\mathbf{u}\right)\right) &= 0 \quad \text{in} \quad \Omega. \end{aligned} \tag{2.17}$$

All components of the stress tensor for the undamaged configuration, $\boldsymbol{\sigma}_0$, are reduced due to the constitutive relationship defined in Equation (2.15). This implies that damage evolution occurs even under compressive stress. To account for asymmetric behavior, the strain energy can be decomposed additively as follows:

$$\psi_0\left(\boldsymbol{\varepsilon}\right) = \psi_d\left(\boldsymbol{\varepsilon}\right) + \psi_s\left(\boldsymbol{\varepsilon}\right), \quad \text{and} \quad \psi\left(\boldsymbol{\varepsilon},\phi\right) = g\left(\phi\right)\psi_d\left(\boldsymbol{\varepsilon}\right) + \psi_s\left(\boldsymbol{\varepsilon}\right), \tag{2.18}$$

where $\psi_d\left(\boldsymbol{\varepsilon}\right)$ represents the dissipated (or damaged) part of the strain energy, while $\psi_s\left(\boldsymbol{\varepsilon}\right)$ corresponds to the stored part of the strain energy, which remains unaffected by the phase field evolution. Based on this additive decomposition of the strain energy, the Cauchy stress can be defined as follows:

$$\boldsymbol{\sigma} = \frac{\partial \psi\left(\boldsymbol{\varepsilon}(\mathbf{u})\right)}{\partial \boldsymbol{\varepsilon}(\mathbf{u})} = g\left(\phi\right) \frac{\partial \psi_d + \left(\boldsymbol{\varepsilon}(\mathbf{u})\right)}{\partial \boldsymbol{\varepsilon}(\mathbf{u})} + \frac{\partial \psi_s\left(\boldsymbol{\varepsilon}(\mathbf{u})\right)}{\partial \boldsymbol{\varepsilon}(\mathbf{u})} = g\left(\phi\right) \boldsymbol{\sigma}^d + \boldsymbol{\sigma}^s, \quad (2.19)$$

where $\boldsymbol{\sigma}^d$ and $\boldsymbol{\sigma}^s$ respectively denote the damaged and non-degraded parts of the Cauchy stress tensor.

Considering the constitutive behavior defined in Equations (2.18) and (2.19), the energy functional can be formulated as:

$$\mathcal{E}_\ell\left(\mathbf{u}, \phi\right) = \int_\Omega \left[g\left(\phi\right) \psi_d\left(\boldsymbol{\varepsilon}\right) + \psi_s\left(\boldsymbol{\varepsilon}\right)\right] \, \mathrm{d}V + \int_\Omega G_c \gamma_\ell\left(\phi, \nabla\phi\right) \, \mathrm{d}V - \int_\Omega \mathbf{b}\cdot\mathbf{u} \, \mathrm{d}V - \int_{\partial\Omega} \mathbf{T}\cdot\mathbf{u} \, \mathrm{d}S, \quad (2.20)$$

Following the same procedure as in Equation (2.16), the weak form of Equation (2.20) is derived using the test functions $\delta\mathbf{u}$ and $\delta\phi$. By applying the Gauss divergence theorem along with the necessary boundary conditions, obtain:

$$\begin{aligned} \nabla \cdot \left[g(\phi)\boldsymbol{\sigma}^d + \boldsymbol{\sigma}^s\right] + \mathbf{b} = \mathbf{0} \quad \text{in} \quad \Omega \\ \frac{G_c}{4c_w\ell}\left(w'(\phi) - \ell^2\Delta\phi\right) + g'(\phi)\,\psi^d\left(\boldsymbol{\varepsilon}\left(\mathbf{u}\right)\right) = 0 \quad \text{in} \quad \Omega \end{aligned} \quad (2.21)$$

2.2.2 Ginzburg-Landau approach

Phase field fracture method can be conceptualized as a form of phase separation, typically represented by reaction-diffusion equations such as the Ginzburg-Landau equation, a variant of the Allen-Cahn equation. In this framework, the material exists in two distinct phases: the intact or pristine phase, denoted by

$\phi = 0$, and the fully fractured phase, denoted by $\phi = 1$, where the material has completely or partially lost its stiffness.

To capture this transition between phases, the volume fractions of the intact and fractured phases as $P_{v1}(\phi)$ and $P_{v2}(\phi)$ are defined, respectively, where these volume fractions are functions of the phase field variable ϕ. For a representative volume element (RVE) of total volume V_{RVE}, the volume fractions are:

$$P_{v1}(\phi) = \frac{V_1}{V_{\text{RVE}}}, \quad P_{v2}(\phi) = 1 - P_{v1}(\phi) = \frac{V_2}{V_{\text{RVE}}}, \tag{2.22}$$

where V_1 and V_2 denote the volumes occupied by the intact and fractured phases, respectively. The total energy of the system, $\mathcal{E}_\ell(\mathbf{u}, \phi)$, comprises the mechanical free energy Ψ^{M}, the fracture energy Ψ^{AC} (regularized using the Allen-Cahn form of the Ginzburg-Landau equation), and contributions from external forces. The total energy functional can thus be expressed as:

$$\mathcal{E}_\ell(\mathbf{u}, \phi) = \Psi^{\text{M}}(\mathbf{u}, \phi) + \Psi^{\text{AC}}(\phi) - \int_\Omega \mathbf{b} \cdot \mathbf{u}\, dV - \int_{\partial\Omega} \mathbf{T} \cdot \mathbf{u}\, dS, \tag{2.23}$$

where $\mathbf{u}$ is the displacement field, and $\mathbf{b}$ and $\mathbf{T}$ represent the body forces and traction forces, respectively. The mechanical free energy, Ψ^{M}, is weighted by the volume fractions of the intact and fractured phases and can be expressed as:

$$\Psi^{\text{M}} = \int_\Omega \left[P_{v1}(\phi)\psi_1^{\text{M}} + P_{v2}(\phi)\psi_2^{\text{M}}\right]\, dV = \int_\Omega \left[P_{v1}(\phi)\psi_1^{\text{M}} + (1 - P_{v1}(\phi))\,\psi_2^{\text{M}}\right]\, dV, \tag{2.24}$$

where ψ_1^{M} and ψ_2^{M} denote the strain energy densities for the intact and fractured

phases, respectively. For an isotropic linear elastic material, the strain energy densities can be formulated as:

$$\psi_i^{\mathrm{M}} = \frac{1}{2}\boldsymbol{\varepsilon} : \boldsymbol{C}_i^{\mathrm{M}} : \boldsymbol{\varepsilon}, \quad i = 1, 2, \tag{2.25}$$

where $\boldsymbol{\varepsilon}$ is the strain tensor, and $\boldsymbol{C}_i^{\mathrm{M}}$ denotes the stiffness tensor of phase i. The resulting stress in the material can then be expressed as:

$$\boldsymbol{\sigma} = P_{v1}(\phi)\boldsymbol{\sigma}_1^{\mathrm{M}} + (1 - P_{v1}(\phi))\,\boldsymbol{\sigma}_2^{\mathrm{M}}, \tag{2.26}$$

where $\boldsymbol{\sigma}_1^{\mathrm{M}}$ and $\boldsymbol{\sigma}_2^{\mathrm{M}}$ represent the stress tensors for the intact and fractured phases, respectively.

The fracture energy is captured by the Allen-Cahn component of the free energy, incorporating the effect of the characteristic length scale ℓ. This term regularizes the sharp crack interface by diffusing it into a transition region. The Allen-Cahn energy is expressed as:

$$\Psi^{\mathrm{AC}}(\phi) = \int_\Omega \left(\frac{G_c}{4c_w\ell} w(\phi) + \frac{G_c\ell}{4c_w} |\nabla\phi|^2 \right) dV, \tag{2.27}$$

where $w(\phi)$ represents the local crack energy density, G_c is the critical energy release rate, and c_w is a constant associated with the profile of the phase field function.

By combining the mechanical energy from Equation (2.24) with the fracture energy from Equation (2.27), the total free energy of the system can be expressed as:

$$\Psi_\ell = \int_\Omega \left(P_{v1}(\phi)\psi_1^{\mathrm{M}} + (1 - P_{v1}(\phi))\,\psi_2^{\mathrm{M}} + \frac{G_c}{4c_w\ell}\left(w(\phi) + \ell^2|\nabla\phi|^2\right)\right) dV. \tag{2.28}$$

The evolution of the phase field ϕ is governed by a relaxation law related to the chemical potential $\mu(\phi)$ (Equation (2.3)), which can be expressed as:

$$\frac{\partial\phi}{\partial t} = -L\frac{\delta\Psi_\ell(\phi)}{\delta\phi} = -L\left(P'_{v1}\left(\psi_1^{\mathrm{M}} - \psi_2^{\mathrm{M}}\right) + \frac{G_c}{4c_w\ell}\left(w'(\phi) - \ell^2\Delta\phi\right)\right), \tag{2.29}$$

where L is a mobility parameter that governs the rate of phase evolution. By introducing a viscous term ζ, which represents the relaxation time constant, Equation (2.29) can be reformulated as:

$$P'_{v1}\left(\psi_1^{\mathrm{M}} - \psi_2^{\mathrm{M}}\right) + \frac{G_c}{4c_w\ell}\left(w'(\phi) - \ell^2\Delta\phi\right) + \zeta\frac{\partial\phi}{\partial t} = 0. \tag{2.30}$$

Under rate-independent conditions, the phase field evolution equation simplifies to an energy minimization problem in which the elastic strain energy drives the fracture process. The driving force for fracture is associated with the strain energy difference, $\psi_d = \psi_1^{\mathrm{M}} - \psi_2^{\mathrm{M}}$, which can be derived through energy decomposition. This is expressed as:

$$\psi(\boldsymbol{\varepsilon},\phi) = g(\phi)\psi_d(\boldsymbol{\varepsilon}) + \psi_s(\boldsymbol{\varepsilon}) \xrightarrow{\psi_d(\boldsymbol{\varepsilon}) = \psi_0(\boldsymbol{\varepsilon}) - \psi_s(\boldsymbol{\varepsilon})} \psi(\boldsymbol{\varepsilon},\phi) = g(\phi)\psi_0(\boldsymbol{\varepsilon}) + (1 - g(\phi))\psi_s(\boldsymbol{\varepsilon}), \tag{2.31}$$

A comparison of Equations (2.24) and (2.31) reveals that the first phase can be

characterized as pristine material homogeneously distributed within a representative elementary volume (RVE), with a volumetric fraction denoted as P_{v1}. This phase may also be interpreted as having its stiffness reduced according to the degradation function $g(\phi)$. Thus, the degradation function $g(\phi)$ effectively represents the volumetric fraction of intact material through homogenization.

Similarly, the second phase corresponds to the material that retains its full stiffness, with its contribution being enhanced as the first phase transitions into the second phase through phase field evolution.

2.2.3 Microforce-based approach

The evolution of phase fields in fracture mechanics can be rigorously derived using the microforce balance law framework introduced by Gurtin [34]. This approach provides a clear separation between the balance laws and the constitutive relations, enabling a thermodynamically consistent formulation applicable to a range of fracture phenomena. Gurtin's framework extends classical balance principles to internal variables, accommodating fracture and damage modeling through phase field methodologies. Specifically, this formulation facilitates the derivation of governing equations such as the Ginzburg-Landau and Cahn-Hilliard equations within a thermodynamically constrained context, forming a robust foundation for phase field fracture theory [6, 35].

In this framework, the phase field variable ϕ is treated as a scalar internal variable conjugate to an internal microforce ω, while the gradient $\nabla\phi$ is associated with a microforce vector $\boldsymbol{\xi}$. The microforce balance law, derived from the principle of virtual power in the absence of external microforces, is expressed as:

$$\nabla \cdot \boldsymbol{\xi} - \omega = 0, \tag{2.32}$$

where ω denotes the internal driving force associated with changes in ϕ, and $\boldsymbol{\xi}$ represents the flux associated with the phase field gradient. This formulation allows for the seamless integration of fracture mechanics with thermodynamic constraints, accommodating complex crack propagation patterns [36].

The microforces' mechanical power, $\mathcal{P}^m$, can be represented as:

$$\mathcal{P}^m = \int_{\partial\Omega} (\boldsymbol{\xi} \cdot \mathbf{n})\dot{\phi}\, \mathrm{d}S = \int_{\Omega} \left(\boldsymbol{\xi} \cdot \nabla\dot{\phi} + \omega\dot{\phi}\right)\, \mathrm{d}V, \tag{2.33}$$

where $\mathbf{n}$ is the outward normal on $\partial\Omega$ and $\dot{\phi}$ denotes the rate of change in ϕ. To uphold thermodynamic consistency, the framework enforces the second law of thermodynamics, which requires the system's total dissipation to be non-negative. This constraint leads to the following dissipation inequality:

$$-\dot{\psi} + \left(\boldsymbol{\xi} \cdot \nabla\dot{\phi} + \omega\dot{\phi}\right) + \boldsymbol{\sigma} : \dot{\boldsymbol{\varepsilon}}(\mathbf{u}) \leq 0, \tag{2.34}$$

where $\dot{\psi}$ is the rate of free energy density change, $\boldsymbol{\sigma}$ is the stress tensor, and $\dot{\boldsymbol{\varepsilon}}(\mathbf{u})$ represents the strain rate. The free energy density $\psi(\mathbf{u}, \phi, \nabla\phi)$ is defined as a function of the displacement field $\mathbf{u}$, the phase field ϕ, and its gradient $\nabla\phi$.

By substituting the free energy expression into Equation (2.34):

$$-\left(\frac{\partial\psi}{\partial\boldsymbol{\varepsilon}(\mathbf{u})} : \dot{\boldsymbol{\varepsilon}}(\mathbf{u}) + \frac{\partial\psi}{\partial\phi}\dot{\phi} + \frac{\partial\psi}{\partial\nabla\phi} \cdot (\dot{\nabla\phi})\right) + \left(\boldsymbol{\xi} \cdot (\dot{\nabla\phi}) + \omega\dot{\phi}\right) + \boldsymbol{\sigma} : \dot{\boldsymbol{\varepsilon}}(\mathbf{u}) \leq 0. \tag{2.35}$$

From the dissipation inequality and the arbitrariness of the rates $\dot{\boldsymbol{\varepsilon}}(\mathbf{u})$, $\dot{\phi}$, and $\nabla\dot{\phi}$, the constitutive relations are derived:

$$\boldsymbol{\sigma} = \frac{\partial\psi(\mathbf{u},\phi,\nabla\phi)}{\partial\boldsymbol{\varepsilon}(\mathbf{u})}, \tag{2.36}$$

$$\omega = \frac{\partial\psi(\mathbf{u},\phi,\nabla\phi)}{\partial\phi}, \tag{2.37}$$

$$\boldsymbol{\xi} = \frac{\partial\psi(\mathbf{u},\phi,\nabla\phi)}{\partial\nabla\phi}. \tag{2.38}$$

Applying the free energy $\psi(\mathbf{u},\phi,\nabla\phi)$ from Equation (2.12), ω and $\boldsymbol{\xi}$ are expresed as:

$$\omega = \frac{\partial\psi(\mathbf{u},\phi,\nabla\phi)}{\partial\phi} = g'(\phi)\psi_d + \frac{G_c}{4c_w\ell}w'(\phi), \tag{2.39}$$

$$\boldsymbol{\xi} = \frac{\partial\psi(\mathbf{u},\phi,\nabla\phi)}{\partial\nabla\phi} = \frac{\ell}{2c_w}G_c\nabla\phi, \tag{2.40}$$

where $g'(\phi)$ is the derivative of the degradation function, ψ_d represents the elastic energy density, G_c is the critical energy release rate, c_w a constant, and ℓ the regularization parameter determining the crack width.

Substituting these into the microforce balance equation (Equation (2.32)), the governing equation for phase field evolution is derived as:

$$\frac{G_c}{2c_w}\left(\frac{w'(\phi)}{2\ell} - \ell\nabla^2\phi\right) + g'(\phi)\psi_d = 0 \quad \text{in } \Omega, \quad \boldsymbol{\xi}\cdot\mathbf{n} = 0 \quad \text{on } \partial\Omega. \tag{2.41}$$

This equation ensures thermodynamic consistency and governs the phase field variable ϕ for describing crack propagation within materials.

2.2.4 Irreversibility in phase field evolution for fracture mechanics

The progression of damage within materials is inherently an irreversible thermodynamic process. Without explicitly constraining the evolution equation for the phase field, healing may unintentionally occur in damaged regions, contradicting the physical principles governing fracture mechanics. Ensuring that the phase field evolution is irreversible, i.e., $\dot{\phi} \geq 0$, is essential and requires additional methodological treatments. Various approaches to this issue have been proposed [37, 38], but this work focuses on two widely accepted methods: the history field method and the penalization method.

The history field method, as proposed by Miehe *et al.* [24], introduces a history field variable, $\mathcal{H}$, which captures the maximum value of the fracture driving force over time. Defined as

$$\mathcal{H} = \max_{t \in [0,\tau]} \psi_d(t), \tag{2.42}$$

this method ensures that fracture energy remains non-decreasing over time, thereby satisfying the Karush-Kuhn-Tucker (KKT) conditions for irreversibility:

$$\psi_d - \mathcal{H} \leq 0, \qquad \dot{\mathcal{H}} \geq 0, \qquad \dot{\mathcal{H}}(\psi_d - \mathcal{H}) = 0. \tag{2.43}$$

Incorporating the history field variable $\mathcal{H}$ into the phase field evolution equation

(see Equation (2.21)a) yields:

$$\frac{G_c}{2c_w}\left(\frac{w'(\phi)}{2\ell} - \ell\nabla^2\phi\right) + g'(\phi)\mathcal{H} = 0, \tag{2.44}$$

which enforces irreversibility. The history field approach is both robust and relatively simple to implement, making it a favored choice for practical applications. However, it has been noted that the formulation may lack full variational consistency, potentially impacting theoretical accuracy [39].

Another approach, the penalization method, imposes the irreversibility condition directly by introducing a penalty term in the energy functional, thereby discouraging any reduction in the phase field variable. The penalized energy functional is expressed as:

$$P(\phi;\gamma) := \frac{\gamma}{2}\int_\Omega \langle \phi - \phi_{n-1}\rangle_-^2 \, \mathrm{d}V, \quad \gamma \gg 1, \tag{2.45}$$

where γ is a large positive penalty parameter, ϕ_{n-1} represents the previous time step's phase field value, and $\langle\cdot\rangle_-$ denotes the Macaulay brackets, defined as:

$$\langle a\rangle_\pm = \frac{a \pm |a|}{2}. \tag{2.46}$$

By adding this term to the energy functional, the phase field evolution equation becomes:

$$\frac{G_c}{2c_w}\left(\frac{w'(\phi)}{2\ell} - \ell\nabla^2\phi\right) + g'(\phi)\psi_d + \gamma\langle \phi - \phi_{n-1}\rangle_- = 0. \tag{2.47}$$

While the penalization method is relatively straightforward and computationally

appealing, selecting an appropriate value for γ is critical to ensure stability and accuracy. A low γ value may inadequately enforce irreversibility, while a high value can lead to numerical instabilities, such as ill-conditioned systems [40].

In this work, the history field method is selected due to its robustness and widespread application in the literature. Although it may exhibit some limitations in variational consistency, its practical benefits outweigh these theoretical concerns, particularly in engineering contexts where robustness and efficiency are prioritized over complete theoretical rigor. Additionally, the history field method circumvents the numerical complexities associated with the penalization method, including the fine-tuning of γ and the associated conditioning challenges.

In summary, while both methods for enforcing irreversibility have their respective advantages, the choice often depends on specific problem requirements, such as computational efficiency, implementation simplicity, and desired theoretical consistency.

2.2.5 Particularising phase field fracture method

In phase field fracture modeling, the degradation function $g(\phi)$, dissipation function $w(\phi)$, and the scaling constant c_w are critical components that govern the fracture process. In this section, a detailed overview of three widely adopted models is presented including the models: the AT2 model proposed by Bourdin et al. [41], the AT1 model introduced by Pham et al. [42], and the cohesive zone model PF-CZM developed by Wu et al. [43, 44]. These models are distinguished primarily by their specific forms of $g(\phi)$ and $w(\phi)$, as well as the values of the scaling constant c_w, which are summarized in Table 2.1.

Table 2.1: Degradation function $g(\phi)$, dissipation function $w(\phi)$, and scaling constant c_w for the AT2, AT1, and PF-CZM models.

Model	$g(\phi)$	$w(\phi)$	c_w
AT2	$(1-\phi)^2 + \kappa$	ϕ^2	$1/2$
AT1	$(1-\phi)^2 + \kappa$	ϕ	$2/3$
PF-CZM	$\dfrac{(1-\phi)^d}{(1-\phi)^d + a\phi(1+b\phi)}$	$2\phi - \phi^2$	$\pi/4$

In Table 2.1, κ is a small, positive constant added to the degradation function to prevent numerical ill-conditioning as $\phi \to 1$. This term ensures the well-posedness of the system near full damage. The constant a in the PF-CZM model is defined as $a = \frac{4EG_c}{\pi \ell \sigma_t^2}$, where σ_t is the tensile strength, E is the Young's modulus, G_c is the critical energy release rate, and ℓ is the length scale parameter. The values of b and d in this model are parameters related to the specific softening law chosen for the simulation, which can be adapted depending on the material behavior [44].

One of the key distinctions between these models is the treatment of the fracture driving force $\mathcal{H}$. In the AT2 model, fracture initiates when $\mathcal{H} > 0$, meaning that no threshold is required for crack propagation. This allows the phase field to evolve whenever there is any driving force for fracture, making it suitable for brittle fracture scenarios.

In contrast, both the AT1 and PF-CZM models introduce a threshold value for $\mathcal{H}$, below which fracture does not occur. This threshold, $\mathcal{H}_{\text{min}}$, ensures that there is a minimum energy requirement for crack propagation. For the AT1 model, the threshold is given by:

$$\mathcal{H}_{\text{min}} = \frac{3G_c}{16\ell}.$$

For the PF-CZM model, the threshold is expressed as:

$$\mathcal{H}_{\text{min}} = \frac{2G_c}{\pi a \ell} = \frac{\sigma_t^2}{2E}.$$

This threshold dependence on the material's tensile strength and stiffness makes the PF-CZM model more representative of cohesive zone behavior, as it incorporates both material strength and toughness into the fracture initiation criterion.

The PF-CZM model offers several advantages over the AT2 and AT1 models, particularly in the context of cohesive fracture. First, it allows for greater flexibility by enabling the user to define the specific form of the softening law, thus making it adaptable to a wide range of material behaviors, including both brittle and quasi-brittle. This user-defined softening behavior can better capture the transition from crack initiation to propagation, which is crucial for materials that exhibit non-linear fracture processes.

Secondly, the PF-CZM model is not sensitive to the length scale parameter ℓ. In traditional phase field models like AT2, ℓ plays a significant role in controlling the width of the diffuse crack zone, and its choice can greatly influence the numerical results. However, in the PF-CZM model, the Griffith's surface energy is replaced by Barenblatt's approximation [1], thus the fracture process becomes independent on ℓ, making it more robust in capturing fracture behavior across different scales without requiring excessive fine-tuning of parameters. This characteristic makes the PF-CZM model particularly suitable for simulations involving complex crack paths or varying length scales.

[1] Barenblatt's approximation of Griffith's brittle fracture addresses limitations in Griffith's original theory by introducing a cohesive zone model. This approach refines the classical fracture mechanics theory to better account for the physical behavior near a crack tip. [44]

2.2.6 Strain energy decomposition as fracture driving force

The strain energy split as a fracture driving force was developed to prevent damage evolution under compressive stress. Several approaches have been proposed to achieve this. Amor *et al.* [45] introduced a volumetric-deviatoric split to exclude energy contributions associated with volumetric compaction. This split can be expressed in terms of the first invariant of the strain tensor, $I_1(\boldsymbol{\varepsilon})$, and the second invariant of the deviatoric part of the strain tensor, $J_2(\boldsymbol{\varepsilon})$, as follows:

$$\begin{aligned} \psi_d(\boldsymbol{\varepsilon}) &= \tfrac{1}{2}K\langle I_1(\boldsymbol{\varepsilon})\rangle_-^2 + 2\mu J_2(\boldsymbol{\varepsilon}) \\ \psi_s(\boldsymbol{\varepsilon}) &= \tfrac{1}{2}K\langle I_1(\boldsymbol{\varepsilon})\rangle_-^2, \end{aligned} \tag{2.48}$$

where K is the bulk modulus, μ is the shear modulus. When the first invariant of the strain tensor, $I_1(\boldsymbol{\varepsilon})$, is negative, the fracture is driven by the energy associated with distortion rather than volumetric compaction.

Miehe *et al.* [24] propose a split based on the decomposition of the principal strain tensor (spectral decomposition) into positive and negative parts, defined as $\boldsymbol{\epsilon}_\pm = \langle\boldsymbol{\epsilon}\rangle_\pm$, and it reads as follows:

$$\begin{aligned} \psi_d(\boldsymbol{\varepsilon}) &= \tfrac{1}{2}\lambda\left(\langle I_1(\boldsymbol{\epsilon})\rangle_+\right)^2 + \mu\left((I_1(\boldsymbol{\epsilon}_+))^2 - 2I_2(\boldsymbol{\epsilon}_+)\right) \\ \psi_s(\boldsymbol{\varepsilon}) &= \tfrac{1}{2}\lambda\left(\langle I_1(\boldsymbol{\epsilon})\rangle_-\right)^2 + \mu\left((I_1(\boldsymbol{\epsilon}_-))^2 - 2I_2(\boldsymbol{\epsilon}_-)\right). \end{aligned} \tag{2.49}$$

where λ is the first Lamé constant, and $I_2(\boldsymbol{\epsilon})$ represents the second invariant of the strain tensor.

Freddy *et al.* [46] developed a decomposition approach for masonry materials, building on the work of Del Piero [47], to address materials that do not sustain tensile loads. Known as the No-tension split, this method can be expressed in

terms of the principal strains ($\epsilon_3 \geq \epsilon_2 \geq \epsilon_1$) as follows:

$$
\begin{array}{llll}
\text{if} & \epsilon_1 > 0 & \text{then} & \begin{cases} \psi_d(\boldsymbol{\varepsilon}) = \frac{E\nu}{2(1+\nu)(1-2v)}\left(\epsilon_1+\epsilon_2+\epsilon_3\right)^2 + \frac{E}{2(1+\nu)}\left(\epsilon_1^2+\epsilon_2^2+\epsilon_3^2\right) \\ \psi_s(\boldsymbol{\varepsilon}) = 0 \end{cases} \\
\text{elseif} & \epsilon_2 + \nu\epsilon_1 > 0 & \text{then} & \begin{cases} \psi_d(\boldsymbol{\varepsilon}) = \frac{Ev}{2(1+v)(1-2v)}\left(\epsilon_3+\epsilon_2+2v\epsilon_1\right)^2 + \frac{E}{2(1+v)}\left[\left(\epsilon_3+v\epsilon_1\right)^2+\left(\epsilon_2+v\epsilon_1\right)^2\right] \\ \psi_s(\boldsymbol{\varepsilon}) = \frac{E}{2}\epsilon_1^2 \end{cases} \\
\text{elseif} & (1-\nu)\epsilon_3 + \nu(\epsilon_1+\epsilon_2) > 0 & \text{then} & \begin{cases} \psi_d(\boldsymbol{\varepsilon}) = \frac{E}{2\left(1-v^2\right)(1-2v)}\left[(1-v)\epsilon_3+v\epsilon_1+v\epsilon_2\right]^2 \\ \psi_s(\boldsymbol{\varepsilon}) = \frac{E}{2\left(1-v^2\right)}\left(\epsilon_1^2+\epsilon_2^2+2v\epsilon_1\epsilon_2\right) \end{cases} \\
 & & \text{else} & \begin{cases} \psi_d(\boldsymbol{\varepsilon}) = 0 \\ \psi_s(\boldsymbol{\varepsilon}) = \frac{Ev}{2(1+\nu)(1-2v)}\left(\epsilon_1+\epsilon_2+\epsilon_3\right)^2 + \frac{E}{2(1+\nu)}\left(\epsilon_1^2+\epsilon_2^2+\epsilon_3^2\right) \end{cases}
\end{array}
\tag{2.50}
$$

where E is Young's modulus and ν is Poisson's ratio. In this model, only positive principal stresses are considered when calculating the fracture driving force.

While most approaches focus on preventing fracture under compressive stress, a recent Drucker-Prager-based model [48] was developed to address material fracture under biaxial loading conditions. In this thesis, a generalized method for strain energy decomposition based on failure surfaces is introduced (See Section 3.4 and [49]), such as the Drucker-Prager model, demonstrating its applicability to the constitutive modeling of material behavior. In this model, the cohesion parameter c [2] is degraded by phase field evolution, while the friction parameter ϕ_f [3] remains constant. The Drucker-Prager model is expressed as follows:

[2] Cohesion c is the component of shear strength in rocks and soils that arises independently of interparticle friction, deriving instead from electrostatic forces, cementation, and negative capillary pressure, among other factors.

[3] The angle of internal friction ϕ_f represents a granular material's inherent resistance to shear stress. This angle reflects the interparticle friction that enables the material to withstand applied forces.

$$\psi_d = \begin{cases} \frac{1}{2}KI_1^2(\boldsymbol{\varepsilon}) + 2\mu J_2(\boldsymbol{\varepsilon}) & \text{for} \quad -6B\sqrt{J_2(\boldsymbol{\varepsilon})} < I_1(\boldsymbol{\varepsilon}) \\ \frac{1}{18B^2K+2\mu}\left(-3BKI_1(\boldsymbol{\varepsilon}) + 2\mu\sqrt{J_2(\boldsymbol{\varepsilon})}\right)^2 & \text{for} \quad -6B\sqrt{J_2(\boldsymbol{\varepsilon})} \geq I_1(\boldsymbol{\varepsilon}) \;\&\; 2\mu\sqrt{J_2(\boldsymbol{\varepsilon})} \geq 3BKI_1(\boldsymbol{\varepsilon}) \\ 0 & \text{for} \quad 2\mu\sqrt{J_2(\boldsymbol{\varepsilon})} < 3BKI_1(\boldsymbol{\varepsilon}) \end{cases}$$

$$\psi_s = \begin{cases} 0 & \text{for} \quad -6B\sqrt{J_2(\boldsymbol{\varepsilon})} < I_1(\boldsymbol{\varepsilon}) \\ \frac{K\mu}{18B^2K+2\mu}\left(I_1(\boldsymbol{\varepsilon}) + 6B\sqrt{J_2(\boldsymbol{\varepsilon})}\right)^2 & \text{for} \quad -6B\sqrt{J_2(\boldsymbol{\varepsilon})} \geq I_1(\boldsymbol{\varepsilon}) \;\&\; 2\mu\sqrt{J_2(\boldsymbol{\varepsilon})} \geq 3BKI_1(\boldsymbol{\varepsilon}) \\ \frac{1}{2}KI_1^2(\boldsymbol{\varepsilon}) + 2\mu J_2(\boldsymbol{\varepsilon}) & \text{for} \quad 2\mu\sqrt{J_2(\boldsymbol{\varepsilon})} < 3BKI_1(\boldsymbol{\varepsilon}) \end{cases} \tag{2.51}$$

where $B(\phi_f)$ is material constants that is function of internal friction ϕ_f.

2.2.7 Phase field length scale as a material parameter

The phase field length scale ℓ is a crucial parameter in phase field fracture models, as it directly influences both the material strength and the fracture process. This relationship can be examined by analyzing the homogeneous solution of the phase field evolution equation in a one-dimensional (1D) scenario under tensile loading.

The governing equation for the AT2 phase field model in 1D, for an applied stress σ, is given by:

$$G_c\left(\frac{\phi}{\ell} - \ell\nabla^2\phi\right) - 2(1-\phi)\left(\frac{\sigma}{2E}\right) = 0, \tag{2.52}$$

By solving Equation (2.52) for the applied stress σ, the maximum stress value σ_t (representing the tensile strength) and the critical strain ε_c which is strain correspond to the tensile strength σ_t can be determined. For the AT2 model, these quantities are expressed as:

$$\sigma_t = \sqrt{\frac{27EG_c}{256\ell}}, \quad \varepsilon_c = \sqrt{\frac{G_c}{3\ell E}}. \tag{2.53}$$

The above relations indicate that both the tensile strength σ_t and the critical strain ε_c are functions of the phase field length scale ℓ, as well as the material properties E and G_c. Specifically, an increase in ℓ leads to a reduction in material strength, implying that larger values of ℓ correspond to more diffuse crack transitions and a lower peak stress.

For the AT1 phase field model, which employs a distinct regularization approach for crack surface density, applying the same procedure yields the following expressions for material strength and critical strain:

$$\sigma_t = \sqrt{\frac{3EG_c}{8\ell}}, \quad \varepsilon_c = \sqrt{\frac{3G_c}{8\ell E}}. \tag{2.54}$$

Comparing Equations (2.53) and (2.54), it is evident that both material strength and critical strain depend on ℓ in similar ways. By recalling the minimum of the history variable in the AT1 model (as discussed in a Section 2.2.5) and substituting it into Equation (2.54), it becomes clear that the maximum stress occurs at the initial stage of phase field evolution in this model.

The phase field length scale ℓ serves as a fundamental parameter, controlling the width of the diffusive crack zone where the material transitions from fully intact to fully damaged. Physically, ℓ can be interpreted as a measure of the material's intrinsic length scale associated with fracture processes.

For a material with fracture energy G_c and Young's modulus E, ℓ influences how the material manages the localization of damage. Smaller values of ℓ correspond to a more localized and sharper crack, implying higher material strength. In con-

trast, larger values of ℓ correspond to a more diffuse damage zone, resulting in reduced material strength.

In both the AT1 and AT2 models, the phase field length scale ℓ directly governs the material strength for a given set of material properties (E, G_c). Specifically, ℓ determines the balance between fracture energy dissipation and damage localization, thereby playing a crucial role in defining the macroscopic fracture behavior. A thorough understanding and careful selection of ℓ are essential for accurately modeling fracture processes in various materials.

3 | SUMMARY OF CONTRIBUTION AND DISCUSSION

In this chapter, a detailed discussion of the findings of this thesis are presented, covering a range of advancements in the prediction and modeling of fracture mechanics in rock-like materials. The results, derived from the combination of theoretical and computational methods, particularly the phase field method, address critical challenges in fracture mechanics. This chapter provides a critical reflection on the outcomes of six key investigations, each contributing uniquely to the overall research objectives.

First, the findings from the first paper Appendix A [50] are discussed in Section 3.1. As mentioned in Section 2.2.7, accurately estimating the length scale ℓ is essential for precise modeling of phase field fractures. While the characteristic length scale ℓ is related to material strength (see Equations (2.53) and (2.54)), accurate estimation of material strength remains a critical aspect in phase field fracture modeling. Tensile strength in rock-like materials is often estimated using the Brazilian test, though there is ongoing debate regarding the accuracy of results obtained from this test. To address this, the Brazilian test is revisited, as discussed in Section 3.1, applying a Griffith-based criterion to assess crack initiation locations. Our study reveals that, under certain conditions, the center of the disk may not always provide the most reliable location for crack initiation, potentially leading to over- or underestimation of tensile strength. Finite element simulations were used to map stress distributions and validate the use of the generalized Griffith criterion, ensuring accuracy in tensile strength estimations across various materials. Our proposed protocol offers a means of verifying the validity of Brazilian test results, allowing for the most accurate estimation of tensile

strength and, consequently, a reliable estimation of the phase field length scale ℓ.

Next, the method for implementing and validating the phase field fracture models are presented in the second and third papers, Appendixes B [51] and C [52], in Section 3.2. For this study, a unified framework for implementing the phase field fracture method is developed. In Section 3.2, the details of phase field fracture approach is outlined using a user material (UMAT) subroutine in Abaqus. This novel method simplifies fracture modeling by avoiding the need for user element subroutine while integrating constitutive models such as AT1, AT2, and PF-CZM. Validation against benchmark problems demonstrates the robustness and accuracy of this approach in simulating crack propagation without introducing complex numerical artifacts. Additionally, several case studies are presented to verify and validate our implementation against existing literature, showcasing the robustness and versatility of our methodology.

In the fourth paper, Appendix D [53], the phase field fracture model is validated using experimental results from the damage mechanics challenge organized by Purdue University, Sandia National Laboratories, and Lawrence Livermore National Laboratory [54]. it is demonstrated that the conventional phase field fracture model is capable of accurately simulating a blind test through the calibration of material parameters for a three-point bending test on a beam with an eccentric notch. However, the failure in the test was primarily driven by tensile stress, a scenario in which the conventional phase field fracture model has already shown good performance.

As mentioned earlier, while the phase field fracture model has demonstrated effectiveness in simulating tensile or shear fractures, many rock-like materials predominantly fail under compression—a failure mode that has been inadequately addressed by phase field fracture models. In our fifth paper, Appendix E [49],

a general framework for constitutive fracture modeling is proposed within the phase field method to address this gap, encompassing a broader range of material behaviors. In Section 3.4, the discussion is extended to constitutive modeling via strain energy decomposition. Here, a generalized framework is introduced which leads to strain energy decomposition based on various failure criteria, focusing on overcoming the limitations of classical models in predicting crack nucleation under compressive stresses. This framework is applied to the Drucker-Prager and Bresler-Pister failure criteria.

Additionally, our unpublished work is presented with providing a deeper discussion of our approach and introducing a method for additive decomposition of strain energy (Section 3.4.2), specifically tailored to the Bresler-Pister criterion in Section 3.4.3. Further, a novel strain energy decomposition approach is developed for materials with voids and inclusions, presented at Complas 2021 [55] (Section 3.4.4).

By addressing compressive failure within the phase field fracture framework, the proposed method is extended to model multiphysics fracture phenomena, particularly in rock-like materials, with a focus on hydraulic fracturing. In Section 3.5, the multiphysics simulations are explored using the phase field method as presented in our sixth paper, Appendix F [56]. This section covers applications to thermomechanical fractures, hydraulic fractures, hydrogen embrittlement, and corrosion-induced stress. The thermal analogy for diffusion-like equations is employed to model phase field fracture, coupled with other governing equations, using the UMATHT subroutine, thereby avoiding the complexity of the UEL subroutine. This approach emphasizes the simplicity of implementation and the versatility of the phase field method in handling coupled physical phenomena, and it demonstrates robustness through validation against experimental, analytical, and numerical data.

Finally, Section 3.6 focuses on hydraulic phase field fracture modeling, which is the subject of our seventh paper G [57]. Building on previous implementations, this study explores the coupling between phase field evolution and permeability tensors in fluid-driven fracture processes using existing methods and a mixed method introduced here. Additionally, The proposed Drucker-Prager based strain energy split (Section 3.4) is introduced into the hydraulic phase field fracture model to address complex geotechnical problems such as stick-slip behavior in faults and slope instability. The key results demonstrate that the phase field method, when integrated with advanced coupling strategies, can accurately predict complex phenomena like fault activation and stick-slip behavior, which are critical for geotechnical engineering applications.

Overall, this chapter synthesizes findings from multiple studies to provide a comprehensive understanding of the role that phase field methods play in fracture modeling of rock-like materials. Each section contributes to enhancing the predictive power and practical applicability of fracture models in industrial and scientific settings. In the subsequent sections, the results and their potential impact on both theoretical research and real-world engineering problems are evaluated and discussed critically.

3.1 Griffith-based analysis of crack initiation location in a Brazilian test

The Brazilian test, or splitting tensile test, is one of the most widely used methods for determining the tensile strength of rock-like materials [58]. Its simplicity and practicality have established it as a standard in both experimental rock mechanics and industry [59]. However, due to the indirect nature of the tensile strength esti-

mation, the test has been the subject of significant debate [60–68]. Traditionally, the Brazilian test assumes that crack initiation occurs at the center of the disk, an assumption that may not hold under different material properties and testing configurations.

In this work (Appendix A) [49], an alternative approach is proposed based on the generalized Griffith criterion [60] to address the inherent limitations of the Brazilian test. The aim is to systematically identify the conditions under which crack initiation occurs at the disk's center, thus validating the test's reliability. By incorporating finite element analysis (FEA) with Griffith's criterion [33, 60], this study provides a comprehensive framework for evaluating the validity of the Brazilian test under various conditions. The work includes maps and a protocol to assess the Brazilian test's validity, emphasizing the importance of ensuring that crack initiation occurs at the center of the disk. This study offers researchers and practitioners a more reliable method for interpreting the results of the Brazilian test, particularly for the experimental determination of tensile strength in brittle materials.

3.1.1 Methodology

The study employed a combination of finite element modeling and the generalized Griffith fracture criterion [60] (Section 2 of Appendix A) to evaluate the conditions for crack initiation in the Brazilian test. The generalized Griffith criterion [60] was selected due to its robust failure envelope, which accounts for both tensile and compressive strengths of materials and is applicable for arbitrary compressive-to-tensile strength ratios, utilizing a parabolic Mohr envelope. The primary objective was to determine under which conditions crack initiation occurs at the center of the disk and when cracking initiates elsewhere, thereby invalidat-

ing the test results.

The finite element simulations modeled the stress distribution within the disk under loading, incorporating geometric variables such as the jaw radius R_j and disk radius R_d, along with material properties, including the elastic moduli of the jaw and disk (E_j and E_d) and Poisson's ratios (ν_j and ν_d).

3.1.2 Key results and findings

The findings are critical in delineating the limitations of the Brazilian test for various rock-like materials and testing standards. A key result indicates that the range of conditions under which the Brazilian test is valid is significantly narrower than previously assumed. The simulations revealed that many commonly used configurations do not guarantee crack initiation at the disk center, thereby challenging assumptions upheld by established standards such as those of the International Society for Rock Mechanics (ISRM) [69] and the American Society for Testing and Materials (ASTM) [70].

The study offered several key insights:

- **Test geometry sensitivity**: The study demonstrated that test geometry has a substantial impact on the stress distribution within the disk (Section 4.3.1 of Appendix A). A large ratio of jaw radius to disk radius (R_j/R_d), or the use of flat jaws as recommended by some standards, often results in crack initiation occurring outside the disk center. Conversely, using jaws with smaller radii promotes crack initiation at the disk center, but only within a specific range of material properties—such as marbles and limestones with high compressive-to-tensile strength ratios (Section 4.4 of Appendix A).
- **Material property dependence**: This study highlighted the influence of

material properties, such as Young's modulus and Poisson's ratio, on the stress distribution within the disk (Sections 4.3.2-4.3.3 of Appendix A). Notably, the tensile-to-compressive strength ratio ($n = -\sigma_c/\sigma_t$) emerged as a critical factor in determining whether a valid test could be achieved. Materials with high compressive-to-tensile strength ratios are more likely to exhibit crack initiation at the disk center (Section 4.4 of Appendix A).

- **The influence of friction**: The analysis indicates that, although friction impacts stress near the jaws, it does not significantly affect the overall validity of the test (Section 4.3.4 of Appendix A). Thus, friction's influence on the Brazilian test's validity appears negligible, as simulations with and without friction produce similar results.

- **Mapping**: Finite element analysis enabled the creation of detailed maps[1] of the stress state within the disk under various geometrical and loading conditions. These maps serve as a valuable tool for predicting whether a Brazilian test will yield valid results based on the specific material properties and testing configuration (Figures 10, 11 of Appendix A).

Case studies on granite, sandstone, limestone, and marble (Figure 3.1) indicate that accurate tensile strength estimates are only achievable with certain configurations, as flat jaws are generally ineffective for most materials (refer to Section 4.4 in Appendix A). In Figure 3.1, each material's range is illustrated by an oval shape, with the area beneath the selected R_j/E_d curve highlighting parameters where crack initiation does not occur at the disk's center for the specified R_j/E_d.

[1]The complete sets of maps are available as supplementary data in [49]: https://doi.org/10.1016/j.ijrmms.2022.105227

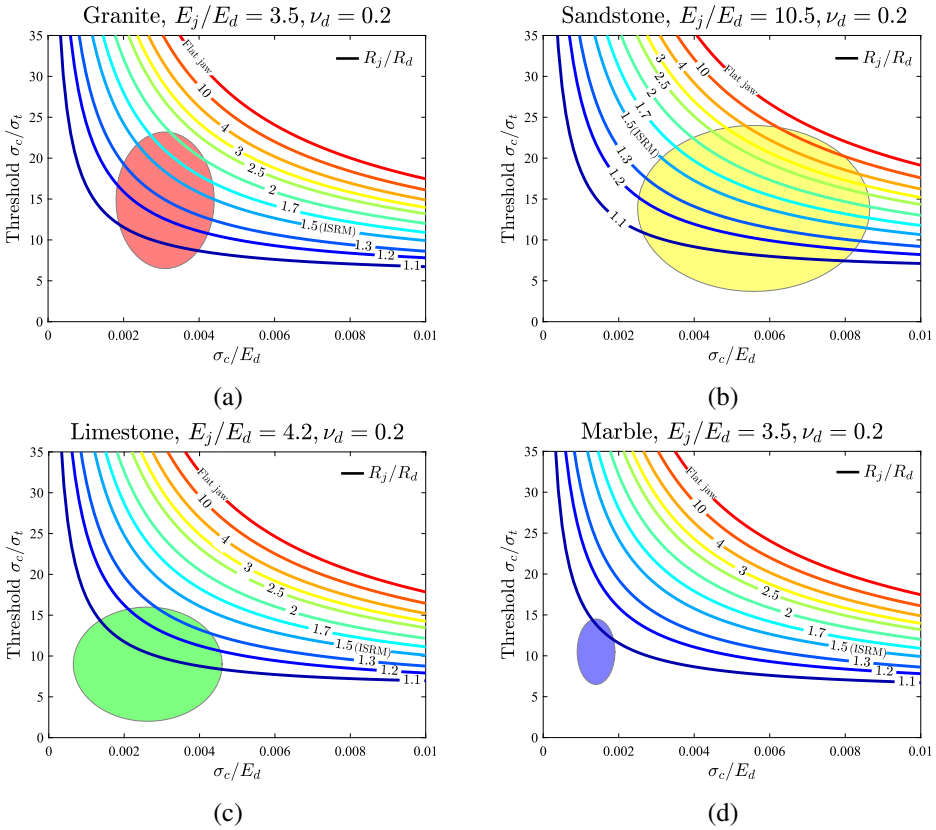

Figure 3.1: Maps to assess if cracking nucleates at the center by comparing the range of material parameters showing in oval shape, application to: (a) granite, (b) sandstone, (c) limestone, and (d) marble.

In addition to these findings, the study provided a set of guidelines to ensure the validity of the Brazilian test (Section 5 of Appendix A). Specifically, it is recommended employing a combination of numerical analysis and the generalized Griffith criterion to evaluate the stress distribution within the disk prior to testing. This approach enables researchers to determine whether the conditions are conducive to a valid test and, if necessary, to adjust the testing configuration accordingly.

3.1.3 Practical applications

The practical contributions of this study are particularly valuable for experimentalists in rock mechanics. A MATLAB App[2] (Appendix A of Appendix A) has been developed to automate the process of assessing Brazilian test validity. This app allows users to input material properties, test configuration, and the results of a Brazilian test, providing an output that indicates whether the test will yield valid results (Figure A.1 of Appendix A). The tool bridges the gap between theoretical insights on the Brazilian test and practical applications, enabling experimentalists to verify that their tests provide accurate estimates of tensile strength.

By offering a user-friendly interface for evaluating test validity, the App helps reduce the risk of inaccurate tensile strength measurements and ensures the reliability of test results.

3.1.4 Conclusion

In conclusion, this work represents a significant advancement in understanding the Brazilian test and its limitations. By integrating finite element analysis with the generalized Griffith criterion, the study provides a robust framework for evaluating the validity of the test across different material and loading conditions. The development of stress maps and the MATLAB App offers practical tools to enhance test reliability, with important implications for both research and industry. The insights gained from this study will improve the accuracy of tensile strength measurements in rock-like materials and contribute to the development of more reliable testing standards in rock mechanics.

[2]The App can be downloaded from https://www.empaneda.com/wp-content/uploads/2022/10/BrazVal.zip

3.2 Implementation and verification of phase field fracture method

In this section, an implementation of the phase field fracture model in Abaqus is introduced using a user material (UMAT) subroutine (Appendixes B, and C). The primary motivation behind this work was to develop an efficient and user-friendly approach for modeling fracture within Abaqus, eliminating the complexities associated with user-defined elements (UEL). Traditionally, implementing phase field models in commercial finite element software like Abaqus has required extensive modifications, including the use of user-defined elements, which can restrict the software's built-in functionality and user accessibility.

Appendix B [51], focuses on the foundational implementation of the phase field fracture method using the UMAT and HETVAL subroutines, enabling users to apply the method without requiring user-defined elements. This approach simplifies the implementation process and leverages the heat transfer analogy, enhancing both efficiency and ease of use.

Appendix C [52], builds upon this foundation by incorporating various constitutive models, including the AT1 [42] and AT2 [41] models, phase field-cohesive zone models (PF-CZM) [43,44], and energy decomposition schemes as defined in Section 2.2.6. This unified implementation enhances flexibility for modeling different fracture mechanisms while retaining the simplicity of using only a UMAT subroutine.

3.2.1 Phase field implementation in Abaqus

The advancement of phase field modeling has enabled significant progress in software for fracture simulation, including platforms like COMSOL [71] and FEniCS [72]. Notable efforts have also been made to integrate phase field methods within Abaqus [73–78], though these typically require user-defined subroutines such as UEL, which can limit post-processing capabilities. This work presents a streamlined implementation approach using UMAT or UMAT with HETVAL (see Section 3 of Appendixes B and C for details), leveraging the similarity between phase field evolution and heat transfer. This implementation supports models like AT2 [41], AT1 [42], and PF-CZM [43,44], incorporates strain energy decompositions to prevent compressive damage [24,45], and accommodates both monolithic and staggered solutions, thereby enhancing simulation robustness.

The phase field evolution equation, Equation (2.44), can be rearranged as follows:

$$\nabla^2\phi = \left(\frac{g'(\phi)\mathcal{H}2c_w}{\ell G_c} + \frac{w'(\phi)}{2\ell^2}\right). \tag{3.1}$$

This partial differential equation (Equation (3.1)) introduces additional complexity to the implementation of phase field fracture in standard FEM software. To address this, the similarity between the phase field and heat transfer equations is leveraged, which allows us to utilize Abaqus' built-in features without requiring additional pre- or post-processing. In the steady-state, the temperature θ for a material with thermal conductivity k and a heat source r is described by:

$$k\nabla^2\theta = -r. \tag{3.2}$$

The resemblance to Equation (3.1) suggests an approach where temperature is

treated as the phase field by setting $k = 1$ and defining r appropriately. In Abaqus 2020 or later, r can be specified directly within a UMAT subroutine, while earlier versions require the use of a HETVAL subroutine. Both approaches are thoroughly detailed, providing a general code[3] for models like AT2, AT1, and PF-CZM. The implementation includes strain energy splitting methods to prevent crack propagation under compressive stresses, incorporating techniques such as spectral decomposition [24] and the volumetric-deviatoric approach [45], and supports anisotropic and hybrid models [79].

As discussed, the analogy between heat transfer and phase field fracture (Table 3.1) can be utilized, where temperature θ corresponds to the phase field ϕ, which ranges from 0 to 1. A UMAT subroutine adjusts the material stiffness and stress based on ϕ, while also defining the heat flux r and its derivative with respect to ϕ. In Abaqus versions prior to 2020, these definitions need to be implemented using a HETVAL subroutine.

Table 3.1: Variable correspondence between heat transfer and phase field evolution equations.

Heat Transfer Equation	Phase Field Evolution Equation
$k\nabla^2\theta = -r$	$\nabla^2\phi = \left(\frac{g'(\phi)\mathcal{H}2c_w}{\ell G_c} + \frac{w'(\phi)}{2\ell^2}\right)$
θ	ϕ
k	1
r	$-\left(\frac{g'(\phi)\mathcal{H}2c_w}{\ell G_c} + \frac{w'(\phi)}{2\ell^2}\right)$

The implementation follows a procedure in which Abaqus supplies strain and phase field (temperature) values at each element's integration points. The UMAT subroutine then computes the material Jacobian $\mathbf{C}$ and Cauchy stress $\boldsymbol{\sigma}$ based on strain, modified by the phase field to account for damage. The strain en-

[3]The codes and documentation are available at: https://www.empaneda.com/wp-content/uploads/2021/07/PhaseFieldUMAT.zip

ergy density is stored in solution-dependent state variables (SDVs) to enforce irreversibility (Equation (2.43)). In the UMAT-only version, the heat flux r and its derivative $\partial r/\partial \phi$ are set as volumetric heat generation and its derivative. In the UMAT+HETVAL implementation, these parameters are defined within HETVAL, with updated SDVs transferring the history field value $\mathcal{H}$, thus avoiding the need for external FORTRAN modules. This process is repeated at each integration point, allowing Abaqus to assemble the global stiffness matrix and residual vectors.

Both monolithic and staggered schemes are supported to ensure computational stability. To maintain a symmetric stiffness matrix, coupling terms $\boldsymbol{K}_{\mathbf{u}\phi}$ and $\boldsymbol{K}_{\phi\mathbf{u}}$ are omitted, thereby preserving a symmetric system in Abaqus. In the monolithic scheme, the phase field and displacement are updated iteratively to solve for deformation and fracture simultaneously. In the staggered scheme, SDVs store the history field $\mathcal{H}_t$ from the previous increment. While staggered methods offer stability, conducting a sensitivity analysis on load increments is recommended.

3.2.2 Phase field fracture verification

The robustness and capabilities of the present implementation are demonstrated by simulating fracture in several benchmark boundary value problems, as detailed in Appendixes B [51] and C [52].

In Appendix B [51], the following benchmarks are modeled:

- **Notched square plate under tension or shear**: Crack initiation and growth in a notched square plate are modeled under uniaxial tension (Section 4.1 of Appendix B) and shear (Section 4.2 of Appendix B), a well-known benchmark in phase field fracture studies [6]. The tension test reveals rapid crack

propagation accompanied by a sudden drop in load capacity (Fig. 4, Appendix B), while the shear case exhibits gradual crack propagation (Fig. 6, Appendix B), both aligning closely with the findings in the literature [80].

- **Screw tension tests**: This study simulates screw fracture under tensile loading [81] (Section 4.3 of Appendix B) across three scenarios: no initial crack, a short crack, and a long crack. Results (Fig. 8, Appendix B) indicate that crack initiation occurs near the screw head in the absence of an initial defect, while defects promote crack propagation along the screw. Screws without defects exhibit higher load capacity, whereas screws with different crack lengths show nearly identical load capacities (Fig. 9, Appendix B).
- **3D Brazilian test**: This case study simulates the 3D Brazilian test (Section 4.4 of Appendix B), a commonly used experiment to measure the tensile strength of brittle materials. The objective is to capture crack initiation and propagation within a circular disk compressed between two jaws. The results indicate that the crack initiates at the center of the disk and rapidly propagates towards the jaws. The model effectively captures the fracture process, with no convergence issues encountered during the simulation.

Figure 3.2 presents the phase field contour for the case studies described above.

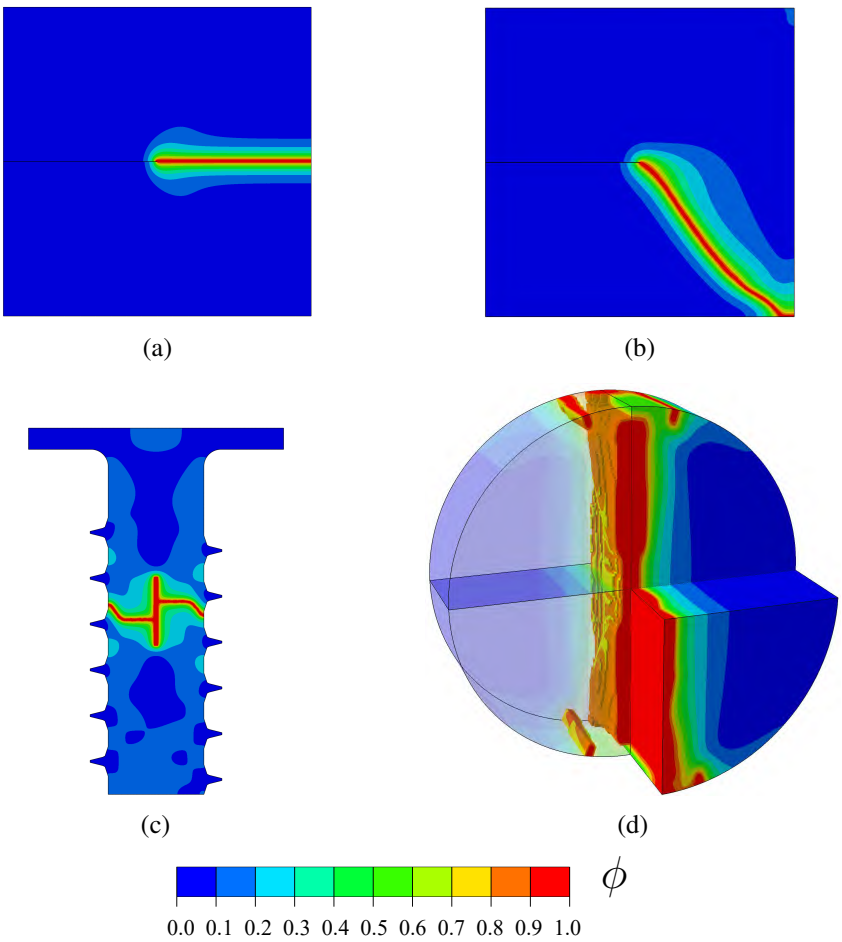

Figure 3.2: Phase field contour of: (a) Notched square plate under tension, (b) Notched square plate unde shear, (c) Screw tension tests, and (d) 3D Brazilian test.

Our initial implementation is extended to a unified phase field formulation, encompassing well-known constitutive models using only the UMAT subroutine. In Appendix C [52], four case studies are presented:

- **Three-point bending test**: This case study models the failure of a beam in a three-point bending test, comparing results with those from Wells and Sluys [82] using a cohesive zone model and partition of unity (Section 4.1 of Appendix C). The objective is to validate the phase field-cohesive zone model (PF-CZM) in capturing fracture behavior. The results show good

agreement, with the crack initiating at the bottom of the beam and propagating straight to the top (Figure 1c of Appendix C). The force-displacement response closely aligns with the cohesive zone model, demonstrating the accuracy of the phase field approach (Figure 2 of Appendix C).

- **Mixed-mode fracture of a single-edge notched concrete beam**: This case study models the mixed-mode fracture of a single-edge notched concrete beam, aiming to compare the phase field model (AT2) with experimental data from Schalangen [83] (Section 4.2 of Appendix C). The setup simulates fracture under complex loading conditions. The results show excellent agreement with experimental observations, as the crack initiates at the notch and follows a crack trajectory similar to that seen in the experiments. The phase field method successfully captures the mixed-mode crack propagation (Figure 5 of Appendix C).

- **Notched plate with an eccentric hole**: This case study investigates the fracture behavior of a notched plate with an eccentric hole, focusing on capturing crack interaction with defects and crack nucleation from arbitrary locations (Section 4.3 of Appendix C). The objective is to validate the robustness of the phase field model in predicting complex crack paths. The results show good agreement with experimental data [79], as the crack initiates from the notch tip, interacts with the hole, and ultimately results in the plate's failure (Figure 6 of Appendix C). The model accurately captures crack deflection and the nucleation of secondary cracks.

- **3D analysis of cracking due to the contact interaction between two gears**: This case study models the 3D cracking behavior of two interacting gears under contact loading (Section 4.4 of Appendix C). The objective is to demonstrate the capability of the phase field model (AT1) in capturing

complex 3D fracture processes, including contact interactions and geometric non-linearities. The results show that cracks initiate at the root of a gear tooth and propagate through the gear, eventually leading to the tooth's failure. The model effectively handles contact interactions and accurately predicts crack growth in a complex 3D geometry.

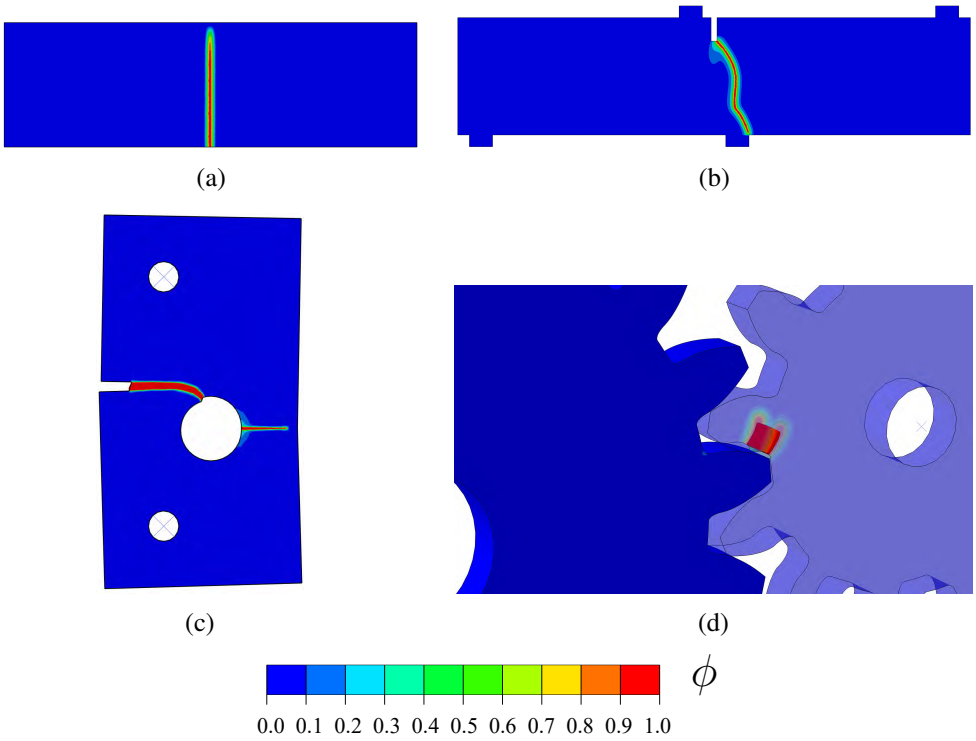

Figure 3.3: Phase field contour of: (a) Three-Point Bending Test, (b) Mixed-Mode Fracture of a Single-Edge Notched Concrete Beam, (c) Notched Plate with an Eccentric Hole, and (d) 3D Analysis of Cracking Due to the Contact Interaction between Two Gears.

3.3 Experimental validation of phase field fracture

In this section, the predictive capabilities of the phase field fracture model is discussed within the context of the Damage Mechanics Challenge, an initiative organized by Purdue University, Sandia National Laboratories, and Lawrence Liver-

more National Laboratory [54]. The challenge was designed to assess the performance of computational methods in predicting the behavior of rock-like materials under complex loading conditions, moving beyond mere curve fitting to experimental data. Our study employs the phase field fracture model to predict failure characteristics in a non-standard three-point bending test performed on 3D-printed rock materials.

The challenge required predictions of the force-displacement response, crack path, and crack surface morphology for an unconventional three-point bending test using a 3D-printed gypsum-like material (Figure 3.4). In this study, the blind predictions had been presented [53] (see Appendix D) before the experimental results were released. These predictions were based solely on the calibration data provided by the challenge organizers, which included standard mechanical tests such as uniaxial compression, Brazilian tensile tests, and traditional three-point bending configurations.

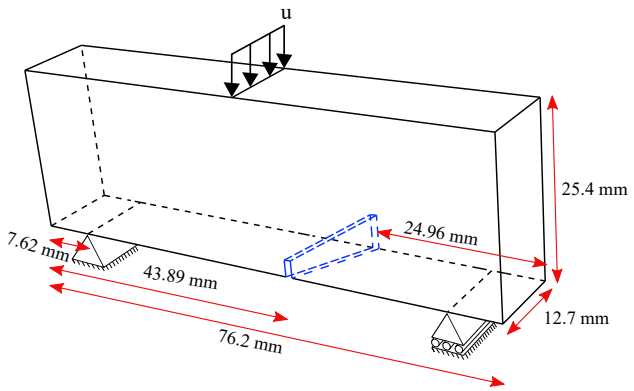

(a)

Figure 3.4: Geometry, dimensions, and boundary conditions of the challenge test.

3.3.1 Methodology

The computational setup for calibrating the phase field fracture model involved simulating three-point bending tests in both 2D and 3D to align with experimental data. The simulations utilized quadrilateral elements in 2D and tetrahedral elements in 3D, with mesh refinement concentrated around regions of potential crack growth. A direct linear solver was employed for the finite element analysis, and the phase field fracture model was implemented using our custom code within Abaqus.

The model employed a volumetric-deviatoric strain energy decomposition to differentiate tensile from compressive behaviors. A monolithic, unconditionally stable solution scheme was used to ensure computational robustness throughout the simulations.

The material parameters were calibrated based on the experimental data provided. Three primary parameters were calibrated: Young's modulus E, fracture toughness G_c, and material strength σ_c, the latter of which is related to the phase field length scale l. Preliminary calibration using a mode I three-point bending test indicated that $E = 600$ MPa, $G_c = 0.13$ kJ/m^2, and $\sigma_c = 4.05$ MPa provided the best fit with the experimental data. These parameters were then applied to predict mixed-mode fracture behavior in subsequent tests.

3.3.2 Key results and findings

Key results from the study include:

- **Model calibration and accuracy**: The rock-like material exhibited distinct properties under tensile and compressive stress due to the presence of

micro-cracks. Using Young's modulus obtained from uniaxial compression tests resulted in an overestimation of stiffness compared to experimental data (Figure 5a in Appendix D). Additionally, the validity of the Brazilian tensile test results provided by the challenge organizers is assessed by applying our method developed in Section 3.1. Our investigation indicated that the Brazilian test results underestimated the material's tensile strength (Sections 2.2.1 and 2.2.3 of Appendix D). Consequently, the phase field fracture model was calibrated using the force-displacement response from a mode I three-point bending test (Section 2.2.3 of Appendix D). The calibrated parameters are Young's modulus $E = 600$ MPa, toughness $G_c = 0.13$ kJ/m^2, and strength $\sigma_c = 4.05$ MPa, demonstrated excellent agreement with experimental data across various test configurations (Figures 6-8 of Appendix D).

- **Blind predictions of complex fracture behavior**: The calibrated model accurately predicted the peak load (Figure 9 of Appendix D), crack trajectory (Figure 10 of Appendix D), and surface crack morphology (Figure 11 of Appendix D) in the challenge test. This test involved a more complex three-point bending experiment with an inclined notch. Our blind predictions, submitted prior to the release of experimental data, showed remarkable agreement with the actual test results [54].

- **Mesh-independent predictions**: The non-local nature of the phase field fracture model ensured mesh-independent results, providing robustness by guaranteeing that predictions are not sensitive to the choice of finite element discretization, provided the mesh is sufficiently refined around the potential crack growth region.

Figure 3.5 compares the experimental and phase field fracture predictions for both

the calibration test (HC) and the challenge test, showing strong agreement.

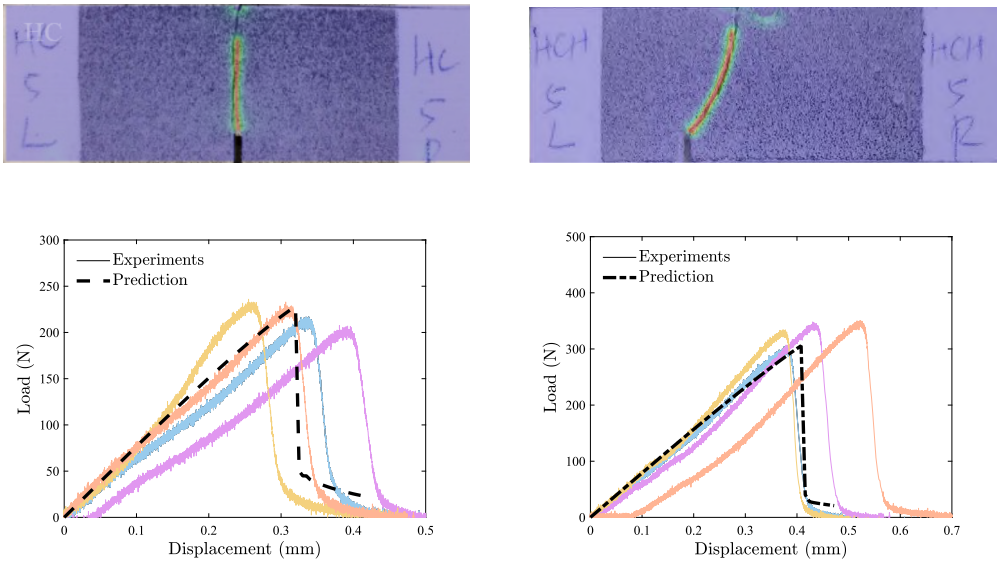

(a) Calibration test HC

(b) Challenge test

Figure 3.5: Comparison between phase field fracture predictions and experimental data: crack trajectories (top) and force versus displacement plots (bottom) for (a) calibration test HC and (b) challenge test.

3.3.3 Conclusion

This work demonstrates the capability of the phase field fracture model to accurately predict fracture behavior in rock-like materials under complex loading conditions. The model's reliance on physical material parameters and its seamless integration into commercial finite element software make it a powerful predictive tool for geomechanical systems. Its performance in the Damage Mechanics Challenge underscores its predictive accuracy and establishes a robust foundation for future research and practical applications.

3.4 Constitutive fracture behavior modeling of material for phase field method

In this section, a novel method of a generalized approach for strain energy decomposition based on failure criteria is demonstrated (Appendix E) [49]. Specifically, the proposed approach is applied to the Drucker-Prager-based split, showcasing its ability to model complex behaviors of rock-like materials, such as dilatancy, friction, and confinement effects. Beyond this novel method, our unpublished works on extending the approach is presented that offering a deeper discussion of our proposed method and introducing an approach for additive decomposition of strain energy, with specific application to the Bresler-Pister failure criterion. Additionally, a new strain energy split tailored for materials containing voids and inclusions is introduced, as presented at Complas 2021 [55].

3.4.1 Fracture driving force based on failure surface

As previously discussed in Section 2.2.6, the decomposition of strain energy serves as a method to prevent damage evolution under compressive states. However, this approach can be extended beyond compression-related damage prevention to model the constitutive fracture behavior of materials. Several studies have explored strain energy decomposition within this context. For example, Zhou et al. [84] and Wang et al. [85] developed a driving force formulations based on the Mohr–Coulomb theory. Additionally, De Lorenzis and Maurini [48] introduced a Drucker–Prager-like energy split to capture fracture nucleation in rock-like materials.

The increasing interest in phase field methods for modeling fracture in concrete

and geomaterials has prompted the development of a novel approach to determine strain energy decomposition for arbitrary failure surfaces. In this work, a general framework for decomposing the phase field fracture driving force is proposed, as detailed in Appendix E. The proposed method introduces a strain energy density decomposition that accommodates any failure criterion within the phase field fracture framework. Since strain energy density governs fracture evolution, this decomposition enables the reproduction of targeted failure surfaces, aligning with the selected failure criterion while preserving the material's mechanical behavior.

The approach primarily focuses on linear elastic solids in their undamaged state. The partial differential equation (PDE) is derived governing the non-dissipative strain energy density, ψ_s, for linear elastic materials and impose a failure envelope to constrain the solution.

As outlined in [46] and grounded in the *Theory of Structured Deformations* [86], a representative volume element (RVE) is defined to incorporate both intact material and micro-cracks, with the phase field ϕ acting as a damage variable. The macroscopic deformation is thus expressed as the sum of the elastic strain in the undamaged regions and the damage-induced strains resulting from the presence of micro-cracks:

$$\boldsymbol{\varepsilon} = \boldsymbol{\varepsilon}^e + \boldsymbol{\varepsilon}^d \,. \tag{3.3}$$

The elastic strain tensor $\boldsymbol{\varepsilon}^e$ is related to the Cauchy stress tensor $\boldsymbol{\sigma}$ through the inverse of the elastic stiffness matrix, defined as $\boldsymbol{\varepsilon}^e = (\mathbf{C}_0)^{-1}\boldsymbol{\sigma}$. If the elastic strain tensor $\boldsymbol{\varepsilon}^e$ and the stress results from damaged strain tensor $\boldsymbol{\sigma}^d = \mathbf{C}_0\boldsymbol{\varepsilon}^d$ are orthogonal ($\boldsymbol{\varepsilon}^e \cdot \boldsymbol{\sigma}^d = 0$), the stored and damaged strain energy densities can be expressed as:

$$\psi_s = \frac{1}{2}\boldsymbol{\varepsilon}^e \mathbf{C}_0 \boldsymbol{\varepsilon}^e \quad \text{and} \quad \psi_d = \frac{1}{2}\boldsymbol{\varepsilon}^d \mathbf{C}_0 \boldsymbol{\varepsilon}^d. \tag{3.4}$$

The total strain energy density ψ is obtained from ψ_s and ψ_d using Equation (2.18). For a pristine material, the strain energy density is a function of the stress invariants:

$$\psi_0(\boldsymbol{\varepsilon}) = \psi_d(\boldsymbol{\varepsilon}^d) + \psi_s(\boldsymbol{\varepsilon}^e) = \frac{1}{18K} I_1^2(\boldsymbol{\sigma}_0(\boldsymbol{\varepsilon})) + \frac{1}{2\mu} J_2(\boldsymbol{\sigma}_0(\boldsymbol{\varepsilon})), \tag{3.5}$$

where K denotes the bulk modulus, μ is the shear modulus, $I_1(\boldsymbol{\sigma}_0)$ represents the first invariant of the undamaged stress (where $\boldsymbol{\sigma}_0 = \partial\psi_0/\partial\boldsymbol{\varepsilon}$), and $J_2(\boldsymbol{\sigma}_0)$ denotes the second invariant of the deviatoric part of the undamaged stress. The stored strain energy density ψ^s can be expressed in terms of the non-degraded stress, defined as $\boldsymbol{\sigma}^s = \partial\psi_s/\partial\boldsymbol{\varepsilon}$, as:

$$\psi_s = \frac{1}{18K} I_1^2(\boldsymbol{\sigma}^s) + \frac{1}{2\mu} J_2(\boldsymbol{\sigma}^s). \tag{3.6}$$

As proved in Appendix A of Appendix E that the following relation holds for any choice of $\psi(I_1(\boldsymbol{\varepsilon}), J_2(\boldsymbol{\varepsilon}))$:

$$I_1(\boldsymbol{\sigma}(\boldsymbol{\varepsilon})) = 3\frac{\partial\psi(\boldsymbol{\varepsilon})}{\partial I_1(\boldsymbol{\varepsilon})}, \quad J_2(\boldsymbol{\sigma}(\boldsymbol{\varepsilon})) = J_2(\boldsymbol{\varepsilon}) \left(\frac{\partial\psi(\boldsymbol{\varepsilon})}{\partial J_2(\boldsymbol{\varepsilon})}\right)^2. \tag{3.7}$$

By substituting Equation (3.7) into Equation (3.6), the partial differential equation (PDE) for the stored strain energy ψ_s is obtained as:

$$\psi_s = \frac{1}{2K}\left(\frac{\partial\psi_s}{\partial I_1(\boldsymbol{\varepsilon})}\right)^2 + \frac{J_2(\boldsymbol{\varepsilon})}{2\mu}\left(\frac{\partial\psi_s}{\partial J_2(\boldsymbol{\varepsilon})}\right)^2. \tag{3.8}$$

On the other hand, the failure criterion imposes additional constraints, expressed as $\mathcal{F}(I_1(\boldsymbol{\sigma}(\boldsymbol{\varepsilon})), J_2(\boldsymbol{\sigma}(\boldsymbol{\varepsilon}))) = 0$. For instance, in the case of a Drucker-Prager failure surface:

$$\sqrt{J_2(\boldsymbol{\sigma})} - BI_1(\boldsymbol{\sigma}) - A = 0\,, \tag{3.9}$$

where A and B are parameters dependent on the material strengthsand they are defined at a fully damage state ($\phi = 1$) as:

$$A(\phi = 1) = 0 \quad \text{and} \quad B(\phi = 1) = B(\phi = 0). \tag{3.10}$$

Similarly, the partial differential equation (PDE) for the failure surface can be derived by substituting the relations from Equation (3.7) into the failure criterion for the fully damaged state. Consequently, the failure envelope function is given by:

$$\mathcal{F}\left(\frac{\partial \psi_s(\boldsymbol{\varepsilon})}{\partial I_1(\boldsymbol{\varepsilon})}, \frac{\partial \psi_s(\boldsymbol{\varepsilon})}{\partial J_2(\boldsymbol{\varepsilon})}\right) = \sqrt{J_2(\boldsymbol{\varepsilon})}\frac{\partial \psi_s(\boldsymbol{\varepsilon})}{\partial J_2(\boldsymbol{\varepsilon})} - 3B\frac{\partial \psi_s(\boldsymbol{\varepsilon})}{\partial I_1(\boldsymbol{\varepsilon})} = 0. \tag{3.11}$$

Now, a system of PDEs should be solved, which includes the PDE for the stored strain energy ψ_s and the PDE for the failure surface, to find their common solution. The detailed procedure is presented in Section 3.1 of Appendix E for the case of the Drucker–Prager failure surface, which is expressed as:

$$\psi_s = \frac{K\mu}{18B^2K + 2\mu}\left(I_1(\boldsymbol{\varepsilon}) + 6B\sqrt{J_2(\boldsymbol{\varepsilon})}\right)^2. \tag{3.12}$$

However, this result is only valid for stress states above the failure envelope. For stress states below the envelope or in other regimes, ψ_s and ψ_d are adjusted ac-

cordingly (see Appendix B of Appendix E):

$$\psi_s = \begin{cases} 0 & \text{for} \quad -6B\sqrt{J_2(\boldsymbol{\varepsilon})} < I_1(\boldsymbol{\varepsilon}) \\ \frac{K\mu}{18B^2K+2\mu}\left(I_1(\boldsymbol{\varepsilon}) + 6B\sqrt{J_2(\boldsymbol{\varepsilon})}\right)^2 & \text{for} \quad -6B\sqrt{J_2(\boldsymbol{\varepsilon})} \geq I_1(\boldsymbol{\varepsilon}) \text{ and } 2\mu\sqrt{J_2(\boldsymbol{\varepsilon})} \geq 3BKI_1(\boldsymbol{\varepsilon}) \\ \frac{1}{2}KI_1^2(\boldsymbol{\varepsilon}) + 2\mu J_2(\boldsymbol{\varepsilon}) & \text{for} \quad 2\mu\sqrt{J_2(\boldsymbol{\varepsilon})} < 3BKI_1(\boldsymbol{\varepsilon}), \end{cases} \tag{3.13}$$

and the damaged strain energy density is given by:

$$\psi_d = \begin{cases} \frac{1}{2}KI_1^2(\boldsymbol{\varepsilon}) + 2\mu J_2(\boldsymbol{\varepsilon}) & \text{for} \quad -6B\sqrt{J_2(\boldsymbol{\varepsilon})} < I_1(\boldsymbol{\varepsilon}) \\ \frac{1}{18B^2K+2\mu}\left(-3BKI_1(\boldsymbol{\varepsilon}) + 2\mu\sqrt{J_2(\boldsymbol{\varepsilon})}\right)^2 & \text{for} \quad -6B\sqrt{J_2(\boldsymbol{\varepsilon})} \geq I_1(\boldsymbol{\varepsilon}) \text{ and } 2\mu\sqrt{J_2(\boldsymbol{\varepsilon})} \geq 3BKI_1(\boldsymbol{\varepsilon}) \\ 0 & \text{for} \quad 2\mu\sqrt{J_2(\boldsymbol{\varepsilon})} < 3BKI_1(\boldsymbol{\varepsilon}). \end{cases} \tag{3.14}$$

The capability of the Drucker-Prager model to capture the compressive failure of brittle materials is demonstrated through the numerical implementation of the resulting strain energy split formulation, applied to four case studies (Section 4 of Appendix E) of particular interest. First, the model's ability to predict friction and dilatancy effects under shear loading is evaluated (Section 4.1 of Appendix E). Second, virtual direct shear tests are conducted to assess fracture predictions under varying normal loads P (Figure 3.6a). In Figure 3.6b, the phase field contour of a concrete cylinder specimen is subjected to uniaxial and triaxial compression to examine the influence of confinement is examined. Finally, the localized failure of a soil slope is predicted using the Drucker-Prager model (Figure 3.6c).

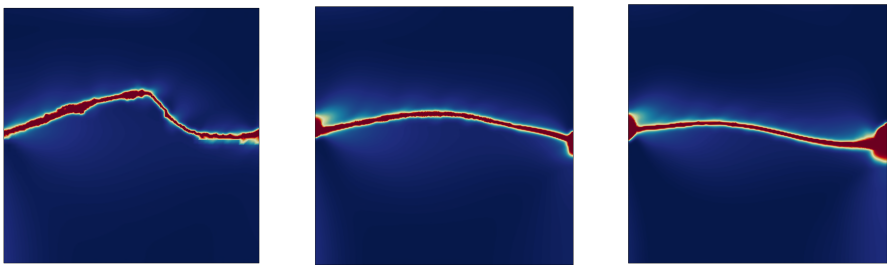

(a) Direct shear test (DST), from left to right, $P = 0$, $P = 10$, and $P = 202$ MPa

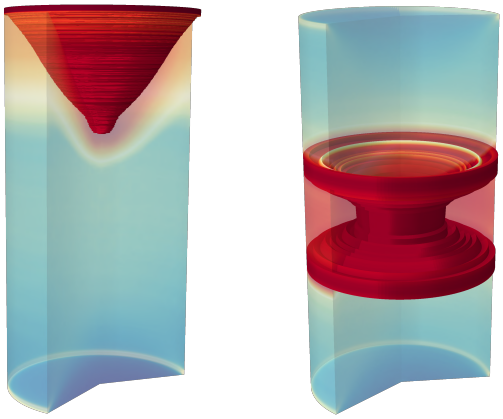

(b) Compressive failure of concrete for unconfined and confined specimens

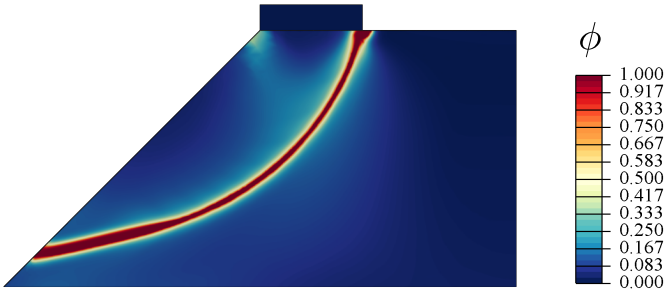

(c) Localised failure of a soil slope

Figure 3.6: Phase field contour of Drucker-Prager based split, (a) direct shear test (DST) for different normal load, (b) compressive failure of concrete, unconfined sample, at the left and confined sample at the right, and (c) Localised failure of a soil slope.

Let's explore the implications of the strain decomposition further. Figure 3.7 illustrates the isolines of the undamaged strain energy ψ_0 (solid line), the dissipated strain energy ψ_d (dashed line), and the stored strain energy ψ_s (dotted line) in the

space of strain invariants for a Drucker-Prager based split. In this context, the first invariant of the strain tensor corresponds to the trace, $tr(\boldsymbol{\varepsilon})$, and $\sqrt{J_2(\boldsymbol{\varepsilon})}$ represents the norm of the deviatoric part of the strain tensor, $||\boldsymbol{\varepsilon}_{\text{dev}}||$. The solid blue line indicates the condition $\psi_d = 0$, corresponding to the Drucker–Prager failure surface, while the solid red line represents the convex set associated with the Drucker–Prager surface where $\psi_s = 0$.

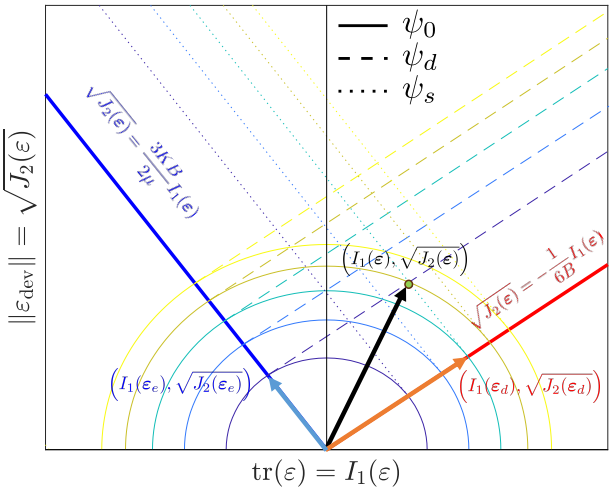

Figure 3.7: Isolines of undamaged strain energy ψ_0, dissipated strain energy ψ_d, and stored strain energy ψ_s for Drucker-Prager strength surface in the space of invariants of strain invariants.

In the case of a fully damaged state ($\phi = 1$), the total strain energy ψ reduces to the stored part of the strain energy ψ_s, which must be minimized according to the principle of minimum strain energy [4]. This minimization process implies that the deviatoric part of the elastic strain tensor $\boldsymbol{\varepsilon}^e_{\text{dev}}$ and the deviatoric part of the damaged strain tensor $\boldsymbol{\varepsilon}^d_{\text{dev}}$ must be collinear [5] to the deviatoric part of the total

[4]The principle of minimum strain energy states that a mechanical system in equilibrium adopts a configuration that minimizes the total strain energy, provided external forces and constraints remain constant [87].

[5]Two tensors $\mathbf{T}_1$ and $\mathbf{T}_2$ are collinear if $\mathbf{T}_2 = \Lambda \mathbf{T}_1$, where Λ is a scalar.

strain tensor ε_{dev} [48].

Based on this fact, the following relations can be established:

$$I_1(\boldsymbol{\varepsilon}) = I_1(\boldsymbol{\varepsilon}^e) + I_1(\boldsymbol{\varepsilon}^d), \quad \sqrt{J_2(\boldsymbol{\varepsilon})} = \sqrt{J_2(\boldsymbol{\varepsilon}^e)} + \sqrt{J_2(\boldsymbol{\varepsilon}^d)}, \tag{3.15}$$

where $I_1(\boldsymbol{\varepsilon}^e)$ and $J_2(\boldsymbol{\varepsilon}^e)$ are the invariants of the elastic strain, and $I_1(\boldsymbol{\varepsilon}^d)$ and $J_2(\boldsymbol{\varepsilon}^d)$ are the invariants of the damage strain. As shown in Figure 3.7, for any strain in this space, the strain invariants $(I_1(\boldsymbol{\varepsilon}), J_2(\boldsymbol{\varepsilon}))$ can be projected onto the Drucker–Prager failure line and its associated convex set. This projection facilitates the decomposition of the strain invariants as described in Equation (3.15).

The total undamaged strain energy for an isotropic linear elastic material, expressed in terms of strain invariants, is given by the equation:

$$\psi_0 = \frac{1}{2} K I_1^2(\boldsymbol{\varepsilon}) + 2\mu J_2(\boldsymbol{\varepsilon}). \tag{3.16}$$

By substituting Equation (3.15) into Equation (3.16), obtained:

$$\psi_0 = \psi_s + \psi_d + K I_1(\boldsymbol{\varepsilon}^e) I_1(\boldsymbol{\varepsilon}^d) + 4\mu \sqrt{J_2(\boldsymbol{\varepsilon}^e)} \sqrt{J_2(\boldsymbol{\varepsilon}^d)}. \tag{3.17}$$

To ensure the additive decomposition of strain energy ($\psi_0 = \psi_s + \psi_d$), the orthogonality condition must be satisfied as:

$$\sqrt{J_2(\boldsymbol{\varepsilon}^e)} \sqrt{J_2(\boldsymbol{\varepsilon}^d)} + \frac{K}{4\mu} I_1(\boldsymbol{\varepsilon}^e) I_1(\boldsymbol{\varepsilon}^d) = 0. \tag{3.18}$$

As mentioned earlier, the decomposition of strain invariants into elastic and damage components lies on the failure line (Figure 3.7) and its associated convex set.

Thus, the following relations can be expressed:

$$\sqrt{J_2(\boldsymbol{\varepsilon}^e)} = \frac{3KB}{2\mu} I_1(\boldsymbol{\varepsilon}^e), \quad \sqrt{J_2(\boldsymbol{\varepsilon}^d)} = -\frac{1}{6B} I_1(\boldsymbol{\varepsilon}^d), \tag{3.19}$$

which satisfies Equation (3.18). Thus, the additive decomposition of strain energy is achieved.

3.4.2 General approach for additive decomposition of strain energy

While developing a common solution for the PDEs of stored energy and the failure surface is a general approach for determining the strain energy split based on the failure surface, the mathematical process becomes increasingly complex when more intricate failure surfaces are involved. In some cases, no known solution procedure may exist. In this section, a solution approach is developed to determine the strain energy based on the failure surface for the additive decomposition of strain energy.

Based on the definitions provided in Eqs. Equation (3.15) and Equation (3.16), the additive decomposition of strain energy can be mathematically expressed such as Equation (3.17). To ensure the validity of this additive decomposition of strain energy, the constraint that is expressed in Equation (3.18) must be satisfied. For improved clarity, this constraint can be reformulated as:

$$2\mu\sqrt{J_2(\boldsymbol{\varepsilon}^e)}\sqrt{J_2(\boldsymbol{\varepsilon}^d)} + \frac{1}{2} K I_1(\boldsymbol{\varepsilon}^e) I_1(\boldsymbol{\varepsilon}^d) = 0. \tag{3.20}$$

Furthermore, the relationships between the invariants of the elastic strain and the

corresponding stress can be expressed as follows:

$$I_1(\boldsymbol{\sigma}^s) = 3KI_1(\boldsymbol{\varepsilon}^e), \quad \sqrt{J_2(\boldsymbol{\sigma}^s)} = 2\mu\sqrt{J_2(\boldsymbol{\varepsilon}^e)}. \tag{3.21}$$

Incorporating these relationships into Equation (3.20) reveals that the elastic strain and damage strain components are orthogonal. This orthogonality can be expressed as:

$$\sqrt{J_2(\boldsymbol{\sigma}^e)}\sqrt{J_2(\boldsymbol{\varepsilon}^d)} + \frac{1}{6}I_1(\boldsymbol{\sigma}^e)I_1(\boldsymbol{\varepsilon}^d) = 0 \quad \text{implying} \quad \boldsymbol{\varepsilon}^d \cdot \boldsymbol{\sigma}^e = 0. \tag{3.22}$$

Similarly, the relationships between the invariants of the damage strain and the corresponding stress invariants are given by:

$$I_1(\boldsymbol{\sigma}^d) = 3KI_1(\boldsymbol{\varepsilon}^d), \quad \sqrt{J_2(\boldsymbol{\sigma}^d)} = 2\mu\sqrt{J_2(\boldsymbol{\varepsilon}^d)}. \tag{3.23}$$

This relationship leads to the following orthogonality condition:

$$\sqrt{J_2(\boldsymbol{\sigma}^d)}\sqrt{J_2(\boldsymbol{\varepsilon}^e)} + \frac{1}{6}I_1(\boldsymbol{\sigma}^d)I_1(\boldsymbol{\varepsilon}^e) = 0 \quad \text{implying} \quad \boldsymbol{\varepsilon}^e \cdot \boldsymbol{\sigma}^d = 0. \tag{3.24}$$

To further elucidate, both the elastic part and the total strain in Equation (3.20), leading to the following formulation:

$$2\mu\sqrt{J_2(\boldsymbol{\varepsilon}^e)}\left(\sqrt{J_2(\boldsymbol{\varepsilon})} - \sqrt{J_2(\boldsymbol{\varepsilon}^e)}\right) + \frac{1}{2}KI_1(\boldsymbol{\varepsilon}^e)\left(I_1(\boldsymbol{\varepsilon}) - I_1(\boldsymbol{\varepsilon}^e)\right) = 0. \tag{3.25}$$

Rearranging this equation results in:

$$\frac{1}{2}KI_1(\boldsymbol{\varepsilon}^e)I_1(\boldsymbol{\varepsilon})+2\mu\sqrt{J_2(\boldsymbol{\varepsilon}^e)}\sqrt{J_2(\boldsymbol{\varepsilon})} = \frac{1}{2}KI_1^2(\boldsymbol{\varepsilon}^e)+2\mu J_2(\boldsymbol{\varepsilon}^e) = \psi_s \quad \text{implying} \quad \frac{1}{2}\boldsymbol{\varepsilon}\cdot\boldsymbol{\sigma}^e = \psi_s. \tag{3.26}$$

Additionally, from considerations of surface strength, derived:

$$\mathcal{F}\left(I_1(\boldsymbol{\varepsilon}^e), J_2(\boldsymbol{\varepsilon}^e)\right) = 0. \tag{3.27}$$

By solving Equations (3.26) and (3.27), the first invariant of the elastic strain can be determined, $I_1(\boldsymbol{\varepsilon}^e)$, as a function of the invariants of the total strain, $(I_1(\boldsymbol{\varepsilon}), J_2(\boldsymbol{\varepsilon}))$:

$$I_1(\boldsymbol{\varepsilon}^e) = \mathcal{G}\left(I_1(\boldsymbol{\varepsilon}), J_2(\boldsymbol{\varepsilon})\right) . \tag{3.28}$$

Similarly, the second invariant of the deviatoric part of the elastic strain, $J_2(\boldsymbol{\varepsilon}^e)$, can be determined through a comparable analysis. Finally, by obtaining $I_1(\boldsymbol{\varepsilon}^e)$ and $J_2(\boldsymbol{\varepsilon}^e)$ and substituting them into the following expression, the stored part of the strain energy ψ_s can be determined as:

$$\psi_s = \frac{1}{2}KI_1^2(\boldsymbol{\varepsilon}^e) + 2\mu J_2(\boldsymbol{\varepsilon}^e). \tag{3.29}$$

The advantage of this method, compared to finding a common solution of two PDEs, is that finding a common solution is complicated for more complex failure criteria.

As a case study, this method is reapplied to obtain the Drucker–Prager decomposition. the Drucker–Prager failure surface is rewritten using Equation (3.21), based

on the invariants of the elastic part of the strain, allowing us to express it as:

$$\mathcal{F}\left(I_1(\boldsymbol{\varepsilon}_e), J_2(\boldsymbol{\varepsilon}_e)\right) = \sqrt{J_2(\boldsymbol{\varepsilon}_e)} - \frac{3KB}{2\mu} I_1(\boldsymbol{\varepsilon}_e) = 0. \tag{3.30}$$

Solving the system of Equations (3.26) and (3.30) allows us to determine the invariants of the elastic strain based on the invariants of the total strain:

$$I_1(\boldsymbol{\varepsilon}_e) = \left(\frac{K\mu}{2\mu + 9K^2B^2}\right)\left(I_1(\boldsymbol{\varepsilon}) + 6B\sqrt{J_2(\boldsymbol{\varepsilon})}\right), \tag{3.31}$$

$$\sqrt{J_2(\boldsymbol{\varepsilon}_e)} = \left(\frac{3KB}{4\mu + 18K^2B^2}\right)\left(I_1(\boldsymbol{\varepsilon}) + 6B\sqrt{J_2(\boldsymbol{\varepsilon})}\right). \tag{3.32}$$

Substituting these relations into Equation (3.28) allows us to determine the stored strain energy ψ_s, as shown in Equation (3.12).

3.4.3 Bresler–Pister based split

Introducing the general approach for additive decomposition of strain energy facilitates finding the strain energy split based on more complex failure surfaces, such as the Bresler–Pister failure criterion. This sophisticated model is designed to predict the strength of concrete under complex multiaxial stress conditions. The Bresler–Pister criterion enhances the Drucker–Prager yield criterion by incorporating additional terms and can be expressed in terms of stress and strain invariants as follows:

$$\sqrt{J_2(\boldsymbol{\sigma})} = CI_1^2(\boldsymbol{\sigma}) + BI_1(\boldsymbol{\sigma}), \quad \sqrt{J_2(\boldsymbol{\varepsilon}_e)} = \frac{9K^2C}{2\mu} I_1^2(\boldsymbol{\varepsilon}_e) + \frac{3KB}{2\mu} I_1(\boldsymbol{\varepsilon}_e). \tag{3.33}$$

In this formulation, the parameters B and C must be carefully selected to ensure that the resulting yield surfaces are physically realistic. To determine these parameters, let σ_c represent the yield stress under uniaxial compression, σ_t the yield stress under uniaxial tension, and σ_b the yield stress under biaxial compression. The parameters B and C are defined by:

$$B = \left(\frac{\sigma_t - \sigma_c}{\sqrt{3}\,(\sigma_t + \sigma_c)}\right)\left(\frac{4\sigma_b^2 - \sigma_b\,(\sigma_c + \sigma_t) + \sigma_c\sigma_t}{4\sigma_b^2 + 2\sigma_b\,(\sigma_t - \sigma_c) - \sigma_c\sigma_t}\right) \tag{3.34}$$

$$C = \left(\frac{1}{\sqrt{3}\,(\sigma_t + \sigma_c)}\right)\left(\frac{\sigma_b\,(3\sigma_t - \sigma_c) - 2\sigma_c\sigma_t}{4\sigma_b^2 + 2\sigma_b\,(\sigma_t - \sigma_c) - \sigma_c\sigma_t}\right). \tag{3.35}$$

Similar to the previous section, the invariants of the elastic tensor is determined based on the invariants of the total strain. By utilizing Equation (3.26) and Equation (3.33), the following expression is derived for the first invariant of the elastic strain:

$$I_1(\boldsymbol{\varepsilon}_e) = \frac{1}{18}\sqrt[3]{4}\Delta + \frac{\sqrt[3]{2}}{27C^2K^3}\frac{Z}{\Delta} - \frac{2B}{9CK}. \tag{3.36}$$

Here, Δ and Z are defined as:

$$\Delta = \frac{1}{C\sqrt[3]{K^4}}\sqrt[3]{X + Y + 1458\sqrt{\frac{(X+Y)^2}{2125764} - \frac{Z^3}{14348907K}}}, \tag{3.37}$$

$$Z = 3KB^2 - \mu + 18CK\mu\sqrt{J_2(\boldsymbol{\varepsilon})}. \tag{3.38}$$

Additionally, X and Y are given by:

$$X = 2B(\mu + B^2K), \quad Y = 9CK\mu\left(I_1(\boldsymbol{\varepsilon}) + 2B\sqrt{J_2(\boldsymbol{\varepsilon})}\right). \tag{3.39}$$

Based on the Bresler-Pister split, the strain and stress spaces are partitioned into four distinct regions, as illustrated in Figure 3.8, considering the invariants space of strain and stress. In the elastic region, irrespective of the phase field variable ϕ, the material exhibits purely elastic behavior with no degradation of stiffness. Conversely, in the fracture region, the stress and stiffness are entirely degraded due to phase field evolution, such that when $\phi = 1$, a traction-free crack is present.

In the frictional region, the material's stiffness becomes anisotropic, reflecting a partial degradation of stress and stiffness caused by the phase field evolution. This anisotropic response is further characterized by the fact that increased pressure leads to higher shear stress. When $\phi = 1$, the stress lies on the failure criterion $\sqrt{J_2(\boldsymbol{\sigma})} = BI_1(\boldsymbol{\sigma})$.

In the frictionless region, the material behavior is analogous to the volumetric-deviatoric decomposition discussed in Section 2.2.6. For $\phi = 1$, the material can sustain hydrostatic stress; however, it lacks the stiffness required to transfer shear stress.

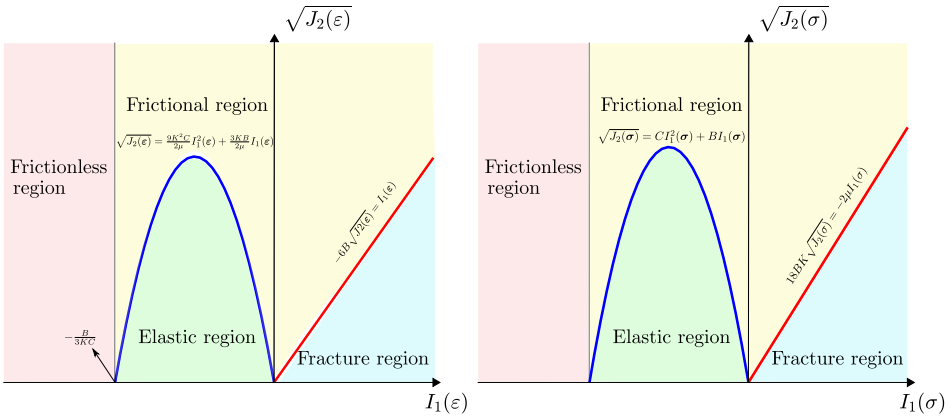

Figure 3.8: Elastic, frictional, frictionless and fracture regions of Drucker-Prager based model, (a) strain space $(I_1(\boldsymbol{\varepsilon}), \sqrt{J_2(\boldsymbol{\varepsilon})})$, and (b) stress space $(I_1(\boldsymbol{\sigma}), \sqrt{J_2(\boldsymbol{\sigma})})$.

Based on the division of the strain space described above, the invariants of the elastic strain for these regions are defined as follows:

$$I_1(\boldsymbol{\varepsilon}_e) = \begin{cases} I_1(\boldsymbol{\varepsilon}) & \text{for } \sqrt{J_2(\boldsymbol{\varepsilon})} \leq \frac{9K^2C}{2\mu} I_1^2(\boldsymbol{\varepsilon}) + \frac{3KB}{2\mu} I_1(\boldsymbol{\varepsilon}) \text{ or } I_1(\boldsymbol{\varepsilon}) < -\frac{B}{3KC} \\ \frac{1}{18K}\sqrt[3]{\frac{4}{K}\Delta} + K\sqrt[3]{2K}\frac{Z}{\Delta} - \frac{2B}{9CK} & \text{for } \sqrt{J_2(\boldsymbol{\varepsilon})} \geq \frac{9K^2C}{2\mu} I_1^2(\boldsymbol{\varepsilon}) + \frac{3KB}{2\mu} I_1(\boldsymbol{\varepsilon}) \text{ and } \sqrt{J_2(\boldsymbol{\varepsilon})} \geq -\frac{I_1(\boldsymbol{\varepsilon})}{6B} \\ 0 & \text{for } \sqrt{J_2(\boldsymbol{\varepsilon})} \leq -\frac{I_1(\boldsymbol{\varepsilon})}{6B}. \end{cases} \tag{3.40}$$

Similarly, the second invariant of the deviatoric part of the elastic strain is given by:

$$\sqrt{J_2(\boldsymbol{\varepsilon}_e)} = \begin{cases} \sqrt{J_2(\boldsymbol{\varepsilon})} & \text{for } \sqrt{J_2(\boldsymbol{\varepsilon})} \leq \frac{9K^2C}{2\mu} I_1^2(\boldsymbol{\varepsilon}) + \frac{3KB}{2\mu} I_1(\boldsymbol{\varepsilon}) \\ \frac{9K^2C}{2\mu} I_1^2(\boldsymbol{\varepsilon}_e) + \frac{3KB}{2\mu} I_1(\boldsymbol{\varepsilon}_e) & \text{for } \sqrt{J_2(\boldsymbol{\varepsilon})} \geq \frac{9K^2C}{2\mu} I_1^2(\boldsymbol{\varepsilon}) + \frac{3KB}{2\mu} I_1(\boldsymbol{\varepsilon}) \text{ and } \sqrt{J_2(\boldsymbol{\varepsilon})} \geq -\frac{I_1(\boldsymbol{\varepsilon})}{6B} \\ 0 & \text{for } \sqrt{J_2(\boldsymbol{\varepsilon})} \leq -\frac{I_1(\boldsymbol{\varepsilon})}{6B} \text{ or } I_1(\boldsymbol{\varepsilon}) < -\frac{B}{3KC}. \end{cases} \tag{3.41}$$

The isolines of the undamaged strain energy, ψ_0, the dissipated part of the strain

energy, ψ_d, and the stored part, ψ_s, are illustrated in Figure 3.9. Let us consider a strain state, $\left(I_1(\boldsymbol{\varepsilon}), \sqrt{J_2(\boldsymbol{\varepsilon})}\right)$, within the frictional region. Based on Equation (3.15), the strain invariants can be decomposed into the invariants of the elastic part and the damaged part of the strain.

As shown in Figure 3.9, the elastic strain lies on the failure surface, while the difference between the total strain and the elastic strain represents the damaged part of the strain. The vectors of invariants corresponding to the elastic and damaged components of the strain point towards the isoline of the isotropic linear elastic form of the strain energy, represented by the semi-oval shape in Figure 3.9.

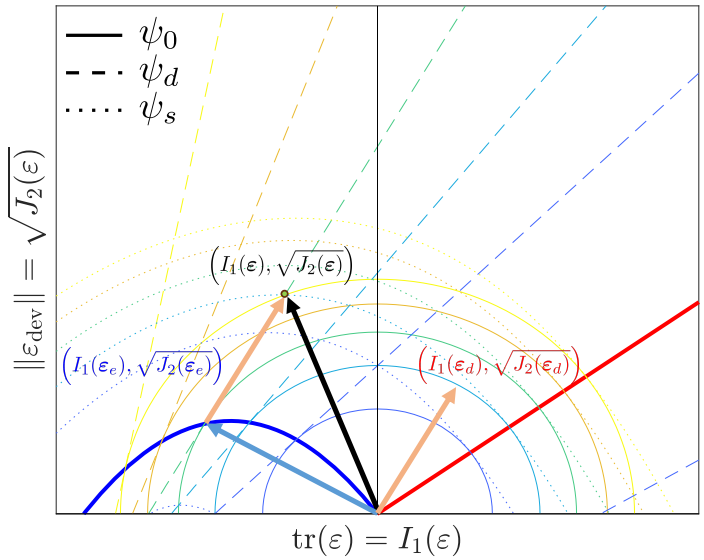

Figure 3.9: Strength surface of Bresler-Pister failure criteria in the space of invariants of strain. The vector shows the decomposition of total tensor into elastic and damage parts.

To better represent the path of the elastic stress $\boldsymbol{\sigma}_e$, and the total stress $\boldsymbol{\sigma}$ a simulation experiment is conducted on a single 3D element with $\phi = 1$ to ensure that it adheres to the behavior of the failure surface ($\boldsymbol{\sigma} = \boldsymbol{\sigma}_e$). AT2 model is used for this analysis. The elasticity parameters, including Young's modulus $E = 25$

GPa and Poisson's ratio $\nu = 0.2$, are considered. The uniaxial tensile strength $\sigma_t = 3.5$ MPa, the uniaxial compressive strength $\sigma_c = 25$ MPa, and the biaxial compressive strength $\sigma_b = 30$ MPa are used, resulting in the strength parameters $B = -0.5551$ and $C = -0.0056$ MPa^{-1}.

Four different scenarios are considered for the stress path of the undamaged configuration $\boldsymbol{\sigma}_0$ under appropriate boundary conditions. Figure 3.10 illustrates the results of these simulations. In Figure 3.10a, the boundary conditions were designed such that $\boldsymbol{\sigma}_0$ starts in the elastic region, transitions into the frictional region, and finally ends in the frictionless region. As observed, $\boldsymbol{\sigma}_e$ coincides with $\boldsymbol{\sigma}_0$ until it reaches the surface strength. Upon transitioning into the frictional region, $\boldsymbol{\sigma}_e$ follows the surface strength until $\boldsymbol{\sigma}_0$ reaches the frictionless region. In the frictionless region, $\boldsymbol{\sigma}_e$ transforms into hydrostatic stress since the material cannot sustain shear stresses.

In Figure 3.10b and Figure 3.10c, $\boldsymbol{\sigma}_0$ starts in the frictional region, above the surface strength, causing $\boldsymbol{\sigma}_e$ to follow the surface strength. In the last case (Figure 3.10d), when $\boldsymbol{\sigma}_0$ is in the fracture region, the overall stiffness of the material degrades, leading to $\boldsymbol{\sigma}_e$ becoming zero throughout this region.

Additionally, the mapping of $\boldsymbol{\sigma}_0$ to $\boldsymbol{\sigma}_e$ is shown for selected stress states in Figure 3.10. The isolines of the stored part of the strain energy, ψ_s, are depicted for these selected stress points. As observed, the lines connecting $\boldsymbol{\sigma}_0$ to $\boldsymbol{\sigma}_e$ are tangent to the isolines of the stored part of the strain energy ψ_s.

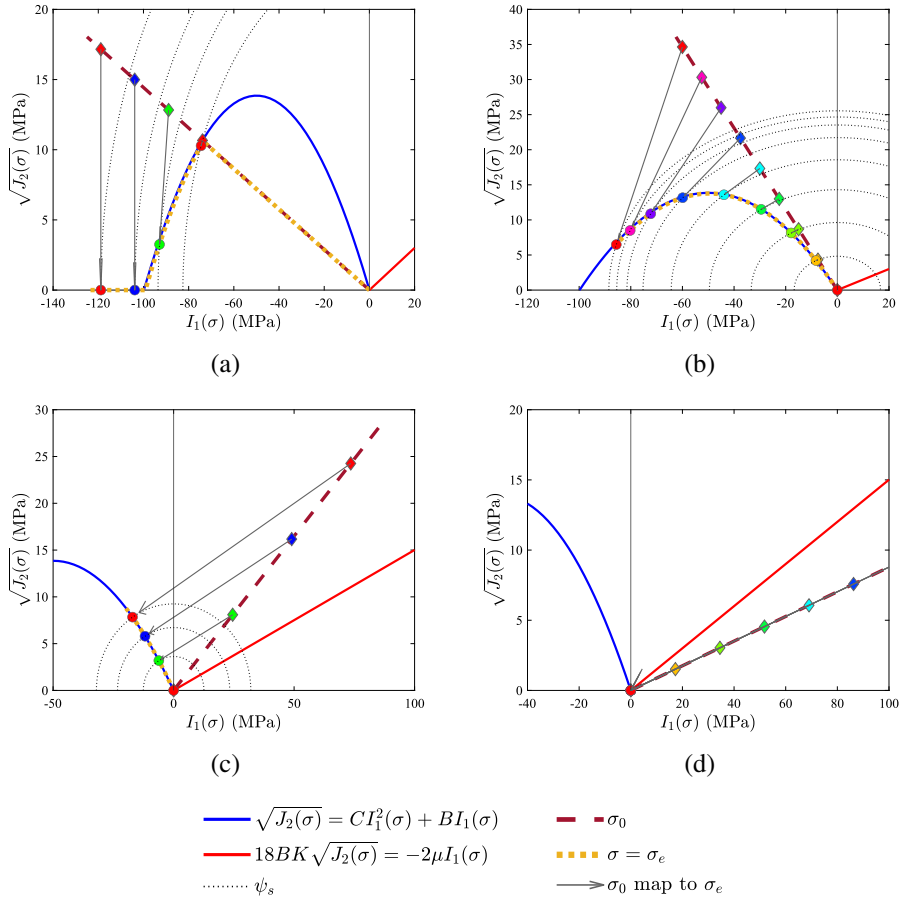

Figure 3.10: Comparison of the stress paths of the undamaged stress $\boldsymbol{\sigma}_0$ and the elastic part of the stress $\boldsymbol{\sigma}_e$ in the invariant stress space $\left(I_1(\boldsymbol{\sigma}), \sqrt{J_2(\boldsymbol{\sigma})}\right)$ for a 3D single element with $\phi = 1$: (a) starting from the elastic region, transitioning into the frictional region, and finally entering the frictionless region; (b), (c) within the frictional region; and (d) within the fracture region.

The Bresler-Pister model is also evaluated under loading-unloading conditions. A 3D single element is considered, with the phase field value $\phi = 0$ at the beginning of the analysis, unlike the previous example. Four scenarios are analyzed, and the results are depicted in Figure 3.11, comparing the undamaged stress $\boldsymbol{\sigma}_0$, the total stress $\boldsymbol{\sigma}$, and the elastic part of the stress $\boldsymbol{\sigma}_e$.

In Figure 3.11a, all stresses are aligned in the elastic region during loading. As the

strength surface is crossed, phase field evolution begins, causing the total stress to degrade, as indicated by the color representing the phase field value. During unloading, the stress path is linear until it touches the strength surface. Beyond this point, the stress path follows the strength surface until it reaches the point where $\boldsymbol{\sigma}_0 = \boldsymbol{\sigma}_e$. At this stage, the stress path re-enters the elastic region and exhibits elastic behavior.

For cases where the stress path of $\boldsymbol{\sigma}_0$ lies within the frictional region (Figure 3.11b, c), damage evolution begins at the outset. In Figure 3.11b, the total stress path follows the strength surface after intersecting it during unloading. Conversely, in Figure 3.11c, if the total stress does not intersect the strength surface, it decreases linearly.

When the stress path of $\boldsymbol{\sigma}_0$ is in the fracture region (Figure 3.11d), all components of the stress tensor degrade. As a result, $\boldsymbol{\sigma}_0$ and $\boldsymbol{\sigma}$ are aligned during both loading and unloading phases.

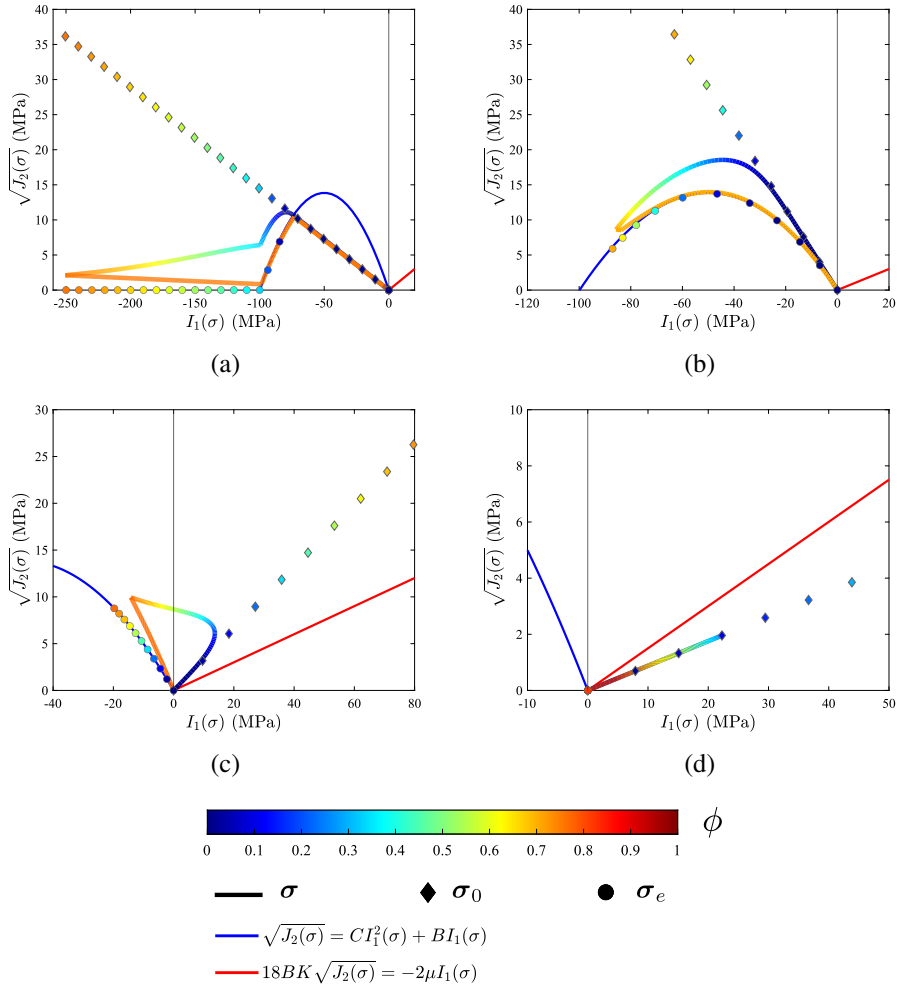

Figure 3.11: Comparison of the stress paths of the total stress $\boldsymbol{\sigma}$, the undamaged stress $\boldsymbol{\sigma}_0$, and the elastic part of the stress $\boldsymbol{\sigma}_e$ in the invariant stress space $\left(I_1(\boldsymbol{\sigma}), \sqrt{J_2(\boldsymbol{\sigma})}\right)$ under loading-unloading conditions for a 3D single element: (a) starting in the elastic region, transitioning into the frictional region, and finally entering the frictionless region; (b), (c) within the frictional region; and (d) within the fracture region. The phase field values are represented by color.

Finally, we simulate the multiaxial loading of concrete using a Bresler-Pister-based model. In this test, a rectangular concrete sample is subjected to multiaxial stress. As shown in Figure 3.12a, the sample is loaded using two steel jaws ($E = 210$ GPa and $\nu = 0.3$), the bottom jaw remains fixed, while the top jaw is subjected

to displacement u. Additionally, traction t is applied to two sides of the sample to create a multiaxial stress state. The material's elastic properties of the sample are characterized by a Young's modulus $E = 25$ GPa and Poisson's ratio $\nu = 0.2$. The concrete's tensile strength is $\sigma_t = 3.5$ MPa, its uniaxial compressive strength is $\sigma_c = 25$ MPa, and its biaxial compressive strength is $\sigma_b = 30$ MPa. The failure surface parameters are $B = -0.5551$ and $C = -0.056$ MPa^{-1}. The fracture properties are defined by a critical fracture energy $G_c = 0.15$ N/m and a characteristic length scale $\ell = 2$ mm. A monolithic scheme is employed in this case study.

The crack propagation path is illustrated using the phase field contour in Figure 3.12b, which exhibits a similar pattern across all cases. Additionally, the corresponding load-displacement curves are presented in Figure 3.12c. It is evident from the results that an increase in confinement leads to a higher peak load when employing the Bresler-Pister-based split formulation. This observation underscores the influence of confinement on the material's mechanical response, further validating the robustness of the chosen modeling approach.

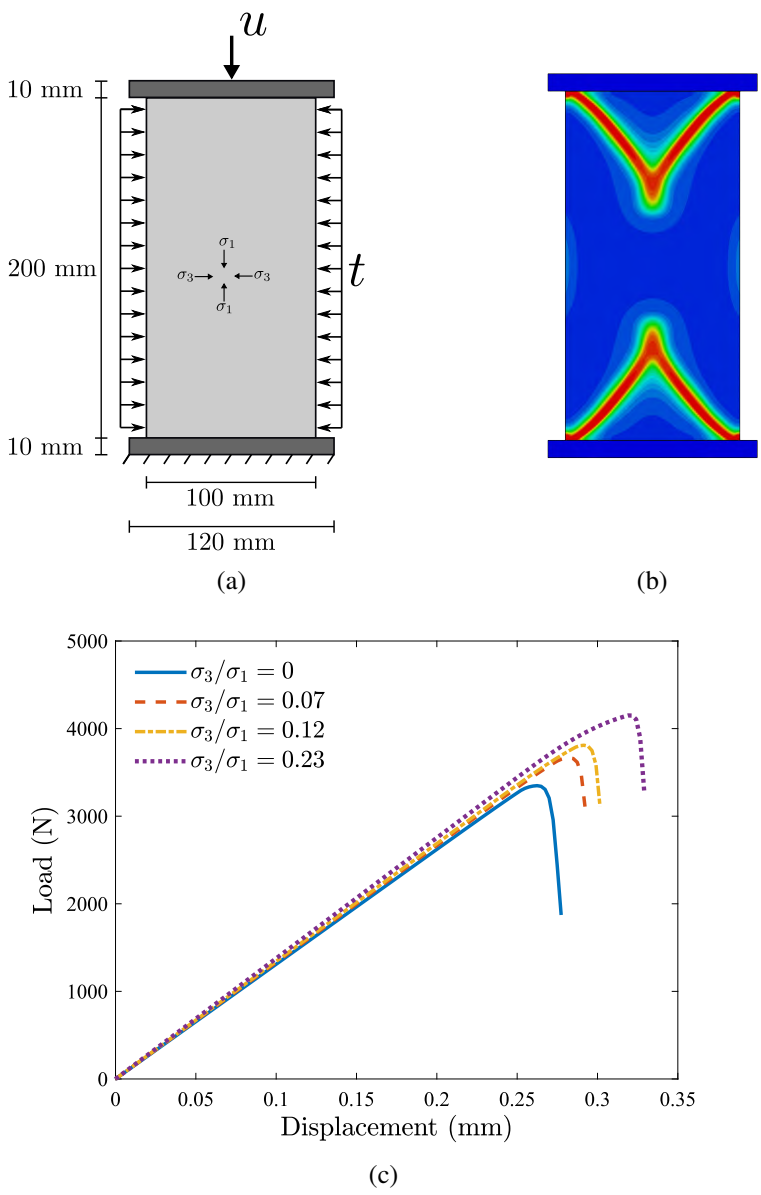

Figure 3.12: Multi-axial compression test on concrete, (a) Boundary conditions and geometry, (b) phase field contour, and (c) comparison of load versus displacement for different case of multiaxial loading.

3.4.4 Strain energy split for material with voids and inclusions

Rock-like materials often contain micro-voids and inclusions that act as stress concentrators, facilitating crack propagation under stress and thereby weakening the material. Over time, the coalescence of these micro-voids and inclusions can lead to macroscopic fractures or material failure. However, the current strain energy splits do not account for this effect when material failure occurs due to mechanisms of volumetric compaction ($I_1(\boldsymbol{\varepsilon}) < 0$). For example, when considering a square domain with voids under pure compression and applying the volumetric-deviatoric split, fractures form between voids under compression (Figure 3.13). In contrast, if the material without explicitly defining the voids is modeled, no degradation in stiffness is observed, underscoring a limitation of current models in accurately capturing the role of voids in fracture under compressive loading.

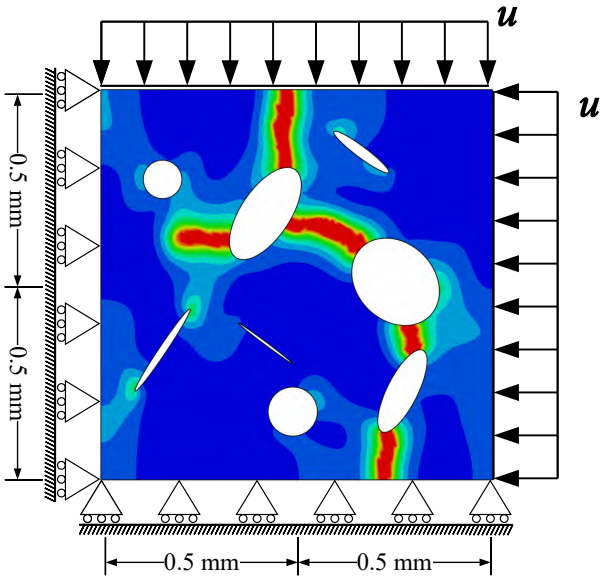

Figure 3.13: Phase field contour of square domain with voids under compression.

However, explicitly defining micro-voids is impractical due to the high compu-

tational cost associated with the requirement for very small element sizes. To address this, the volumetric-deviatoric split is modified to account for the effect of inclusions by introducing a parameter a, which represents the contribution of volumetric compaction to the fracture driving force [55]. The dissipated and stored parts of the strain energy can then be redefined as follows:

$$\begin{aligned} \psi_d(\boldsymbol{\varepsilon}) &= \left(\tfrac{1}{2}K - a\right)\langle I_1(\boldsymbol{\varepsilon})\rangle_+^2 + \left(\tfrac{2}{3}\mu + a\right) I_1^2(\boldsymbol{\varepsilon}) - 2\mu I_2(\boldsymbol{\varepsilon}) \\ \psi_s(\varepsilon) &= \left(\tfrac{1}{2}K - a\right)\langle I_1(\boldsymbol{\varepsilon})\rangle_-^2 \end{aligned} \quad , \tag{3.42}$$

where material constant $0 \leq a \leq \frac{1}{2}K$ to ensure a non-negative fracture driving force. As shown in Equation (3.42), the parameter a represents a fraction of the bulk modulus that accounts for the contribution of voids. By selecting $a = 0$, Equation (3.42) reduces to the standard volumetric-deviatoric split of strain energy (Equation (2.48)), while setting $a = 0.5K$ results in no strain energy split. Any value of a between these limits allows for the modeling of the effects of voids and inclusions.

To investigate the effect of the parameter a, a square domain with an inclined crack at the center is subjected to uniaxial compression is considered, as depicted in Figure 3.14a. Three distinct values of the parameter are considered: $a = \{0, 0.45K, 0.5K\}$. The phase field contours for these three models are illustrated in Figure 3.14b–c. As shown, when the volumetric-deviatoric split [45] ($a = 0$) is applied, the crack propagation direction remains nearly parallel to the pre-existing initial crack, indicating that fracture occurs predominantly due to shear failure. However, by increasing the parameter a, the effect of voids and inclusions is more pronounced. Figure 3.14c demonstrates that the crack propagation path forms a lower angle with the horizontal compared to the initial inclined crack, indicating the combined influence of both shear and compressive forces

due to the presence of voids and inclusions. Finally, when no split is applied ($a = 0.5K$), the failure occurs primarily under compression, with the crack propagating almost horizontally.

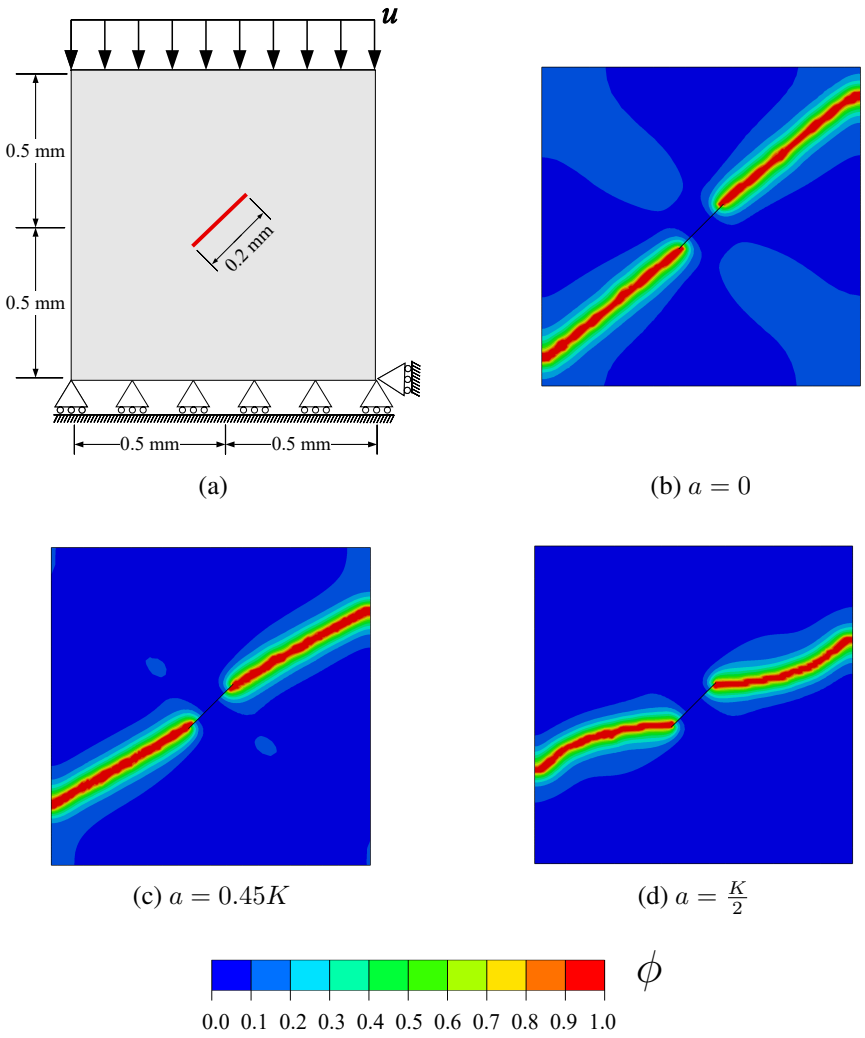

Figure 3.14: Square domain with inclined crack at the center subjected under uniaxial compression, (a) geometry, dimensions and boundary conditions. phase field contour to show crack path for, (b) volumetric-deviatoric split $a = 0$ [45], (c) $a = 0.45K$, and (d) no split of strain energy $a = 0.5K$.

The force versus displacement of this three different value of parameter a are compared in Figure 3.15. The volumetric-deviatoric split $a = 0$ shows the highest

peak load due to considering just distortion energy as fracture driving force. by increasing the value of parameter a, the effect of inclusions and voids are coming to play a roll and contribute the compression to fracture driving force additional to shear energy. The peak load related to the case of no split of strain energy when the material fail under compression in this case study.

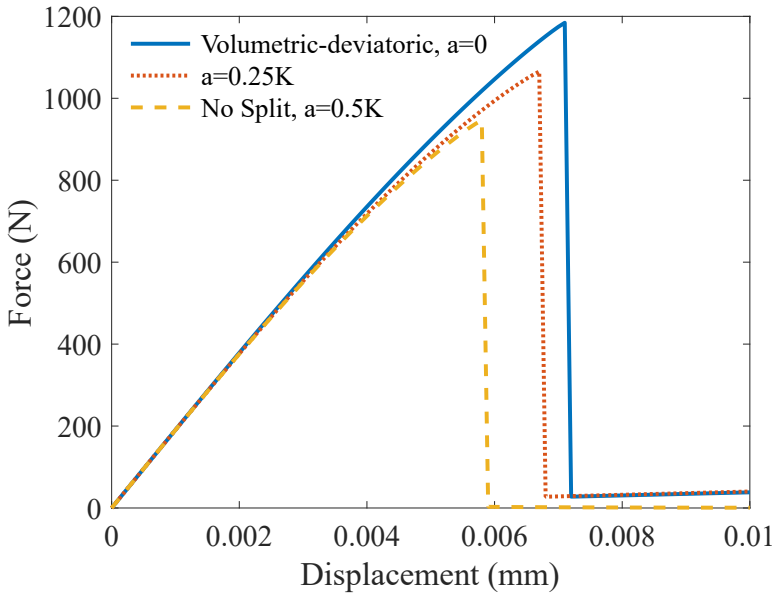

Figure 3.15: Comparison of the force versus displacement of square domain with inclined crack at the center subjected under uniaxial compression for volumetric-deviatoric split $a = 0$ [45], $a = 0.45K$, no split of strain energy $a = 0.5K$.

3.4.5 Conclusions

A comprehensive framework is developed for determining the strain energy decomposition associated with various constitutive behaviors and failure criteria. This advancement is crucial for phase field fracture modeling, as it enables the integration of multi-axial failure surfaces, thereby accurately capturing crack nucleation across a wide range of materials. This capability is particularly essential

for predicting the compressive failure of brittle and quasi-brittle solids, such as concrete and geomaterials. To demonstrate the efficacy of the proposed framework, this method is applied specifically to the Drucker-Prager model and the Bresler-Pister failure surface. This approach paves the way for incorporating multi-axial failure criteria into phase field fracture modeling, significantly enhancing the model's predictive power and broadening its applicability in various engineering and material science domains. Additionally, a new strain energy split is developed for materials with voids and inclusions, where compression can significantly contribute to failure.

3.5 Multiphysics phase field fracture method

The multiphysics phase field method has emerged as a versatile computational tool for simulating fracture processes involving interactions between multiple physical phenomena, such as thermal, hydraulic, and chemical processes. This approach extends traditional phase field modeling by incorporating the coupling of mechanical deformation with other fields, allowing for the simulation of complex fracture behaviors in various materials and loading conditions. In this thesis, we investigate phase-field modeling for thermal fracture and hydraulic fracture. Furthermore, we present our generalized approach for modeling hydrogen embrittlement and stress-corrosion cracking, demonstrating its applicability to these complex fracture mechanisms. For a detailed explanation of the implementation and examples, refer to Appendix F [56]. Here, we briefly review the fundamental equations governing thermal fracture and hydraulic fracture.

3.5.1 Thermal fracture modeling

In thermal fracture modeling, the phase field method is applied to simulate crack propagation under thermo-mechanical loading (see Section 3.1 of Appendix F). The strain tensor is decomposed into an elastic component and a thermal component, allowing stress to be calculated solely from the elastic strain. Heat transfer is coupled with the phase field evolution by considering thermal conductivity as a function of the phase field variable, thus modeling heat flow through cracks [88–90]. This coupling facilitates the prediction of crack initiation and propagation in materials subjected to thermal gradients. The heat transfer equation can be expressed as:

$$\rho c_\theta \dot{\theta} + k_\theta(\phi)\Delta\theta = q_\theta \tag{3.43}$$

where ρ is the density, c_θ is specific heat, k_θ is thermal conductivity wiht is degraded by phase field evolution, and q_θ is the heat source.

3.5.2 Hydraulic fracture simulation

The phase field method has also been adapted for hydraulic fracture modeling (see Section 3.2 of Appendix F). Here, the fluid flow is coupled with the mechanical and fracture processes using poroelasticity theory, which governs the fluid pressure evolution and its interaction with the deformation of the solid matrix [91–97]. There are different method for coupling fluid flow into phase field, such the approach divides the domain into different regions (reservoir, fracture, and transition zones) and adjusts material properties accordingly to capture the influence of fluid injection on crack growth. The fluid flow equation is defined as follows:

$$\rho_{fl}\left(S(\alpha(\phi),\varepsilon_p(\phi))\dot{p}+\alpha(\phi)\chi_r(\phi)\dot{\varepsilon}_{vol}\right)+\nabla\cdot\left(-\rho_{fl}\frac{\boldsymbol{K}_f l(\phi)}{\mu}\nabla p\right)=q_m \quad (3.44)$$

where ρ_{fl} is the density of fluid, α is Biot's coefficient, ε_p is porosity, S is storage coefficient, p is fluid pressure and χ_r is reservior domain indicator and q_m is source fluid.

3.5.3 Implementation in Abaqus

The phase field fracture method is implemented in the ABAQUS FEA package using a heat transfer analogy with UMAT and UMATHT subroutines, avoiding the need for user element subroutines (UEL) [51, 52]. This implementation at the integration point level leverages ABAQUS's built-in features, including various element types and contact algorithms, enabling phase field fracture modeling through a heat transfer analogy.

UMATHT offers advantages over using UMAT alone by supporting a general form of diffusion equations and allowing transient analysis. Both UMAT and UMATHT utilize definitions of the heat source, internal heat energy, and heat flux to construct the residual vector and stiffness matrix, along with their derivatives with respect to temperature and its gradient.

For modeling multiphysics problems, such as coupled mechanical, phase field, and diffusion processes, an additional degree of freedom (DOF), η, is introduced using a thermal analogy. This is achieved by creating a secondary part (PART-2) that mirrors the primary part's (PART-1) geometry and mesh but with distinct material properties. The temperature DOF in PART-1 represents the phase field ($\phi \equiv \theta$), while in PART-2, it represents η ($\eta \equiv \theta$). The use of conjugate element

pairs allows for data exchange between the two parts, effectively introducing additional DOFs in the model.

The procedure begins with the UMAT subroutine to compute the Cauchy stress and material Jacobian, followed by UMATHT for heat-related calculations. In PART-2, where displacement DOFs are not considered, the stress and Jacobian are set to zero to ensure zero residual and stiffness. Data transfer between subroutines is facilitated by state variables (SDVs) and FORTRAN modules, with SDVs enabling data exchange within the same material.

Different solution schemes are employed: a monolithic (implicit) approach is used for equations within the same part, while a staggered (explicit) approach is applied for inter-part coupling. The staggered scheme sequentially updates variables, with options for a single-pass scheme (more robust, requiring smaller increments) and a multi-pass scheme (requiring more iterations for convergence but allowing larger increments).

3.5.4 Multiphysics phase field validation

To validate the phase field modeling approach, several representative examples were analyzed, including thermo-mechanical fracture (Section 5.1 of Appendix F), hydraulic fracture (Section 5.2 of Appendix F), hydrogen embrittlement (Section 5.3 of Appendix F), and stress-assisted corrosion (Section 5.4 of Appendix F). These examples demonstrate the model's accuracy in capturing complex fracture behavior and are compared with experimental data or analytical solutions.

- **Thermo-mechanical fracture, quenching**: This case study simulates the thermal shock fracture of a ceramic plate during quenching (Section 5.1 of Appendix F). The aim is to validate the phase field thermal fracture model

by comparing it with experimental results [98]. The simulation captures crack initiation and propagation due to the high temperature gradient, showing good agreement with experimental observations (Figure. 4 of Appendix F). The study also compares results with and without degraded thermal conductivity, revealing that non-degraded conductivity produces better matches with experimental data.

- **Hydraulic fracture**: Two case studies are presented to validate the phase field hydraulic fracture model (Section 5.2 of Appendix F). The first case involves a pressurized crack in a square domain to determine the critical pressure for crack propagation. The results are compared to analytical solutions, showing good agreement (Figure. 7 of Appendix F). The second case explores crack interaction in a square domain with two pre-existing cracks under fluid injection. The results highlight how the phase field method captures the evolution of crack interaction and pressure distribution effectively (Figure. 9 of Appendix F).

These validation cases confirm the robustness of the phase field approach for modeling different types of fractures under various physical conditions (Figure 3.16).

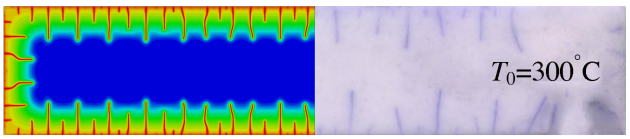

(a)

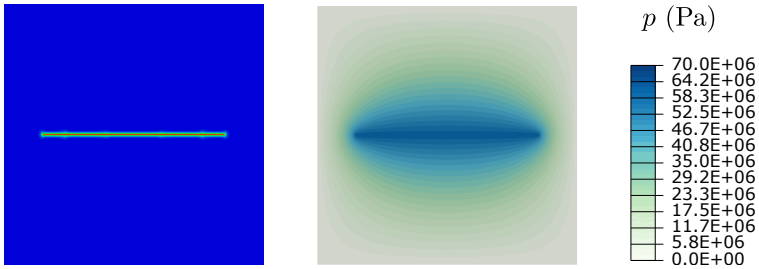

(b) Time=1200 sec, $p_{\text{center}} = 60$ MPa

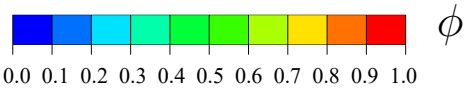

Figure 3.16: Phase field multiphysics: (a) comparison of phase field contour (at the left) and crack pattern from experiments [98] of quenching, and (b) phase field contours and pressure for a pressurized crack at Time=1200 sec, $p_{\text{center}} = 60$ MPa of pressurized crack.

3.6 Hydraulic phase field fracture modeling

Hydraulic fracturing plays a pivotal role in industries such as petroleum engineering and geothermal energy extraction, motivating extensive research across theoretical, numerical, and experimental domains. The phase field fracture method has emerged as a powerful tool for modeling hydraulic fractures, especially due to its ability to handle complex crack propagation without requiring explicit crack tracking. Bourdin *et al.* [99] pioneered the application of phase field methods in hydraulic fracturing, and subsequent researchers have refined these techniques to enhance their applicability [93, 95, 96, 100–103].

In this work (Appendix G, [57]), our previous phase field hydraulic fracture im-

plementation is extended, as described in Section 3.5.2. This extension introduces new strategies and modifications to existing methods for coupling the phase field variable with the permeability tensor. Additionally, the impact of various strain energy decomposition methods is investigated on fracture propagation. Furthermore, the proposed Drucker-Prager-based strain energy split is applied to demonstrate the ability of the phase field model to capture stick-slip behavior, a phenomenon critical in geotechnical engineering problems, such as fault activation induced by pore pressure changes. This paper aims to advance the implementation of the phase field fracture method in Abaqus, utilizing UMAT and UMATHT subroutines to address the complexities of damage evolution and pore pressure in hydraulic fracturing.

Key contributions of this work include:

- The development of a coupled phase field and poroelasticity model for hydraulic fractures, grounded in Biot's theory of poroelasticity.
- A comprehensive analysis of strain energy decomposition into stored and dissipative components, essential for accurately capturing fracture evolution in hydraulic fracturing scenarios.
- An in-depth exploration of various methods for coupling fluid flow and fracture mechanics, including domain decomposition and permeability modeling strategies.

This framework enhances existing methods by incorporating features such as anisotropic permeability and a Drucker-Prager split, which better represent the interaction between fluid pressure and rock mechanics. This advancement is crucial in fields like reservoir engineering and fault activation.

3.6.1 Methodology

Our phase field hydraulic fracture implementation in Abaqus was extended using the UMAT and UMATHT subroutines, as detailed in Section 3.5.3. two primary coupling methods for integrating the phase field evolution equation with the fluid flow equation are explored. The first method is based on the work of Lee *et al.* [101], and has been widely adopted in studies such as [104, 105]. This method divides the domain into three regions—the reservoir (Ω_r), fracture (Ω_f), and transient (Ω_t)—using linear domain indicators χ_r and χ_f to to be defined permeability as a function of phase field variable ϕ. The second method, proposed by Miehe *et al.* [100], employs a Poiseuille-type flow model by modifying Darcy's law to capture fluid flow within cracks. Our contribution introduces a novel hybrid approach that combines the advantages of these two methods while addressing their limitations.

Also, the effects of different strain energy decompositions are examined, as described in Section 2.2.6, to assess their influence on phase field hydraulic fracture modeling. Furthermore, the phase field hydraulic fracture implementation is extended to include the Drucker-Prager based split, broadening its applicability to geotechnical engineering problems such as fault activation.

The methodology centers around a phase field fracture model implemented in Abaqus, eliminating the need for explicit crack tracking and enabling the simulation of complex crack propagation behaviors.

3.6.2 Key results and sindings

Four case studies are presented which explore the impact of permeability coupling on crack behavior, stick-slip modeling, crack interaction under different energy

splits, and multiaxial stress conditions. These case studies highlight the model's ability to capture fracture behavior across diverse conditions and geometries. The key findings include:

- **Coupling strategies**: Three different methods for coupling fluid flow and phase field variables were evaluated, each with distinct advantages (Section 4.1 of Appendix G). The domain decomposition method [101] is robust but does not account for anisotropic permeability or crack opening effects. The modified Darcy method [100] addresses these effects but poses numerical challenges due to the anisotropic nature of permeability. The mixed method, which combines these two approaches, was found to offer the best balance between flexibility and accuracy.

- **Drucker-Prager fracture model**: The inclusion of a Drucker-Prager-based phase field model (Section 4.2 of Appendix G) enabled the simulation of stick-slip behavior, commonly observed in fault activation scenarios. The stress path for different scenarios was analyzed to demonstrate the effects of varying stress states on fracture propagation.

- **Effect of strain energy decomposition**: By applying different strain energy decomposition techniques, it is observed how tensile and shear energies drive crack propagation differently (Section 4.3 of Appendix G). Spectral decomposition led to more tensile-driven fracture behavior, while the Drucker-Prager model better captured shear-driven fracture propagation.

Figure 3.17 shows selected result from our investigation including the comparison of crack path (at the left)in crack interaction problem for various strain energy split and fluid pressure distribution and fluid flux vector at the right for the case wihtiout decomposition of strain energy (Figure 3.17a). The crack path using contour of phase field is shown for simultaneous injection into a axisymetric boundary

with inital stress in (Figure 3.17b).

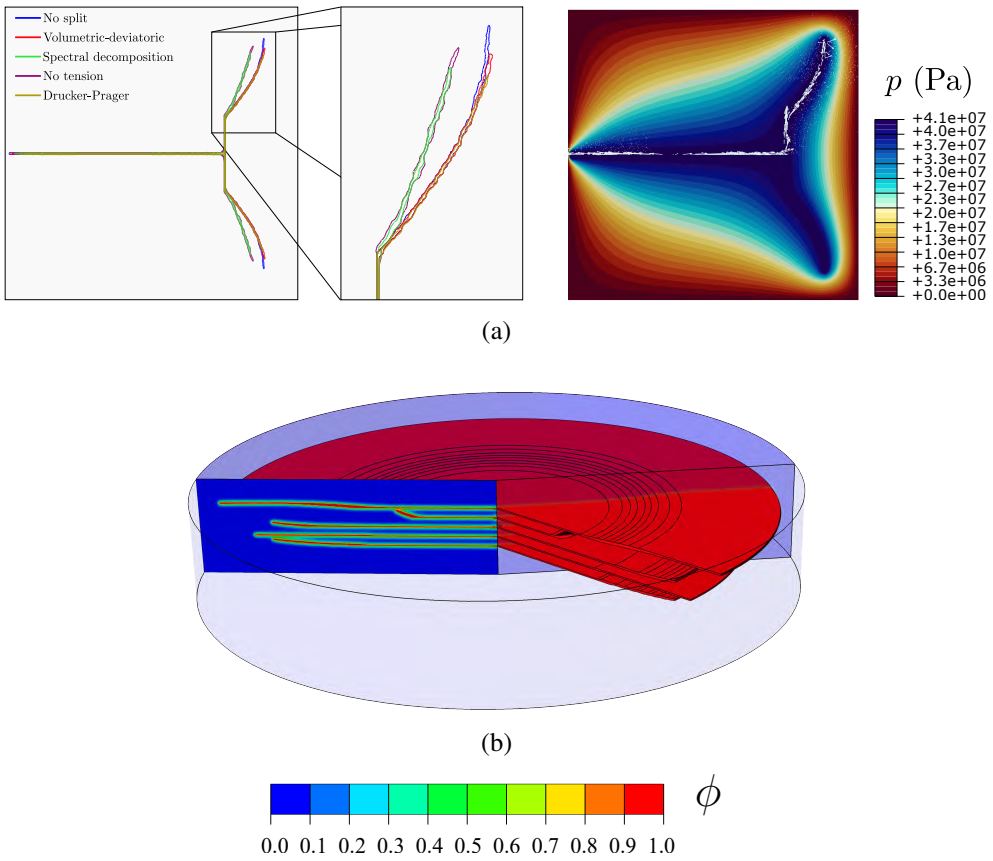

Figure 3.17: Hydraulic fracture, (a) Crack-interaction, at the left: crack path for different fracture driving forces and at the right: fluid pressure p contour and fluid flux vector for the steady state of the case without strain energy decomposition, and (b) contour of phase field of s simultaneous injection into a axisymetric boundary with inital stress case study.

3.6.3 Practical applications

The implementation of the phase field hydraulic fracture model in Abaqus holds significant potential for practical applications in reservoir engineering, geothermal energy, and fault activation scenarios. The use of UMAT and UMATHT subroutines enables seamless integration into Abaqus (see Section 6 of Appendix G), eliminating the need for user element subroutines (UEL) and facilitating indus-

trial adoption. Moreover, the mixed coupling method offers a more accurate and flexible approach to modeling fluid-driven fracture propagation in porous media.

Additionally, the inclusion of pre-configured case studies and the framework's ability to handle complex boundary conditions—such as multiaxial stresses and fluid injection—make it a valuable tool for engineers and researchers working on hydraulic fracturing problems.

3.6.4 Conclusion

This work presents a flexible and comprehensive approach to modeling hydraulic fractures using the phase field method within Abaqus. By coupling fluid flow with fracture mechanics and incorporating a variety of constitutive models, the framework enables accurate simulation of complex fracture phenomena in geomechanical contexts. The robustness of the implementation and its ease of integration into Abaqus make it a valuable resource for future research and practical applications in hydraulic fracturing and subsurface engineering.

4 | CONCLUSIONS

This thesis has advanced the field of fracture mechanics by focusing on the application and extension of the phase field fracture method, specifically in the modeling of rock-like materials under complex loading conditions. The research presented here has made significant contributions to both theoretical and practical aspects of fracture modeling, addressing key challenges in simulating compressive failure modes, multiphysics coupling, and the validation of tensile strength measurements from the Brazilian test. This chapter summarizes the major findings and highlights the contributions to the field.

4.1 Key Findings

The primary contributions of this thesis can be summarized as follows:

- **Validation of the Brazilian test:** The study on the Brazilian test has revealed significant limitations in traditional tensile strength measurements for rock-like materials, challenging prevailing assumptions about crack initiation and the validity of test geometries. Through finite element analysis and the application of the Griffith criterion, it was shown that cracks do not consistently originate at the center of the test disk, contrary to what widely accepted standards suggest. The research introduced a novel methodology to validate Brazilian test outcomes, including the development of a MATLAB App (BrazVal) and validity maps that provide a more accurate assessment of tensile strength by identifying optimal testing conditions. Key findings indicate that the use of jaws with large radii promotes crack initiation in compressive regions away from the disk's center, invalidating test

results. Furthermore, crack location is highly sensitive to testing geometry and, to a lesser extent, the sample's stiffness, while Poisson's ratio and friction play minimal roles in most configurations. By mapping critical load against stress states at the disk center, this work enables more precise tensile strength estimates, eliminating reliance on Hondros's equation and offering a two-step protocol for experimental validation. These insights will allow researchers to determine the suitable test conditions, thus advancing the accuracy and reliability of tensile strength measurements in rock-like materials.

- **Implementation of phase field models in Abaqus:** A unified implementation of the phase field fracture model has been developed within Abaqus using a UMAT subroutine, which eliminates the complexities associated with using user element subroutines and simplifies pre- and post-processing. This versatile approach leverages Abaqus's built-in capabilities, enabling seamless application to 2D, 3D, and axisymmetric problems. The implementation supports both staggered and monolithic solution schemes, enhancing flexibility for diverse fracture modeling needs. Additionally, it allows for the integration of any constitutive model of the phase field approach, including AT1, AT2, and PF-CZM, with various strain energy decomposition methods. This setup accommodates both hybrid and anisotropic formulations, offering a robust toolset for phase field fracture analysis across a broad range of applications.

- **Phase field fracture verification:** The phase field fracture model was validated through a series of case studies, including both established examples from literature and newly designed tests, demonstrating the implementation's robustness in handling complex fracture scenarios. Results consistently showed that the model accurately simulates fracture propagation un-

der tensile, shear, and mixed loading conditions in both 2D and 3D configurations. This consistent accuracy across various fracture modes highlights the capability of the implementation to model complex fracture processes reliably, showcasing its effectiveness for diverse applications in fracture mechanics. However, a notable limitation is that the conventional phase field model was not originally designed to model failure under compressive loading.

- **Constitutive phase field fracture modeling:** A novel generalized framework for strain energy decomposition has been introduced, advancing the phase field fracture method's ability to accurately model compressive failure in rock-like materials. This framework integrates the Drucker-Prager failure criterion, enabling the simulation of a wider range of fracture behaviors and addressing limitations in traditional methods for modeling compressive fractures—a common and complex issue in rock mechanics. The Drucker-Prager based strain energy split successfully captures essential rock-like behaviors, such as dilatancy, confinement, and friction, creating a more realistic representation of these materials under stress. Furthermore, a new strain energy formulation has been developed to effectively simulate materials with voids and inclusions, expanding the model's capabilities in complex geological and material science applications. The efficacy of the developed model has been demonstrated through case studies, including Direct Shear Tests, uniaxial and triaxial compression tests of concrete, and the localized failure of soil slopes—all scenarios that were challenging to simulate accurately with existing strain energy splits. These validations illustrate the model's strength in capturing complex, compression-driven fracture behaviors, marking a significant advancement in the phase field fracture method's application to real-world materials and enhancing its utility in comprehen-

sive fracture analysis.

- **Multiphysics fracture modeling:** The research expanded the phase field fracture method to address multiphysics problems, utilizing a new thermal analogy-based approach that simplifies the implementation within Abaqus by avoiding the complexities of a user element subroutine. This innovative method allows for modeling complex multiphysics phenomena, such as hydraulic fracturing, thermomechanical fractures, hydrogen embrittlement, and corrosion-stress interactions. By coupling phase field evolution with other physical fields, particularly fluid flow, the model successfully replicates benchmark cases from the literature, demonstrating its reliability and accuracy. This novel approach establishes a streamlined, robust pathway for implementing complex interactions involving multiple degrees of freedom (DoFs), significantly enhancing the phase field method's applicability to real-world multiphysics problems and broadening its utility in engineering and materials science.

- **Phase field hydraulic fracture modeling:** The study examined the effects of various coupling methods between phase field and flow equations, comparing two established approaches and introducing a novel mixed method. This new combined coupling approach, which links permeability with the phase field variable, enhances control over permeability transitions by integrating the advantages of both the domain decomposition method and the modified Darcy method. Additionally, incorporating a Drucker-Prager based strain energy split as the fracture-driving force in phase field hydraulic fracturing enables the model to capture geotechnical phenomena like fault activation, broadening its applicability to realistic subsurface conditions. The influence of different strain energy split methods was also analyzed through a crack interaction problem, highlighting distinct responses based

on the stress environment. Specifically, the crack path remains consistent when major stress is tensile; however, the presence of shear stress leads to variations in crack trajectory depending on the chosen strain energy split. This insight underscores the importance of selecting an appropriate strain energy decomposition method to accurately model fracture paths under different loading conditions, offering a refined approach for complex geotechnical and rock mechanics applications

4.2 Implications and contributions

This research addresses several key challenges in the field of fracture mechanics and has wide-ranging implications for both academic research and industrial applications. By advancing the phase field fracture method and improving the accuracy of tensile strength estimation, this work contributes to the development of more reliable tools for predicting and managing fractures in rock-like materials. The practical implementations developed as part of this thesis provide researchers and engineers with computational tools that can be directly applied to complex fracture problems in industries such as mining, oil and gas extraction, geothermal energy, and civil engineering.

The introduction of a generalized strain energy decomposition framework extends the applicability of phase field methods to a wider range of fracture scenarios, particularly in the modeling of compressive failures. This is particularly significant in geotechnical engineering, where compressive failure modes are common but challenging to simulate accurately.

In conclusion, this thesis provides a comprehensive framework for modeling fractures in rock-like materials using the phase field method. The contributions made

to the field of fracture mechanics have the potential to significantly improve the accuracy and reliability of fracture predictions in both research and practical applications, paving the way for future advancements in the field.

5 | FUTURE WORKS

Despite the significant advancements achieved in this thesis, several limitations persist. The proposed models, while effective in simulating a range of fracture behaviors, remain computationally intensive, particularly for large-scale problems involving complex multiphysics interactions. Future research should aim to enhance the computational efficiency of the current implementation. This can be achieved through different methods:

- **Adaptive mesh refinement (AMR)** is a computational technique that enhances the efficiency and accuracy of numerical simulations by dynamically adjusting the mesh resolution where needed. In phase field fracture modeling, where the simulation captures the evolution of cracks in materials, AMR plays a crucial role in balancing computational resources with solution accuracy, especially in regions where cracks develop and propagate. AMR increases mesh density (refinement) around critical areas—like the crack tip or evolving fracture path—where solution gradients are high. Conversely, regions far from the fracture zones can use a coarser mesh, reducing computational cost without sacrificing accuracy [106, 107]. This can be achieved using the UMESHMOTION subroutine within Abaqus.

- **Alternate minimization (AM)** is an iterative technique widely used in phase field fracture methods to solve the variational form of fracture problems. It decomposes a complex, coupled minimization problem into subproblems by alternately minimizing the system's total energy with respect to each field independently, simplifying the solution procedure and improving computational efficiency.

  The AM procedure involves two main steps:

1. **Displacement minimization**: Starting with an initial phase field ϕ, the total energy is minimized with respect to the displacement field $\mathbf{u}$, treating ϕ as fixed.

2. **Phase field minimization**: Using the updated displacement field $\mathbf{u}$, the energy is then minimized with respect to ϕ, keeping $\mathbf{u}$ fixed.

This alternate process repeats until convergence, defined as minimal changes in both $\mathbf{u}$ and ϕ across iterations. By transforming a non-convex problem into two convex sub-problems, AM ensures stability and robust solutions, even for large-scale simulations [6,25,45,108]. Since the problem is divided into two distinct problems, implementation within Abaqus can be feasible through Python scripting to run a series of iterative problems.

- **Active and inactive phase field domains method** is a simple and robust approach to reduce computational cost. In this method, the fracture path is first predicted with a coarse mesh model, then the domain is decomposed into a region where the phase field degree of freedom is not defined (or set to zero) and a region where phase field evolution can occur. This method is straightforward and cost-effective but is recommended for the AT1 model over the AT2 model due to boundary conditions being enforced at the domain with an active phase field degree of freedom. This method has already been tested in Abaqus [109] and can be extended to more complex multi-physics problems.

Additionally, while the phase field method has been successfully extended to address compressive fractures, further investigation is required to explore the interactions among tensile, compressive, and shear failure modes. The proposed generalized method can be used to determine strain energy for various failure criteria, including:

- **Hoek-Brown criterion** [110] is an empirical strength criterion widely used in rock mechanics to estimate the strength and failure characteristics of jointed rock masses. The Hoek-Brown criterion is especially useful in applications like tunnel and underground excavation design, slope stability analysis, and more, providing a realistic approximation of rock mass strength, particularly in heterogeneous or fractured rock masses.

- **Generalized Griffith criterion** [60] is an extension of Griffith's criterion applicable for arbitrary strength ratios, as demonstrated in Section 3.1. It can be expressed in terms of stress invariants, enabling strain energy split determination for further studies on the Brazilian test using the phase field fracture method.

- **Unified strength theory (UST)** is a comprehensive framework in mechanics and material science that generalizes classical strength theories to model materials under complex stress states [111–113]. UST overcomes limitations of traditional theories like Tresca, von Mises, and Mohr-Coulomb by considering intermediate principal stress, essential for accurate predictions in 3D stress scenarios. Applicable to various materials such as metals, plastics, rocks, and soils, UST is adaptable through parameter adjustments. Its accuracy makes it valuable in fields like geotechnical and structural engineering, especially under triaxial stress conditions. UST's mathematical model integrates shear and normal stresses, enhancing predictions for material failure in multidimensional stress environments.

Moreover, the new strain energy split based on failure criteria can be applied to advancing elasto-plastic ductile fracture using the phase field method. The phase field fracture method has been extensively used to model ductile fracture by accounting for plasticity effects, with recent studies demonstrating how elastic

and plastic strain energies contribute distinctly to fracture modeling [114–117]. Building on this methodology, further studies could apply a generalized approach for strain energy splitting based on failure criteria (Section 3.4), allowing for advanced ductile fracture modeling when failure criteria and yield surfaces coincide. This approach aims to better represent material behavior by incorporating damage and plastic evolution comprehensively.

The multiphysics framework could be extended to accommodate more complex problems involving three or more field variables, such as geothermal energy modeling [118], which integrates mechanical, phase field, fluid flow, and thermal equations. This coupling can be performed by various methods, which may or may not be variationally consistent. For instance, material, fluid, and heat analysis parameters could directly depend on the phase field variable ϕ, decomposing the domain as discussed in Section 3.6.

Finally, the current model could be further developed to incorporate dynamic effects, enabling its extension to explicit simulation frameworks like Abaqus/Explicit [119]. Most existing implementations use an explicit version of a user-defined elaccounting for the effect of porosity and void fraction on material strengthement subroutine (VUEL); however, by introducing a thermal analogy for phase field fracture, it is possible to use subroutines that work at the integration level, such as VHETVAL and VUMATHT. This approach enables dynamic problem modeling, including multiphysics problems, in a more computationally robust environment.

4 | CONCLUSIONES

Esta tesis ha avanzado el campo de la mecánica de fractura al enfocarse en la aplicación y extensión del método de fractura de campo de fase, específicamente en el modelado de materiales similares a roca bajo condiciones de carga complejas. La investigación presentada aquí ha realizado contribuciones significativas tanto en aspectos teóricos como prácticos del modelado de fracturas, abordando desafíos clave en la simulación de modos de falla compresiva, acoplamiento multifísico y la validación de mediciones de resistencia a tracción a partir del ensayo brasileño. Este capítulo resume los hallazgos principales y destaca las contribuciones al campo.

4.1 Hallazgos Clave

Las principales contribuciones de esta tesis pueden resumirse de la siguiente manera:

- ***Validación del ensayo brasileño:*** *El estudio sobre el ensayo brasileño ha revelado limitaciones significativas en las mediciones tradicionales de resistencia a tracción para materiales similares a roca, cuestionando las suposiciones prevalecientes sobre la iniciación de grietas y la validez de las geometrías de prueba. A través del análisis de elementos finitos y la aplicación del criterio de Griffith, se demostró que las grietas no se originan consistentemente en el centro del disco de prueba, contrariamente a lo que sugieren los estándares ampliamente aceptados. La investigación introdujo una metodología novedosa para validar los resultados del ensayo brasileño, incluyendo el desarrollo de una aplicación en MATLAB (BrazVal) y*

mapas de validez que proporcionan una evaluación más precisa de la resistencia a tracción al identificar condiciones óptimas de prueba. Los hallazgos clave indican que el uso de mordazas con grandes radios promueve la iniciación de grietas en regiones compresivas alejadas del centro del disco, invalidando los resultados de la prueba. Además, la ubicación de la grieta es altamente sensible a la geometría de la prueba y, en menor medida, a la rigidez de la muestra, mientras que el coeficiente de Poisson y la fricción juegan roles mínimos en la mayoría de las configuraciones. Al mapear la carga crítica contra los estados de esfuerzo en el centro del disco, este trabajo permite estimaciones más precisas de la resistencia a tracción, eliminando la dependencia de la ecuación de Hondros y ofreciendo un protocolo de dos pasos para la validación experimental. Estos conocimientos permitirán a los investigadores determinar las condiciones de prueba adecuadas, avanzando así en la precisión y confiabilidad de las mediciones de resistencia a tracción en materiales similares a roca.

- ***Implementación de modelos de campo de fase en Abaqus:*** *Se ha desarrollado una implementación unificada del modelo de fractura de campo de fase dentro de Abaqus utilizando una subrutina UMAT, lo que elimina las complejidades asociadas con el uso de subrutinas de elementos de usuario y simplifica el pre- y pos-procesamiento. Este enfoque versátil aprovecha las capacidades integradas de Abaqus, permitiendo una aplicación sin problemas a problemas 2D, 3D y axisimétricos. La implementación soporta tanto esquemas de solución escalonados como monolíticos, mejorando la flexibilidad para diversas necesidades de modelado de fracturas. Además, permite la integración de cualquier modelo constitutivo del enfoque de campo de fase, incluyendo AT1, AT2 y PF-CZM, con varios métodos de descomposición de energía de deformación. Esta configuración acomoda*

tanto formulaciones híbridas como anisotrópicas, ofreciendo un conjunto de herramientas robusto para el análisis de fracturas por campo de fase en una amplia gama de aplicaciones.

- ***Verificación de fractura de campo de fase:*** *El modelo de fractura de campo de fase fue validado a través de una serie de estudios de caso, incluyendo tanto ejemplos establecidos de la literatura como pruebas diseñadas recientemente, demostrando la robustez de la implementación en el manejo de escenarios complejos de fractura. Los resultados mostraron consistentemente que el modelo simula con precisión la propagación de fracturas bajo condiciones de carga de tracción, corte y mixtas en configuraciones 2D y 3D. Esta precisión constante en varios modos de fractura destaca la capacidad de la implementación para modelar procesos de fractura complejos de manera confiable, mostrando su efectividad para diversas aplicaciones en mecánica de fracturas. Sin embargo, una limitación notable es que el modelo de campo de fase convencional no fue diseñado originalmente para modelar fallas bajo carga compresiva.*

- ***Modelado constitutivo de fractura de campo de fase:*** *Se ha introducido un marco generalizado novedoso para la descomposición de energía de deformación, avanzando en la capacidad del método de fractura de campo de fase para modelar con precisión la falla compresiva en materiales similares a roca. Este marco integra el criterio de falla de Drucker-Prager, permitiendo la simulación de una gama más amplia de comportamientos de fractura y abordando las limitaciones de los métodos tradicionales para modelar fracturas compresivas, un problema común y complejo en la mecánica de rocas. La descomposición de energía de deformación basada en Drucker-Prager captura con éxito comportamientos esenciales de materiales similares a roca, como dilatancia, confinamiento y fricción, creando*

una representación más realista de estos materiales bajo tensión. Además, se ha desarrollado una nueva formulación de energía de deformación para simular eficazmente materiales con vacíos e inclusiones, ampliando las capacidades del modelo en aplicaciones complejas de geología y ciencia de materiales. La eficacia del modelo desarrollado ha sido demostrada a través de estudios de caso, incluyendo Pruebas de Corte Directo, pruebas de compresión uniaxial y triaxial de concreto, y la falla localizada de taludes de suelo, todos escenarios difíciles de simular con precisión con las descomposiciones de energía de deformación existentes. Estas validaciones ilustran la fortaleza del modelo para capturar comportamientos de fractura complejos impulsados por compresión, marcando un avance significativo en la aplicación del método de fractura de campo de fase a materiales del mundo real y mejorando su utilidad en análisis de fractura integrales.

- ***Modelado de fractura multifísica:*** *La investigación amplió el método de fractura de campo de fase para abordar problemas multifísicos, utilizando un nuevo enfoque basado en una analogía térmica que simplifica la implementación en Abaqus al evitar las complejidades de una subrutina de elemento de usuario. Este método innovador permite modelar fenómenos multifísicos complejos, como fracturación hidráulica, fracturas termomecánicas, fragilización por hidrógeno e interacciones corrosión-esfuerzo. Al acoplar la evolución del campo de fase con otros campos físicos, particularmente el flujo de fluidos, el modelo replicó exitosamente casos de referencia de la literatura, demostrando su confiabilidad y precisión. Este enfoque novedoso establece una vía simplificada y robusta para implementar interacciones complejas que involucran múltiples grados de libertad (DoFs), mejorando significativamente la aplicabilidad del método de campo de fase a problemas multifísicos del mundo real y ampliando su utilidad*

en ingeniería y ciencia de materiales.

- ***Modelado de fractura hidráulica de campo de fase:*** *El estudio examinó los efectos de varios métodos de acoplamiento entre el campo de fase y las ecuaciones de flujo, comparando dos enfoques establecidos e introduciendo un nuevo método mixto. Este nuevo enfoque de acoplamiento combinado, que vincula la permeabilidad con la variable de campo de fase, mejora el control sobre las transiciones de permeabilidad al integrar las ventajas tanto del método de descomposición del dominio como del método de Darcy modificado. Además, la incorporación de una descomposición de energía de deformación basada en Drucker-Prager como la fuerza impulsora de fractura en la fracturación hidráulica de campo de fase permite que el modelo capture fenómenos geotécnicos como la activación de fallas, ampliando su aplicabilidad a condiciones realistas del subsuelo. La influencia de diferentes métodos de descomposición de energía de deformación también fue analizada a través de un problema de interacción de grietas, destacando respuestas distintas en función del entorno de esfuerzo. Específicamente, la trayectoria de la grieta permanece consistente cuando el esfuerzo principal es de tracción; sin embargo, la presencia de esfuerzo de corte conduce a variaciones en la trayectoria de la grieta según el método de descomposición de energía de deformación elegido. Este hallazgo subraya la importancia de seleccionar un método de descomposición de energía adecuado para modelar con precisión las trayectorias de fractura bajo diferentes condiciones de carga, ofreciendo un enfoque refinado para aplicaciones complejas en mecánica de rocas y geotécnica.*

4.2 Implicaciones y contribuciones

Esta investigación aborda varios desafíos clave en el campo de la mecánica de fracturas y tiene implicaciones de gran alcance tanto para la investigación académica como para aplicaciones industriales. Al avanzar en el método de fractura de campo de fase y mejorar la precisión de la estimación de resistencia a tracción, este trabajo contribuye al desarrollo de herramientas más confiables para predecir y gestionar fracturas en materiales similares a roca. Las implementaciones prácticas desarrolladas como parte de esta tesis proporcionan a investigadores e ingenieros herramientas computacionales que pueden aplicarse directamente a problemas complejos de fractura en industrias como la minería, la extracción de petróleo y gas, la energía geotérmica y la ingeniería civil.

La introducción de un marco generalizado para la descomposición de energía de deformación extiende la aplicabilidad de los métodos de campo de fase a una gama más amplia de escenarios de fractura, particularmente en el modelado de fallas compresivas. Esto es especialmente significativo en la ingeniería geotécnica, donde los modos de falla compresiva son comunes pero difíciles de simular con precisión.

En conclusión, esta tesis proporciona un marco integral para el modelado de fracturas en materiales similares a roca utilizando el método de campo de fase. Las contribuciones realizadas al campo de la mecánica de fracturas tienen el potencial de mejorar significativamente la precisión y confiabilidad de las predicciones de fractura tanto en la investigación como en aplicaciones prácticas, allanando el camino para futuros avances en el campo.

5 | TRABAJO FUTURO

A pesar de los avances significativos logrados en esta tesis, persisten varias limitaciones. Los modelos propuestos, si bien son efectivos en la simulación de una variedad de comportamientos de fractura, siguen siendo intensivos en términos computacionales, especialmente para problemas a gran escala que involucran interacciones multifísicas complejas. La investigación futura debería enfocarse en mejorar la eficiencia computacional de la implementación actual. Esto se puede lograr mediante diferentes métodos:

- ***Refinamiento de malla adaptativo (AMR)** es una técnica computacional que mejora la eficiencia y precisión de las simulaciones numéricas ajustando dinámicamente la resolución de la malla donde sea necesario. En el modelado de fractura de campo de fase, donde la simulación captura la evolución de grietas en materiales, el AMR juega un papel crucial en equilibrar los recursos computacionales con la precisión de la solución, especialmente en las regiones donde se desarrollan y propagan las grietas. El AMR incrementa la densidad de malla (refinamiento) alrededor de áreas críticas, como la punta de la grieta o el camino de fractura en evolución, donde los gradientes de la solución son altos. Por el contrario, las regiones alejadas de las zonas de fractura pueden usar una malla más gruesa, reduciendo el costo computacional sin sacrificar precisión [106, 107]. Esto se puede lograr utilizando la subrutina UMESHMOTION dentro de Abaqus.*

- ***Minimización alternante (AM)** es una técnica iterativa ampliamente utilizada en los métodos de fractura de campo de fase para resolver la forma variacional de los problemas de fractura. Descompone un problema complejo y acoplado de minimización en subproblemas, minimizando alterna-*

tivamente la energía total del sistema con respecto a cada campo de forma independiente, simplificando el procedimiento de solución y mejorando la eficiencia computacional.

El procedimiento AM involucra dos pasos principales:

1. ***Minimización del desplazamiento**: Comenzando con un campo de fase inicial ϕ, se minimiza la energía total con respecto al campo de desplazamiento* $\mathbf{u}$*, tratando a* ϕ *como fijo.*

2. ***Minimización del campo de fase**: Utilizando el campo de desplazamiento actualizado* $\mathbf{u}$*, la energía se minimiza con respecto a* ϕ*, manteniendo* $\mathbf{u}$ *fijo.*

Este proceso alternante se repite hasta la convergencia, definida como cambios mínimos en ambos $\mathbf{u}$ *y* ϕ *a través de las iteraciones. Al transformar un problema no convexo en dos subproblemas convexos, el AM asegura estabilidad y soluciones robustas, incluso para simulaciones a gran escala [6, 25, 45, 108]. Dado que el problema se divide en dos problemas distintos, la implementación dentro de Abaqus puede ser factible mediante scripting en Python para ejecutar una serie de problemas iterativos.*

- ***Método de dominios de campo de fase activos e inactivos** es un enfoque simple y robusto para reducir el costo computacional. En este método, el camino de fractura se predice primero con un modelo de malla gruesa, luego el dominio se descompone en una región donde el grado de libertad del campo de fase no está definido (o se establece en cero) y una región donde puede ocurrir la evolución del campo de fase. Este método es sencillo y rentable, pero se recomienda para el modelo AT1 sobre el modelo AT2 debido a que las condiciones de contorno se imponen en el dominio con un grado de libertad de campo de fase activo. Este método ya ha sido probado en*

Abaqus [109] y puede extenderse a problemas multifísicos más complejos.

Además, aunque el método de campo de fase se ha extendido exitosamente para abordar fracturas compresivas, se requiere una investigación adicional para explorar las interacciones entre los modos de falla por tracción, compresión y corte. El desdoblamiento basado en Bresler-Pister propuesto puede implementarse y probarse en diferentes estudios de caso, como el modelado de concreto bajo carga multiaxial compleja. Además, el método generalizado propuesto se puede utilizar para determinar la energía de deformación para varios criterios de falla, incluyendo:

- ***Criterio de Hoek-Brown** [110] es un criterio empírico de resistencia ampliamente utilizado en mecánica de rocas para estimar las características de resistencia y falla de masas rocosas fracturadas. El criterio de Hoek-Brown es especialmente útil en aplicaciones como el diseño de túneles y excavaciones subterráneas, análisis de estabilidad de taludes, y más, proporcionando una aproximación realista de la resistencia de la masa rocosa, particularmente en masas rocosas heterogéneas o fracturadas.*

- ***Criterio de Griffith generalizado** [60] es una extensión del criterio de Griffith aplicable para relaciones de resistencia arbitrarias, como se demuestra en Section 3.1. Puede expresarse en términos de invariantes de esfuerzo, permitiendo la determinación del desdoblamiento de energía de deformación para estudios adicionales sobre el ensayo brasileño utilizando el método de fractura de campo de fase.*

- ***Teoría de resistencia unificada (UST)** es un marco integral en mecánica y ciencia de materiales que generaliza las teorías clásicas de resistencia para modelar materiales bajo estados de esfuerzo complejos [111–113]. La UST supera las limitaciones de teorías tradicionales como Tresca, von Mises y*

Mohr-Coulomb al considerar el esfuerzo principal intermedio, esencial para predicciones precisas en escenarios de esfuerzo 3D. Aplicable a diversos materiales como metales, plásticos, rocas y suelos, la UST es adaptable mediante ajustes de parámetros. Su precisión la hace valiosa en campos como la ingeniería geotécnica y estructural, especialmente bajo condiciones de esfuerzo triaxial. El modelo matemático de la UST integra esfuerzos de corte y normales, mejorando las predicciones de falla de materiales en entornos de esfuerzo multidimensional.

Además, el nuevo desdoblamiento de energía de deformación basado en criterios de falla puede aplicarse al avance de la fractura dúctil elasto-plástica utilizando el método de campo de fase. El método de fractura de campo de fase se ha utilizado extensamente para modelar fracturas dúctiles al tener en cuenta los efectos de la plasticidad, con estudios recientes que demuestran cómo las energías de deformación elástica y plástica contribuyen distintivamente al modelado de fracturas [114–117]. Basándose en esta metodología, estudios adicionales podrían aplicar un enfoque generalizado para el desdoblamiento de energía de deformación basado en criterios de falla (Section 3.4), permitiendo un modelado avanzado de fractura dúctil cuando los criterios de falla y las superficies de fluencia coinciden. Este enfoque busca representar mejor el comportamiento del material al incorporar de manera integral la evolución de daño y plasticidad.

El marco multifísico podría extenderse para acomodar problemas más complejos que involucren tres o más variables de campo, como el modelado de energía geotérmica [118], que integra ecuaciones mecánicas, de campo de fase, de flujo de fluidos y térmicas. Este acoplamiento puede realizarse mediante diversos métodos, que pueden o no ser variacionalmente consistentes. Por ejemplo, los parámetros de análisis de material, fluido y calor podrían depender directamente de la variable de campo de fase ϕ, descomponiendo el dominio como se discute en

Section 3.6.

Finalmente, el modelo actual podría desarrollarse aún más para incorporar efectos dinámicos, permitiendo su extensión a marcos de simulación explícitos como Abaqus/Explicit [119]. La mayoría de las implementaciones existentes utilizan una versión explícita de una subrutina de elemento definida por el usuario (VUEL); sin embargo, al introducir una analogía térmica para la fractura de campo de fase, es posible usar subrutinas que funcionen a nivel de integración, como VHETVAL y VUMATHT. Este enfoque permite el modelado de problemas dinámicos, incluyendo problemas multifísicos, en un entorno computacionalmente más robusto.

Bibliography

[1] O. Zienkiewicz, R. Taylor, The Finite Element Method: Its Basis and Fundamentals, The Finite Element Method, Elsevier Science, 2013.

[2] J. W. Thomas, Numerical partial differential equations: finite difference methods, Vol. 22, Springer Science & Business Media, 2013.

[3] S. Crouch, Boundary element methods in solid mechanics, London: Allen & Unwin/Allen & Unwin 322 (1983) 322.

[4] A. Needleman, A Continuum Model for Void Nucleation by Inclusion Debonding, Journal of Applied Mechanics 54 (3) (1987) 525–531.

[5] N. Moës, J. Dolbow, T. Belytschko, A finite element method for crack growth without remeshing, International Journal for Numerical Methods in Engineering 46 (1) (1999) 131–150.

[6] C. Miehe, F. Welshinger, M. Hofacker, Thermodynamically consistent phase-field models of fracture: Variational principles and multi-field FE implementations, International Journal for Numerical Methods in Engineering 83 (45-48) (2010) 1273–1311.

[7] J.-Y. Wu, V. P. Nguyen, C. T. Nguyen, D. Sutula, S. Sinaie, S. P. Bordas, Phase-field modeling of fracture, Advances in applied mechanics 53 (2020) 1–183.

[8] S. A. Silling, Reformulation of elasticity theory for discontinuities and long-range forces, Journal of the Mechanics and Physics of Solids 48 (1) (2000) 175–209.

[9] C. Desai, J. Christian, Numerical Methods in Geotechnical Engineering, McGraw-Hill Series in Industrial Engineering and Management, McGraw-Hill, 1977.

[10] F. M. Aliabadi, Boundary element methods, in: Encyclopedia of continuum mechanics, Springer, 2020, pp. 182–193.

[11] A. Wilde, M. Aliabadi, Boundary element analysis of geomechanical fracture, International journal for numerical and analytical methods in geomechanics 23 (12) (1999) 1195–1214.

[12] P. A. Cundall, O. D. Strack, A discrete numerical model for granular assemblies, geotechnique 29 (1) (1979) 47–65.

[13] J. V. Lemos, Discrete element modeling of the seismic behavior of masonry construction, Buildings 9 (2) (2019) 43.

[14] D. O. Potyondy, P. A. Cundall, A bonded-particle model for rock, International journal of rock mechanics and mining sciences 41 (8) (2004) 1329–1364.

[15] L. Jing, O. Stephansson, Fundamentals of discrete element methods for rock engineering: theory and applications, Elsevier, 2007.

[16] A. A. Munjiza, The combined finite-discrete element method, John Wiley & Sons, 2004.

[17] E. Schlangen, E. J. Garboczi, Fracture simulations of concrete using lattice models: computational aspects, Engineering fracture mechanics 57 (2-3) (1997) 319–332.

[18] T. Koyama, L. Jing, Effects of model scale and particle size on micro-mechanical properties and failure processes of rocks-a particle mechan-

ics approach, Engineering Analysis with Boundary Elements 31 (5) (2007) 458–472, innovative Numerical Methods for Micro and Nano Mechanics and Structures - Part I.

[19] S. M. Allen, J. W. Cahn, A microscopic theory for antiphase boundary motion and its application to antiphase domain coarsening, Acta Metallurgica 27 (6) (1979) 1085–1095.

[20] J. W. Cahn, J. E. Hilliard, Free Energy of a Nonuniform System. I. Interfacial Free Energy, The Journal of Chemical Physics 28 (2) (1958) 258–267.

[21] W. Boettinger, J. Warren, C. Beckermann, A. Karma, Phase-field simulation of solidification, Annual Review of Materials Research 32 (1) (2002) 163–194.

[22] A. Karma, W.-J. Rappel, Phase-field model of dendritic sidebranching with thermal noise, Phys. Rev. E 60 (1999) 3614–3625.

[23] I. Steinbach, Phase-field models in materials science, Modelling and Simulation in Materials Science and Engineering 17 (7) (2009) 073001.

[24] C. Miehe, M. Hofacker, F. Welschinger, A phase field model for rate-independent crack propagation: Robust algorithmic implementation based on operator splits, Computer Methods in Applied Mechanics and Engineering 199 (45-48) (2010) 2765–2778.

[25] B. Bourdin, G. A. Francfort, J. J. Marigo, The variational approach to fracture, Springer Netherlands, 2008.

[26] C. Kuhn, R. Müller, A continuum phase field model for fracture, Engineering Fracture Mechanics 77 (18) (2010) 3625–3634.

[27] L. Q. Chen, Phase-field models for microstructure evolution, Annual Review of Materials Science 32 (2002) 113–140.

[28] D. Jacqmin, Calculation of two-phase navier–stokes flows using phase-field modeling, Journal of Computational Physics 155 (1) (1999) 96–127.

[29] H. DING, P. D. M. SPELT, Inertial effects in droplet spreading: a comparison between diffuse-interface and level-set simulations, Journal of Fluid Mechanics 576 (2007) 287–296.

[30] V. Badalassi, H. Ceniceros, S. Banerjee, Computation of multiphase systems with phase field models, Journal of Computational Physics 190 (2) (2003) 371–397.

[31] A. Moure, H. Gomez, Phase-field model of cellular migration: Three-dimensional simulations in fibrous networks, Computer Methods in Applied Mechanics and Engineering 320 (2017) 162–197.

[32] P. Gerlee, A. R. Anderson, An evolutionary hybrid cellular automaton model of solid tumour growth, Journal of Theoretical Biology 246 (4) (2007) 583–603.

[33] A. A. Griffith, The Phenomena of Rupture and Flow in Solids, Philosophical Transactions A, 221 (1920) 163–198.

[34] M. E. Gurtin, Generalized ginzburg-landau and cahn-hilliard equations based on a microforce balance, Physica D: Nonlinear Phenomena 92 (3) (1996) 178–192.

[35] M. J. Borden, C. V. Verhoosel, M. A. Scott, T. J. R. Hughes, C. M. Landis, A phase-field description of dynamic brittle fracture, Computer Methods in Applied Mechanics and Engineering 217-220 (2012) 77–95.

[36] Y. S. Lo, T. J. Hughes, C. M. Landis, Phase-field fracture modeling for large structures, Journal of the Mechanics and Physics of Solids 171 (November 2022) (2023) 105118.

[37] B. Bourdin, Numerical implementation of the variational formulation for quasi-static brittle fracture, Interfaces and Free Boundaries 9 (3) (2007) 411 – 430, cited by: 293; All Open Access, Bronze Open Access.

[38] A. Marengo, A. Patton, M. Negri, U. Perego, A. Reali, A rigorous and efficient explicit algorithm for irreversibility enforcement in phase-field finite element modeling of brittle crack propagation, Computer Methods in Applied Mechanics and Engineering 387 (2021) 114137.

[39] P. K. Kristensen, C. F. Niordson, E. Martínez-Pañeda, An assessment of phase field fracture: crack initiation and growth, Philosophical Transactions of the Royal Society A: Mathematical, Physical and Engineering Sciences 379 (2021) 20210021.

[40] T. Gerasimov, L. De Lorenzis, On penalization in variational phase-field models of brittle fracture, Computer Methods in Applied Mechanics and Engineering 354 (2019) 990–1026.

[41] B. Bourdin, G. A. Francfort, J.-J. Marigo, Numerical experiments in revisited brittle fracture, Journal of the Mechanics and Physics of Solids 48 (4) (2000) 797–826.

[42] K. Pham, H. Amor, J. J. Marigo, C. Maurini, Gradient damage models and their use to approximate brittle fracture, International Journal of Damage Mechanics 20 (4) (2011) 618–652.

[43] J.-Y. Wu, A unified phase-field theory for the mechanics of damage and quasi-brittle failure, Journal of the Mechanics and Physics of Solids 103

(2017) 72–99.

[44] J.-Y. Wu, V. P. Nguyen, A length scale insensitive phase-field damage model for brittle fracture, Journal of the Mechanics and Physics of Solids 119 (2018) 20–42.

[45] H. Amor, J. J. Marigo, C. Maurini, Regularized formulation of the variational brittle fracture with unilateral contact: Numerical experiments, Journal of the Mechanics and Physics of Solids 57 (8) (2009) 1209–1229.

[46] F. Freddi, G. Royer-Carfagni, Regularized variational theories of fracture: A unified approach, Journal of the Mechanics and Physics of Solids 58 (8) (2010) 1154–1174.

[47] G. Del Piero, Constitutive equation and compatibility of the external loads for linear elastic masonry-like materials, Meccanica 24 (3) (1989) 150–162.

[48] L. De Lorenzis, C. Maurini, Nucleation under multi-axial loading in variational phase-field models of brittle fracture, International Journal of Fracture 237 (1-2) (2022) 61–81.

[49] Y. Navidtehrani, C. Betegón, E. Martínez-Pañeda, A general framework for decomposing the phase field fracture driving force, particularised to a drucker–prager failure surface, Theoretical and Applied Fracture Mechanics 121 (2022) 103555.

[50] Y. Navidtehrani, C. Betegón, R. W. Zimmerman, E. Martínez-Pañeda, Griffith-based analysis of crack initiation location in a brazilian test, International Journal of Rock Mechanics and Mining Sciences 159 (2022) 105227.

[51] Y. Navidtehrani, C. Betegón, E. Martínez-Pañeda, A simple and robust abaqus implementation of the phase field fracture method, Applications in

Engineering Science 6 (2021) 100050.

[52] Y. Navidtehrani, C. Betegón, E. Martínez-Pañeda, A unified abaqus implementation of the phase field fracture method using only a user material subroutine, Materials 14 (8) (2021).

[53] Y. Navidtehrani, R. Duddu, E. Martínez-Pañeda, Damage mechanics challenge: Predictions based on the phase field fracture model, Engineering Fracture Mechanics 301 (2024) 110046.

[54] J. P. Morris, L. J. Pyrak-Nolte, H. Yoon, A. Bobet, L. Jiang, The damage Mechanics challenge Results: Participant predictions compared with experiment, Engineering Fracture Mechanics 310 (2024) 110421.

[55] Y. Navidtehrani, C. Betegón, E. Martínez-Pañeda, On strain energy splits and fracture driving forces in phase field fracture modelling, Proceedings of the International Conference on Computational Plasticity, Barcelona, Spain, 2021.

[56] Y. Navidtehrani, C. Betegón, E. Martínez-pañeda, A generalised framework for phase field-based modelling of coupled problems : Application to thermo-mechanical fracture , hydraulic fracture , hydrogen embrittlement and corrosion, Engineering Fracture Mechanics 326 (2025) 111363.

[57] Y. Navidtehrani, C. Betegón, J. Vallejos, E. Martínez-Pañeda, A phase field model for hydraulic fracture: Drucker–Prager driving force and a hybrid coupling strategy, Computer Methods in Applied Mechanics and Engineering 444 (2025) 118155.

[58] D. Li, L. N. Y. Wong, The brazilian disc test for rock mechanics applications: Review and new insights, Rock Mechanics and Rock Engineering 46 (2) (2013) 269–287.

[59] F. Carneiro, A new method to determine the tensile strength of concrete, in: Proceedings of the 5th meeting of the Brazilian Association for Technical Rules, Vol. 3, 1943, pp. 126–129.

[60] C. Fairhurst, On the validity of the 'Brazilian' test for brittle materials, International Journal of Rock Mechanics and Mining Sciences and 1 (4) (1964) 535–546.

[61] J. A. Hudson, E. T. Brown, F. Rummel, The controlled failure of rock discs and rings loaded in diametral compression, International Journal of Rock Mechanics and Mining Sciences and 9 (2) (1972) 241–248.

[62] M. I. Alvarez-Fernandez, C. C. Garcia-Fernandez, C. Gonzalez-Nicieza, D. J. Guerrero-Miguel, Effect of the Contact Angle in the Failure Pattern in Slate Under Diametral Compression, Rock Mechanics and Rock Engineering 53 (5) (2020) 2123–2139.

[63] C. F. Markides, S. K. Kourkoulis, The influence of jaw's curvature on the results of the Brazilian disc test, Journal of Rock Mechanics and Geotechnical Engineering 8 (2) (2016) 127–146.

[64] R. Gutiérrez-Moizant, M. Ramírez-Berasategui, S. Sánchez-Sanz, S. Santos-Cuadros, Experimental verification of the boundary conditions in the success of the Brazilian test with loading arcs. An uncertainty approach using concrete disks, International Journal of Rock Mechanics and Mining Sciences 132 (April) (2020) 104380.

[65] M. F. Bouali, M. Bouassida, Numerical simulation of the effect of loading angle on initial cracks position point: Application to the Brazilian test, Applied Sciences 11 (8) (2021).

[66] C. C. Garcia-Fernandez, C. Gonzalez-Nicieza, M. I. Alvarez-Fernandez, R. A. Gutierrez-Moizant, Analytical and experimental study of failure onset during a Brazilian test, International Journal of Rock Mechanics and Mining Sciences 103 (June 2017) (2018) 254–265.

[67] Z. Zhao, W. Sun, S. Chen, D. Yin, H. Liu, B. Chen, Determination of critical criterion of tensile-shear failure in Brazilian disc based on theoretical analysis and meso-macro numerical simulation, Computers and Geotechnics 134 (January) (2021) 104096.

[68] Z. Aliabadian, G. F. Zhao, A. R. Russell, Failure, crack initiation and the tensile strength of transversely isotropic rock using the Brazilian test, International Journal of Rock Mechanics and Mining Sciences 122 (July) (2019) 104073.

[69] I. S. for Rock Mechanics. Commission on Standardization of Laboratory, F. T. C. on Laboratory Tests, Suggested methods for determining tensile strength of rock materials, The Society, 1977.

[70] ASTM International, Standard test method for splitting tensile strength of cylindrical concrete specimens (c496/c496m-17) (2017).

[71] S. Zhou, T. Rabczuk, X. Zhuang, Phase field modeling of quasi-static and dynamic crack propagation: COMSOL implementation and case studies, Advances in Engineering Software 122 (March) (2018) 31–49.

[72] Hirshikesh, S. Natarajan, R. K. Annabattula, A FEniCS implementation of the phase field method for quasi-static brittle fracture, Frontiers of Structural and Civil Engineering 13 (2) (2019) 1–17.

[73] M. A. Msekh, J. M. Sargado, M. Jamshidian, P. M. Areias, T. Rabczuk, Abaqus implementation of phase-field model for brittle fracture, Computa-

tional Materials Science 96 (PB) (2015) 472–484.

[74] G. Liu, Q. Li, M. A. Msekh, Z. Zuo, Abaqus implementation of monolithic and staggered schemes for quasi-static and dynamic fracture phase-field model, Computational Materials Science 121 (2016) 35–47.

[75] G. Molnár, A. Gravouil, 2D and 3D Abaqus implementation of a robust staggered phase-field solution for modeling brittle fracture, Finite Elements in Analysis and Design 130 (March) (2017) 27–38.

[76] J. Fang, C. Wu, T. Rabczuk, C. Wu, C. Ma, G. Sun, Q. Li, Phase field fracture in elasto-plastic solids: Abaqus implementation and case studies, Theoretical and Applied Fracture Mechanics 103 (February) (2019) 102252.

[77] G. Molnár, A. Gravouil, R. Seghir, J. Réthoré, An open-source Abaqus implementation of the phase-field method to study the effect of plasticity on the instantaneous fracture toughness in dynamic crack propagation, Computer Methods in Applied Mechanics and Engineering 365 (2020) 113004.

[78] J.-Y. Wu, Y. Huang, Comprehensive implementations of phase-field damage models in Abaqus, Theoretical and Applied Fracture Mechanics 106 (2020) 102440.

[79] M. Ambati, T. Gerasimov, L. De Lorenzis, A review on phase-field models of brittle fracture and a new fast hybrid formulation, Computational Mechanics 55 (2015) 383–405.

[80] P. K. Kristensen, E. Martínez-Pañeda, Phase field fracture modelling using quasi-Newton methods and a new adaptive step scheme, Theoretical and Applied Fracture Mechanics 107 (2020) 102446.

[81] D. Wick, T. Wick, R. J. Hellmig, H. J. Christ, Numerical simulations of crack propagation in screws with phase-field modeling, Computational Ma-

terials Science 109 (2015) 367–379.

[82] G. N. Wells, L. J. Sluys, A new method for modelling cohesive cracks using finite elements, International Journal for Numerical Methods in Engineering 50 (12) (2001) 2667–2682.

[83] E. Schalangen, Experimental and numerical analysis of fracture process in concrete, Heron 38 (2) (1993) 1–17.

[84] S. Zhou, X. Zhuang, T. Rabczuk, Phase field modeling of brittle compressive-shear fractures in rock-like materials: A new driving force and a hybrid formulation, Computer Methods in Applied Mechanics and Engineering 355 (2019) 729–752.

[85] T. Wang, X. Ye, Z. Liu, D. Chu, Z. Zhuang, Modeling the dynamic and quasi-static compression-shear failure of brittle materials by explicit phase field method, Computational Mechanics 64 (6) (2019) 1537–1556.

[86] G. Del Piero, D. R. Owen, Structured deformations of continua, Archive for Rational Mechanics and Analysis 124 (2) (1993) 99–155.

[87] I. S. Sokolnikoff, Mathematical theory of elasticity, McGraw-Hill, 1946.

[88] D. Chu, X. Li, Z. Liu, Study the dynamic crack path in brittle material under thermal shock loading by phase field modeling, International Journal of Fracture 208 (1-2) (2017) 115–130.

[89] A. Schlüter, C. Kuhn, R. Müller, M. Tomut, C. Trautmann, H. Weick, C. Plate, Phase field modelling of dynamic thermal fracture in the context of irradiation damage, Continuum Mechanics and Thermodynamics 29 (4) (2017) 977–988.

[90] H. Badnava, M. A. Msekh, E. Etemadi, T. Rabczuk, An h-adaptive thermo-mechanical phase field model for fracture, Finite Elements in Analysis and Design 138 (April 2017) (2018) 31–47.

[91] B. Bourdin, C. Chukwudozie, K. Yoshioka, A variational approach to the numerical simulation of hydraulic fracturing, Proceedings - SPE Annual Technical Conference and Exhibition 2 (2012) 1442–1452.

[92] C. Miehe, H. Dal, L.-M. Schanzel, A. Raina, A phase-field model for chemo-mechanical induced fracture in lithium-ion battery electrode particles, International Journal for Numerical Methods in Engineering 106 (2016) 683–711.

[93] Z. A. Wilson, C. M. Landis, Phase-field modeling of hydraulic fracture, Journal of the Mechanics and Physics of Solids 96 (2016) 264–290.

[94] M. F. Wheeler, T. Wick, W. Wollner, An augmented-Lagrangian method for the phase-field approach for pressurized fractures, Computer Methods in Applied Mechanics and Engineering 271 (2014) 69–85.

[95] Y. Heider, B. Markert, A phase-field modeling approach of hydraulic fracture in saturated porous media, Mechanics Research Communications 80 (2017) 38–46.

[96] W. Ehlers, C. Luo, A phase-field approach embedded in the Theory of Porous Media for the description of dynamic hydraulic fracturing, Computer Methods in Applied Mechanics and Engineering 315 (2017) 348–368.

[97] Y. Heider, A review on phase-field modeling of hydraulic fracturing, Engineering Fracture Mechanics 253 (June) (2021) 1–24.

[98] C. P. Jiang, X. F. Wu, J. Li, F. Song, Y. F. Shao, X. H. Xu, P. Yan, A study of the mechanism of formation and numerical simulations of crack patterns in ceramics subjected to thermal shock, Acta Materialia 60 (11) (2012) 4540–4550.

[99] B. Bourdin, C. Chukwudozie, K. Yoshioka, A variational approach to the numerical simulation of hydraulic fracturing, Proceedings - SPE Annual Technical Conference and Exhibition 2 (2012) 1442–1452.

[100] C. Miehe, S. Mauthe, S. Teichtmeister, Minimization principles for the coupled problem of Darcy-Biot-type fluid transport in porous media linked to phase field modeling of fracture, Journal of the Mechanics and Physics of Solids 82 (2015) 186–217.

[101] S. Lee, M. F. Wheeler, T. Wick, Pressure and fluid-driven fracture propagation in porous media using an adaptive finite element phase field model, Comput. Methods Appl. Mech. Engrg 305 (2016) 111–132.

[102] F. Aldakheel, N. Noii, T. Wick, P. Wriggers, A global–local approach for hydraulic phase-field fracture in poroelastic media, Computers and Mathematics with Applications 91 (2021) 99–121.

[103] F. Aldakheel, A microscale model for concrete failure in poro-elasto-plastic media, Theoretical and Applied Fracture Mechanics 107 (2020) 102517.

[104] S. Zhou, X. Zhuang, H. Zhu, T. Rabczuk, Phase field modelling of crack propagation, branching and coalescence in rocks, Theoretical and Applied Fracture Mechanics 96 (April) (2018) 174–192.

[105] S. Zhou, X. Zhuang, T. Rabczuk, A phase-field modeling approach of fracture propagation in poroelastic media, Engineering Geology 240 (2018) 189–203.

[106] A. Gupta, U. M. Krishnan, T. K. Mandal, R. Chowdhury, V. P. Nguyen, An adaptive mesh refinement algorithm for phase-field fracture models: Application to brittle, cohesive, and dynamic fracture, Computer Methods in Applied Mechanics and Engineering 399 (2022) 115347.

[107] H.-Y. Kim, H.-G. Kim, A novel adaptive mesh refinement scheme for the simulation of phase-field fracture using trimmed hexahedral meshes, International Journal for Numerical Methods in Engineering 122 (6) (2021) 1493–1512.

[108] E. Tanné, T. Li, B. Bourdin, J.-J. Marigo, C. Maurini, Crack nucleation in variational phase-field models of brittle fracture, Journal of the Mechanics and Physics of Solids 110 (2018) 80–99.

[109] H. Ahmadian, M. R. Mehraban, M. R. Ayatollahi, Y. Navidtehrani, B. Bahrami, Phase-field approach for fracture prediction of brittle cracked components, Engineering Fracture Mechanics 309 (2024) 110417.

[110] E. Hoek, E. T. Brown, Empirical strength criterion for rock masses, Journal of the geotechnical engineering division 106 (9) (1980) 1013–1035.

[111] M. YU, L. HE, Ts2e4 - a new model and theory on yield and failure of materials under the complex stress state, in: M. JONO, T. INOUE (Eds.), Mechanical Behaviour of Materials VI, Pergamon, Oxford, 1992, pp. 841–846.

[112] M.-H. Yu, J.-C. Li, Computational plasticity: With emphasis on the application of the unified strength theory, Springer Science & Business Media, 2012.

[113] M.-H. Yu, Y.-W. Zan, J. Zhao, M. Yoshimine, A unified strength criterion for rock material, International Journal of Rock Mechanics and Mining Sci-

ences 39 (8) (2002) 975–989.

[114] M. Ambati, T. Gerasimov, L. De Lorenzis, Phase-field modeling of ductile fracture, Computational Mechanics 55 (5) (2015) 1017–1040.

[115] R. Alessi, J.-J. Marigo, S. Vidoli, Gradient damage models coupled with plasticity and nucleation of cohesive cracks, Archive for Rational Mechanics and Analysis 214 (2014) 575–615.

[116] R. Alessi, J.-J. Marigo, C. Maurini, S. Vidoli, Coupling damage and plasticity for a phase-field regularisation of brittle, cohesive and ductile fracture: One-dimensional examples, International Journal of Mechanical Sciences 149 (2018) 559–576.

[117] C. Miehe, M. Hofacker, L. M. Schänzel, F. Aldakheel, Phase field modeling of fracture in multi-physics problems. Part II. Coupled brittle-to-ductile failure criteria and crack propagation in thermo-elastic-plastic solids, Computer Methods in Applied Mechanics and Engineering 294 (2015) 486–522.

[118] V. Putra, K. Furui, Phase-field modeling of coupled thermo-hydromechanical processes for hydraulic fracturing analysis in enhanced geothermal systems, Energies 16 (24) (2023).

[119] X. Hu, S. Tan, D. Xia, L. Min, H. Xu, W. Yao, Z. Sun, P. Zhang, T. Quoc Bui, X. Zhuang, T. Rabczuk, An overview of implicit and explicit phase field models for quasi-static failure processes, implementation and computational efficiency, Theoretical and Applied Fracture Mechanics 124 (2023) 103779.

A | Paper 1

Griffith-based analysis of crack initiation location in a Brazilian test

Authors:

Yousef Navidtehrani, Covadonga Betegón, Robert W. Zimmerman, Emilio Martínez-Pañeda

Journal:

International Journal of Rock Mechanics and Mining Sciences

Year of Publication:

2022

Impact Factor:

7.0 - Q1

International Journal of Rock Mechanics & Mining Sciences 159 (2022) 105227

Contents lists available at ScienceDirect

International Journal of Rock Mechanics and Mining Sciences

journal homepage: www.elsevier.com/locate/ijrmms

Griffith-based analysis of crack initiation location in a Brazilian test

Yousef Navidtehrani [a], Covadonga Betegón [a], Robert W. Zimmerman [b], Emilio Martínez-Pañeda [c,*]

[a] Department of Construction and Manufacturing Engineering, University of Oviedo, Gijón 33203, Spain
[b] Department of Earth Science and Engineering, Imperial College London, London SW7 2AZ, UK
[c] Department of Civil and Environmental Engineering, Imperial College London, London SW7 2AZ, UK

ARTICLE INFO

Keywords:
Rock mechanics
Brazilian test
Fracture
Finite element analysis
Griffith

ABSTRACT

The Brazilian test has been extremely popular while prompting significant debate. The main source of controversy is rooted in its *indirect* nature; the material tensile strength is inferred upon assuming that cracking initiates at the centre of the sample. Here, we use the Griffith criterion and finite element analysis to map the conditions (jaws geometry and material properties) that result in the nucleation of a centre crack. Unlike previous studies, we do not restrict ourselves to evaluating the stress state at the disk centre; the failure envelope of the generalised Griffith criterion is used to establish the crack nucleation location. We find that the range of conditions where the Brazilian test is valid is much narrower than previously assumed, with current practices and standards being inappropriate for a wide range of rock-like materials. The results obtained are used to develop a protocol that experimentalists can follow to obtain a valid estimate of the material tensile strength. This is showcased with specific case studies and examples of valid and invalid tests from the literature. Furthermore, the uptake of this protocol is facilitated by providing a MATLAB App that determines the validity of the experiment for arbitrary test conditions.

1. Introduction

The Brazilian test, also known as the Splitting Tensile Strength test, is arguably the most popular laboratory experiment for estimating the tensile strength of rocks and other quasi-brittle materials.[1] It was, independently, first proposed by Carneiro[2] and Akazawa[3] in 1943, and has been considered a standardised test since 1978, when it was included as a Suggested Method of the International Society for Rock Mechanics (ISRM).[4] As shown in Fig. 1, the test is comprised of two loading jaws, typically made of steel, and a disc-shaped sample. The jaws are configured so as to contact the sample at diametrically-opposed surfaces. Critical variables are the jaw radius, R_j, the disk radius, R_d, the disk thickness t, the measured reaction force P, and the contact angle α.

Assuming isotropic, linear elastic material behaviour, Hondros[5] derived an equation that relates the measured load P and contact angle α with the maximum principal stress at the centre of the disk:

$$\left(\sigma_1\right)_{x=0,y=0} = \frac{2P}{\pi R_d t \alpha}\left(\sin\alpha - \frac{\alpha}{2}\right). \tag{1}$$

Thus, from the critical values of P and α at failure, one can use Eq. (1) to estimate the material tensile strength σ_t upon assuming that the maximum value of σ_1 is attained at the centre of the disk: $\sigma_t = \left(\sigma_1\right)_{x=0,y=0}$. However, Eq. (1) is derived assuming the application of a uniform pressure. Moreover, being able to experimentally measure the contact angle at failure is far from trivial. Consequently, standards are built upon the assumption of a zero contact angle, simplifying Eq. (1) to the case of a concentrated load:

$$\left(\sigma_1\right)_{x=0,y=0} = \frac{P}{\pi R_d t}, \quad \text{for} \quad \alpha \to 0. \tag{2}$$

Eq. (2) is often referred to as the Hondros's point load solution or the Hertz solution.[6] Using Eq. (2), the material tensile strength can be readily estimated from the critical load (P_c): $\sigma_t = \left(\sigma_1\right)_{x=0,y=0} = P_c/(\pi R_d t)$. However, this *indirect* approach builds upon a number of assumptions; most notably: (i) the load is assumed to be a concentrated point load, and (ii) cracking initiates from the centre of the disk. In practice, fulfilling these two assumptions depends on the choices of test geometry and material. Numerical computations show the existence of three regimes. Sufficiently low contact angles will satisfy Eq. (2) and lead to a maximum value of σ_1 at the disk centre. As the contact angle increases, Eq. (2) is no longer satisfied, but the maximum magnitude of the tensile principal stress is still attained at the centre. And finally, if the contact angle is sufficiently large then not only is Eq. (2) not satisfied but also the location of the maximum tensile stress moves away from the disk centre. Thus, the validity of the Brazilian test is sensitive to the contact angle at failure, which is itself dependent

* Corresponding author.
E-mail address: e.martinez-paneda@imperial.ac.uk (E. Martínez-Pañeda).

https://doi.org/10.1016/j.ijrmms.2022.105227
Received 19 March 2022; Received in revised form 17 August 2022; Accepted 13 September 2022
Available online 6 October 2022

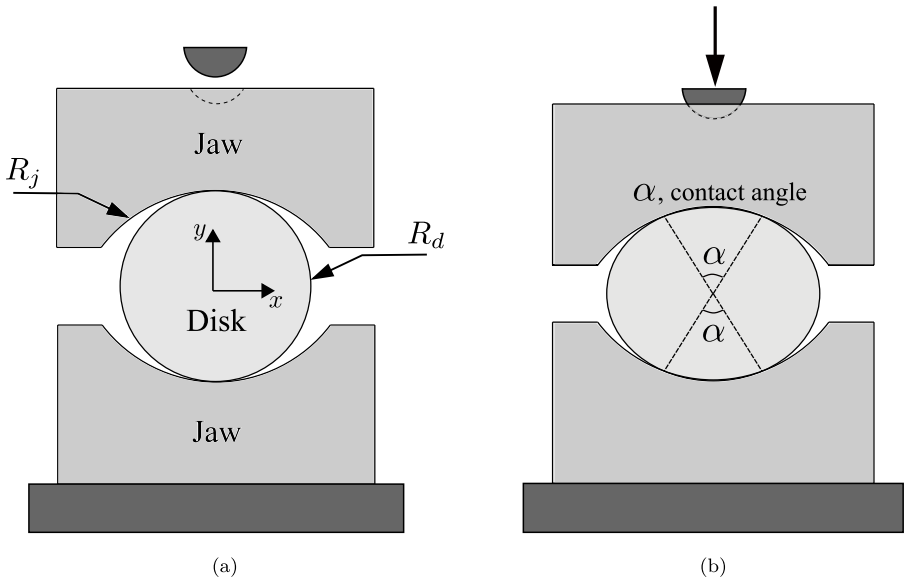

Fig. 1. Brazilian test configuration in the (a) undeformed, and (b) deformed states. The sketch shows the main variables: the jaw radius R_j, the disk radius R_d, and the contact angle at failure α. A reaction force P is measured.

on the elastic properties of the disk and jaws (Young's moduli E_d, E_j; Poisson's ratios ν_d, ν_j), the sample and jaw radii (R_d, R_j), and the critical load (i.e., the material strength). Not surprisingly, this sensitivity to material and test parameters has fostered significant discussion in the academic literature. Despite the current popularity of the Brazilian test, early studies highlighted the sensitivity of the crack initiation location to the contact angle and questioned its use.[7,8] The debate is very much open and a myriad of papers have been published trying to shed light on the validity regimes of the Brazilian test using theoretical, numerical and experimental tools. Recent examples include the work of Alvarez-Fernandez and co-workers[9], who investigated, experimentally and analytically, the influence of the contact angle in the stress distribution and the failure load in slate. They reported that contact angles in the range $23-32°$ were the most suitable to achieve crack initiation near the disk centre. Markides and Kourkoulis[10] used analytical methods to evaluate the sensitivity of the stress state to the jaw's curvature, delimiting the conditions where Eq. (2) is applicable. Gutierrez-Moizant et al.[11] conducted Brazilian tests in concrete with various contact angles and recommended using a loading arc of 20°. Bouali and Bouassida[12] investigated the role of the contact angle for both concrete and mortar, concluding that 20° was the most suitable contact angle for concrete while 10° was recommended for mortar. Garcia-Fernandez et al.[13] conducted Brazilian tests in PMMA samples, which enabled them to visualise the crack initiation process and demonstrated the important role of the contact angle. Zhao and co-workers[14] used acoustic emission to investigate the role of the experiment setup on the crack nucleation event. Aliabadian et al.[15] showed, using Digital Image Correlation (DIC), that the location of crack nucleation was sensitive to the contact angle and estimated a value of $\alpha = 25°$ as the most appropriate one for sandstone. Alternative testing configurations have also been proposed (see, e.g., Refs. 16, 17 and Refs. therein). The aforementioned studies provide material-specific estimations of test geometry (contact angles) that result in a stress state where the maximum tensile stress is attained at the centre of the disk. This can be achieved by using a sufficiently large jaw radius (sufficiently small contact angle). However, small contact angles result in high contact stresses that cause premature cracking near the loading region.[18] Thus, finding a suitable testing configuration involves striking a balance between ensuring that the contact angle is both: (i) small enough such that the maximum tensile stress is attained at the centre and Eq. (2) is satisfied, and (ii) large enough such that cracking does not occur in the compressive region beneath the jaw. This is not straightforward as it depends on a number of testing and material parameters and even today technical standards differ in their recommendations (see, e.g., Refs. 4, 19). There is a need for a generalised approach that will enable mapping the regimes of validity of the Brazilian test for arbitrary choices of material and test configuration.

In this work, we use the generalised Griffith criterion[7,20] to gain insight into the location of crack initiation in the Brazilian test. By considering the entire failure envelope, we ensure that not only is the maximum tensile stress attained at the centre of the sample at the moment of failure but also that this crack nucleation event is not preceded by cracking elsewhere in the sample. Finite element calculations are conducted to build maps that enable assessing the experiment viability for any material and test geometry. First, we analyse the stress state at the disk centre as a function of the load and quantify the error associated with Hondros's solutions, Eqs. (1) and (2), for relevant material properties and testing configurations. Second, we map the conditions that lead to crack nucleation at the disk centre and thus to a valid test. Calculations span the main classes of rocks and assess the suitability of current testing standards. We find that the range of conditions where a Brazilian test is valid is much narrower than previously thought. A protocol is presented to ensure that the experiment leads to a valid estimate of the material tensile strength. This is exemplified with specific case studies and facilitated by providing a MATLAB App that takes as input the test data and provides as output the validity of the experiment and the magnitude of the tensile strength.

2. Generalised Griffith criterion for crack initiation

Griffith[20] studied the fracture of brittle materials under compressive loads by assuming that the rupture process was driven by local flaws within the material. As shown in Fig. 2, local tensile stresses will develop near existing flaws when these are oriented at an angle relative to the principal directions of the applied stress. Denoting the major and minor principal stresses as σ_1 and σ_3, respectively, Griffith's[20] two-part criterion for the onset of fracture is given as follows,[d]

$$\begin{cases} \sigma_1 = \sigma_t & \text{if} \quad 3\sigma_1 + \sigma_3 \geq 0 \\ (\sigma_1 - \sigma_3)^2 = -8\sigma_t(\sigma_1 + \sigma_3) & \text{if} \quad 3\sigma_1 + \sigma_3 < 0 \end{cases} \tag{3}$$

[d] A detailed derivation can be found in Ref. 21.

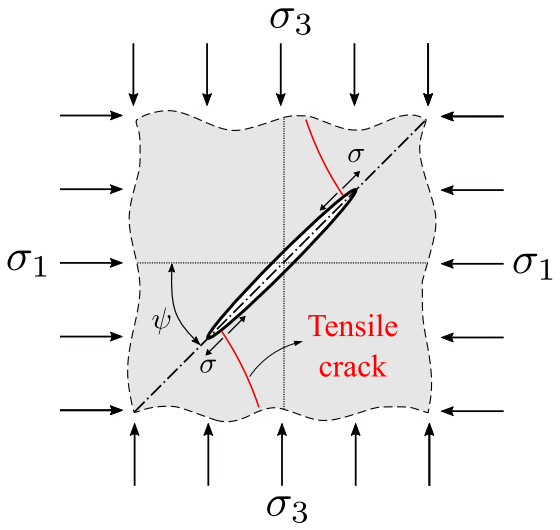

Fig. 2. Local stress state in a Griffith micro-crack, with ψ denoting the crack inclination angle. When the local tensile stresses reach the material tensile strength σ_t, wing cracks nucleate near the edges of the original micro-crack.

with the initial crack orientation being respectively given by the angles:

$$\begin{cases} \psi = \pi/2 & \text{if} \quad 3\sigma_1 + \sigma_3 \geq 0 \\ \psi = \frac{1}{2}\cos^{-1}\left(\frac{\sigma_1 - \sigma_3}{2(\sigma_1 + \sigma_3)}\right) & \text{if} \quad 3\sigma_1 + \sigma_3 < 0 \end{cases} \tag{4}$$

Two aspects must be emphasised. First, it is observed that for a regime where σ_1 is tensile and σ_3 is compressive with an absolute value lower than three times σ_1, conditions of purely tensile failure take place, with cracks parallel to the original flaw[22]. Second, the criterion indicates that the material compressive strength σ_c is eight times its tensile strength as Eq. (3)b gives $\sigma_3 = \sigma_c = -8\sigma_t$ under uniaxial compression ($\sigma_1 = 0$). While this is of the right order of magnitude, it limits the application of the criterion to materials with a compressive-to-tensile strength ratio of 8. To overcome this and generalise Griffith's criterion, Fairhurst[7] proposed an extension to allow for arbitrary compression-to-tensile strength ratios. This is achieved by defining a parabolic Mohr envelope that encloses the uniaxial tensile and compressive strength circles, with the former being touched at its vertex and the latter being tangent to the envelope — see Fig. 3a. Accordingly, defining n as the compressive-to-tensile strength ratio ($n = -\sigma_c/\sigma_t$), the relation describing the compressive strength circle is given by,

$$\left(\sigma + \frac{n\sigma_t}{2}\right)^2 + \tau^2 = \left(\frac{n\sigma_t}{2}\right)^2 \tag{5}$$

with σ and τ respectively denoting the normal and shear stresses.

In terms of the principal stress space, the generalised Griffith criterion reads:

$$\begin{cases} \sigma_1 = \sigma_t & \text{if} \quad m(m-2)\sigma_1 + \sigma_3 \geq 0 \\ \sigma_3 = \sigma_1 - (1-m)^2\sigma_t + 2(1-m)\sqrt{\sigma_t\left(\sigma_t - \sigma_1\right)} & \text{if} \quad m(m-2)\sigma_1 + \sigma_3 < 0 \end{cases} \tag{6}$$

where m is a material parameter defined as $m = \sqrt{n+1}$. The failure envelope is shown graphically in Fig. 3b. The generalised Griffith criterion particularises to the original Griffith criterion (3) for $n = 8$ and otherwise extends it to arbitrary tensile and compressive material strengths. It is worth noting that the adoption of the generalised Griffith criterion necessarily implies that the Brazilian test is, generally, not a suitable experiment for measuring the tensile strength of materials with $n < 8$; see Eq. ((6)a) and Fig. 3b and consider the fact that $\sigma_3 \approx -3\sigma_1$ at the disk centre for zero or small contact angles.[21]

3. The application of Griffith's criterion to the Brazilian test

During the Brazilian split test, the material points in the disk undergo a stress state that is characterised by two domains in the principal stress state — see Fig. 4. In some regions, such as in the vicinity of the jaws, material points exhibit compressive major and minor principal stresses ($\sigma_1 < 0 \& \sigma_3 < 0$). However, near the centre of the disk, the stress state is characterised by a maximum principal stress in tension ($\sigma_1 > 0$) and a minimum principal stress in compression ($\sigma_3 < 0$).

As discussed in Section 1, the controversy surrounding the Brazilian test is related to the crack initiation location. For the experiment to provide a valid estimate of the material tensile strength, the onset of cracking must take place at the centre of the disk and the relation between the critical load and σ_1 at the disk centre must be known. One can use the failure envelope of the generalised Griffith criterion (Fig. 3) to analyse the stress state in the disk and map the conditions of validity. This is shown in a schematic manner in Fig. 5, where a cloud of points is used to represent the potential stress states in a discrete number of material points distributed within the disk, $(\sigma_1, \sigma_3)_{(x,y)}$. Two scenarios can essentially occur. On the one hand, Fig. 5a, the test is invalid if the first material point reaching the failure envelope is not located in the centre of the disk. This is, for example, what happens when cracking is observed close to the loading jaws. On the other hand, Fig. 5b, if the failure envelope is reached first by the material point located at the disk centre ($x = 0$, $y = 0$), then a valid estimate of the tensile strength is obtained: $\sigma_t = (\sigma_1)_{(0,0)}$.

For a given applied load, test geometry and elastic properties of jaws and disk, the validity of the test will be determined by the failure envelope (i.e., the magnitude of σ_c and σ_t). Fig. 5c shows a scenario where one of the conditions of validity of the Brazilian test has been met: the centre of the disk (green dot) is in a stress state where $(\sigma_1)_{(0,0)} = \sigma_t$. However, the test is still not valid if the ratio σ_c/σ_t is sufficiently low — several material points are above the envelope, implying that failure has occurred elsewhere at a smaller load. This scenario is illustrated with a red dotted curve in Fig. 5c. If the ratio σ_c/σ_t is sufficiently large (green dashed curve), then the only point in contact with the envelope is the centre one, and the experiment is valid.

The limiting case is that where the failure envelope is met at two or more points at the same time, one of which is located at the disk centre. This is illustrated in Fig. 5c with an orange dash-dotted line and provides the threshold of admissible σ_c/σ_t ratios for a Brazilian test to be valid. Thus, for a given load, geometry and material parameters, one can use numerical analysis to estimate the stress state at any point in the disk $(\sigma_1, \sigma_3)_{(x,y)}$ and utilise the generalised Griffith criterion to determine the compressive strength associated with a failure envelope passing through that point; i.e., re-arranging Eq. (6)b:

$$(\sigma_c)_{(x,y)} = -\sigma_t \left(\frac{\left(\sigma_t - \sqrt{\sigma_t\left(\sigma_t - (\sigma_1)_{(x,y)}\right)} + \sqrt{\sigma_t\left(\sigma_t - (\sigma_3)_{(x,y)}\right)}\right)^2}{{\sigma_t}^2} - 1 \right) \tag{7}$$

For the failure condition to be first met at the disk centre, the maximum value of $(\sigma_c)_{(x,y)}$ among all material points in the disk, as estimated *via* Eq. (7), must be equal or smaller than the real material compressive strength σ_c. Hence, since σ_c is a known material property that can be measured independently, one can combine numerical analysis and the generalised Griffith's criterion to map the conditions that lead to failure initiation from the centre of the disk. In this way, the two validity conditions of the Brazilian test – cracking initiating at the centre (0,0) and $(\sigma_1)_{(0,0)} = \sigma_t$ – can be incorporated in the analysis, as shown below.

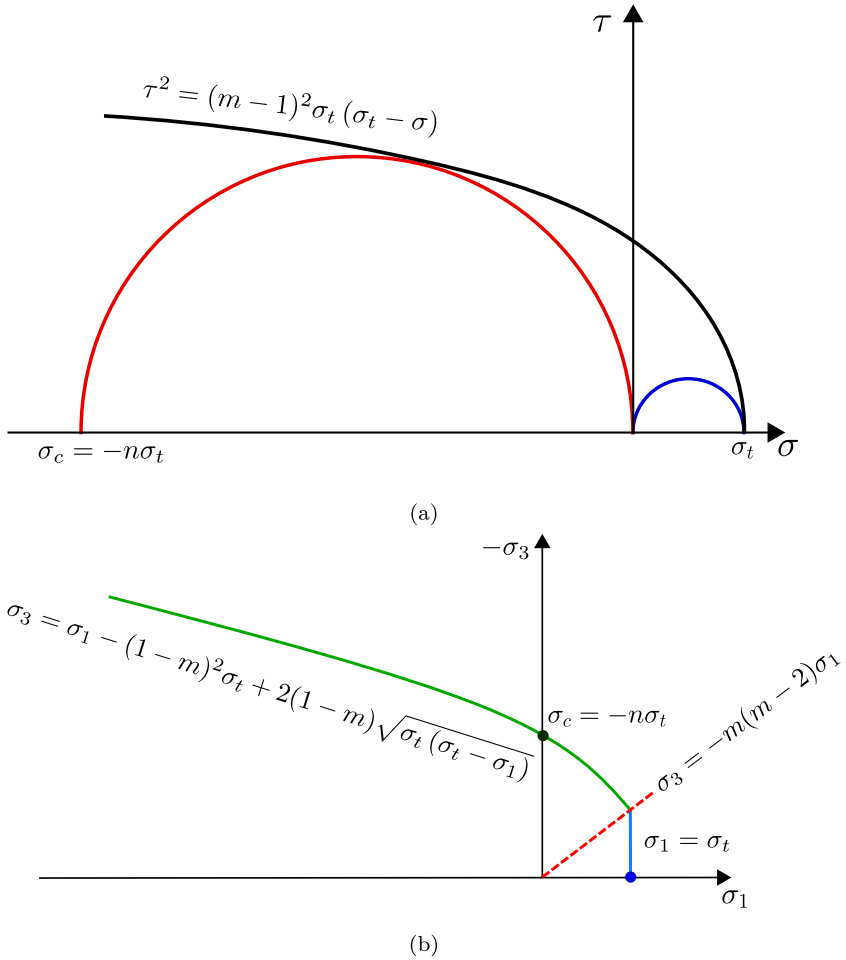

Fig. 3. Generalised Griffith criterion. Mohr diagram showing the generalised parabolic failure envelope in terms of: (a) normal σ and shear τ stresses, and (b) minor σ_3 and major σ_1 principal stresses. Here, $n = -\sigma_c/\sigma_t$ and $m = \sqrt{n+1}$.

4. Analysis

We proceed to combine finite element analysis and the generalised Griffith criterion to map the regimes of validity of the Brazilian test.

4.1. Preliminaries

The location of crack initiation in the Brazilian test is a function of 2 geometrical and 6 material parameters: the jaw radius (R_j), the disk radius (R_d), the elastic properties of the disk (E_d, ν_d) and jaws (E_j, ν_j), and the tensile (σ_t) and compressive (σ_c) strengths of the material being tested. Assuming that cracking initiates along the vertical middle axis of the disk, the crack initiation location can be fully characterised by a variable Y, equal to 0 at the centre and to R_d at the edge. Then, dimensional analysis dictates that the solution is a function of the following non-dimensional sets:

$$\frac{Y}{R_d} = F\left(\frac{R_j}{R_d}, \frac{E_j}{E_d}, \nu_j, \nu_d, \frac{\sigma_c}{E_d}, \frac{\sigma_t}{E_d}\right). \tag{8}$$

Further assuming that crack nucleation takes place at the centre of the disk ($Y/R_d = 0$), as required for the test to be valid, then Eq. (8) can be re-arranged to:

$$\frac{\sigma_c}{\sigma_t} = G\left(\frac{R_j}{R_d}, \frac{E_j}{E_d}, \nu_j, \nu_d, \frac{\sigma_c}{E_d}\right). \tag{9}$$

Thus, conducting calculations over relevant ranges of the five non-dimensional sets in Eq. (9) will enable mapping the conditions that lead to cracking at the disk centre.

We use the GRANTA Material library[23] to define a suitable range of material properties. The Young's modulus, Poisson's ratio, tensile strength and compressive strength of the most widely used rock-like materials are shown in Figs. 6a–6c. To conduct a comprehensive analysis, we vary the Young's modulus of the disk from 5 to 150 GPa. Also, Poisson's ratio is varied within the range 0.1 to 0.4. The jaws are typically made of steel and thus the following elastic properties are assumed: $E_j = 210$ GPa and $\nu = 0.3$. Given that E_j and ν_j are fixed (and known), the dimensional analysis conducted above suggests that the two critical non-dimensional sets are σ_c/σ_t and σ_c/E_d. Thus, we proceed to plot their relationship for a wide range of materials in Fig. 6d. It can be observed that relevant ranges of σ_c/σ_t and σ_c/E_d are approximately 2–30 and 0.0001–0.01, respectively.

To determine the stress state within the disk we conduct finite element analysis of the contact between the jaws and the sample and the subsequent material deformation. The commercial finite element package ABAQUS is used. Only one quarter of the test is simulated, taking advantage of symmetry. The radius of the disk equals $R_d = 10$ mm while the jaw radius is varied from $R_j = 11$ mm to the case of a flat jaw geometry ($R_j \to \infty$). Quadratic quadrilateral finite elements with full integration are used to discretise the disk and the jaw. Plane strain conditions are assumed. After a sensitivity analysis, a total of 28,241 elements are used to discretise the disk and between 4102 and 4459 elements are used for the jaw. The mesh is particularly fine in the disk and in the regions of the jaw that are in contact with the disk. A uniform negative vertical displacement is applied at the top of the jaw and the resulting reaction force is measured. The contact behaviour is modelled as follows. For the normal behaviour, we

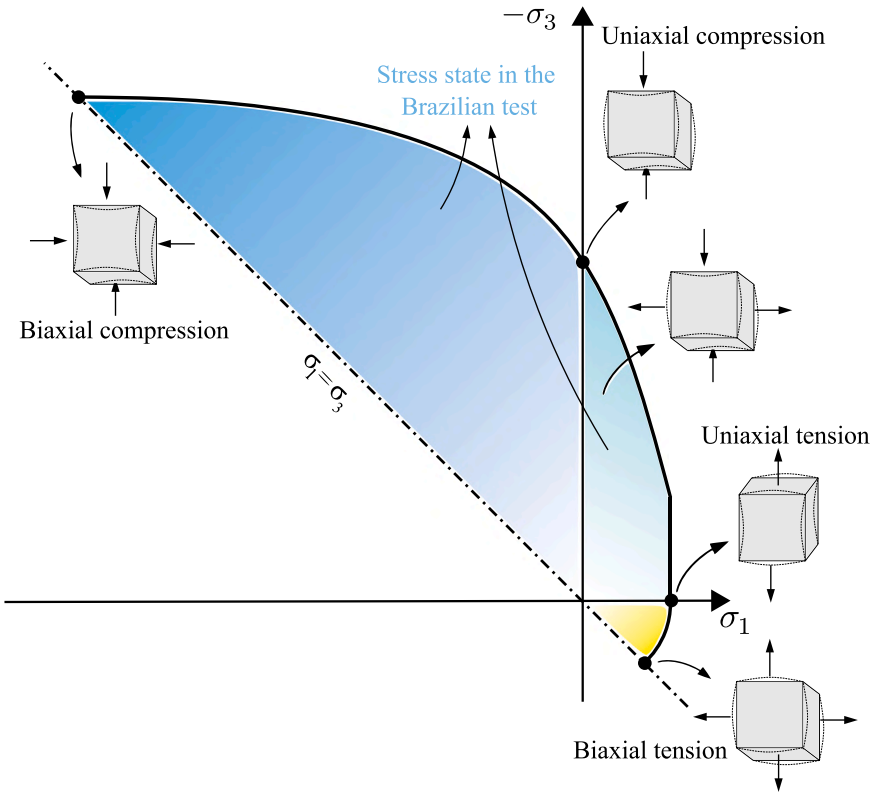

Fig. 4. Stress states and typical failure envelope for rock-like materials, emphasising the two regimes relevant to the Brazilian test. The stress states are shown in the principle stress diagram, with tensile stresses being positive and σ_1 and σ_3 respectively denoting the major and minor principal stresses.

consider surface-to-surface hard contact, where Lagrangian multipliers are used to ensure that the contact pressure and the contact constraint minimise overclosure. For the tangential behaviour, frictionless contact is generally assumed although the role of friction is also investigated (see Section 4.3.4), revealing a negligible influence.

4.2. Mapping the stress state at the disk centre

We shall start by quantifying the relationship between the load P and the stress state at the centre of the disk under a wide range of conditions. The goal is to map the scenarios where Eqs. (1) and (2) are valid. We shall start by assessing the validity of Eq. (2), an intrinsic assumption in the standards. The finite element results obtained are shown in Fig. 7 in terms of the stress state at the centre of the disk ($x = 0, y = 0$) versus the load for a wide range of E_j/E_d values and selected choices of jaw radius, as given by the ratio R_j/R_d. In terms of test geometry, three scenarios are considered: $R_j/R_d = 1.1$, $R_j/R_d = 1.5$ (as in the ISRM standard) and flat jaws (one of the configurations recommended by the ASTM standard). The limits of the x-axis are chosen so as to encompass a wide range of realistic contact angles; the upper limit ($P/(\pi R_d t) = 0.0003 E_j$) corresponds to a tensile strength of roughly 60 MPa if a steel jaw ($E_j = 210$ GPa) is considered in Eq. (2), which is sufficiently high to cover the vast majority of rock-like materials.

The results reveal that Eq. (2) is only valid for low load magnitudes and small E_j/E_d ratios. The error is particularly significant for low R_j/R_d values — note the y axis limits in Fig. 7a. But even for the case of flat jaws, as recommended by the ASTM standard, $(\sigma_1)_{(0,0)}/(P/\pi R_d t)$ is only equal to 1 for low contact angles (low P) and small Young's modulus mismatch. Consider for example a sandstone with $E_d = 20$ GPa ($E_j/E_d = 10.5$) and tensile strength $\sigma_t = 20$ MPa ($P/(\pi R_d t) \approx 0.0001 E_j$), see Fig. 6; in all cases Eq. (2) is not fulfilled, with the errors being of roughly 5%, 2% and 0.5% for, respectively, the cases of $R_j/R_d = 1.1$, $R_j/R_d = 1.5$ (as suggested by ISRM) and flat jaws (as suggested by the ASTM standard). The maximum errors observed for these three configurations, relevant to materials with high tensile strength and low stiffness, are respectively 36%, 13% and 5%. However, these maps enable a precise determination of the stress state in the centre of the disk and, accordingly, of the material tensile strength σ_t. One can use them to assess if the error intrinsic to the adoption of the point load equation is admissible, or directly as a replacement to Eq. (2), as these maps enable determining the precise value of $\sigma_1 (= \sigma_t)$ at the disk centre as a function of the material properties, test geometry and critical load.

The results obtained for a wide range of jaw radii are given in Fig. 8. Maps are provided as a function of the normalised load, using the Young's modulus of the rock as normalising parameter. Two figures are shown, corresponding to the lower and upper bounds of the elastic modulus; $E_j/E_d = 42$ ($E_d \approx 5$ GPa, Fig. 8a) and $E_j/E_d = 1.4$ ($E_d \approx 150$ GPa, Fig. 8b). Maps for other scenarios are provided in the Supplementary Material, so that experimentalists can accurately determine the stress state at the disk centre for arbitrary materials and test conditions. See also the Matlab App described in Appendix A. In agreement with expectations and with the results shown in Fig. 7, stiffer materials bring the stress state close to that fulfilling Eq. (2). Also, the error is relatively small when large jaw radii are used, with the limiting case being given by the flat jaws recommended by ASTM.[19]

Let us assume that the contact angle can be experimentally determined and assess the accuracy of Hondros's analytical solution for $\alpha > 0$, Eq. (1). The finite element prediction of maximum principal stress at the disk centre is shown in Fig. 9 normalised by Hondros's analytical solution for a uniformly distributed load. Results are shown for the lower and upper bounds of the elastic modulus considered above, and as a function of the jaw radius. Differences are overall small, as could be expected from Saint-Venant's principle. However, the assumption of a uniform pressure, intrinsic to Hondros's solution, leads to errors above 3% for softer rocks and curved jaw configurations such as that of the ISRM standard. As in Figs. 7 and 8, the error becomes negligible for rocks on upper end of the stiffness spectrum and for jaws with

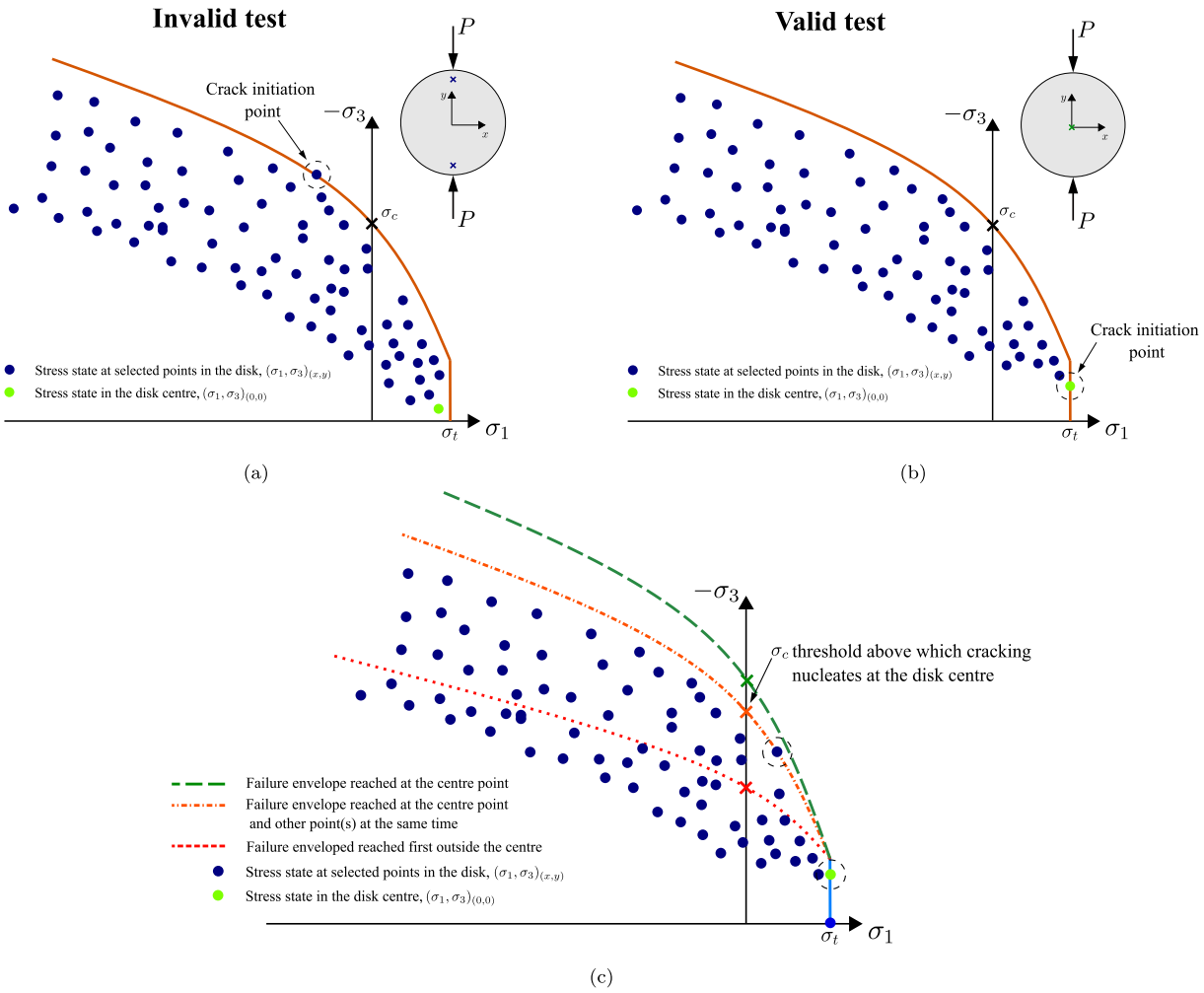

Fig. 5. Stress state at a discrete number of material points within the Brazilian disk and failure envelopes based on the generalised Griffith criterion. (a) Conditions leading to an invalid test; failure is attained outside from the disk centre. (b) Conditions leading to a valid test; $\sigma_1 = \sigma_t$ at the centre of the sample (0,0). (c) Validity of the test as a function of the failure envelope (σ_c, σ_t) for a given stress state associated with a load P. A green dot is used to denote the stress state at the disk centre (0,0).

large radius. Notwithstanding, as discussed below, the use of a large jaw radius favours the nucleation of cracking far from the disk centre, making the test invalid.

4.3. Mapping the conditions that lead to cracking at the disk centre

Low contact angles lead to stress states that are close to the Hondros equations. However, this is not sufficient for the test to be valid as cracking can nucleate outside of the disk centre, as it is often reported when flat or large-radius jaws are used (see, e.g., Refs. 12, 24, 25). While the maps presented in Section 4.2 provide a relationship between the critical load and the tensile strength (even if Eq. (2) is not met), this is only meaningful if the critical load is associated with the initiation of cracks at the disk centre and not elsewhere. To determine the location of crack nucleation, we combine the generalised Griffith failure envelope and finite element analysis (see Section 3). To achieve this, we start by assuming that cracking initiates at the disk centre, where $\sigma_1 = \sigma_t$, and assess that assumption by comparing the compressive-to-tensile strength ratio resulting from the test with the admissible range of σ_c/σ_t ratios. If the latter is greater than the former, then cracking initiates outside of the disk centre and the test is invalid. Specifically, for each combination of material and test parameters, the process is as follows. Firstly, a finite element analysis is conducted to estimate the principal stresses (σ_1, σ_3) at each integration point for a wide range of load increments. Secondly, Eq. (7) is used to compute the minimum admissible σ_c (i.e., the maximum σ_c among all material points). Finally, from the threshold σ_c and the assumption $(\sigma_1)_{(0,0)} = \sigma_t$, a data point is established relating the material and test parameters to the threshold of admissible σ_c/σ_t values. Each map, such as Fig. 10a, is built using approximately 20,000 of these data points and interpolating in-between. The process is automated by means of Python and MATLAB scripts.[26]

4.3.1. The influence of the jaw radius

We start by mapping the influence of the jaw radius on the validity of the Brazilian test. Fig. 10 shows, following the procedure described above, the relation between the jaw radius (as given by R_j/R_d), the non-dimensional set σ_c/E_d and the minimum acceptable compressive-to-tensile strength ratio. Maps are provided for two limit cases of disk elastic properties: $E_j/E_d = 42$ (i.e., $E_d \approx 5$ GPa) and $E_j/E_d = 1.4$ (i.e., $E_d \approx 150$ GPa), with the majority of rock-like materials expected to fall between these two cases. By comparing Figs. 10a and 10b, it can be seen that while E_j/E_d influences the results, the role appears to be of secondary nature relative to the influence of the jaw radius.

The results reveal the following trends. First, for a given jaw radius, the range of admissible σ_c/σ_t ratios increases with increasing σ_c/E_d, as valid tests (centre cracking) are those above the σ_c/σ_t threshold. When the compressive strength increases, the likelihood of cracking nucleating outside of the disk centre decreases. For example, consider the specific case $E_j/E_d = 42$ and $R_j/R_d = 1.5$. When $\sigma_c/E_d = 0.002$, the

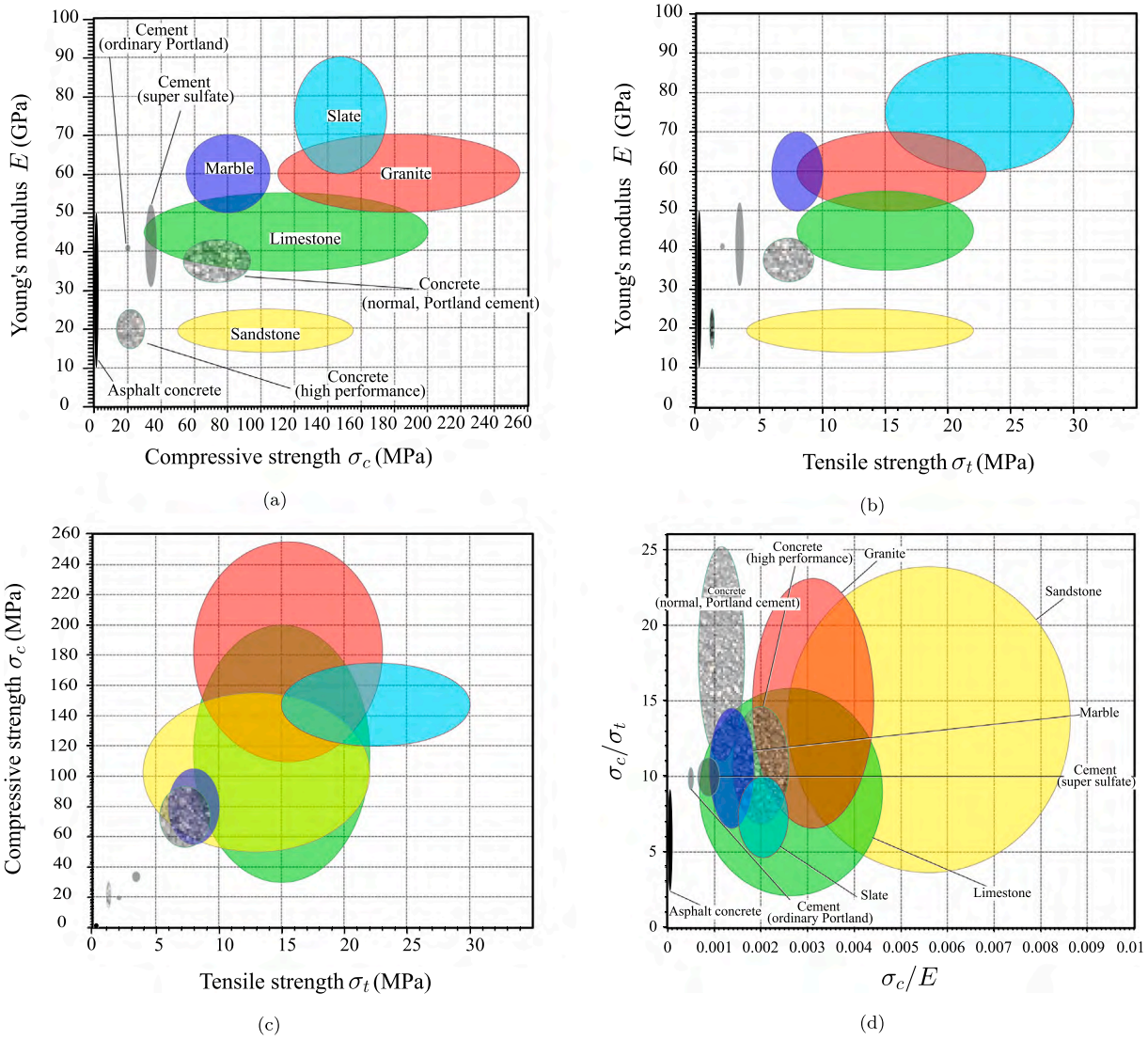

Fig. 6. Material property range of rock-like materials. Ashby charts showing the relations between (a) Young's modulus (E) and compressive strength (σ_c), (b) Young's modulus (E) and tensile strength (σ_t), (c) compressive (σ_c) and tensile (σ_t) strengths, and (d) ratio of compressive-to-tensile strength (σ_c/σ_t) and ratio of compressive strength to elasticity modulus σ_c/E. The data is taken from the GRANTA Material library[23] for granite, slate, marble, sandstone, limestone, concrete, cement and asphalt. The typical ranges for the Poisson's ratio of these materials are: granite $\nu = 0.15 - 0.26$, slate $\nu = 0.22 - 0.3$, marble $\nu = 0.14 - 0.22$, sandstone $\nu = 0.22 - 0.29$, limestone $\nu = 0.2 - 0.26$, concrete $\nu = 0.1 - 0.2$, cement $\nu = 0.2 - 0.24$, and asphalt $\nu = 0.35 - 0.36$.

region of validity is $\sigma_c/\sigma_t > 28$, whereas when $\sigma_c/E_d = 0.01$, the ratio σ_c/σ_t needs only to exceed 11. Also, lower E_d values result in larger contact angles and thus less chances of cracking occurring nearby the loading jaws. This is also observed by comparing Figs. 10a and 10b; the stiffer the sample the more likely that cracking will occur in the compressive regions. Importantly, the results provide σ_c/σ_t thresholds below which it is not possible to obtain a valid Brazilian test. Thus, it is not possible to obtain a valid result if $\sigma_c/\sigma_t < 7$, independently of the jaw radius. For σ_c/E_d ratios as high as 0.01, the ISRM ($R_j/R_d = 1.5$) configuration provides thresholds of σ_c/σ_t equal to 11 (Fig. 10a) and 8 (Fig. 10b). While the ASTM (flat jaws) configuration gives σ_c/σ_t thresholds of 20 (Fig. 10a) and 14 (Fig. 10b). Hence, as it can be seen in Fig. 6(d), conducting Brazilian tests in agreement with the ISRM and (particularly) ASTM guidelines will lead to invalid results for a range of rocky materials, independently of the jaw radius.

4.3.2. The influence of Young's modulus

We proceed to report the effect of the Young's modulus of the sample (E_d) for selected testing geometries. Specifically, results are shown for a small jaw radius ($R_j/R_d = 1.1$) and the ISRM ($R_j/R_d = 1.5$) and ASTM (flat jaws) recommended configurations. The maps obtained are presented in Fig. 11.

Several observations can be drawn. First, the flatter the jaws the higher the sensitivity to the elastic stiffness of the sample. The map is wider and more significant differences can be observed between the admissible limits for a given σ_c/E_d value. A smaller range of admissible σ_c/σ_t ratios (i.e., lower threshold values) is predicted with increasing jaw radius. This is consistent with expectations in terms of contact angles; high contact angles can readily be achieved with curved jaws while flat or large radius jaws can only do so if the disk is soft. Second, the figure emphasises the limitations of current standardised procedures. As shown in Fig. 6(d), many materials lie within the region delimited by 0.001–0.004 σ_c/E_d and 5–15 σ_c/σ_t. However, the maps obtained for the ISRM and ASTM standards fall above this region, implying that the tests will necessarily result in estimates below the admissible σ_c/σ_t threshold and thus cracking is predicted to occur in the compressive region, rather than in the disk centre.

4.3.3. The influence of Poisson's ratio

The role of the disk's Poisson's ratio is examined in Fig. 12. Two limit values are considered, $\nu_d = 0.1$ and $\nu_d = 0.4$, and results are

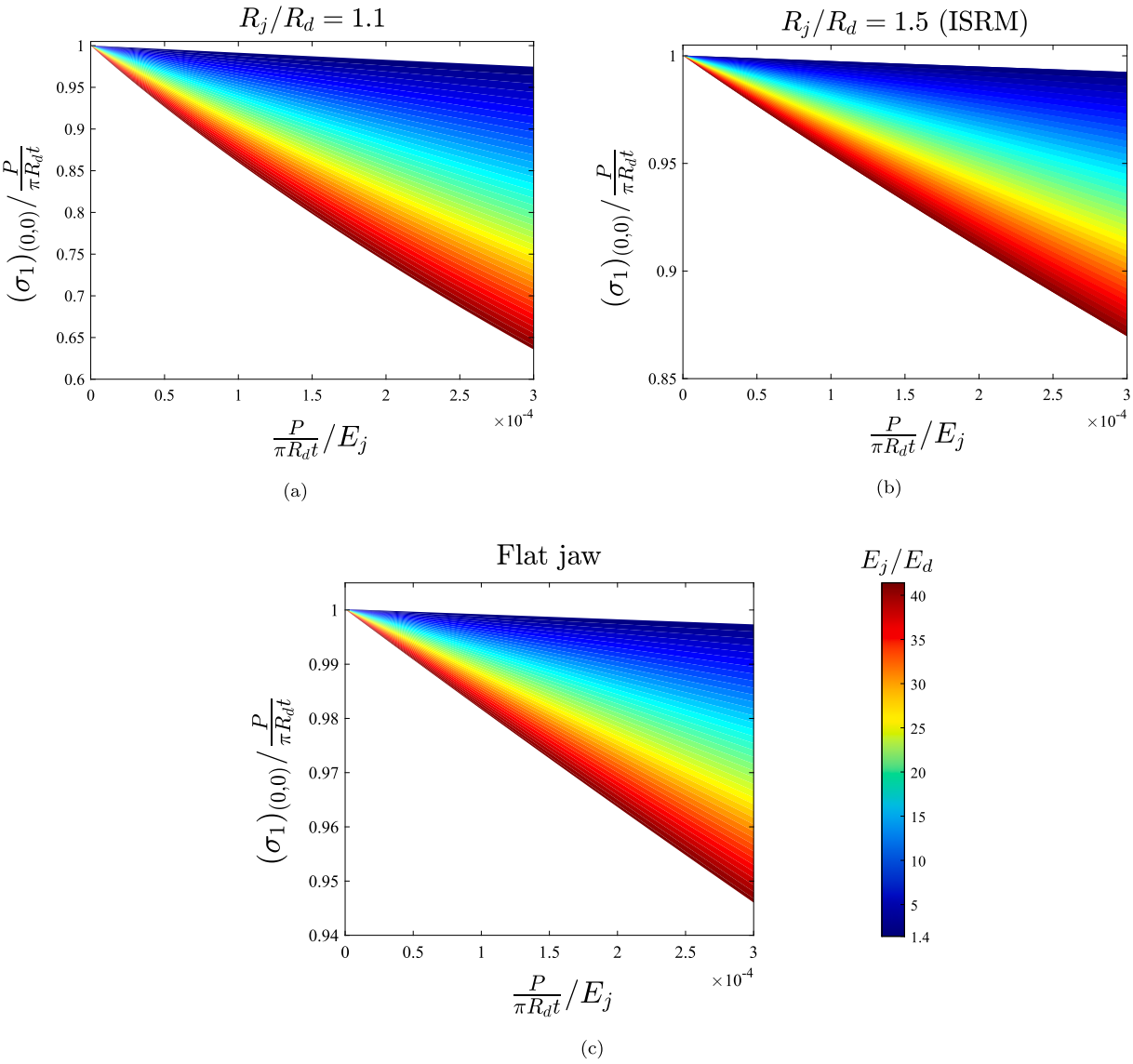

Fig. 7. Maps to quantify the stress state at the disk centre as a function of the material properties, test geometry and critical load. Normalised major principal stress versus dimensionless load for a wide range of E_j/E_d values and the following test geometries: (a) $R_j/R_d = 1.1$, (b) $R_j/R_d = 1.5$ (as recommended by ISRM), and (c) flat jaws (as recommended by ASTM). Poisson's ratio in the disk is taken to be $\nu_d = 0.2$.

obtained for limit cases of E_j/E_d and R_j/R_d so as to span all scenarios. Overall, Poisson's ratio seems to play a very secondary role. The effect is negligible for low jaw radii ($R_j/R_d = 1.1$) and this appears to be insensitive to the elastic modulus mismatch (E_j/E_d). Some differences are observed for jaws with a large radius, with smaller Poisson's ratios further reducing the range of admissible compressive-to-tensile strength ratios. This implies that the appropriate value of Poisson's ratio must be used when assessing the validity of the Brazilian test in a configuration with flat or large-radius jaws, as in the ASTM standard.[19]

4.3.4. The influence of friction

To investigate the role of friction, simulations are conducted with a friction coefficient of $\mu = 0.8$, an upper bound with respect to the values that may be expected for rock/metal interfaces. A penalty method is used to incorporate friction into the model. As in the Poisson's ratio study, we consider limit values of E_j/E_d and R_j/R_d, to span all relevant conditions. The results are shown in Fig. 13 for a Poisson's ratio of $\nu_d = 0.1$; consistent with the observations above, other values of the disk's Poisson's ratio led to identical conclusions. As it can be observed, no noticeable differences are seen between the simulations with and without friction. This also holds for other values of the friction coefficient (results not shown) and is in agreement with the secondary role of friction reported in the literature.[27–30] While friction is known to influence the stress state of material points near the jaws,[31] these points appear to play a secondary role in our analysis of the validity of the Brazilian test.

4.4. Representative case studies

Let us now showcase the importance of the maps presented above by particularising them to the study of common rock materials. Fig. 14 shows the results obtained for granite, sandstone, limestone and marble. To build the maps, a Poisson's ratio of $\nu_d = 0.2$ is adopted in all cases, while the Young's modulus equals $E_d = 60$ GPa ($E_j/E_d = 3.5$) for granite, $E_d = 20$ GPa ($E_j/E_d = 10.5$) for sandstone, $E_d = 50$ GPa ($E_j/E_d = 4.2$) for limestone, and $E_d = 60$ GPa ($E_j/E_d = 3.5$) for marble. The space that these materials occupy in a compressive-to-tensile strength ratio versus σ_c/E_d plot is shown by means of ellipses, based on the material properties available in the GRANTA Material library[23] (see Fig. 6(d)). As before, estimates of the admissible σ_c/σ_t

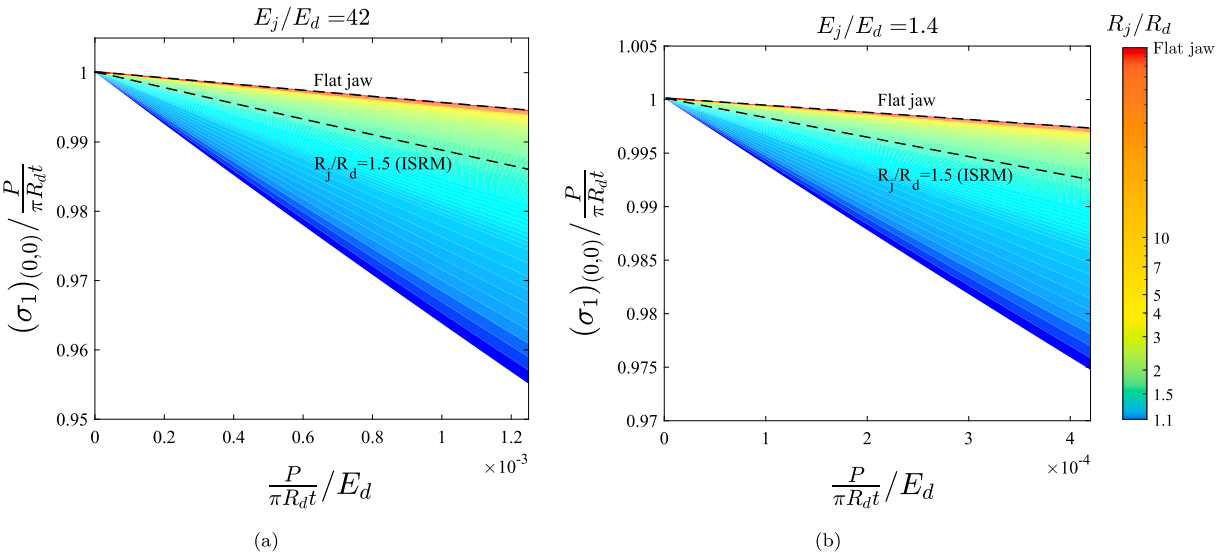

Fig. 8. Maps to quantify the stress state at the disk centre as a function of the material properties, test geometry and critical load. Normalised major principal stress versus dimensionless load for a wide range of R_j/R_d values and the following bounds of the elastic stiffness: (a) $E_j/E_d = 42$, and (b) $E_j/E_d = 1.4$. Poisson's ratio in the disk is taken to be $\nu_d = 0.2$.

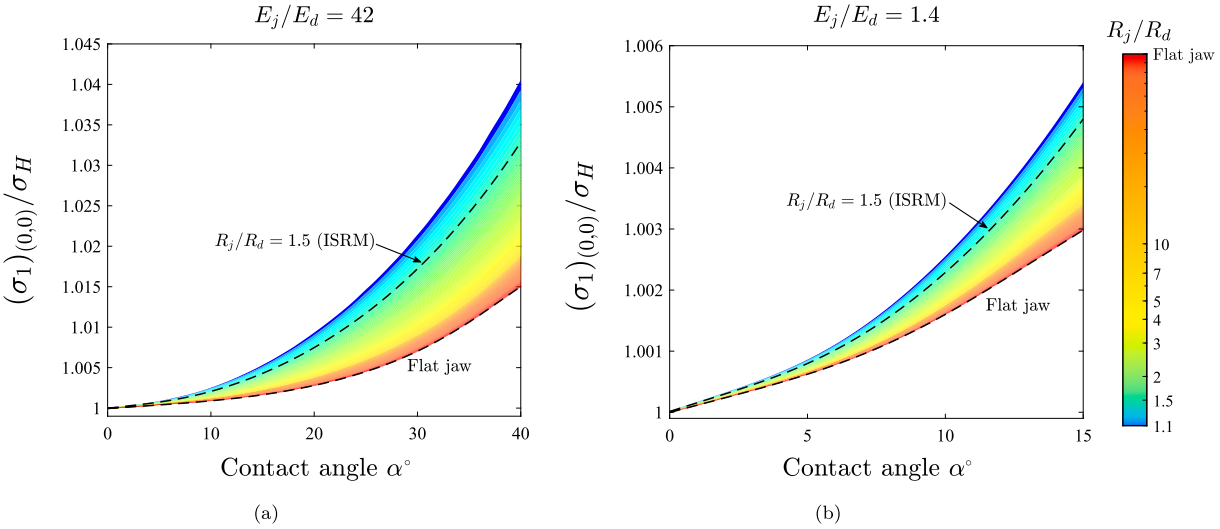

Fig. 9. Maps to evaluate the accuracy of Hondros's analytical solution for a uniformly distributed load, Eq. (1). The finite element predictions of the maximum principal stress at the disk centre are normalised by Hondros's stress solution, denoted as σ_H. The results are obtained for a wide range of R_j/R_d values and the following bounds of the elastic stiffness: (a) $E_j/E_d = 42$, and (b) $E_j/E_d = 1.4$.

ratios are provided for jaw radii varying from $R_j/R_d = 1.1$ to the flat jaws recommended by the ASTM standard.[19]

Consider first the case of granite, Fig. 14a. Flaw radii from $R_j/R_d = 1.1$ to $R_j/R_d = 2.2$ can be used to obtain valid estimates for granite materials within the upper estimates of compressive-to-tensile strength ratios. This includes the ISRM configuration ($R_j/R_d = 1.5$), which appears to be suited for some classes of granite. The number of suitable testing configurations improves for sandstone, see Fig. 14b. Types of sandstone can be adequately tested with jaw radius up to $R_j/R_d = 7$ but the use of flat jaws would lead to an invalid result and no testing configuration is suitable for sandstones with low σ_c/σ_t ratios. In the case of limestone, see Fig. 14c, only jaw radii from $R_j/R_d = 1.1$ to $R_j/R_d = 1.3$ can be used and these cover only those limestones with high compressive strength. In this case, it is not possible to get a valid estimate of σ_t with the ISRM testing configuration for any type of limestone. Finally, the results obtained for marble (Fig. 14d) show that only a small class of marbles can be adequately characterised with the Brazilian test, and this requires using the smallest jaw radius considered ($R_j/R_d = 1.1$). Again, as in the case of limestone, it does not appear to be possible to measure the tensile strength of any class of marble using the Brazilian test configuration suggested by the ISRM. Remarkably, the flat jaws recommended by the ASTM standard are shown to be generally unsuited to provide a valid estimate of the tensile strength, across the wide range of granites, sandstones, limestones and marbles considered.

The maps presented can be used by experimentalists to assess the validity of the their testing configuration, as described below. To facilitate this, we provide as Supplementary Material admissible σ_c/σ_t maps for relevant ranges of material properties and testing parameters. Moreover, as described in Appendix A, a MATLAB App is provided that includes a convenient graphical user interface to readily confirm the validity of the test, based on the criteria and analyses conducted here.

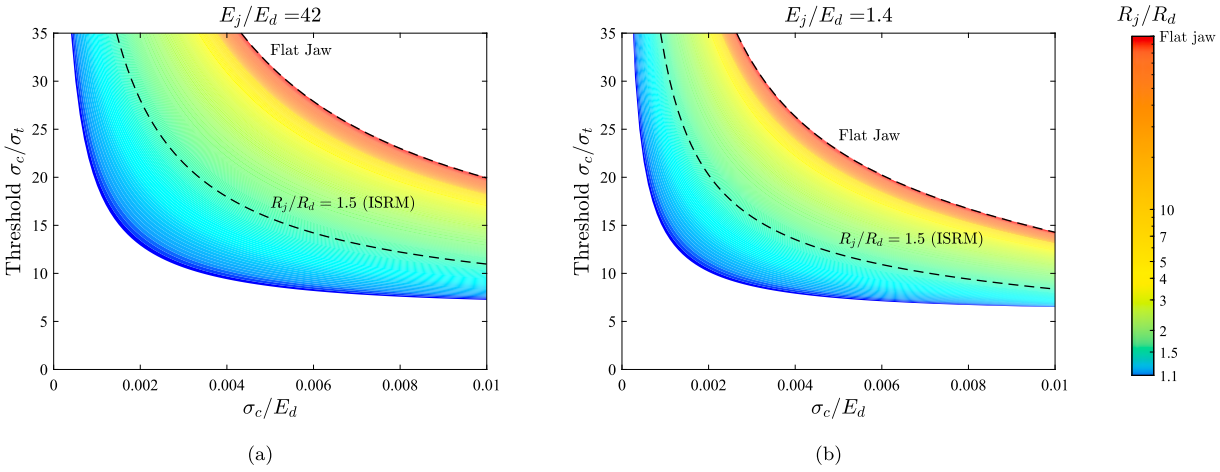

Fig. 10. Maps to assess if cracking nucleates at the centre. Influence of the jaw radius on the minimum acceptable ratio of compressive-to-tensile strength for (a) $E_j/E_d = 42$ and (b) $E_j/E_d = 1.4$. The disk's Poisson's ratio equals $\nu_d = 0.2$. Dashed lines are used to define the conditions relevant to the ASTM[19] and ISRM[4] standards.

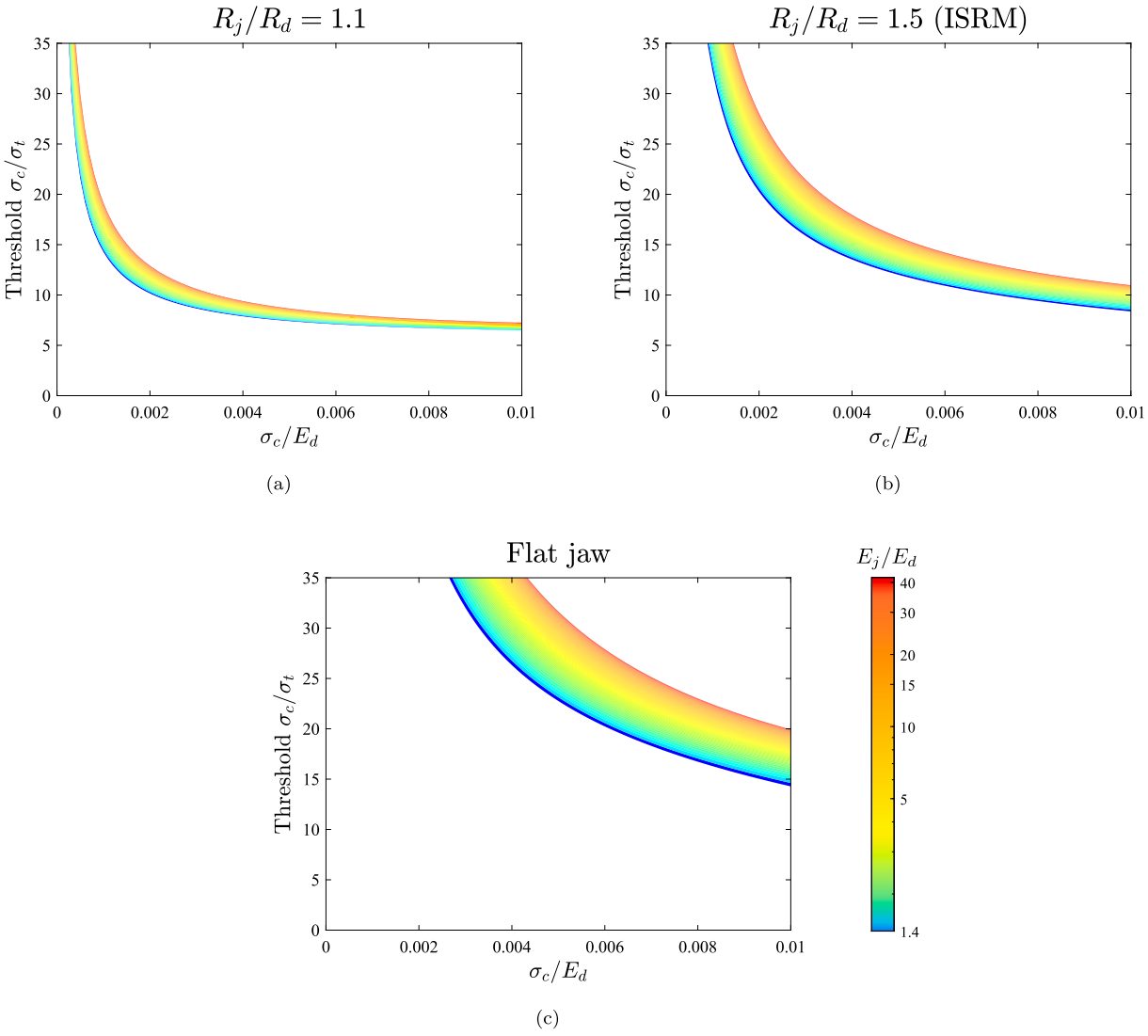

Fig. 11. Maps to assess if cracking nucleates at the centre. Influence of the elastic modulus of the material on the minimum acceptable ratio of compressive-to-tensile strength for (a) $R_j/R_d = 1.1$ (a low jaw radius), (b) $R_j/R_d = 1.5$ (the ISRM configuration), and (c) flat jaws (the ASTM configuration). The disk's Poisson's ratio equals $\nu_d = 0.2$.

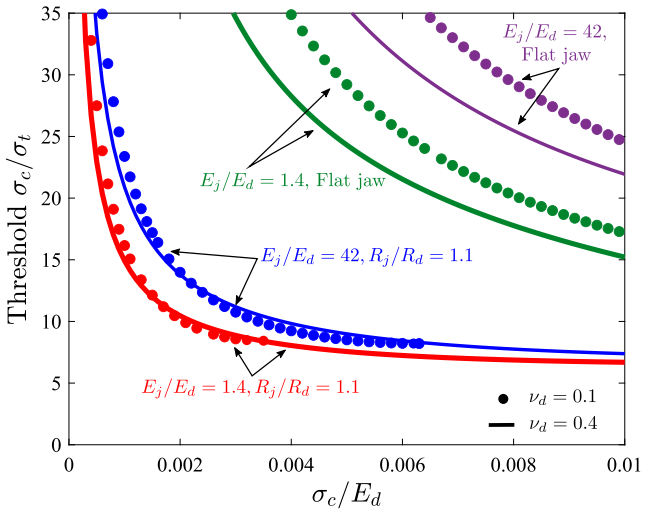

Fig. 12. Maps to assess if cracking nucleates at the centre. Influence of the Poisson ratio of the material on the minimum acceptable ratio of compressive-to-tensile strength. Results are obtained for the lower and upper bounds of ν_d (0.1, 0.4), E_j/E_d (1.4, 42) and R_j/R_d (1.1, 100).

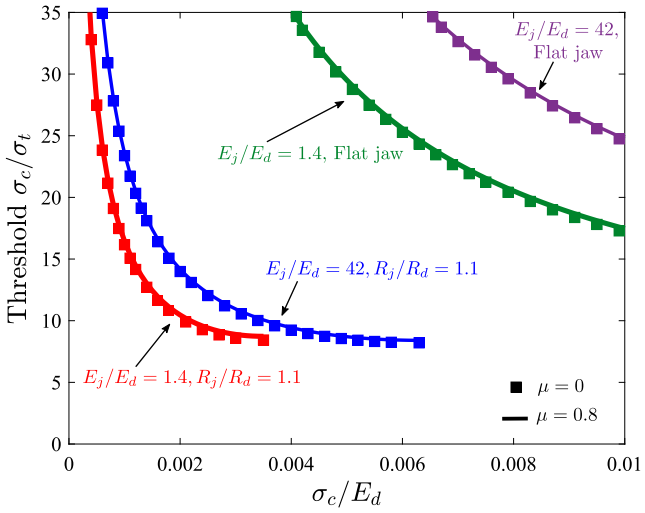

Fig. 13. Maps to assess if cracking nucleates at the centre. Influence of friction on the minimum acceptable ratio of compressive-to-tensile strength. Results are obtained without friction and for a friction coefficient of $\mu = 0.8$, for the lower and upper bounds of E_j/E_d (1.4, 42) and R_j/R_d (1.1, 100). The disk's Poisson's ratio equals $\nu_d = 0.1$.

5. A protocol for evaluating the validity of the Brazilian test

Identifying experimentally the location of crack nucleation in the Brazilian split test is hindered by the brittle behaviour of rocks; theoretical endeavours are needed to map the conditions of validity of the Brazilian test. The generalised Griffith criterion provides a suitable platform to achieve this as its failure envelope is given by two material properties: the tensile strength σ_t, which is estimated from the Brazilian test, and the compressive strength σ_c, which can be measured independently. In the following, we use the maps presented in Section 4 to provide a protocol to assess the validity of the Brazilian test as a function of the material and testing parameters. This is illustrated with examples of valid and invalid tests taken from the literature.

The protocol is a two-step process. First, one has to determine what is the maximum principal stress at the centre of the disk and second, one has to assess if cracking nucleated at the disk centre or elsewhere. Hondros's equations provide an estimate for the first step, but we have seen in Section 4.2 that these can be inaccurate. Thus, it is suggested that the maps provided in Section 4.2 and in the Supplementary Material are used instead to accurately determine the stress state at the disk centre. This corresponds with the material tensile strength ($\sigma_1 = \sigma_t$) if cracking initiated at the centre. The location of crack initiation is assessed by using the maps presented in Section 4.3; since σ_c and E_d are known (they can be measured independently) we can estimate what is the admissible compressive-to-tensile strength ratio σ_c/σ_t for a choice of jaw radius R_j/R_d. If the magnitude of σ_c/σ_t resulting from the test is below this admissible threshold, then the test is invalid as cracking has nucleated outside of the centre of the disk. Alternatively, one can use this information before the test, using approximate expected values of σ_t (e.g., taken from the literature) to decide what is the most suitable testing geometry (R_j/R_d).

The protocol is exemplified with two examples of valid and invalid tests, taken from the literature. Specifically, we take as case studies the experiments by Sun and Wu[32] on sandstone using the ISRM test configuration and the work by Duevel and Haimson[33] on granite, also using the ISRM recommended testing geometry. In both cases the jaws were made of steel, with elastic properties $E_j = 210$ GPa and $\nu_j = 0.3$. For the sandstone tested in Ref. 32, the reported elastic properties are $E_d = 19.15$ GPa and $\nu_d = 0.17$ and the material compressive strength is $\sigma_c = 99.93$ MPa. For the pink Lac du Bonnet granite study by Duevel and Haimson, the elastic properties are given by $E_d = 74.2$ GPa and $\nu_d = 0.25$, while the compressive strength was found to be $\sigma_c = 219$ MPa.[33,34] The Brazilian tests conducted in Ref. 32 and Ref. 33 led to tensile strengths of $\sigma_t = 7.51$ MPa and $\sigma_t = 11.4$ MPa, respectively. Following

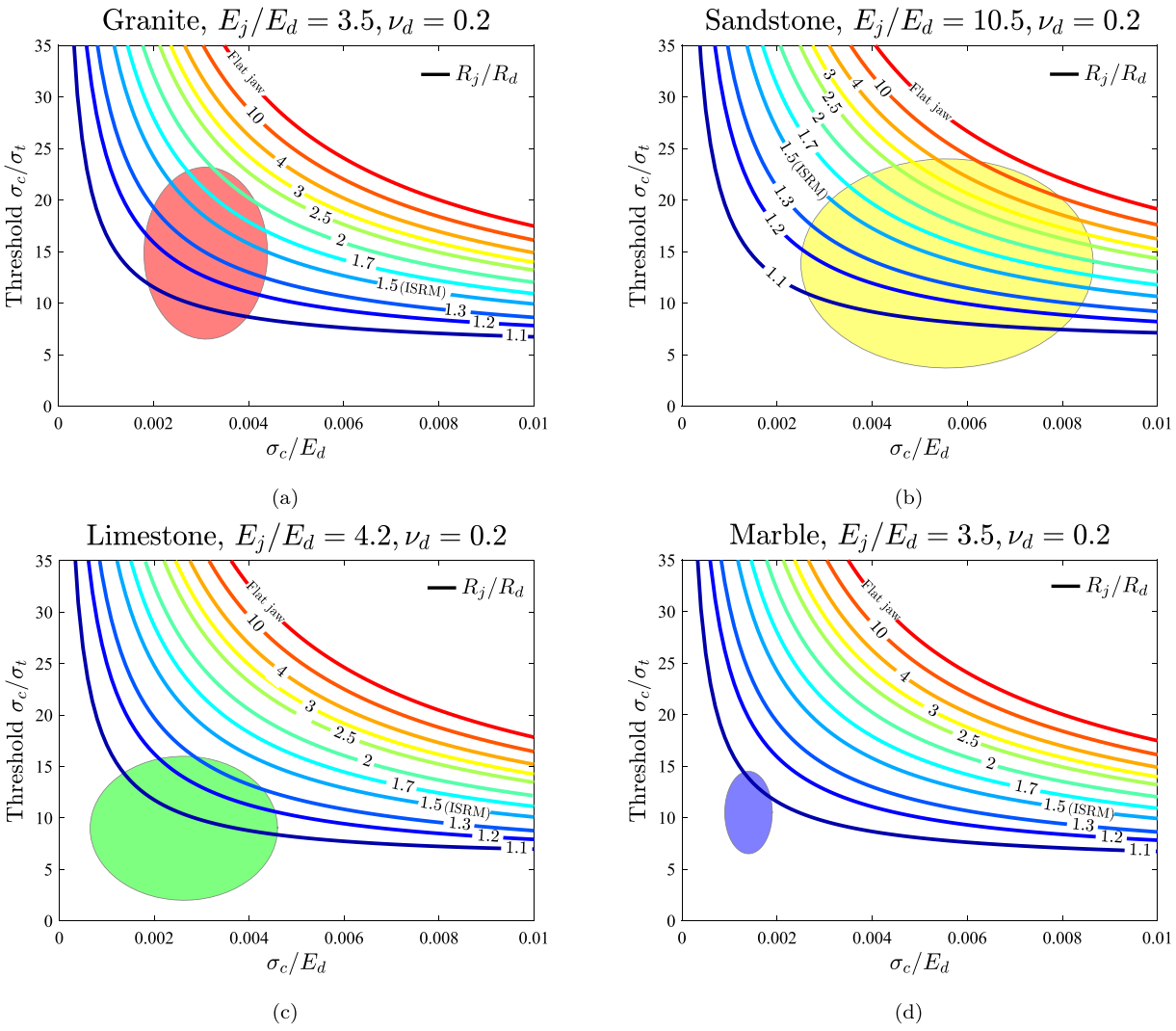

Fig. 14. Maps to assess if cracking nucleates at the centre: application to: (a) granite, (b) sandstone, (c) limestone, and (d) marble. The figure shows admissible compressive-to-tensile strength ratios as a function of the jaw radius (R_j/R_d) for the material properties of: (a) granite (E_j/E_d = 1.5, ν_d = 0.2), (b) sandstone (E_j/E_d = 10.5, ν_d = 0.2), (c) limestone (E_j/E_d = 4.2, ν_d = 0.2), and (d) marble (E_j/E_d = 3.5, ν_d = 0.2). Also, the domain of relevance of each material in a σ_c/σ_t vs σ_c/E_d plot is shown superimposed, as extracted from the GRANTA Material library.[23]

the protocol presented above, we shall start by assessing the stress state at the disk centre at the critical load.

As described above, the first step lies in finding the maximum principal stress σ_1 at the centre for the critical applied load. Fig. 15 shows the maps presented in Section 4.2 particularised for the two case studies considered here: a sandstone with E_j/E_d = 10.96 and ν_d = 0.17 (Fig. 15a) and a granite with E_j/E_d = 2.83 and ν_d = 0.25 (Fig. 15b). The results of Fig. 15 reveal that, while in both case studies the stress state in the disk centre is not described by the point load equation, this approximation provides a good estimate. In the case of the sandstone study by Sun and Wu[32] the error relative to Eq. (2) is below 0.5% while in the granite experiment by Duevel and Haimson[33] the error is roughly 0.2%. As shown in the figure, a better approximation can be obtained with flat jaws. In any case, Fig. 15 provides a way of obtaining an accurate estimate of the maximum principal stress at the disk centre, which equals σ_1 = 7.47 and σ_1 = 11.38 MPa for, respectively, the sandstone and the granite under consideration. These magnitudes correspond to the material tensile strengths, provided that cracking nucleates at the disk centre.

The second and last step involves assessing the crack nucleation location. For the test to be valid, cracking must begin from the disk centre and, following the Griffith's generalised criterion, this will only happen if the compressive-to-tensile strength ratio is above the threshold of admissible values. Thus, given that σ_c and E_d are known, we can take the σ_t value obtained from the experiment in step 1 and see where the experimental data point lies in the maps presented in Section 4.3; this is done in Fig. 16 for both case studies and the testing geometries recommended by ASTM and ISRM, being the latter the one used in the tests.

The results of Fig. 16 show that while the granite study of Duevel and Haimson[33] provides a valid estimate of the material tensile strength, this is not the case for the sandstone experiment of Sun and Wu.[32] The experimental data point lies below the contour corresponding to the testing geometry employed (R_j/R_d = 1.5), suggesting that

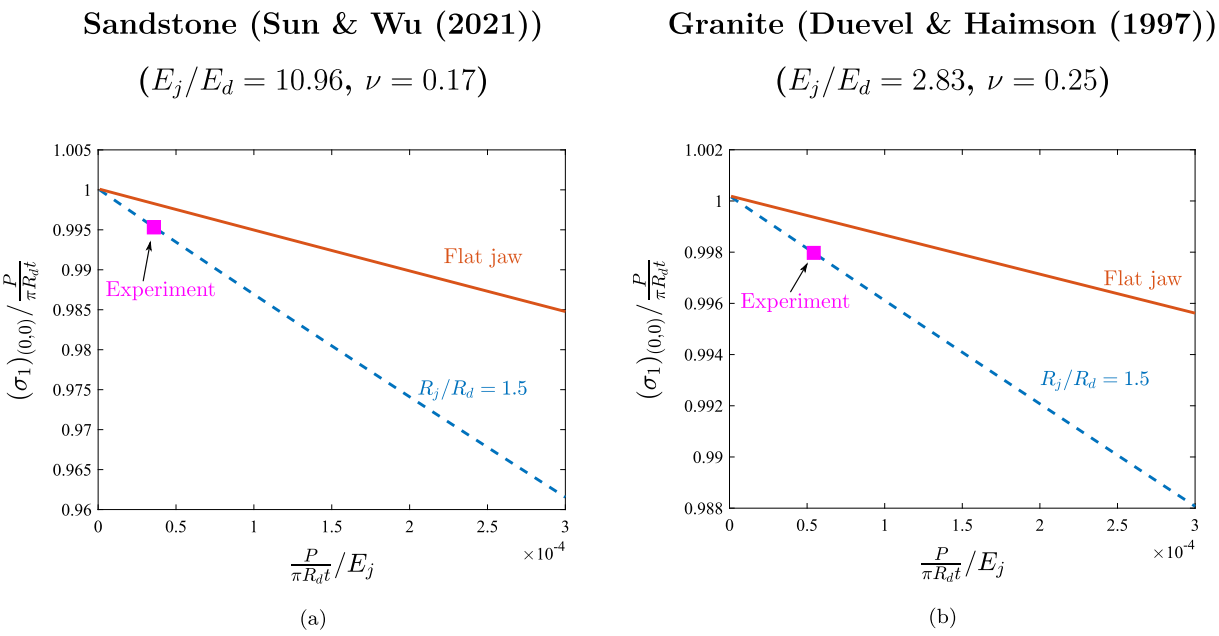

Fig. 15. A protocol for assessing the validity of the Brazilian test. Step 1 - evaluating the stress state at the disk centre for (a) the sandstone tested by Sun and Wu,[32] and (b) the granite tested by Duevel and Haimson.[33] The material properties and critical load are $E_j/E_d = 10.96$, $\nu_d = 0.17$ and $P/(\pi R_d t) = 0.0000357 E_j$ for (a), and $E_j/E_d = 2.83$, $\nu_d = 0.25$ and $P/(\pi R_d t) = 0.000054 E_j$ for (b). The maps provided in Section 4.2 and the Supplementary Material are particularised for the two case studies under consideration and the ISRM ($R_j/R_d = 1.5$) and ASTM (flat jaws) testing configurations.

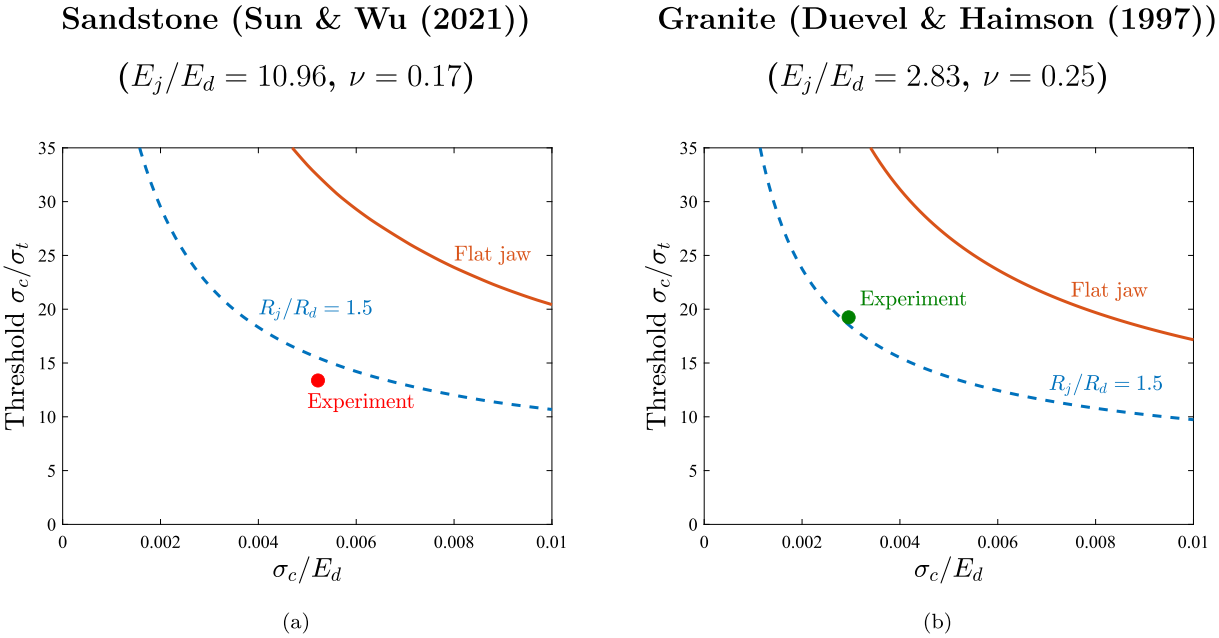

Fig. 16. A protocol for assessing the validity of the Brazilian test. Step 2 - evaluating the crack nucleation location for (a) the sandstone tested by Sun and Wu,[32] and (b) the granite tested by Duevel and Haimson.[33] The material properties are $E_j/E_d = 10.96$, $\nu_d = 0.17$, $\sigma_c/E_d = 0.0052$ and $\sigma_c/\sigma_t = 13.37$ for (a), and $E_j/E_d = 2.83$, $\nu_d = 0.25$, $\sigma_c/E_d = 0.00295$ and $\sigma_c/\sigma_t = 19.24$ for (b). The maps provided in Section 4.3 and the Supplementary Material are particularised for the two case studies under consideration and the ISRM ($R_j/R_d = 1.5$) and ASTM (flat jaws) testing configurations. The admissible compression-to-tensile strengths establishes the threshold below which cracking initiates outside of the disk centre and the test becomes invalid.

cracking has initiated outside of the centre of the sample. This was also inferred from active and passive ultrasonic techniques in the study by Sun and Wu[32], who concluded that cracking had initiated close to the jaws. Their comprehensive analysis, including numerical and experimental analysis of multiple testing configurations, showcased the limitations of the Brazilian test. The protocol and maps provided here (see also the Supplementary Material and Appendix A) enable establishing the conditions where the Brazilian test is valid, upon assuming that crack propagation is well approximated by the generalised Griffith criterion.

6. Conclusions

We have combined the generalised Griffith criterion and finite element analysis to theoretically assess the validity of the Brazilian split test. Maps have been provided to evaluate, as a function of material properties and test geometry, the fulfilment of the two assumptions inherent to the indirect estimate of the material tensile strength provided by the Brazilian test; that (i) the load is related to the maximum principal stress at the disk centre through Hondros's equations, and that (ii) cracking starts at the centre of the sample. The use of the generalised Griffith criterion enables assessing (ii) using a failure envelope that is solely a function of two material properties that can be independently measured: the tensile (σ_t) and compressive (σ_c) strengths. Our main findings are the following:

- For relevant contact angles, there is a noticeable deviation from the stress solution for a point load. However, the error remains small (below 5%) for a wide range of rock-like materials if flat or large-radii jaws are used.
- The use of the Hondros's stress solution for a uniformly distributed load ensures that the error does not exceed 4% for relevant ranges of stiffness mismatch and jaw radius. However, unlike the maps provided, requires an experimental characterisation of the contact angle at failure.
- The use of jaws with large radii favours the initiation of cracking in the compressive region, far from the disk centre, making the test invalid.
- The location of crack initiation is particularly sensitive to the testing geometry and, to a lesser degree, to the stiffness of the sample. Poisson's ratio plays a negligible role in jaws with a small radius but has an effect in the case of flat jaws. No influence of friction is observed.
- The analysis of the main classes of rocks reveals that the Brazilian test is not a suitable experiment for a wide range of materials. Only a small set of marbles and limestones (those with high σ_c/σ_t) can be adequately characterised and this requires the use of jaws with small radii. On the other hand, large-radius jaws can be used to test a range of granites and sandstones. The ISRM configuration ($R_j/R_d = 1.5$) appears to be solely suitable for these two latter classes of rocks, while the ASTM test geometry (flat jaws) was found to be unsuited to provide a valid estimate of tensile strength for any of the rock-like materials considered.

These findings suggest that the regimes of validity of the Brazilian test are much smaller than previously thought. To overcome these shortcomings and determine the range of conditions that lead to a valid Brazilian test, we have provided:

- Maps that relate the critical load with the stress state at the disk centre. These allow for accurately estimating the tensile strength without the need of using the approximation provided by the Hondros's equations.
- Maps that quantify the admissible compression-to-tensile strength ratios above which cracking initiates at the centre of the disk. These allow determining if the test is valid *a posteriori* or making *a priori* decisions of adequate test geometries based on expected σ_t values.
- A two-step protocol that will allow experimentalists to determine the validity of the test and accurately estimate the material tensile strength. The protocol is demonstrated with examples of valid and invalid tests from the literature. To facilitate uptake, this is encapsulated into a MATLAB App with an easy user interface.

Declaration of competing interest

The authors declare that they have no known competing financial interests or personal relationships that could have appeared to influence the work reported in this paper.

Data availability

Data will be made available on request.

Acknowledgements

The authors acknowledge financial support from the Ministry of Science, Innovation and Universities of Spain through grant PGC2018-099695-B-I00. E. Martínez-Pañeda additionally acknowledges financial support from the Royal Commission for the 1851 Exhibition, UK through their Research Fellowship programme (RF496/2018).

Appendix A. BrazVal: A MATLAB App to assess the validity of the Brazilian test

A Matlab App is provided to facilitate the assessment of the validity of the Brazilian test, as per the Griffith generalised criterion and the analysis described in this manuscript. As shown in Fig. A.1, the MATLAB App contains a simple graphical user interface where the user provides as input variables the parameters related to the disk sample (radius R_d, Young's modulus E_d, Poisson's ratio ν_d, compressive strength σ_c and thickness t) and to the jaws (radius R_j, Young's modulus E_j, Poisson's ratio ν_j), as well as the critical load measured P_c. Upon clicking the button `Run`, the App provides the material tensile strength σ_t. If the test is deemed invalid, the message `INVALID` will be shown instead. In addition, the App provides the user with the tensile stress estimate based on Eq. (2), the actual tensile stress at the disk centre (which will coincide with σ_t if the test is valid) and the maximum allowable tensile strength, as determined from the threshold σ_c/σ_t ratio that ensures that cracking nucleates earlier at the disk centre than elsewhere.

The information provided by the App is based on a data grid generated by performing finite element calculations such as those described in Section 4. For scenarios for which data points do not exist, an estimate is attained by using linear interpolation (MATLAB's function `griddedInterpolant`). The App can be downloaded from www.empaneda.com/codes

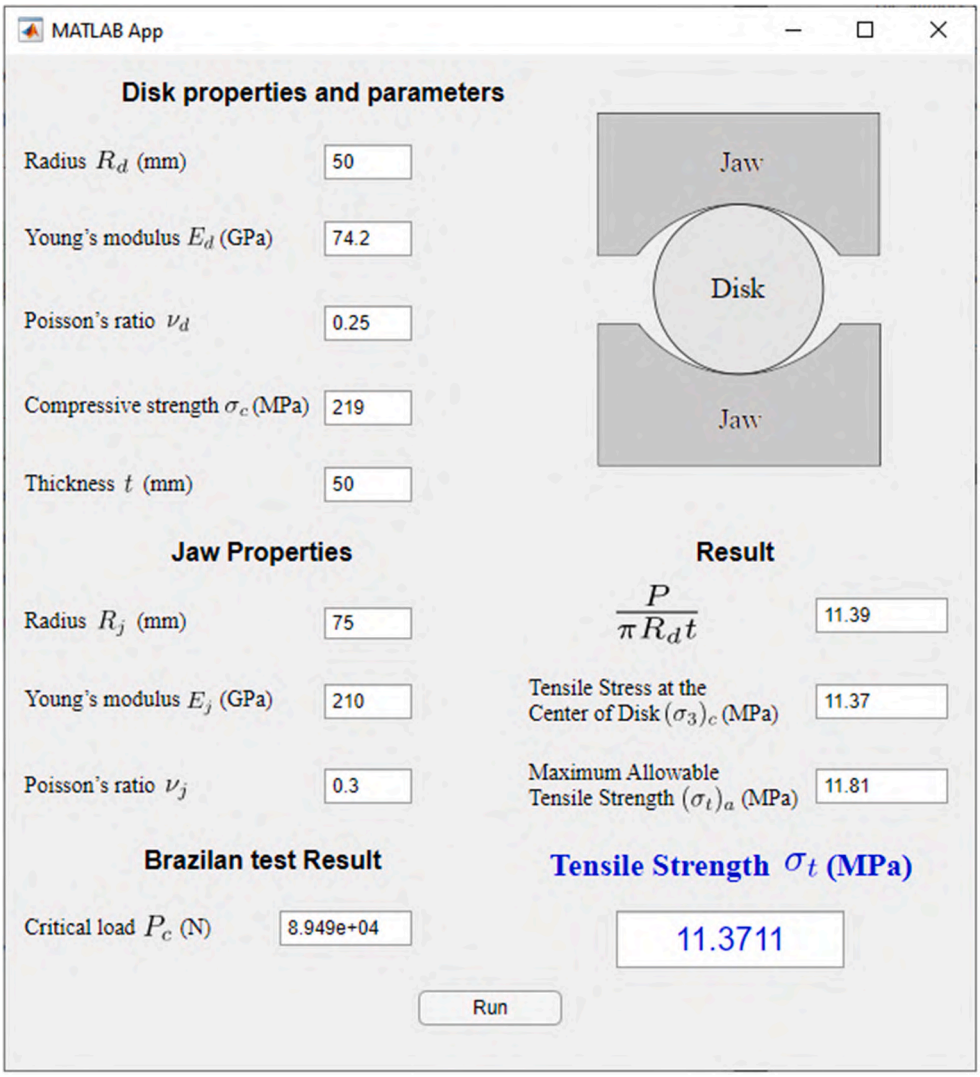

Fig. A.1. Graphical User Interface (GUI) of BrazVal, a MATLAB App to assess the validity of the Brazilian test, as a function of material and testing parameters. The App can be downloaded from www.empaneda.com/codes.

Appendix B. Supplementary data

Supplementary material related to this article can be found online at https://doi.org/10.1016/j.ijrmms.2022.105227.

References

1. Li D, Wong LNY. The Brazilian disc test for rock mechanics applications: Review and new insights. *Rock Mech Rock Eng.* 2013;46(2):269–287.
2. Carneiro F. A new method to determine the tensile strength of concrete. In: *Proceedings of the 5th Meeting of the Brazilian Association for Technical Rules, Section 3d.* 1943.
3. Akazawa T. New test method for evaluating internal stress due to compression of concrete. *J Japan Soc Civ Eng.* 1943;29:777–787.
4. Bieniawski ZT, Hawkes I. Suggested methods for determining tensile strength of rock materials. *Int J Rock Mech Min Sci.* 1978;15(3):99–103.
5. Hondros G. The evaluation of Poisson's ratio and the modulus of materials of a low tensile resistance by the Brazilian (indirect tensile) test with particular reference to concrete. *Aust J Appl Sci.* 1959;10(3):243–268.
6. Timoshenko S, Goodier J. *Theory of Elasticity*. McGraw-Hill; 1951.
7. Fairhurst C. On the validity of the 'Brazilian' test for brittle materials. *Int J Rock Mech Min Sci.* 1964;1(4):535–546.
8. Hudson JA, Brown ET, Rummel F. The controlled failure of rock discs and rings loaded in diametral compression. *Int J Rock Mech Min Sci.* 1972;9(2):241–248.
9. Alvarez-Fernandez MI, Garcia-Fernandez CC, Gonzalez-Nicieza C, Guerrero-Miguel DJ. Effect of the contact angle in the failure pattern in slate under diametral compression. *Rock Mech Rock Eng.* 2020;53(5):2123–2139.
10. Markides CF, Kourkoulis SK. The influence of jaw's curvature on the results of the Brazilian disc test. *J Rock Mech Geotech Eng.* 2016;8(2):127–146.
11. Gutiérrez-Moizant R, Ramírez-Berasategui M, Sánchez-Sanz S, Santos-Cuadros S. Experimental verification of the boundary conditions in the success of the Brazilian test with loading arcs, an uncertainty approach using concrete disks. *Int J Rock Mech Min Sci.* 2020;132:104380.
12. Bouali MF, Bouassida M. Numerical simulation of the effect of loading angle on initial cracks position point: Application to the Brazilian test. *Appl Sci.* 2021;11(8).
13. Garcia-Fernandez CC, Gonzalez-Nicieza C, Alvarez-Fernandez MI, Gutierrez-Moizant RA. Analytical and experimental study of failure onset during a Brazilian test. *Int J Rock Mech Min Sci.* 2018;103:254–265.
14. Zhao Z, Sun W, Chen S, Yin D, Liu H, Chen B. Determination of critical criterion of tensile-shear failure in Brazilian disc based on theoretical analysis and meso-macro numerical simulation. *Comput Geotech.* 2021;134:104096.
15. Aliabadian Z, Zhao GF, Russell AR. Failure, crack initiation and the tensile strength of transversely isotropic rock using the Brazilian test. *Int J Rock Mech Min Sci.* 2019;122:104073.
16. Erarslan N, Liang ZZ, Williams DJ. Experimental and numerical studies on determination of indirect tensile strength of rocks. *Rock Mech Rock Eng.* 2012;45(5):739–751.
17. Yu H, Andersen DH, He J, Zhang Z. Is it possible to measure the tensile strength and fracture toughness simultaneously using flattened Brazilian disk? *Eng Fract Mech.* 2021;247:107633.
18. Komurlu E, Kesimal A. Evaluation of indirect tensile strength of rocks using different types of jaws. *Rock Mech Rock Eng.* 2015;48(4):1723–1730.
19. *ASTM D3697 Standard Test Method for Splitting Tensile Strength of Intact Rock Core Specimens*. West Conshohocken, PA, ASTM International.
20. Griffith AA. The theory of rupture. In: *Proc. First International Congress for Applied Mechanics*. 1924:55–63.

21. Jaeger J, Cook N, Zimmerman R. *Fundamentals of Rock Mechanics*. Oxford, UK: Blackwell Publishing; 2009.
22. Hoek E, Martin CD. Fracture initiation and propagation in intact rock - A review. *J Rock Mech Geotech Eng*. 2014;6(4):287–300.
23. *Ansys Granta EduPack*. Cambridge, UK: ANSYS Inc.; 2021.
24. Lin H, Xiong W, Zhong W, Xia C. Location of the crack initiation points in the Brazilian disc test. *Geotech Geol Eng*. 2014;32(5):1339–1345.
25. Yuan R, Shen B. Numerical modelling of the contact condition of a Brazilian disk test and its influence on the tensile strength of rock. *Int J Rock Mech Min Sci*. 2017;93(December 2015):54–65.
26. Papazafeiropoulos G, Muñiz-Calvente M, Martínez-Pañeda E. Abaqus2Matlab: A suitable tool for finite element post-processing. *Adv Eng Softw*. 2017;105:9–16.
27. Lavrov A, Vervoort A. Theoretical treatment of tangential loading effects on the Brazilian test stress distribution. *Int J Rock Mech Min Sci*. 2002;39(2):275–283.
28. Markides CF, Pazis DN, Kourkoulis SK. Influence of friction on the stress field of the Brazilian tensile test. *Rock Mech Rock Eng*. 2011;44(1):113–119.
29. Markides CF, Pazis DN, Kourkoulis SK. The Brazilian disc under non-uniform distribution of radial pressure and friction. *Int J Rock Mech Min Sci*. 2012;50:47–55.
30. Markides CF, Kourkoulis SK. Naturally accepted boundary conditions for the Brazilian disc test and the corresponding stress field. *Rock Mech Rock Eng*. 2013;46(5):959–980.
31. Hooper JA. The failure of glass cylinders in diametral compression. *J Mech Phys Solids*. 1971;19(4):179–188.
32. Sun W, Wu S. A study of crack initiation and source mechanism in the Brazilian test based on moment tensor. *Eng Fract Mech*. 2021;246:107622.
33. Duevel B, Haimson B. Mechanical characterization of pink Lac du Bonnet granite: Evidence on nonlinearity and anisotropy. *Int J Rock Mech Min Sci Geomech Abstracts*. 1997;34(3–4):543.
34. Cai M. Practical estimates of tensile strength and Hoek-Brown strength parameter mi of brittle rocks. *Rock Mech Rock Eng*. 2010;43(2):167–184.

B | Paper 2

A simple and robust Abaqus implementation of the phase field fracture method

Authors:

Yousef Navidtehrani, Covadonga Betegón, Emilio Martínez-Pañeda

Journal:

Applications in Engineering Science

Year of Publication:

2021

Impact Factor:

2.2 - Q2

Applications in Engineering Science 6 (2021) 100050

Contents lists available at ScienceDirect

Applications in Engineering Science

journal homepage: www.elsevier.com/locate/apples

A simple and robust Abaqus implementation of the phase field fracture method

Yousef Navidtehrani [a], Covadonga Betegón [a], Emilio Martínez-Pañeda [b,*]

[a] Department of Construction and Manufacturing Engineering, University of Oviedo, Gijón 33203, Spain
[b] Department of Civil and Environmental Engineering, Imperial College London, London SW7 2AZ, UK

ARTICLE INFO

Keywords:
Phase field fracture
Abaqus
Fracture
Finite element analysis
User subroutines

ABSTRACT

The phase field fracture method is attracting significant interest. Phase field approaches have enabled predicting - on arbitrary geometries and dimensions - complex fracture phenomena such as crack branching, coalescence, deflection and nucleation. In this work, we present a simple and robust implementation of the phase field fracture method in the commercial finite element package Abaqus. The implementation exploits the analogy between the phase field evolution law and the heat transfer equation, enabling the use of Abaqus' in-built features and circumventing the need for defining user elements. The framework is general, and is shown to accommodate different solution schemes (staggered and monolithic), as well as various constitutive choices for preventing damage under compression. The robustness and applicability of the numerical framework presented is demonstrated by addressing several 2D and 3D boundary value problems of particular interest. Focus is on the solution of paradigmatic case studies that are known to be particularly demanding from a convergence perspective. The results reveal that our phase field fracture implementation can be readily combined with other advanced computational features, such as contact, and deliver robust and precise solutions. The code developed can be downloaded from www.empaneda.com/codes.

1. Introduction

Modelling the morphology of an evolving interface is considered to be a longstanding mathematical and computational challenge. Tracking interface boundaries explicitly is hindered by the need of defining moving interfacial boundary conditions and manually adjusting the interface topology with arbitrary criteria when merging or division occurs (Biner, 2017). Phase field formulations have proven to offer a pathway for overcoming these challenges. In the phase field modelling paradigm, the interface is smeared over a *diffuse* region using an auxiliary field variable ϕ, which takes a distinct value for each of the two phases (e.g., 0 and 1) and exhibits a smooth change between these values near the interface. The temporal evolution of the phase field variable ϕ is described by a partial differential equation (PDE) and thus the method enables the simulation of complex interface evolution phenomena by integrating a set of PDEs for the whole system, avoiding the explicit treatment of interface conditions.

The phase field paradigm has quickly gained significant traction in the condensed matter and materials science communities, becoming the *de facto* tool for modelling microstructural evolution (Provatas and Elder, 2011). The change in shape and size of microstructural features such as grains can be predicted by defining the evolution of the phase field in terms of other fields (temperature, concentration, strain, etc.) through a thermodynamic free energy. This success has been extended to other interfacial problems, such as corrosion, where the phase field smoothens the metal-electrolyte interface (Cui et al., 2021), or fracture mechanics, where the phase field is used to implicitly track the evolution of the crack-solid boundary (Bourdin et al., 2000). The coupling of the phase field paradigm with the variational approach to fracture presented by Bourdin et al. (2008) has opened new horizons in the modelling of cracking phenomena, from predicting complex crack trajectories to simulating inertia-driven crack branching. Moreover, this can be achieved on the original finite element mesh, without *ad hoc* crack propagation criteria, and for arbitrary geometries and dimensions. Not surprisingly, the popularity of phase field methods for fracture has rocketed in recent years; applications include the prediction of fracture (and fatigue) in fibre-reinforced composites (Quintanas-Corominas et al., 2019; Tan and Martínez-Pañeda, 2021), hydrogen-embrittled alloys (Martínez-Pañeda et al., 2018; Kristensen et al., 2020a), batteries (Klinsmann et al., 2016; Miehe et al., 2016),

* Corresponding author.
E-mail address: e.martinez-paneda@imperial.ac.uk (E. Martínez-Pañeda).

https://doi.org/10.1016/j.apples.2021.100050
Received 19 December 2020; Received in revised form 6 April 2021; Accepted 14 April 2021
Available online 20 April 2021

rock-like materials (Zhou et al., 2019; Schuler et al., 2020), solar-grade silicon (Paggi et al., 2018), functionally graded materials (Hirshikesh et al., 2019; Kumar et al., 2021), hyperelastic solids (Loew et al., 2019; Mandal et al., 2020), piezo-electric materials (Abdollahi and Arias, 2012) and shape memory alloys (Simoes and Martínez-Pañeda, 2021) - see (Wu et al., 2020b) for a comprehensive review.

The success of phase field fracture methods has also triggered a notable interest for the development of robust solution algorithms to solve the coupled deformation-fracture problem (Miehe et al., 2010b; Gerasimov and De Lorenzis, 2016; Wu et al., 2020a; Kristensen and Martínez-Pañeda, 2020). The total potential energy functional, including the contributions from the bulk and fracture energies, is minimised with respect to the two primary kinematic variables: the displacement field $\boldsymbol{u}$ and the phase field ϕ. Thus, the phase field ϕ, a damage-like variable, is solved for at the finite element nodes, as an additional degree of freedom. This requires performing the numerical implementation at the element level, as opposed to local damage models, which are implemented at the integration point level. In the context of commercial finite element packages, solving for the phase field as a degree-of-freedom requires the development of user element subroutines. The commercial finite element package Abaqus has received particular attention in the phase field fracture community, and a vast literature has emerged on the implementation of the phase field fracture method on this popular software suite (Liu et al., 2016; Molnár and Gravouil, 2017; Fang et al., 2019; Molnár et al., 2020b; Wu and Huang, 2020). These implementations require programming an *ad hoc* finite element, effectively using Abaqus as a solver and not being able to exploit most of its in-built features. In this work, we circumvent this issue by exploiting the analogy between the heat conduction equation and the phase field evolution law. This approach enables using the vast majority of Abaqus' in-built features, including the coupled temperature-displacement elements from its finite element library, which avoids coding user-defined elements and the associated complications in meshing and visualisation (e.g., Abaqus2Matlab is frequently used to pre-process input files, Papazafeiropoulos et al., 2017). Moreover, the phase field implementation presented can accommodate both staggered and monolithic solution schemes, ensuring convergence in all cases. We demonstrate the potential and robustness of the implementation presented by addressing several paradigmatic 2D and 3D boundary value problems. The framework provided is general and can be easily implemented in other finite element packages.

The remainder of this manuscript is organised as follows. In Section 2 we describe the theory underlying the phase field fracture method. The analogy with the heat transfer problem and the implementation details are given in Section 3. Representative results are shown in Section 4. First, unstable fracture is addressed with the paradigmatic benchmark of a cracked square plate under uniaxial tension. Secondly, convergence under stable crack propagation conditions is investigated using a cracked square plate subjected to shear. The performance of monolithic and staggered schemes is compared. Thirdly, the screw tension tests presented by Wick et al. (2015) are examined. Finally, we simulate the so-called Brazilian laboratory test, which is widely used for measuring the tensile strength of rock-like materials. A comprehensive 3D analysis is conducted, including the modelling of the contact between the jaws and the specimen. The manuscript ends with concluding remarks in Section 5.

2. Phase field fracture model

The phase field fracture method builds upon Griffith's thermodynamics framework (Griffith, 1920). In agreement with the first law of thermodynamics, a crack can form (or grow) only if this process causes the total energy of the system to decrease or remain constant. Accordingly, a critical condition for fracture can be defined upon the assumption of equilibrium conditions - no net change in total energy. Consider an elastic solid containing a crack. In the absence of external forces, the variation of the total energy $\mathcal{E}$ due to an incremental increase in the crack area $\mathrm{d}A$ is given by

$$\frac{\mathrm{d}\mathcal{E}}{\mathrm{d}A} = \frac{\mathrm{d}\psi(\boldsymbol{\varepsilon}(\boldsymbol{u}))}{\mathrm{d}A} + \frac{\mathrm{d}W_c}{\mathrm{d}A} = 0 \tag{1}$$

where W_c is the work required to create new surfaces and ψ is the strain energy density, which is a function of the displacement field $\boldsymbol{u}$ and the strain field $\boldsymbol{\varepsilon} = \left(\nabla \boldsymbol{u}^T + \nabla \boldsymbol{u}\right)/2$. The last term in Eq. (1) is the so-called critical energy release rate $G_c = \mathrm{d}W_c/\mathrm{d}A$, a material property that characterises the fracture resistance. Thus, Griffth's premise is a local minimality principle for the sum of the elastic and fracture energies. For an arbitrary body $\Omega \subset \mathbb{R}^n$ $(n \in [1,2,3])$ with internal discontinuity boundary Γ, this minimality principle can be expressed in a variational form as (Bourdin et al., 2008),

$$\mathcal{E}(\boldsymbol{u}) = \int_\Omega \psi(\boldsymbol{\varepsilon}(\boldsymbol{u}))\,\mathrm{d}V + \int_\Gamma G_c\,\mathrm{d}S, \tag{2}$$

Thus, within this framework, crack growth along any trajectory can be predicted without arbitrary criteria, driven by global minimality and the transformation of stored energy into fracture energy. However, minimisation of the variational Griffith energy functional (2) is hindered by the complexities associated with tracking the propagating fracture surface Γ. The problem can be made computationally tractable by employing an auxiliary phase field ϕ that enables tracking the crack interface. The phase field ϕ can be interpreted as a damage-like variable that goes from 0 in intact regions to 1 inside of the crack. Accordingly, following continuum damage mechanics arguments, a degradation function $g(\phi) = (1-\phi)^2$ can be defined to reduce the material stiffness with evolving damage. Hence, the regularised energy functional is given by,

$$\mathcal{E}_\ell(\boldsymbol{u},\phi) = \int_\Omega (1-\phi)^2 \psi_0(\boldsymbol{\varepsilon}(\boldsymbol{u}))\,\mathrm{d}V + \int_\Omega G_c \gamma_\ell(\phi)\,\mathrm{d}V, \tag{3}$$

where ℓ is a length scale parameter that governs the size of the fracture process zone and γ_ℓ is the crack density function. A common choice for γ_ℓ reads,

$$\gamma_\ell(\phi) = \frac{\phi^2}{2\ell} + \frac{\ell}{2}|\nabla\phi|^2. \tag{4}$$

As rigorously proven using Gamma-convergence, the $(\boldsymbol{u},\phi)$ sequence that constitutes a global minimum for the regularised functional $\mathcal{E}_\ell$ converges to that of $\mathcal{E}$ for a fixed $\ell \to 0^+$. Thus, ℓ can be interpreted as a regularising parameter in its vanishing limit. However, for $\ell > 0^+$ a finite material strength is introduced and thus ℓ becomes a material property governing the strength (Tanné et al., 2018); e.g., for plane stress:

$$\sigma_f \propto \sqrt{\frac{G_c E}{\ell}} = \frac{K_{Ic}}{\sqrt{\ell}} \tag{5}$$

where K_{Ic} is the material fracture toughness. It has been shown that the consideration of a finite $\ell > 0^+$ enables to accurately predict crack nucleation, capturing its transition from strength-driven to fracture-driven (Tanné et al., 2018), and in agreement with the predictions from the coupled criterion in finite fracture mechanics (Molnár et al., 2020a).

We will restrict our analysis to the behaviour of linear elastic materials, such that the strain energy density of the intact material is given by,

$$\psi_0 = \frac{1}{2}\boldsymbol{\varepsilon} : \boldsymbol{C}_0 : \boldsymbol{\varepsilon}, \tag{6}$$

where $\boldsymbol{C}_0$ is the (undamaged) linear elastic stiffness tensor. Accordingly, the Cauchy stress tensor is defined as

$$\boldsymbol{\sigma} = (1-\phi)^2 \boldsymbol{\sigma}_0 = (1-\phi)^2 \frac{\partial \psi_0(\boldsymbol{\varepsilon})}{\partial \boldsymbol{\varepsilon}} \tag{7}$$

where the undamaged Cauchy stress is given by $\boldsymbol{\sigma}_0 = \boldsymbol{C}_0 : \boldsymbol{\varepsilon}$.

Considering the constitutive choices just described and taking the first variation of the $\mathcal{E}_\ell$ with respect to the primal kinematic variables $\boldsymbol{u}$ and ϕ renders,

$$\int_\Omega \Big[(1-\phi)^2 \boldsymbol{\sigma}_0 \,:\, \mathrm{sym}\nabla\delta\boldsymbol{u} - 2(1-\phi)\,\psi_0(\boldsymbol{\varepsilon}(\boldsymbol{u}))\delta\phi + G_c\left(\frac{\phi}{\ell}\delta\phi + \ell\nabla\phi\cdot\nabla\delta\phi\right)\Big]\,\mathrm{d}V = 0 \tag{8}$$

The local force balances can be readily derived by applying Gauss' divergence theorem and noting that (8) must hold for any kinematically admissible variations of the virtual quantities. Thus, the coupled field equations read,

$$\begin{aligned} \nabla\cdot\left[(1-\phi)^2\boldsymbol{\sigma}_0\right] &= \boldsymbol{0} \quad \text{in} \quad \Omega \\ G_c\left(\frac{\phi}{\ell} - \ell\Delta\phi\right) - 2(1-\phi)\,\psi_0(\boldsymbol{\varepsilon}(\boldsymbol{u})) &= 0 \quad \text{in} \quad \Omega \end{aligned} \tag{9}$$

The discretised forms of the field equations can be solved using a monolithic scheme, where $\boldsymbol{u}$ and ϕ are solved simultaneously, or by means of a so-called staggered scheme, where an alternate minimisation strategy is used.

3. Finite element implementation

We shall describe the numerical framework proposed. First, we introduce a history field to ensure damage irreversibility. Secondly, the analogy with heat transfer is presented. Thirdly, the particularities of the Abaqus implementation are described. Finally, we show how our implementation can accommodate different solution schemes, and discuss the advantages and limitations of the options available. For the sake of brevity, we limit our description to the constitutive and implementation choices inherent to the code provided, and describe in Appendix A other potential extensions, which are considered in the numerical examples.

3.1. Damage irreversibility

A history variable field H is introduced to prevent crack healing, ensuring that the following condition is always met

$$\phi_{t+\Delta t} \geq \phi_t, \tag{10}$$

where $\phi_{t+\Delta t}$ is the phase field variable in the current time increment while ϕ_t denotes the value of the phase field on the previous increment. For both loading and unloading scenarios, the history field must satisfy the Kuhn-Tucker conditions

$$\psi_0 - H \leq 0, \qquad \dot{H} \geq 0, \qquad \dot{H}(\psi_0 - H) = 0. \tag{11}$$

Accordingly, the history field for a current time t can be written as:

$$H = \max_{\tau\in[0,t]} \psi_0(\tau). \tag{12}$$

3.2. Heat Transfer Analogy

For a solid with thermal conductivity k, specific heat c_p and density ρ, the field equation for heat transfer in the presence of a heat source r reads:

$$k\nabla^2 T - \rho c_p \frac{\partial T}{\partial t} = r, \tag{13}$$

where T is the temperature field. Under steady-state conditions the rate term vanishes and Eq. (13) is reduced to,

$$k\nabla^2 T = r \tag{14}$$

The analogy of this elliptic partial differential equation (PDE) with the phase field evolution law is evident, with the temperature field acting as the phase field $T \equiv \phi$. Making use of the history field described above, one can reformulate the phase field local force balance, Eq. (9)b, as

$$\nabla^2\phi = \frac{\phi}{\ell^2} - \frac{2(1-\phi)}{G_c\ell}H. \tag{15}$$

And thus (14) and (15) are equivalent upon assigning the value of unity to the thermal conductivity ($k = 1$) and defining the following heat flux due to internal heat generation,

$$r = \frac{\phi}{\ell^2} - \frac{2(1-\phi)}{G_c\ell}H. \tag{16}$$

Finally, for the computation of the Jacobian matrix, one should also define the rate of change of heat flux (r) with temperature ($T \equiv \phi$),

$$\frac{\partial r}{\partial\phi} = \frac{1}{\ell^2} + \frac{2H}{G_c\ell} \tag{17}$$

We have restricted ourselves to the steady-state scenario, treating the phase field evolution law as rate-independent. This is, by far, the most common formulation for phase field fracture. However, one can also introduce a viscous regularisation term in the phase field equation by exploiting instead the transient problem - Eq. (13). In such scenario, the quantity ρc_p is analogous to a viscosity parameter (Miehe et al., 2010a). The heat capacity terms help stabilising the solution and thus one might wish to address a rate-independent (steady-state) problem by conducting instead a transient analysis over a long time. However, as demonstrated in the numerical examples below, we do not see the need to consider viscous regularisation to achieve convergence.

3.3. Abaqus particularities

The heat transfer analogy described can be readily implemented in Abaqus by making use of user material (UMAT) and heat flux (HETVAL) subroutines. The process is outlined in Fig. 1. Taking advantage of the heat transfer analogy enables carrying out the implementation at the integration point level, using in-built displacement-temperature elements such as the Abaqus CPE4T type for the case of 4-node bilinear quadrilateral elements. For a given element, Abaqus provides to the integration point-level subroutines the values of strain and phase field (temperature), as interpolated from the nodal solutions. Within each integration point loop, the user material subroutine (UMAT) is called first. Inside of the UMAT, the material Jacobian $\boldsymbol{C}_0$ and the Cauchy stress $\boldsymbol{\sigma}$ can be readily computed from the strain tensor. The current value of the phase field (temperature) is then used to account for the damage degradation of these two quantities. The strain energy density can be stored in so-called solution dependent state variables (SDVs), enabling to enforce the irreversibility condition (Section 3.1). The updated value of the SDVs is transferred to the heat flux (HETVAL) subroutine; this is used to transfer the current value of the history field H, without the need for external Fortran modules. In the HETVAL subroutine we define the internal heat flux r, Eq. (16), and its derivative with respect to the temperature (phase field) $\partial r/\partial\phi$, Eq. (17). The process is repeated for every integration point, enabling Abaqus to externally build the element stiffness matrices and residuals and assembling the global system of equations, see Fig. 1. It is worth emphasising that the coupling terms in the stiffness matrix are not defined: $\boldsymbol{K}_{\boldsymbol{u}\phi} = \boldsymbol{K}_{\phi\boldsymbol{u}} = \boldsymbol{0}$, making the stiffness matrix symmetric. By default, Abaqus assumes a non-symmetric system for coupled displacement-temperature analyses but this can be modified by defining a separated solution technique. It should be noted that parallel calculations using versions of Abaqus older than 2016 only execute the solver in parallel (if the separated solution technique is used).

To avoid editing the user subroutine, mechanical and fracture property are defined in the input file only, as user material property, and are then transferred between subroutines using solution dependent variables. Consistent with the heat transfer analogy outlined above, one must activate the heat generation option and define as material property the thermal conductivity k, with a value of unity. Also, one should assign an initial temperature distribution of $T(t=0) = 0\,\forall\,\boldsymbol{x}$. No additional pre-processing or post-processing steps are needed, all actions can be conducted within the Abaqus/CAE graphical user interface and the phase field solution can be visualised by plotting the nodal solution temperature (NT11).

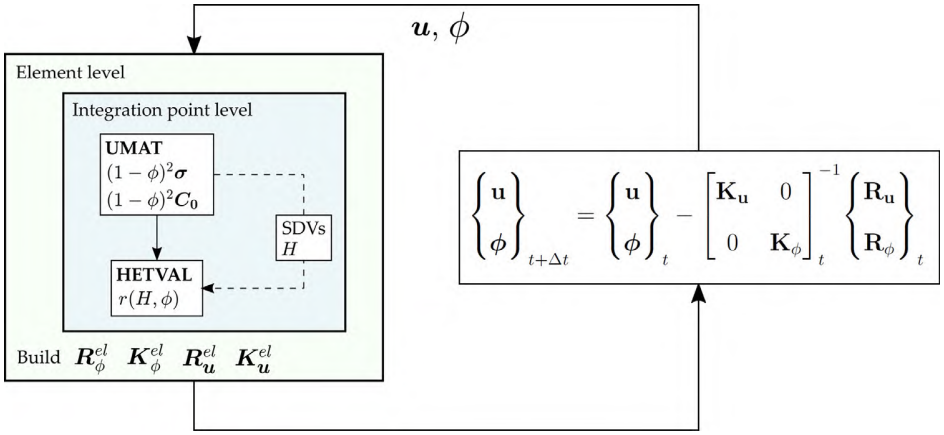

Fig. 1. User subroutine flowchart for the implementation of a coupled deformation - phase field fracture model exploiting the analogy with heat transfer.

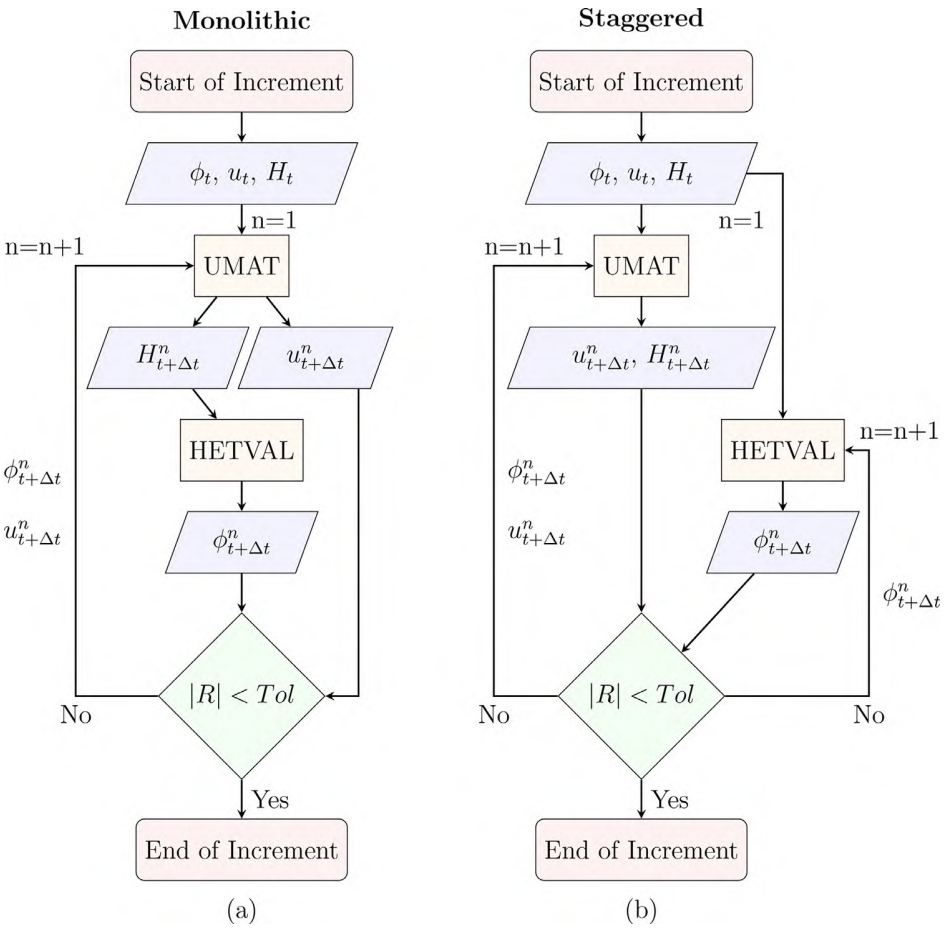

Fig. 2. Phase field fracture solution flowchart at each integration point for a specific increment: (a) monolithic, and (b) staggered schemes.

3.4. Solution schemes

The global system of equations, shown in Fig. 1, can be solved in either a *monolithic* or a *staggered* manner. In a monolithic approach, the displacement sub-system $\boldsymbol{K_u u} = \boldsymbol{R_u}$ and the phase field sub-system $\boldsymbol{K_\phi \phi} = \boldsymbol{R_\phi}$ are solved simultaneously. On the other hand, a staggered solution scheme entails an alternative minimisation approach, by which the sub-systems are solved sequentially. Monolithic solution strategies are unconditionally stable and, therefore, more efficient (in principle). However, the total potential energy functional (3) is non-convex with respect to $\boldsymbol{u}$ and ϕ. As a consequence, the Jacobian matrix in Newton's method becomes indefinite, hindering convergence when solving for the displacement and the phase field at the same time. It has been recently shown that the use of quasi-Newton methods such as the Broyden-Fletcher-Goldfarb-Shanno (BFGS) algorithm enables the implementation of robust monolithic schemes that are very efficient and do not exhibit convergence issues (Kristensen and Martínez-Pañeda, 2020; Wu et al., 2020a) - see also (Kristensen et al., 2020b; Wu et al., 2021) for application examples. Unfortunately, the quasi-Newton solution scheme is not available in Abaqus for thermo-mechanical problems. Accordingly, we implement a conventional monolithic scheme, based on Newton's method, and a staggered scheme of the single-pass type. The flowchart associated with each of these solution schemes is presented in Fig. 2. In the staggered case, the residual and the stiffness matrix for the

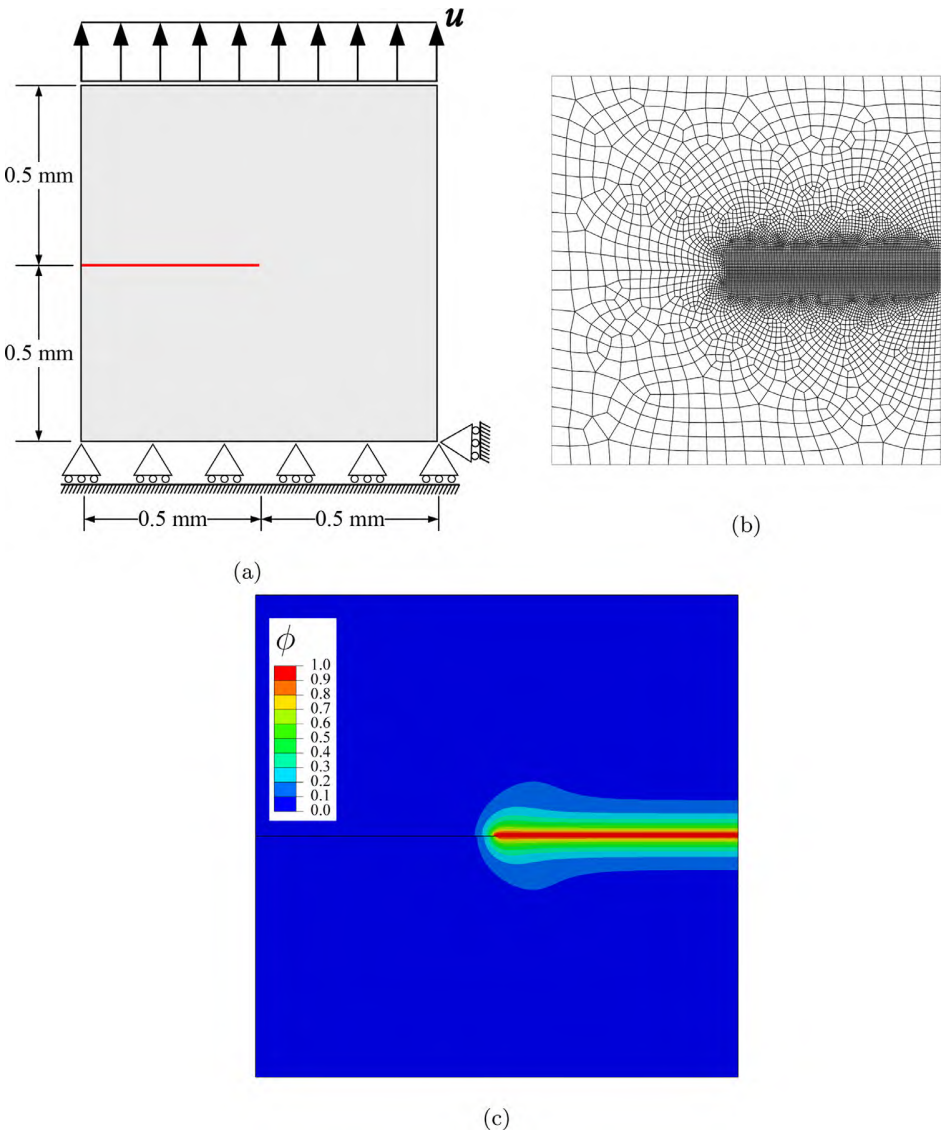

Fig. 3. Notched square plate under tension: (a) geometry, dimensions and boundary conditions, (b) finite element mesh, and (c) contour of the phase field ϕ after rupture.

phase field sub-system are built considering the history field of the previous increment H_t; i.e., the history field is frozen during the iterative procedure, facilitating convergence in demanding problems at the cost of scarifying unconditional stability. A recursive iteration or multi-pass staggered scheme can be implemented by using a Fortran module to transfer the history field between the UMAT and the HETVAL. Thus, we provide a general framework that provides flexibility to enhance robustness or efficiency, as required for the problem at hand. This trade-off between efficiency and robustness, and the differences in performance between solution schemes, are addressed in the numerical examples below.

4. Results

We shall show the robustness and capabilities of the present implementation by simulating fracture in several paradigmatic boundary value problems. First, crack initiation and growth in a notched square plate is addressed under both uniaxial tension (Section 4.1) and shear (Section 4.2). Then, the failure of screws subjected to tension, with and without initial cracks, is simulated in Section 4.3. Finally, in Section 4.4, a 3D model of the Brazilian test is developed, including the contact between the jaws and the sample, to determine the nucleation and coalescence of cracks.

4.1. Notched square plate under tension

First, we shall consider the case of unstable crack growth in a notched squared plate undergoing uniaxial tension. This is a paradigmatic benchmark in the phase field fracture community since the early work by Miehe et al. (2010b). The geometry and boundary conditions are shown in Fig. 3a. The sample is subjected to mode I fracture conditions, with a vertical displacement being prescribed in the remote boundary. The mechanical behaviour is characterised by a Young's modulus $E = 210$ GPa and a Poisson's ratio $\nu = 0.3$, while the fracture properties read $\ell = 0.024$ mm and $G_c = 2.7$ N/mm (Kristensen and Martínez-Pañeda, 2020). We discretise the model using linear quadrilateral elements for coupled displacement-thermal analyses, CPE4T in Abaqus terminology. A total of 8,532 elements are used. As shown in Fig. 3b, the mesh is refined along the expected crack path, such that the characteristic element size is at least five times smaller than the phase field length scale ℓ. For this case study, the monolithic implementation is used and no strain energy decomposition is assumed. The predicted crack path is showcased in Fig. 3c by plotting the contours of the phase field variable ϕ.

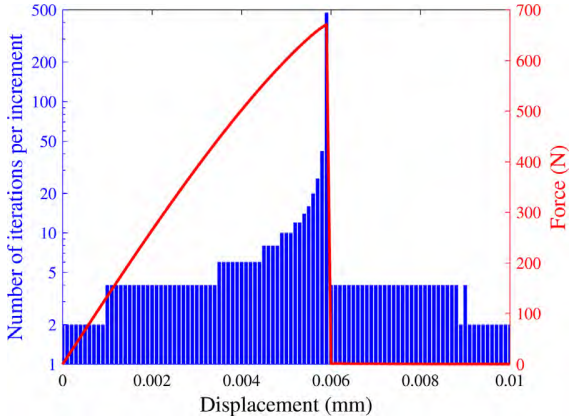

Fig. 4. Notched square plate under tension. Number of iterations per increment, with the force versus displacement curve superimposed.

The force versus displacement response predicted is shown in Fig. 4. The result agrees with that of Kristensen and Martínez-Pañeda (2020), which was obtained using a quasi-Newton solution scheme. Cracking is unstable, with the crack extending through the ligament instantaneously. This leads to a dramatic drop in the load carrying capacity, as shown in Fig. 4. However, despite this drastic change in the structural response, convergence can be attained and the fracture event is captured in one single load increment. Fig. 4 also shows the number of iterations required to achieve convergence in each increment, superimposed to the force versus displacement response. We use time increments of constant size and resolve the analysis with a total of 100 load increments. Convergence throughout can be achieved with as few as 10 increments, but using a larger number facilitates capturing the sudden load drop with greater fidelity. An adaptive time stepping scheme, such as the one developed by Kristensen and Martínez-Pañeda (2020), can be easily incorporated. This will allow for the increment size to increase or decrease as needed, enabling accurate results at an even smaller computational cost. In any case, it can be observed that the problem can be solved efficiently, with most time increments requiring a small number of iterations to achieve convergence (10 or fewer). However, resolving the fracture event requires a load increment with over 400 iterations. Unlike other computational fracture methods, the Newton-Raphson algorithm can converge after hundreds of iterations in phase field models (Gerasimov and De Lorenzis, 2016). The solution controls of Abaqus have to be edited to increase the maximum number of iterations that are allowed before convergence is deemed unlikely and the load increment is aborted (see the accompanying input file, to be downloaded from www.empaneda.com/codes). It must be noted that, despite the good performance observed, this boundary value

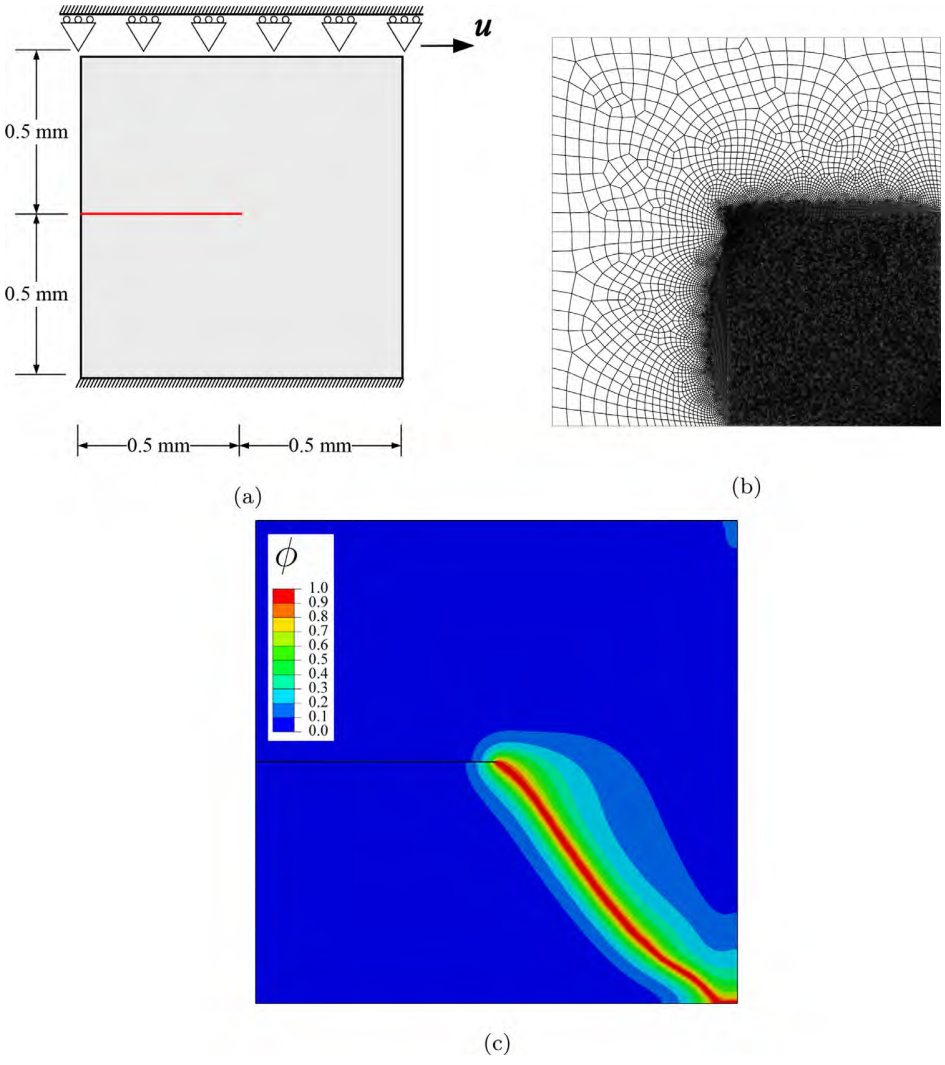

Fig. 5. Notched square plate under shear: (a) geometry, dimensions and boundary conditions, (b) finite element mesh, and (c) contour of the phase field ϕ after rupture.

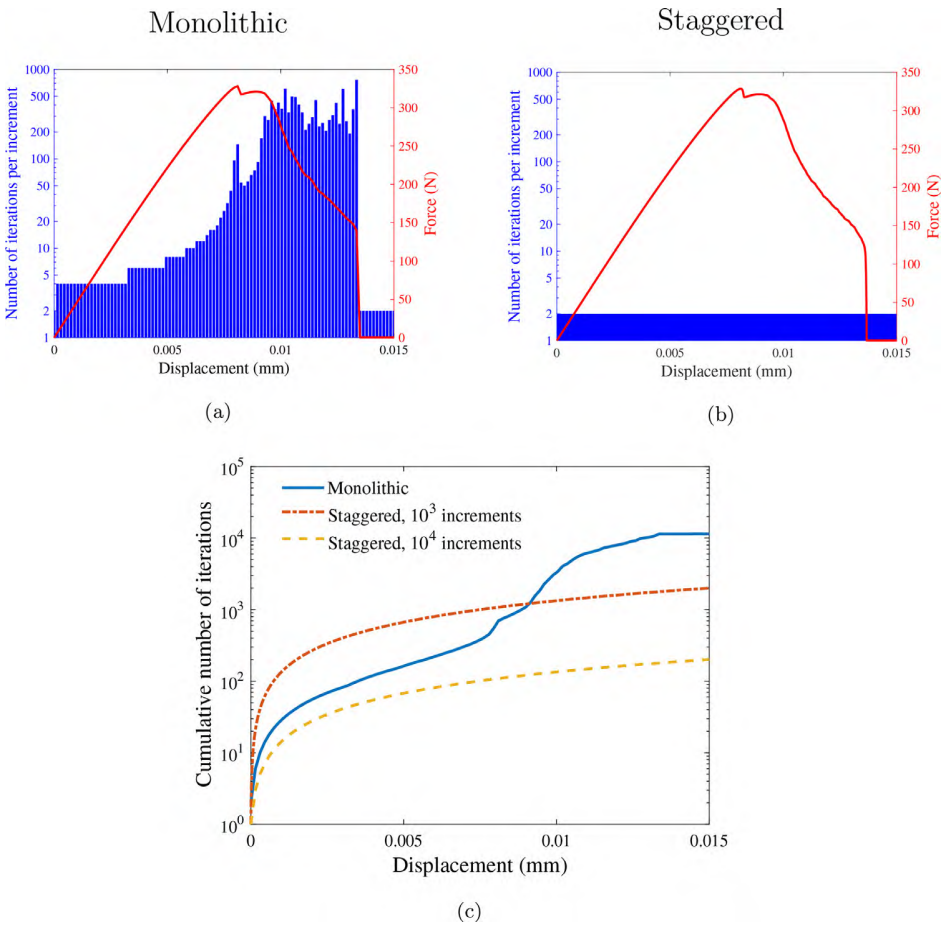

Fig. 6. Notched square plate under shear: (a) Number of iterations per increment for the monolithic scheme, with the force versus displacement curve superimposed; (b) number of iterations per increment for the staggered scheme with 10,000 increments, with the force versus displacement curve superimposed; and (c) cumulative number of iterations for both staggered and monolithic results.

problem can be resolved more efficiently using quasi-Newton solution schemes (see Kristensen and Martínez-Pañeda, 2020).

4.2. Notched square plate under shear

We shall now address the case of stable crack growth by simulating the fracture of the notched square plate considered in Section 4.1, but subjected to shear loading. As shown in Fig. 5a, a horizontal displacement is prescribed at the top edge of the plate, while the bottom edge is fully constrained $u_x = u_y = 0$. The dimensions of the initial crack and the sample are identical to those considered for the uniaxial tension case study. Also, the same material properties are assumed. On this occasion, the volumetric-deviatoric split of the strain energy density proposed by Amor et al. (2009) is adopted - see Appendix A. This is implemented using the so-called hybrid approach by Ambati et al. (2015), such that the displacement field equation remains as in Eq. (9a). Based on the literature (see, e.g., Ambati et al., 2015; Kristensen and Martínez-Pañeda, 2020), the crack is expected to deflect towards the bottom-right corner. Accordingly, the mesh is refined in the bottom half of the sample - see Fig. 5b. A total of 73,714 linear quadrilateral elements with full integration are used, with the characteristic element size being ten times smaller than the phase field length scale. The phase field contours at the end of the analysis are provided in Fig. 5c, showing the final crack trajectory. The crack path predicted agrees with that observed in previous studies using the volumetric-deviatoric split (Ambati et al., 2015; Kristensen and Martínez-Pañeda, 2020).

The force versus displacement response is shown in Fig. 6, along with the size of each increment and the number of iterations that were needed to achieve convergence. The crack propagates in a stable manner, leading to a progressive reduction in the reaction force. Again, the results agree with those obtained by Kristensen and Martínez-Pañeda (2020) using a monolithic quasi-Newton solution scheme. This boundary value problem is known to be particularly challenging from a convergence viewpoint and is thus used to compare the monolithic and staggered solution schemes. Consider first the monolithic analysis, Fig. 6a. While the entire crack propagation process can be captured, many increments require a very significant number of iterations to achieve convergence - unlike in the uniaxial tension case where cracking is unstable. It is clear that, for this boundary value problem, the monolithic implementation struggles to converge and becomes inefficient. Now let us examine the output of the staggered case. The results obtained with the single-pass staggered implementation also make use of a uniform increment size, with the entire analysis being conducted using 10^4 load steps. This is a sufficiently large number of increments such that the solution is similar to that obtained with the unconditionally stable monolithic model - see Fig. 6b. In the staggered case, all load increments converge after two iterations. Notwithstanding, as discussed before, this solution scheme is not unconditionally stable and results can be sensitive to the number of time increments. We also conduct the analysis using 10^3 load steps; the crack trajectory and the maximum force attained agree with those predicted with the monolithic scheme but the force versus displacement result differs in the softening region (not shown). The staggered implementation appears to be more robust and efficient than the monolithic one for this specific case study; as quantified in Fig. 6c, the total number of iterations is larger in the monolithic case. However, one should note that both implementations are significantly outperformed by a monolithic approach based on the quasi-Newton solution method. As shown in (Kristensen and

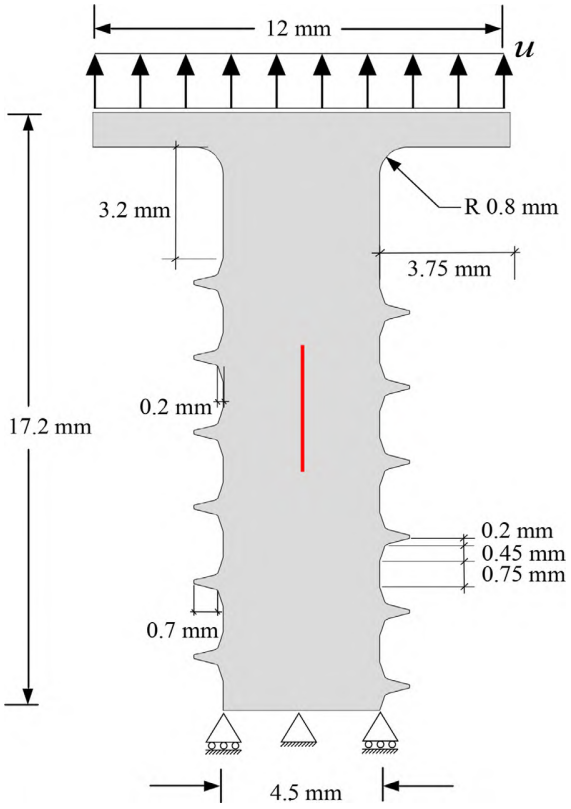

Fig. 7. Screw tension tests: geometry, dimensions and boundary conditions.

Martínez-Pañeda, 2020), a precise solution to this specific boundary value problem can be obtained with a number of iterations that is one order of magnitude smaller than the accurate staggered solution.

4.3. Screw tension tests

We proceed now to simulate the fracture of a screw subjected to tension, following the work by Wick et al. (2015). The geometry, dimensions and boundary conditions mimic those of (Wick et al., 2015) and are shown in Fig. 7. Three different cases are considered. First, we model a screw with no initial damage; i.e., without the initial crack displayed in Fig. 7. Secondly, we will assume that the screw contains an initial short crack, with size $a = 3$ mm. Thirdly, a screw with a long crack will be modelled, where $a = 6$ mm. In all cases, the initial cracks are introduced by defining as initial condition $\phi = 1$. Moreover, the initial crack is vertical, as shown in Fig. 7, has a thickness of 0.16 mm, and its bottom tip is located at a distance of 7 mm to the bottom of the screw. Following Wick et al. (2015), the material properties are taken to be $E = 210$ GPa, $\nu = 0.3$, $\ell = 0.2$ mm, and $G_c = 2.7$ N/mm. The screws are discretised using approximately 70,000 linear quadrilateral elements. The samples are meshed uniformly so as to remove any bias of the mesh on the crack trajectory, with the characteristic element size being 5 times smaller than the phase field length scale. Computations are conducted with the monolithic scheme and no strain energy density split is considered.

The crack growth trajectories predicted for the three cases described above are shown in Fig. 8, by plotting the phase field contours. The results agree qualitatively with those obtained by Wick et al. (2015). In the absence of an initial defect, crack nucleation takes place near the head of the screw. This is in agreement with expectations, as the first winding of the thread carries the highest load (see Kristensen et al., 2020b). However, when an initial defect is present, two cracks branch from it and propagate until reaching the sides of the screw.

The force versus displacement response is shown in Fig. 9a. In agreement with expectations, the sample without an initial defect is able to carry a larger load. In regard to the screws with an existing defect, the stiffness of the solid is degraded faster in the case of a long crack, relative to the sample with a smaller crack, but the magnitude of the maximum force attained is similar in both cases. The number of iterations required to achieve convergence is shown for every load increment in Figs. 9b-d for, respectively, the case without an initial defect, the case with an initial long crack and the case with an initial short crack. In all three cases convergence can be readily attained. The crack grows in an unstable fashion and the situation thus resembles that of Section 4.1; convergence can be readily attained but one specific increment requires more than 100 iterations to do so.

Finally, we investigate the role of using extrapolation to speed up the solution. By default, Abaqus uses linear extrapolation to determine the first guess of the incremental solution. Fig. 10 shows the accumulated number of iterations for the case of a screw with a short initial defect, as a function of the applied displacement and with the force versus displacement response superimposed. It can be readily seen that enabling extrapolation facilitates convergence before cracking occurs, but eventually the solution without extrapolation becomes more efficient as it requires less iterations to resolve the crack propagation process. Thus, computational gains might be attained by deactivating the extrapolation option.

4.4. 3D Brazilian test

Finally, we showcase the potential of the framework presented in capturing structural failure in 3D solids. We do so by simulating the

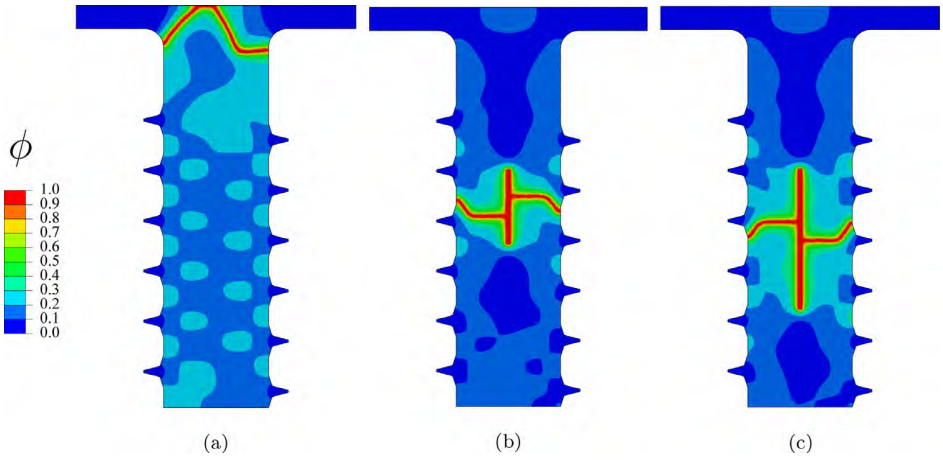

Fig. 8. Screw tension tests: final phase field contours for the cases of (a) a screw with no initial crack, (b) a screw with a short ($a = 3$ mm) initial crack, and (c) a screw with a long ($a = 6$ mm) initial crack.

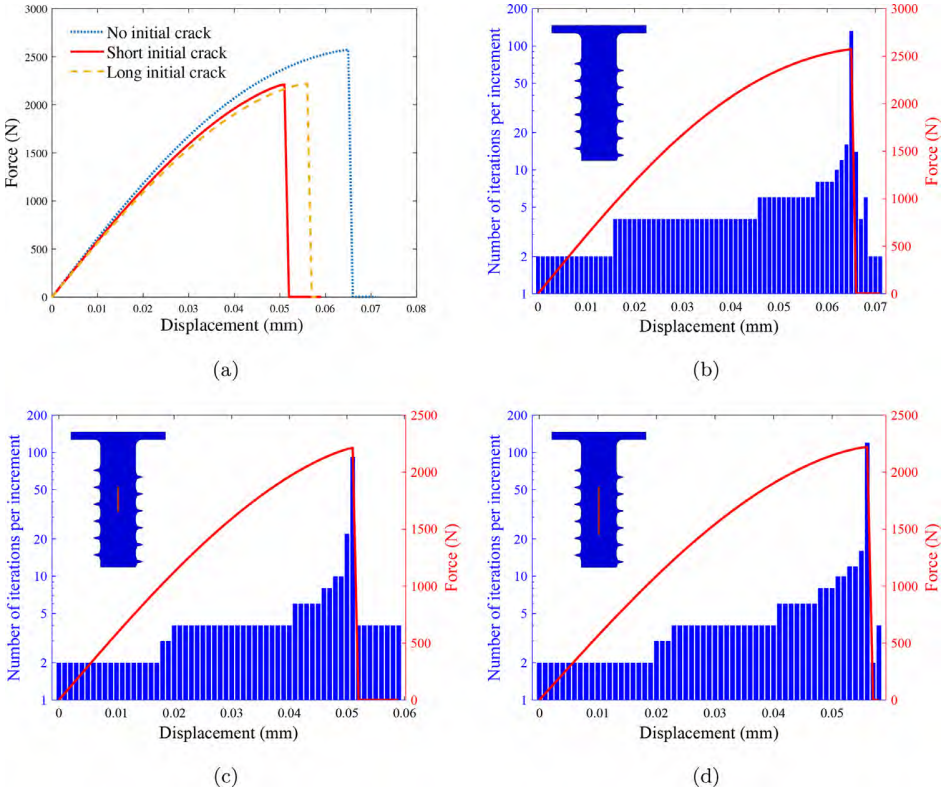

Fig. 9. Screw tension tests: (a) force versus displacement curve for each of the three cases considered, together with the number of iterations per increment for (b) a screw with no initial crack, (c) a screw with a short ($a = 3$ mm) initial crack, and (d) a screw with a long ($a = 6$ mm) initial crack.

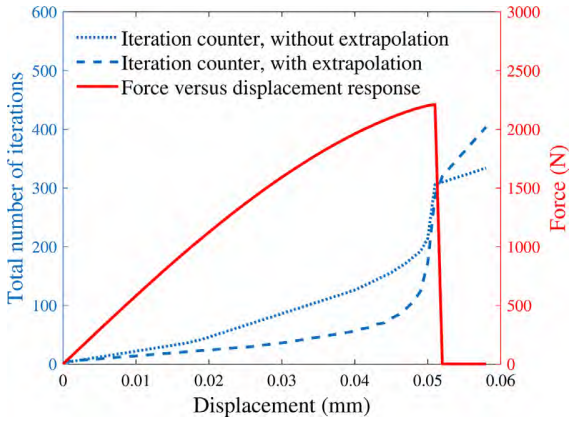

Fig. 10. Screw tension test: assessing the influence of the extrapolation technique. Force versus displacement response and cumulative number of iterations required to achieve convergence with and without extrapolation.

fracture of a brittle solid subjected to the Brazilian test. The Brazilian test is a laboratory experiment widely used in the rock mechanics community to indirectly measure the tensile strength of brittle materials. As shown in Fig. 11a, a circular disk is compressed between two jaws until fracture occurs. Upon the assumption that failure occurs at the centre of the disk, closed form expressions can be used to determine the material tensile strength from the remote load (Garcia-Fernandez et al., 2018). As shown in Fig. 11b, we take advantage of symmetry and model one-eighth of the experiment applying suitable boundary conditions. Thus, we prescribe $u_z = 0$ in the xy plane at $z = 0$ for both the disk and the jaw. To account for symmetry about a plane with x=constant, we prescribe $u_x = 0$ along the yz plane at $x = 0$ on the surfaces of the disk and the jaw. Finally, to account for symmetry along the y axis, we constrain $u_y = 0$ on the bottom surface of the disk. The compressive load state is achieved by prescribing a negative u_y displacement on the nodes located on the top surface of the jaw. This one-eighth part of the complete testing configuration is discretised using 58,925 linear brick elements. The characteristic element length equals 0.1 mm and the calculations involved 254,384 degrees-of-freedom.

The material properties are defined as follows. On the one side, the jaws are typically made of steel, for which $E = 210$ GPa and $\nu = 0.3$ are assumed. For the disk we consider a brittle solid with elastic properties $E = 25$ GPa and $\nu = 0.2$ and fracture properties $\ell = 0.5$ mm and $G_c = 0.16$ N/mm. The jaws radius to disk radius ratio is chosen to be $R_j/R_d = 1.5$. The contact between the jaws and the disk is defined as surface to surface contact with a finite sliding formulation. The normal behaviour is based on a hard contact formulation, where the contact constraint is enforced with a Lagrange multiplier representing the contact pressure in a mixed formulation. The tangential contact behaviour is assumed to be frictionless. To prevent damage under compression, the spectral tension-compression decomposition by Miehe et al. (2010a) is adopted - see Appendix A. Also, an *anisotropic* formulation is used, such that the strain energy density split is accounted for in the balance equation for the displacement problem (see Appendix A for details).

The results obtained are shown in Fig. 12 in terms of the phase field contours for the different loading stages. The evolution of the phase field is also shown in Video 1, provided in the online version of this manuscript. Sub-figures 12 (a)-(c) show in red colour the phase field contours where $\phi > 0.9$. The crack appears to initiate at the centre of the disk and propagates towards the jaws very fast. Also, smaller cracks nucleate near the loading region. These calculations have been obtained using 345 load increments and with the monolithic implementation, no convergence issues were observed.

5. Conclusions

We have presented a simple and robust implementation of the phase field fracture method in Abaqus. The framework developed does

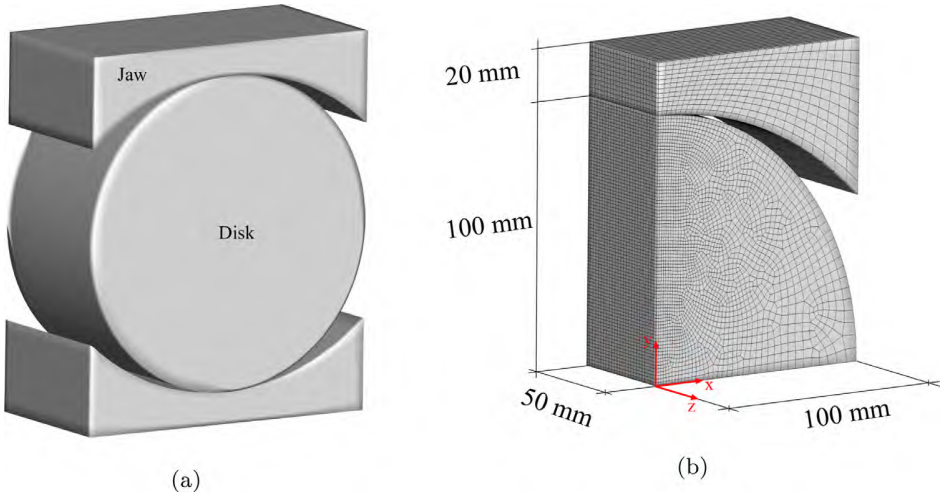

Fig. 11. 3D Brazilian test: (a) complete geometry of the test and (b) geometry, boundary conditions and mesh of the computational model. One-eighth of the problem is simulated, taking advantage of symmetry.

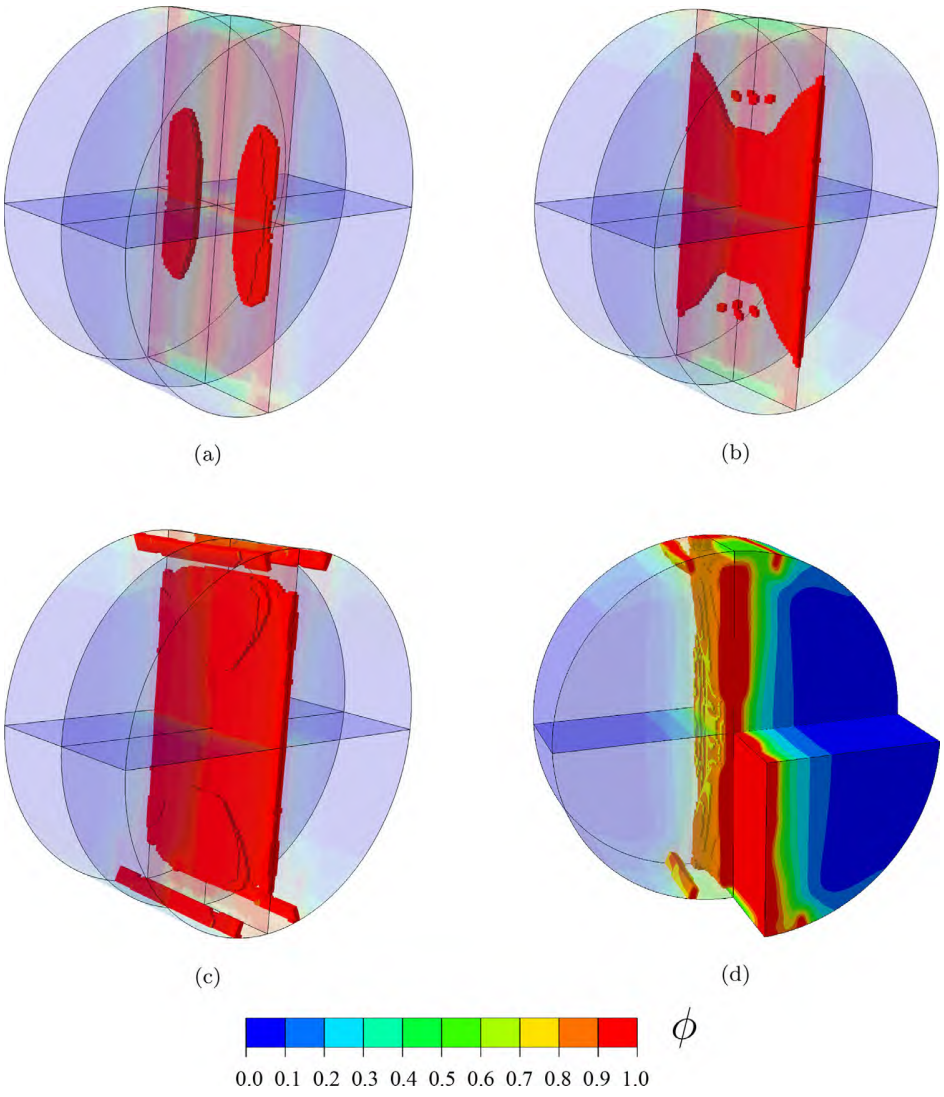

Fig. 12. 3D Brazilian test: contours of the phase field ϕ showcasing different stages of the fracture process. Sub-figures (a)-(c) show a transparent cross-section of the disk with $\phi > 0.9$ contours for the the following values of the remote displacement: (a) $u_y = -0.0668$ mm, (b) $u_y = -0.0670$ mm, and (c) $u_y = -0.0676$ mm. Sub-figure (d) shows the complete phase field ϕ contours for a jaw displacement of $u_y = -0.0676$ mm.

not require the coding of user-defined elements and therefore enables exploiting the majority of the in-built features of commercial finite element codes. This is achieved by taking advantage of the similarities between the heat transfer and the phase field evolution equations. The model can be developed entirely in Abaqus' graphical user interface and the implementation can be accomplished by combining a user material (UMAT) and a heat flux (HETVAL) subroutine. The code, which is provided open-source at www.empaneda.com/codes, can be used without changes for both 2D and 3D problems. The framework is general and can accommodate a wide variety of solution schemes and constitutive choices. Specifically, we incorporate both the spectral tension-compression (Miehe et al., 2010a) and the volumetric-deviatoric (Amor et al., 2009) strain energy decompositions. Moreover, we implement both monolithic and staggered solution schemes, providing a suitable trade-off between efficiency and robustness.

The potential of the framework is demonstrated by addressing four 2D and 3D paradigmatic boundary value problems. First, unstable fracture is examined using a notched square plate subjected to tension. Secondly, stable crack growth is investigated by subjecting the square plate to shear loading. Thirdly, the fracture of screws with and without internal cracks is investigated. Finally, the Brazilian test is simulated, including the modelling of the contact between the jaws and the disk. We observe that the monolithic standard Newton implementation provided is able to reach convergence in all cases. However, a single-pass staggered scheme appears to be more efficient in convergence-wise demanding problems. Computations are efficient but both schemes seem to perform worse than quasi-Newton methods (Kristensen and Martínez-Pañeda, 2020; Wu et al., 2020a). We also find that the use of interpolation schemes might not lead to efficiency improvements in phase field fracture. The framework can be very easily extended to other material models (e.g., plasticity) and damage mechanisms, such as fatigue.

Declaration of Competing Interest

The authors declare that they have no known competing financial interests or personal relationships that could have appeared to influence the work reported in this paper.

Acknowledgements

The authors would like to acknowledge financial support from the Ministry of Science, Innovation and Universities of Spain through grant PGC2018-099695-B-I00. E. Martínez-Pañeda additionally acknowledges financial support from the EPSRC (grants EP/R010161/1 and EP/R017727/1) and from the Royal Commission for the 1851 Exhibition (RF496/2018).

Appendix A. Additional details of numerical implementation

The framework can be easily extended to incorporate other constitutive choices. Specifically, as shown in the results section, a tension-compression split of the driving force for fracture should be considered to prevent damage from developing under compressive stresses. Alternative strain energy splits are described below, together with an anisotropic phase field formulation where the split is incorporated into the linear momentum equation. All these extensions are implemented in the user material (UMAT) subroutine.

A1. Strain energy density decomposition

The two most widely used strain energy splits are considered: the Miehe et al. (2010a) tension-compression spectral decomposition and the Amor et al. (2009) volumetric-deviatoric split. In both cases, the strain energy density is decomposed as follows,

$$\psi_0 = (1-\phi)^2\psi_0^+ + \psi_0^-, \tag{A.1}$$

and only ψ_0^+ is considered in the evaluation of the history field H, Eq. (12). In regard to the specific constitutive definition of ψ_0^+, the volumetric-deviatoric split assumes that the compressive part of the volumetric strain energy does not contribute to the fracture process. Accordingly,

$$\psi_0^+ = \frac{1}{2}K\langle \mathrm{tr}(\boldsymbol{\varepsilon})\rangle_+^2 + \mu\left(\boldsymbol{\varepsilon}' : \boldsymbol{\varepsilon}'\right) \tag{A.2}$$

$$\psi_0^- = \frac{1}{2}K\langle \mathrm{tr}(\boldsymbol{\varepsilon})\rangle_-^2 \tag{A.3}$$

where K is the bulk modulus, μ is the shear modulus, $\langle\rangle$ denote the Macaulay brackets, such that $\langle a\rangle_\pm = (a \pm |a|)/2$, and $\boldsymbol{\varepsilon}'$ is the deviatoric part of the strain tensor, such that $\boldsymbol{\varepsilon}' = \boldsymbol{\varepsilon} - tr(\boldsymbol{\varepsilon})\mathbf{1}/3$. Here, $\mathbf{1}$ is the second-order unit tensor.

On the other hand, the spectral decomposition considers,

$$\psi_0^+ = \frac{1}{2}\lambda\langle \mathrm{tr}\left(\boldsymbol{\varepsilon}^+\right)\rangle^2 + \mu\,\mathrm{tr}\left[\left(\boldsymbol{\varepsilon}^+\right)^2\right] \tag{A.4}$$

$$\psi_0^- = \frac{1}{2}\lambda\langle \mathrm{tr}(\boldsymbol{\varepsilon}^-)\rangle^2 + \mu\,\mathrm{tr}\left[(\boldsymbol{\varepsilon}^-)^2\right] \tag{A.5}$$

where λ is the first Lamé constant and a spectral decomposition is applied to the strain tensor, such that:

$$\boldsymbol{\varepsilon} = \sum_{I=1}^{3}\langle \varepsilon_I\rangle\, \boldsymbol{n}_I \otimes \boldsymbol{n}_I \tag{A.6}$$

where ε_I and $\boldsymbol{n}_I$ are the principal strains and principal strain directions (with $I = 1, 2, 3$). The components $\boldsymbol{\varepsilon}^+$ and $\boldsymbol{\varepsilon}^-$ are obtained by considering in (A.6) the tensile and compressive principal strains, respectively.

A2. Anisotropic formulation

While the majority of the representative results presented are obtained using the hybrid approach proposed by Ambati et al. (2015), we have also extended our implementation to incorporate the so-called *anisotropic* approach (Miehe et al., 2010a). Thus, the decomposition into tension and compression components is also considered in the field equation for the displacement problem, such that the Cauchy stress (7) would instead read,

$$\boldsymbol{\sigma} = (1-\phi)^2\frac{\partial\psi_0^+(\boldsymbol{\varepsilon})}{\partial\boldsymbol{\varepsilon}} + \frac{\partial\psi_0^-(\boldsymbol{\varepsilon})}{\partial\boldsymbol{\varepsilon}} \tag{A.7}$$

From an implementation perspective, this translates into a more elaborate computation of the material Jacobian, $\boldsymbol{C} = \partial\boldsymbol{\sigma}/\partial\boldsymbol{\varepsilon}$. Thus, the material behaviour is characterised by the following 4th order elasticity tensor:

$$\boldsymbol{C} = \lambda\left\{\left[(1-\phi)^2\right]H_\varepsilon(\mathrm{tr}(\boldsymbol{\varepsilon})) + H_\varepsilon(-\mathrm{tr}(\boldsymbol{\varepsilon}))\right\}\boldsymbol{J} + 2\mu\left\{\left[(1-\phi)^2\right]\boldsymbol{P}^+ + \boldsymbol{P}^-\right\} \tag{A.8}$$

where H_ε is the Heaviside function, such that $H_\varepsilon(x) = 1$ for $x \geq 0$ or $H_\varepsilon(x) = 0$ for $x < 0$, and $\boldsymbol{J} \equiv J_{ijkl} = \delta_{ij}\delta_{kl}$, with δ_{ij} being the Kronecker delta. Also, the projection tensor $\boldsymbol{P}^+ = \partial_\varepsilon\left[\boldsymbol{\varepsilon}_+(\boldsymbol{\varepsilon})\right]$ is computed as (Miehe, 1998)

$$P^+_{ijkl} = \sum_{a=1}^{3}\sum_{b=1}^{3} H_\varepsilon\left(\varepsilon_a\right)\delta_{ab}n_{ai}n_{aj}n_{bk}n_{bl} + \sum_{a=1}^{3}\sum_{b\neq a}^{3}\frac{1}{2}\frac{\langle\varepsilon_a\rangle_+ - \langle\varepsilon_b\rangle_+}{\varepsilon_a - \varepsilon_b}n_{ai}n_{bj}\left(n_{ak}n_{bl} + n_{bk}n_{al}\right) \tag{A.9}$$

where n_{xi} is the i^{th} component of the principal strain directions vector n_x. On the other hand: $\boldsymbol{P}^- = \boldsymbol{I} - \boldsymbol{P}^+$, with $\boldsymbol{I}$ being the fourth-order identity tensor. If $\varepsilon_a = \varepsilon_b$ then P^+_{ijkl} (A.9) cannot be evaluated. Under such circumstances we replace the term $\left(\langle\varepsilon_a\rangle_+ - \langle\varepsilon_b\rangle_+\right)/\left(\varepsilon_a - \varepsilon_b\right)$ with $H_\varepsilon\left(\varepsilon_a\right)$.

References

Abdollahi, A., Arias, I., 2012. Phase-field modeling of crack propagation in piezoelectric and ferroelectric materials with different electromechanical crack conditions. Journal of the Mechanics and Physics of Solids 60 (12), 2100–2126.

Ambati, M., Gerasimov, T., De Lorenzis, L., 2015. A review on phase-field models of brittle fracture and a new fast hybrid formulation. Computational Mechanics 55, 383–405.

Amor, H., Marigo, J.J., Maurini, C., 2009. Regularized formulation of the variational brittle fracture with unilateral contact: Numerical experiments. Journal of the Mechanics and Physics of Solids 57 (8), 1209–1229.

Biner, S.B., 2017. Programming Phase-Field Modeling. Springer.

Bourdin, B., Francfort, G.A., Marigo, J.-J., 2000. Numerical experiments in revisited brittle fracture. Journal of the Mechanics and Physics of Solids 48 (4), 797–826.

Bourdin, B., Francfort, G.A., Marigo, J.J., 2008. The variational approach to fracture. Springer Netherlands.

Cui, C., Ma, R., Martínez-Pañeda, E., 2021. A phase field formulation for dissolution-driven stress corrosion cracking. Journal of the Mechanics and Physics of Solids 147, 104254.

Fang, J., Wu, C., Rabczuk, T., Wu, C., Ma, C., Sun, G., Li, Q., 2019. Phase field fracture in elasto-plastic solids: Abaqus implementation and case studies. Theoretical and Applied Fracture Mechanics 103 (December 2018).

Garcia-Fernandez, C.C., Gonzalez-Nicieza, C., Alvarez-Fernandez, M.I., Gutierrez–Moizant, R.A., 2018. Analytical and experimental study of failure onset during a Brazilian test. International Journal of Rock Mechanics and Mining Sciences 103 (December 2017), 254–265.

Gerasimov, T., De Lorenzis, L., 2016. A line search assisted monolithic approach for phase–field computing of brittle fracture. Computer Methods in Applied Mechanics and Engineering 312, 276–303.

Griffith, A., 1920. The Phenomena of Rupture and Flow in Solids. Philosophical Transactions A, 221, 163–198.

Hirshikesh, Natarajan, S., Annabattula, R.K., Martínez-Pañeda, E., 2019. Phase field modelling of crack propagation in functionally graded materials. Composites Part B: Engineering 169, 239–248.

Klinsmann, M., Rosato, D., Kamlah, M., McMeeking, R.M., 2016. Modeling crack growth during Li insertion in storage particles using a fracture phase field approach. Journal of the Mechanics and Physics of Solids 92, 313–344.

Kristensen, P.K., Martínez-Pañeda, E., 2020. Phase field fracture modelling using quasi-Newton methods and a new adaptive step scheme. Theoretical and Applied Fracture Mechanics 107, 102446.

Kristensen, P.K., Niordson, C.F., Martínez-Pañeda, E., 2020. A phase field model for elastic-gradient-plastic solids undergoing hydrogen embrittlement. Journal of the Mechanics and Physics of Solids 143, 104093.

Kristensen, P.K., Niordson, C.F., Martínez-Pañeda, E., 2020. Applications of phase field fracture in modelling hydrogen assisted failures. Theoretical and Applied Fracture Mechanics 110, 102837.

Kumar, P.K.A.V., Dean, A., Reinoso, J., Lenarda, P., Paggi, M., 2021. Phase field modeling of fracture in Functionally Graded Materials : G -convergence and mechanical insight on the effect of grading. Thin-Walled Structures 107234.

Liu, G., Li, Q., Msekh, M.A., Zuo, Z., 2016. Abaqus implementation of monolithic and staggered schemes for quasi-static and dynamic fracture phase-field model. Computational Materials Science 121, 35–47.

Loew, P.J., Peters, B., Beex, L.A., 2019. Rate-dependent phase-field damage modeling of rubber and its experimental parameter identification. Journal of the Mechanics and Physics of Solids 127, 266–294.

Mandal, T.K., Gupta, A., Nguyen, V.P., Chowdhury, R., de Vaucorbeil, A., 2020. A length scale insensitive phase field model for brittle fracture of hyperelastic solids. Engineering Fracture Mechanics 236 (June), 107196.

Martínez-Pañeda, E., Golahmar, A., Niordson, C.F., 2018. A phase field formulation for hydrogen assisted cracking. Computer Methods in Applied Mechanics and Engineering 342, 742–761.

Miehe, C., 1998. Comparison of two algorithms for the computation of fourth-order isotropic tensor functions. Computers and Structures 66 (1), 37–43.

Miehe, C., Dal, H., Schanzel, L.-M., Raina, A., 2016. A phase-field model for chemo-mechanical induced fracture in lithium-ion battery electrode particles. International Journal for Numerical Methods in Engineering 106, 683–711.

Miehe, C., Hofacker, M., Welschinger, F., 2010. A phase field model for rate-independent crack propagation: Robust algorithmic implementation based on operator splits. Computer Methods in Applied Mechanics and Engineering 199 (45-48), 2765–2778.

Miehe, C., Welshinger, F., Hofacker, M., 2010. Thermodynamically consistent phase-field models of fracture: Variational principles and multi-field FE implementations. International Journal for Numerical Methods in Engineering 83, 1273–1311.

Molnár, G., Doitrand, A., Estevez, R., Gravouil, A., 2020. Toughness or strength? Regularization in phase-field fracture explained by the coupled criterion. Theoretical and Applied Fracture Mechanics 109 (June), 102736.

Molnár, G., Gravouil, A., 2017. 2D and 3D Abaqus implementation of a robust staggered phase-field solution for modeling brittle fracture. Finite Elements in Analysis and Design 130 (March), 27–38.

Molnár, G., Gravouil, A., Seghir, R., Réthoré, J., 2020. An open-source Abaqus implementation of the phase-field method to study the effect of plasticity on the instantaneous fracture toughness in dynamic crack propagation. Computer Methods in Applied Mechanics and Engineering 365, 113004.

Paggi, M., Corrado, M., Reinoso, J., 2018. Fracture of solar-grade anisotropic polycrystalline Silicon: A combined phase fieldcohesive zone model approach. Computer Methods in Applied Mechanics and Engineering 330, 123–148.

Papazafeiropoulos, G., Muñiz-Calvente, M., Martínez-Pañeda, E., 2017. Abaqus2Matlab: A suitable tool for finite element post-processing. Advances in Engineering Software 105, 9–16.

Provatas, N., Elder, K., 2011. Phase-Field Methods in Materials Science and Engineering. John Wiley & Sons.

Quintanas-Corominas, A., Reinoso, J., Casoni, E., Turon, A., Mayugo, J.A., 2019. A phase field approach to simulate intralaminar and translaminar fracture in long fiber composite materials. Composite Structures 220, 899–911.

Schuler, L., Ilgen, A.G., Newell, P., 2020. Chemo-mechanical phase-field modeling of dissolution-assisted fracture. Computer Methods in Applied Mechanics and Engineering 362, 112838.

Simoes, M., Martínez-Pañeda, E., 2021. Phase field modelling of fracture and fatigue in Shape Memory Alloys. Computer Methods in Applied Mechanics and Engineering 373, 113504.

Tan, W., Martínez-Pañeda, E., 2021. Phase field predictions of microscopic fracture and R-curve behaviour of fibre-reinforced composites. Composites Science and Technology 202, 108539.

Tanné, E., Li, T., Bourdin, B., Marigo, J.-J., Maurini, C., 2018. Crack nucleation in variational phase-field models of brittle fracture. Journal of the Mechanics and Physics of Solids 110, 80–99.

Wick, D., Wick, T., Hellmig, R.J., Christ, H.J., 2015. Numerical simulations of crack propagation in screws with phase-field modeling. Computational Materials Science 109, 367–379.

Wu, J.Y., Huang, Y., 2020. Comprehensive implementations of phase-field damage models in Abaqus. Theoretical and Applied Fracture Mechanics 106, 102440.

Wu, J.-Y., Huang, Y., Nguyen, V.P., 2020. On the BFGS monolithic algorithm for the unified phase field damage theory. Computer Methods in Applied Mechanics and Engineering 360, 112704.

Wu, J.-Y., Huang, Y., Nguyen, V.P., 2021. Three-dimensional phase-field modeling of mode I + II / III failure in solids. Computer Methods in Applied Mechanics and Engineering 373, 113537.

Wu, J.-Y., Nguyen, V.P., Nguyen, C.T., Sutula, D., Sinaie, S., Bordas, S., 2020. Phase-field modelling of fracture. Advances in Applied Mechanics 53, 1–183.

Zhou, S., Zhuang, X., Rabczuk, T., 2019. Phase field modeling of brittle compressive-shear fractures in rock-like materials: A new driving force and a hybrid formulation. Computer Methods in Applied Mechanics and Engineering 355, 729–752.

C | Paper 3

A Unified Abaqus Implementation of the Phase Field Fracture Method Using Only a User Material Subroutine

Authors:

Yousef Navidtehrani, Covadonga Betegón, Emilio Martínez-Pañeda

Journal:

Materials

Year of Publication:

2021

Impact Factor:

3.1 - Q2

materials

MDPI

Article

A Unified Abaqus Implementation of the Phase Field Fracture Method Using Only a User Material Subroutine

Yousef Navidtehrani [1], Covadonga Betegón [1] and Emilio Martínez-Pañeda [2,*]

[1] Department of Construction and Manufacturing Engineering, University of Oviedo, 33203 Gijón, Spain; navidtehraniyousef@uniovi.es (Y.N.); cova@uniovi.es (C.B.)
[2] Department of Civil and Environmental Engineering, Imperial College London, London SW7 2AZ, UK
* Correspondence: e.martinez-paneda@imperial.ac.uk

Abstract: We present a simple and robust implementation of the phase field fracture method in Abaqus. Unlike previous works, only a user material (UMAT) subroutine is used. This is achieved by exploiting the analogy between the phase field balance equation and heat transfer, which avoids the need for a user element mesh and enables taking advantage of Abaqus' in-built features. A unified theoretical framework and its implementation are presented, suitable for any arbitrary choice of crack density function and fracture driving force. Specifically, the framework is exemplified with the so-called `AT1`, `AT2` and phase field-cohesive zone models (`PF-CZM`). Both staggered and monolithic solution schemes are handled. We demonstrate the potential and robustness of this new implementation by addressing several paradigmatic 2D and 3D boundary value problems. The numerical examples show how the current implementation can be used to reproduce numerical and experimental results from the literature, and efficiently capture advanced features such as complex crack trajectories, crack nucleation from arbitrary sites and contact problems. The code developed is made freely available.

Keywords: Abaqus; phase field fracture; finite element analysis; UMAT; fracture mechanics

Citation: Navidtehrani, Y.; Betegón, C.; Martínez-Pañeda, E. A Unified Abaqus Implementation of the Phase Field Fracture Method Using Only a User Material Subroutine. *Materials* **2021**, *14*, 1913. https://doi.org/10.3390/ma14081913

Academic Editor: Carmine Maletta and Francesco Freddi

Received: 14 March 2021
Accepted: 8 April 2021
Published: 11 April 2021

1. Introduction

Variational phase field methods for fracture are enjoying a notable success [1,2]. Among many others, applications include shape memory alloys [3], glass laminates [4,5], hydrogen-embrittled alloys [6,7], dynamic fracture [8,9], fiber-reinforced composites [10–13], functionally graded materials [14–16], fatigue crack growth [17,18], and masonry structures [19]. The key to the success of the phase field paradigm in fracture mechanics is arguably three-fold. First, the phase field paradigm can override the computational challenges associated with direct tracking of the evolving solid-crack interface. The interface is made spatially diffuse by using an auxiliary variable, the phase field ϕ, which varies smoothly between the solid and crack phases and evolves based on a suitable governing equation. Such a paradigm has also opened new horizons in the modelling of other interfacial problems such as microstructural evolution [20] or corrosion [21]. Secondly, phase field modelling has provided a suitable platform for the simple yet rigorous fracture thermodynamics principles first presented by Griffith [22]. This energy-based approach enables overcoming the issues associated with local approaches based on stress intensity factors, such as the need for *ad hoc* criteria for determining the crack propagation direction [23,24]. Thirdly, phase field fracture modelling has shown to be very compelling and robust from a computational viewpoint. Advanced fracture features such as complex crack trajectories, crack branching, nucleation, and merging can be captured in arbitrary geometries and dimensions, and on the original finite element mesh (see, e.g., [25–28]). Also, computations can be conducted in a Backward Euler setting without the convergence issues observed when using other computational fracture methods. One reason behind this robustness

is the flexibility introduced by solving the phase field, a damage-like variable, independently from the deformation problem. So-called *staggered* solution schemes have been presented to exploit this flexibility by computing sequentially the displacement and phase field solutions [29], avoiding computationally demanding phenomena such as snap-backs.

The success of phase field modelling has been, not surprisingly, accompanied by a vast literature devoted to the development of open-source codes and finite element implementations of variational phase field methods for fracture. These works have been aimed at both commercial finite element packages, such as COMSOL [30], and open-source platforms like FEniCS [31]. The development of phase field fracture implementations in the commercial package Abaqus has received particular attention [32–38], due to its popularity in the solid mechanics community. However, these works require the use of multiple user subroutines, most often including a user element (UEL) subroutine. Abaqus' in-built elements cannot be employed due to the need for solving for the phase field ϕ as a nodal degree-of-freedom. Having to adopt a user-defined finite element carries multiple limitations; namely post-processing requires the use of a *dummy* mesh or *ad hoc* scripts, and most in-built features of Abaqus cannot be exploited, as the software suite is effectively used as a solver. In this work, we overcome these limitations by presenting a new implementation that only requires the use of a user material (UMAT) subroutine. The simple yet robust implementation presented is achieved by taking advantage of the analogy between the phase field evolution equation and heat transfer. This not only greatly simplifies the use of Abaqus for conducting phase field fracture studies but also enables taking advantage of the many in-built features provided by this commercial package. In addition, we present a generalized theoretical and numerical framework that encapsulates what are arguably the three most popular phase field fracture models presented to date: (i) the so-called `AT2` model [24], based on the Ambrosio and Tortorelli regularization of the Mumford-Shah functional [39], (ii) the `AT1` model [40], which includes an elastic phase in the damage response, and (iii) the phase field-cohesive zone model `PF-CZM` [41,42], aimed at providing an explicit connection to the material strength. Our framework also includes two strain energy decompositions to prevent damage in compressive states: the spectral split [29] and the volumetric-deviatoric one [43]—both available in the context of *anisotropic* and *hybrid* formulations [44]. Moreover, the implementation can use both *monolithic* and *staggered* solution schemes, enhancing its robustness. Two example codes are provided with this work (www.empaneda.com/codes), both capable of handling 2D and 3D analyses without any modification. One is a simple 33-line code, which showcases the simplicity of this approach by adopting the most widely used constitutive choices (`AT2`, no split). The other one is an extended version, with all the features mentioned above, aimed at providing a unified implementation for phase field fracture. To the authors' knowledge, the present work provides the simplest Abaqus implementation of the phase field fracture method.

The remainder of this manuscript is organised as follows. In Section 2 we provide a generalised formulation for phase field fracture, which can accommodate a myriad of constitutive choices. This is exemplified with the `AT2`, `AT1` and `CZ-PFM` models. Then, in Section 3, the details of the finite element implementation are presented, including the analogy with heat transfer and the particularities of the Abaqus usage. The potential of the implementation presented is showcased in Section 4, where several boundary value problems of particular interest are addressed. Specifically, (i) a three-point bending test, to compare with the results obtained with other numerical methods; (ii) a concrete single-edge notched beam, to compare with experimental data; (iii) a notched plate with a hole, to simulate complex crack paths, merging and nucleation; and (iv) a 3D gear, where cracking occurs due to contact between the teeth. Finally, concluding remarks are given in Section 5.

2. A Generalised Formulation for Phase Field Fracture

In this section, we formulate our generalised formulation, suitable for arbitrary constitutive choices of crack density function and fracture driving force. Consider an elastic

body occupying an arbitrary domain $\Omega \subset \mathbb{R}^n$ ($n \in [1,2,3]$), with an external boundary $\partial\Omega \subset \mathbb{R}^{n-1}$ with outwards unit normal $\mathbf{n}$.

2.1. Kinematics

The primary kinematic variables are the displacement field vector $\mathbf{u}$ and the damage phase field ϕ. In this work, we limit our attention to small strains and isothermal conditions. Consequently, the strain tensor $\boldsymbol{\varepsilon}$ reads

$$\boldsymbol{\varepsilon} = \frac{1}{2}\left(\nabla \mathbf{u}^T + \nabla \mathbf{u}\right). \tag{1}$$

The nucleation and growth of cracks are described by using a smooth continuous scalar *phase field* $\phi \in [0;1]$. The phase field describes the degree of damage, being $\phi = 0$ when the material point is in its intact state and $\phi = 1$ when the material point is fully broken. Since ϕ is smooth and continuous, discrete cracks are represented in a diffuse manner. The smearing of cracks is controlled by a phase field length scale ℓ. The aim of this diffuse representation is to introduce, over a discontinuous surface Γ, the following approximation of the fracture energy [24]:

$$\Phi = \int_\Gamma G_c \, \mathrm{d}S \approx \int_\Omega G_c \gamma(\phi, \nabla\phi) \, \mathrm{d}V, \qquad \text{for } \ell \to 0, \tag{2}$$

where γ is the so-called crack surface density functional and G_c is the material toughness [22,45]. This approximation circumvents the need to track discrete crack surfaces, a well-known challenge in computational fracture mechanics.

2.2. Principle of Virtual Work. Balance of Forces

Now, we shall derive the balance equations for the coupled deformation-fracture system using the principle of virtual work. The Cauchy stress $\boldsymbol{\sigma}$ is introduced, which is work conjugate to the strains $\boldsymbol{\varepsilon}$. Also, a traction $\mathbf{T}$ is defined on the boundary of the solid $\partial\Omega$, work conjugate to the displacements $\mathbf{u}$. Regarding fracture, we introduce a scalar stress-like quantity ω, which is work conjugate to the phase field ϕ, and a phase field microstress vector $\boldsymbol{\xi}$, that is work conjugate to the gradient of the phase field $\nabla\phi$. The phase field is assumed to be driven solely by the solution to the displacement problem. Thus, no external traction is associated with ϕ. In the absence of body forces, the principle of virtual work reads:

$$\int_\Omega \left\{\boldsymbol{\sigma} : \delta\boldsymbol{\varepsilon} + \omega\delta\phi + \boldsymbol{\xi} \cdot \delta\nabla\phi\right\} \mathrm{d}V = \int_{\partial\Omega} (\mathbf{T} \cdot \delta\mathbf{u}) \, \mathrm{d}S \tag{3}$$

where δ denotes a virtual quantity. This equation must hold for an arbitrary domain Ω and for any kinematically admissible variations of the virtual quantities. Thus, by application of the Gauss divergence theorem, the local force balances are given by:

$$\begin{aligned} \nabla \cdot \boldsymbol{\sigma} &= 0 \\ \nabla \cdot \boldsymbol{\xi} - \omega &= 0 \end{aligned} \qquad \text{in } \Omega, \tag{4}$$

with natural boundary conditions:

$$\begin{aligned} \boldsymbol{\sigma} \cdot \mathbf{n} &= \mathbf{T} \\ \boldsymbol{\xi} \cdot \mathbf{n} &= 0 \end{aligned} \qquad \text{on } \partial\Omega. \tag{5}$$

2.3. Constitutive Theory

The constitutive theory is presented in a generalised fashion, and the `AT1` [40], `AT2` [24] and `PF-CZM` [41,42] models are then derived as special cases. The total potential energy of the solid reads,

$$W(\boldsymbol{\varepsilon}(\mathbf{u}), \phi, \nabla\phi) = \psi(\boldsymbol{\varepsilon}(\mathbf{u}), g(\phi)) + \varphi(\phi, \nabla\phi) \tag{6}$$

where ψ is the elastic strain energy density and φ is the fracture energy density. The former diminishes with increasing damage through the degradation function $g(\phi)$, which must fulfill the following conditions:

$$g(0) = 1, \qquad g(1) = 0, \qquad g'(\phi) \leq 0 \ \text{ for } \ 0 \leq \phi \leq 1\,. \tag{7}$$

We proceed to formulate the fracture energy density as,

$$\varphi(\phi, \nabla\phi) = G_c\gamma(\phi, \nabla\phi) = G_c\frac{1}{4c_w\ell}\Big(w(\phi) + \ell^2|\nabla\phi|^2\Big)\,. \tag{8}$$

where ℓ is the phase field length scale and $w(\phi)$ is the geometric crack function. The latter must fulfill the following conditions:

$$w(0) = 0, \qquad w(1) = 1, \qquad w'(\phi) \geq 0 \ \text{ for } \ 0 \leq \phi \leq 1\,. \tag{9}$$

Also, c_w is a scaling constant, related to the so-called geometric crack function:

$$c_w = \int_0^1 \sqrt{w(\zeta)}\,\mathrm{d}\zeta\,. \tag{10}$$

Damage is driven by the elastic energy stored in the solid, as characterized by the undamaged elastic strain energy density ψ_0. To prevent cracking under compressive strain states, the driving force for fracture can be decomposed into active ψ_0^+ and inactive ψ_0^- parts. Accordingly, the elastic strain energy density can be defined as [46]:

$$\psi(\boldsymbol{\varepsilon}(\mathbf{u}), g(\phi)) = \psi^+(\boldsymbol{\varepsilon}(\mathbf{u}), \phi) + \psi_0^-(\boldsymbol{\varepsilon}(\mathbf{u})) = g(\phi)\psi_0^+(\boldsymbol{\varepsilon}(\mathbf{u})) + \psi_0^-(\boldsymbol{\varepsilon}(\mathbf{u})) \tag{11}$$

Also, damage is an irreversible process: $\dot{\phi} \geq 0$. To enforce irreversibility, a history field variable $\mathcal{H}$ is introduced, which must satisfy the Karush–Kuhn–Tucker (KKT) conditions:

$$\psi_0^+ - \mathcal{H} \leq 0, \qquad \dot{\mathcal{H}} \geq 0, \qquad \dot{\mathcal{H}}(\psi_0^+ - \mathcal{H}) = 0\,. \tag{12}$$

Accordingly, for a current time t, over a total time τ, the history field can be defined as,

$$\mathcal{H} = \max_{t\in[0,\tau]}\psi_0^+(t)\,. \tag{13}$$

Consequently, the total potential energy of the solid (6) can be re-formulated as,

$$W = g(\phi)\mathcal{H} + \frac{G_c}{4c_w}\left(\frac{1}{\ell}w(\phi) + \ell|\nabla\phi|^2\right) \tag{14}$$

Now we proceed to derive, in a generalised fashion, the fracture micro-stress variables ω and $\boldsymbol{\xi}$. The scalar micro-stress ω is defined as:

$$\omega = \frac{\partial W}{\partial\phi} = g'(\phi)\mathcal{H} + \frac{G_c}{4c_w\ell}w'(\phi)\,, \tag{15}$$

while the phase field micro-stress vector $\boldsymbol{\xi}$ reads,

$$\boldsymbol{\xi} = \frac{\partial W}{\partial\nabla\phi} = \frac{\ell}{2c_w}G_c\nabla\phi\,. \tag{16}$$

Inserting these into the phase field balance Equation (4b), one reaches the following phase field evolution law:

$$\frac{G_c}{2c_w}\left(\frac{w'(\phi)}{2\ell} - \ell\nabla^2\phi\right) + g'(\phi)\mathcal{H} = 0 \tag{17}$$

We shall now make specific constitutive choices, particularising the framework to the so-called `AT2`, `AT1` and `PF-CZM` models.

Degradation function $g(\phi)$. Both `AT2` and `AT1` models were originally formulated using a quadratic degradation function:

$$g(\phi) = (1-\phi)^2 + \kappa \tag{18}$$

where κ is a small, positive-valued constant that is introduced to prevent ill-conditioning when $\phi = 1$. A value of $\kappa = 1 \times 10^{-7}$ is adopted throughout this work. Alternatively, the `PF-CZM` model typically uses the following degradation function,

$$g(\phi) = \frac{(1-\phi)^d}{(1-\phi)^d + a\phi(1+b\phi)}\,, \tag{19}$$

with,

$$a = \frac{4EG_c}{\pi \ell f_t^2}, \tag{20}$$

where E denotes Young's modulus and f_t is the tensile strength of the material. The choices of b and d depend on the softening law employed. Two commonly used softening laws are the linear one, with $b = -0.5$ and $d = 2$, and the exponential one, with $b = 2^{(5/3)} - 3$ and $d = 2.5$.

Dissipation function. The dissipation function is governed by the magnitude of w and, consequently, c_w. For the `AT2` model: $w(\phi) = \phi^2$ and $c = 1/2$. Since $w'(0) = 0$, this choice implies a vanishing threshold for damage. An initial, damage-free linear elastic branch is introduced in the `AT1` model, with the choices $w(\phi) = \phi$ and $c = 2/3$. Finally, in the `PF-CZM` case we have $w(\phi) = 2\phi - \phi^2$ and $c = \pi/4$.

Fracture driving force ψ_0^+. The variationally consistent approach, as proposed in the original `AT2` model, is often referred to as the *isotropic* formulation:

$$\psi_0^+(\boldsymbol{\varepsilon}) = \frac{1}{2}\boldsymbol{\varepsilon} : \boldsymbol{C}_0 : \boldsymbol{\varepsilon} = \frac{1}{2}\lambda \mathrm{tr}^2(\boldsymbol{\varepsilon}) + \mu \mathrm{tr}(\boldsymbol{\varepsilon}^2)\,, \quad \psi_0^-(\boldsymbol{\varepsilon}) = 0\,. \tag{21}$$

where $\boldsymbol{C}_0$ is the undamaged elastic stiffness tensor and λ and μ are the Lamé parameters. In the context of the `AT1` and `AT2` models, damage under compression is prevented by decomposing the strain energy density following typically two approaches. One is the so-called *volumetric-deviatoric* split, proposed by Amor et al. [43], which reads

$$\psi_0^+(\boldsymbol{\varepsilon}) = \frac{1}{2}K\langle \mathrm{tr}(\boldsymbol{\varepsilon})\rangle_+^2 + \mu\left(\boldsymbol{\varepsilon}' : \boldsymbol{\varepsilon}'\right), \quad \psi_0^-(\boldsymbol{\varepsilon}) = \frac{1}{2}K\langle \mathrm{tr}(\boldsymbol{\varepsilon})\rangle_-^2\,. \tag{22}$$

Here, K is the bulk modulus, $\langle a \rangle_\pm = (a \pm |a|)/2$, and $\boldsymbol{\varepsilon}' = \boldsymbol{\varepsilon} - \mathrm{tr}(\boldsymbol{\varepsilon})\boldsymbol{I}/3$. The second one is the so-called *spectral* decomposition, proposed by Miehe et al. [46], which builds upon the spectral decomposition of the strain tensor $\boldsymbol{\varepsilon}^\pm = \sum_{a=1}^3 \langle \varepsilon_I \rangle_\pm \mathbf{n}_I \otimes \mathbf{n}_I$, with ε_I and $\mathbf{n}_I$ being, respectively, the strain principal strains and principal strain directions (with $I = 1, 2, 3$). The strain energy decomposition then reads [46]:

$$\psi_0^\pm(\boldsymbol{\varepsilon}) = \frac{1}{2}\lambda\langle \mathrm{tr}(\boldsymbol{\varepsilon})\rangle_\pm^2 + \mu \mathrm{tr}\left[\left(\boldsymbol{\varepsilon}^\pm\right)^2\right] \tag{23}$$

The split can be applied not only to the phase field balance law but also to the balance of linear momentum. Considering the split only in the phase field balance (17) is typically

referred to as the *hybrid* approach [44]. Alternatively, an *anisotropic* formulation can be used, such that the damaged version of the stress tensor $\boldsymbol{\sigma}$ is computed as,

$$\boldsymbol{\sigma}(\mathbf{u},\phi) = g(\phi)\frac{\partial \psi_0^+(\boldsymbol{\varepsilon})}{\partial \boldsymbol{\varepsilon}} + \frac{\partial \psi_0^-(\boldsymbol{\varepsilon})}{\partial \boldsymbol{\varepsilon}}\,. \tag{24}$$

On the other hand, in the `PF-CZM` model the driving force for fracture is defined as [41]:

$$\psi_0^+ = \frac{\langle \sigma_1 \rangle_+^2}{2E}, \tag{25}$$

with the other term of the split being given by,

$$\psi_0^- = \frac{1}{2E}\Big[\sigma_1\langle\sigma_1\rangle_- + \sigma_2^2 + \sigma_3^2 - 2\nu(\sigma_2\sigma_3 + \sigma_1\sigma_3 + \sigma_1\sigma_2)\Big], \tag{26}$$

where ν is Poisson's ratio and σ_i are the principal stresses, with σ_1 being the maximum principal (undamaged) stress. The variational consistency is lost but the failure surface of concrete under dominant tension can be well captured [41]. This formulation is only used with the *hybrid* approach.

In addition, it is important to note that for the `AT1` and `PF-CZM` models there is a minimum value of the fracture driving force, which we denote as $\mathcal{H}_{min}$. This is needed as otherwise $\phi \leq 0$, as can be observed by setting $\phi = 0$ and solving the balance Equation (17). The magnitude of $\mathcal{H}_{min}$ is then given by the solution of (17) for $\mathcal{H}$ under $\phi = 0$. For the `AT1` case: $\mathcal{H}_{min} = 3G_c/(16\ell)$; while for the `PF-CZM` model: $\mathcal{H}_{min} = 2G_c/(\pi a\ell) = f_t^2/(2E)$.

3. Finite Element Implementation

We proceed to present our finite element model. The unified phase field fracture theory presented in Section 2 is numerically implemented in Abaqus using only a user material (UMAT) subroutine; i.e., at the integration point level. This is achieved by taking advantage of the similitude between the heat transfer law and the Helmholtz-type phase field balance equation. The analogy between heat transfer and phase field fracture is described in Section 3.1, while the specific details of the Abaqus implementation are given in Section 3.2. The present implementation does not require the coding of residual and stiffness matrix terms; however, these are provided in Appendix A for completeness.

3.1. Heat Transfer Analogy

Consider a solid with thermal conductivity k, specific heat c_p and density ρ. In the presence of a heat source r, the evolution of the temperature field T in time t is given by the following balance law:

$$k\nabla^2 T - \rho c_p \frac{\partial T}{\partial t} = -r\,, \tag{27}$$

Under steady-state conditions the $\partial T/\partial t$ term vanishes and Equation (27) is reduced to,

$$k\nabla^2 T = -r \tag{28}$$

Now, rearrange the phase field evolution law (17) as,

$$\nabla^2\phi = \frac{g'(\phi)\mathcal{H}2c_w}{\ell G_c} + \frac{w'(\phi)}{2\ell^2}\,. \tag{29}$$

Equations (28) and (29) are analogous upon considering the temperature to be equivalent to the phase field $T \equiv \phi$, assuming a unit thermal conductivity $k = 1$, and defining the following heat flux due to internal heat generation,

$$r = -\frac{g'(\phi)\mathcal{H}2c_w}{\ell G_c} - \frac{w'(\phi)}{2\ell^2}\,. \tag{30}$$

Finally, we also define the rate of change of heat flux (r) with temperature ($T \equiv \phi$),

$$\frac{\partial r}{\partial \phi} = -\frac{g''(\phi)\mathcal{H}2c_w}{\ell G_c} - \frac{w''(\phi)}{2\ell^2}, \tag{31}$$

as required for the computation of the Jacobian matrix.

3.2. Abaqus Particularities

The analogy between heat transfer and phase field fracture lays the grounds for a straightforward implementation of variational phase field fracture models in Abaqus. Only a user material (UMAT) subroutine is needed, as it is possible to define within the UMAT a volumetric heat generation source (30) and its variation with respect to the temperature (31). It must be noted that a recent version of Abaqus should be used, as the UMAT volumetric heat generation option does not function properly for versions older than 2020. The alternative for versions 2019 or older is to combine the UMAT with a heat flux (HETVAL) subroutine [38].

Abaqus' in-built displacement-temperature elements can be used, significantly facilitating model development. The same process as for a standard Abaqus model can be followed, with a few exceptions. The user should employ an analysis step of the type coupled temperature-displacement, with a steady-state response. Also, one should define as material properties the thermal conductivity k, the density ρ and the specific heat c_p, all of them with a value of unity. To avoid editing the UMAT subroutine, the mechanical and fracture properties are provided as mechanical constants in the user material definition. Also, one should define a zero-temperature initial condition $T(t = 0) = 0 \,\forall\, \boldsymbol{x}$. No other pre-processing or post-processing steps are needed, everything can be done within the Abaqus/CAE graphical user interface, and the phase field solution can be visualized by plotting the nodal solution temperature (NT11). Inside of the UMAT, the material Jacobian $\boldsymbol{C}_0$ and the Cauchy stress $\boldsymbol{\sigma}_0$ are computed from the strain tensor. The current (undamaged) stress-strain state is used to determine the driving force for fracture, $\mathcal{H}$. Both $\boldsymbol{C}_0$ and $\boldsymbol{\sigma}_0$ are degraded using the current value of the phase field ϕ (temperature), which is passed to the subroutine by Abaqus, such that $\boldsymbol{C} = g(\phi)\boldsymbol{C}_0$ and $\boldsymbol{\sigma} = g(\phi)\boldsymbol{\sigma}_0$. Finally, $\mathcal{H}$ and ϕ are used to compute r (30) and $\partial r/\partial \phi$ (31), defined as the volumetric heat generation and its derivative with respect to the temperature. In its simplest form, the code requires only 33 lines.

The implementation also accommodates both *monolithic* and *staggered* schemes, enabling convergence even in computationally demanding problems. We choose not to define the non-diagonal, coupling terms of the displacement-phase field stiffness matrix; i.e., $\boldsymbol{K}_{\boldsymbol{u}\phi} = \boldsymbol{K}_{\phi\boldsymbol{u}} = \boldsymbol{0}$. This makes the stiffness matrix symmetric. By default, Abaqus assumes a non-symmetric system for coupled displacement-temperature analyses but one can configure the solver to deal with a symmetric system by using the separated solution technique. The current values of the phase field (temperature) and displacement solutions are provided to the subroutine, so they can used to update the relevant variables ($\boldsymbol{C}_0$, $\boldsymbol{\sigma}$, r and $\partial r/\partial \phi$), such that the deformation and fracture problems are solved in a simultaneous (monolithic) manner. Conversely, one can use solution dependent state variables (SDVs) to store and use the history field of the previous increment $\mathcal{H}_t$, effectively freezing its value during the iterative procedure taking place for the current load increment. This is known as a single-pass staggered solution scheme. Although single-pass staggered schemes are very robust, unconditional stability no longer holds and one should conduct a sensitivity analysis to ensure that the load increments employed are sufficiently small. Robustness and unconditional stability can be achieved by using quasi-Newton methods [47,48], but such option is not currently available in Abaqus for coupled temperature-displacement analyses. Independently of the solution scheme, it is known that phase field fracture analyses can achieve convergence after many iterations [48,49]. Thus, the solution controls are modified to enable this (see the example input file provided in www.empaneda.com/codes).

4. Results

We address several paradigmatic boundary value problems to showcase the various features of the implementation, as well as its robustness and potential. First, we use the `PF-CZM` model to simulate fracture in a three-point bending experiment and compare the results with those obtained by Wells and Sluys [50] using an enriched cohesive zone model. Secondly, we model mixed-mode fracture in a concrete beam to compare the crack trajectories predicted by the `AT2` model to those observed experimentally [51]. Thirdly, cracking in a mortar plate with an eccentric hole is simulated to benchmark our predictions with the numerical and experimental results of Ambati et al. [44]. Finally, the `AT1` model is used in a 3D analysis of crack nucleation and growth resulting from the interaction between two gears.

4.1. Three-Point Bending Test

First, we follow the work by Wells and Sluys [50] and model the failure of a beam subjected to three-point bending. In their analysis, Wells and Sluys combined the concepts of cohesive zone modelling and partition of unity, using an exponential traction-separation law [50]. To establish a direct comparison, we choose to adopt the so-called phase field-cohesive zone model (`PF-CZM`) [41,42] using the exponential degradation function.

The geometry, dimensions and boundary conditions are shown in Figure 1a. A vertical displacement of 1.5 mm is applied at the top of the beam, at a horizontal distance of 5 mm to each of the supports. No initial crack is defined in the beam. Following Ref. [50], the mechanical behaviour of the beam is characterized by a Young's modulus of $E = 100$ MPa and a Poisson's ratio of $\nu = 0$, while the fracture behaviour is characterized by a tensile strength of $f_t = 1$ MPa and a toughness of $G_c = 0.1$ N/mm. Recall that in the `PF-CZM` model the material strength is explicitly incorporated into the constitutive response and, as a consequence, results become largely insensitive to the choice of phase field length scale, which is here assumed to be $\ell = 0.1$ mm. The model is discretised using 4-node coupled temperature-displacement plane strain elements (CPE4T in Abaqus notation). As shown in Figure 1b, the mesh is refined in the center of the beam, where the crack is expected to nucleate and grow. The characteristic element is at least five times smaller than the phase field length scale and the total number of elements equals 5820. Results are computed using the monolithic scheme.

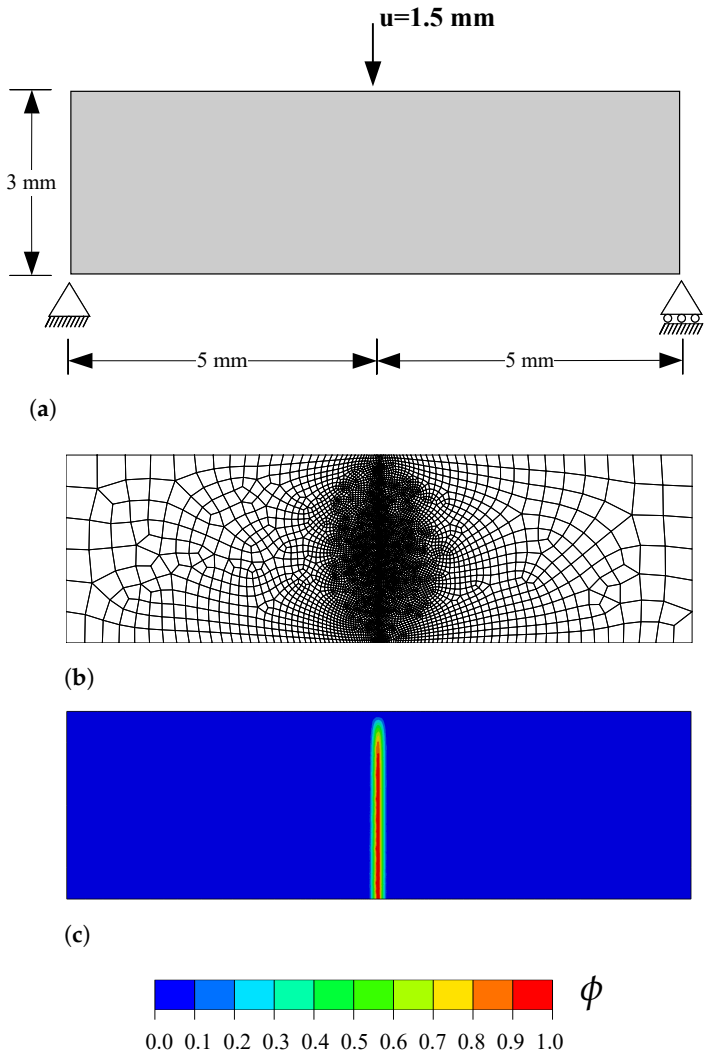

Figure 1. Three-point bending test: (**a**) geometry, dimensions and boundary conditions, (**b**) finite element mesh, and (**c**) phase field contour at the end of the analysis.

In agreement with expectations and with the results by Wells and Sluys [50], a crack nucleates at the bottom of the beam, in the center of the beam axis. The crack then propagates in a straight manner until reaching the top, as shown in Figure 1c. The resulting force versus displacement response reveals a quantitative agreement with the predictions by Wells and Sluys [50]—see Figure 2.

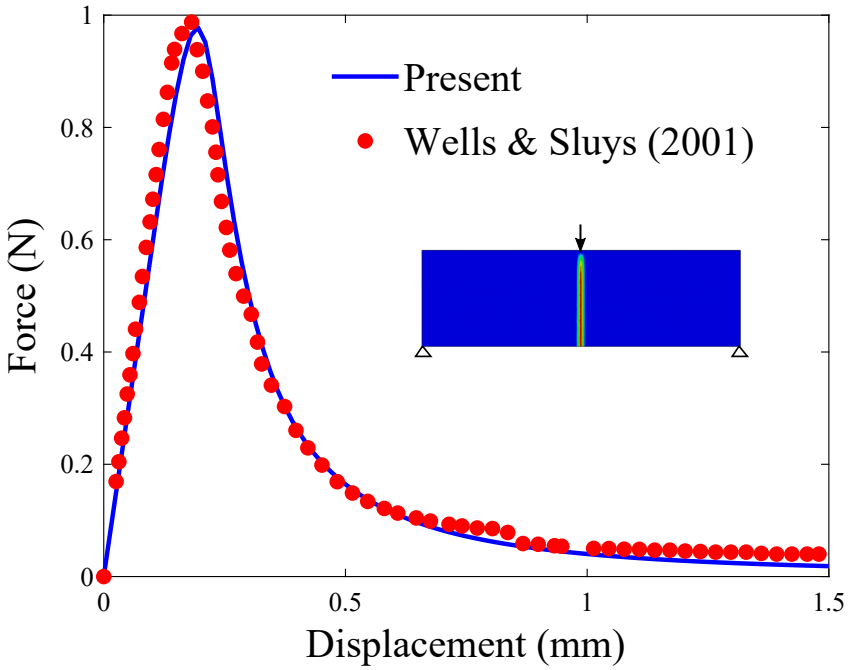

Figure 2. Three-point bending test: force versus displacement response. The results obtained with the present phase field fracture framework are compared with the results computed by Wells and Sluys [50] using an enriched cohesive zone model.

4.2. Mixed-Mode Fracture of a Single-Edge Notched Concrete Beam

We proceed to model the failure of a concrete beam containing a notch. The aim is to compare the predictions obtained with the `AT2` model with the experimental observations by Schalangen [51]. Schalangen subjected a concrete beam to the loading configuration shown in Figure 3. The beam is supported at four locations, and each support is connected to a girder beam through a rod. The cross-sections of the outer rods are smaller than those of the inner rods, to ensure an equal elongation. The load is applied to the center of the girder beams and then transferred through the rods to the concrete beam. The resulting fracture is stable and mixed-mode.

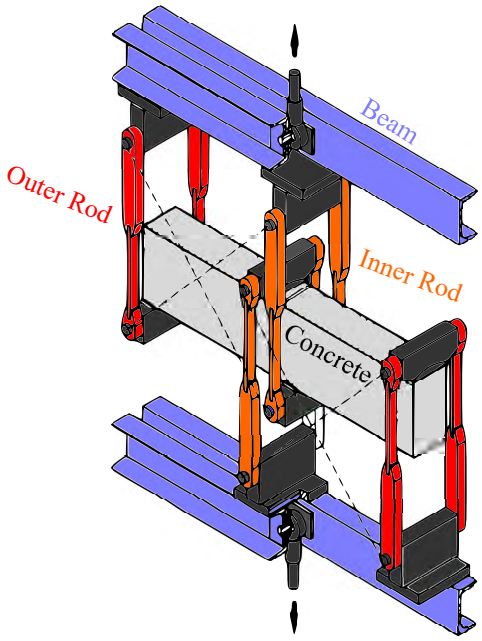

Figure 3. Mixed-mode fracture of a concrete beam: experimental testing configuration, following Ref. [51].

The geometry and boundary conditions of our finite element model aim at mimicking the experimental configuration, see Figure 4a. Two rigid beams are defined, tied to the reference points RP1 and RP2, where the boundary conditions are applied. Both girder beams can rotate around their reference points. The steel rods and supports are modelled and assigned a Young's modulus $E = 210$ GPa and a Poisson's ratio equal to $\nu = 0.3$. The cross-section of the inner rods equals 1000 mm^2 while the cross-section of the outer rods is taken to be ten times smaller, in agreement with the experimental configuration. As shown in Figure 4a, both horizontal and vertical displacements are constrained at the reference point RP1, while RP2 has its horizontal displacement constrained but is subjected to a vertical displacement of 0.5 mm.

Fracture is simulated using the `AT2` model. To prevent failure of elements under compression, the strain energy density is divided into tensile and compressive parts employing the strain spectral decomposition proposed by Miehe et al. [29], using the anisotropic formulation (24). The material properties of the concrete beam are taken to be: Young's modulus $E = 35$ GPa, Poisson's ratio $\nu = 0.2$, and toughness $G_c = 0.1$ N/mm. The phase field length scale is assumed to be equal to $\ell = 2$ mm and, consequently, the characteristic size of the elements along the potential crack propagation region equals 0.5 mm (see Figure 4b). The rods are modelled using truss elements, while the concrete beam is discretised with a total of 28,265 linear quadrilateral coupled temperature-displacement plane strain elements. The results obtained are presented in Figure 5. Both experimental (Figure 5a) and numerical (Figure 5b) results are shown. A very good agreement can be observed, with the crack initiating in both cases at the right corner of the notch and deflecting, following a very similar trajectory, towards the right side of the bottom support.

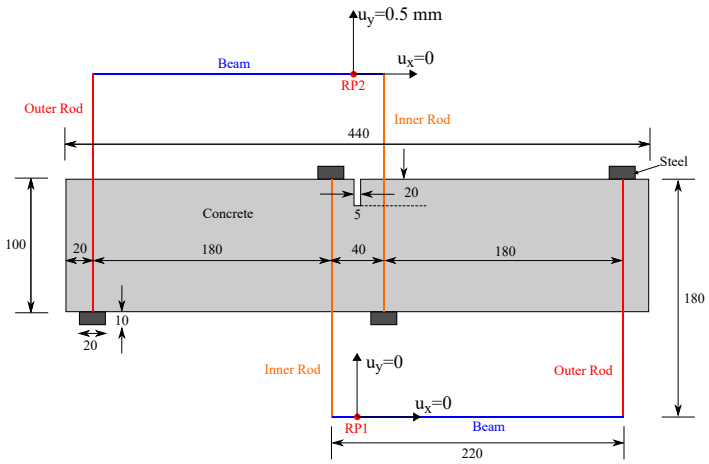

(**a**)

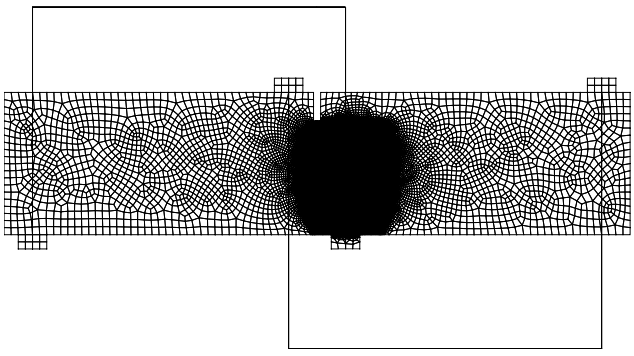

(**b**)

Figure 4. Mixed-mode fracture of a concrete beam: (**a**) geometry, dimensions (in mm) and boundary conditions, and (**b**) finite element mesh.

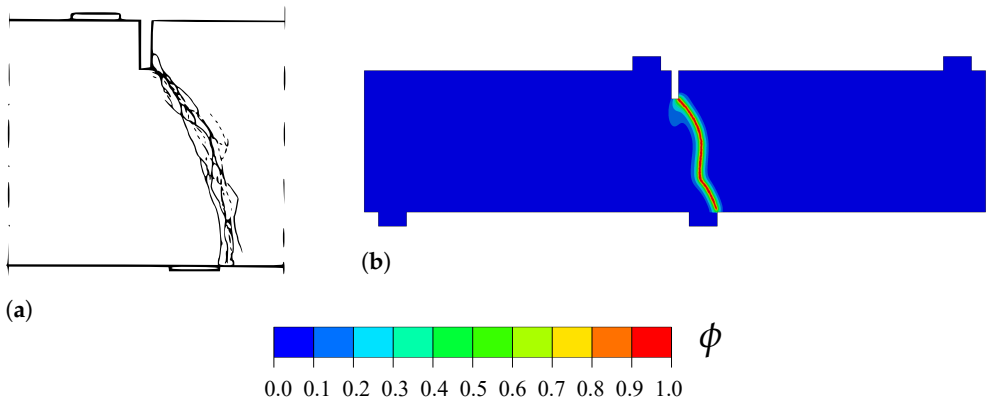

Figure 5. Mixed-mode fracture of a concrete beam: (**a**) Experimental crack patterns [51], and (**b**) predicted crack trajectory, as given by the phase field contour.

4.3. Notched Plate with an Eccentric Hole

In this case study, we demonstrate the capabilities of the framework in capturing the interaction of cracks with other defects, and in predicting crack nucleation from arbitrary sites. This is achieved by using the monolithic scheme and without observing convergence issues. Specifically, we chose to model the failure of a mortar plate, which has been experimentally and numerically investigated by Ambati et al. [44]. As shown in Figure 6a, the plate contains a 10 mm notch and an eccentric hole of 10 mm radius. Mimicking the experimental setup, the plate contains two loading pin holes; the bottom one is fixed in both vertical and horizontal directions, while a vertical displacement of 2 mm is applied to the top one. The material properties are $E = 5982$ MPa, $\nu = 0.22$, $\ell = 0.25$ mm and $G_c = 2.28$ N/mm. The `AT2` phase field model is considered, with no split applied to the strain energy density. We discretise the plate with 56,252 linear plane stress coupled displacement-thermal elements (CPS4T, in Abaqus notation). The characteristic element length in the regions surrounding the notch and the hole is five times smaller than the phase field length scale.

The results obtained, in terms of the crack trajectory, are shown in Figure 6. A very good agreement with the experimental observations is attained (Figure 6b). As shown in Figure 6c, the crack starts from the notch tip and deflects towards the hole. The location of the point of interaction between the hole and the crack originating from the notch appears to be the same for experiments and simulations. Upon increasing the applied load, a new crack eventually nucleates from the right side of the hole, and propagates until reaching the end of the plate. The resulting force versus displacement response is shown in Figure 7, where various images of the crack path have been superimposed to facilitate interpretation. The curve exhibits a linear behaviour until crack nucleation occurs ($u \approx 0.28$ mm), when a sudden drop in the load carrying capacity is observed. The interaction between the crack and the hole induces mixed-mode conditions and crack deflection, which is reflected in the force versus displacement curve. Once the crack has reached the hole, the applied displacement can be further increased without a drop in the load. This is observed until the nucleation of the second crack, which leads to the complete failure of the plate.

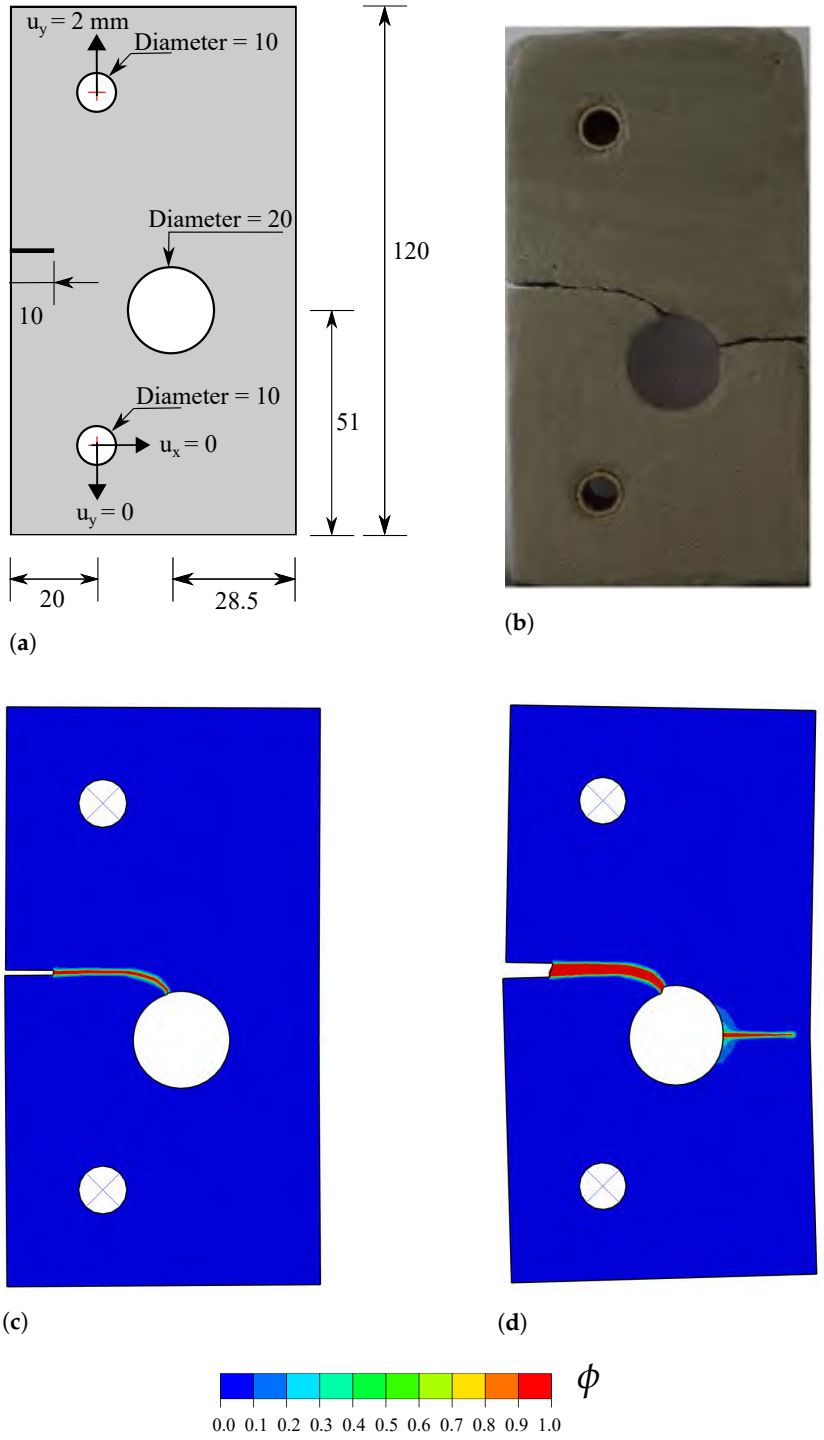

Figure 6. Notched plate with an eccentric hole: (**a**) geometry, dimensions (in mm) and boundary conditions, (**b**) experimental observation [44], and predicted phase field ϕ contours at (**c**) $u = 0.4$ mm and (**d**) $u = 2$ mm.

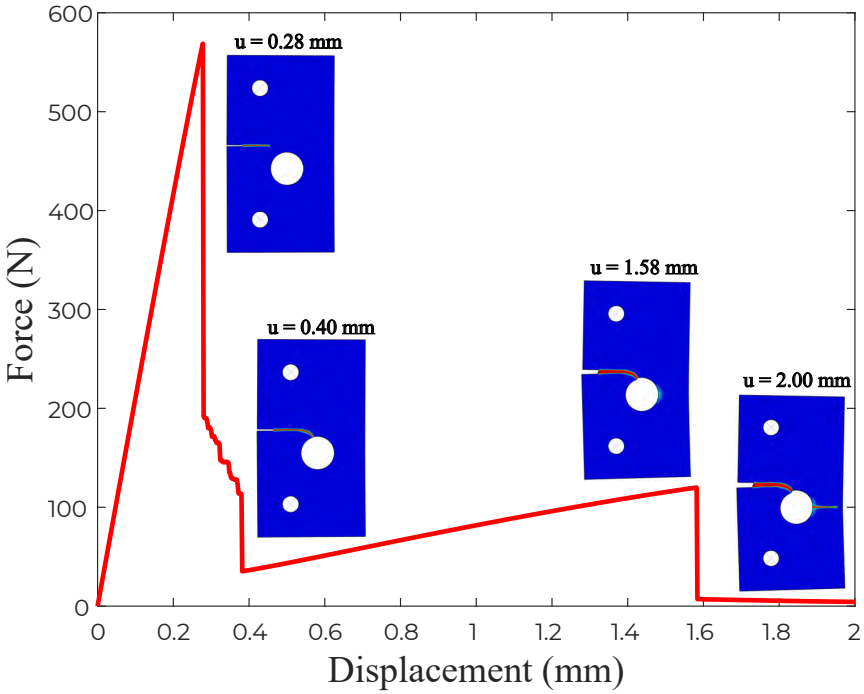

Figure 7. Notched plate with an eccentric hole: force versus displacement curve, with several snapshots of several cracking events superimposed.

4.4. 3D Analysis of Cracking Due to the Contact Interaction between Two Gears

Finally, we proceed to showcase the abilities of the model in simulating complex 3D boundary value problems, involving advanced features such as contact. It should be emphasized that the same subroutine is used for both 2D and 3D analyses as the implementation is conducted at the integration point level. We chose to simulate the nucleation and growth of cracks in the teeth of two interacting gears, a problem of important technological relevance. The geometries of the two gears are shown in Figure 8, with dimensions given in mm. The circular pitch equals 8 mm, the pressure angle is 20° and both the clearance and the backlash equal 0.05 mm. Both gears have a thickness of 3 mm. The boundary conditions are also depicted in Figure 8. The inner hole of each gear is tied to the gear center point. The center of the small, right gear is subjected to a rotation of 1 radian, while a linear rotational spring is considered at the center of the large, left gear. The stiffness of the rotational spring is 7×10^6 N·mm/rad.

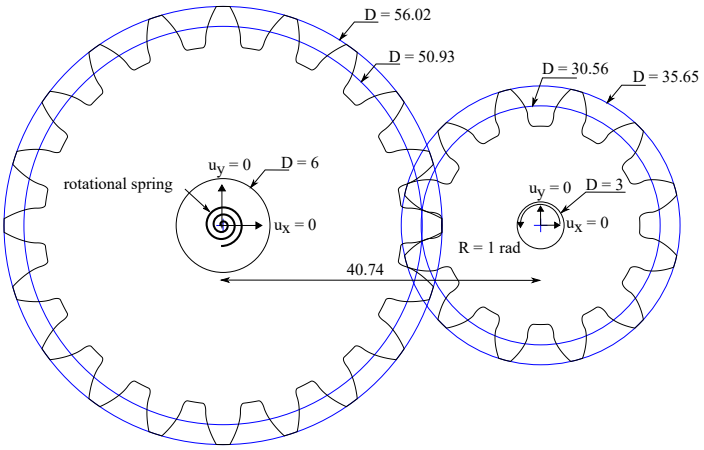

Figure 8. Cracking in interacting gears: geometry, dimensions (in mm) and boundary conditions.

The modelling requires a non-linear geometrical analysis and the use of a contact algorithm to simulate the interaction between the gear teeth. Frictionless contact is assumed for the tangential contact behaviour, which is enforced by making the Lagrangian multiplier equal to zero. The normal contact behaviour is considered to be a hard contact with a surface-to-surface interaction. The penetration of the slave surface into the master surface is minimised under hard contact conditions. The normal contact constraint is enforced through a Lagrangian multiplier. The material properties read $E = 210$ GPa, $\nu = 0.3$, $\ell = 0.25$ mm, and $G_c = 2.7$ N/mm. Fracture is predicted using the `AT1` model and no split is used for the strain energy density. The model is discretised with more than 120,000 three-dimensional coupled temperature-displacement brick elements. The results obtained are shown in Figure 9, in terms of phase field ϕ contours. Cracking initiates from the root of one of the teeth from the smaller gear and propagates towards the opposite root until the rupture of the gear teeth.

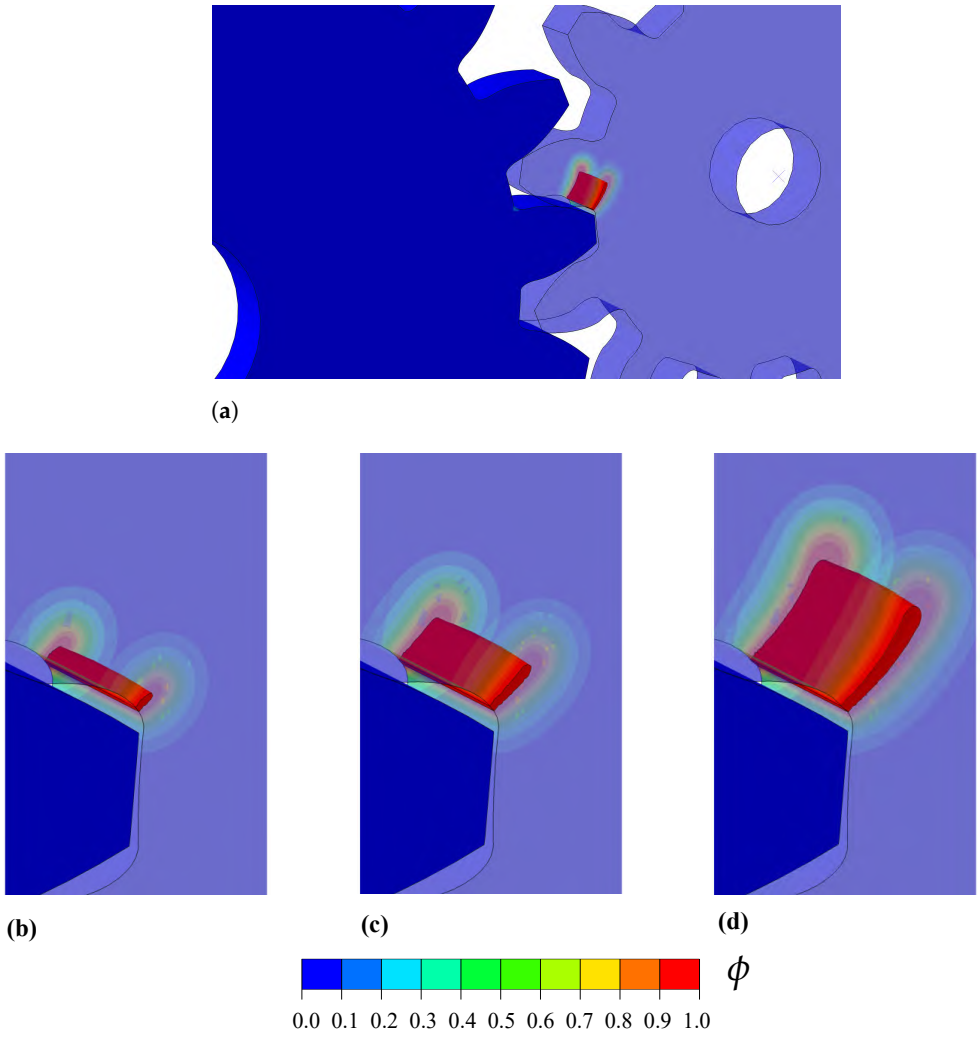

Figure 9. Cracking in interacting gears: phase field contours, (**a**) overall view at an advanced stage of cracking, and detail at (**b**) $0.028 + 2 \times 10^{-7}$ rad, (**c**) $0.028 + 5 \times 10^{-7}$ rad and (**d**) $0.028 + 9 \times 10^{-7}$ rad.

5. Conclusions

We have presented a unified Abaqus implementation of the phase field fracture method. Unlike previous works, our implementation requires only one user subroutine, of the user material type (UMAT). This enables avoiding the use of user elements, with the associated complications in pre- and post-processing, as well as exploiting most Abaqus' in-built features. The implementation is compact, requiring only 33 lines of code in its simpler form, and can be used indistinctly for 2D and 3D problems. It is

also robust, as both staggered and monolithic solution schemes have been incorporated. Moreover, the implementation can accommodate any constitutive choice of phase field model. We present a unified theoretical framework that resembles the code, and particularize it to three of the most widely used phase field models: `AT1`, `AT2` and `PF-CZM`. In addition, several strain energy splits are considered, in the framework of both hybrid and anisotropic formulations.

We have demonstrated the robustness and capabilities of the framework presented by addressing several boundary value problems of particular interest. First, we showed that the `PF-CZM` version leads to an excellent agreement with the enriched cohesive zone model analysis by Wells and Sluys [50] of crack nucleation and growth in a beam subjected to three-point bending. Secondly, we validated the crack trajectories predicted by the `AT2` model with the experimental observations by Schalangen [51] on a concrete beam exhibiting mixed-mode fracture. Thirdly, we simulated the failure of a mortar plate with an eccentric hole to showcase the capabilities of the framework in capturing the interaction between cracks and other defects, as well as the nucleation of secondary cracks. The simulations agree qualitatively and quantitatively with the results obtained by Ambati et al. [44]. Finally, we used the `AT1` version to model cracking due to the interaction between gears to showcase the capabilities of the model in dealing with 3D problems incorporating complex computational features, such as contact and geometric non-linearity. The codes developed have been made freely available, with examples and documentation at www.empaneda.com/codes.

Author Contributions: Conceptualization, E.M.-P., Y.N., C.B.; methodology, Y.N.; software, E.M.-P., Y.N.; validation, E.M.-P., Y.N.; data curation, Y.N.; writing—original draft preparation, E.M.-P.; writing—review and editing, E.M.-P., Y.N., C.B.; project administration, E.M.-P., C.B.; funding acquisition, E.M.-P., C.B. All authors have read and agreed to the published version of the manuscript.

Funding: The authors would like to acknowledge financial support from the Ministry of Science, Innovation and Universities of Spain through grant PGC2018-099695-B-I00. E. Martínez-Pañeda additionally acknowledges financial support from the Royal Commission for the 1851 Exhibition (RF496/2018).

Data Availability Statement: The codes used have been made freely available at www.empaneda.com/codes.

Conflicts of Interest: The authors declare no conflict of interest.

Appendix A. Weak Formulation and Finite Element Implementation

The heat transfer analogy enables implementing the phase field fracture method in Abaqus using only an integration point level user subroutine. Thus, the definition of the element stiffness matrix $\boldsymbol{K}^e$ and the element residual vector $\boldsymbol{R}^e$ are carried out by Abaqus internally. However, both are provided here for the sake of completeness. Consider the principle of virtual work presented in Section 2. Decoupling the deformation and fracture problems, the weak form reads,

$$\int_\Omega \Big\{ \big[g(\phi) + \kappa \big] \boldsymbol{\sigma}_0 : \delta\boldsymbol{\varepsilon} \Big\} \mathrm{d}V = 0 \,. \tag{A1}$$

$$\int_\Omega \left\{ g'(\phi)\delta\phi\, \mathcal{H} + \frac{1}{2c_w} G_c \left[\frac{1}{2\ell} w'(\phi)\delta\phi - \ell \nabla\phi \nabla\delta\phi \right] \right\} \mathrm{d}V = 0 \,. \tag{A2}$$

Now let us proceed with the finite element discretisation. Adopting Voig notation, the nodal variables for the displacement field $\hat{\mathbf{u}}$, and the phase field $\hat{\phi}$ are interpolated as:

$$\mathbf{u} = \sum_{i=1}^{m} \boldsymbol{N}_i \hat{\mathbf{u}}_i, \qquad \phi = \sum_{i=1}^{m} N_i \hat{\phi}_i \,, \tag{A3}$$

where N_i is the shape function associated with node i and $\boldsymbol{N}_i$ is the shape function matrix, a diagonal matrix with N_i in the diagonal terms. Also, m is the total number of nodes per

element such that $\hat{\mathbf{u}}_i = \{u_x, u_y, u_z\}^T$ and $\hat{\phi}_i$ respectively denote the displacement and phase field at node i. Consequently, the associated gradient quantities can be discretised using the corresponding **B**-matrices, containing the derivative of the shape functions, such that:

$$\boldsymbol{\varepsilon} = \sum_{i=1}^{m} \boldsymbol{B}_i^{\boldsymbol{u}} \hat{\mathbf{u}}_i, \qquad \nabla\phi = \sum_{i=1}^{m} \mathbf{B}_i \hat{\phi}_i \,. \tag{A4}$$

Considering the discretisation (A3)–(A4), we derive the residuals for each primal kinematic variable as:

$$\mathbf{R}_i^{\mathbf{u}} = \int_\Omega \left\{ [g(\phi) + \kappa] (\boldsymbol{B}_i^{\mathbf{u}})^T \boldsymbol{\sigma}_0 \right\} \mathrm{d}V \,, \tag{A5}$$

$$R_i^{\phi} = \int_\Omega \left\{ g'(\phi) N_i \mathcal{H} + \frac{G_c}{2 c_w \ell} \left[\frac{w'(\phi)}{2} N_i + \ell^2 \left(\mathbf{B}_i\right)^T \nabla\phi \right] \right\} dV \,. \tag{A6}$$

Finally, the consistent tangent stiffness matrices $\boldsymbol{K}$ are obtained by differentiating the residuals with respect to the incremental nodal variables as follows:

$$\boldsymbol{K}_{ij}^{\mathbf{u}} = \frac{\partial \boldsymbol{R}_i^{\boldsymbol{u}}}{\partial \boldsymbol{u}_j} = \int_\Omega \left\{ [g(\phi) + \kappa] (\boldsymbol{B}_i^{\boldsymbol{u}})^T \boldsymbol{C}_0 \, \boldsymbol{B}_j^{\boldsymbol{u}} \right\} \mathrm{d}V \,, \tag{A7}$$

$$\boldsymbol{K}_{ij}^{\phi} = \frac{\partial R_i^{\phi}}{\partial \phi_j} = \int_\Omega \left\{ \left(g''(\phi) \mathcal{H} + \frac{G_c}{4 c_w \ell} w''(\phi) \right) N_i N_j + \frac{G_c \ell}{2 c_w} \mathbf{B}_i^T \mathbf{B}_j \right\} \mathrm{d}V \,, \tag{A8}$$

References

1. Wu, J.Y.; Nguyen, V.P.; Nguyen, C.T.; Sutula, D.; Sinaie, S.; Bordas, S. Phase-field modelling of fracture. *Adv. Appl. Mech.* **2020**, *53*, 1–183.
2. Kristensen, P.K.; Niordson, C.F.; Martínez-Pañeda, E. An assessment of phase field fracture: Crack initiation and growth. *Philos. Trans. R. Soc. A-Math. Phys. Eng. Sci.* **2021**, in press.
3. Simoes, M.; Martínez-Pañeda, E. Phase field modelling of fracture and fatigue in Shape Memory Alloys. *Comput. Methods Appl. Mech. Eng.* **2021**, *373*, 113504. [CrossRef]
4. Freddi, F.; Mingazzi, L. Phase field simulation of laminated glass beam. *Materials* **2020**, *13*, 3218. [CrossRef]
5. Schmidt, J.; Zemanová, A.; Zeman, J.; Šejnoha, M. Phase-field fracture modelling of thin monolithic and laminated glass plates under quasi-static bending. *Materials* **2020**, *13*, 5153. [CrossRef]
6. Martínez-Pañeda, E.; Golahmar, A.; Niordson, C.F. A phase field formulation for hydrogen assisted cracking. *Comput. Methods Appl. Mech. Eng.* **2018**, *342*, 742–761. [CrossRef]
7. Kristensen, P.K.; Niordson, C.F.; Martínez-Pañeda, E. A phase field model for elastic-gradient-plastic solids undergoing hydrogen embrittlement. *J. Mech. Phys. Solids* **2020**, *143*, 104093. [CrossRef]
8. Borden, M.J.; Verhoosel, C.V.; Scott, M.A.; Hughes, T.J.R.; Landis, C.M. A phase-field description of dynamic brittle fracture. *Comput. Methods Appl. Mech. Eng.* **2012**, *217–220*, 77–95. [CrossRef]
9. McAuliffe, C.; Waisman, H. A coupled phase field shear band model for ductile-brittle transition in notched plate impacts. *Comput. Methods Appl. Mech. Eng.* **2016**, *305*, 173–195. [CrossRef]
10. Alessi, R.; Freddi, F. Phase-field modelling of failure in hybrid laminates. *Compos. Struct.* **2017**, *181*, 9–25. [CrossRef]
11. Quintanas-Corominas, A.; Reinoso, J.; Casoni, E.; Turon, A.; Mayugo, J.A. A phase field approach to simulate intralaminar and translaminar fracture in long fiber composite materials. *Compos. Struct.* **2019**, *220*, 899–911. [CrossRef]
12. Alessi, R.; Freddi, F. Failure and complex crack patterns in hybrid laminates: A phase-field approach. *Compos. Part B Eng.* **2019**, *179*, 107256. [CrossRef]
13. Tan, W.; Martínez-Pañeda, E. Phase field predictions of microscopic fracture and R-curve behaviour of fibre-reinforced composites. *Compos. Sci. Technol.* **2021**, *202*, 108539. [CrossRef]
14. Hirshikesh; Natarajan, S.; Annabattula, R.K.; Martínez-Pañeda, E. Phase field modelling of crack propagation in functionally graded materials. *Compos. Part B Eng.* **2019**, *169*, 239–248. [CrossRef]
15. Kumar, P.K.A.V.; Dean, A.; Reinoso, J.; Lenarda, P.; Paggi, M. Phase field modeling of fracture in Functionally Graded Materials: G-convergence and mechanical insight on the effect of grading. *Thin Walled Struct.* **2021**, *159*, 107234. [CrossRef]
16. Hirshikesh; Martínez-Pañeda, E.; Natarajan, S. Adaptive phase field modelling of crack propagation in orthotropic functionally graded materials. *Def. Technol.* **2021**, *17*, 185–195. [CrossRef]
17. Lo, Y.S.; Borden, M.J.; Ravi-Chandar, K.; Landis, C.M. A phase-field model for fatigue crack growth. *J. Mech. Phys. Solids* **2019**, *132*, 103684. [CrossRef]

18. Carrara, P.; Ambati, M.; Alessi, R.; De Lorenzis, L. A framework to model the fatigue behavior of brittle materials based on a variational phase-field approach. *Comput. Methods Appl. Mech. Eng.* **2020**, *361*, 112731. [CrossRef]
19. Freddi, F.; Royer-Carfagni, G. Variational fracture mechanics to model compressive splitting of masonry-like materials. *Ann. Solid Struct. Mech.* **2011**, *2*, 57–67. [CrossRef]
20. Provatas, N.; Elder, K. *Phase-Field Methods in Materials Science and Engineering*; John Wiley & Sons: Weinheim, Germany, 2011.
21. Cui, C.; Ma, R.; Martínez-Pañeda, E. A phase field formulation for dissolution-driven stress corrosion cracking. *J. Mech. Phys. Solids* **2021**, *147*, 104254. [CrossRef]
22. Griffith, A.A. The Phenomena of Rupture and Flow in Solids. *Philos. Trans. A* **1920**, *221*, 163–198.
23. Francfort, G.A.; Marigo, J.J. Revisiting brittle fracture as an energy minimization problem. *J. Mech. Phys. Solids* **1998**, *46*, 1319–1342. [CrossRef]
24. Bourdin, B.; Francfort, G.A.; Marigo, J.J. Numerical experiments in revisited brittle fracture. *J. Mech. Phys. Solids* **2000**, *48*, 797–826. [CrossRef]
25. Borden, M.J.; Hughes, T.J.R.; Landis, C.M.; Anvari, A.; Lee, I.J. A phase-field formulation for fracture in ductile materials: Finite deformation balance law derivation, plastic degradation, and stress triaxiality effects. *Comput. Methods Appl. Mech. Eng.* **2016**, *312*, 130–166. [CrossRef]
26. Miehe, C.; Aldakheel, F.; Raina, A. Phase field modeling of ductile fracture at finite strains: A variational gradient-extended plasticity-damage theory. *Int. J. Plast.* **2016**, *84*, 1–32. [CrossRef]
27. Kristensen, P.K.; Niordson, C.F.; Martínez-Pañeda, E. Applications of phase field fracture in modelling hydrogen assisted failures. *Theor. Appl. Fract. Mech.* **2020**, *110*, 102837. [CrossRef]
28. Wu, J.Y.; Huang, Y.; Nguyen, V.P. Three-dimensional phase-field modeling of mode I + II/III failure in solids. *Comput. Methods Appl. Mech. Eng.* **2021**, *373*, 113537. [CrossRef]
29. Miehe, C.; Hofacker, M.; Welschinger, F. A phase field model for rate-independent crack propagation: Robust algorithmic implementation based on operator splits. *Comput. Methods Appl. Mech. Eng.* **2010**, *199*, 2765–2778. [CrossRef]
30. Zhou, S.; Rabczuk, T.; Zhuang, X. Phase field modeling of quasi-static and dynamic crack propagation: COMSOL implementation and case studies. *Adv. Eng. Softw.* **2018**, *122*, 31–49. [CrossRef]
31. Hirshikesh; Natarajan, S.; Annabattula, R.K. A FEniCS implementation of the phase field method for quasi-static brittle fracture. *Front. Struct. Civ. Eng.* **2019**, *13*, 1–17.
32. Msekh, M.A.; Sargado, J.M.; Jamshidian, M.; Areias, P.M.; Rabczuk, T. Abaqus implementation of phase-field model for brittle fracture. *Comput. Mater. Sci.* **2015**, *96*, 472–484. [CrossRef]
33. Liu, G.; Li, Q.; Msekh, M.A.; Zuo, Z. Abaqus implementation of monolithic and staggered schemes for quasi-static and dynamic fracture phase-field model. *Comput. Mater. Sci.* **2016**, *121*, 35–47. [CrossRef]
34. Molnár, G.; Gravouil, A. 2D and 3D Abaqus implementation of a robust staggered phase-field solution for modeling brittle fracture. *Finite Elem. Anal. Des.* **2017**, *130*, 27–38. [CrossRef]
35. Fang, J.; Wu, C.; Rabczuk, T.; Wu, C.; Ma, C.; Sun, G.; Li, Q. Phase field fracture in elasto-plastic solids: Abaqus implementation and case studies. *Theor. Appl. Fract. Mech.* **2019**, *103*, 102252. [CrossRef]
36. Molnár, G.; Gravouil, A.; Seghir, R.; Réthoré, J. An open-source Abaqus implementation of the phase-field method to study the effect of plasticity on the instantaneous fracture toughness in dynamic crack propagation. *Comput. Methods Appl. Mech. Eng.* **2020**, *365*, 113004. [CrossRef]
37. Wu, J.Y.; Huang, Y. Comprehensive implementations of phase-field damage models in Abaqus. *Theor. Appl. Fract. Mech.* **2020**, *106*, 102440. [CrossRef]
38. Navidtehrani, Y.; Betegón, C.; Martínez-Pañeda, E. A simple and robust Abaqus implementation of the phase field fracture method. *Appl. Eng. Sci.* **2021**, in press.
39. Ambrosio, L.; Tortorelli, V.M. Approximation of functionals depending on jumps by elliptic functionals via gamma-convergence. *Commun. Pure Appl. Math.* **1991**, *43*, 999–1036. [CrossRef]
40. Pham, K.; Amor, H.; Marigo, J.J.; Maurini, C. Gradient damage models and their use to approximate brittle fracture. *Int. J. Damage Mech.* **2011**, *20*, 618–652. [CrossRef]
41. Wu, J.Y. A unified phase-field theory for the mechanics of damage and quasi-brittle failure. *J. Mech. Phys. Solids* **2017**, *103*, 72–99. [CrossRef]
42. Wu, J.Y.; Nguyen, V.P. A length scale insensitive phase-field damage model for brittle fracture. *J. Mech. Phys. Solids* **2018**, *119*, 20–42. [CrossRef]
43. Amor, H.; Marigo, J.J.; Maurini, C. Regularized formulation of the variational brittle fracture with unilateral contact: Numerical experiments. *J. Mech. Phys. Solids* **2009**, *57*, 1209–1229. [CrossRef]
44. Ambati, M.; Gerasimov, T.; De Lorenzis, L. A review on phase-field models of brittle fracture and a new fast hybrid formulation. *Comput. Mech.* **2015**, *55*, 383–405. [CrossRef]
45. Irwin, G.R. *Onset of Fast Crack Propagation in High Strength Steel and Aluminum Alloys*; Naval Research Lab.: Washington, DC, USA, 1956; Volume 2, pp. 289–305.
46. Miehe, C.; Welshinger, F.; Hofacker, M. Thermodynamically consistent phase-field models of fracture: Variational principles and multi-field FE implementations. *Int. J. Numer. Methods Eng.* **2010**, *83*, 1273–1311. [CrossRef]

47. Wu, J.Y.; Huang, Y.; Nguyen, V.P. On the BFGS monolithic algorithm for the unified phase field damage theory. *Comput. Methods Appl. Mech. Eng.* **2020**, *360*, 112704. [CrossRef]
48. Kristensen, P.K.; Martínez-Pañeda, E. Phase field fracture modelling using quasi-Newton methods and a new adaptive step scheme. *Theor. Appl. Fract. Mech.* **2020**, *107*, 102446. [CrossRef]
49. Gerasimov, T.; De Lorenzis, L. A line search assisted monolithic approach for phase-field computing of brittle fracture. *Comput. Methods Appl. Mech. Eng.* **2016**, *312*, 276–303. [CrossRef]
50. Wells, G.N.; Sluys, L.J. A new method for modelling cohesive cracks using finite elements. *Int. J. Numer. Methods Eng.* **2001**, *50*, 2667–2682. [CrossRef]
51. Schalangen, E. Experimental and numerical analysis of fracture process in concrete. *Heron* **1993**, *38*, 1–17.

D | Paper 4

Damage Mechanics Challenge: Predictions based on the phase field fracture model

Authors:

Yousef Navidtehrani, Ravindra Duddu, Emilio Martínez-Pañeda

Journal:

Engineering Fracture Mechanics journal

Year of Publication:

2024

Impact Factor:

4.7 - Q1

Engineering Fracture Mechanics 301 (2024) 110046

Contents lists available at ScienceDirect

Engineering Fracture Mechanics

journal homepage: www.elsevier.com/locate/engfracmech

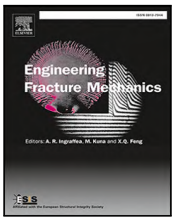

Damage Mechanics Challenge: Predictions based on the phase field fracture model

Yousef Navidtehrani [a], Ravindra Duddu [b], Emilio Martínez-Pañeda [c,d,*]

[a] Department of Construction and Manufacturing Engineering, University of Oviedo, Gijón 33203, Spain
[b] Department of Civil and Environmental Engineering and Department of Mechanical Engineering, Vanderbilt University, PMB 351831, Nashville, TN 37235-1831, USA
[c] Department of Engineering Science, University of Oxford, Oxford OX1 3PJ, UK
[d] Department of Civil and Environmental Engineering, Imperial College London, London SW7 2AZ, UK

ARTICLE INFO

Keywords:
Phase field fracture
Damage mechanics challenge
Brittle fracture
Rock fracture
Finite element analysis

ABSTRACT

In this work, we describe our contribution to the Purdue-SANDIA-LLNL *Damage Mechanics Challenge*. The phase field fracture model is adopted to blindly estimate the failure characteristics of the challenge test, an unconventional three-point bending experiment on an additively manufactured rock resembling a type of gypsum. The model is formulated in a variationally consistent fashion, incorporating a volumetric–deviatoric strain energy decomposition, and the numerical implementation adopts a monolithic unconditionally stable solution scheme. Our focus is on providing an efficient and simple yet rigorous approach capable of delivering accurate predictions based solely on physical parameters. Model inputs are Young's modulus E, Poisson's ratio ν, toughness G_c and strength σ_c (as determined by the choice of phase field length scale ℓ). We show that a single mode I three-point bending test is sufficient to calibrate the model, and that the calibrated model can then reliably predict the force versus displacement responses, crack paths and surface crack morphologies of more intricate three-point bending experiments that are inherently mixed-mode. Importantly, our peak load, crack trajectory and crack surface morphology predictions for the challenge test, submitted before the experimental data was released, show a remarkable agreement with experiments. The characteristics of the challenge, and how changes in these can impact the predictive abilities of phase field fracture models, are also discussed.

1. Introduction

This work presents our contribution to the *Damage Mechanics Challenge* organised by Purdue University, Sandia National Laboratories and the Lawrence Livermore National Laboratory. The aim of the *Damage Mechanics Challenge* is to assess and showcase the ability of computational methods to predict (as opposed to fit) the failure of rock-like materials. As detailed below, a certain degree of information was provided on the deformation and fracture characteristics of the material under consideration, a 3D-printed rock, and then participants were asked to predict – using the computational approach of their choosing – the failure behaviour (force vs displacement response, crack trajectory and morphology) in a new test configuration.

We chose to employ the phase field fracture model [1,2] to predict the fracture behaviour of the additively manufactured rock samples, due to its robustness and rigorous physical basis. The phase field fracture model has been enjoying an ever-growing popularity in recent years. Grounded on Griffith's energy balance [3], the phase field model enables predicting complex

* Corresponding author at: Department of Engineering Science, University of Oxford, Oxford OX1 3PJ, UK.
E-mail address: emilio.martinez-paneda@eng.ox.ac.uk (E. Martínez-Pañeda).

https://doi.org/10.1016/j.engfracmech.2024.110046
Received 16 December 2023; Received in revised form 17 February 2024; Accepted 26 March 2024
Available online 28 March 2024

cracking phenomena based on the thermodynamics of fracture, including arbitrary crack branching, coalescence and arbitrary crack trajectories. The approach is also known to be mesh objective and computationally robust [4,5]. Hence, not surprisingly, phase field-based fracture models have been developed to simulate material failure across a wide range of engineering applications, including dynamic fracture [6–8], hydrogen embrittlement [9,10], fatigue damage [11,12], fibre-reinforced composites [13–15], functionally graded materials [16,17], smart materials [18–20], and Li-Ion battery degradation [21,22]. Notably, phase field fracture methods have been recently applied to study crack propagation in rock-like materials [23–27] and glaciers [28,29].

In the following, we proceed to describe how we have successfully predicted the required experimental outcome of the *Damage Mechanics Challenge* using the phase field fracture model and the provided experimental calibration data. The aim was to demonstrate robust predictive capabilities with minimal model complexity. As such, a conventional phase field fracture model (so-called `AT2` model [2]) is employed, such that predictions depend only on four material properties: Young's modulus E, Poisson's ratio ν, fracture energy G_c, and strength σ_c, with the last one being indirectly defined through the choice of phase field length scale ℓ. It is worth emphasising that this contribution deals with a piece of work that was conducted as part of the standard *Damage Mechanics Challenge*; i.e., the results presented are *blind* predictions, which were submitted to the challenge organisers before the experimental data of the benchmark test was released.

2. Approach: Phase field fracture modelling

In the following, we proceed to describe the numerical approach employed and the characteristics of the boundary value problem under consideration. This study was carried out by three researchers based at the University of Oviedo, University of Oxford, and Vanderbilt University with previous collaborative experience in related endeavours.

2.1. A phase field description of fracture

2.1.1. Background

The phase field fracture model builds upon Griffith's foundational thermodynamic framework [3]. In concordance with the principles of the first law of thermodynamics, the initiation or propagation of a crack is contingent upon the proviso that the total energy of the system either diminishes or remains constant. Thus, the condition for fracture is critically determined through equilibrium considerations, whereby the overall energy remains unaltered. Consider an elastic solid including a crack, the perturbation in the total energy $\mathcal{E}$ attributable to infinitesimal growth in the crack area, denoted as $\mathrm{d}A$, can be articulated as:

$$\frac{\mathrm{d}\mathcal{E}}{\mathrm{d}A} = \frac{\mathrm{d}\Pi}{\mathrm{d}A} + \frac{\mathrm{d}W_c}{\mathrm{d}A} = \frac{\mathrm{d}\Psi\left(\boldsymbol{\varepsilon}\left(\mathbf{u}\right)\right)}{\mathrm{d}A} + \frac{\mathrm{d}W_e}{\mathrm{d}A} + \frac{\mathrm{d}W_c}{\mathrm{d}A} = 0 \tag{1}$$

where W_c denotes the energy expenditure required to generate two new surfaces, and Π is the total potential energy supplied by the internal strain energy Ψ and the external forces W_e. The last term in Eq. (1) is the so-called fracture energy or critical energy release rate, $G_c = \mathrm{d}W_c/\mathrm{d}A$; a constant, material-specific parameter characterising its resilience against fracture. The internal strain energy Ψ is a function of the strain field $\boldsymbol{\varepsilon}$, which is itself a function of the displacement field; for small strains, $\boldsymbol{\varepsilon} = \left(\nabla\mathbf{u}^T + \nabla\mathbf{u}\right)/2$. Thus, in the case of prescribed/fixed displacements, although no external work is done on the body ($W_e = 0$), a crack would grow if the energy stored in the solid equates to the energy required to create two new surfaces. As such, Griffith's hypothesis describes a localised principle of minimality governing the cumulative stored and fracture energies. Within an arbitrary domain $\Omega \subset \mathrm{IR}^n$ ($n \in [1,2,3]$) encompassing an internal discontinuity boundary Γ, this principle of minimality can be expressed through a variational representation as:

$$\mathcal{E}\left(\mathbf{u}\right) = \int_\Omega \psi\left(\boldsymbol{\varepsilon}\left(\mathbf{u}\right)\right)\mathrm{d}V + \int_\Gamma G_c\,\mathrm{d}S - \int_\Omega \mathbf{b}\cdot\mathbf{u}\,\mathrm{d}V - \int_{\partial\Omega} \mathbf{T}\cdot\mathbf{u}\,\mathrm{d}S \tag{2}$$

where the external work is characterised by the body force $\mathbf{b}$ and the external traction vector $\mathbf{T}$, and their dot product with the displacement vector $\mathbf{u}$. Thus, the trajectory of crack growth can be predicted devoid of arbitrary criteria, grounded in the principles of global minimality and the conversion of stored energy into fracture energy. Nonetheless, minimising the Griffith energy functional (2) is hindered by the intricacies associated with the tracking of the advancing fracture surface Γ. This computational challenge can be addressed by making use of a scalar phase field variable ϕ, which can be interpreted as a damage field variable, transitioning from 0 in undamaged regions to 1 within the confines of the crack. In alignment with the rationale of continuum damage mechanics, a degradation function $g(\phi) = (1-\phi)^2$ is also used, so as to modulate the material stiffness in accordance with the evolving damage. Consequently, the regularised energy functional takes the form:

$$\mathcal{E}_\ell\left(\mathbf{u},\phi\right) = \int_\Omega (1-\phi)^2\,\psi_0\left(\boldsymbol{\varepsilon}\left(\mathbf{u}\right)\right)\mathrm{d}V + \int_\Omega G_c\gamma_\ell\left(\phi\right)\mathrm{d}V - \int_\Omega \mathbf{b}\cdot\mathbf{u}\,\mathrm{d}V - \int_{\partial\Omega} \mathbf{T}\cdot\mathbf{u}\,\mathrm{d}S \tag{3}$$

where γ_ℓ is the so-called crack density function, which for the conventional `AT2` model reads [2]:

$$\gamma_\ell\left(\phi\right) = \frac{\phi^2}{2\ell} + \frac{\ell}{2}|\nabla\phi|^2. \tag{4}$$

The crack density function includes the gradient of the phase field order parameter and accordingly a length scale ℓ, which enables mesh objectivity. This phase field length scale ℓ is directly related to the material strength, as can be illustrated by plotting the solution to the homogeneous, 1D coupled deformation-phase field fracture problem, which gives a maximum stress of,

$$\sigma_c = \sqrt{\frac{27EG_c}{256\ell}} \tag{5}$$

Accordingly, for plane stress conditions, $\sigma_c \propto \sqrt{G_c E/\ell} = K_{Ic}/\sqrt{\ell}$, and the choice of ℓ will define the material strength for a given Young's modulus E and critical fracture energy G_c (or fracture toughness K_{Ic}). The ability of the phase field fracture model to go beyond Griffith's fracture and incorporate the concept of material strength is essential to predict crack nucleation [30], and as a result, the phase field fracture model can capture the transition from toughness-driven failures to strength-driven failures [31], naturally encompassing the transition flaw size concept. Thus, the structure of the phase field model ensures its alignment with conventional fracture mechanics theory and this has been shown computationally (see, e.g. Refs. [30–32]) and theoretically - e.g., Γ-convergence studies have shown that the regularised functional (3) converges to the Griffith functional (2) in both discrete and continuous systems [33,34].

One relevant aspect to consider is that the conventional phase field fracture model, akin to Griffith's work, assumes a symmetric fracture behaviour in tension and compression. To break this symmetry and hinder cracking in compressive regions, a number of authors have proposed modifications to the model that aim at decomposing the fracture driving force, the strain energy density. Accordingly, the (undamaged) strain energy density, which is typically defined as follows for elastic solids,

$$\psi_0(\boldsymbol{\varepsilon}(\mathbf{u})) = \frac{1}{2}\boldsymbol{\varepsilon}(\mathbf{u}) : \boldsymbol{C}_0 : \boldsymbol{\varepsilon}(\mathbf{u}), \tag{6}$$

with $\boldsymbol{C}_0$ denoting the undamaged stiffness tensor, can be decomposed into a tensile part, ψ_0^+, and a compressive part, ψ_0^-, such that

$$\psi_0(\boldsymbol{\varepsilon}(\mathbf{u})) = \psi_0^+(\boldsymbol{\varepsilon}(\mathbf{u})) + \psi_0^-(\boldsymbol{\varepsilon}(\mathbf{u})), \tag{7}$$

Herein, we adopt the so-called volumetric–deviatoric split [35], rendering

$$\begin{aligned} \psi_0^+(\varepsilon(\mathbf{u})) &= \frac{1}{2}K\langle \mathrm{tr}(\boldsymbol{\varepsilon}(\mathbf{u}))\rangle_+^2 + \mu\left(\varepsilon'(\mathbf{u}) : \boldsymbol{\varepsilon}'(\mathbf{u})\right) \\ \psi_0^-(\varepsilon(\mathbf{u})) &= \frac{1}{2}K\langle \mathrm{tr}(\varepsilon(\mathbf{u}))\rangle_-^2, \end{aligned} \tag{8}$$

where K denotes the bulk modulus, μ represents the shear modulus, and $\langle\rangle$ are used to denote the Macaulay brackets, defined as $\langle a\rangle_\pm = (a \pm |a|)/2$. Furthermore, $\boldsymbol{\varepsilon}'(\mathbf{u})$ is the deviatoric part of the strain tensor, defined as $\boldsymbol{\varepsilon}'(\mathbf{u}) = \boldsymbol{\varepsilon}(\mathbf{u}) - \mathrm{tr}(\boldsymbol{\varepsilon}(\mathbf{u}))\mathbf{1}/3$, where $\mathbf{1}$ denotes the second-order unit tensor.

2.1.2. Balance equations

We now proceed to formulate the relevant partial differential equations of the modelling framework in their weak and strong forms. To this end, it is convenient to define the elastic strain energy density, considering the volumetric–deviatoric split considered above,

$$\psi(\boldsymbol{\varepsilon}(\mathbf{u})) = (1-\phi)^2\,\psi_0^+(\boldsymbol{\varepsilon}(\mathbf{u})) + \psi_0^-(\boldsymbol{\varepsilon}(\mathbf{u}))\,. \tag{9}$$

Then, in a variationally consistent fashion, the Cauchy stress is defined as,

$$\boldsymbol{\sigma} = \frac{\partial\psi\,(\boldsymbol{\varepsilon}(\mathbf{u}))}{\partial\boldsymbol{\varepsilon}(\mathbf{u})} = (1-\phi)^2\,\frac{\partial\psi_0^+\,(\boldsymbol{\varepsilon}(\mathbf{u}))}{\partial\boldsymbol{\varepsilon}(\mathbf{u})} + \frac{\partial\psi_0^-\,(\boldsymbol{\varepsilon}(\mathbf{u}))}{\partial\boldsymbol{\varepsilon}(\mathbf{u})} = (1-\phi)^2\,\boldsymbol{\sigma}_0^+ + \boldsymbol{\sigma}_0^-, \tag{10}$$

where $\boldsymbol{\sigma}_0^+$ denotes the positive part of the undamaged Cauchy stress tensor, which undergoes degradation due to the evolution of damage, while $\boldsymbol{\sigma}_0^-$ represents the corresponding negative counterpart. Then, considering both the strain energy decomposition (7) and the choice of crack density function (4), the regularised functional (3) can be expressed as,

$$\begin{aligned} \mathcal{E}_\ell\,(\mathbf{u},\phi) = &\int_\Omega \left[(1-\phi)^2\,\psi_0^+\,(\boldsymbol{\varepsilon}\,(\mathbf{u})) + \psi_0^-\,(\boldsymbol{\varepsilon}\,(\mathbf{u}))\right]\,\mathrm{d}V \\ &+ \int_V G_c\left(\frac{1}{2\ell}\phi^2 + \frac{\ell}{2}|\nabla\phi|^2\right)\,\mathrm{d}V - \int_\Omega \mathbf{b}\cdot\mathbf{u}\,\mathrm{d}V - \int_{\partial\Omega}\mathbf{T}\cdot\mathbf{u}\,\mathrm{d}S \end{aligned} \tag{11}$$

Consequently, taking the stationary of the functional (11), using Gauss' divergence theorem and noting that the resulting expression must hold for any kinematically admissible variations of virtual quantities, the local balance equations of the problem are obtained as follows:

$$\begin{aligned} \nabla\cdot\left[(1-\phi)^2\,\boldsymbol{\sigma}_0^+ + \boldsymbol{\sigma}_0^-\right] + \boldsymbol{b} = 0 \quad &\text{in} \quad \Omega \\ G_c\left(\frac{\phi}{\ell} - \ell\,\Delta\phi\right) - 2(1-\phi)\psi_0^+\,(\boldsymbol{\varepsilon}\,(\mathbf{u})) = 0 \quad &\text{in} \quad \Omega \end{aligned} \tag{12}$$

Finally, one should note that crack healing is possible in the absence of supplementary constraints in the phase field evolution Eq. (12)b. To preclude this phenomenon, a history field $\mathcal{H}$ can be introduced, $\mathcal{H} = \max_{\tau\in[0,t]}\psi_0^+(\tau)$, replacing ψ_0^+ as the fracture driving force [4]. Also, a residual stiffness can be added to the degradation function to prevent ill-conditioning in fully damaged regions, such that $g(\phi) = (1-\phi)^2 + \kappa$, where κ is a small number ($\kappa = 1\times10^{-7}$).

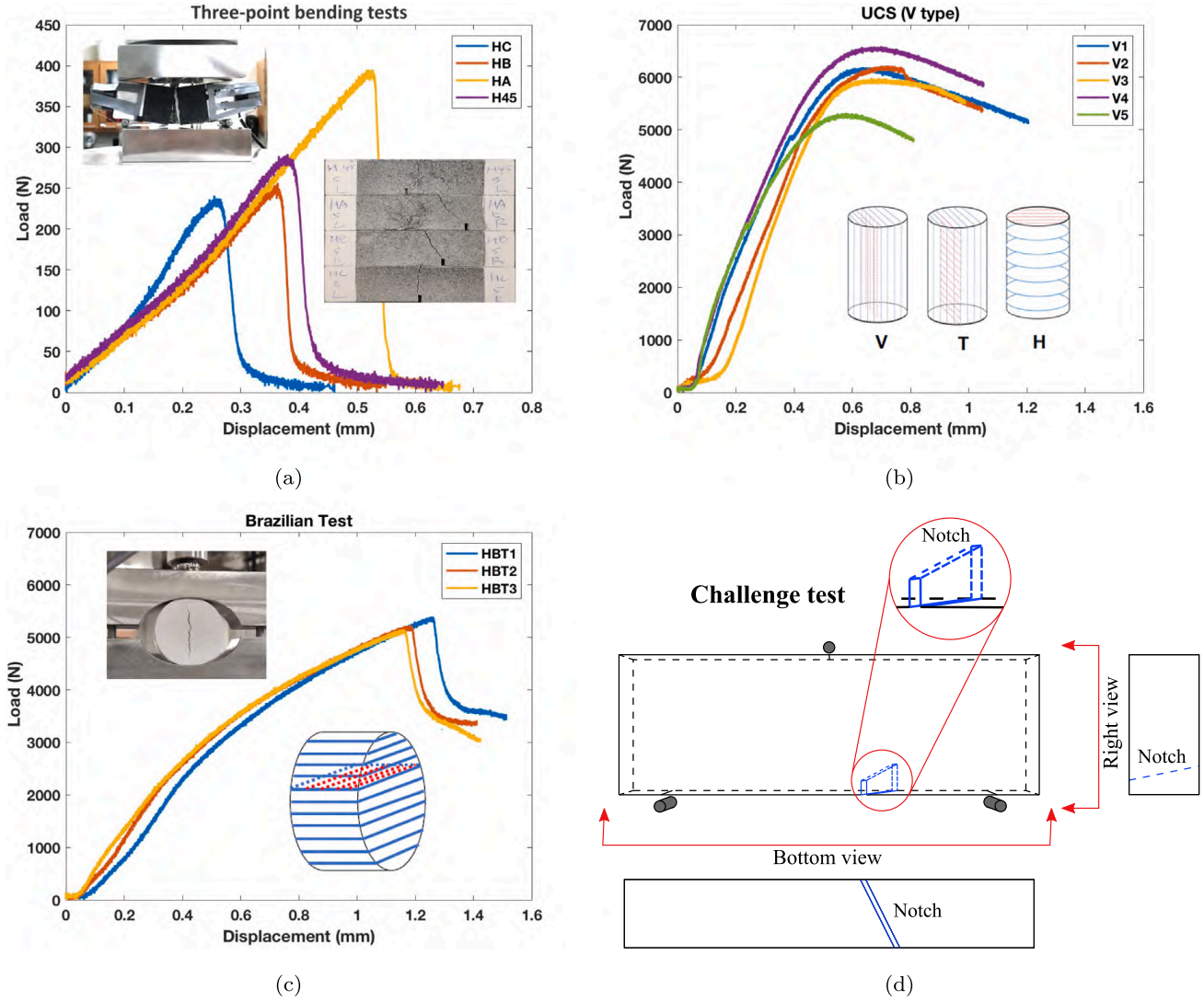

Fig. 1. Damage Mechanics Challenge data: calibration and to-be-predicted experiments. The calibration data included force versus displacement measurements for: (a) four three-point bending configurations (of equal dimensions but different notch configurations), (b) unconfined compressive tests, and (c) Brazilian disk tests. Based on this information, participants were asked to blindly estimate the cracking characteristics (peak load, crack trajectory and morphology) of an unconventional three-point bending test with an inclined, unsymmetric notch (d).

2.1.3. Numerical implementation

The coupled system of equations is solved using the finite element method. As described in Appendix A, the components of the stiffness matrix and the residuals can be obtained from Eq. (11) using the finite element discretisation. Here, the focus is on simplicity and accordingly, the model is implemented in the commercial finite element package `Abaqus` without the need for an element-level implementation. As shown in Appendix B, the phase field evolution equation, Eq. ((12)b), takes the form of Poisson's equation, such that one can exploit the analogy with the steady-state heat transfer equation and use in-built `Abaqus` capabilities. By treating the phase field variable ϕ akin to the temperature field and applying the crack driving force via an appropriate (nonlinear) heat source, one can easily implement the phase field model at the integration point level, using a user material (UMAT) subroutine. Details of the implementation are provided in Appendix B and Refs. [36,37]. A monolithic solution scheme was used to solve the coupled displacement and phase field equations, ensuring unconditional stability and thus maximising efficiency.

2.2. Numerical experiments: defining the boundary value problem

2.2.1. Challenge data, requisitions and characteristics

The phase field fracture model was used to conduct numerical experiments with the aim of benchmarking model predictions against calibration data and providing a blind estimate of the required outputs. The samples needed for the challenge experiment and the calibration data were manufactured by the hosts of the *Damage Mechanics Challenge* using additive manufacturing. The material employed was a special type of gypsum, which resulted from the bonding of calcium sulphate hemihydrate layers (bassanite powders with a deposition layer thickness of 0.1 mm) with a proprietary water-based binder (ProJet X60 VisiJet PXL). For consistency, all

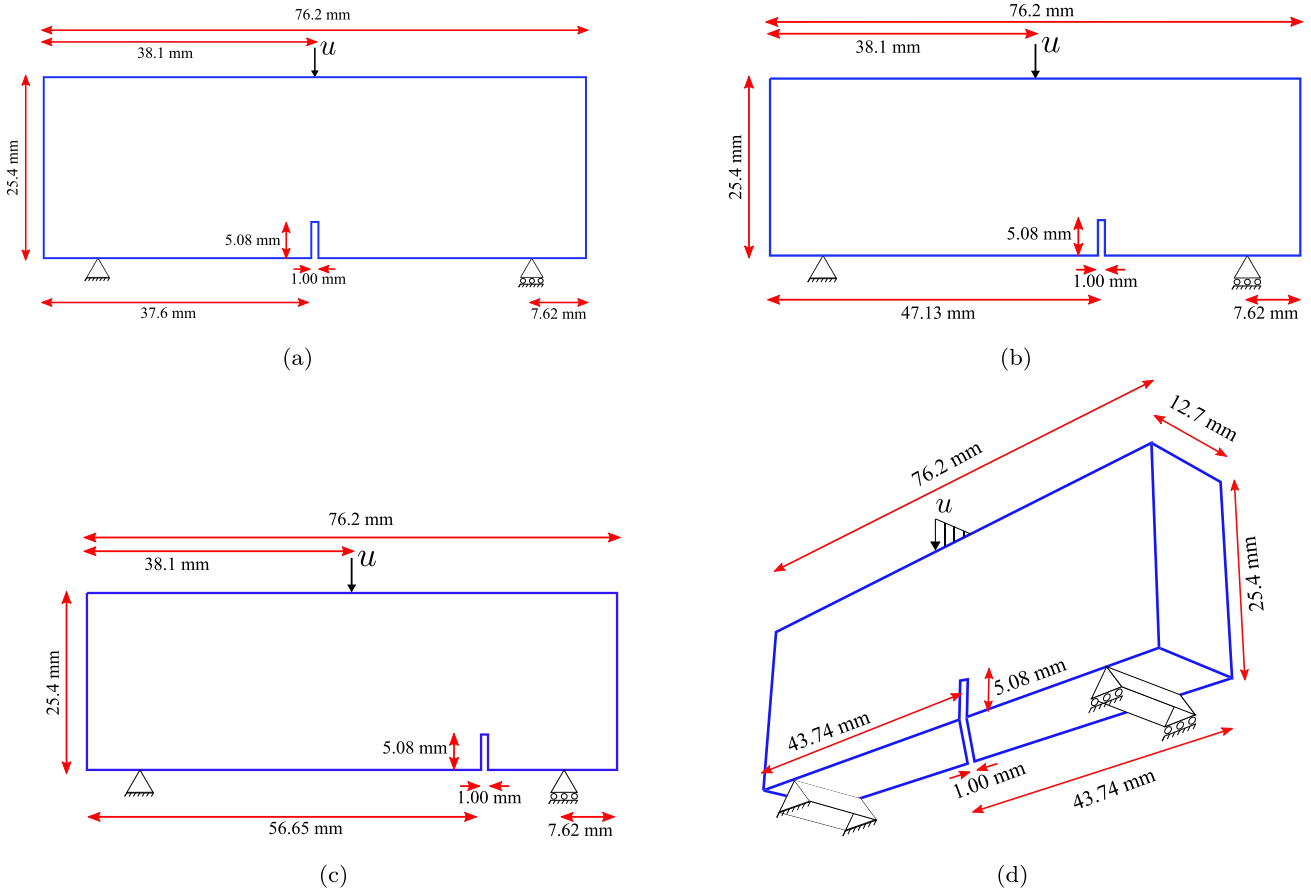

Fig. 2. Three-point bending tests used for generating calibration data: geometry, dimensions and boundary conditions. The tests included a conventional three-point bending experiment, denoted as HC (a), two tests where the notch was placed eccentric, HB (b) and HA (c), and a fourth experiment where the notch was inclined 45° along the thickness, requiring a 3D analysis, H45 (d).

samples were obtained from the same 3D printing build. As summarised in Fig. 1, the calibration data included: (i) three-point bending tests on four types of notched samples, differentiated by the location of their notch, (ii) uniaxial loading tests to measure the unconfined compressive strength (UCS), and (iii) Brazilian tests to measure the tensile strength. Based on this information, participants were provided with the geometry of the challenge test, a three-point bending test with an inclined notch — see Fig. 1d, and asked to numerically predict:

- The force versus displacement response.
- The crack trajectory to benchmark against Digital Image Correlation (DIC) images.
- The crack surface morphology to benchmark against laser profilometry measurements.

Because the growth of a pre-existing notch in a three-point bending test is likely to be driven by tensile stress states, we disregarded the UCS values measured in the calibration unconfined compressive tests. However, these experiments can be useful in providing a rough estimate of the material's Young's modulus E. Specifically, the data provided in Fig. 1b can be well-fitted with E values between 900 and 1100 MPa. Nevertheless, it is important to emphasise that this is likely to be a higher value than that relevant to tensile loading, due to the additional stiffness provided by existing defects under compression. The Brazilian test data provided was also disregarded. While the Brazilian test is an experiment frequently used to estimate a material's tensile strength, the analysis of the experiment with the `BrazVal` App [38] revealed that the conditions of validity of the test were not fulfilled. As elaborated in Ref. [38], jaws with sufficiently small radii must be used to ensure that cracking initiates in the disk centre. If this is not the case, the tensile strength obtained from the peak load measurement is an underestimation of the real material tensile strength. As a result, the tensile strength corresponding to the average peak load in the Brazilian tests conducted (5200 N, $\sigma_c \approx 2.5$ MPa) is deemed to be an unsuitable value and can only serve as a lower bound. Accordingly, the calibration three-point bending tests were used to estimate the three parameters of our phase field fracture model: Young's modulus E, strength σ_c and toughness G_c. Poisson's ratio was assumed to be equal to $\nu = 0.2$ as is commonly the case in rock-like materials and calculations with other values (results not shown here) indicate negligible differences. While a mode I fracture experiment can serve to independently calibrate each of these parameters, it is important to emphasise that they all have a physical meaning and can be independently measured.

Three-point bending tests were conducted on five types of samples, with the results obtained for four of them provided as calibration data. These samples are illustrated in Fig. 2, providing details of their geometry and boundary conditions. All the samples

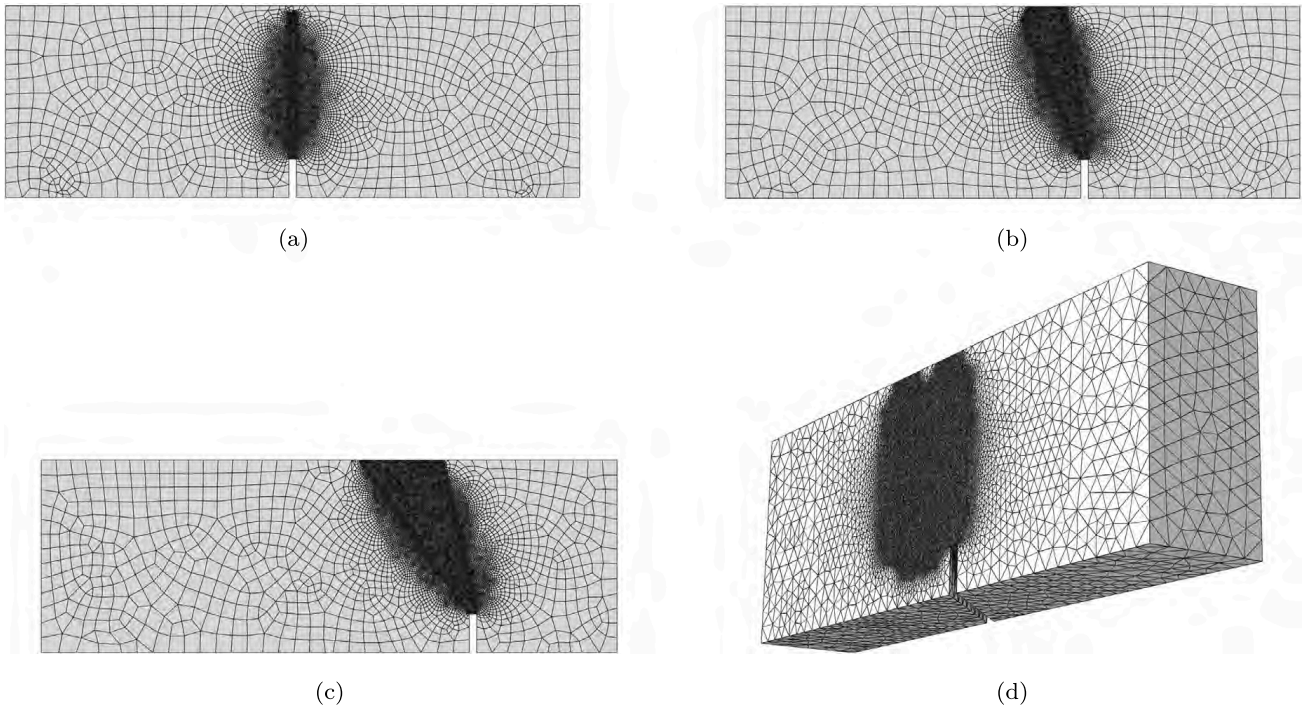

Fig. 3. Finite element discretisation of the three-point bending tests used for generating calibration data. The model HC (a) employs a total of 8888 bi-linear quadrilateral elements, the model HB (b) uses 11,242 bi-linear quadrilateral elements, the model HA (c) uses 14,622 bi-linear quadrilateral elements, and the three-dimensional model H45 employs 1,953,053 linear tetrahedral elements. Since the crack trajectory is not known a priori, the mesh is strategically refined in regions of potential crack growth.

had the following dimensions: 25.4 mm × 76.2 mm × 12.7 mm. The tests denoted HC correspond to a standard three-point bending configuration, with the notch located in the centre of the sample and aligned with the applied load. In tests HB and HA the notch was placed eccentric to break the symmetry of the beam and induce mixed-mode fracture conditions. A fourth calibration test, denoted H45, included a notch inclined 45° along the thickness, requiring full 3D analysis. On the other hand, the challenge experiment was based on a more intricate geometry, containing a crack that was not only inclined along the out-of-plane direction but also exhibited a variation in notch depth along the sample thickness — see Figs. 1d and 4. An important point to emphasise is that, as will be shown below, the mode I HC three-point bending experiment suffices to estimate the parameters of the phase field fracture model; the model can predict (without any additional fitting) the mixed mode behaviour of the remaining three-point bending as crack trajectories are naturally captured following the path of maximum energy release rate.

2.2.2. Computational details

The finite element meshes employed for each of the calibration three-point bending tests are given in Fig. 3. Plane strain conditions were assumed for calibration tests HA, HB and HC, whereas a 3D model has to be employed for H45. Three and four degrees of freedom per node are respectively employed in the 2D and 3D models, involving the components of the displacement vector and the scalar phase field variable. A key computational advantage of the phase field fracture model is its ability to deliver mesh-independent results, due to its non-local nature. However, this requires a mesh sufficiently fine to resolve the phase field length scale ℓ. Specifically, it has been shown that the characteristic element size has to be five times smaller than ℓ to ensure mesh objectivity [31]. This rule is followed in all our calculations, requiring the use of a refined mesh along the potential crack propagation region. Since the crack path is not known a priori, the mesh is refined over a relevant, sufficiently large region near the notch — see Fig. 3.

Four-node quadrilateral elements with full integration are employed for the 2D case studies, while four-node linear tetrahedral elements are used for the 3D benchmark. For the sake of comparison, both tetrahedral and brick elements are used in the predictions of the challenge test, as discussed below. As quantified in the caption of Fig. 3, the finite element meshes range from 8000 to 15,000 elements, in the 2D cases, while close to 2 million elements are employed for the 3D analysis. Calculation times go from 30 min for the 2D analyses (using a single core) to eight days for the 3D model (using 8 cores). A direct linear solver is employed. In the case of the challenge test, the total number of DOFs was close to 4 million, and calculations exceeded ten days on an Intel(R) Xeon(R) Gold 6242R workstation using 16 cores. These calculation times are intrinsically related to the choice of a fully monolithic scheme, which provides accuracy and unconditional stability at the expense of poor convergence. Calculation times can be very significantly reduced through the use of staggered or BFGS-based monolithic approaches. The geometry, mesh and boundary conditions of the challenge test are provided in Fig. 4.

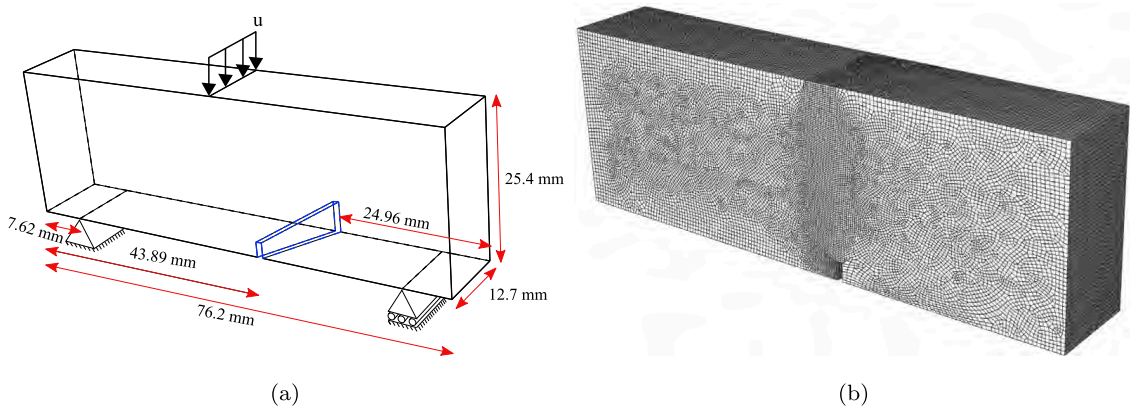

Fig. 4. Details of the challenge test: (a) Geometry, dimensions and boundary conditions, and (b) finite element discretisation, employing a total of 904,429 linear brick elements.

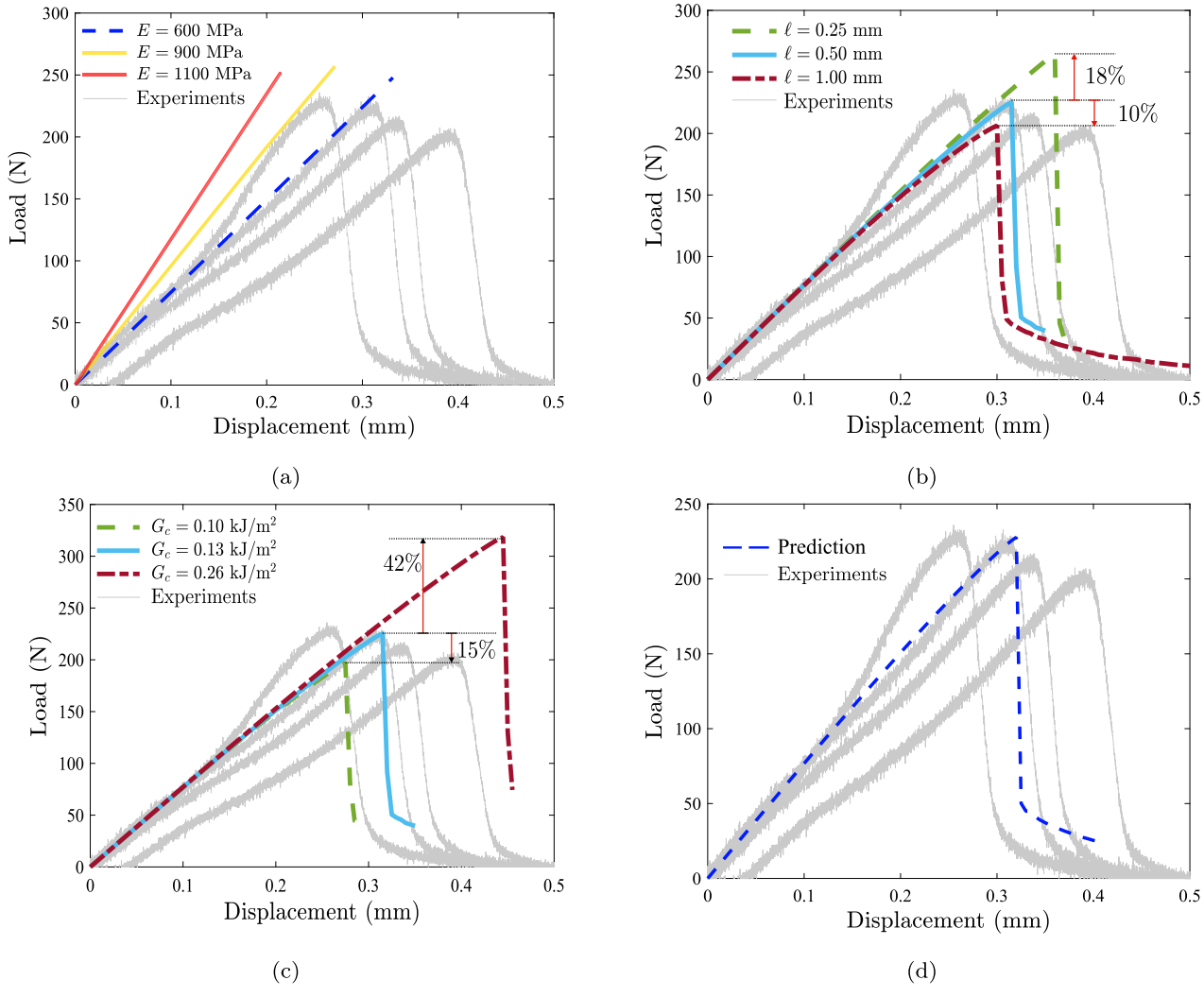

Fig. 5. Using the mode I three-point bending experiment (HC) to estimate the three input parameters to the phase field fracture model: Young's modulus E, toughness G_c and phase field length scale ℓ (or strength σ_c). Numerical force versus displacement results, and comparison with experiments, for varying (a) E, (b) ℓ, and (c) G_c. Lastly, (d) shows the prediction obtained with the choices $E = 600$ MPa, $\nu = 0.2$, $G_c = 0.13$ kJ/m^2 and $\ell = 0.5$ mm. These choices give a strength of $\sigma_c = 4.05$ MPa.

2.2.3. Calibration of the material parameters

Preliminary calculations were conducted to estimate the values of the three input parameters of the model: Young's modulus E, toughness G_c and strength σ_c, with the last one being fixed by an appropriate choice of the phase field length scale ℓ. As discussed

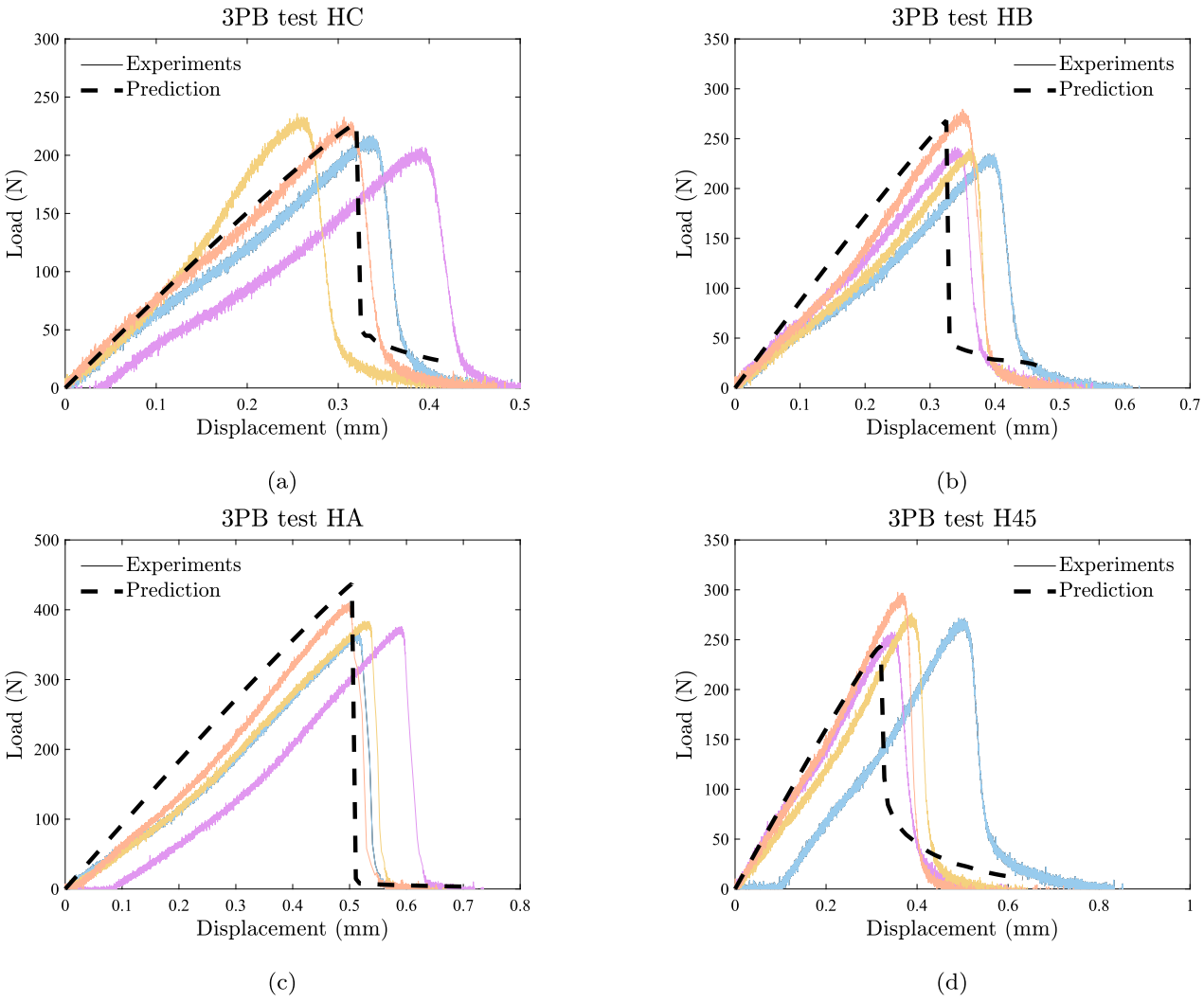

Fig. 6. Numerical predictions of the force versus displacement response of the three-point bending tests provided as part of the challenge data. Four types of tests have been conducted: (a) HC, (b) HB, (c) HA, and (d) H45. A black dashed line is used for the finite element results and solid coloured lines are used for the experimental data consisting of four replicate experiments per testing configuration.

above, the mode I three-point bending test (denoted HC) suffices to calibrate these variables, and the quality of the calibration was then benchmarked by predicting the failure of the other three three-point bending tests, which are more intricate and inherently mixed-mode. The calibrated and verified model was then used to deliver a blind estimate for the test challenge.

Let us consider first the case of Young's modulus E. As shown in Fig. 5a, the numerical results obtained show that the range of values inferred from the UCS experiments (900–1100 MPa) overestimates the stiffness shown in the three-point bending tests. Instead, a value of $E = 600$ MPa appears to provide a much better agreement. As discussed above, these discrepancies between the stiffness of tensile and compressive tests are likely to be related to the influence of defect dilation in the former (as opposed to defect closure and friction in the latter). We proceed then to determine the fracture parameters, G_c and σ_c (or ℓ). Recall that the choice of ℓ defines the strength, as per Eq. (5). A higher sensitivity to the choice of G_c is expected because the samples contain large pre-existing defects and thus failures are likely to be toughness-controlled (as opposed to strength-controlled) [31]. This is shown in Figs. 5b and 5c; doubling the value of G_c brings an increase of 42% in the critical load, while the critical load only changes by 10% when the value of ℓ is halved. But qualitatively, changes in G_c and ℓ have the same effect — changing the magnitude of the critical load. Accordingly, we make a judicious choice and pick a pair of G_c and ℓ values that provide a good agreement with the experimentally measured peak load while falling within the range of expected values for rock-like materials. These are $G_c = 0.13$ kJ/m^2 and $\sigma_c = 4.05$ MPa ($\ell = 0.5$ mm). As discussed below, this choice of parameters gives a remarkable agreement with the other (mixed-mode) four three-point bending tests and with the challenge test, in terms of peak load, crack trajectory and crack morphology.

3. Results

We proceed to showcase the numerical results obtained using the model and boundary value problems described in Section 2. First, from a set of parameters calibrated with the mode I three-point bending test, we examine the ability of the model to predict

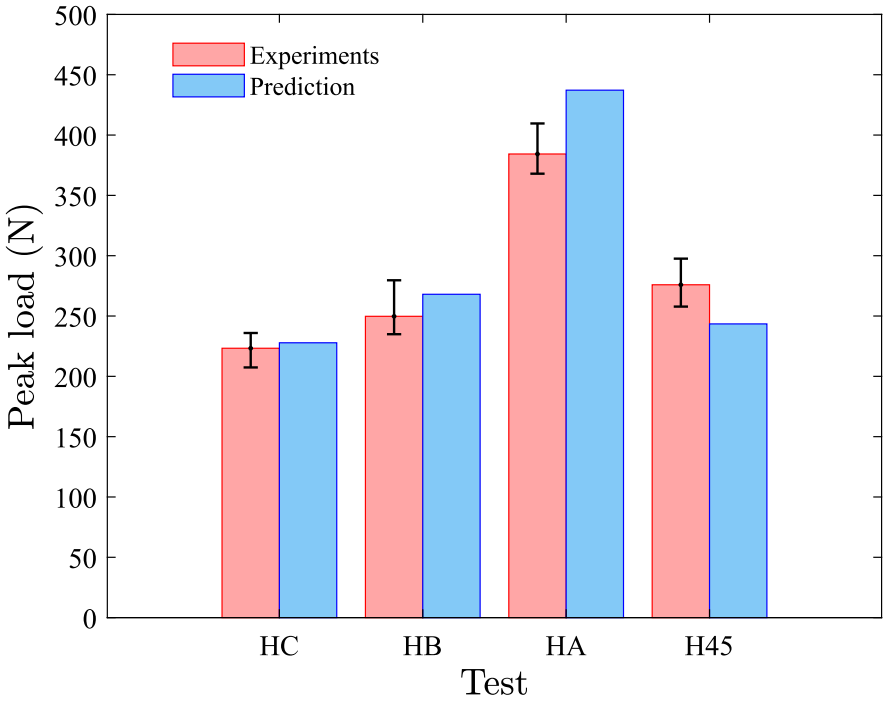

Fig. 7. Numerical and experimental estimations of the critical (peak) load for the three-point bending tests provided as part of the challenge data. The experimental data is reported as the average peak load with an error bar.

cracking in the four mixed-mode three-point bending data calibration experiments (Section 3.1). Then, we provide blind estimates of the failure characteristics of the challenge test (Section 3.2).

3.1. Model benchmarking against calibration data

Numerically predicted force versus displacement responses for the four three-point bending calibration tests are given in Fig. 6, next to the experimental results (4 repeated tests per configuration). The fit is particularly good for the HC case, unsurprisingly as it was used as a calibration benchmark, but a good agreement is overall attained both in terms of peak load and critical displacement. A more quantitative comparison is provided in Fig. 7, where the peak load is shown for both simulations and experiments. In the latter, the average of the four experiments conducted per test is reported and error bars have been included to quantify the experimental scatter. While the agreement is overall good, numerical simulations of test HA and H45 appear to respectively overestimate and underestimate the peak load. Nevertheless, even in those cases, numerical predictions deviate only ~10% from the average peak load and the error is less than 7% from the closest experimental measurement. This level of differences is arguably to be expected considering that the model assumes that the 3D-printed rock is homogeneous and isotropic.

Next, crack trajectories are compared with DIC measurements. In addition, the predicted crack morphology in the 3D case study (H45) is also compared to the laser profilometry profile. The results are shown in Fig. 8. Fig. 8b shows the predicted 2D crack trajectories, with red colour denoting the regions with $\phi = 1$ (i.e., cracks), and Fig. 8c overlaps the experimental (Fig. 8a) and computational (Fig. 8b) results. This overlap reveals an almost perfect agreement between the two, showcasing the ability of the model to capture complex crack trajectories that have not been predefined. A good agreement is also attained in the predictions of crack morphology for the 3D analysis (case H45), as shown in Fig. 8d, with the predicted crack morphology exhibiting the same shape and contortions as the laser profilometry-based measurements.

3.2. Blind predictions of the challenge test

Finally, we use our phase field model to deliver *blind* estimates of force versus displacement behaviour, crack trajectory and crack surface morphology for the challenge test. Our results, submitted to the challenge prior to the release of the corresponding data, are shown here and compared to the outcome of the laboratory tests. It should be noted that calculations were conducted with two types of elements (brick and tetrahedral) and while the results were similar, some differences were found, which are discussed in Appendix C. The results presented in this Section correspond to those calculated using brick elements. After a mesh sensitivity study, the 3D model employed uses a total of 904,429 8-node trilinear brick elements, with the mesh being selectively refined in the regions of potential crack growth (see Fig. 4b).

First, we compare our numerical predictions of the macroscopic force versus displacement response; the results are shown in Fig. 9. The numerical model appears to succeed in predicting with reasonable accuracy the force versus displacement behaviour,

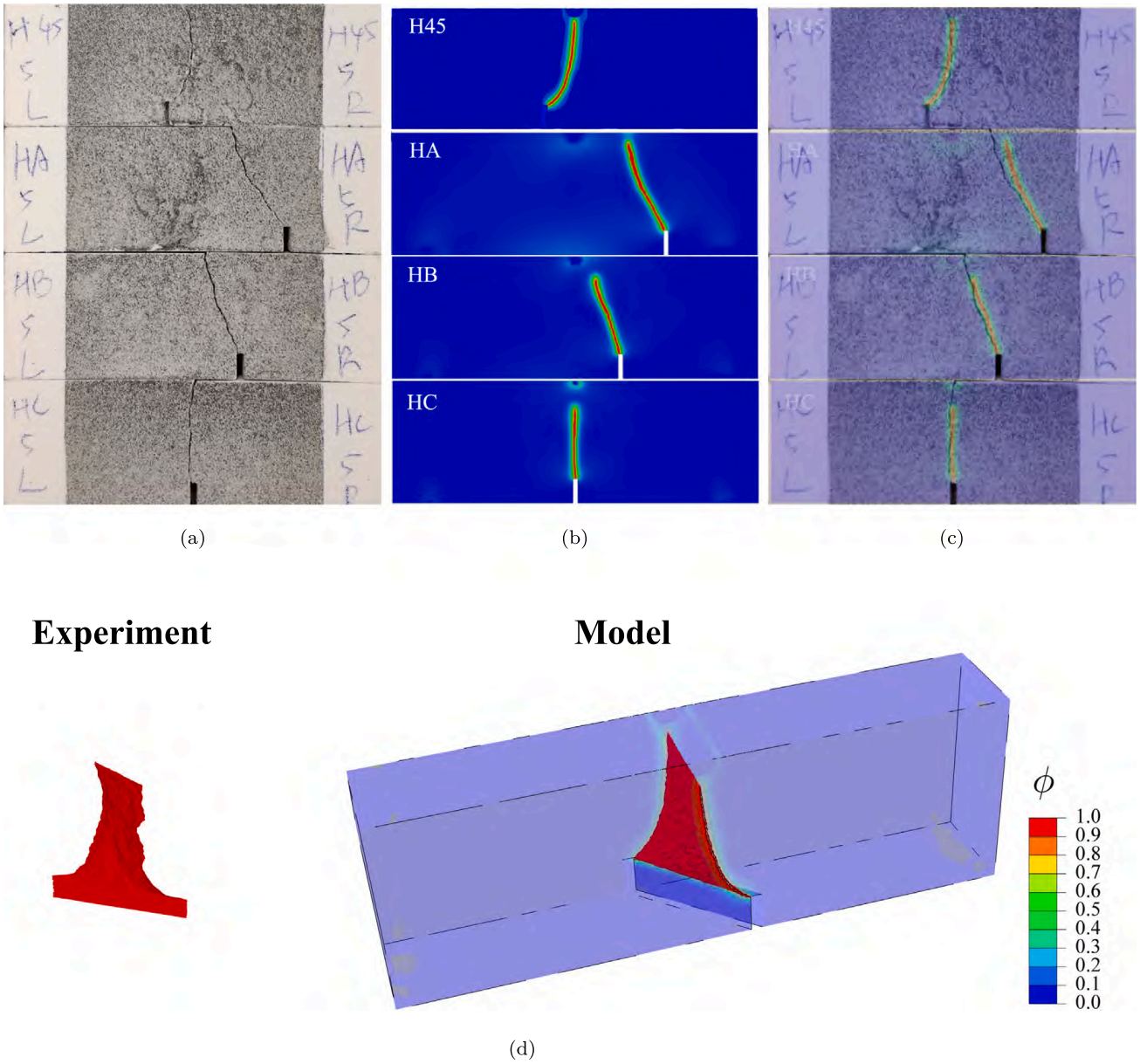

Fig. 8. Numerical and experimental results of crack trajectories and morphology for the three-point bending tests provided as part of the challenge data: (a) experimental crack paths, (b) phase field fracture model predictions, (c) overlap between experimental and numerical results, and (d) comparison of crack morphologies for H45.

providing a peak load and a critical displacement that lie within the experimental data. As shown in Fig. 9b, the peak load appears to be slightly lower than the test average but falls within the experimental scatter.

The crack path predictions are provided in Fig. 10, as depicted by the phase field ϕ contours. The experimental results are also provided (Fig. 10a), together with an overlap of model and experimental crack trajectories (Fig. 10c). The results show a remarkable agreement between computations and experiments, showcasing the ability of the phase field fracture model presented to deliver accurate blind estimations.

Finally, model predictions are benchmarked against the last piece of data provided: crack surface morphology, as measured using laser profilometry. The experimental data, provided as asperity data for 250 rows and 120 columns in 0.1 mm intervals, is plotted using MATLAB. The results are compared in Fig. 11. As can be observed, the crack surface morphology predicted with the phase field model appears to be in good agreement with the experimentally determined crack surface profile, which was released after the submission of the model predictions.

4. Summary, conclusions and outlook

We have described our contribution to the *Damage Mechanics Challenge*, which exploited the strengths of the phase field fracture model [2] to deliver *blind* estimates (i.e., predictions submitted before the challenge data was released). Phase field fracture models

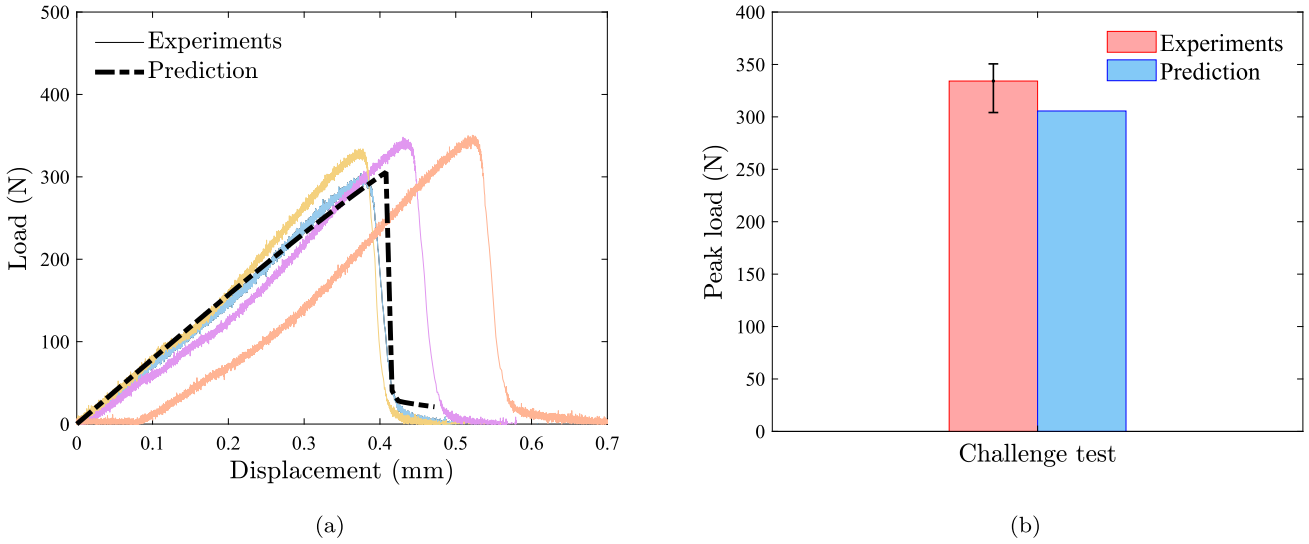

Fig. 9. Comparison between phase field fracture predictions and experimental data, released a posteriori, for the challenge test: (a) force versus displacement response, showing numerical results (dashed line) and four replicate experiments, and (b) peak load, with the experimental data reported as the average peak load with an error bar.

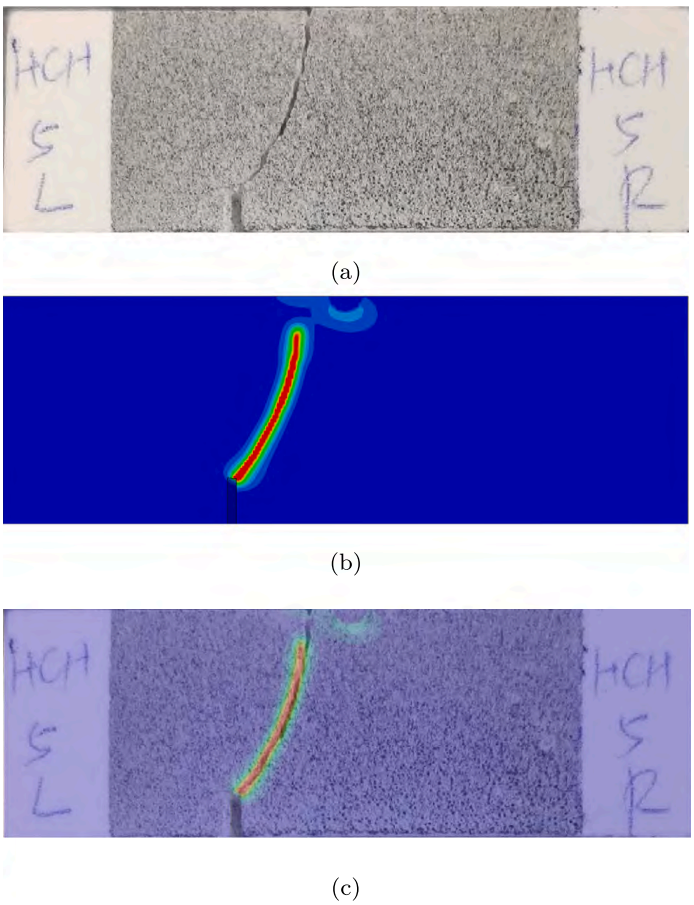

Fig. 10. Crack trajectories. Comparison between phase field fracture predictions and experimental data, released a posteriori, for the challenge test: (a) experimental results, (b) phase field contours, and (c) overlap of numerical and experimental results.

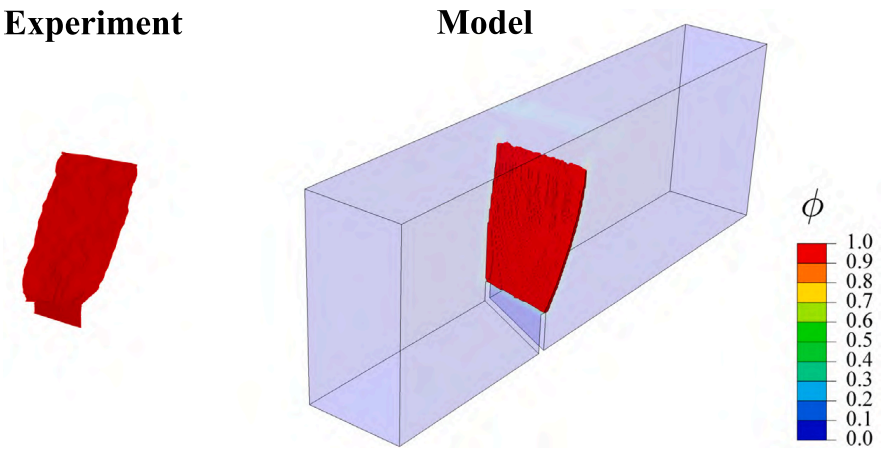

Fig. 11. Three-dimensional crack surface morphology. Comparison between phase field fracture predictions and experimental data, as measured with laser profilometry.

are grounded on Griffith's energy balance and the thermodynamics of fracture, and accordingly deliver predictions in agreement with the conventional fracture mechanics theory. The aim was to demonstrate the predictive potential of simple, physically-sound models based on a well-established theory. Maximising computational efficiency and simplifying implementation were also targets of this work, which used an unconditionally stable monolithic solution scheme and straightforwardly implemented the model in a commercial finite element package by exploiting the analogy between heat transfer and the phase field evolution equations [36,37].

Our model predictions relied only on four parameters, with a clear physical interpretation: Young's modulus E, Poisson's ratio ν, toughness G_c and strength σ_c, with the last one being defined through the choice of phase field length scale ℓ [30,31]. Our study showed that a simple, mode I three-point bending test was sufficient to calibrate the model parameters, with the calibrated model accurately predicting the failure characteristics of the other three three-point bending experiments provided as calibration data, which were more intricate and intrinsically mixed-mode. A very good agreement with experiments was observed across all available data: force versus displacement response, crack trajectory and 3D crack morphology. Furthermore, the submitted predictions for the challenge test were shown to deliver a remarkable agreement with the experimental data, released a posteriori. The agreement was found to be excellent across all the data provided: force versus displacement response, crack propagation paths and surface crack profile.

The results presented further showcase the ability of phase field fracture models to capture complex cracking phenomena in a physically sound fashion. Only the force versus displacement curve of one conventional, mode I three-point bending test sufficed to calibrate a model that could deliver reliable predictions not only for the challenge test but also for the remaining calibration data, across a wide range of scenarios, data (load carrying capacity, crack paths and morphology) and loading configurations. This is despite the challenge being based on an additively manufactured material (a type of gypsum mortar) that is rare and for which little information is available. Phase field approaches link damage and fracture mechanics, providing the computational robustness of non-local damage models while delivering predictions based on well-established fracture parameters and in agreement with decades of fracture mechanics development and understanding. However, one could envisage ways to complicate the challenge that would have potentially showcased the limitations of phase field fracture modelling and other state-of-the-art computational models. For example, rocks are typically heterogeneous porous materials yet material heterogeneity played a secondary role in this challenge. Within this realm, several classes of heterogeneous rocks have been shown to exhibit distinct mode I and mode II critical energy release rates (G_c^I, G_c^{II}). This was not observed in the challenge data, where cracks appear to grow according to the direction of maximum energy release rate. In any case, phase field models have been recently developed to account for material anisotropy [39,40] and shear fracture characteristics [26,41]. Additionally, conventional phase field models assume a failure surface that is symmetric over the tensile and compressive regimes. This was appropriate for this challenge, as the chosen loading configuration (three-point bend testing) resulted in crack growth due to tensile stress states. However, rock-like materials are known to exhibit asymmetric failure surfaces and these would have played a role under more intricate loading conditions. Fortunately, recent years have seen the development of phase field models capable of accommodating arbitrary failure surfaces, such as Drucker–Prager [42,43]. A new edition of this challenge, which could potentially test these complex regimes, would be very welcomed.

CRediT authorship contribution statement

Yousef Navidtehrani: Writing – review & editing, Writing – original draft, Visualization, Validation, Software, Methodology, Investigation, Formal analysis, Data curation, Conceptualization. **Ravindra Duddu:** Writing – review & editing, Supervision, Methodology, Investigation, Funding acquisition, Conceptualization. **Emilio Martínez-Pañeda:** Writing – review & editing, Writing – original draft, Supervision, Software, Resources, Project administration, Methodology, Investigation, Funding acquisition, Conceptualization.

Declaration of competing interest

The authors declare that they have no known competing financial interests or personal relationships that could have appeared to influence the work reported in this paper.

Data availability

Data will be made available on request.

Acknowledgements

Y. Navidtehrani acknowledges financial support from the Ministry of Science, Innovation and Universities of Spain, Spain through grant PGC2018-099695-B-I00. E. Martínez-Pañeda was supported by an UKRI Future Leaders Fellowship, UK (grant MR/V024124/1). R. Duddu acknowledges the funding support from the National Science Foundation's Office of Polar Programs, USA via CAREER grant no. PLR-1847173.

Appendix A. Finite element implementation of phase field fracture

For the sake of facilitating reproducibility, in the following we proceed to describe the characteristics of a finite element implementation of the phase field fracture model. It is emphasised that this information, required for an element-level implementation, is not required if the heat transfer analogy approach is followed, as discussed in Section 2.1.3.

We start by taking into account the outlined constitutive selections, including the definition of a history field $\mathcal{H}$, and calculate the stationary of $\mathcal{E}_\ell$ with respect to the primal variables $\mathbf{u}$ and ϕ; the resultant expression takes the form:

$$\partial\mathcal{E}_\ell(\mathbf{u},\phi) = \int_\Omega \Bigg\{ \left[(1-\phi)^2 \frac{\partial \psi_0^+(\boldsymbol{\varepsilon}(\mathbf{u}))}{\partial \boldsymbol{\varepsilon}(\mathbf{u})} + \frac{\partial \psi_0^-(\boldsymbol{\varepsilon}(\mathbf{u}))}{\partial \boldsymbol{\varepsilon}(\mathbf{u})} \right] \delta\boldsymbol{\varepsilon}(\mathbf{u}) - 2(1-\phi)\delta\phi\mathcal{H} + G_c \left[\frac{1}{\ell}\phi\delta\phi + \ell\nabla\phi\cdot\nabla\delta\phi \right] - \mathbf{b}\cdot\delta\mathbf{u} \Bigg\} \mathrm{d}V - \int_{\partial\Omega} \mathbf{T}\cdot\delta\mathbf{u}\,\mathrm{d}S = 0\,. \tag{A.1}$$

where $\delta\mathbf{u}$ and $\delta\phi$ are arbitrary fields (test functions). Then, considering the stress definition, Eq. (10), one can reformulate Eq. (A.1) into two coupled weak form equations

$$\int_\Omega \left\{ \left[(1-\phi)^2 \boldsymbol{\sigma}_{\mathbf{0}}^+ + \boldsymbol{\sigma}_{\mathbf{0}}^- \right] : \delta\boldsymbol{\varepsilon}(\mathbf{u}) - \mathbf{b}\cdot\delta\mathbf{u} \right\} \mathrm{d}V - \int_{\partial\Omega} \mathbf{T}\cdot\delta\mathbf{u}\ \mathrm{d}S = 0 \tag{A.2}$$

$$\int_\Omega \left\{ -2(1-\phi)\delta\phi\,\mathcal{H} + G_c \left[\frac{1}{\ell}\phi\delta\phi + \ell\nabla\phi\nabla\delta\phi \right] \right\} \mathrm{d}V = 0\,, \tag{A.3}$$

We define a finite element discretisation to formulate the element stiffness matrix $\boldsymbol{K}^e$ and the residual vector $\mathbf{R}^e$. Using Voigt notation, the nodal variables for the displacement field, denoted as $\hat{\mathbf{u}}$, and the phase field $\hat{\phi}$, are interpolated as follows

$$\mathbf{u} = \sum_{i=1}^{m} \boldsymbol{N}_i\hat{\mathbf{u}}_i, \qquad \phi = \sum_{i=1}^{m} N_i\hat{\phi}_i\,, \tag{A.4}$$

where N_i represents the shape function associated with node i, and $\boldsymbol{N}_i$ is the shape function matrix. Additionally, m denotes the total number of nodes per element, while $\hat{\mathbf{u}}_i$ and $\hat{\phi}_i$ respectively represent the displacement and phase field at node i. In a similar manner, the associated gradient quantities can be discretised using the corresponding $\mathbf{B}$-matrices, which contain the derivatives of the shape functions;

$$\boldsymbol{\varepsilon} = \sum_{i=1}^{m} \boldsymbol{B}_i^{\mathbf{u}}\hat{\mathbf{u}}_i, \qquad \nabla\phi = \sum_{i=1}^{m} \mathbf{B}_i\hat{\phi}_i\,. \tag{A.5}$$

The discretised residuals for each of the primal kinematic variables are then expressed as:

$$\mathbf{R}_i^{\mathbf{u}} = \int_\Omega \left\{ (1-\phi)^2 \left(\boldsymbol{B}_i^{\mathbf{u}}\right)^T \boldsymbol{\sigma}_0^+ + \left(\boldsymbol{B}_i^{\mathbf{u}}\right)^T \boldsymbol{\sigma}_0^- \right\} \mathrm{d}V - \int_\Omega \left(\mathbf{N}_i^{\mathrm{u}}\right)^T \mathbf{b}\ \mathrm{d}V - \int_{\partial\Omega_h} \left(\mathbf{N}_i^{\mathrm{u}}\right)^T \mathbf{T}\ \mathrm{d}S, \tag{A.6}$$

$$\mathbf{R}_i^{\phi} = \int_\Omega \left\{ -2(1-\phi)N_i\mathcal{H} + G_c \left[\frac{1}{\ell}N_i\phi + \ell \left(\mathbf{B}_i^{\phi}\right)^T \nabla\phi \right] \right\} \mathrm{d}V \tag{A.7}$$

The consistent tangent stiffness matrices $\boldsymbol{K}$ are then determined by differentiating the residuals with respect to the incremental nodal variables:

$$\boldsymbol{K}_{ij}^{\mathbf{u}} = \frac{\partial \mathbf{R}_i^{\mathbf{u}}}{\partial \mathbf{u}_j} = \int_\Omega \left\{ (1-\phi)^2 (\boldsymbol{B}_i^{\mathbf{u}})^T \boldsymbol{C}_0^+ \boldsymbol{B}_j^{\mathbf{u}} + (\boldsymbol{B}_i^{\mathbf{u}})^T \boldsymbol{C}_0^- \boldsymbol{B}_j^{\mathbf{u}} \right\} \mathrm{d}V\,, \tag{A.8}$$

$$\boldsymbol{K}_{ij}^{\phi} = \frac{\partial R_i^{\phi}}{\partial \phi_j} = \int_\Omega \left\{ \left(2\mathcal{H} + \frac{G_c}{\ell} \right) N_i N_j + G_c\ell\, \mathbf{B}_i^T \mathbf{B}_j \right\} \mathrm{d}V\,, \tag{A.9}$$

where $\boldsymbol{C}_0^{\pm} = \partial\boldsymbol{\sigma}_0^{\pm}/\partial\boldsymbol{\varepsilon}(\mathbf{u})$ are the tangent matrices for the positive and negative parts.

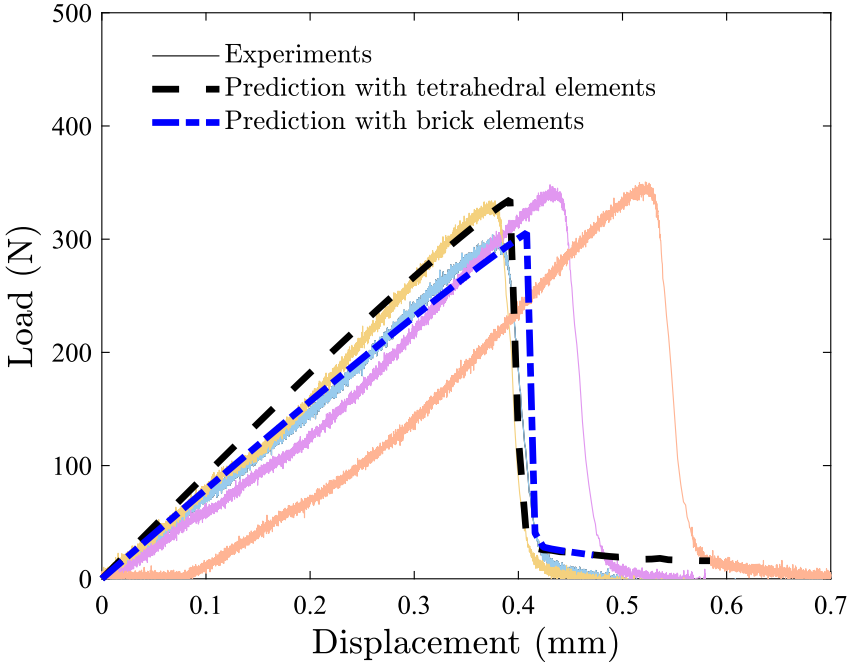

Fig. C.1. Assessing the role of the element type: load versus force results for the challenge test, as obtained using tetrahedral and brick elements.

Appendix B. Heat transfer analogy

As elaborated in Refs. [36,37], one can leverage the analogy with heat transfer to simplify the numerical implementation of the phase field evolution equation in commercial finite element packages. In the presence of a heat source denoted as r, the steady-state equation for heat transfer takes the following form:

$$k\nabla^2 T = -r \tag{B.1}$$

where, T represents temperature, and k is the thermal conductivity. Eq. (B.1) is analogous to the phase field evolution equation ((12)b) upon assuming $T \equiv \phi$, $k = 1$, and defining the nonlinear heat source r as follows

$$r = \frac{2(1-\phi)\mathcal{H}}{\ell G_c} - \frac{\phi}{\ell^2} \tag{B.2}$$

Finally, to determine the Jacobian or tangent matrix, we must provide the gradient of the heat source with respect to the phase field (temperature), which reads

$$\frac{\partial r}{\partial \phi} = -\frac{2\mathcal{H}}{\ell G_c} - \frac{1}{\ell^2} \tag{B.3}$$

Appendix C. On the influence of the element type

To investigate the sensitivity of model predictions to numerical discretisation choices, calculations for the challenge test were conducted using two types of elements, linear tetrahedral elements and linear brick (hexahedral) elements. Overall, a small influence was found, as is to be expected when using sufficiently fine meshes. However, given the size of the 3D models, with millions of degrees-of-freedom (DOFs), an effort was made to use a finite element mesh as coarse as possible outside of the regions of crack growth, and this can result in some sensitivity to the element choice. Thus, to assess this, calculations were conducted with two models, one employing 2,438,970 linear tetrahedral elements (1,673,512 DOFs) and another one employing 904,429 linear brick elements (3,735,636 DOFs). The results obtained are compared in Fig. C.1 in terms of their predicted force versus displacement responses. The experimental results, released a posteriori, are also included. While small, some differences can be observed; the tetrahedral response is stiffer and this leads to a slightly higher peak load. This is to be expected, to a certain extent, as linear tetrahedral elements are known to display stiffer responses if the mesh is not sufficiently fine [44]. Nonetheless, both sets of numerical results provide a good agreement with experiments.

References

[1] Francfort GA, Marigo J-J. Revisiting brittle fracture as an energy minimization problem. J Mech Phys Solids 1998;46(8):1319–42.
[2] Bourdin B, Francfort GA, Marigo JJ. The variational approach to fracture. Springer Netherlands; 2008.

[3] Griffith AA. The Phenomena of Rupture and Flow in Solids. Philos Trans A 1920;221:163–98.
[4] Miehe C, Hofacker M, Welschinger F. A phase field model for rate-independent crack propagation: Robust algorithmic implementation based on operator splits. Comput Methods Appl Mech Engrg 2010;199(45–48):2765–78.
[5] Kristensen PK, Martínez-Pañeda E. Phase field fracture modelling using quasi-newton methods and a new adaptive step scheme. Theor Appl Fract Mech 2020;107:102446.
[6] Borden MJ, Verhoosel CV, Scott MA, Hughes TJR, Landis CM. A phase-field description of dynamic brittle fracture. Comput Methods Appl Mech Engrg 2012;217–220:77–95.
[7] McAuliffe C, Waisman H. A coupled phase field shear band model for ductile–brittle transition in notched plate impacts. Comput Methods Appl Mech Engrg 2016;305:173–95.
[8] Mandal TK, Nguyen VP, Wu JY. Evaluation of variational phase-field models for dynamic brittle fracture. Eng Fract Mech 2020;235:107169.
[9] Martínez-Pañeda E, Golahmar A, Niordson CF. A phase field formulation for hydrogen assisted cracking. Comput Methods Appl Mech Engrg 2018;342:742–61.
[10] Cui C, Ma R, Martínez-Pañeda E and. A generalised, multi-phase-field theory for dissolution-driven stress corrosion cracking and hydrogen embrittlement. J Mech Phys Solids 2022;166:104951.
[11] Carrara P, Ambati M, Alessi R, De Lorenzis L. A framework to model the fatigue behavior of brittle materials based on a variational phase-field approach. Comput Methods Appl Mech Engrg 2020;361:112731.
[12] Golahmar A, Niordson CF, Martínez-Pañeda E. A phase field model for high-cycle fatigue: Total-life analysis. Int J Fatigue 2023;170:107558.
[13] Quintanas-Corominas A, Reinoso J, Casoni E, Turon A, Mayugo JA. A phase field approach to simulate intralaminar and translaminar fracture in long fiber composite materials. Compos Struct 2019;220:899–911.
[14] Tan W, Martínez-Pañeda E. Phase field predictions of microscopic fracture and R-curve behaviour of fibre-reinforced composites. Compos Sci Technol 2021;202:108539.
[15] Gao Y, Berger M, Duddu R. Cnn-based surrogate for the phase field damage model: Generalization across microstructure parameters for composite materials. J Eng Mech 2023;149(6):04023025.
[16] Natarajan Hirshikesh S, Annabattula RK, Martínez-Pañeda E. Phase field modelling of crack propagation in functionally graded materials. Composites B 2019;169:239–48.
[17] Kumar PKAV, Dean A, Reinoso J, Lenarda P, Paggi M. Phase field modeling of fracture in functionally graded materials: G -convergence and mechanical insight on the effect of grading. Thin-Walled Struct 2021;159:107234.
[18] Simoes M, Martínez-Pañeda E. Phase field modelling of fracture and fatigue in shape memory alloys. Comput Methods Appl Mech Engrg 2021;373:113504.
[19] Simoes M, Braithwaite C, Makaya A, Martínez-Pañeda E. Modelling fatigue crack growth in shape memory alloys. Fatigue Fract Eng Mater Struct 2022.
[20] Quinteros L, García-Macías E, Martínez-Pañeda E. Micromechanics-based phase field fracture modelling of CNT composites. Composit B 2022;236:109788.
[21] Klinsmann M, Rosato D, Kamlah M, McMeeking RM. Modeling crack growth during li extraction in storage particles using a fracture phase field approach. J Electrochem Soc 2016;163(2):A102–18.
[22] Boyce AM, Martínez-Pañeda E, Wade A, Zhang YS, Bailey JJ, Heenan TM, et al. Shearing, cracking predictions of lithium-ion battery electrodes by X-ray computed tomography and modelling. J Power Sources 2022;526:231119.
[23] Liu S, Wang Y, Peng C, Wu W. A thermodynamically consistent phase field model for mixed-mode fracture in rock-like materials. Comput Methods Appl Mech Engrg 2022;392:114642.
[24] Hug L, Potten M, Stockinger G, Thuro K, Kollmannsberger S. A three-field phase-field model for mixed-mode fracture in rock based on experimental determination of the mode II fracture toughness. Eng Comput 2022;38(6):5563–81.
[25] Xu B, Xu T, Xue Y, Heap MJ, Ranjith PG, Wasantha PL, Li Z. Phase-field modeling of crack growth and interaction in rock. Geomech Geophys Geo-Energy Geo-Resour 2022;8(6):1–18.
[26] Bryant EC, Sun WC. A mixed-mode phase field fracture model in anisotropic rocks with consistent kinematics. Comput Methods Appl Mech Engrg 2018;342:561–84.
[27] Santillán D, Juanes R, Cueto-Felgueroso L. Phase field model of fluid-driven fracture in elastic media: Immersed-fracture formulation and validation with analytical solutions. J Geophys Res Solid Earth 2017;122(4):2565–89.
[28] Sun X, Duddu R, Hirshikesh. A poro-damage phase field model for hydrofracturing of glacier crevasses. Extreme Mech Lett 2021;45:101277.
[29] Clayton T, Duddu R, Siegert M, Martínez-Pañeda E. A stress-based poro-damage phase field model for hydrofracturing of creeping glaciers and ice shelves. Eng Fract Mech 2022;272:108693.
[30] Tanné E, Li T, Bourdin B, Marigo J-J, Maurini C. Crack nucleation in variational phase-field models of brittle fracture. J Mech Phys Solids 2018;110:80–99.
[31] Kristensen PK, Niordson CF, Martínez-Pañeda E. An assessment of phase field fracture: crack initiation and growth. Phil Trans R Soc A 2021;379:20210021.
[32] Klinsmann M, Rosato D, Kamlah M, McMeeking RM. An assessment of the phase field formulation for crack growth. Comput Methods Appl Mech Engrg 2015;294:313–30.
[33] Bellettini G, Coscia A. Discrete approximation of a free discontinuity problem. Numer Funct Anal Optim 1994;15(3–4):201–24.
[34] Chambolle A. An approximation result for special functions with bounded deformation. J Math Pures Appl 2004;83(7):929–54.
[35] Amor H, Marigo JJ, Maurini C. Regularized formulation of the variational brittle fracture with unilateral contact: Numerical experiments. J Mech Phys Solids 2009;57(8):1209–29.
[36] Navidtehrani Y, Betegón C, Martínez-Pañeda E. A simple and robust Abaqus implementation of the phase field fracture method. Appl Eng Sci 2021;6:100050.
[37] Navidtehrani Y, Betegón C, Martínez-Pañeda E. A unified abaqus implementation of the phase field fracture method using only a user material subroutine. Materials 2021;14(8):1913.
[38] Navidtehrani Y, Betegón C, Zimmerman RW, Martínez-Pañeda E. Griffith-based analysis of crack initiation location in a brazilian test. Int J Rock Mech Min Sci 2022;159:105227.
[39] Teichtmeister S, Kienle D, Aldakheel F, Keip MA. Phase field modeling of fracture in anisotropic brittle solids. Int J Non-Linear Mech 2017;97:1–21.
[40] Bleyer J, Alessi R. Phase-field modeling of anisotropic brittle fracture including several damage mechanisms. Comput Methods Appl Mech Engrg 2018;336:213–36.
[41] Feng Y, Li J. Phase-field method with additional dissipation force for mixed-mode cohesive fracture. J Mech Phys Solids 2022;159:104693.
[42] De Lorenzis L, Maurini C. Nucleation under multi-axial loading in variational phase-field models of brittle fracture. Int J Fract 2022;237(1–2):61–81.
[43] Navidtehrani Y, Betegón C, Martínez-Pañeda E. A general framework for decomposing the phase field fracture driving force, particularised to a Drucker–Prager failure surface. Theor Appl Fract Mech 2022;121:103555.
[44] Puso MA, Solberg J. A stabilized nodally integrated tetrahedral. Internat J Numer Methods Engrg 2006;67(6):841–67.

E | Paper 5

A general framework for decomposing the phase field fracture driving force, particularised to a Drucker-Prager failure surface

Authors:

Yousef Navidtehrani, Covadonga Betegón, Emilio Martínez-Pañeda

Journal:

Theoretical and Applied Fracture Mechanics

Year of Publication:

2022

Impact Factor:

5.0 - Q1

Theoretical and Applied Fracture Mechanics 121 (2022) 103555

Contents lists available at ScienceDirect

Theoretical and Applied Fracture Mechanics

journal homepage: www.elsevier.com/locate/tafmec

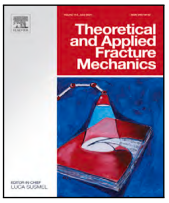

A general framework for decomposing the phase field fracture driving force, particularised to a Drucker–Prager failure surface

Yousef Navidtehrani [a], Covadonga Betegón [a], Emilio Martínez-Pañeda [b,*]

[a] Department of Construction and Manufacturing Engineering, University of Oviedo, Gijón 33203, Spain
[b] Department of Civil and Environmental Engineering, Imperial College London, London SW7 2AZ, UK

ARTICLE INFO

Keywords:
Phase field fracture
Fracture driving force
Brittle fracture
Drucker–Prager criterion
Strain energy split

ABSTRACT

Due to its computational robustness and versatility, the phase field fracture model has become the preferred tool for predicting a wide range of cracking phenomena. However, in its conventional form, its intrinsic tension–compression symmetry in damage evolution prevents its application to the modelling of compressive failures in brittle and quasi-brittle solids, such as concrete or rock materials. In this work, we present a general methodology for decomposing the phase field fracture driving force, the strain energy density, so as to reproduce asymmetrical tension–compression fracture behaviour. The generalised approach presented is particularised to the case of linear elastic solids and the Drucker–Prager failure criterion. The ability of the presented model to capture the compressive failure of brittle materials is showcased by numerically implementing the resulting strain energy split formulation and addressing four case studies of particular interest. Firstly, insight is gained into the capabilities of the model in predicting friction and dilatancy effects under shear loading. Secondly, virtual direct shear tests are conducted to assess fracture predictions under different pressure levels. Thirdly, a concrete cylinder is subjected to uniaxial and triaxial compression to investigate the influence of confinement. Finally, the localised failure of a soil slope is predicted and the results are compared with other formulations for the strain energy decomposition proposed in the literature. The results provide a good qualitative agreement with experimental observations and demonstrate the capabilities of phase field fracture methods to predict crack nucleation and growth under multi-axial loading in materials exhibiting asymmetric tension–compression fracture behaviour.

1. Introduction

The application of the phase field paradigm to fracture mechanics has enabled predicting cracking phenomena of arbitrary complexity [1,2]. These include not only hitherto complex crack trajectories but also crack branching, nucleation and merging, without *ad hoc* criteria and cumbersome tracking techniques, in both two and three dimensions [3,4]. In phase field methods, the crack–solid interface is not explicitly modelled but instead smeared over a finite domain and characterised by an auxiliary phase field variable ϕ, which takes two distinct values in each of the phases (e.g., $\phi = 0$ in intact material points and $\phi = 1$ inside of the crack). Hence, interfacial boundary conditions are replaced by a differential equation that describes the evolution of the phase field ϕ. Phase field fracture methods have become the *de facto* choice for modelling a wide range of cracking phenomena. New phase field formulations have been presented for ductile fracture [5,6], composite materials [7–9], shape memory alloys [10,11], functionally graded materials [12,13], fatigue damage [14,15] and hydrogen embrittlement [16,17], among others (see Refs. [18,19] for an overview).

Most frequently, the phase field is defined to evolve in agreement with Griffith's energy balance [20] - crack growth is predicted by the exchange between elastic and fracture energies. While thermodynamically rigorous, this leads to a symmetric fracture behaviour in tension and compression, implying that crack interpenetration can occur in compressive stress states, and that the compressive strength is assumed to be equal to the tensile strength. In metals, which often fail in compression by buckling, crumbling or 45-degree shearing, this leads to nonphysical predictions of crack nucleation in compressive regions, such as the vicinity of loading pins in standardised experiments like three-point bending or compact tension. For brittle and quasi brittle solids, such as concrete or geomaterials, the assumption of tension–compression symmetry is unrealistic as compressive-to-tensile strength

* Corresponding author.
E-mail address: e.martinez-paneda@imperial.ac.uk (E. Martínez-Pañeda).

https://doi.org/10.1016/j.tafmec.2022.103555
Received 1 May 2022; Received in revised form 19 August 2022; Accepted 22 August 2022
Available online 28 August 2022

ratios typically range between $\sigma_c/\sigma_t = 2$ and $\sigma_c/\sigma_t = 25$ [21]. In brittle materials, compressive failure takes place due to the linkage of pre-existing micro-cracks growing under local tensile stresses [22], while tensile brittle fractures are typically due to unstable crack propagation. Thus, extending the use of phase field to the prediction of compressive failures in brittle solids requires the development of new formulations that can accommodate appropriate failure surfaces. To achieve this goal, we here present a general approach for decomposing the phase field fracture driving force, the strain energy density. We then particularise such approach to the case of a Drucker–Prager failure surface and numerically show that it can adequately capture cracking patterns in concrete and geomaterials.

2. The variational phase field fracture framework

We shall begin by providing a brief introduction to the variational phase field fracture formulation; the reader is referred to Ref. [1] for a comprehensive description. Considering a body Ω with a crack surface Γ, where the displacement field $\mathbf{u}$ might be discontinuous, the energy functional can be formulated as the sum of the elastic energy stored in the cracked body and the energy required to grow the crack [23]:

$$\mathcal{E} = \int_\Omega \psi\left(\boldsymbol{\varepsilon}\left(\mathbf{u}\right)\right) \mathrm{d}V + \int_\Gamma G_c \,\mathrm{d}\Gamma\,, \tag{1}$$

where ψ is the elastic strain energy density, which is a function of the strain tensor $\boldsymbol{\varepsilon}\left(\mathbf{u}\right)$, and G_c is a measure of the energy required to create two new surfaces, the material toughness. Eq. (1) postulates Griffith's minimality principle in a global manner and its minimisation enables predicting arbitrary cracking phenomena solely as a result of the exchange between elastic and fracture energies. However, minimising Griffith's functional $\mathcal{E}$ is hindered by the unknown nature of the crack surface Γ. This can be overcome by the use of the phase field paradigm; diffusing the interface over a finite region and tracking its evolution by means of an auxiliary phase field variable ϕ. Accordingly, Eq. (1) can be approximated by the following regularised functional:

$$\mathcal{E}_\ell = \int_\Omega g\left(\phi\right)\psi_0\left(\boldsymbol{\varepsilon}\left(\mathbf{u}\right)\right) \mathrm{d}V + \int_V G_c \gamma\left(\phi, \nabla\phi, \ell\right) \mathrm{d}V\,, \tag{2}$$

where ψ_0 denotes the elastic strain energy density of the undamaged solid, $g(\phi)$ is a degradation function to reduce the stiffness of the solid with increasing damage, and $\gamma\left(\phi, \nabla\phi, \ell\right)$ is the so-called crack density function. For simplicity, and without loss of generality, we adopt the constitutive choices of the so-called conventional or AT2 phase field model [24], such that

$$g\left(\phi\right) = \left(1-\phi\right)^2 \quad \text{and} \quad \gamma(\phi, \nabla, \ell\phi) = \frac{1}{2\ell}\phi^2 + \frac{\ell}{2}|\nabla\phi|^2 \tag{3}$$

where ℓ is the phase field length scale, inherently arising due to the non-local nature of the model. The strong form of the balance equations can be derived by taking the first variation of $\mathcal{E}_\ell$ with respect to the primal kinematic variables $(\mathbf{u}, \phi)$ and making use of Gauss' divergence theorem, rendering

$$\begin{aligned} \nabla\cdot\left[\left(1-\phi\right)^2\boldsymbol{\sigma}_0\right] &= \mathbf{0} \quad \text{in} \quad \Omega \\ G_c\left(\frac{\phi}{\ell} - \ell\nabla^2\phi\right) - 2\left(1-\phi\right)\psi_0 &= 0 \quad \text{in} \quad \Omega \end{aligned} \tag{4}$$

where $\boldsymbol{\sigma}_0$ is the undamaged stress tensor. As seen in (4)b, the evolution of the phase field is governed by the (undamaged) elastic strain energy density which, for linear elastic isotropic solids, is given by

$$\psi_0 = \frac{1}{2}\lambda\mathrm{tr}\left(\boldsymbol{\varepsilon}\right)^2 + \mu\,\boldsymbol{\varepsilon} : \boldsymbol{\varepsilon}\,, \tag{5}$$

where λ and μ are the Lamé coefficients. It follows that the phase field is insensitive to the compressive or tensile nature of the mechanical fields (tension–compression symmetry in damage evolution). To enforce a distinction between tension and compression behaviour, several formulations have been proposed. Initially, the motivation was the need to avoid crack interpenetration and achieve the resistance to cracking under compression observed in some materials such as metals. Examples of strain energy decompositions formulated with this objective include the volumetric–deviatoric split by Amor et al. [25], the spectral decomposition by Miehe and co-workers [26], and the purely tensile splits (so-called 'no-tension' models) of Freddi and Royer-Carfagni [27,28] and Lo et al. [29]. On the other hand, rising interest in using phase field methods to model fracture in concrete and geomaterials has led to the development of driving force definitions that accommodate non-symmetric failure surfaces [30]. Zhou et al. [31] and Wang et al. [32] developed new driving force formulations based on Mohr–Coulomb theory. And very recently, de Lorenzis and Maurini [33] presented an analytical study where the strain energy split was defined based on a Drucker–Prager failure surface. The majority of these works adopt the following structure. The elastic strain energy density is decomposed into two parts: (i) a part affected by damage, ψ_d, and (ii) a stored residual elastic part ψ_s, which is independent of the damage variable and thus not susceptible to dissipation. Accordingly,

$$\psi_0\left(\boldsymbol{\varepsilon}\right) = \psi_d\left(\boldsymbol{\varepsilon}\right) + \psi_s\left(\boldsymbol{\varepsilon}\right), \quad \text{and} \quad \psi\left(\boldsymbol{\varepsilon}, \phi\right) = g\left(\phi\right)\psi_d\left(\boldsymbol{\varepsilon}\right) + \psi_s\left(\boldsymbol{\varepsilon}\right), \tag{6}$$

which necessarily implies,

$$\psi\left(\boldsymbol{\varepsilon}, \phi\right) = g\left(\phi\right)\psi_0\left(\boldsymbol{\varepsilon}\right) + \left(1 - g\left(\phi\right)\right)\psi_s\left(\boldsymbol{\varepsilon}\right). \tag{7}$$

And this decomposition of the strain energy density gives rise to an analogous decomposition of the Cauchy stress tensor, such that

$$\boldsymbol{\sigma}\left(\boldsymbol{\varepsilon}, \phi\right) = g\left(\phi\right)\frac{\partial\psi_d\left(\boldsymbol{\varepsilon}\right)}{\partial\boldsymbol{\varepsilon}} + \frac{\partial\psi_s\left(\boldsymbol{\varepsilon}\right)}{\partial\boldsymbol{\varepsilon}} = g\left(\phi\right)\boldsymbol{\sigma}^d + \boldsymbol{\sigma}^s\,. \tag{8}$$

where $\boldsymbol{\sigma}^d$ and $\boldsymbol{\sigma}^s$ respectively denote the damaged and non-degraded parts of the Cauchy stress tensor.

The aim of this work is to present a generalised approach to identify $\psi_s\left(\boldsymbol{\varepsilon}\right)$ (and subsequently $\psi_d\left(\boldsymbol{\varepsilon}\right)$) as a function of the failure surface and the constitutive behaviour of the pristine material. This is presented below, in Section 3, where the framework is exemplified with a Drucker–Prager [34] failure surface.

3. A general approach for decomposing the strain energy density based on failure criteria

We proceed to present a general approach for decomposing the strain energy density so as to incorporate any arbitrary failure criterion in the phase field fracture method. As the strain energy density is the driving force for fracture, a suitable choice of strain energy decomposition can enable reproducing the desired failure surface. Such a choice must satisfy the failure criterion assumed while recovering the constitutive behaviour of the pristine material. Here, for simplicity, we choose to focus on solids exhibiting linear elastic behaviour in the undamaged state. However, the framework is general and can be extended to other constitutive responses, such as hyperelasticity. We shall first derive the partial differential equation (PDE) that characterises the possible solutions for the non-dissipative stored strain energy density ψ_s in linear elastic solids. Then, we consider the failure envelope function that provides the constraint required to obtain a solution to this PDE. The process is exemplified with a Drucker–Prager failure surface, and the section concludes with brief details of the numerical implementation.

As in Ref. [27], the *Theory of Structured Deformations* [35] is applied to a damaged continuum solid. We confine our attention to infinitesimal deformations, such that the total strain tensor can be estimated from the displacement vector as,

$$\boldsymbol{\varepsilon} = \frac{1}{2}\left(\nabla\mathbf{u}^T + \nabla\mathbf{u}\right) \tag{9}$$

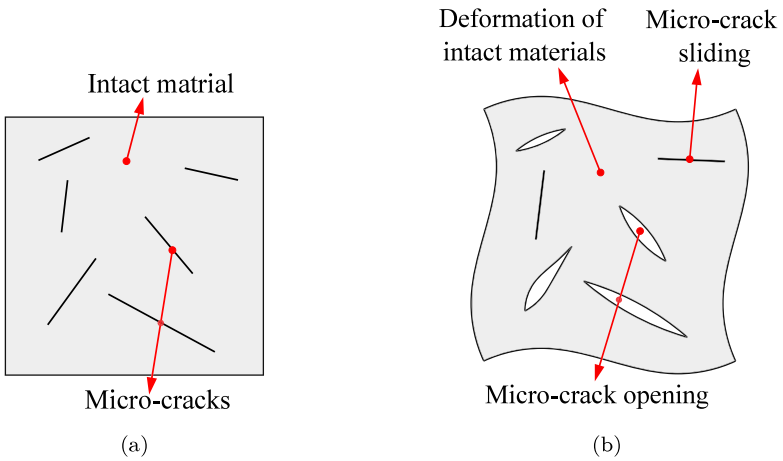

Fig. 1. Meso-scale Representative Volume Element (RVE) of a damaged solid, showing regions of micro-cracks and intact material in the: (a) undeformed, and (b) deformed states, with the latter emphasising the effect of micro-crack opening and sliding.

A Representative Volume Element (RVE) can be defined, see Fig. 1, such that the meso-scale representation of the material involves regions of intact material and micro-cracks. In this context, the phase field ϕ is akin to a damage variable, and describes the integrity of the RVE (the extent of dominance of intact and cracked regions, within the two limiting cases of $\phi = 0$ and $\phi = 1$). The macroscopic deformation is then the sum of two contributions: an elastic straining of the intact material regions, and the opening and sliding of micro-cracks, that can coalescence into macroscopic cracks. Accordingly,

$$\boldsymbol{\varepsilon} = \boldsymbol{\varepsilon}^e + \boldsymbol{\varepsilon}^d\,, \tag{10}$$

where $\boldsymbol{\varepsilon}^e$ are the elastic (recoverable) strains due to the deformation of the undamaged structure, while $\boldsymbol{\varepsilon}^d$ denotes the inelastic strains associated with microscopic damage mechanisms.

The elastic strain tensor $\boldsymbol{\varepsilon}^e$ is related to the Cauchy stress tensor through the inverse of the elastic stiffness matrix $\boldsymbol{\varepsilon}^e = (C_0)^{-1}\,\boldsymbol{\sigma}$ and, if $\boldsymbol{\varepsilon}^e$ and $\boldsymbol{\varepsilon}^d$ are orthogonal, the stored and damaged strain energy densities of effective configuration (see Section 2) can be estimated as,

$$\psi_s = \frac{1}{2}\boldsymbol{\varepsilon}^e C_0 \boldsymbol{\varepsilon}^e \quad \text{and} \quad \psi_d = \frac{1}{2}\boldsymbol{\varepsilon}^d C_0 \boldsymbol{\varepsilon}^d \tag{11}$$

with the total strain energy density ψ being computed from ψ_s and ψ_d using Eq. (6). Now, let us consider the strain energy density of pristine material as a function of the effective stress invariants $(I_1(\boldsymbol{\sigma}_0), J_2(\boldsymbol{\sigma}_0))$;

$$\psi_0(\boldsymbol{\varepsilon}) = \frac{1}{18K} I_1^2(\boldsymbol{\sigma}_0(\boldsymbol{\varepsilon})) + \frac{1}{2\mu} J_2(\boldsymbol{\sigma}_0(\boldsymbol{\varepsilon}))\,, \tag{12}$$

where K is the bulk modulus, μ is the shear modulus, I_1 is the first invariant of a tensor, and J_2 is the second invariant of the deviatoric part of a tensor. Eq. (12) holds for any linear elastic isotropic solid. The stiffness and material behaviour associated with the non-degraded strain energy density ψ^s and stress $\boldsymbol{\sigma}^s$ corresponds to that of intact material and, accordingly,

$$\psi_s = \frac{1}{18K} I_1^2(\boldsymbol{\sigma}^s) + \frac{1}{2\mu} J_2(\boldsymbol{\sigma}^s)\,. \tag{13}$$

Then, for any choice of $\psi(I_1(\boldsymbol{\varepsilon}), J_2(\boldsymbol{\varepsilon}))$, it is possible to describe the relation between the invariants of strain and stress as follows (see Appendix A):

$$I_1(\boldsymbol{\sigma}(\boldsymbol{\varepsilon})) = 3\frac{\partial \psi(\boldsymbol{\varepsilon})}{\partial I_1(\boldsymbol{\varepsilon})}, \quad J_2(\boldsymbol{\sigma}(\boldsymbol{\varepsilon})) = J_2(\boldsymbol{\varepsilon})\left(\frac{\partial \psi(\boldsymbol{\varepsilon})}{\partial J_2(\boldsymbol{\varepsilon})}\right)^2 \tag{14}$$

By substituting Eq. (14) into Eq. (13), one can obtain the PDE for the stored strain energy density,

$$\psi_s = \frac{1}{2K}\left(\frac{\partial \psi_s}{\partial I_1(\boldsymbol{\varepsilon})}\right)^2 + \frac{J_2(\boldsymbol{\varepsilon})}{2\mu}\left(\frac{\partial \psi_s}{\partial J_2(\boldsymbol{\varepsilon})}\right)^2 \tag{15}$$

Upon the appropriate constraints and boundary conditions, one can solve the PDE (15) to obtain the non-dissipative stored part of the strain energy density for any level of material damage. The additional constraint needed comes from the definition of the failure criterion under consideration. Any arbitrary failure envelope can be defined in terms of the stress invariants for the fully damaged state. For illustration, let us consider a failure surface defined in terms of I_1 and J_2; i.e., $f\left(I_1(\boldsymbol{\sigma}^f), J_2(\boldsymbol{\sigma}^f)\right) = 0$, where $\boldsymbol{\sigma}^f = \boldsymbol{\sigma}(\boldsymbol{\varepsilon}, \phi = 1)$. Accordingly, considering Eq. (14), the following failure envelope function can be defined:

$$f\left(\frac{\partial \psi_s(\boldsymbol{\varepsilon})}{\partial I_1(\boldsymbol{\varepsilon})}, \frac{\partial \psi_s(\boldsymbol{\varepsilon})}{\partial J_2(\boldsymbol{\varepsilon})}\right) = 0 \tag{16}$$

and ψ_s can be found from the common solution to Eqs. (15) and (16) upon the application of appropriate boundary conditions. This is showcased below for a Drucker–Prager failure envelope.

3.1. Particularisation to the Drucker–Prager failure surface

Drucker–Prager's failure criterion was developed for pressure-dependent materials like rock, concrete, foams and polymers. In terms of invariants of stress, the Drucker–Prager criterion is expressed as follows,

$$\sqrt{J_2(\boldsymbol{\sigma})} = A + BI_1(\boldsymbol{\sigma})\,, \tag{17}$$

where A and B are a function of the uniaxial tensile (σ_t) and compressive (σ_c) strengths, such that

$$A = \frac{2}{\sqrt{3}}\left(\frac{\sigma_c\sigma_t}{\sigma_c + \sigma_t}\right)\,; \qquad B = \frac{1}{\sqrt{3}}\left(\frac{\sigma_t - \sigma_c}{\sigma_c + \sigma_t}\right)\,. \tag{18}$$

A material point sitting inside the Drucker–Prager failure envelope can be assumed to behave in a linear elastic manner, with damage-driven non-linear behaviour being triggered when the stress state reaches the failure surface. Assuming that the same degradation function $g(\phi)$ applies to the tensile and compressive strengths, then the sensitivity of the parameters A and B to the phase field variable is characterised by,

$$\begin{aligned} A(\phi) &= \frac{2}{\sqrt{3}}\left(\frac{g(\phi)\sigma_c g(\phi)\sigma_t}{g(\phi)\sigma_c + g(\phi)\sigma_t}\right) = g(\phi)\frac{2}{\sqrt{3}}\left(\frac{\sigma_c\sigma_t}{\sigma_c + \sigma_t}\right) = g(\phi)A(\phi = 0) \\ B(\phi) &= \frac{1}{\sqrt{3}}\left(\frac{g(\phi)\sigma_t - g(\phi)\sigma_c}{g(\phi)\sigma_c + g(\phi)\sigma_t}\right) = \frac{1}{\sqrt{3}}\left(\frac{\sigma_t - \sigma_c}{\sigma_c + \sigma_t}\right) = B(\phi = 0) \end{aligned} \tag{19}$$

Accordingly, for the fully damaged state ($\phi = 1$), the Drucker–Prager parameters read,

$$A(\phi = 1) = 0\,; \qquad B(\phi = 1) = B(\phi = 0)\,. \tag{20}$$

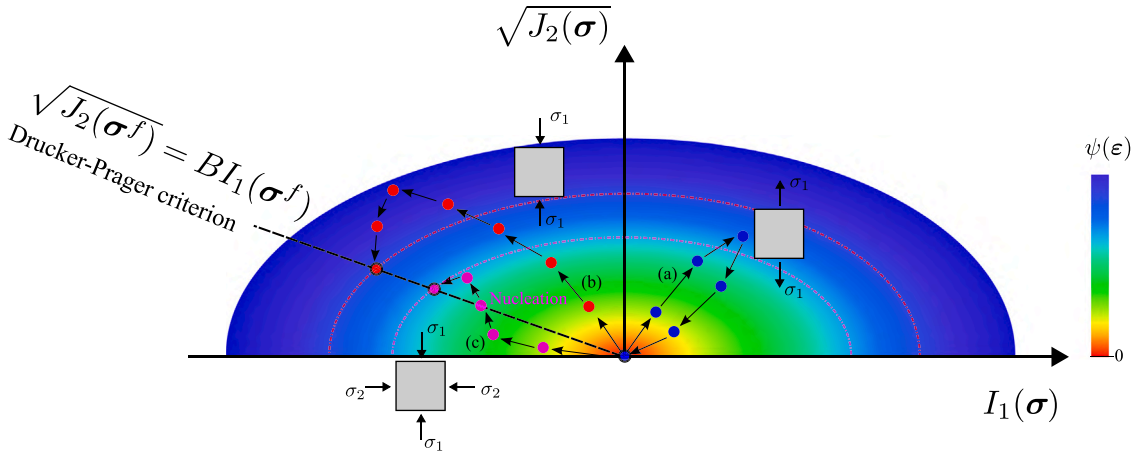

Fig. 2. Stress states in the $\left(I_1(\boldsymbol{\sigma}), \sqrt{J_2(\boldsymbol{\sigma})}\right)$. Three loading paths have been schematically incorporated to showcase the three potential scenarios discussed in Eqs. (27) and (28), and colour contours denote the magnitude of the total strain energy (increasing as we move away from the origin). Circles with an outer black domain denote fully damaged states ($\phi = 1$).

I.e., A is degraded as the phase field evolves, while the parameter B is insensitive to the damage state. This can be physically interpreted through the cohesion parameter c and the friction angle θ of Mohr–Coulomb's criterion, and their relationship with Drucker–Prager's coefficients:

$$A(\theta, c) = \frac{6c\cos\theta}{\sqrt{3}(3+\sin\theta)}; \quad B(\theta) = \frac{2\sin\theta}{\sqrt{3}(3+\sin\theta)}. \tag{21}$$

As seen in Eq. (21), B is only a function of the friction angle, while A is also a function of c, exhibiting a linear relationship with the cohesion parameter. Since damage translates into a loss of cohesion, both A and c degrade with evolving damage, and eventually vanish in fully cracked state.

In addition, consistent with Eq. (17), the stress state in the fully damaged configuration satisfies,

$$\sqrt{J_2(\boldsymbol{\sigma}^f)} = BI_1(\boldsymbol{\sigma}^f), \tag{22}$$

as the stress state goes back to the failure envelope for $\phi = 1$ (see Fig. 2).

As discussed above, our general approach requires a function describing the failure condition in terms of the strain energy density and the strains—see Eq. (16). This can be achieved by combining Eqs. (14) and (22), reaching

$$f\left(\frac{\partial\psi_s(\boldsymbol{\varepsilon})}{\partial I_1(\boldsymbol{\varepsilon})}, \frac{\partial\psi_s(\boldsymbol{\varepsilon})}{\partial J_2(\boldsymbol{\varepsilon})}\right) = \sqrt{J_2(\boldsymbol{\varepsilon})}\frac{\partial\psi_s(\boldsymbol{\varepsilon})}{\partial J_2(\boldsymbol{\varepsilon})} - 3B\frac{\partial\psi_s(\boldsymbol{\varepsilon})}{\partial I_1(\boldsymbol{\varepsilon})} = 0 \tag{23}$$

An isotropic linear elastic material must satisfy Eq. (15) and, if obeying the Drucker–Prager failure criterion, also Eq. (23). Hence, the common solution to these two PDEs will give us the stored (elastic) strain energy density ψ_s. Let us obtain this common solution by first finding the general solution of Eq. (23), which is of the form

$$\psi_s = a_1\left(I_1(\boldsymbol{\varepsilon}) + 6B\sqrt{J_2(\boldsymbol{\varepsilon})}\right)^2 + a_2 \tag{24}$$

where a_1 and a_2 are unknowns. These can be estimated by applying suitable boundary conditions and substituting the general solution into the second PDE. Hence, considering the boundary condition $\psi_s(I_1(\boldsymbol{\varepsilon}) = 0, J_2(\boldsymbol{\varepsilon}) = 0) = 0$, one finds that $a_2 = 0$. Then, the remaining unknown is obtained by deriving Eq. (24) with respect to $I_1(\boldsymbol{\varepsilon})$ and $J_2(\boldsymbol{\varepsilon})$ and substituting into Eq. (15), rendering

$$a_1 = \frac{K\mu}{18B^2K + 2\mu}. \tag{25}$$

Accordingly, upon substitution in Eq. (24), the stored (elastic) strain energy density associated with the Drucker–Prager failure envelope is found to be:

$$\psi_s = \frac{K\mu}{18B^2K + 2\mu}\left(I_1(\boldsymbol{\varepsilon}) + 6B\sqrt{J_2(\boldsymbol{\varepsilon})}\right)^2 \tag{26}$$

However, one should note that Eq. (26) is only valid for stress states that are above the failure envelope. Three potential scenarios exist: (1) the first invariant of stress is positive, $I_1(\boldsymbol{\sigma}) > 0$; (2) the stress state is above the failure criterion, $\sqrt{J_2(\boldsymbol{\sigma})} \geq BI_1(\boldsymbol{\sigma})$; and (3) the stress state is below the failure criterion, $\sqrt{J_2(\boldsymbol{\sigma})} < BI_1(\boldsymbol{\sigma})$. With scenarios (2) and (3) being only relevant when $I_1(\boldsymbol{\sigma}) < 0$. We then proceed to generalise Eq. (26) to encompass those three regimes (see Appendix B), such that

$$\psi_s = \begin{cases} 0 & \text{for} \quad -6B\sqrt{J_2(\boldsymbol{\varepsilon})} < I_1(\boldsymbol{\varepsilon}) \\ \frac{K\mu}{18B^2K+2\mu}\left(I_1(\boldsymbol{\varepsilon}) + 6B\sqrt{J_2(\boldsymbol{\varepsilon})}\right)^2 & \text{for} \quad -6B\sqrt{J_2(\boldsymbol{\varepsilon})} \geq I_1(\boldsymbol{\varepsilon}) \\ & \quad \& \; 2\mu\sqrt{J_2(\boldsymbol{\varepsilon})} \geq 3BKI_1(\boldsymbol{\varepsilon}) \\ \frac{1}{2}KI_1^2(\boldsymbol{\varepsilon}) + 2\mu J_2(\boldsymbol{\varepsilon}) & \text{for} \quad 2\mu\sqrt{J_2(\boldsymbol{\varepsilon})} < 3BKI_1(\boldsymbol{\varepsilon}) \end{cases} \tag{27}$$

And the damaged part of the strain energy density can be readily estimated using Eq. (6), rendering

$$\psi_d = \begin{cases} \frac{1}{2}KI_1^2(\boldsymbol{\varepsilon}) + 2\mu J_2(\boldsymbol{\varepsilon}) & \text{for} \quad -6B\sqrt{J_2(\boldsymbol{\varepsilon})} < I_1(\boldsymbol{\varepsilon}) \\ \frac{1}{18B^2K+2\mu}\left(-3BKI_1(\boldsymbol{\varepsilon}) + 2\mu\sqrt{J_2(\boldsymbol{\varepsilon})}\right)^2 & \text{for} \quad -6B\sqrt{J_2(\boldsymbol{\varepsilon})} \geq I_1(\boldsymbol{\varepsilon}) \\ & \quad \& \; 2\mu\sqrt{J_2(\boldsymbol{\varepsilon})} \geq 3BKI_1(\boldsymbol{\varepsilon}) \\ 0 & \text{for} \quad 2\mu\sqrt{J_2(\boldsymbol{\varepsilon})} < 3BKI_1(\boldsymbol{\varepsilon}) \end{cases} \tag{28}$$

The different stress states are illustrated in Fig. 2 in terms of their location in the $\left(I_1(\boldsymbol{\sigma}), \sqrt{J_2(\boldsymbol{\sigma})}\right)$ space, where the colour contours denote the magnitude of the total strain energy (increasing as we move away from the origin). The loading path illustrated with blue dots, path (a), illustrates the case where the first invariant of stress is positive $I_1(\boldsymbol{\sigma}) > 0$. In such a scenario, the failure process is driven by ψ_d, with the fully damage state achieved by returning to the origin (where the loading path intersects the Drucker–Prager failure criterion). In regards to the stress states on the left side of the figure ($I_1(\boldsymbol{\sigma}) < 0$), their behaviour is differentiated by their location relative to the Drucker–Prager criterion, which is represented by the $\sqrt{J_2(\boldsymbol{\sigma})} = BI_1(\boldsymbol{\sigma})$ line. Thus, the red loading path (b) is above the Drucker–Prager criterion and both ψ_s and ψ_c are active, see Eqs. (27)b and (28)b. Eventually, the loading path intersects again the $\sqrt{J_2(\boldsymbol{\sigma})} = BI_1(\boldsymbol{\sigma})$ line, reaching the fully damaged state and the associated residual strain energy density

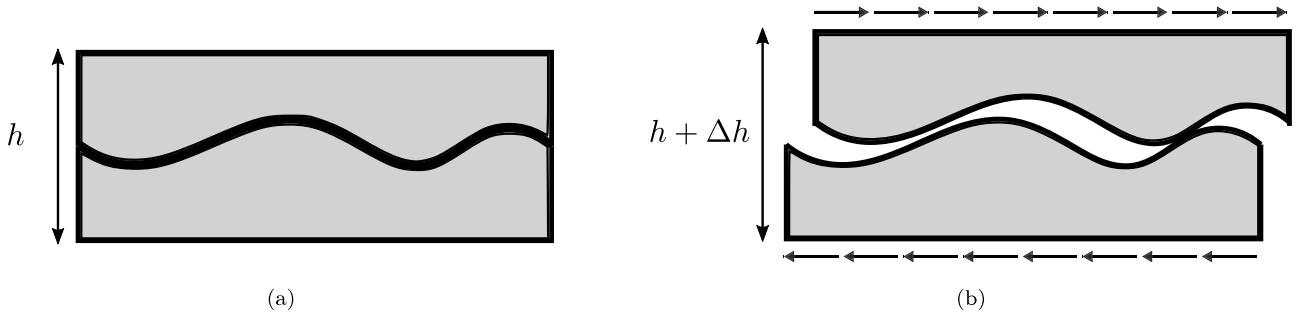

Fig. 3. Sketch showcasing the dilatancy effect on geomaterials, also known as Reynolds dilatancy. Bulk expansion takes place due to the lever motion that occurs between neighbouring grains as a result of interlocking.

ψ_s. Finally, loading paths within the $I_1(\boldsymbol{\sigma}) < 0$ domain can also lie below the failure criterion, as showcased by the purple circles, path (c). In this case, $\psi_d = 0$, see Eq. (28)c, and consequently $\phi = 0$. As shown in Fig. 2, changes in stress state associated with the loading path might lead to an intersection with the Drucker–Prager failure line, in what would constitute a micro-fracturing nucleation event ($\phi > 0$). Subsequently, final rupture ($\phi = 1$) would be attained when the loading path intersects again with the failure line, rendering a residual strain energy density ψ_s.

This phase field fracture formulation built upon Drucker–Prager's failure criterion is numerically implemented using the finite element method. Retaining unconditional stability, we solve in a monolithic fashion the coupled system of equations that results from restating the local force balances,

$$\begin{aligned} &\nabla \cdot \left[(1-\phi)^2 \frac{\partial \psi_d(\boldsymbol{\varepsilon})}{\partial \boldsymbol{\varepsilon}} + \frac{\partial \psi_s(\boldsymbol{\varepsilon})}{\partial \boldsymbol{\varepsilon}}\right] = \mathbf{0} \quad \text{in} \quad \Omega \\ &G_c \left(\frac{\phi}{\ell} - \ell \nabla^2 \phi\right) - 2(1-\phi)\mathcal{H} = 0 \quad \text{in} \quad \Omega \end{aligned} \tag{29}$$

into their weak form. Here, $\mathcal{H} = \max \psi_d(t)$ is a history field introduced to enforce damage irreversibility [26]. As described in Appendix C, we take advantage of the analogy between the phase field evolution law and the heat transfer equation to implement the model into the finite element package ABAQUS using solely a user-material subroutine (UMAT) (see Refs. [36,37]).

4. Representative results

Now, we shall illustrate the potential of enriching the phase field fracture description with a failure envelope of our choice. Specifically, through numerical examples, we will showcase how a formulation based on the Drucker–Prager failure criterion can capture the compressive failure of brittle materials such as concrete or geomaterials, along with capturing frictional behaviour and the dilatancy effect. Firstly, in Section 4.1, we gain insight into the material behaviour resulting from the Drucker–Prager strain energy split adopted by investigating the response of a single element undergoing shear. Secondly, numerical experiments using the Direct Shear Test (DST) configuration are conducted in Section 4.2. The goal is to investigate the fracture predictions obtained under the conditions relevant to the determination of the failure properties of frictional materials. The third case study, shown in Section 4.3, involves conducting virtual uniaxial and triaxial compression tests on concrete, so as to investigate the confinement effect. Finally, in Section 4.4, the predictions obtained from three strain energy splits are compared in the modelling of the localised failure of a soil slope. Our finite element calculations extend the very recent analytical study by de Lorenzis and Maurini [33], where a Drucker–Prager failure surface was also adopted.

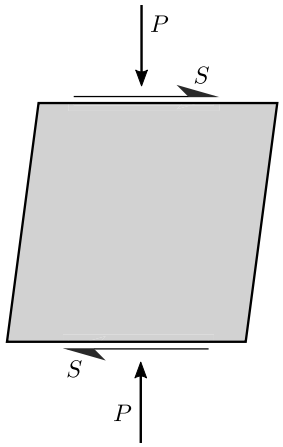

Fig. 4. Configuration of a single element under pressure and shear stress.

4.1. Single element under shear deformation

We begin our numerical experiments by conducting shear tests on a single element. The aim is to investigate the ability of the Drucker–Prager based formulation presented in capturing frictional behaviour and the dilatancy effect. The latter is the volume change observed in granular materials subjected to shear deformations, due to the interlocking between grains and interfaces (see Fig. 3).

As shown in Fig. 4, a single plane strain element is considered undergoing both shear and uniaxial pressure. Specifically, a vertical constant pressure is first applied, followed by shear displacement at the top and bottom edges. In this and all other case studies, the Neumann boundary condition $\nabla\phi \cdot \mathbf{n} = 0$ is adopted for the phase field. The constitutive behaviour of the element is characterised by linear elasticity, with a Young's modulus of $E = 25$ GPa and a Poisson's ratio of $\nu = 0.2$. The fracture behaviour is described by a material toughness of $G_c = 0.15$ kJ/m^2 and a phase field length scale of $\ell = 2$ mm.

We aim at assessing the frictional behaviour of the model, for which it is convenient to formulate the relation between the shear strain ε_{xy} and the shear stress σ_{xy}, as a function of the pressure and Drucker–Prager's B parameter. For the fully damaged state ($\phi = 1$), this relation reads

$$(\sigma_f)_{xy} = \frac{\partial \psi_c(\boldsymbol{\varepsilon})}{\partial \varepsilon_{xy}} = \frac{K\mu}{9B^2K + \mu}\left(\frac{I_1(\boldsymbol{\varepsilon})}{\sqrt{J_2(\boldsymbol{\varepsilon})}} + 6B\right)\varepsilon_{xy} \tag{30}$$

First, let us consider the case of no pressure ($P = 0$). Fig. 5(a) shows the shear stress versus shear strain curves obtained for different B values. The role played by damage evolution can be readily observed, with calculations obtained for low absolute B values exhibiting a peak in the shear stress response. For the fully cracked state ($\phi = 1$), the shear stress drops to zero only if $B = 0$. Hence, the expected influence

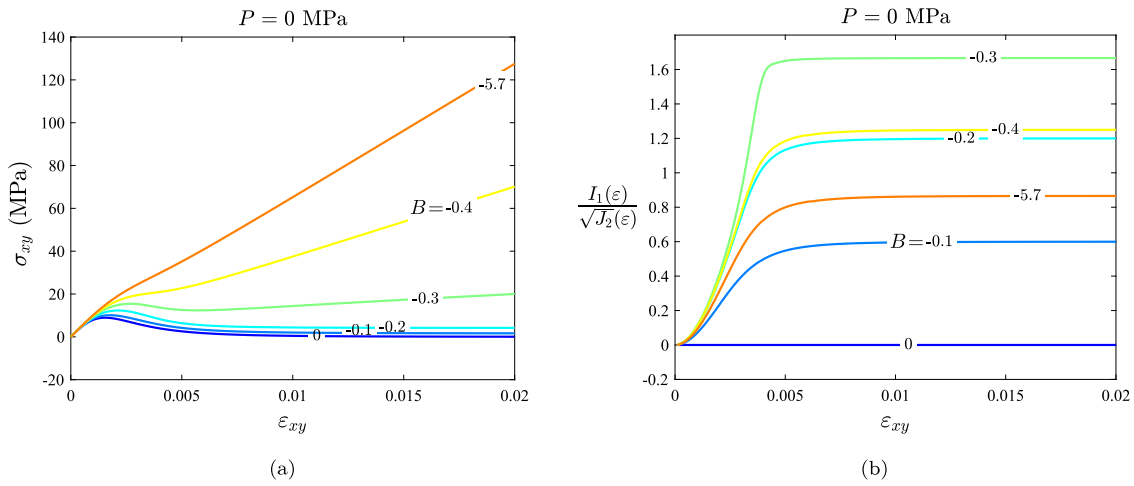

Fig. 5. Single element under shear deformation. Results obtained without vertical pressure ($P = 0$ MPa) for selected choices of B: (a) shear stress σ_{xy} versus shear strain ϵ_{xy}, and (b) $I_1(\boldsymbol{\epsilon})/\sqrt{J_2(\boldsymbol{\epsilon})}$ versus shear strain ϵ_{xy}.

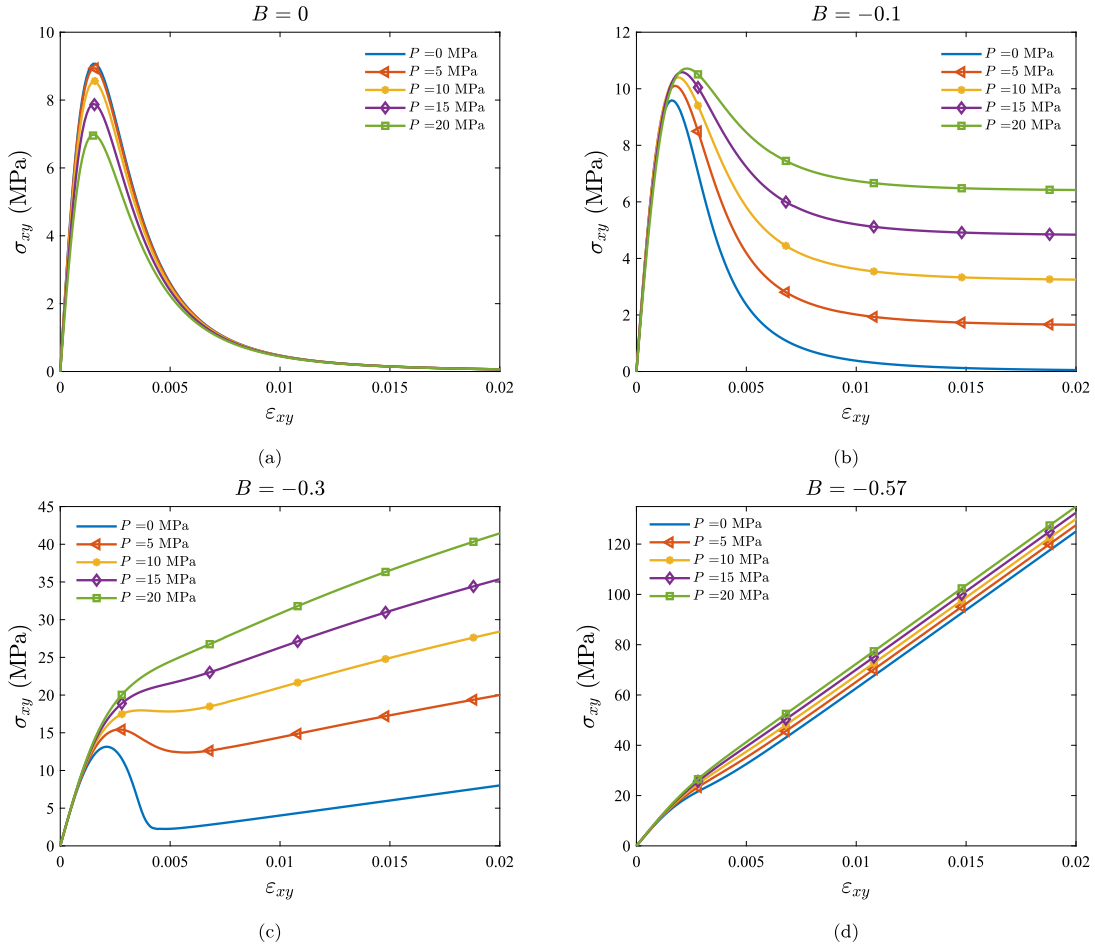

Fig. 6. Single element under shear deformation. Shear stress versus shear strain predictions as a function of P for selected values of the B parameter: (a) $B = 0$, (b) $B = -0.1$, (c) $B = -0.3$, and (c) $B = -0.57$.

of dilatancy on the stress–strain curve is attained for $B \neq 0$, and the effect increases with increasing its absolute magnitude ($|B|$). This load bearing capacity that is retained after reaching the fully cracked state due to dilatancy arises due to two contributions. One is the term $6B$ in Eq. (30). The second one is the term $I_1(\boldsymbol{\epsilon})/\sqrt{J_2(\boldsymbol{\epsilon})}$ - as shown in Fig. 5(b), it attains a positive constant value for $\phi = 1$ and $B \neq 0$. However, the relation between B and $I_1(\boldsymbol{\epsilon})/\sqrt{J_2(\boldsymbol{\epsilon})}$ is non-linear.

Next, the influence of vertical pressure is examined. The results obtained for selected values of P and B are shown in Fig. 6. For the case of $B = 0$ (Fig. 6(a)), the shear stress shows a negligible sensitivity to the vertical pressure and no frictional effect (σ_{xy} drops to zero as $\phi \to 1$). The peak stress value shows some sensitivity to P due to the interplay between damage and the applied pressure. The results seen for $B = 0$ contrast with those obtained for non-zero B values (Figs. 6b–d). For

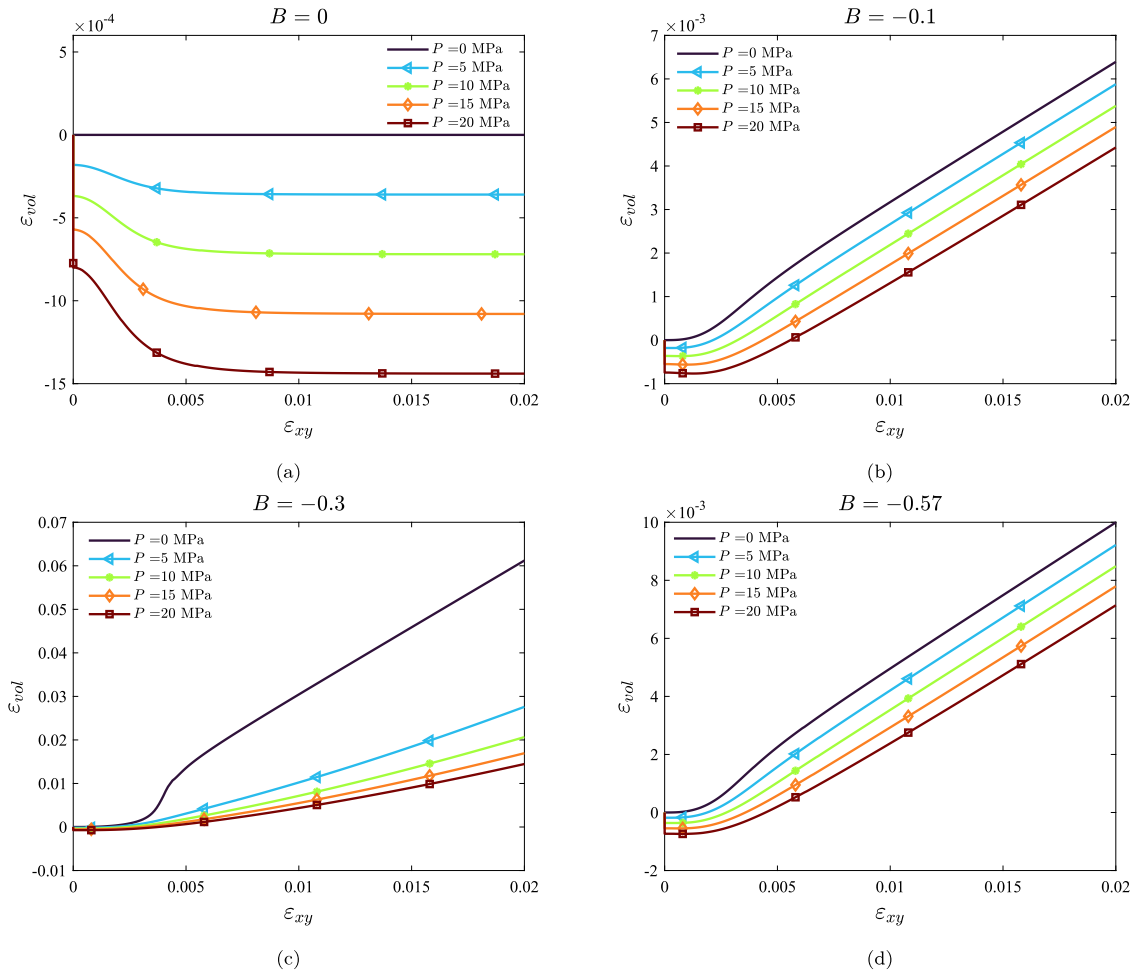

Fig. 7. Single element under shear deformation. Volumetric strain versus shear strain predictions as a function of P for selected values of the B parameter: (a) $B = 0$, (b) $B = -0.1$, (c) $B = -0.3$, and (c) $B = -0.57$.

$B \neq 0$, friction plays a noticeable role with the shear stress increasing with P. Also, the slope of the shear stress–strain curve increases with the absolute value of B.

The ability of the Drucker–Prager based split model to capture the dilatancy effect is further explored by plotting the predictions of volumetric strain $\varepsilon_{vol} = \varepsilon_{xx} + \varepsilon_{yy} + \varepsilon_{zz}$ for selected values of the parameter B and the applied pressure P. As shown in Fig. 7, the volumetric strain ε_{vol} increases with the shear strain ε_{xy} in all cases except for that of $B = 0$. The effect of dilatancy is clear in all $B \neq 0$ calculations (Fig. 7b–d). In addition, the results show that higher pressures lead to reductions in volume as a result of material damage.

4.2. Virtual Direct Shear Tests (DST)

Next, the Direct Shear Test (DST) is simulated to evaluate the model behaviour in an experimental configuration that is widely used for finding the frictional parameters of soil and rock materials, such as cohesion and friction angle. The geometry and boundary conditions of the model are shown in Fig. 8. A vertical pressure P is applied at the top edge, followed by a horizontal displacement u_x over a 24 mm long region of the left edge. We consider three scenarios to assess the role of the vertical pressure: $P = 20$ MPa, $P = 10$ MPa and no pressure ($P = 0$). The elastic properties are taken as $E = 25$ GPa and $\nu = 0.2$, while the fracture parameters are given by $G_c = 0.15$ kJ/m^2 and $\ell = 0.2$ mm. The model is discretised with approximately 80,000 4-node plane strain quadrilateral elements with full integration. The mesh is refined along the expected crack propagation region, such that the characteristic element size is at least half of the phase field length scale ℓ.

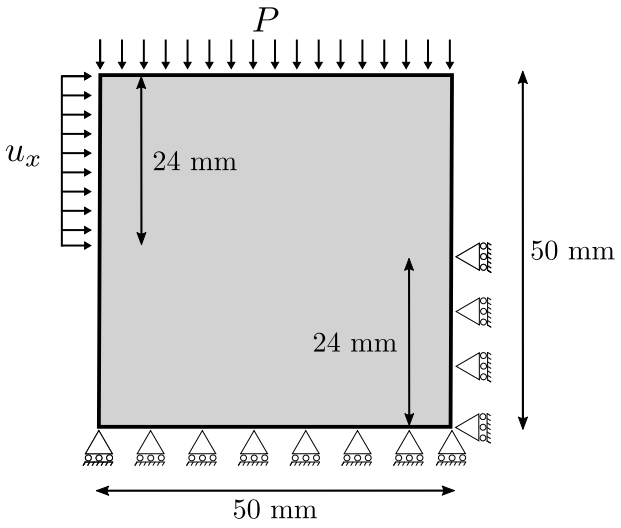

Fig. 8. Direct shear test (DST) model. Geometry and boundary conditions.

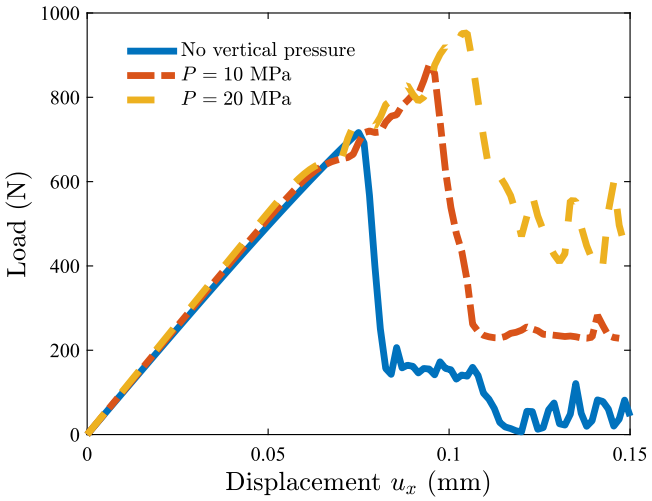

Fig. 9. Direct shear test (DST). Shear load versus applied displacement results as a function of the applied pressure P.

The results obtained are shown in Fig. 9, in terms of the shear force versus the applied displacement u_x, and as a function of the applied pressure P. The case of no pressure shows a complete drop of the load carrying capacity as a result of damage, in agreement with experimental DST observations on geomaterials. However, a residual load is retained when a vertical pressure is applied, and this increases with the magnitude of P. Also, in all cases some oscillations can be seen in the force versus displacement response, which can be attributed to the effect of grain interlocking.

Finally, the predicted crack trajectories are shown in Fig. 10, as a function of P, by plotting contours of the phase field order parameter ϕ. The results reveal an influence of the applied pressure on the cracking pattern. The lower the vertical pressure the more tortuous the crack path. Also, increasing the applied pressure leads to an accumulation of damage at the edges of the loading region, which are then connected through a crack that propagates across the sample.

4.3. Uniaxial and triaxial compression testing of concrete

The third case study involves the failure of concrete samples undergoing uniaxial and triaxial compression. The aim is to investigate the abilities of the Drucker–Prager formulation presented to capture the effect of confinement. Mimicking the commonly used experimental setup, a cylindrical specimen is subjected to a compressive displacement at the top, while its surface is subjected to a confinement pressure. In the numerical model, we take advantage of axial symmetry and simulate a 2D section of the sample. The dimensions and loading configuration of the model are given in Fig. 11. To reproduce with fidelity the experimental conditions, we choose to simulate the contact between the jaws and the concrete sample. The jaws are assumed to be made of steel, with elastic properties $E = 210$ GPa and $\nu = 0.3$. The contact between the jaws and the disc is defined as a surface to surface contact with a finite sliding formulation. The tangential contact behaviour is assumed to be frictionless while the normal behaviour is based on a hard contact scheme, where the contact constraint is enforced with a Lagrange multiplier representing the contact pressure in a mixed formulation. The material properties of concrete are taken to be $E = 25$ GPa, $\nu = 0.2$, $\ell = 0.4$ mm, $G_c = 0.15$ kJ/m^2, and $B = -0.12$. Linear quadrilateral axisymmetric elements are used to discretise the model. In particular, approximately 35,000 elements are used to discretise the concrete sample while 1500 elements are employed in each of the jaws. The characteristic element size in the areas of interest is below 0.2 mm, half of the phase field length scale. The ratio between the applied pressure and the prescribed displacement equals $P/u_y = 10$ MPa/mm.

The force versus displacement responses predicted with and without a confinement pressure are shown in Fig. 12. It can be seen that, in agreement with expectations, the application of a confinement pressure increases the magnitude of the critical load. The ultimate strength of the sample with confinement is found to be almost 40% higher than the unconfined one. Also, a more brittle behaviour is observed in the unconfined sample, with a sharper drop in the load carrying capacity at the moment of failure.

Qualitative differences are found between the cracking patterns observed for the confined and unconfined experiments. As shown in Fig. 13, in the unconfined specimen the crack starts from the edge and propagates gradually towards the centre, creating a cone shape fracture. This is in agreement with the cracking patterns observed experimentally for brittle solids in the absence of confinement [38,39]. However, in the confined specimen, see Fig. 14, the crack nucleates at the centre of the sample and then propagates towards the surface, exhibiting a double shear failure mode. Such a cracking pattern has also been reported in experiments conducted under confinement pressures [39]. Of interest for future work is the analysis of the influence of friction between the sample and the compression plates, which can be readily be incorporated into the present framework and has been argued to influence cracking patterns [28,40].

4.4. Localised failure of a soil slope

Finally, in our last case study, we compare the predictions of the Drucker–Prager strain energy decomposition formulation to those obtained with what are arguably the most widely use strain energy decompositions in the literature: the volumetric–deviatoric split by Amor et al. [25] and the spectral decomposition by Miehe and co-workers [26]. First, the damaged and stored (elastic) strain energy

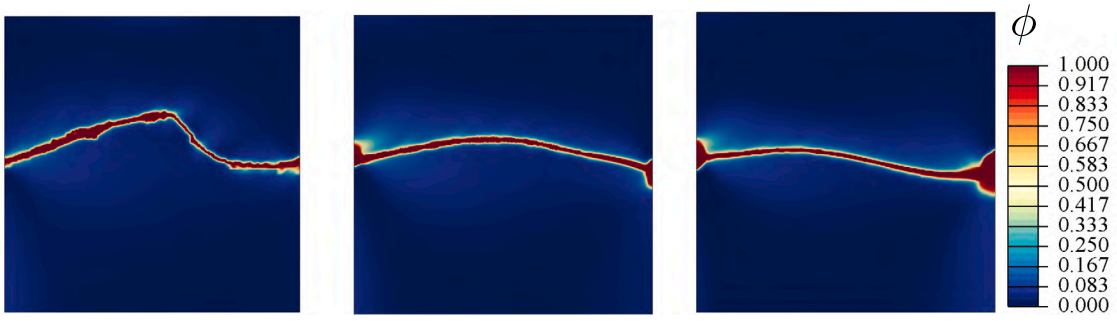

(a) $P = 0$ MPa (b) $P = 10$ MPa (c) $P = 20$ MPa

Fig. 10. Direct shear test (DST). Predicted cracking patterns, as shown through contours of the phase field ϕ for selected values of the applied pressure: (a) $P = 0$, (b) $P = 10$ MPa, and (c) $P = 20$ MPa.

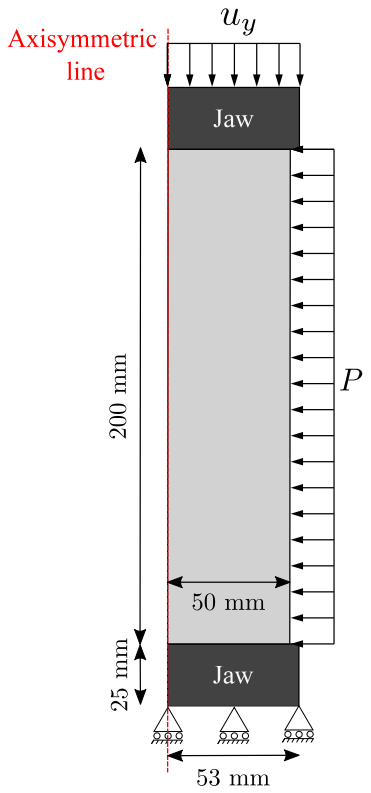

Fig. 11. Compressive failure of concrete. Model geometry, dimensions and boundary conditions.

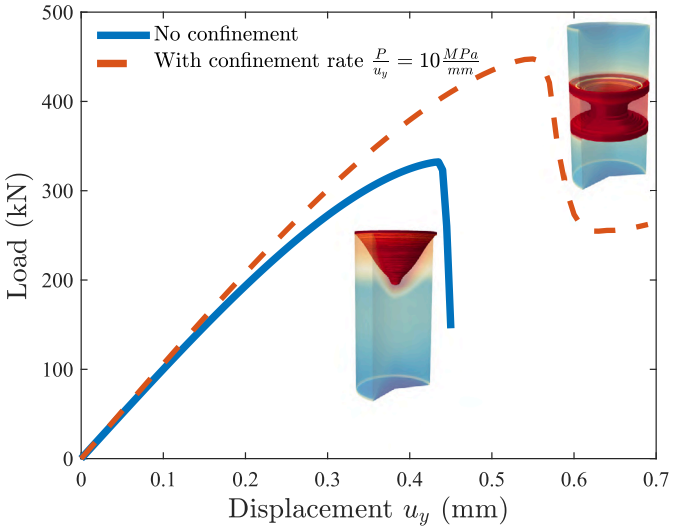

Fig. 12. Compressive failure of concrete. Predicted load versus displacement curves for a sample without confinement pressure and one with a confinement pressure-prescribed displacement ratio of $P/u_y = 10$ MPa/mm.

densities are defined for these two approaches, following the terminology of Section 2. Thus, the volumetric–deviatoric split is characterised by,

$$\psi_d(\boldsymbol{\varepsilon}) = \frac{1}{2}K\langle \mathrm{tr}(\boldsymbol{\varepsilon})\rangle_+^2 + \mu\left(\boldsymbol{\varepsilon}' : \boldsymbol{\varepsilon}'\right), \qquad \psi_s(\boldsymbol{\varepsilon}) = \frac{1}{2}K\langle \mathrm{tr}(\boldsymbol{\varepsilon})\rangle_-^2. \tag{31}$$

Here, $\langle a\rangle_\pm = (a \pm |a|)/2$, and $\boldsymbol{\varepsilon}' = \boldsymbol{\varepsilon} - \mathrm{tr}(\boldsymbol{\varepsilon})\boldsymbol{I}/3$. While the strain energy decomposition by Miehe et al. [26] reads,

$$\psi_d(\boldsymbol{\varepsilon}) = \frac{1}{2}\lambda\langle \mathrm{tr}(\boldsymbol{\varepsilon})\rangle_+^2 + \mu\mathrm{tr}\left[\left(\boldsymbol{\varepsilon}^+\right)^2\right], \qquad \psi_s(\boldsymbol{\varepsilon}) = \frac{1}{2}\lambda\langle \mathrm{tr}(\boldsymbol{\varepsilon})\rangle_-^2 + \mu\mathrm{tr}\left[(\boldsymbol{\varepsilon}^-)^2\right], \tag{32}$$

where a spectral decomposition is applied to the strain tensor, such that $\boldsymbol{\varepsilon}^\pm = \sum_{a=1}^3 \langle \varepsilon_I\rangle_\pm \mathbf{n}_I \otimes \mathbf{n}_I$, with ε_I and $\mathbf{n}_I$ being, respectively, the principal strains and principal strain directions (with $I = 1, 2, 3$).

The boundary value problem under consideration is inspired by the work by Regueiro and Borja [41], where a strong discontinuity approach was used to predict the stability of a soil slope. This problem was also recently investigated by Fei and Choo [42] using a phase field-based frictional shear fracture model. The geometry, dimensions and boundary conditions are given in Fig. 15. A rigid foundation is placed at the crest of the slope, as shown in Fig. 15. First, a gravity load is applied, followed by a vertical displacement that is prescribed at the centre of the rigid foundation. The material properties of the soil are given by $E = 10$ MPa, $\nu = 0.4$, $\ell = 0.1$ m, $G_c = 0.2$ kJ/m^2, and $B = 0.12$. Approximately 50,000 quadrilateral linear elements are used, with the mesh being refined in the crack propagation region through an iterative process. In all cases, the characteristic size of the elements in the damaged region is five times smaller than the phase field length scale ℓ.

The results obtained are given in Fig. 16. The cracking patterns are shown for each of the three strain energy decompositions considered, by means of contours of the phase field order parameter ϕ. As shown in Fig. 16a, the volumetric–deviatoric split by Amor et al. [25] predicts a localised failure under the rigid foundation. The spectral decomposition by Miehe and co-workers [26] is also unable to adequately capture the localised failure of the soil slope. As shown in Fig. 16b, damage accumulates under the rigid foundation, showing a V-type of failure. On the other hand, the Drucker–Prager formulation presented in Section 3 is able to appropriately simulate the localised failure of the soil slope. Cracking initiates from the right corner of the foundation and propagates towards the edge of the slope, in a very similar pattern to that reported by other numerical experiments [41,42].

5. Discussion

The aim of the present work is to present a general approach to decompose the phase field fracture driving force, the strain energy density, so as to encompass any arbitrary choice of failure criteria. One important motivation for this work lies in the need to enrich the phase field fracture method to go beyond its assumed symmetric tension–compression fracture behaviour to adequately predict crack nucleation and growth in multi-axial stress states. The potential of the general methodology presented is demonstrating by particularising it to the Drucker–Prager failure surface. In doing so, we establish a connection with the recent work by De Lorenzis and Maurini [33]. De Lorenzis and Maurini [33] showed analytically that phase field fracture can be generalised to accommodate arbitrary multiaxial failure surfaces and thus faithfully predict crack nucleation without the need to recur to non-variational models. They also chose to particularise their approach to a Drucker–Prager failure surface. Thus, both works reach the same theoretical outcome from different angles. Since our paper also includes a numerical implementation, it complements and extends the work by De Lorenzis and Maurini [33], confirming their findings. It is also worth noting that our analysis is not limited to nucleation but also considers the propagation of cracks until failure. To achieve this, it is here assumed that the same surface in the multiaxial stress space characterises the limit of the elastic domain ($\phi > 0$) and the fully damaged state ($\phi = 1$). Several numerical experiments are reported to showcase the ability of the model to predict crack nucleation and growth in boundary value problems exhibiting multi-axial loading and mixed-mode fracture conditions. An alternative approach is that proposed by Kumar et al. [43], where an external driving force is defined to recover a Drucker–Prager failure surface. However, this comes at the cost of losing the variational consistency.

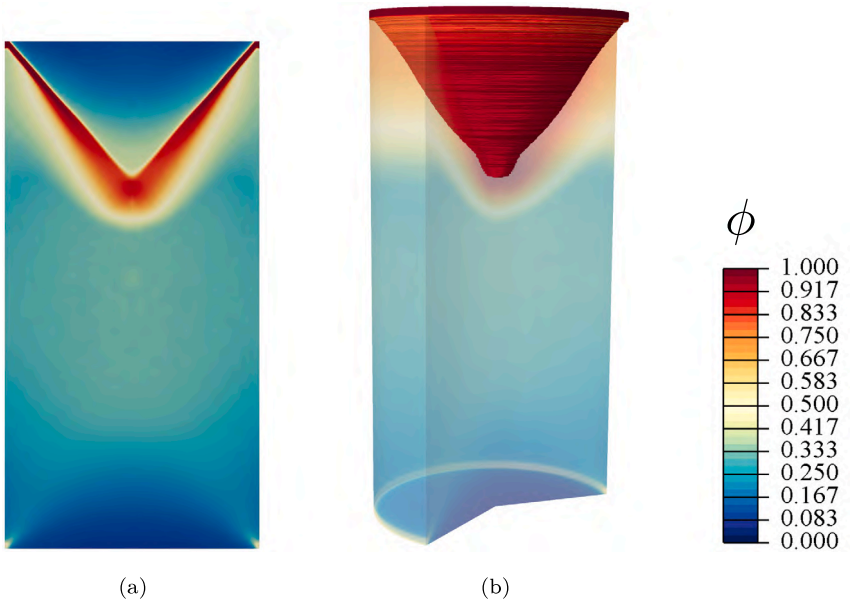

Fig. 13. Compressive failure of concrete. Cracking patterns for the unconfined sample, as described by the phase field ϕ contours: (a) axisymmetric 2D results, and (b) 3D visualisation.

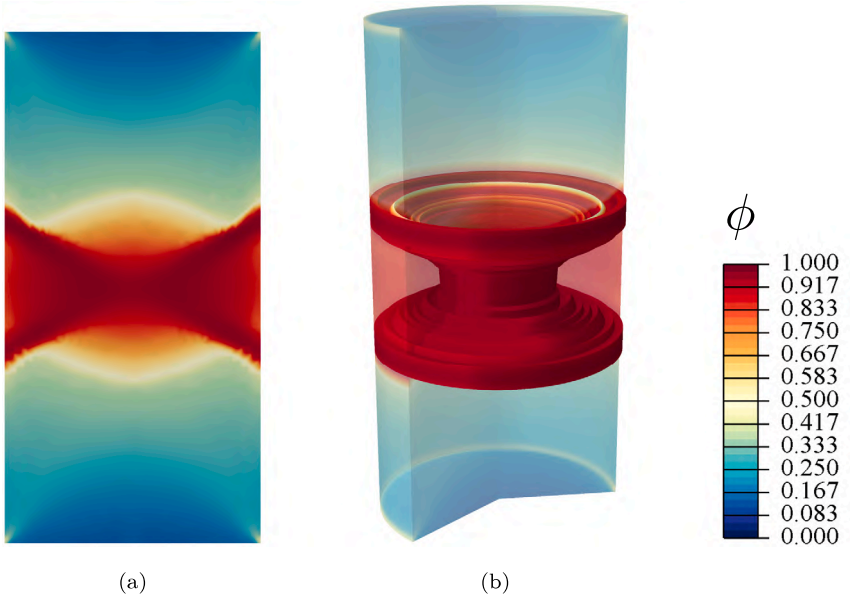

Fig. 14. Compressive failure of concrete. Cracking patterns for the confined sample, as described by the phase field ϕ contours: (a) axisymmetric 2D results, and (b) 3D visualisation. The ratio between the applied pressure and the prescribed displacement equals $P/u_y = 10$ MPa/mm.

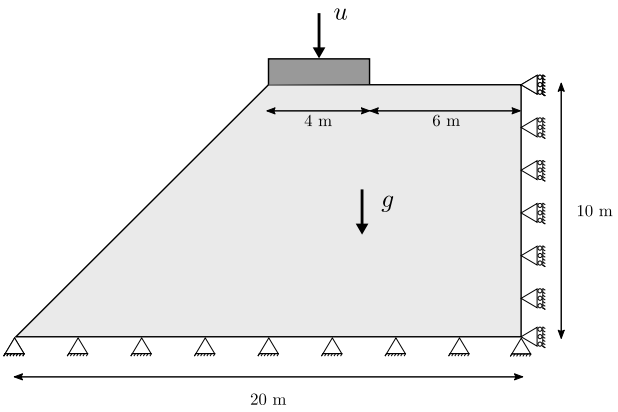

Fig. 15. Localised failure of a soil slope. Geometry and boundary conditions.

6. Conclusions

We have presented a general framework for determining the strain energy decomposition associated with arbitrary choices of constitutive behaviour and failure criterion. This is of importance for phase field fracture modelling as it opens a new avenue for incorporating multi-axial failure surfaces and thus appropriately capturing crack nucleation in a wide range of materials. In particular, this is needed to predict the compressive failure of brittle and quasi-brittle solids such as concrete and geomaterials. Accordingly, we chose to illustrate our framework by particularising it to the case of a Drucker–Prager failure surface. We numerically implemented the resulting formulation for the strain energy decomposition and used it to simulate fracture phenomena in brittle materials. Specifically, the potential of the Drucker–Prager based formulation presented was showcased by addressing four paradigmatic case studies. The behaviour of a single element undergoing shear deformations and vertical pressure was investigated first. The results showed that the model is capable of capturing the role of friction and dilatancy. The magnitude of the shear stresses attained was highest for higher values of the pressure and of Drucker–Prager's parameter B. Direct Shear Tests (DST) were subsequently simulated showing a noticeable influence of the applied pressure. The lower the pressure, the more tortuous the crack path and the lower the magnitude of the residual load predicted. Thirdly, the failure of cylindrical samples under uniaxial and triaxial compression was investigated. The results revealed a qualitative impact of the confinement pressure on both the cracking patterns and the force versus displacement response predicted. Cracking predictions appear to agree with experimental observations, shifting from a cone shape fracture to a double shear failure mode with increasing confinement. Finally, we simulated the localised failure of a soil slope using three different strain energy splits: our Drucker–Prager approach and the widely used volumetric–deviatoric [25] and spectral [26] decompositions. The results show that only the Drucker–Prager based formulation is able to adequately predict the fracture behaviour. Accordingly, the present work: (i) opens a new avenue for incorporating multi-axial failure criteria in phase field fracture modelling, and (ii) demonstrates the potential of Drucker–Prager based phase field formulations for predicting compressive failures in materials exhibiting asymmetric tension–compression fracture behaviour.

CRediT authorship contribution statement

Yousef Navidtehrani: Conceptualization, Methodology, Software, Validation, Formal analysis, Investigation, Data curation, Writing – original draft, Visualization. **Covadonga Betegón:** Conceptualization, Writing – review & editing, Supervision, Project administration, Funding acquisition. **Emilio Martínez-Pañeda:** Conceptualization, Methodology, Software, Investigation, Resources, Writing – review & editing, Supervision, Project administration, Funding acquisition.

Declaration of competing interest

The authors declare that they have no known competing financial interests or personal relationships that could have appeared to influence the work reported in this paper.

Data availability

Data will be made available on request.

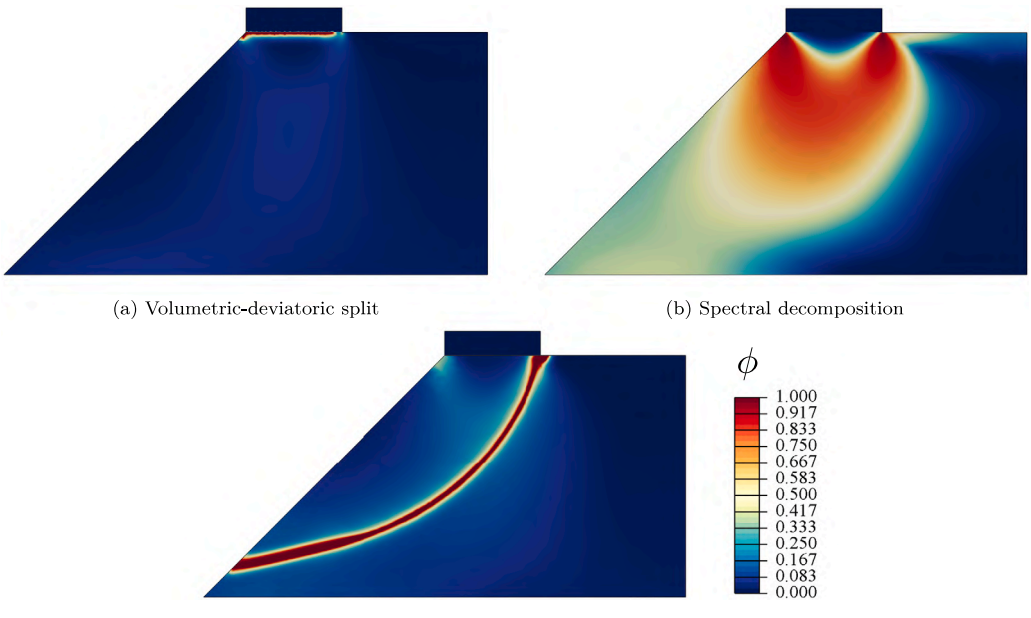

Fig. 16. Localised failure of a soil slope. Failure patterns as described by the contours of the phase field order parameter for: (a) the volumetric–deviatoric split, Eq. (31), (b) the spectral decomposition, Eq. (32), and (c) the Drucker–Prager based split presented, Eqs. (27)–(28).

Acknowledgements

The authors acknowledge financial support from the Ministry of Science, Innovation and Universities of Spain through grant PGC2018-099695-B-I00. E. Martínez-Pañeda was supported by an UKRI Future Leaders Fellowship (grant MR/V024124/1).

Appendix A. The relation of stress and strain invariants

In the following, we shall show how Eq. (14) can be derived for any choice of strain energy density in the form of $\psi(I_1(\boldsymbol{\varepsilon}), J_2(\boldsymbol{\varepsilon}))$. First, let us express the Cauchy stress as:

$$\begin{aligned}\boldsymbol{\sigma}(\boldsymbol{\varepsilon}) &= \frac{\partial \psi(I_1(\boldsymbol{\varepsilon}), J_2(\boldsymbol{\varepsilon}))}{\partial \boldsymbol{\varepsilon}} \\ &= \frac{\partial \psi(I_1(\boldsymbol{\varepsilon}), J_2(\boldsymbol{\varepsilon}))}{\partial I_1(\boldsymbol{\varepsilon})}\frac{\partial I_1(\boldsymbol{\varepsilon})}{\partial \boldsymbol{\varepsilon}} + \frac{\partial \psi(I_1(\boldsymbol{\varepsilon}), J_2(\boldsymbol{\varepsilon}))}{\partial J_2(\boldsymbol{\varepsilon})}\frac{\partial J_2(\boldsymbol{\varepsilon})}{\partial \boldsymbol{\varepsilon}}.\end{aligned} \tag{A.1}$$

The variations of the first two invariants of the strain tensor are written as,

$$\frac{\partial I_1(\boldsymbol{\varepsilon})}{\partial \boldsymbol{\varepsilon}} = \boldsymbol{I}, \quad \frac{\partial J_2(\boldsymbol{\varepsilon})}{\partial \boldsymbol{\varepsilon}} = \boldsymbol{\varepsilon}' \tag{A.2}$$

where $\boldsymbol{I}$ denotes the identity tensor and $\boldsymbol{\varepsilon}'$ is the deviatoric part of strain tensor. On the other side, the first invariant of the Cauchy stress tensor is given by

$$\begin{aligned}I_1(\boldsymbol{\sigma}) &= \mathrm{tr}(\boldsymbol{\sigma}) = \mathrm{tr}\left(\frac{\partial \psi(I_1(\boldsymbol{\varepsilon}), J_2(\boldsymbol{\varepsilon}))}{\partial \boldsymbol{\varepsilon}}\right) \\ &= \frac{\partial \psi(I_1(\boldsymbol{\varepsilon}), J_2(\boldsymbol{\varepsilon}))}{\partial I_1(\boldsymbol{\varepsilon})}\mathrm{tr}\left(\frac{\partial I_1(\boldsymbol{\varepsilon})}{\partial \boldsymbol{\varepsilon}}\right) + \frac{\partial \psi(I_1(\boldsymbol{\varepsilon}), J_2(\boldsymbol{\varepsilon}))}{\partial J_2(\boldsymbol{\varepsilon})}\mathrm{tr}\left(\frac{\partial J_2(\boldsymbol{\varepsilon})}{\partial \boldsymbol{\varepsilon}}\right)\end{aligned} \tag{A.3}$$

Eq. (A.3) can be simplified by considering $\mathrm{tr}\left(\partial I_1(\boldsymbol{\varepsilon})/\partial \boldsymbol{\varepsilon}\right) = 3$ and $\mathrm{tr}\left(\partial J_2(\boldsymbol{\varepsilon})/\partial \boldsymbol{\varepsilon}\right) = 0$, such that

$$I_1(\boldsymbol{\sigma}) = 3\frac{\partial \psi(I_1(\boldsymbol{\varepsilon}), J_2(\boldsymbol{\varepsilon}))}{\partial I_1(\boldsymbol{\varepsilon})}. \tag{A.4}$$

which corresponds to Eq. (14)a, the equation relating the first invariant of stress $I_1(\boldsymbol{\sigma})$ with the first invariant of strain $I_1(\boldsymbol{\varepsilon})$. Next, we use Eqs. (A.1) and (A.4) to formulate the deviatoric part of the Cauchy stress tensor $\boldsymbol{\sigma}'$ as

$$\boldsymbol{\sigma}' = \boldsymbol{\sigma} - \frac{1}{3}\mathrm{tr}(\boldsymbol{\sigma})\,\boldsymbol{I} = \boldsymbol{\varepsilon}'\frac{\partial \psi(I_1(\boldsymbol{\varepsilon}), J_2(\boldsymbol{\varepsilon}))}{\partial J_2(\boldsymbol{\varepsilon})}. \tag{A.5}$$

Then, Eq. (14)b, relating the second stress invariant $J_2(\boldsymbol{\sigma})$ with its strain-based counterpart $J_2(\boldsymbol{\varepsilon})$ can be obtained by substituting Eq. (A.5) into the definition of $J_2(\boldsymbol{\sigma})$, rendering

$$\begin{aligned}J_2(\boldsymbol{\sigma}) &= \frac{1}{2}\mathrm{tr}\left((\boldsymbol{\sigma}')^2\right) = \frac{1}{2}\mathrm{tr}\left((\boldsymbol{\varepsilon}')^2\right)\left(\frac{\partial \psi(I_1(\boldsymbol{\varepsilon}), J_2(\boldsymbol{\varepsilon}))}{\partial J_2(\boldsymbol{\varepsilon})}\right)^2 \\ &= J_2(\boldsymbol{\varepsilon})\left(\frac{\partial \psi(I_1(\boldsymbol{\varepsilon}), J_2(\boldsymbol{\varepsilon}))}{\partial J_2(\boldsymbol{\varepsilon})}\right)^2.\end{aligned} \tag{A.6}$$

Appendix B. Strain-based mapping of the stress state scenarios

Any relevant stress state can be classified as one of three potential scenarios in the $(I_1(\boldsymbol{\sigma}),\ \sqrt{J_2(\boldsymbol{\sigma})})$ stress space. However, for numerical reasons, the stored (reversible) ψ_s and damaged ψ_d strain energy densities are formulated in terms of the strain tensor $\boldsymbol{\varepsilon}$, see Eqs. (27)–(28). Thus, for completeness, we proceed to describe the derivation of Eqs. (27)–(28) for the stress scenarios discussed in Section 3.

Consider first the third regime, given by Eqs. (27)c and (28)c, where $I_1(\boldsymbol{\sigma}) < 0$ and the stress state is below the failure envelope. Under these conditions, damage does not evolve and consequently the stored part of the strain energy density equals the total one $\psi_s(\boldsymbol{\varepsilon}) = \psi_0(\boldsymbol{\varepsilon})$. Specifically, the stress state in this regime fulfils the following:

$$\sqrt{J_2(\boldsymbol{\sigma})} < BI_1(\boldsymbol{\sigma}) \quad \text{and} \quad I_1(\boldsymbol{\sigma}) \leq 0. \tag{B.1}$$

Where the stress invariants can be written as,

$$\begin{aligned}I_1(\boldsymbol{\sigma}) &= 3\frac{\partial \psi(\boldsymbol{\varepsilon})}{\partial I_1(\boldsymbol{\varepsilon})} = 3\ g(\phi)\frac{\partial \psi_0(\boldsymbol{\varepsilon})}{\partial I_1(\boldsymbol{\varepsilon})} + 3(1-g(\phi))\frac{\partial \psi_s(\boldsymbol{\varepsilon})}{\partial I_1(\boldsymbol{\varepsilon})}, \\ J_2(\boldsymbol{\sigma}) &= J_2(\boldsymbol{\varepsilon})\left(\frac{\partial \psi(\boldsymbol{\varepsilon})}{\partial J_2(\boldsymbol{\varepsilon})}\right)^2 = g(\phi)J_2(\boldsymbol{\varepsilon})\left(\frac{\partial \psi_0(\boldsymbol{\varepsilon})}{\partial J_2(\boldsymbol{\varepsilon})}\right)^2 \\ &\quad + (1-g(\phi))J_2(\boldsymbol{\varepsilon})\left(\frac{\partial \psi_s(\boldsymbol{\varepsilon})}{\partial J_2(\boldsymbol{\varepsilon})}\right)^2.\end{aligned} \tag{B.2}$$

Considering that, in this scenario, $\psi_s(\boldsymbol{\varepsilon}) \equiv \psi_0(\boldsymbol{\varepsilon})$ and inserting Eq. (B.2) into the first condition of Eq. (B.1), one reaches

$$\sqrt{J_2(\boldsymbol{\varepsilon})}\frac{\partial \psi_0(\boldsymbol{\varepsilon})}{\partial J_2(\boldsymbol{\varepsilon})} < 3B\frac{\partial \psi_0(\boldsymbol{\varepsilon})}{\partial I_1(\boldsymbol{\varepsilon})} \tag{B.3}$$

Now, recalling the definition of ψ_0, Eq. (13), Eq. (B.3) can be re-formulated as

$$2\mu\sqrt{J_2(\boldsymbol{\varepsilon})} < 3BKI_1(\boldsymbol{\varepsilon}) \tag{B.4}$$

On the other side, the second condition of Eq. (B.1) can be described as a function of the strain tensor as follows,

$$3\frac{\partial \psi_0(\boldsymbol{\varepsilon})}{\partial I_1(\boldsymbol{\varepsilon})} \leq 0 \tag{B.5}$$

Implying that $I_1(\boldsymbol{\varepsilon}) \leq 0$. However, this has already been satisfied by Eq. (B.4) as $\sqrt{J_2(\boldsymbol{\varepsilon})}$ is a positive value and the parameter B is always zero or negative, such that $I_1(\boldsymbol{\varepsilon})$ must be negative to satisfy Eq. (B.3).

The second regime in the $(I_1(\boldsymbol{\sigma}),\ \sqrt{J_2(\boldsymbol{\sigma})})$ stress space corresponds to that where $I_1(\boldsymbol{\sigma}) \leq 0$ and the stress state is above the failure criterion; i.e.,

$$\sqrt{J_2(\boldsymbol{\sigma})} \geq BI_1(\boldsymbol{\sigma}) \quad \text{and} \quad I_1(\boldsymbol{\sigma}) \leq 0. \tag{B.6}$$

Given that Eq. (B.3) provides the strain condition for the case where the stress state is below the failure criterion, it follows that the relevant condition for the second regime where the stress state is above the failure criterion is given by

$$2\mu\sqrt{J_2(\boldsymbol{\varepsilon})} \geq 3BI_1(\boldsymbol{\varepsilon}) \tag{B.7}$$

Then, the second condition in Eq. (B.6) can be expressed as:

$$g(\phi)KI_1(\boldsymbol{\varepsilon}) + \frac{K\mu}{9B^2K+\mu}(1-g(\phi))\left(I_1(\boldsymbol{\varepsilon}) + 6B\sqrt{J_2(\boldsymbol{\varepsilon})}\right) \leq 0. \tag{B.8}$$

Which, considering that $g(\phi = 1) = 0$, can be reduced to,

$$I_1(\boldsymbol{\varepsilon}) \leq -6B\sqrt{J_2(\boldsymbol{\varepsilon})} \tag{B.9}$$

Accordingly, the conditions for the second regime, in terms of the strain tensor, are given by (B.7) and (B.9).

The remaining conditions are applicable for the first regime in the stress space, where $I_1(\boldsymbol{\sigma})$ is positive:

$$\mu\sqrt{J_2(\boldsymbol{\varepsilon})} \geq 3BKI_1(\boldsymbol{\varepsilon}); \qquad -6B\sqrt{J_2(\boldsymbol{\varepsilon})} < I_1(\boldsymbol{\varepsilon}), \tag{B.10}$$

where the first condition can be neglected as it is satisfied by the second one.

Appendix C. Additional details of the finite element implementation

C.1. Strong and weak formulations

Considering Eq. (2) and the constitutive choices in Eq. (3), Griffith's regularised energy functional can be formulated as,

$$\mathcal{E}_\ell = \int_\Omega \psi_s(\boldsymbol{\varepsilon}(\mathbf{u})) + (1-\phi)^2\psi_d(\boldsymbol{\varepsilon}(\mathbf{u}))\,\mathrm{d}V + \int_V G_c\left(\frac{1}{2\ell}\phi^2 + \frac{\ell}{2}|\nabla\phi|^2\right)\mathrm{d}V \tag{C.1}$$

The stationary of $\mathcal{E}_\ell$ with respect to the primal kinematic variables renders,

$$\partial\mathcal{E}_\ell = \int_\Omega \left\{ \left[(1-\phi)^2 \frac{\partial \psi_d(\boldsymbol{\varepsilon})}{\partial \boldsymbol{\varepsilon}} + \frac{\partial \psi_s(\boldsymbol{\varepsilon})}{\partial \boldsymbol{\varepsilon}} \right] \delta\boldsymbol{\varepsilon} - 2(1-\phi)\delta\phi\psi_d(\boldsymbol{\varepsilon}) + G_c \left[\frac{1}{\ell}\phi\delta\phi + \ell \nabla\phi\cdot\nabla\delta\phi \right] \right\} \mathrm{d}V \tag{C.2}$$

Accordingly, the strong form can be readily derived by considering the variation in the external work,

$$\delta W_{ext} = \int_\Omega \mathbf{b}\cdot\delta\mathbf{u}\mathrm{d}V + \int_{\partial\Omega_h} \mathbf{h}\cdot\delta\mathbf{u}\mathrm{d}A \tag{C.3}$$

enforcing equilibrium of the external and internal virtual works,

$$\partial\mathcal{E}_\ell - \delta W_{ext} = 0 \tag{C.4}$$

and making use of Gauss' divergence theorem,

$$\begin{aligned} &\nabla\cdot\left[(1-\phi)^2 \frac{\partial \psi_d(\boldsymbol{\varepsilon})}{\partial \boldsymbol{\varepsilon}} + \frac{\partial \psi_s(\boldsymbol{\varepsilon})}{\partial \boldsymbol{\varepsilon}} \right] + \mathbf{b} = \mathbf{0} \quad \text{in} \quad \Omega \\ &G_c\left(\frac{\phi}{\ell} - \ell\nabla^2\phi \right) - 2(1-\phi)\psi_d = 0 \quad \text{in} \quad \Omega \end{aligned} \tag{C.5}$$

C.2. Heat transfer analogy

As discussed in Refs. [36,37], we exploit the analogy with heat transfer to facilitate the numerical implementation of the phase field evolution equation. In the presence of a heat source r, the steady state equation for heat transfer has the following form,

$$k\nabla^2 T = -r \tag{C.6}$$

where T is the temperature, and k is the thermal conductivity. Eq. (C.6) is analogous to the phase field evolution equation ((C.5)b) upon assuming $T \equiv \phi$, $k = 1$, and defining the heat source r as follows:

$$r = \frac{2(1-\phi)\mathcal{H}}{\ell G_c} - \frac{\phi}{\ell^2} \tag{C.7}$$

where, as discussed in Section 3, $\mathcal{H} = \max \psi_d(t)$ is a history field introduced to enforce damage irreversibility. Finally, the variation of the heat source with respect to the phase field (temperature) is derived as,

$$\frac{\partial r}{\partial \phi} = -\frac{2\mathcal{H}}{\ell G_c} - \frac{1}{\ell^2} \tag{C.8}$$

C.3. Finite element discretisation

By exploiting the heat transfer analogy, one can implement the phase field formulation described in this paper into the finite element package ABAQUS using only a user material subroutine (UMAT). I.e., there is no need to explicitly define and implement the element stiffness matrix $\boldsymbol{K}^e$ and the element residual vector $\boldsymbol{R}^e$. However, these are derived here for completeness. Consider the equilibrium of the external and internal virtual works presented in Appendix C.1. Decoupling the displacement and phase field problems, the weak form equations read,

$$\int_\Omega \left\{ \left[(1-\phi)^2 \frac{\partial \psi_d(\boldsymbol{\varepsilon})}{\partial \boldsymbol{\varepsilon}} + \frac{\partial \psi_s(\boldsymbol{\varepsilon})}{\partial \boldsymbol{\varepsilon}} \right] : \delta\boldsymbol{\varepsilon} - \mathbf{b}\cdot\delta\mathbf{u} \right\} \mathrm{d}V - \int_{\partial\Omega_h} \mathbf{h}\cdot\delta\mathbf{u}\mathrm{d}A = 0\,. \tag{C.9}$$

$$\int_\Omega \left\{ -2(1-\phi)\delta\phi\,\mathcal{H} + G_c\left[\frac{1}{\ell}\phi\delta\phi + \ell\nabla\phi\nabla\delta\phi \right] \right\} \mathrm{d}V = 0\,. \tag{C.10}$$

Now, consider the following finite element discretisation. Adopting Voigt notation, the nodal variables for the displacement field $\hat{\mathbf{u}}$, and the phase field $\hat{\phi}$ are interpolated as:

$$\mathbf{u} = \sum_{i=1}^{m} \boldsymbol{N}_i\hat{\mathbf{u}}_i, \qquad \phi = \sum_{i=1}^{m} N_i\hat{\phi}_i\,, \tag{C.11}$$

where N_i is the shape function associated with node i and $\boldsymbol{N}_i$ is the shape function matrix, a diagonal matrix with N_i in the diagonal terms. Also, m is the total number of nodes per element and $\hat{\mathbf{u}}_i$ and $\hat{\phi}_i$ respectively denote the displacement and phase field at node i. In a similar manner, the associated gradient quantities can be discretised using the corresponding **B**-matrices, containing the derivative of the shape functions, such that:

$$\boldsymbol{\varepsilon} = \sum_{i=1}^{m} \boldsymbol{B}_i^{\mathbf{u}}\hat{\mathbf{u}}_i, \qquad \nabla\phi = \sum_{i=1}^{m} \mathbf{B}_i\hat{\phi}_i\,. \tag{C.12}$$

The discretised residuals for each primal kinematic variable are then given by:

$$\begin{aligned} \mathbf{R}_i^{\mathbf{u}} = &\int_\Omega \left\{ (1-\phi)^2 \left(\boldsymbol{B}_i^{\mathbf{u}}\right)^T \frac{\partial \psi_d(\boldsymbol{\varepsilon})}{\partial \boldsymbol{\varepsilon}} + \left(\boldsymbol{B}_i^{\mathbf{u}}\right)^T \frac{\partial \psi_s(\boldsymbol{\varepsilon})}{\partial \boldsymbol{\varepsilon}} \right\} \mathrm{d}V \\ &- \int_\Omega \left(\mathbf{N}_i^{\mathbf{u}}\right)^T \mathbf{b}\mathrm{d}V - \int_{\partial\Omega_h} \left(\mathbf{N}_i^{\mathbf{u}}\right)^T \mathbf{h}\mathrm{d}A, \end{aligned} \tag{C.13}$$

$$\mathbf{R}_i^{\phi} = \int_\Omega \left\{ -2(1-\phi)N_i\mathcal{H} + G_c\left[\frac{1}{\ell}N_i\phi + \ell\left(\mathbf{B}_i^{\phi}\right)^T\nabla\phi \right] \right\} \mathrm{d}V \tag{C.14}$$

And the consistent tangent stiffness matrices $\boldsymbol{K}$ are obtained by differentiating the residuals with respect to the incremental nodal variables:

$$\boldsymbol{K}_{ij}^{\mathbf{u}} = \frac{\partial \boldsymbol{R}_i^{\boldsymbol{u}}}{\partial \boldsymbol{u}_j} = \int_\Omega \left\{ (1-\phi)^2 (\boldsymbol{B}_i^{\boldsymbol{u}})^T \boldsymbol{C}_d\, \boldsymbol{B}_j^{\boldsymbol{u}} + (\boldsymbol{B}_i^{\boldsymbol{u}})^T \boldsymbol{C}_s\, \boldsymbol{B}_j^{\boldsymbol{u}} \right\} \mathrm{d}V\,, \tag{C.15}$$

$$\boldsymbol{K}_{ij}^{\phi} = \frac{\partial R_i^{\phi}}{\partial \phi_j} = \int_\Omega \left\{ \left(2\mathcal{H} + \frac{G_c}{\ell} \right) N_i N_j + G_c\ell\, \mathbf{B}_i^T\mathbf{B}_j \right\} \mathrm{d}V\,, \tag{C.16}$$

Here, the material Jacobian $\boldsymbol{C}_s$ can be defined as:

$$\boldsymbol{C}_s = \frac{\partial \psi_s}{\partial \boldsymbol{\varepsilon}\partial \boldsymbol{\varepsilon}} = \begin{cases} 0 & \text{for } -6B\sqrt{J_2(\boldsymbol{\varepsilon})} < I_1(\boldsymbol{\varepsilon}) \\ \boldsymbol{C}_s^{DP} & \text{for } -6B\sqrt{J_2(\boldsymbol{\varepsilon})} \geq I_1(\boldsymbol{\varepsilon}) \;\&\; 2\mu\sqrt{J_2(\boldsymbol{\varepsilon})} \geq 3BKI_1(\boldsymbol{\varepsilon}) \\ \boldsymbol{C}_0 & \text{for } 2\mu\sqrt{J_2(\boldsymbol{\varepsilon})} < 3BKI_1(\boldsymbol{\varepsilon}) \end{cases} \tag{C.17}$$

where $\boldsymbol{C}_0$ is undamaged elastic tangent stiffness and $\boldsymbol{C}_s^{DP}$ can be written as:

$$\begin{aligned} (C_s^{DP})_{ijkl} = &\frac{K\mu}{9B^2K+\mu}\left(\frac{\partial I_1}{\partial \varepsilon_{ij}} + \frac{3B}{\sqrt{J_2}}\frac{\partial J_2}{\partial \varepsilon_{ij}} \right)\left(\frac{\partial I_1}{\partial \varepsilon_{kl}} + \frac{3B}{\sqrt{J_2}}\frac{\partial J_2}{\partial \varepsilon_{Kl}} \right) + \\ &\left(\frac{6Ba_1\left(I_1 + 6B\sqrt{J_2}\right)}{\sqrt{J_2}} \right)\left(\frac{\partial^2 J_2}{\partial \varepsilon_{ij}\partial \varepsilon_{kl}} - \frac{1}{2J_2}\frac{\partial J_2}{\partial \varepsilon_{ij}}\frac{\partial J_2}{\partial \varepsilon_{kl}} \right) \end{aligned} \tag{C.18}$$

Finally, $\boldsymbol{C}_d$ is obtained by exploiting the fact that $\psi_d = \psi_0 - \psi_s$:

$$\boldsymbol{C}_d = \frac{\partial \psi_d}{\partial \boldsymbol{\varepsilon}\partial \boldsymbol{\varepsilon}} = \frac{\partial \psi_0}{\partial \boldsymbol{\varepsilon}\partial \boldsymbol{\varepsilon}} - \frac{\partial \psi_s}{\partial \boldsymbol{\varepsilon}\partial \boldsymbol{\varepsilon}} = \boldsymbol{C}_0 - \boldsymbol{C}_s \tag{C.19}$$

References

[1] B. Bourdin, G.A. Francfort, J.J. Marigo, The variational approach to fracture, Springer Netherlands, 2008.

[2] A.J. Pons, A. Karma, Helical crack-front instability in mixed-mode fracture, Nature 464 (7285) (2010) 85–89.

[3] M.J. Borden, C.V. Verhoosel, M.A. Scott, T.J.R. Hughes, C.M. Landis, A phase-field description of dynamic brittle fracture, Comput. Methods Appl. Mech. Eng. 217-220 (2012) 77–95.

[4] P.K. Kristensen, E. Martínez-Pañeda, Phase field fracture modelling using quasi-Newton methods and a new adaptive step scheme, Theor. Appl. Fract. Mech. 107 (2020) 102446.

[5] M.J. Borden, T.J.R. Hughes, C.M. Landis, A. Anvari, I.J. Lee, A phase-field formulation for fracture in ductile materials: Finite deformation balance law derivation plastic degradation, and stress triaxiality effects, Comput. Methods Appl. Mech. Eng. 312 (2016) 130–166.

[6] S.S. Shishvan, S. Assadpour-asl, E. Martínez-Pañeda, A mechanism-based gradient damage model for metallic fracture, Eng. Fract. Mech. 255 (2021) 107927.

[7] Hirshikesh S. Natarajan, R.K. Annabattula, E. Martínez-Pañeda, Phase field modelling of crack propagation in functionally graded materials, Composites B 169 (2019) 239–248.
[8] A. Quintanas-Corominas, A. Turon, J. Reinoso, E. Casoni, M. Paggi, J.A. Mayugo, A phase field approach enhanced with a cohesive zone model for modeling delamination induced by matrix cracking, Comput. Methods Appl. Mech. Engrg. 358 (2020) 112618.
[9] W. Tan, E. Martínez-Pañeda, Phase field fracture predictions of microscopic bridging behaviour of composite materials, Compos. Struct. 286 (2022) 115242.
[10] M. Simoes, E. Martínez-Pañeda, Phase field modelling of fracture and fatigue in shape memory alloys, Comput. Methods Appl. Mech. Engrg. 373 (2021) 113504.
[11] M. Simoes, C. Braithwaite, A. Makaya, E. Martínez-Pañeda, Modelling fatigue crack growth in shape memory alloys, Fatigue Fract. Eng. Mater. Struct. 45 (2022) 1243–1257.
[12] W. Tan, E. Martínez-Pañeda, Phase field predictions of microscopic fracture and R-curve behaviour of fibre-reinforced composites, Compos. Sci. Technol. 202 (2021) 108539.
[13] P.K.A.V. Kumar, A. Dean, J. Reinoso, P. Lenarda, M. Paggi, Phase field modeling of fracture in functionally graded materials: G -convergence and mechanical insight on the effect of grading, Thin-Walled Struct. 159 (2021) 107234.
[14] P. Carrara, M. Ambati, R. Alessi, L. De Lorenzis, A framework to model the fatigue behavior of brittle materials based on a variational phase-field approach, Comput. Methods Appl. Mech. Engrg. 361 (2020) 112731.
[15] Z. Khalil, A.Y. Elghazouli, E. Martínez-Pañeda, A generalised phase field model for fatigue crack growth in elastic – plastic solids with an efficient monolithic solver, Comput. Methods Appl. Mech. Engrg. 388 (2022) 114286.
[16] E. Martínez-Pañeda, A. Golahmar, C.F. Niordson, A phase field formulation for hydrogen assisted cracking, Comput. Methods Appl. Mech. Engrg. 342 (2018) 742–761.
[17] J.-Y. Wu, T.K. Mandal, V.P. Nguyen, A phase-field regularized cohesive zone model for hydrogen assisted cracking, Comput. Methods Appl. Mech. Engrg. 358 (2020) 112614.
[18] J.-Y. Wu, V.P. Nguyen, C.T. Nguyen, D. Sutula, S. Sinaie, S. Bordas, Phase-field modelling of fracture, Adv. Appl. Mech. 53 (2020) 1–183.
[19] P.K. Kristensen, C.F. Niordson, E. Martínez-Pañeda, An assessment of phase field fracture: crack initiation and growth, Phil. Trans. R. Soc. A 379 (2021) 20210021.
[20] A.A. Griffith, The phenomena of rupture and flow in solids, Philos. Trans. A 221 (1920) 163–198.
[21] Y. Navidtehrani, C. Betegón, R.W. Zimmerman, E. Martínez-Pañeda, Griffith-based analysis of crack initiation location in a brazilian test, Int. J. Rock Mech. Min. Sci. (2022) in press.
[22] C.G. Sammis, M.F. Ashby, The failure of brittle porous solids under compressive stress states, Acta Metall. 34 (3) (1986) 511–526.
[23] G.A. Francfort, J.-J. Marigo, Revisiting brittle fracture as an energy minimization problem, J. Mech. Phys. Solids 46 (8) (1998) 1319–1342.
[24] B. Bourdin, G.A. Francfort, J.-J. Marigo, Numerical experiments in revisited brittle fracture, J. Mech. Phys. Solids 48 (4) (2000) 797–826.
[25] H. Amor, J.J. Marigo, C. Maurini, Regularized formulation of the variational brittle fracture with unilateral contact: Numerical experiments, J. Mech. Phys. Solids 57 (8) (2009) 1209–1229.
[26] C. Miehe, M. Hofacker, F. Welschinger, A phase field model for rate-independent crack propagation: Robust algorithmic implementation based on operator splits, Comput. Methods Appl. Mech. Engrg. 199 (45–48) (2010) 2765–2778.
[27] F. Freddi, G. Royer-Carfagni, Regularized variational theories of fracture: A unified approach, J. Mech. Phys. Solids 58 (8) (2010) 1154–1174.
[28] F. Freddi, G. Royer-Carfagni, Variational fracture mechanics to model compressive splitting of masonry-like materials, Ann. Solid Struct. Mech. 2 (2–4) (2011) 57–67.
[29] Y.S. Lo, M.J. Borden, K. Ravi-Chandar, C.M. Landis, A phase-field model for fatigue crack growth, J. Mech. Phys. Solids 132 (2019) 103684.
[30] J. Choo, W.C. Sun, Coupled phase-field and plasticity modeling of geological materials: From brittle fracture to ductile flow, Comput. Methods Appl. Mech. Engrg. 330 (2018) 1–32.
[31] S. Zhou, X. Zhuang, T. Rabczuk, Phase field modeling of brittle compressive-shear fractures in rock-like materials: A new driving force and a hybrid formulation, Comput. Methods Appl. Mech. Engrg. 355 (2019) 729–752.
[32] T. Wang, X. Ye, Z. Liu, D. Chu, Z. Zhuang, Modeling the dynamic and quasi-static compression-shear failure of brittle materials by explicit phase field method, Comput. Mech. 64 (6) (2019) 1537–1556.
[33] L.D. Lorenzis, C. Maurini, Nucleation under multi-axial loading in variational phase-field models of brittle fracture, Int. J. Fract. (2022) in press.
[34] D.C. Drucker, W. Prager, Soil mechanics and plastic analysis for limit design, Quart. Appl. Math. 10 (2) (1952) 157–165.
[35] G. Del Piero, D.R. Owen, Structured deformations of continua, Arch. Ration. Mech. Anal. 124 (2) (1993) 99–155.
[36] Y. Navidtehrani, C. Betegón, E. Martínez-Pañeda, A unified abaqus implementation of the phase field fracture method using only a user material subroutine, Materials 14 (8) (2021) 1913.
[37] Y. Navidtehrani, C. Betegón, E. Martínez-Pañeda, A simple and robust abaqus implementation of the phase field fracture method, Appl. Eng. Sci. 6 (2021) 100050.
[38] D.D. Pollard, R.C. Fletcher, Fundamentals of Structural Geology, Cambridge University Press, 2010.
[39] K. Hoshhino, Mechanical properties of Japanese Tertiary sedimentary rocks under high confining pressures, Tech. rep., 1972.
[40] J. Jaeger, N. Cook, R. Zimmerman, Fundamentals of rock mechanics, Blackwell Publishing, Oxford, UK, 2009.
[41] R.A. Regueiro, R.I. Borja, Plane strain finite element analysis of pressure sensitive plasticity with strong discontinuity, Int. J. Solids Struct. 38 (21) (2001) 3647–3672.
[42] F. Fei, J. Choo, A phase-field model of frictional shear fracture in geologic materials, Comput. Methods Appl. Mech. Engrg. 369 (2020) 113265.
[43] A. Kumar, B. Bourdin, G.A. Francfort, O. Lopez-Pamies, Revisiting nucleation in the phase-field approach to brittle fracture, J. Mech. Phys. Solids 142 (2020) 104027.

F | Paper 6

A generalised framework for phase field-based modelling of coupled problems: application to thermo-mechanical fracture, hydraulic fracture, hydrogen embrittlement and corrosion

Authors:

Yousef Navidtehrani, Covadonga Betegón, Emilio Martínez-Pañeda

Journal:

Engineering Fracture Mechanics journal

Year of Publication:

2025

Impact Factor:

4.7 - Q1

212

Engineering Fracture Mechanics 326 (2025) 111363

Contents lists available at ScienceDirect

Engineering Fracture Mechanics

journal homepage: www.elsevier.com/locate/engfracmech

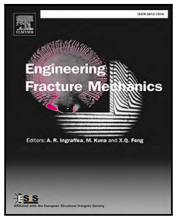

A generalised framework for phase field-based modelling of coupled problems: Application to thermo-mechanical fracture, hydraulic fracture, hydrogen embrittlement and corrosion

Yousef Navidtehrani [a], Covadonga Betegón [a], Emilio Martínez-Pañeda [b,*]

[a] Department of Construction and Manufacturing Engineering, University of Oviedo, Gijón 33203, Spain
[b] Department of Engineering Science, University of Oxford, Oxford OX1 3PJ, UK

ARTICLE INFO

Keywords:
Phase field
Multiphysics modelling
Abaqus
Hydraulic fracture
Thermo-mechanical fracture
Stress corrosion cracking

ABSTRACT

We present a novel, generalised formulation to treat coupled structural integrity problems by combining phase field and multi-physics modelling. The approach exploits the versatility of the heat transfer equation and is therefore well suited to be adopted in commercial finite element packages, requiring only integration point-level implementation. This aspect is demonstrated here by implementing coupled, multi-variable phenomena through simple `UMAT` and `UMATHT` subroutines in the finite element package `Abaqus`. The generalised theoretical and computational framework presented is particularised to four problems of engineering and scientific relevance: thermo-mechanical fracture, hydraulic fracture, hydrogen-assisted cracking and metallic corrosion. 2D and 3D problems are considered. The results reveal a very good agreement with experimental data, and existing numerical and analytical solutions. The user subroutines developed are made freely available at https://mechmat.web.ox.ac.uk/codes.

1. Introduction

Phase field models are enjoying remarkable popularity. Grounded on the foundational work by John W. Cahn and John E. Hilliard [1], the phase field paradigm exploits a diffuse representation of otherwise sharp interfaces to capture complex morphologies and transitions, based on variational principles. The versatility of phase field models has led to their widespread adoption across science and engineering disciplines, including solidification and phase transformations [2], general microstructural evolution problems [3], voiding in all-solid-state batteries [4], and fluid–structure interactions [5]. This success has also reached the discipline of structural integrity, with phase field formulations opening new horizons in the modelling of fracture mechanics [6–8] and corrosion [9,10]. In the case of phase field fracture models, the phase field order parameter ϕ regularises the crack - undamaged material interface, while for the corrosion ones, ϕ describes the evolution of the corrosion front (i.e., the corrosive electrolyte - metal interface). Corrosion and fracture phase field models have been developed independently although we will show here how both classes of phase field models can be encapsulated within a generalised framework. The success of phase field models in the area of structural integrity has been notable, spanning nearly all engineering and natural materials; these include fibre-reinforced composites [11,12], shape memory materials [13,14], metals [15,16], ice-sheets [17,18], rocks [19–21], concrete [22,23], and functionally graded materials [24,25].

One of the key strengths of phase field models is their seamless integration into coupled multi-variable problems, as the phase field (interface) equation can be easily combined with differential equations describing various physical phenomena. Interfacial

* Corresponding author.
E-mail address: emilio.martinez-paneda@eng.ox.ac.uk (E. Martínez-Pañeda).

https://doi.org/10.1016/j.engfracmech.2025.111363
Received 19 March 2025; Received in revised form 16 June 2025; Accepted 24 June 2025
Available online 10 July 2025

Nomenclature

$(\boldsymbol{C}_2^{\mathrm{M}})'$	Material Jacobian in the principal direction of the second phase
α_b	Biot's coefficient
α_{r}	Biot's coefficient in the reservoir domain
α_T	Thermal expansion coefficient
$\boldsymbol{\epsilon}^t$	Principal tensile strain tensor
$\boldsymbol{\epsilon}$	Principal strain tensor
$\boldsymbol{\sigma}$	Stress tensor
$\boldsymbol{\sigma}^{\mathrm{eff}}$	Effective stress tensor
$\boldsymbol{\sigma}_0$	Stress tensor in the undamaged configuration
$\boldsymbol{\varepsilon}$	Strain tensor
$\boldsymbol{\varepsilon}_e$	Elastic strain tensor
$\boldsymbol{\varepsilon}_p$	Plastic strain tensor
$\boldsymbol{\varepsilon}_T$	Thermal strain tensor
$\boldsymbol{a}$	Transpose of the direction cosines matrix for the principal directions
$\boldsymbol{C}$	Elasticity tensor
$\boldsymbol{C}'$	Tangential stiffness matrix in the principal direction
$\boldsymbol{C}_0$	Elastic stiffness tensor in the undamaged configuration
$\boldsymbol{C}_1^{\mathrm{M}}$	Elastic tensor of the first phase
$\boldsymbol{C}_2^{\mathrm{M}}$	Elastic tensor of the second phase
$\boldsymbol{I}$	Identity tensor
$\boldsymbol{K}$	Stiffness matrix
$\boldsymbol{K}_{\mathrm{fl}}$	Permeability tensor
$\boldsymbol{K}_{\mathrm{f}}$	Permeability tensor in the fracture domain
$\boldsymbol{K}_{\mathrm{r}}$	Permeability tensor in the reservoir domain
$\boldsymbol{v}_i$	The ith of the principal vectors of the strain tensor
χ_{H}	Hydrogen damage coefficient
χ_{f}	Fracture domain indicator field
χ_{r}	Reservoir domain indicator field
Δg_b^0	Gibbs free energy
δ_{ij}	Kronecker delta
ℓ	Phase field fracture length scale
ℓ_m	Interface thickness
γ	Interface energy
$\mathbf{b}$	Body force vector
$\mathbf{f}$	Heat flux vector
$\mathbf{f}_\xi$	Flux vector of the diffusion field
$\mathbf{J}$	Flux of metal ions
$\mathbf{J}_{\mathrm{H}}$	Flux of hydrogen atoms
$\mathbf{R}$	Residual vector
$\mathbf{T}$	Surface traction
$\mathbf{u}$	Displacement vector
$\mathbf{v}_{\mathrm{fl}}$	Fluid velocity vector
$\mathcal{F}_\ell$	Regularised energy functional
$\mathcal{H}$	History field in phase field fracture
μ	Chemical potential of metal ions
μ_{H}	Chemical potential of hydrogen atoms
μ_{fl}	Fluid viscosity
∇^2	Laplace operator
ν	Poisson's ratio
Ω	Domain of the system
ω	Height of the double-well potential
Ω_{f}	Fracture domain

Ω_{r}	Reservoir domain
Ω_{t}	Transition domain
$\partial\Omega$	Boundary of the domain
ψ_0^+	Positive part of the undamaged strain energy density
ψ_0^-	Negative part of the undamaged strain energy density
ψ^{ch}	Chemical free energy density
$\psi_{\mathrm{L}}^{\mathrm{ch}}$	Chemical free energy density of the liquid phase
$\psi_{\mathrm{S}}^{\mathrm{ch}}$	Chemical free energy density of the solid phase
ψ^{M}	Strain energy density
ψ_1^{M}	Strain energy density of the first phase
ψ_2^{M}	Strain energy density of the second phase
$\psi_{\mathrm{S}}^{\mathrm{M}}$	Undamaged strain energy of solid phase
ψ_{S}^{e}	Elastic energy density of the solid phase
ψ_{S}^{p}	Plastic energy density of the solid phase
ρ	Mass density
ρ_{fl}	Mass density of the fluid
σ_f	Flow stress
σ_h	Hydrostatic stress
σ_y	Yield stress
θ	Hydrogen coverage
ε^p	Equivalent plastic strain
ε_f	Critical strain for film rupture
$\varepsilon_{\mathrm{vol}}$	Volumetric strain
ξ	Diffusion field
ζ_{fl}	Mass fluid content
A	Curvature of the free energy density
a_0	Length of the initial crack
b	Transient parameter
c	Normalised concentration of metal ions
c_1	First constant for domain indicator fields
c_2	Second constant for domain indicator fields
c_m	Concentration of dissolved ions
c_{H}	Hydrogen concentration
c_{env}	Environmental hydrogen concentration
C_{fl}	Fluid compressibility
c_{Le}	Normalised equilibrium concentration for the liquid phase
c_{L}	Normalised concentration of the liquid phase
c_{sat}	Saturation concentration
c_{Se}	Normalised equilibrium concentration for the solid phase
c_{solid}	Concentration of atoms in the metal
c_{S}	Normalised concentration of the solid phase
c_T	Specific heat
D_m	Diffusion coefficient of metal ions
D_{H}	Diffusion coefficient for hydrogen transport
E	Young's modulus
E'	Young's modulus for plane strain
f_{b1}	Bulk free energy density of the first phase
f_{b2}	Bulk free energy density of the second phase
f_ξ	Diffusion field flux
G_c	Critical energy release rate
i	Corrosion current density
i_0	Corrosion current density of the bare metal
K	Bulk modulus

k	Film stability coefficient
k_0	Thermal conductivity of the pristine material
k_{m}	Mechanocorrosion coefficient
k_T	Thermal conductivity
L	Interface kinetics coefficient
L_0	Reference interface kinetics coefficient
M	Mobility coefficient
N	Strain hardening exponent
N_i	shape functions of node i
n_{pr}	Porosity in the reservoir domain
n_{p}	Porosity
p	Fluid pressure
p_c	Critical fluid pressure
q_m	External fluid source
q_ξ	Flux of the diffusion equation
q_ξ	Flux of the diffusion field
q_T	Heat source
R	Gas constant
r	Heat source
S	Storage coefficient
T	Temperature
t	Time
T_0	Initial temperature
t_0	Time interval before corrosion decay begins in a repassivated metal
T_{k}	Absolute temperature
T_a	Ambient temperature
t_f	Drop time during a film rupture event
U	Internal heat energy
U_ξ	Internal energy of diffusion equation
V_m	Partial molar volume
V_{H}	Partial molar volume of hydrogen
V_{b}	Bulk volume of porous medium
V_{p}	Volume of pores in porous medium
β_i	Representative field variable
η	Relaxation time constant
κ	Gradient energy coefficient
$\mathbf{B}$	Set of field variables
$\mathbf{n}$	Outward unit normal vector
$\mathcal{F}$	Free energy
$\mathcal{F}_{\mathrm{bulk}}$	Bulk free energy
$\mathcal{F}_{\mathrm{int}}$	Interface free energy
∇	Gradient operator in a spatial frame
ϕ	Phase field
f_{b}	Bulk free energy density
f_{int}	Interface free energy density
g	Degradation function
V_{l}	Volume occupied by the first phase
V_{RVE}	Volume of a representative volume element
w	Double-well potential

electro-thermo-chemo-mechanical phenomena can be captured within a single, thermodynamically-consistent framework. As such, phase field-based models have been developed to tackle a wide range of coupled fracture problems, including hydraulic fracture [26,27], Li-Ion battery degradation [28,29], hydrogel fracture [30,31], concrete corrosion-induced cracking [32,33], thermo-mechanical fracture [34,35], hydrogen-assisted cracking [36,37], and electro-mechanical fracture [38,39]. More recently – and independently – phase field models have been developed to tackle the long-standing challenge of predicting corrosion, both uniform and localised; see Ref. [40] for a review. Different from their fracture counterparts, phase field corrosion models are built following the framework used for phase transformation problems (solidification, microstructural evolution). This hinders the coupling of phase field fracture and corrosion models, as needed to tackle important technological problems such as corrosion-fatigue and stress corrosion cracking [41]. Hence, there is a need to establish a unified framework and move beyond *ad hoc* numerical implementations; the aim of this work. Thus, the novelty of the work is two-fold. To start with, we present a theoretical and computational formulation that encapsulates a wide range of coupled phase field problems, for the first time providing a common root for phase field fracture and corrosion models. This generalised formulation enables a versatile and straightforward numerical implementation, allowing us to present the first integration point-level implementation of coupled problems such as thermo-mechanical fracture, corrosion, hydraulic fracture and hydrogen embrittlement. This is demonstrated in the commercial finite element package Abaqus through simple user material (`UMAT` and `UMATHT`) subroutines, which are freely provided. The remainder of this manuscript begins with the presentation of a generalised phase field formulation that encapsulates both fracture and corrosion models (Section 2). Then, this formulation is extended to general coupled (multi-physics) problems (Section 3). In Section 4, details of the numerical implementation are provided, which is done at the integration point level by exploiting the thermal analogy, as demonstrated with user material subroutines in the commercial finite element package Abaqus. Representative results are presented in Section 5 and concluding remarks are given in Section 6. The main body of text is complemented by Appendices aiming at providing additional theoretical and numerical details.

2. A generalised phase field model

We establish a generalised treatment of phase field fracture and phase field corrosion models from the Allen–Cahn equation, a fundamental mathematical framework in phase transition modelling [1,42]. The Allen–Cahn equation typically models non-conserved order parameters, distinguishing it from the Cahn–Hilliard equation, which is used for conserved quantities.

The total free energy of a system involving two phases can be expressed as the sum of the bulk free energy $\mathcal{F}_{\text{bulk}}$ and the interface free energy $\mathcal{F}_{\text{int}}$. For a given body $\Omega \subset \mathbb{R}^n$ (where $n \in \{1,2,3\}$), the total free energy is given by:

$$\mathcal{F} = \mathcal{F}_{\text{bulk}} + \mathcal{F}_{\text{int}} = \int_{\Omega} \left(f_{\text{b}}(\{\beta_i\}, \phi) + f_{\text{int}}(\nabla\phi) \right) \mathrm{d}V, \tag{1}$$

where $f_{\text{b}}(\{\beta_i\}, \phi)$ is the bulk free energy density, depending on the phase field (order parameter) ϕ and a set of field variables $\mathbf{B} = \{\beta_1, \beta_2, \dots, \beta_k \mid \beta_i \in \mathbb{B}\}$, related to mechanical or chemical processes. The interface free energy density $f_{\text{int}}(\nabla\phi)$ depends on the gradient of the phase field $\nabla\phi$.

The bulk free energy density $f_{\text{b}}(\{\beta_i\}, \phi)$ can be defined as:

$$f_{\text{b}}(\{\beta_i\}, \phi) = g(\phi) f_{\text{b1}}(\{\beta_i\}) + (1 - g(\phi)) f_{\text{b2}}(\{\beta_i\}) + w(\phi), \tag{2}$$

where f_{b1} and f_{b2} represent the free energy densities for the first and second phases, respectively. By assuming that each material point is a mixture of the first and second phases, the function $g(\phi)$, known as the degradation or interpolation function, defines the volume fraction of the first phase in a representative volume element (RVE):

$$g(\phi) = \frac{V_1}{V_{\text{RVE}}}, \tag{3}$$

where V_1 is the volume occupied by the first phase and V_{RVE} is the volume of the RVE. The double-well potential $w(\phi)$ ensures that the order parameter favours distinct phases by penalising intermediate values.

The interface energy density is defined as:

$$f_{\text{int}}(\nabla\phi) = \frac{\kappa}{2} |\nabla\phi|^2, \tag{4}$$

where κ is the gradient energy coefficient, which controls the energetic cost associated with creating interfaces. Substituting Eqs. (2) and (4) into the total free energy expression (1), we obtain:

$$\mathcal{F} = \int_{\Omega} \left(g(\phi) f_{\text{b1}}(\{\beta_i\}) + (1 - g(\phi)) f_{\text{b2}}(\{\beta_i\}) + w(\phi) + \frac{\kappa}{2} |\nabla\phi|^2 \right) \mathrm{d}V. \tag{5}$$

The last two terms in Eq. (5) represent the Allen–Cahn energy, capturing the energetic cost of phase interfaces. This energy reflects the tendency of a system to minimise interface area during phase transitions [43]. The Allen–Cahn equation describes the evolution of the phase field by applying the following relaxation law, which drives the system towards equilibrium:

$$\eta \frac{\partial \phi}{\partial t} = -\frac{\delta \mathcal{F}}{\delta \phi} = \kappa \nabla^2 \phi - w'(\phi) - g'(\phi) \left(f_{\text{b1}}(\{\beta_i\}) - f_{\text{b2}}(\{\beta_i\}) \right). \tag{6}$$

Here, η is the relaxation time constant, which characterises the rate at which equilibrium is approached. The Neumann boundary condition is defined as:

$$\nabla\phi \cdot \mathbf{n} = 0 \quad \text{on} \quad \partial\Omega, \tag{7}$$

where $\mathbf{n}$ is the outward unit normal vector on the surface of the domain Ω.

2.1. Phase field fracture method

Let us now show how the Allen–Cahn-based framework introduced so far can encompass existing phase field fracture models. In phase field fracture modelling, the phase field variable ϕ is taken to be a representation of damage, in a continuum mechanics sense, and thus degrades the material stiffness. Consider a body Ω with two phases of materials undergoing mechanical deformation: the first phase represents the material with pristine stiffness ($\phi = 0$), while the second phase corresponds to the fully damaged configuration ($\phi = 1$). We shall then define a material toughness or critical energy release rate G_c, describing the material's resistance to fracture, and a characteristic length scale ℓ which governs the size of the interface thickness and the fracture process zone. Then, considering (for illustrative purposes) the original AT2 phase field fracture model [7], expressions for the double-well potential and the gradient energy coefficient in Eq. (5) can be found:

$$w(\phi) = \frac{G_c\,\phi^2}{2\ell}, \quad \kappa = \frac{\ell\,G_c}{2} \tag{8}$$

Let us denote the bulk free energy due to mechanical work as ψ^{M}. Thus, for each phase we can write $f_{\mathrm{b1}}(\mathbf{u}) = \psi_1^{\mathrm{M}}(\boldsymbol{\varepsilon}(\mathbf{u}))$ and $f_{\mathrm{b2}}(\mathbf{u}) = \psi_2^{\mathrm{M}}(\boldsymbol{\varepsilon}(\mathbf{u}))$. Based on Eq. (5), the total potential energy of the deformation-fracture system can be written as:

$$\mathcal{F}_\ell = \int_\Omega \left[G_c \left(\frac{\ell}{2}|\nabla\phi|^2 + \frac{\phi^2}{2\ell} \right) + g(\phi)\psi_1^{\mathrm{M}}(\boldsymbol{\varepsilon}(\mathbf{u})) + (1 - g(\phi))\psi_2^{\mathrm{M}}(\boldsymbol{\varepsilon}(\mathbf{u})) \right] \mathrm{d}V. \tag{9}$$

In this expression, ψ_1^{M} and ψ_2^{M} denote the strain energy densities for the pristine (first phase) and fully degraded (second phase) materials, respectively. The displacement vector is denoted by $\mathbf{u}$, and the strain tensor is defined as $\boldsymbol{\varepsilon} = \left(\nabla\mathbf{u}^T + \nabla\mathbf{u}\right)/2$. The volume fraction of the first phase, referred to as the degradation function, is given by the quadratic form $g(\phi) = (1-\phi)^2$. Assuming that the second phase has no stiffness and consequently no strain energy ($\psi_2^{\mathrm{M}} = 0$), Eq. (9) simplifies to:

$$\mathcal{F}_\ell = \int_\Omega \left[G_c \left(\frac{\ell}{2}|\nabla\phi|^2 + \frac{\phi^2}{2\ell} \right) + g(\phi)\psi_1^{\mathrm{M}}(\boldsymbol{\varepsilon}(\mathbf{u})) \right] \mathrm{d}V. \tag{10}$$

The evolution equation for the phase field in the fracture model is derived from Eq. (6) and the potential energy in Eq. (10), assuming rate-independent damage evolution ($\eta = 0$):

$$G_c \left(-\ell\nabla^2\phi + \frac{\phi}{\ell} \right) + g'(\phi)\psi_1^{\mathrm{M}}(\boldsymbol{\varepsilon}(\mathbf{u})) = 0. \tag{11}$$

Eq. (11) is arguably the most recognised form of the phase field evolution law, as it corresponds to the balance equation for the so-called AT2 phase field model. However, Eq. (11) does not distinguish between compressive and tensile stress states, and this has led to various extensions of the AT2 phase field model to ensure that damage only occurs under tension or to embed arbitrary failure surfaces [44–48]. An asymmetric tension–compression behaviour can be captured by defining a non-zero stiffness for the second phase, such that

$$G_c \left(-\ell\nabla^2\phi + \frac{\phi}{\ell} \right) + g'(\phi)\left(\psi_1^{\mathrm{M}}(\boldsymbol{\varepsilon}(\mathbf{u})) - \psi_2^{\mathrm{M}}(\boldsymbol{\varepsilon}(\mathbf{u}))\right) = 0. \tag{12}$$

whereby $\psi_1^M - \psi_2^M$ is the driving force for fracture. In the literature, the variable ψ_0^+ is often used to describe a fracture driving force based on the tensile part of a decomposed strain energy density (i.e., $\psi_0^+ = \psi_1^M - \psi_2^M$). Adopting the notation most commonly found in the literature, the (undamaged) strain energy density can be decomposed into a tensile and a compressive part as $\psi_0 = \psi_0^+ + \psi_0^-$ and, accordingly, the total strain energy density in the damaged configuration reads,

$$\psi = g(\phi)\psi_0^+ + \psi_0^- = g(\phi)\psi_0 + (1 - g(\phi))\psi_0^-\,. \tag{13}$$

Comparing Eqs. (9) and (13) one finds that the strain energy density of the undamaged configuration equals the strain energy of the first phase ($\psi_0 = \psi_1^{\mathrm{M}}$), while the strain energy of the second phase corresponds to the compressive part of the undamaged strain energy density ($\psi_0^- = \psi_2^{\mathrm{M}}$). For the formulation to be variationally consistent, this asymmetric degradation must also be considered in the deformation problem. Hence, the stress tensor $\boldsymbol{\sigma}$ reads,

$$\boldsymbol{\sigma} = g(\phi)\frac{\partial\psi_1^{\mathrm{M}}(\boldsymbol{\varepsilon}(\mathbf{u}))}{\partial\boldsymbol{\varepsilon}(\mathbf{u})} + (1 - g(\phi))\frac{\partial\psi_2^{\mathrm{M}}(\boldsymbol{\varepsilon}(\mathbf{u}))}{\partial\boldsymbol{\varepsilon}(\mathbf{u})}. \tag{14}$$

With the strong form of the coupled deformation–diffusion problem being given by,

$$\nabla\cdot\boldsymbol{\sigma} + \mathbf{b} = 0 \tag{15}$$

$$G_c \left(-\ell\nabla^2\phi + \frac{\phi}{\ell} \right) + g'(\phi)\mathcal{H} = 0. \tag{16}$$

with $\mathbf{b}$ being a body force vector. Here, Eq. (15) can be readily derived by taking the variation of Eq. (9) with respect to the displacement vector $\mathbf{u}$ and applying the divergence theorem. Also, a history field $\mathcal{H} = \max_{t\in[0,\tau]}(\psi_1^{\mathrm{M}}(t) - \psi_2^{\mathrm{M}}(t))$ has been defined to ensure damage irreversibility.

2.2. Phase field corrosion

The generalised framework presented before can also be particularised to the study of corrosion, the degradation of materials due to environmental chemical interactions. The dissolution of metals due to corrosion results in an evolving interface, separating the solid metal (electrode) from the liquid corrosive electrolyte. Defining the solid phase as the first phase and the liquid phase as the second one, the phase field variable is taken to be $\phi = 1$ in the metal and $\phi = 0$ in the aqueous electrolyte. In its simplest form, a phase field model for corrosion needs to capture two phenomena: the dissolution of the metal (short-range interactions) and the subsequent transport of metal ions (long-range interactions). In terms of the generalised formulation presented above, this implies particularising the bulk free energy density to the chemical free energy density ψ^{ch} and considering an additional primary variable, the normalised concentration of metal ions, equal to $c = 1$ in the metal phase and equal to $c = 0$ in electrolyte regions very far from the corrosion interface. Accordingly, the energy functional in Eq. (1) is given by

$$\mathcal{F} = \int_{\Omega} \left(\psi^{\text{ch}} + \frac{\kappa}{2} |\nabla \phi|^2 \right) \mathrm{d}V. \tag{17}$$

The chemical free energy density ψ^{ch} can be expressed as a weighted sum of the chemical free energy densities of the solid ($\psi_{\text{S}}^{\text{ch}}$) and liquid ($\psi_{\text{L}}^{\text{ch}}$) phases, using the interpolation function $g(\phi)$, as

$$\psi^{\text{ch}}(\phi, c) = g(\phi)\psi_{\text{S}}^{\text{ch}} + (1 - g(\phi))\psi_{\text{L}}^{\text{ch}} + w(\phi). \tag{18}$$

The interpolation function $g(\phi)$, characterising the volume fraction, as defined in Eq. (3), is typically chosen to be $g(\phi) = -2\phi^3 + 3\phi^2$ in the phase field corrosion community, while the double-well potential $w(\phi)$ is typically defined as $w(\phi) = \omega\phi^2(1-\phi)^2$, with ω being the height of the double-well potential.

Following the literature, the chemical free energy densities of solid ($\psi_{\text{S}}^{\text{ch}}$) and liquid ($\psi_{\text{L}}^{\text{ch}}$) phases are defined as:

$$\psi_{\text{S}}^{\text{ch}} = A(c_{\text{S}} - c_{\text{Se}}), \quad \psi_{\text{L}}^{\text{ch}} = A(c_{\text{L}} - c_{\text{Le}}), \tag{19}$$

where A is the curvature of the free energy density, and c_{S} and c_{L} are the normalised concentrations of the solid and liquid phases. Also, $c_{\text{Se}} = c_{\text{solid}}/c_{\text{solid}} = 1$, and $c_{\text{Le}} = c_{\text{sat}}/c_{\text{solid}}$ are the normalised equilibrium concentrations for the solid and liquid phases, with c_{sat} being the saturation concentration. Accordingly, Eq. (18) can be reformulated as,

$$\psi^{\text{ch}}(c, \phi) = A\left(c - g(\phi)(c_{\text{Se}} - c_{\text{Le}}) - c_{\text{Le}}\right)^2 + \omega\phi^2(1-\phi)^2. \tag{20}$$

The interface energy density follows the same notation and definition as in Eq. (4). An interface energy γ and interface thickness ℓ_m can be defined based ω and κ as [49]:

$$\gamma = \sqrt{\frac{\kappa\omega}{18}}, \quad \ell_m = \sqrt{\frac{8\kappa}{\omega}}. \tag{21}$$

The corrosion phase field evolution equation can derived using the relaxation law, see Eq. (6), as:

$$\frac{1}{L}\dot{\phi} = \kappa\nabla^2\phi - \frac{\partial \psi^{\text{ch}}(c, \phi)}{\partial \phi} \tag{22}$$

where L is the interface kinetics coefficient. For more details, see Ref. [10].

It remains to define the transport of the mass conserved quantity: the normalised concentration of metal ions $c = c_m(\mathbf{x}, t)/c_{\text{solid}}$, with c_{solid} being the concentration of atoms in the metal and $c_m(\mathbf{x}, t)$ being the concentration of dissolved ions. The mass conservation law then reads

$$\dot{c}c_{\text{solid}} + \nabla \cdot \mathbf{J} = 0, \tag{23}$$

As the medium is a mixture of solid and liquid phases, the normalised concentration c can be expressed as a function of the normalised concentration in the solid (c_S) and liquid (c_L) phases,

$$c = g(\phi)c_{\text{S}} + (1 - g(\phi))c_{\text{L}}. \tag{24}$$

The mass transport is derived from the chemical potential using the relationships in Eq. (19), given as:

$$\mu = -\frac{1}{c_{\text{solid}}}\frac{\partial \psi^{\text{ch}}}{\partial c} = -\frac{2A}{c_{\text{solid}}}\left(c - g(\phi)(c_{\text{Se}} - c_{\text{Le}}) - c_{\text{Le}}\right). \tag{25}$$

Using a Fick's law-type relation, the flux $\mathbf{J}$ can be expressed as:

$$\mathbf{J} = \frac{D_m}{2A} \cdot c_{\text{solid}} \cdot \nabla\mu = -c_{\text{solid}} \cdot D_m \nabla\left(c - g(\phi)(c_{\text{Se}} - c_{\text{Le}}) - c_{\text{Le}}\right), \tag{26}$$

where D_m is the diffusion coefficient of metal ions. Substituting Eq. (26) into Eq. (23), the mass conservation law reads:

$$\dot{c} - \nabla \cdot \left[D_m \nabla\left(c - g(\phi)(c_{\text{Se}} - c_{\text{Le}}) - c_{\text{Le}}\right)\right] = 0. \tag{27}$$

3. Extension and particularisation to coupled problems

Let us now extend this generalised formulation to the analysis of coupled problems, where solids undergo mechanical deformation, phase transitions, and a diffusion-type process. Considering as primary variables the displacement vector $\mathbf{u}$, the phase field ϕ, and the diffusion field ξ, the coupled system of equations for a body Ω can be formulated as follows:

$$\nabla \cdot \boldsymbol{\sigma}(\mathbf{u}, \phi, \xi) + \mathbf{b} = 0, \tag{28}$$

$$\kappa \nabla^2 \phi - w'(\phi) - g'(\phi)\big(f_{\mathrm{b1}}(\mathbf{u}, \xi) - f_{\mathrm{b2}}(\mathbf{u}, \xi)\big) - \eta \dot{\phi} = 0, \tag{29}$$

$$\rho \dot{U}_{\xi}(\xi, \nabla\xi, \mathbf{u}, \phi) + \nabla \cdot \mathbf{f}_{\xi}(\xi, \nabla\xi, \mathbf{u}, \phi) - q_{\xi} = 0, \tag{30}$$

Here, Eq. (28) represents the linear momentum equation, Eq. (29) is the phase field evolution equation, and Eq. (30) corresponds to a diffusion-type field equation. In the following subsections, we explore four specific cases for multiphysics phase field modelling, each one addressing different coupling mechanisms and physical phenomena. More specifically, this general framework will be particularised to the analysis of thermal fracture ($\xi = T$, Section 3.1), hydraulic fracture ($\xi = p$, Section 3.2), hydrogen embrittlement ($\xi = c_{\mathrm{H}}$, Section 3.3), and stress-assisted corrosion ($\xi = c$, Section 3.4).

3.1. Thermal fracture

Thermal fractures are commonplace in a wide range of engineering applications and sectors, from aerospace [50] to nuclear energy [51]. Changes in temperature lead to thermal strains, which can result in fractures [52].

In thermoelasticity, the strain tensor is decomposed into an elastic part, $\boldsymbol{\varepsilon}_e$, and a thermal part, $\boldsymbol{\varepsilon}_T$, as follows:

$$\boldsymbol{\varepsilon} = \boldsymbol{\varepsilon}_e + \boldsymbol{\varepsilon}_T \,, \tag{31}$$

where the thermal strain, $\boldsymbol{\varepsilon}_T$, is defined in terms of the thermal expansion coefficient α_T:

$$\boldsymbol{\varepsilon}_T = \alpha_T (T - T_0)\boldsymbol{I} \,, \tag{32}$$

with T_0 representing the initial temperature and $\boldsymbol{I}$ being the identity tensor. Since only the elastic (stored) strain contributes to stress, Eqs. (28) and (29) can be respectively rewritten as:

$$\nabla \cdot \boldsymbol{\sigma}(\boldsymbol{\varepsilon}_e, \phi) + \mathbf{b} = \mathbf{0} \quad \text{in} \quad \Omega, \tag{33}$$

$$G_c \left(\frac{\phi}{\ell} - \ell \nabla^2 \phi \right) - 2(1 - \phi)\mathcal{H}(\boldsymbol{\varepsilon}_e) = 0 \quad \text{in} \quad \Omega. \tag{34}$$

While Eq. (30) is particularised to the heat transfer equation, given by:

$$\rho c_T \dot{T} - k_T \nabla^2 T = q_T \,, \tag{35}$$

where ρ is the material density, c_T is the specific heat, k_T is the thermal conductivity, and q_T is the heat source. Often, heat transfer and phase field fracture are assumed to interact through a damage-dependent thermal conductivity, such that

$$\rho c_T \dot{T} - k_T(\phi) \nabla^2 T = q_T \,, \tag{36}$$

where the thermal conductivity $k_T(\phi)$ is defined as $k_T(\phi) = g(\phi) k_0$, with k_0 representing the thermal conductivity of the pristine material.

3.2. Hydraulic fracture

Hydraulic fracture is a process of crack nucleation and propagation caused by changes in pore pressure within a solid body due to fluid injection or natural forces. This phenomenon occurs in both natural settings and engineering applications, with hydraulic fracture modelling being widely used in geotechnical engineering, oil and gas extraction, environmental management, and other fields to predict and control fracture behaviour for resource extraction and infrastructure stability [17,18,53,54].

Particularising the above-presented generalised formulation to the study of hydraulic fracture requires defining a balance equation for the evolution of fluid pressure p. This is achieved by particularising Eq. (30) to the mass balance equation governing fluid flow within a porous medium. When considering an external fluid source q_m, the fluid mass balance equation is defined as:

$$\dot{\zeta}_{\mathrm{fl}} + \nabla \cdot (\rho_{\mathrm{fl}} \mathbf{v}_{\mathrm{fl}}) = q_m, \tag{37}$$

where ζ_{fl} is the mass fluid content, corresponding to the mass of fluid per unit bulk volume and $\mathbf{v}_{\mathrm{fl}}$ is the fluid velocity vector. This can be defined using porosity (n_{p}) and the density of the fluid (ρ_{fl}) as:

$$\zeta_{\mathrm{fl}} = \rho_{\mathrm{fl}} n_{\mathrm{p}}, \tag{38}$$

where porosity $n_{\mathrm{p}} = V_{\mathrm{p}}/V_{\mathrm{b}}$ is the ratio of the volume of pores (V_{p}) to the bulk volume (V_{b}) of the medium. Using Biot's theory of poroelasticity and Darcy's law, the mass balance equation can be rewritten as:

$$\rho_{\mathrm{fl}}\left(S\dot{p} + \alpha_b \dot{\varepsilon}_{\mathrm{vol}}\right) + \nabla \cdot \left(-\rho_{\mathrm{fl}} \frac{\boldsymbol{K}_{\mathrm{fl}}}{\mu_{\mathrm{fl}}} \nabla p\right) = q_m, \tag{39}$$

where α_b is Biot's coefficient, $\dot{\varepsilon}_{\mathrm{vol}}$ is the rate of volumetric strain, $\boldsymbol{K}_{\mathrm{fl}}$ is the permeability tensor, μ_{fl} is the fluid viscosity, and S is the storage coefficient, defined as:

$$S = \frac{(1-\alpha_b)(\alpha_b - n_{\mathrm{p}})}{K} + n_{\mathrm{p}} C_{\mathrm{fl}}, \tag{40}$$

with K being the bulk modulus and C_{fl} the fluid compressibility.

Next, Biot's theory of poroelasticity is utilised to establish a constitutive relationship between stress and strain. In a saturated porous medium, the total strain arises from the stress acting on the solid skeleton (effective stress $\boldsymbol{\sigma}^{\mathrm{eff}}$), and the pore pressure of fluid. Under static conditions or slow fluid flow, the pore pressure contributes only to changes in volumetric strain. Consequently, the total stress is expressed as the sum of the effective stress $\boldsymbol{\sigma}^{\mathrm{eff}} = \boldsymbol{C} : \boldsymbol{\varepsilon}$, and the pore fluid pressure scaled by Biot's coefficient α_b, resulting in:

$$\boldsymbol{\sigma} = \boldsymbol{C} : \boldsymbol{\varepsilon} - \alpha_b p \boldsymbol{I} = \boldsymbol{\sigma}^{\mathrm{eff}} - \alpha_b p \boldsymbol{I}, \tag{41}$$

where $\boldsymbol{I}$ is the identity tensor. In the context of phase field hydraulic fracture, and considering a decomposition of the strain energy density, the effective stress is defined as:

$$\boldsymbol{\sigma}^{\mathrm{eff}} = g(\phi)\frac{\partial \psi_0^+(\boldsymbol{\varepsilon})}{\partial \boldsymbol{\varepsilon}} + \frac{\partial \psi_0^-(\boldsymbol{\varepsilon})}{\partial \boldsymbol{\varepsilon}}. \tag{42}$$

Thus, Eq. (28) can be reformulated as:

$$\nabla \cdot \left[\boldsymbol{\sigma}^{\mathrm{eff}} - \alpha_b p \boldsymbol{I}\right] = \boldsymbol{0} \quad \text{in} \quad \Omega. \tag{43}$$

One must also consider the interplay between cracking phenomena and fluid flow. Building on the work of Lee et al. [55], we couple the fluid and phase field equations by dividing the domain into three distinct regions: the reservoir (Ω_{r}), fracture (Ω_{f}), and transition (Ω_{t}) domains. These regions are distinguished using domain indicator fields as functions of the phase field variable ϕ and material constants c_1 and c_2. The domain indicator fields ($\chi_{\mathrm{r}}, \chi_{\mathrm{f}}$) can be defined as:

$$\chi_{\mathrm{r}}(\phi) = \begin{cases} 1 & \phi \le c_1 \\ \frac{c_2-\phi}{c_2-c_1} & c_1 < \phi < c_2 \\ 0 & c_2 \le \phi, \end{cases} \qquad \chi_{\mathrm{f}}(\phi) = \begin{cases} 0 & \phi \le c_1 \\ \frac{\phi-c_1}{c_2-c_1} & c_1 < \phi < c_2 \\ 1 & c_2 \le \phi, \end{cases} \tag{44}$$

Thus, the fluid and solid parameters between the reservoir and fracture domains are defined as:

$$\alpha_b = \chi_{\mathrm{r}}\alpha_{\mathrm{r}} + \chi_{\mathrm{f}}, \tag{45}$$

$$n_{\mathrm{p}} = \chi_{\mathrm{r}} n_{\mathrm{pr}} + \chi_{\mathrm{f}}, \tag{46}$$

$$\boldsymbol{K}_{\mathrm{fl}} = \chi_{\mathrm{r}}\boldsymbol{K}_{\mathrm{r}} + \chi_{\mathrm{f}}\boldsymbol{K}_{\mathrm{f}}, \tag{47}$$

where α_{r}, n_{pr}, and $\boldsymbol{K}_{\mathrm{r}}$ denote Biot's coefficient, porosity, and the permeability tensor of the reservoir domain, respectively. $\boldsymbol{K}_{\mathrm{f}}$ is the permeability tensor of the fracture domain. Finally, we can write the fluid flow equation in a form valid across all domains using the domain indicator fields χ_{r} and χ_{f}:

$$\rho_{\mathrm{fl}}\left(S(\alpha_b(\phi), n_{\mathrm{p}}(\phi))\dot{p} + \alpha_b(\phi)\chi_{\mathrm{r}}(\phi)\dot{\varepsilon}_{\mathrm{vol}}\right) + \nabla \cdot \left(-\rho_{\mathrm{fl}} \frac{\boldsymbol{K}_{\mathrm{fl}}(\phi)}{\mu} \nabla p\right) = q_m. \tag{48}$$

3.3. Hydrogen embrittlement

When metallic materials are exposed to hydrogen-containing environments, such as seawater or hydrogen gas, they experience a phenomenon known as *hydrogen embrittlement*, whereby the absorption of hydrogen atoms into the metal results in a dramatic degradation of their ductility, fracture toughness and fatigue crack growth resistance [56,57]. Hydrogen embrittlement phenomena can be captured in a phase field setting, as first achieved by Martínez-Pañeda and co-workers [58–60].

Predicting hydrogen-assisted failures requires solving a three-field system, modelling deformation, hydrogen diffusion and fracture. The transport of hydrogen can be simulated considering an equation of the type (30), with the primary variable being the diffusible hydrogen concentration c_{H}. Considering the balance of mass, hydrogen transport can be described as,

$$\dot{c}_{\mathrm{H}} + \nabla \cdot \mathbf{J}_{\mathrm{H}} = 0, \tag{49}$$

where the hydrogen flux, $\mathbf{J}_{\mathrm{H}}$, is defined based on the gradient of the chemical potential μ_{H}:

$$\mathbf{J}_{\mathrm{H}} = -\frac{D_{\mathrm{H}} c_{\mathrm{H}}}{R T_{\mathrm{k}}} \nabla \mu_{\mathrm{H}} = -D_{\mathrm{H}} \nabla c_{\mathrm{H}} + \frac{D_{\mathrm{H}}}{R\, T_{\mathrm{k}}} c_{\mathrm{H}} V_{\mathrm{H}} \nabla \sigma_h, \tag{50}$$

with D_{H} being the diffusion coefficient, R the gas constant, T_{k} the absolute temperature, V_{H} the partial molar volume of hydrogen in solid solution, and σ_h the hydrostatic stress. Hydrogen accumulates in regions of high hydrostatic stress, providing a source of coupling between the solid mechanics and diffusion problems.

An important source of coupling is how hydrogen degrades the fracture resistance of metals. This is naturally captured in phase field by defining the material toughness as a function of the hydrogen content: $G_c(c_{\mathrm{H}})$. Among the multiple ways available for defining this relationship, we follow Ref. [58], and use an atomistically-informed linear degradation law:

$$G_c(c_{\mathrm{H}}) = G_c(\theta) = (1 - \chi_{\mathrm{H}} \theta) G_c(0), \tag{51}$$

where χ_{H} is an atomistically-estimated damage coefficient that quantifies the reduction in fracture energy due to the presence of hydrogen and θ is the hydrogen coverage. The latter can be related to the hydrogen concentration through Oriani's equilibrium or the Langmuir–McLean's isotherm,

$$\theta = \frac{c_{\mathrm{H}}}{c_{\mathrm{H}} + \exp\left(\frac{-\Delta g_b^0}{R T_{\mathrm{k}}}\right)}, \tag{52}$$

where the hydrogen content is here expressed in units of impurity mole fraction, and Δg_b^0 is the Gibbs free energy difference between the decohering interface and the surrounding material.

3.4. Stress-assisted corrosion

The interplay between mechanical deformation and corrosion is what underpins localised corrosion failures. Mechanical stresses can rupture the protective passive film and accelerate corrosion kinetics, while metal dissolution alters stress distributions - a two-way coupling problem. These can be coupled by extending the formulation in Section 2.2 to define a bulk free energy density that encompasses both mechanical and chemical contributions:

$$f_{\mathrm{b}}(\mathbf{u}, \phi, c) = \psi^{\mathrm{M}}(\mathbf{u}, \phi) + \psi^{\mathrm{ch}}(c, \phi), \tag{53}$$

where $\psi^{\mathrm{M}}(\mathbf{u})$ is the mechanical free energy (i.e., the strain energy density), and $\psi^{\mathrm{ch}}(c)$ is the chemical free energy density, as defined in Eq. (18). Since the liquid phase is assumed not to carry stress, the mechanical free energy can be written as:

$$\psi^{\mathrm{M}} = g(\phi) \psi_{\mathrm{S}}^{\mathrm{M}}(\mathbf{u}) = g(\phi)(\psi_{\mathrm{S}}^{e} + \psi_{\mathrm{S}}^{p}) \tag{54}$$

where $\psi_{\mathrm{S}}^{\mathrm{M}}$ is the undamaged strain energy of the solid phase and $g(\phi)$ is the degradation function, as defined in Section 2.2, which satisfies $g(0) = 0$ for the electrolyte phase ($\phi = 0$) and $g(1) = 1$ for the undissolved solid ($\phi = 1$). In Eq. (54), both elastic and plastic contributions to the strain energy density are considered, as respectively denoted by the e and p superscripts. Assuming J2 plasticity, the elastic and plastic strain energy densities are given by:

$$\psi_{\mathrm{S}}^{e}\left(\boldsymbol{\varepsilon}_e\right) = \frac{1}{2}\left(\boldsymbol{\varepsilon}_e\right)^{T} : \boldsymbol{C}_0 : \boldsymbol{\varepsilon}_e \tag{55}$$

$$\psi_{\mathrm{S}}^{p} = \int_0^t \boldsymbol{\sigma_0} : \dot{\boldsymbol{\varepsilon}}_p \, \mathrm{d}t, \tag{56}$$

where $\boldsymbol{\varepsilon}_e$ and $\boldsymbol{\varepsilon}_p$ are the elastic and plastic parts of the strain tensor, and $\boldsymbol{C}_0$ is the elastic stiffness matrix. Accordingly, the undamaged stress $\boldsymbol{\sigma}_0$ and total stress $\boldsymbol{\sigma}$ are defined as:

$$\boldsymbol{\sigma} = g(\phi)\boldsymbol{\sigma}_0 = g(\phi)\, \boldsymbol{C}_0 : (\boldsymbol{\varepsilon}_e - \boldsymbol{\varepsilon}_p). \tag{57}$$

Work hardening is considered by means of an isotropic power law relationship:

$$\sigma_f = \sigma_y \left(1 + \frac{E\varepsilon^p}{\sigma_y}\right)^N, \tag{58}$$

where E is Young's modulus, σ_f is the flow stress, σ_y is the initial yield stress and N is the strain hardening exponent ($0 \leq N \leq 1$). The equivalent plastic strain is defined as $\varepsilon^p = \sqrt{(2/3)\, \boldsymbol{\varepsilon}_p : \boldsymbol{\varepsilon}_p}$.

Using the aforementioned definitions of the mechanical and chemical free energy densities, the total free energy can then be written as:

$$\mathcal{F} = \int_\Omega \left(g(\phi)(\psi_{\mathrm{S}}^{e} + \psi_{\mathrm{S}}^{p}) + \psi^{\mathrm{ch}}(c, \phi) + \frac{\kappa}{2} |\nabla \phi|^2 \right) \mathrm{d}V. \tag{59}$$

From Eq. (59), the linear momemtum balance equation can be readily obtained by taking the stationary of the functional with respect to the displacement field:

$$\nabla \cdot \boldsymbol{\sigma}(\mathbf{u}, \phi) = \nabla \cdot \left[g(\phi)\, \boldsymbol{C}_0 : (\boldsymbol{\varepsilon}_e - \boldsymbol{\varepsilon}_p) \right] = 0 \tag{60}$$

However, as extensively discussed in Ref. [40], defining the phase field evolution equation in a variationally consistent way results in non-physical behaviour, with mechanical strains impacting corrosion not only during activation-controlled corrosion, as observed experimentally, but also during diffusion-controlled corrosion. To work around this, Cui and co-workers [10] suggested instead to enrich the description of the phase field mobility coefficient L to make it a function of mechanical fields, such that the phase field corrosion evolution equation reads,

$$\frac{1}{L\left(\sigma_h, \varepsilon^p\right)}\dot{\phi} = \kappa\nabla^2\phi - \frac{\partial\psi^{\mathrm{ch}}(c,\phi)}{\partial\phi} \tag{61}$$

where σ_h is the hydrostatic stress. The precise definition of $L\left(\sigma_h, \varepsilon^p\right)$ is aimed at incorporating the two main mechanisms by which mechanics interplays with corrosion: (i) enhancement of corrosion kinetics, and (ii) film rupture.

To incorporate the role of mechanical fields in enhancing corrosion kinetics, we define the mobility coefficient as,

$$L = k_{\mathrm{m}}\left(\varepsilon^p, \sigma_h\right) L_0 = \left(\frac{\varepsilon^p}{\varepsilon_y} + 1\right) \exp\left(\frac{\sigma_h V_m}{RT_{\mathrm{k}}}\right) L_0, \tag{62}$$

where L_0 is the reference mobility coefficient, which can be quantitatively related to the corrosion current density [10], V_m is the molar volume, and k_m is the so-called mechanochemical coefficient. Eq. (62) incorporates the impact on corrosion kinetics of both lattice expansion and dislocation phenomena through the hydrostatic stress and the effective plastic strain rate, respectively.

The interplay between mechanics and film rupture and re-passivation is an important one. Mechanical strains lead to localised rupture of the protective film in corrosion-resistant materials, leading to localised corrosion phenomena (pitting, stress corrosion cracking), which are very detrimental and difficult to predict. The process is a cyclic one, with film rupture being followed by material dissolution and subsequent repassivation (film formation). This phenomenon is known as the film-rupture-dissolution-repassivation (FRDR) mechanism [61], and for a corrosion current density i, can be expressed as,

$$i\left(t_i\right) = \begin{cases} i_0, & \text{if } 0 < t_i \leqslant t_0 \\ i_0 \exp\left(-k\left(t_i - t_0\right)\right), & \text{if } t_0 < t_i \leqslant t_0 + t_f, \end{cases} \tag{63}$$

where i_0 is the corrosion current density of the bare metal, t_0 is the time interval before decay begins, t_f is the drop time during a film rupture event, t_i is the current time (within a specific cycle) and k is a parameter that characterises the sensitivity of the corrosion rates to the stability of the passive film, as dictated by the material and the environment. Following experimental observations, the decay in corrosion current density with the improvement of the film stability in time is characterised by an exponential function. The time t_f at which a rupture event will happen is dictated by straining kinetics. This is often described by considering the accumulated plastic strain - over a FRDR cycle ε_i^p (i.e., undergone by the newly developed oxide layer) - with failure occurring when a critical value is reached ($\varepsilon_i^p = \varepsilon_f \approx 0.001$). As elaborated in Ref. [41], this is effectively captured by exploiting the proportionality relationship between the phase field mobility coefficient and the corrosion current density. Hence, considering as well Eq. (62), the mobility coefficient can be defined as,

$$L = \begin{cases} k_{\mathrm{m}}\left(\varepsilon^p, \sigma_h\right) L_0, & \text{if } 0 < t_i \leqslant t_0 \\ k_{\mathrm{m}}\left(\varepsilon^p, \sigma_h\right) L_0 \exp\left(-k(t_i - t_0)\right), & \text{if } t_0 < t_i \leqslant t_0 + t_f. \end{cases} \tag{64}$$

4. Numerical implementation exploiting the thermal analogy

In Sections 3.1–3.4, we have illustrated that a wide range of physical phenomena can be modelled using a diffusion type equation, Eq. (30). One such phenomenon is heat transfer, which has been widely implemented across in-house and commercial finite element packages. Therefore, leveraging the thermal analogy of diffusion-type equations, these physical processes can be incorporated into these codes with minimal effort. We demonstrate this here, exploiting this heat transfer analogy to straightforwardly implement the coupled problems discussed before in the commercial finite element package Abaqus.

The heat transfer equation can be expressed in a general form as:

$$\rho\dot{U} + \nabla\cdot\mathbf{f} - r = 0\,, \tag{65}$$

where U denotes internal heat energy, $\mathbf{f}$ is the heat flux vector, and r is the heat source. Using Eq. (65) as a foundation, any diffusion-type equation can be reformulated analogously, as shown below.

General phase field. Consider the general phase field evolution equation given in Eq. (6). Taking the phase field variable as the temperature ($\phi \equiv T$), Eq. (6) can be reformulated to resemble Eq. (65) as,

$$\underbrace{1}_{\rho}\underbrace{\left(-\eta\frac{\partial\phi}{\partial t} - w'(\phi) - g'(\phi)\left(f_{b1}(\beta) - f_{b2}(\beta)\right)\right)}_{\dot{U}} + \nabla\cdot\underbrace{(\kappa\nabla\phi)}_{\mathbf{f}} = 0. \tag{66}$$

with $r = 0$.

Phase field fracture. The specific case of phase field fracture, given by Eq. (16), can also readily be expressed in a way that resembles the heat transfer PDE:

$$\underbrace{1}_{\rho}\underbrace{\left(\frac{\phi}{\ell^2} + g'(\phi)\frac{\mathcal{H}}{G_c\ell}\right)}_{\dot{U}} + \nabla\cdot\underbrace{(-\nabla\phi)}_{\mathbf{f}} = 0 \tag{67}$$

with the heat source term being also $r = 0$ and $\phi \equiv T$.

Phase field corrosion. The modelling of stress-assisted corrosion requires defining a phase field equation to describe material dissolution and an equation to describe the long-range transport of metal ions, in addition to considering mechanical equilibrium. The heat transfer analogy can be exploited to model both short-range interactions (corrosion) and long-range interactions (metal ion transport). The latter is given by Eq. (27), which can be reformulated as,

$$\underbrace{1}_{\rho}\underbrace{\dot{c}}_{\dot{U}} + \nabla\cdot\underbrace{\left[-D_m\nabla\left(c - h(\phi)(c_{\mathrm{Se}} - c_{\mathrm{Le}}) - c_{\mathrm{Le}}\right)\right]}_{\mathbf{f}} = 0. \tag{68}$$

with $r = 0$ and the primary variable, the normalised concentration of metal ions, being analogous to the temperature ($c \equiv T$). On the other side, the phase field evolution equation for the corrosion problem, Eq. (61), can be expressed as,

$$\underbrace{1}_{\rho}\underbrace{\left(-\frac{1}{L}\dot{\phi} - \frac{\partial\psi^{\mathrm{ch}}(c,\phi)}{\partial\phi}\right)}_{\dot{U}} + \nabla\cdot\underbrace{(\kappa\nabla\phi)}_{\mathbf{f}} = 0. \tag{69}$$

where $r = 0$ and $\phi \equiv T$.

Hydraulic fracture. In addition to using the thermal analogy to implement the phase field fracture equation, tackling hydraulic fracture problems requires determining the evolution of the fluid pressure p. This can readily be achieved by establishing $p \equiv T$, and reformulating the mass conservation Eq. (48) as:

$$\underbrace{\rho_{\mathrm{fl}}}_{\rho}\underbrace{\left(S(\alpha(\phi), n_{\mathrm{p}}(\phi))\dot{p} + \alpha_b(\phi)\chi_{\mathrm{r}}(\phi)\dot{\varepsilon}_{\mathrm{vol}}\right)}_{\dot{U}} + \nabla\cdot\underbrace{\left(-\rho_{\mathrm{fl}}\frac{\boldsymbol{K}_{\mathrm{fl}}(\phi)}{\mu_{\mathrm{fl}}}\nabla p\right)}_{\mathbf{f}} - \underbrace{q_m}_{r} = 0. \tag{70}$$

Hydrogen embrittlement. The prediction of hydrogen-assisted fractures using phase field requires solving the phase field evolution equation, as discussed above, but also considering the role of hydrogen in degrading G_c, and the hydrogen transport equation. The latter can also be made analogous to the heat transfer problem by taking $c_{\mathrm{H}} \equiv T$ and reformulating the hydrogen transport problem, Eqs. (49)–(50), as

$$\underbrace{1}_{\rho}\underbrace{\dot{c}_{\mathrm{H}}}_{\dot{U}} + \nabla\cdot\underbrace{\left(-D_{\mathrm{H}}\nabla c_{\mathrm{H}} + \frac{D_{\mathrm{H}}}{RT_{\mathrm{k}}}c_{\mathrm{H}}V_{\mathrm{H}}\nabla\sigma_h\right)}_{\mathbf{f}} = 0. \tag{71}$$

with $r = 0$.

Finally, we also provide for generality how the balance equation of the heat transfer problem, Eq. (36), can be given in the form of Eq. (65); i.e.,

$$\rho\underbrace{c_T\dot{T}}_{\dot{U}} + \nabla\cdot\underbrace{(-k_T\nabla T)}_{\mathbf{f}} - \underbrace{q_T}_{r} = 0\,, \tag{72}$$

For numerical implementation purposes, one also needs to build the appropriate terms of the stiffness matrix, which requires defining the variation of internal thermal energy per unit mass with respect to temperature $\partial U/\partial T$, the variation of internal thermal energy per unit mass with respect to the spatial gradients of temperature $\partial U/\partial(\nabla T)$, the variation of the heat flux vector with respect to temperature $\partial\mathbf{f}/\partial T$, and the variation of the heat flux vector with respect to the spatial gradients of temperature $\partial\mathbf{f}/\partial(\nabla T)$. These are provided in Appendix A for each of the physical phenomena considered here. For the sake of generality, complement implementation details (including definition of discretised residuals and stiffness matrix components) are given in Appendix B, although these details are not used here, where the implementation is carried out entirely at the integration point level.

4.1. Abaqus implementation

Exploiting the thermal analogy can significantly simplify the numerical implementation. This is here demonstrated in the context of the commercial software Abaqus, showing how complex multi-field coupled problems can be implemented at the integration point level. In the past, we showed how the coupled deformation-phase field fracture problem could be implemented into Abaqus using only a user material (UMAT) subroutine [62] or, for versions older than 2020, a user material (UMAT) subroutine and an internal heat generation (HETVAL) user subroutine [63]. A notable advantage of these methods is their ability to operate at the integration point level, thereby eliminating the need for element-level implementation. This approach also enables the use of Abaqus's built-in features, such as various element types and contact interactions. However, a new paradigm is needed here, as the heat analogy is exploited to treat simultaneously two or more equations and only one temperature degree of freedom can be defined in Abaqus.

First, the use of a user material heat transfer (UMATHT) subroutine is suggested, in combination with a UMAT. This provides greater flexibility as it enables to conduct transient analyses with history-dependent variables. This is, for example, required to implement the phase field corrosion equation, Eq. (61), as exploiting the heat transfer analogy using a UMAT (or HETVAL) only allows to define the quantity ρc_p as the coefficient multiplying $\partial T/\partial t$; ρc_p is a constant quantity, with c_p being the specific heat, but the equivalent term $1/L(\sigma_h, \varepsilon^p)$ is not constant in time. In terms of computational efficiency, both approaches (UMAT/HETVAL vs UMAT/UMATHT) are equivalent.

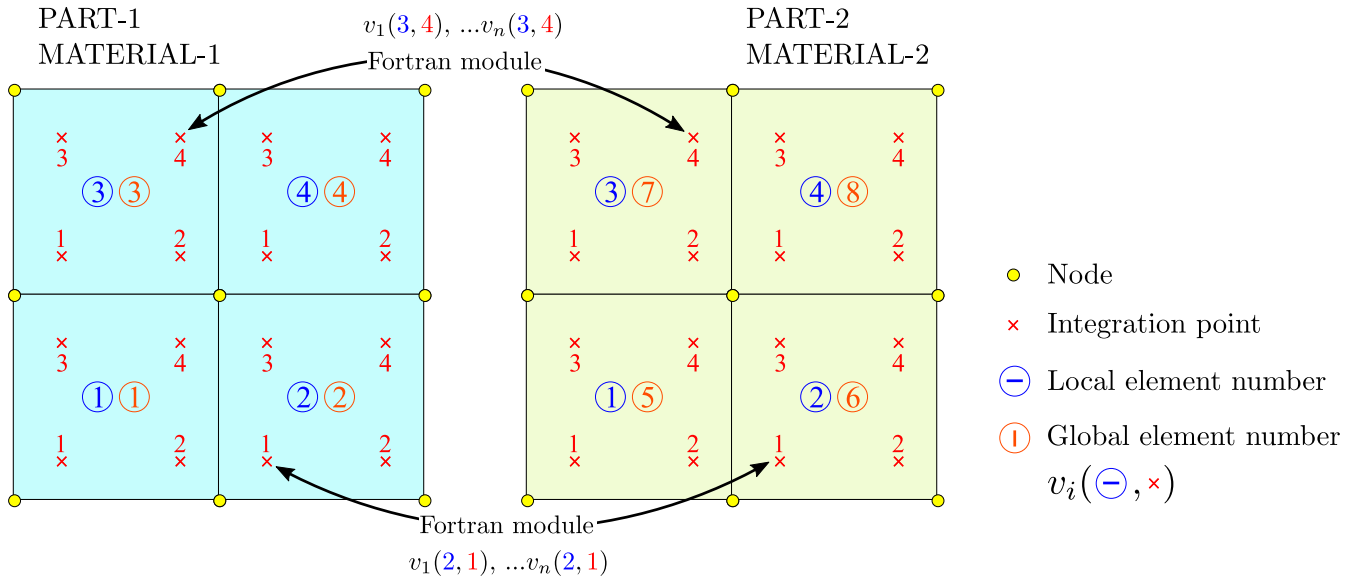

Fig. 1. Conjugate pairs of elements for identical geometry and mesh discretisation.

The second key innovation of our implementation is the treatment of multiple temperature-like degrees-of-freedom, as required to simultaneously solve several diffusion-like equations (e.g., phase field fracture and hydrogen transport, in the case of hydrogen embrittlement). Thus, we introduce a *twin-part* method, whereby a second part (`PART-2`) is defined, which duplicates the geometry and mesh of the primary part (`PART-1`). This is straightforward in Abaqus, as it just implies creating a copy of `PART-1`, once meshed. While both parts share geometric properties and meshing, they differ in material definitions (`MATERIAL-1` for `PART-1` and `MATERIAL-2` for `PART-2`) and boundary conditions. Each part includes degrees of freedom for displacement and temperature, and hence the use of conjugate elements enables additional degrees of freedom. For example, the temperature degree of freedom in `PART-1` represents the phase field ($\phi \equiv T$), while in `PART-2`, an additional degree of freedom ξ is taken to be analogous to temperature ($\xi \equiv T$). Materials can be differentiated within `UMAT` and `UMATHT` subroutines using the `CMNAME` variable, which allows assignment of distinct materials to each part. Data transfer within the parts is facilitated by the identical local element numbering used by Abaqus when a geometrically identical part with the same mesh is created; the idea of *conjugate elements*, as illustrated in Fig. 1. In Abaqus, both global and local element numbering systems are used, with local element numbering being specific to each part instance within the model assembly.

The procedure proposed for implementing coupled problems involving multiple diffusion-type equations in Abaqus is described in Fig. 2. Abaqus proceeds following the global element number. Thus, for the first element (belonging to `PART-1`) and the first integration point, the `UMAT` subroutine is called first. There, the Cauchy stress $\boldsymbol{\sigma}$ and material Jacobian $\boldsymbol{C}$ are computed from the strain tensor $\boldsymbol{\epsilon}$ and any other relevant variable, coming from either the inputs of the `UMAT` (e.g., T, representing ϕ) or from the Fortran module used to communicate between the parts (e.g. ξ). The stress tensor and material Jacobian are used by Abaqus to construct the relevant residual and stiffness matrix components. Then, within that first integration point, the `UMATHT` subroutine is called. There, the internal heat energy U and the heat flux vector $\mathbf{f}$ must be defined to construct the residual vector $\mathbf{R}$, along with their variations with respect to temperature T and its gradient ∇T to form the stiffness matrix $\boldsymbol{K}$. This is done in agreement with the definitions provided previously in this section and those given in Appendix A. Data exchange between the `UMAT` and `UMATHT` subroutines can be done in a straightforward manner using state variables (SDVs).

Once Abaqus has looped over all the elements (integration points) in `PART-1`, it proceeds to `PART-2`. The `UMAT` is first called, where $\boldsymbol{\sigma} = 0$ and $\boldsymbol{C} = 0$ for the material of the second part (`MATERIAL-2`). Then, the `UMATHT` subroutine is called, where one defines U, $\mathbf{f}$, and their derivatives for ξ, the additional variable of interest. To communicate between the parts, a Fortran module is used, together with the Abaqus utility routine `GETPARTINFO`, which provides the local element number.

In terms of solving the coupled equations, various schemes exist. The monolithic scheme updates all variables simultaneously using the backward Euler method, which is unconditionally stable but can suffer from convergence issues. Conversely, the staggered method, akin to the forward Euler method, updates some primary variables while holding others constant, being more stable but potentially requiring small increments for accuracy. In our approach, the variables solved within one part can be coupled in a monolithic way but the coupling with the third variable must be done in a staggered fashion. Both single-pass and multi-pass staggered approaches are possible, as illustrated in Fig. 3, where data exchange is shown for an increment n and an iteration i. The inability to incorporate fully monolithic approaches, which can be made robust through the use of quasi-Newton schemes [64], is a disadvantage of this approach relative to user element-based implementations. However, the present approach circumvents the coding, validation, and pre- and post-processing issues associated with developing user element subroutines. The present implementation can also be extended to an arbitrary number of fields governed by diffusion-type equations by defining additional `PARTs` for each new diffusion field — for example, to simultaneously account for hydrogen effects and corrosion. The user subroutines developed are shared freely with the community and are available to download at https://mechmat.web.ox.ac.uk/codes.

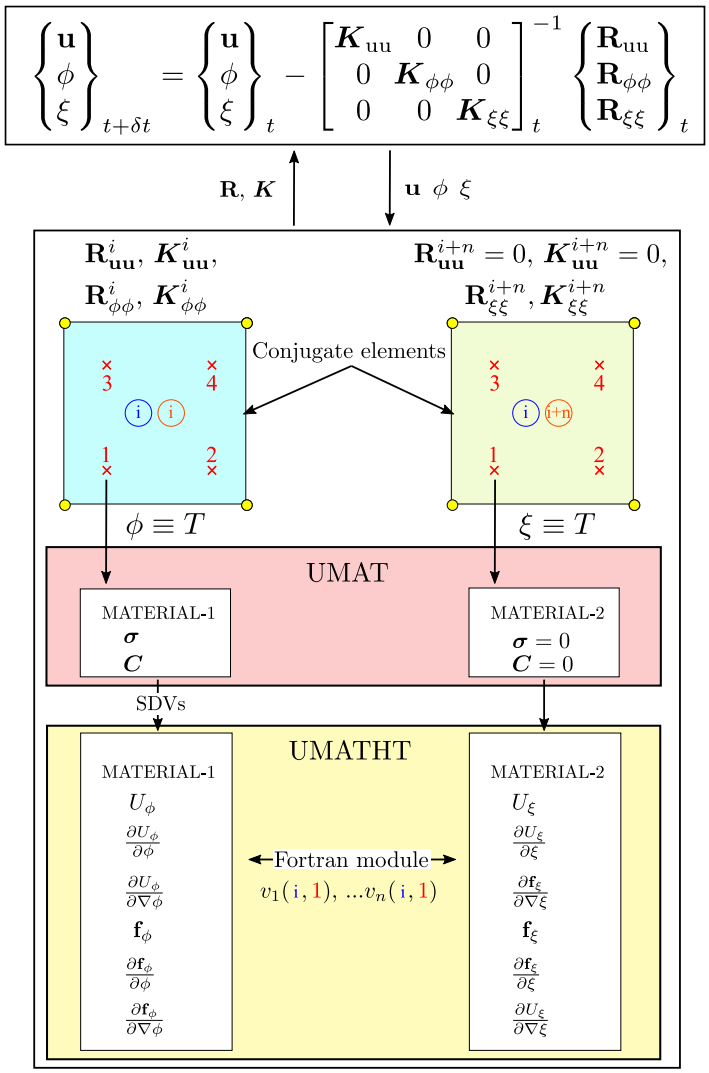

Fig. 2. Twin-part procedure to implement coupled problems in Abaqus involving multiple diffusion-type equations. Sketch describing the protocol followed by Abaqus at the integration point level, the element level, and the global equation level. For illustrative purposes, the first part is used to define the balance equations for the displacement field and the phase field, while the second part is used for an additional variable, but this can be changed depending on the solution scheme desired.

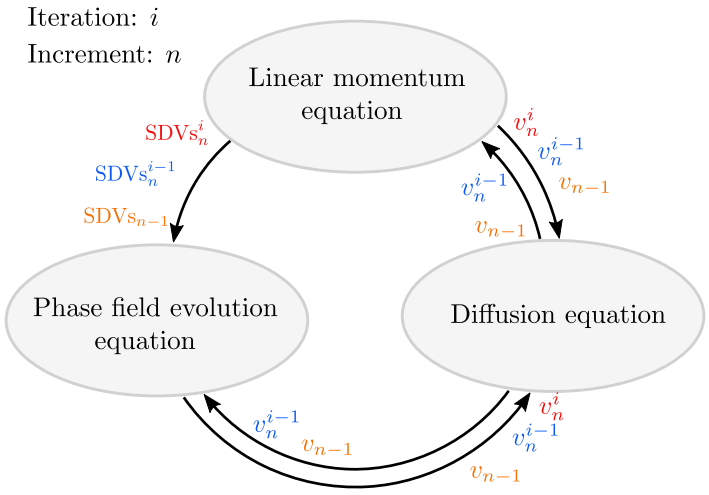

Fig. 3. Solution and data exchange schemes available in the current implementation.

Table 1
Material properties for the quenching case study [65–67].

Parameter	Value	Unit
Density ρ	3980	kg/m^3
Young's modulus E	370	GPa
Poisson's ratio ν	0.3	
Phase field length scale ℓ	0.1	mm
Toughness G_c	42.47	J/m^2
Undamaged thermal conductivity k_0	31	W/(m K)
Specific heat c_T	880	J/(kg K)
Thermal expansion coefficient α_T	7.5×10^{-6}	K^{-1}

5. Representative examples

In this section, we aim to validate and illustrate the capabilities of our multiphysics phase field implementation across different applications. This section includes detailed simulations that replicate established experiments and simulation benchmarks, showcasing the model's versatility and accuracy in various coupled problems. Specifically, we explore case studies involving thermo-mechanical fracture (Section 5.1), modelling quenching in ceramic materials; hydraulic fracture (Section 5.2), under conditions that allow validating against an analytical solution for the critical fluid pressure; hydrogen embrittlement (Section 5.3), addressing a key validation benchmark; and stress-assisted corrosion (Section 5.4), whereby two classic numerical experiments are conducted.

5.1. Thermo-mechanical fracture: quenching

To validate our phase field thermal fracture model, we replicate the classic quenching experiment by Jiang et al. [65]. The experiment involves immersing a ceramic plate (50 mm × 10 mm), which has been pre-heated up to a temperature T_0, into a water bath held at ambient temperature ($T_a = 20\,^\circ$C). The resulting change in temperature causes thermal fracture, with cracks nucleating at the outer surface and growing in parallel towards the centre of the plate. This problem has been used widely as a benchmark of thermal phase field fracture modelling. The material properties used, taken from the literature [65–67], are listed in Table 1.

The ceramic plate is discretised using a uniform grid of 4-node plane strain thermally coupled quadrilateral elements (CPE4T in Abaqus) with a characteristic element size of 0.0025 mm. The staggered scheme couples the linear momentum and phase field equations, using a fixed increment size of 0.1 ms over 200 ms of total simulation time. No decomposition of strain energy is considered for the fracture driving force. Due to symmetry, only a quarter of the plate is modelled, as shown in Fig. 4a. The range of initial temperatures considered is $T_0 = \{300, 350, 400, 500, 600\}\,^\circ$C and the boundary condition prescribed in the outer surface of the plate is $T_a = 20\,^\circ$C.

The results obtained are shown in Fig. 4b,c, in terms of the phase field contour, for the cases where the thermal conductivity is independent of the phase field ($k_T = k_0$) and for the case where it is degraded ($k_T = g(\phi)k_0$). The high-temperature gradient causes uniform damage at the perimeter of the plate, with cracks propagating inwards with uniform spacing. In both experiments and simulations, higher initial temperatures (i.e., higher gradients) result in a higher number of cracks, as expected. The agreement between modelling and experiments is notable, in terms of the number of cracks, their spacing and their extension. Numerical predictions are also in good agreement with the computational literature [34,67–70]. Differences between the degraded and undegraded thermal conductivity calculations are small, but the latter appears to be in closer agreement with experiments (fewer and longer cracks), likely due to anisotropic thermal conductivity post-cracking and potential heat transfer through closed cracks. It is also worth noting that the conventional AT2 phase field model does not include a damage threshold, which can result in a larger degree of distributed damage near the outer surface.

5.2. Hydraulic fracture

The verification of the hydraulic phase field fracture implementation is carried out through two case studies. In the first one, we examine the growth of a pressurised crack located in the centre of a square domain. This analysis aims to validate our estimation of the critical pressure, which represents the water pressure at the time of crack propagation and is denoted as p_c. To this end, a comparison with an existing analytical solution is conducted. Subsequently, the second case study is dedicated to simulating an injection-driven fracture scenario in a 3D model, shedding light on the interaction of preexisting cracks. The material parameters listed in Table 2 are considered for both case studies. Also, in these analyses, we adopt the no-tension strain energy decomposition [46,71] as the fracture driving force, accounting for the anisotropic influence of strain energy decomposition (see Appendix D).

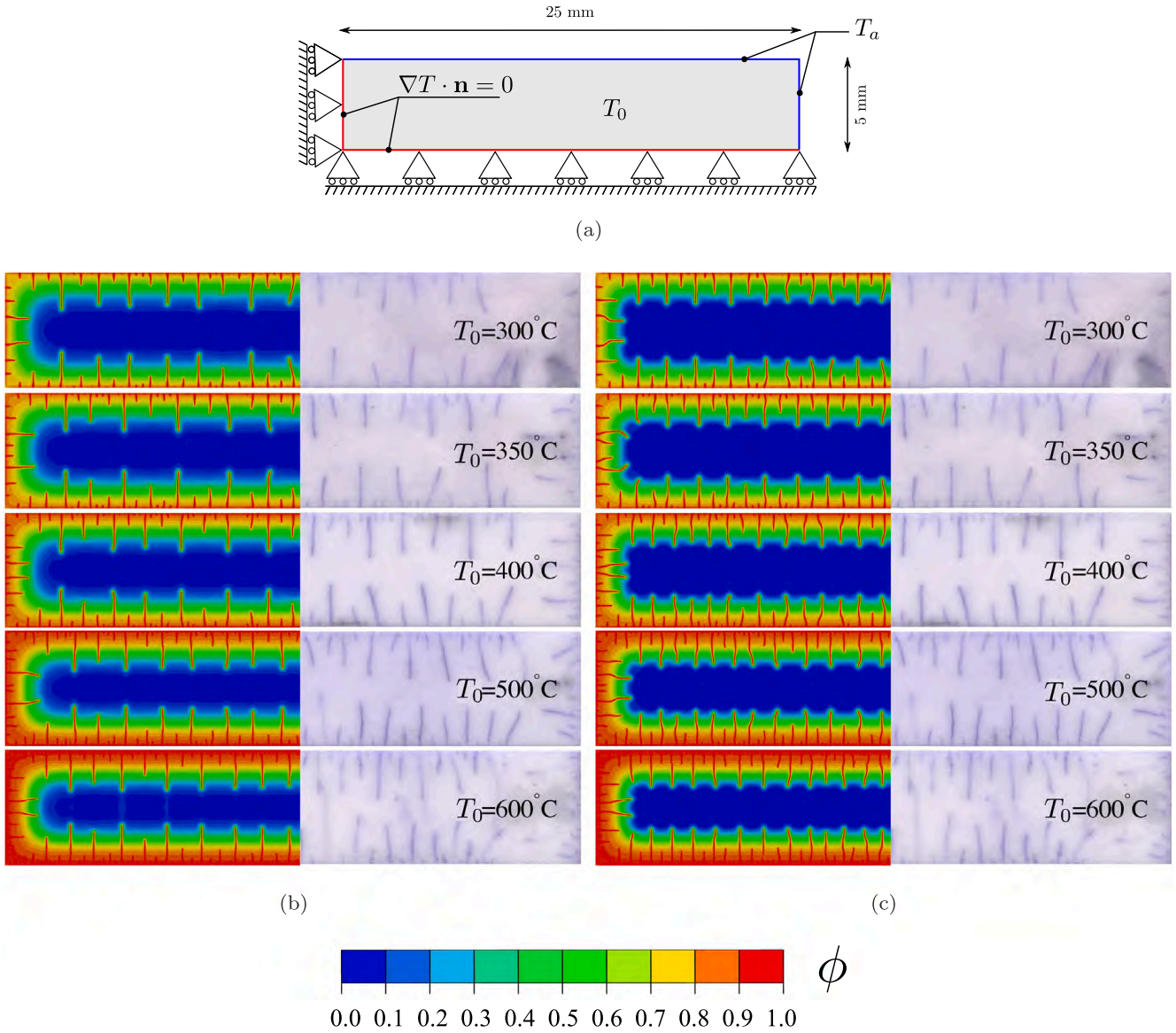

Fig. 4. Thermo-mechanical fracture (quenching) case study. (a) Geometry and boundary conditions. Comparison between simulation (phase field contours ϕ) and experimental crack patterns [65]. Two scenarios are considered: (b) a non-degraded thermal conductivity ($k_T = k_0$), and (c) a degraded thermal conductivity $k_T = g(\phi)k_0$.

Table 2
Solid and fluid materials parameters for hydraulic fracture case studies adopted in the analysis of hydraulic fracture.

Parameter	Value	Unit
Young's modulus E	210	GPa
Poisson's ratio ν	0.3	
Characteristic length scale ℓ	4	mm
Toughness G_c	2700	J/m^2
Biot's coefficient of reservoir domain α_r	2×10^{-3}	
Porosity in the reservoir domain n_{pr}	2×10^{-3}	
Mass density of the fluid ρ_{fl}	1000 kg/m^3	kg/m^3
Fluid viscosity μ_{fl}	1×10^{-3}	Pa s
Fluid compressibility C_{fl}	1×10^{-8}	Pa^{-1}
Permeability tensor of reservoir domain $\boldsymbol{K}_r$	$1 \times 10^{-15}\boldsymbol{I}$	m^2
Permeability tensor of fracture domain $\boldsymbol{K}_f$	$1.333 \times 10^{-6}\boldsymbol{I}$	m^2
First constants for domain indicator fields c_1	0.4	
Second constants for domain indicator fields c_2	1	

5.2.1. Pressurised crack

The first case study involves a square domain featuring a centred crack, subjected to a gradually increasing pressure up to $p = 100$ MPa over a period of 2000 s. In practice, this is implemented by defining a temperature Dirichlet boundary condition,

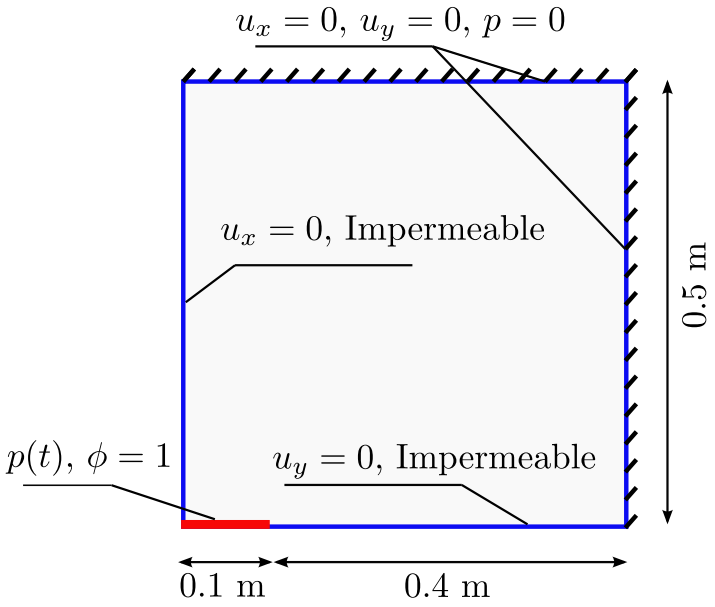

Fig. 5. Geometry, dimensions, and boundary conditions of the pressurised crack case study.

exploiting the analogy between pressure and temperature. The geometric configuration and boundary conditions of the model are depicted in Fig. 5, with only a quarter of the model simulated to exploit its inherent double symmetry.

The finite element mesh comprised 14,443 eight-node biquadratic displacement, bilinear temperature elements (Abaqus type CPE8T). The mesh was refined in the region where cracking was anticipated, ensuring that the smallest element size was maintained at one-fifth of the characteristic length ℓ. The monolithic scheme was employed to solve the coupled deformation-fracture problem, while a multi-pass staggered scheme is adopted to handle the coupling with the fluid equation. 100 increments are used, each spanning 20 s.

The evolution of the crack and the pressure distribution are shown in Fig. 6 for three selected time intervals: 1140, 1200 and 1400 s. The initiation of crack growth occurs at a time of 1140 s, as shown in Fig. 6(a), with a central domain pressure p_{center} of 57 MPa. Subsequently, the crack extends along the mode I crack trajectory until reaching the edge of the domain, with the associated increase in pressure along the cracked domain being appropriately captured by the model, see Figs. 6b and 6c.

We proceed to compare the critical pressure p_c estimates of the model with the analytical solution by Yoshioka and Bourdin [72] (see also Ref. [73]). The dependency of p_c on the initial crack length a_0, material toughness G_c and elastic properties is given by,

$$p_c = \left(\frac{4E'G_c}{\pi a_0}\right)^{\frac{1}{2}}, \tag{73}$$

where $E' = E/(1-\nu^2)$ is the plane strain Young's modulus, with ν being Poisson's ratio. The comparison between the critical pressure estimates from Eq. (73) and those from the present phase field-based numerical framework are shown in Fig. 7. Results are obtained for various choices of the material toughness G_c. Overall, the analytical and numerical results are in very good agreement, with the numerical results slightly underpredicting the fluid pressure at the time at crack propagation.

5.2.2. 3D cracking due to an injected fluid

The second case study investigates the interaction of pre-existing cracks in a three-dimensional configuration. A cubic domain with a characteristic length of 0.5 m is considered, featuring two cracks in the XY plane, prolonged along the Z direction (Fig. 8a), each with a length of 0.05 m. One crack is positioned horizontally at the centre of the domain in the XY plane, while the other crack is inclined and located away from the centre, as illustrated in Fig. 8b. The domain is discretised using approximately 268,000 8-node thermally coupled brick, trilinear displacement and temperature elements (C3D8T), with the characteristic finite element length being 2 mm. Different to the previous case study, crack growth is here driven by fluid injection. Specifically, a fluid source of $q_m = 4000\,\text{kg}/(\text{m}^3\ \text{s})$ is applied and held constant over a time of 300 s. This is achieved by defining a body heat flux (r in Eq. (65)) on the elements located in the central crack. A staggered solution scheme is employed in this model with a time increment of 1 s.

The results obtained are shown in Fig. 9. The crack path is shown using the phase field contour in Fig. 9a for time of $t = 300$ s. The pressure contour at that time, the steady state situation, is given in Fig. 9b. The fluid flux vector, computed based on Darcy's law ($\mathbf{q} = -\rho_{\text{fl}}\frac{\boldsymbol{K}_{\text{fl}}}{\mu_{\text{fl}}}\nabla p$), is also superimposed on the figure. This quantity is equivalent to the heat flux vector $\mathbf{f}$ in the thermal analogy presented in Eq. (70). The time evolution of the pressure at the centre of the domain is given in Fig. 9c. Insets of the phase field contour are also included to depict crack evolution over time. The result shows that the pressure increases upon water injection until the initiation of crack growth. At this point, the maximum water pressure exceeds 150 MPa. As crack propagation occurs, the pressure starts to decrease, with a sharper decline when the two cracks approach each other. Over time, both cracks propagate

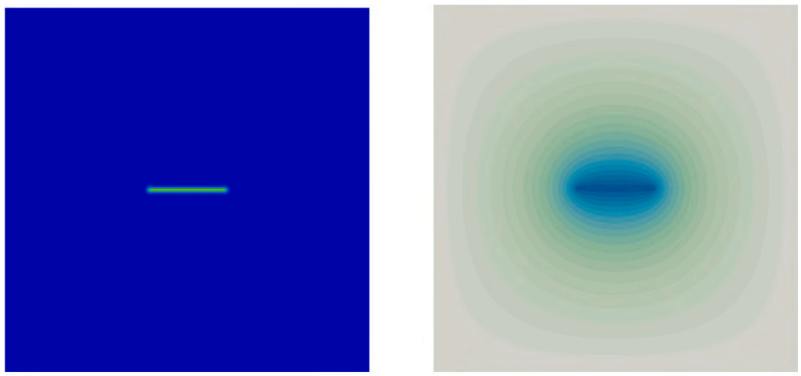

(a) Time $t = 1140$ s, $p_{\text{center}} = 57$ MPa

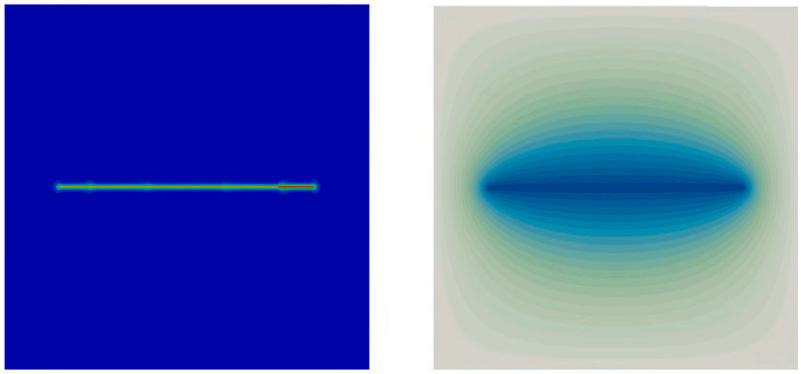

(b) Time $t = 1200$ s, $p_{\text{center}} = 60$ MPa

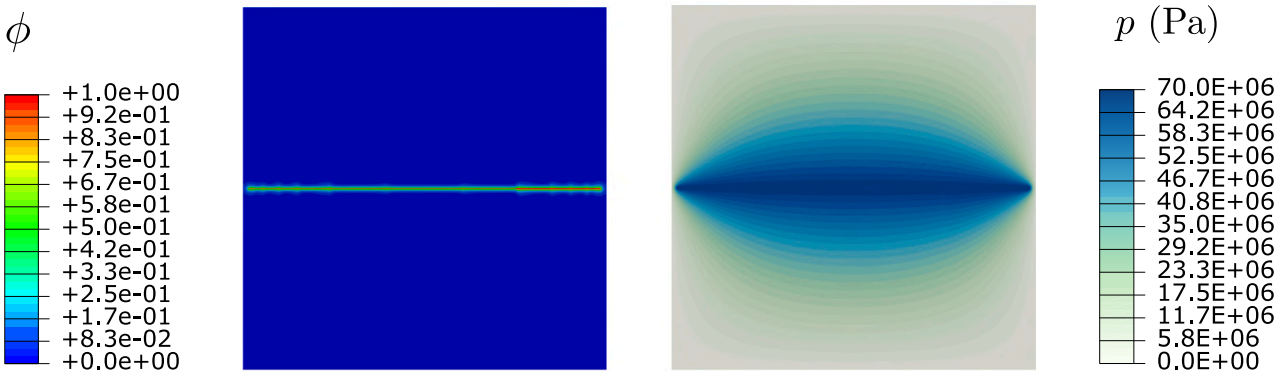

(c) Time $t = 1400$ s, $p_{\text{center}} = 70$ MPa

Fig. 6. Contours of phase field ϕ (left) and fluid pressure p (right) for a pressurised crack at different times: (a) $t = 1140$ s, $p_{\text{center}} = 57$ MPa, (b) $t = 1200$ s, $p_{\text{center}} = 60$ MPa, and (c) $t = 1400$ s, $p_{\text{center}} = 70$ MPa.

and coalesce. However, after reaching a steady state, which is characterised by a constant pressure at the centre, no further crack propagation is observed.

5.3. Hydrogen embrittlement

The ability of the present framework to simulate hydrogen-assisted fractures is here demonstrated by benchmarking against literature results of the classic edge-cracked square plate boundary value problem, first studied by Martínez-Pañeda et al. [36]. The geometry and loading configuration are given in Fig. 10. The specimen is initially saturated with a constant hydrogen concentration c_{H}, equivalent to the environmental concentration c_{env}. Subsequently, a displacement is applied to the top of the plate over 10^7 s in 2000 increments. The mechanical and hydrogen transport parameters are listed in Table 3.

The domain is discretised into approximately 36,000 8-node plane strain thermally coupled quadrilateral elements with biquadratic displacement and bilinear temperature discretisation (denoted as CPE8T in Abaqus). The mesh around the predicted

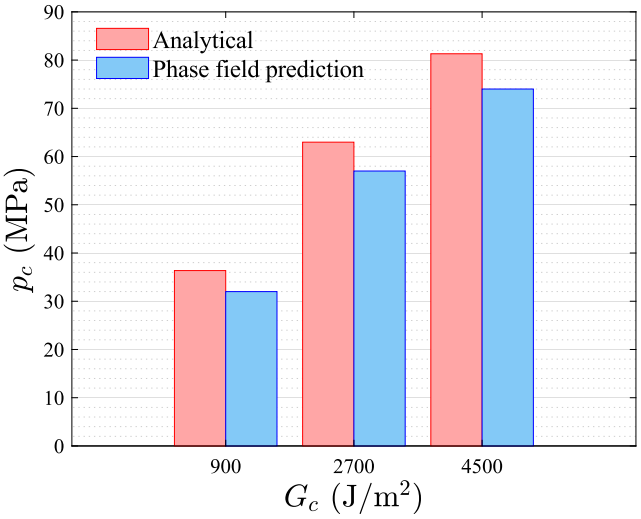

Fig. 7. Comparison of critical fluid pressure p_c predictions, as obtained from the analytical solution given in Eq. (73) and through the present phase field model.

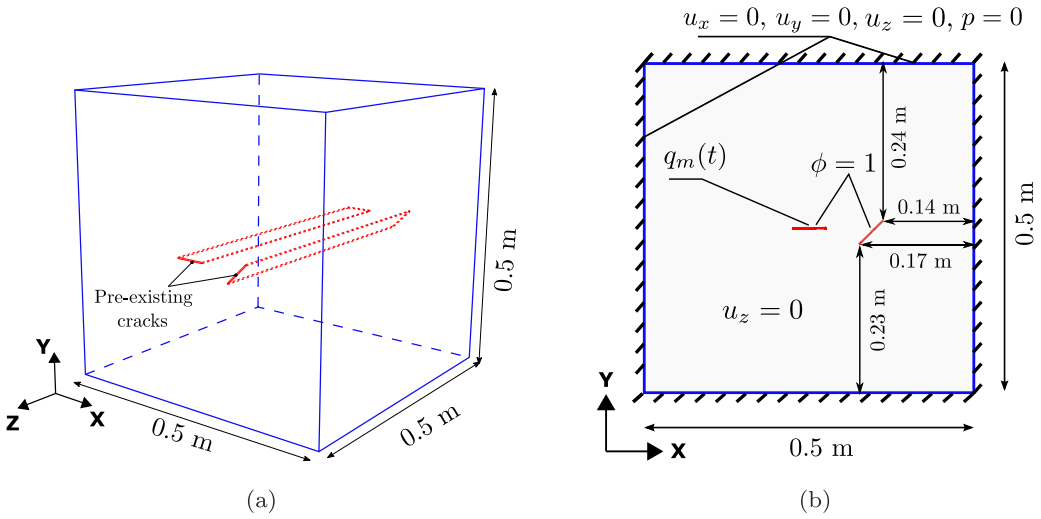

Fig. 8. Boundary value problem: Cubic domain with two preexisting cracks, (a) 3D geometry, and (b) boundary conditions shown in XY plane.

Table 3
Material properties for hydrogen embrittlement.

Parameter	Value	Unit
Young's modulus E	210	GPa
Poisson's ratio ν	0.3	
Phase field length scale ℓ	0.0075	mm
Toughness G_c	2.7	kJ/m^2
Hydrogen diffusion coefficient D_{H}	0.0127	mm^2/s
Trap binding energy Δg_b^0	30	kJ/mol
Hydrogen damage coefficient χ_{H}	0.89	
Temperature T_{k}	300	K

crack path was refined, with the element size being five times smaller than the characteristic phase field length ℓ. As shown in Eq. (71), one must compute the gradient of hydrostatic stress $\nabla\sigma_h$. This is achieved here by extrapolating the integration point values of σ_h to the nodes using appropriate shape functions. To build these shape functions, at the beginning of the analysis we store all the relevant information (node numbers and coordinates, and element connectivity), using a `UEXTERNALDB` subroutine (as shown in the codes provided). Then, the strain–displacement matrices (so-called $\boldsymbol{B}$-matrices) are used to estimate $\nabla\sigma_h$ at the integration points. A staggered solution scheme was employed.

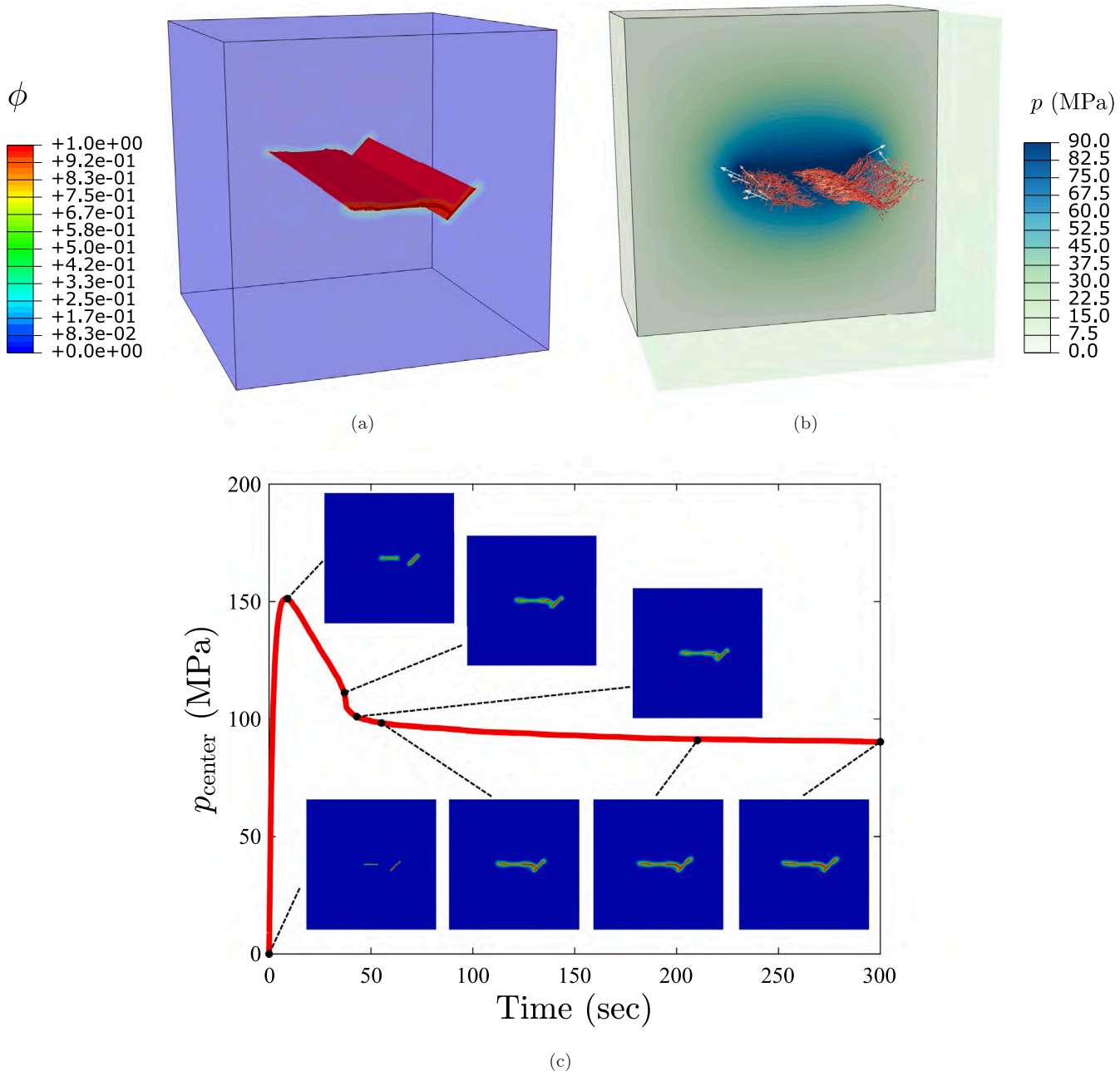

Fig. 9. Cracking due to an injected fluid in a cube: (a) phase field contours depicting the crack trajectory, (b) fluid flux vector and fluid pressure contour p in the XY plane at $Z = -0.25$ m, and (c) fluid pressure at the centre of the domain p_{center} versus time, also showing phase field contours at selected times.

The comparison of the load versus displacement responses obtained with our numerical framework and those from Cui et al. [41] are given in Fig. 11. The agreement is satisfactory but not excellent. Differences could be due to the loading rate (not reported in Ref. [41]), the different approach employed to estimate the gradient of the hydrostatic stress σ_h, the lack of a penalty boundary condition on our simulation, or the use of fully integrated elements (as opposed to reduced integration elements in Ref. [41]). For both cases, it can be seen that increasing hydrogen content results in a drop in the peak load and a reduction in the failure displacement. A sharper softening is observed in our simulation, suggesting a more accurate representation of material behaviour (unstable crack growth is expected).

The evolution of the phase field contour and of the normalised hydrogen concentration are illustrated in Fig. 12, for selected time steps and the case of $c_{\text{env}} = 0.5$ wppm. It can be seen that the model captures the accumulation of hydrogen near the crack tip, due to the role that hydrostatic stresses play in driving hydrogen diffusion. The hydrogen concentration contours are smooth and follow the crack tip as it propagates, as a result of the low load rate considered. The good agreement attained with experimentally-validated models (see, e.g., Refs. [74,75]) demonstrates that the present framework is also capable of predicting hydrogen-assisted failures in laboratory and practical conditions.

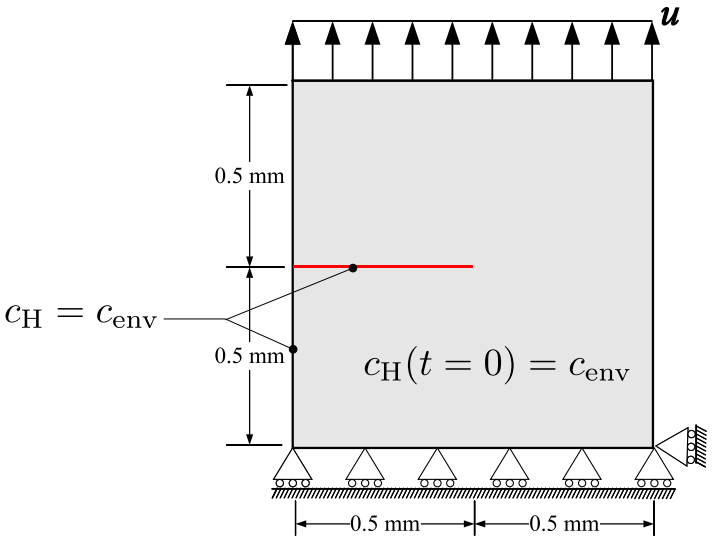

Fig. 10. Geometry and boundary conditions for the notched square plate under tension exposed to hydrogen.

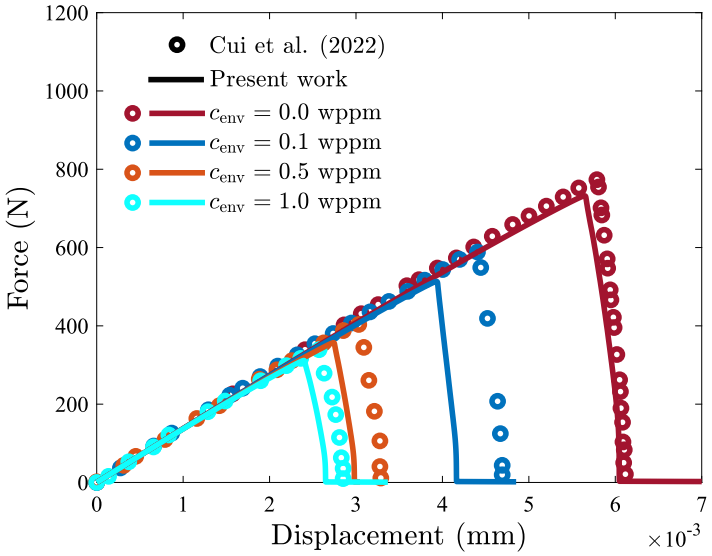

Fig. 11. Hydrogen embrittlement of a square plate under tension. Load versus applied displacement predictions for various hydrogen contents, as obtained with the present implementation and as reported in the work by Cui et al. [41].

Finally, calculations are conducted under selected loading rates, to showcase the model's ability to capture the qualitative trend observed in experiments and bring insight into the differences observed with the predictions by Cui et al. [41]. For slow loading rates, there is less time for the hydrogen to accumulate in the fracture process zone and therefore, a higher resistance to fracture is expected. The results obtained are given in Fig. 13, for the case of $c_{\text{env}} = 0.5$ wppm. The two limit cases of $\dot{u} \to 0$ (where c_H follows the steady state solution) and $\dot{u} \to 0$ (where the hydrogen concentration is uniform and equal to the initial hydrogen concentration), together with four selected intermediate cases. The results show that the model is able to capture the sensitivity to loading rate and reveal the variation in critical load that can be attained with changes in loading rate.

5.4. Stress corrosion cracking

The last case study showcases the ability of the present framework to simulate stress-assisted corrosion. This is achieved by considering two boundary value problems involving localised corrosion phenomena: pitting and (anodic dissolution-driven) stress corrosion cracking. The first example examines a plate with a semi-circular pit in the absence of mechanical load, to validate the phase field corrosion implementation, while the second involves a plate with a semi-elliptical pit subjected to a remote displacement. Our results are compared with findings from the literature. In both case studies, a monolithic scheme is used to couple displacement with the phase field evolution equation, while the metallic ion transport equation is coupled via a multi-pass staggered method.

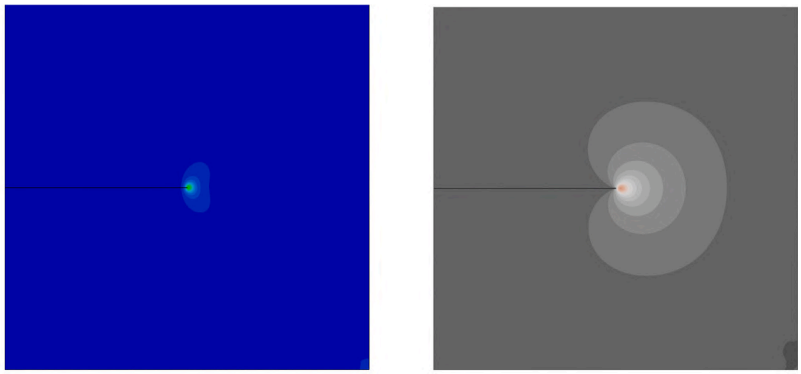

(a) $u = 0.00273$ mm

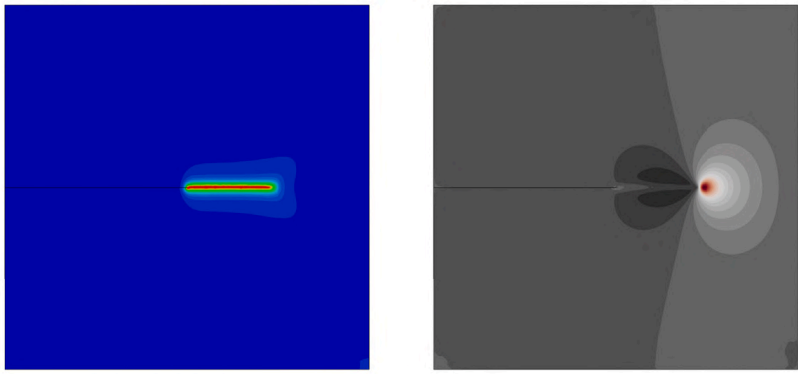

(b) $u = 0.00287$ mm

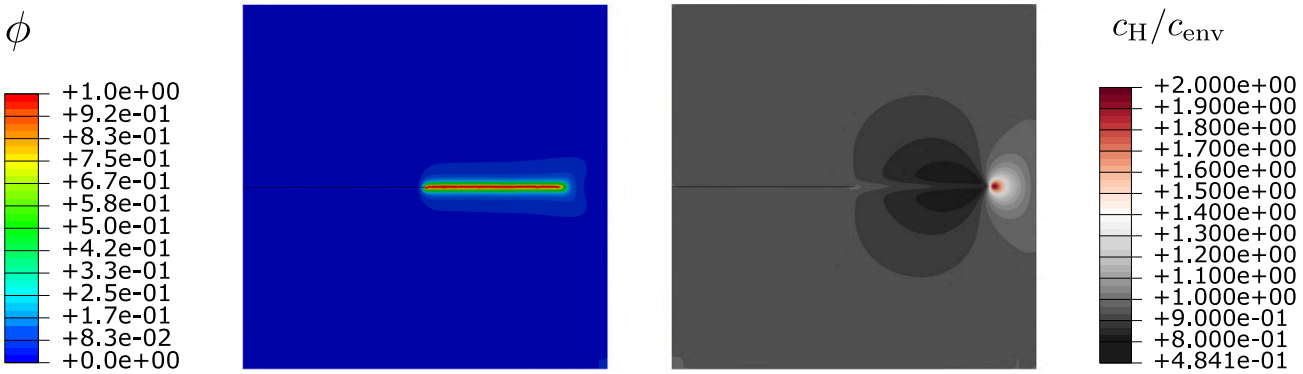

(c) $u = 0.00294$ mm

Fig. 12. Phase field contours (left) and normalised hydrogen concentration (right) for $c_{env} = 0.5$ wppm in the square plate under tension at different displacements u: (a) $u = 0.00273$ mm, (b) $u = 0.00287$ mm, and (c) $u = 0.00294$ mm.

5.4.1. Growth of a semi-circular pit

We validate pit growth in the absence of stress using a rectangular plate with an initial semi-circular pit. This setup was previously simulated by Duddu [76] using the level set method and by Mai et al. [9], Gao et al. [77], and Cui et al. [41] using the phase field method. The geometry and boundary conditions are shown in Fig. 14, and the material parameters considered are listed in Table 4. To achieve diffusion-controlled pit growth, a large value of L_0 is considered. The minimum element size is set to 0.001 mm, and approximately 30,000 8-node reduced integration elements that provide biquadratic discretisation for the displacement field and bilinear discretisation for the temperature field are adopted (denoted as CPE8RT in Abaqus). No film rupture or repassivation effects are considered in this case study (i.e., $k = 0$).

The results obtained are shown in Figs. 15a and 15b, depicting pit growth by means of phase field contours. The results are shown for a time of 50 s for our implementation and that by Cui et al. [41], respectively. An excellent agreement is observed. Moreover, predictions match the experimental results by Ernst and Newman [78], showing that a semi-circular pit remains semi-circular in

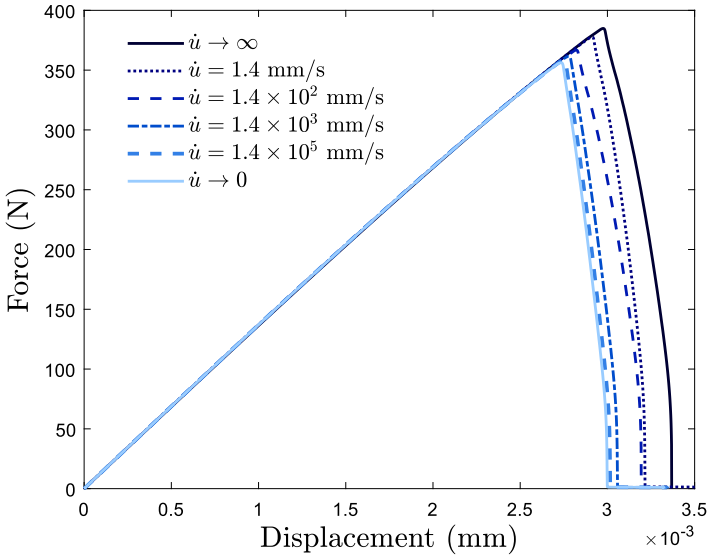

Fig. 13. Hydrogen embrittlement of a square plate under tension: effect of the loading rate. Load versus applied displacement predictions for various loading rates (including the two limit cases of very fast and very slow tests) for the case of $c_{\text{env}} = 0.5$ wppm.

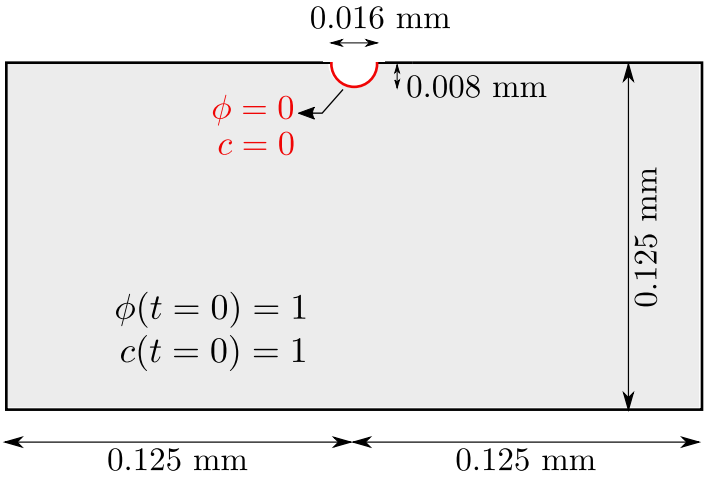

Fig. 14. Geometry and boundary conditions for the semi-circular pit example.

Table 4
Material parameters for the stress-assisted corrosion case study.

Parameter	Value	Unit
Gradient energy coefficient κ	51×10^{-6}	J/m
Height of the double-well potential ω	35.3×10^6	J/m^3
Temperature T	300	K
Diffusion coefficient of metal ion D_m	8.5×10^{-4}	mm^2/s
Interface kinetics coefficient L_0	2×10^6	mm^2/(N s)
Free energy density curvature A	53.5	N/mm^2
Average concentration of metal c_{solid}	143	mol/L
Average saturation concentration c_{sat}	5.1	mol/L

the absence of stress during corrosion. The evolution of pit depth over time is quantitatively compared with the predictions by Cui et al. [41] in Fig. 15c, showing a very good agreement.

5.4.2. Growth of a semi-elliptical pit under stress

The ability to couple corrosion and mechanical phenomena is investigated by predicting the evolution of a pre-existing semi-elliptical pit in a stainless steel plate subjected to a remote displacement. This case study was first simulated by Cui et al. [10] and reproduced by others since. The geometry and boundary conditions are illustrated in Fig. 16. A uniform displacement of $u = 0.0002$ mm is applied linearly over 1 s to both the right and left sides and then maintained constant throughout the simulation.

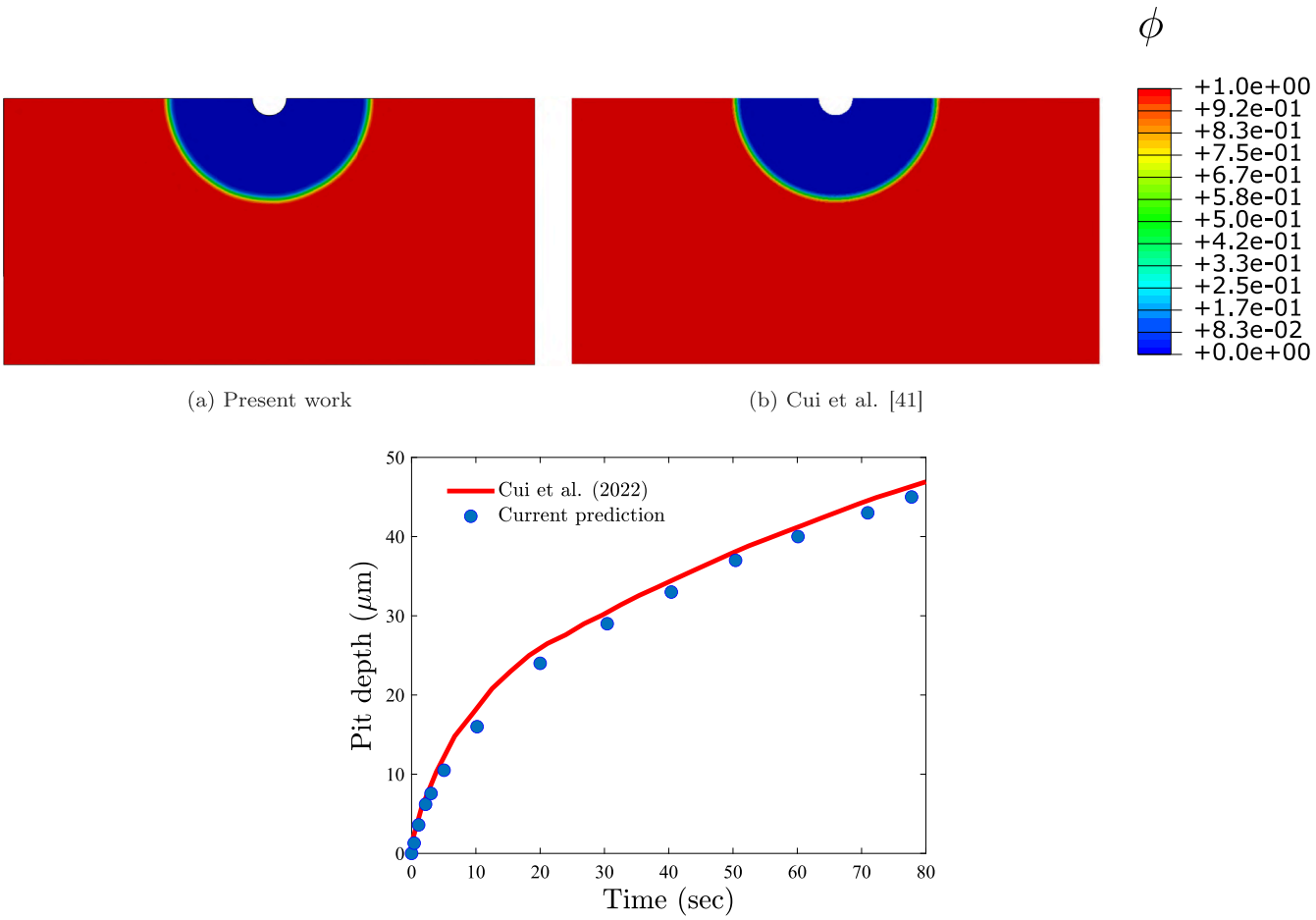

Fig. 15. Pit growth for a semi-circular pit. Phase field contours at a time of $t = 50$ s, as obtained with (a) our current implementation, and (b) by Cui et al. [41]. A quantitative comparison of pit depth versus time is given in (c).

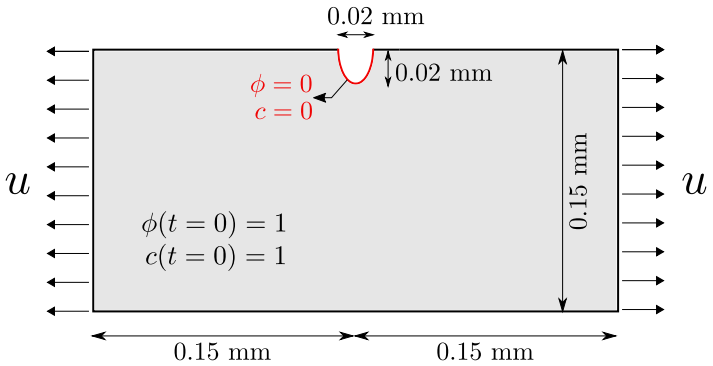

Fig. 16. Geometry and boundary conditions of the semi-elliptical pit.

Over the pit domain (red line in Fig. 16), we enforce $\phi = 0$ and $c = 0$, while the remaining regions are initialised with $\phi(t = 0) = 1$ and $c(t = 0) = 1$. Unless otherwise specified, the material parameters adopted correspond to those used in the previous case study and provided in Table 4. A stability parameter of $k = 5 \times 10^{-4}$ is considered, with a time interval before decay begins set at $t_0 = 10$ s and a critical strain for film rupture of $\varepsilon_f = 3 \times 10^{-3}$. The initial interface kinetics coefficient is given as $L_0 = 0.001$ mm^2/ (N s). The mechanical parameters include a Young's modulus of $E = 190$ GPa, a Poisson's ratio of $\nu = 0.3$, an initial yield stress of $\sigma_y = 520$ MPa, and a strain hardening exponent of $N = 0.067$. The computational domain is discretised using over 13,000 8-node elements with reduced integration (CPE8RT). The characteristic element size in the central region is set to 0.005 mm.

The results of the present study are illustrated in Fig. 17. Upon applying the prescribed boundary conditions, the phase field corrosion process initiates and evolves over time. As corrosion progresses, the material undergoes degradation, leading to a reduction in its stiffness, as evidenced by the contours of hydrostatic stress σ_h and the phase field variable ϕ at different time steps shown in Fig. 17a-c. The role of the evolving corrosion pit in acting as a stress concentrator is also shown. Fig. 17d presents the distributions

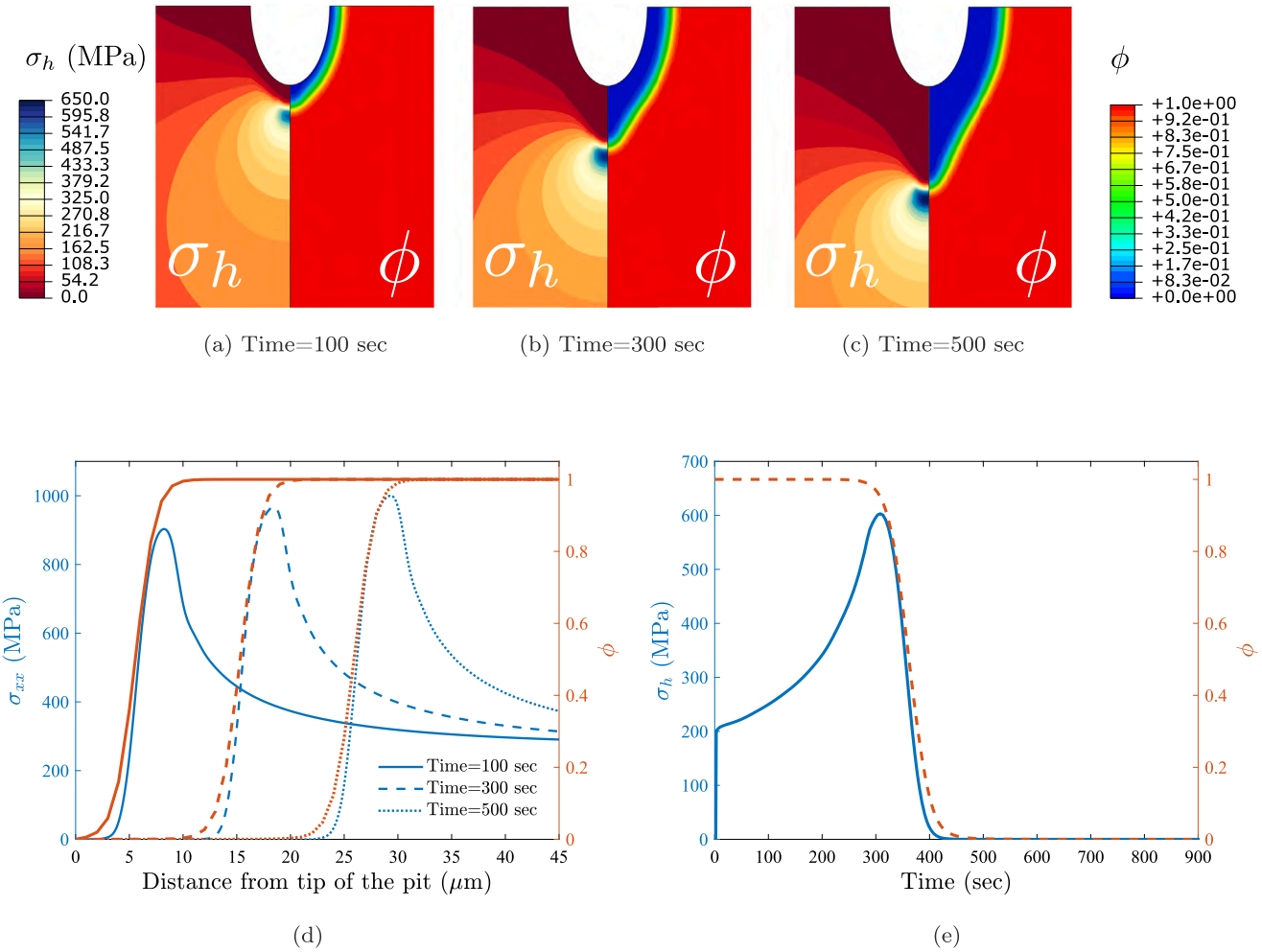

Fig. 17. Stress-assisted corrosion originating from a semi-elliptical pit. Contours of hydrostatic stress σ_h (left) and phase field variable ϕ (right) are shown for: (a) t = 100 s, (b) t = 300 s, and (c) t = 500 s. The distributions of normal stress σ_{xx} and phase field variable ϕ along the vertical line from the pit tip at $t = \{100, 300, 500\}$ s are presented in (d). The temporal evolution of hydrostatic stress σ_h and phase field variable ϕ at a vertical distance of 20 μm from the pit tip is shown in (e).

of normal stress σ_{xx} and the phase field variable ϕ along a vertical line extending from the initial pit tip at times $t = \{100, 300, 500\}$ s. These results show how the stress vanishes in regions where $\phi = 0$, representing fully corroded material. Fig. 17e shows the temporal evolution of hydrostatic stress and the phase field variable at a point located 20 μm below the initial pit tip. As observed, hydrostatic stress initially increases during the first second due to the application of displacement. Subsequently, as the pit grows and the corrosion front approaches this point, the hydrostatic stress continues to rise. However, once the solid material at this location transitions to the electrolyte phase (i.e., as ϕ approaches 0), the loss of stiffness leads to a decrease in hydrostatic stress.

The results are compared with those obtained from the UEL code provided by Cui et al. [10]. A comparison of the phase field contours from our current simulation (Fig. 18a) with those from the UEL code by Cui et al. [10] (Fig. 18b) demonstrates an excellent agreement. This is corroborated further by the quantitative comparison of pit depth versus time shown in Fig. 18c. It is important to note that the reference results by Cui et al. [10] have been computed using the UEL code provided, which corresponds to the formulation used in Ref. [41]. Slight differences exist due to the arrangement of the weak form, as discussed in Appendix C.

6. Conclusions

We have presented a generalised formulation to handle coupled phase field fracture and corrosion problems under the same theoretical structure. The versatility of the heat transfer equation is then exploited to provide a novel computational framework capable of handling coupled phase field problems. This significantly facilitates the numerical implementation, which can be done at the integration point level in commercial finite element packages. This is demonstrated in Abaqus but the approach is universal and could be adopted in other platforms. The applications explored span hydraulic fracture, thermal fracture, hydrogen embrittlement and stress-assisted corrosion. 2D and 3D problems are considered. The associated user material subroutines are made freely available to showcase the simplicity of the approach. The results obtained with the novel computational framework presented are well-aligned with experimental and computational results from the literature involving the quenching of ceramic plates, the propagation of

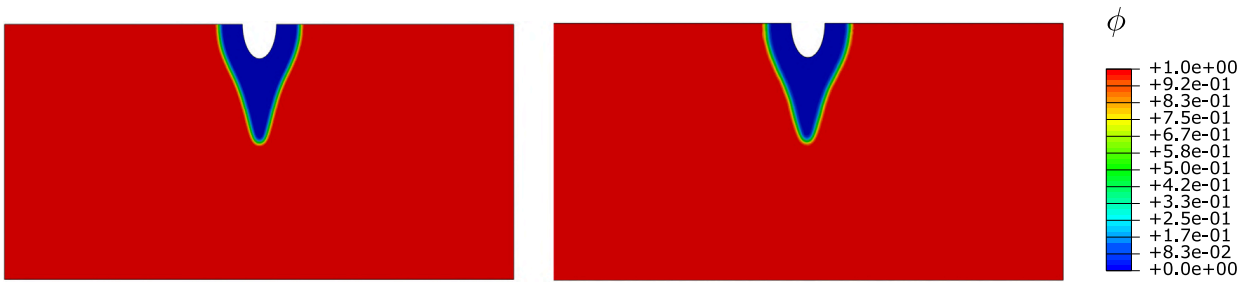

(a) Present work (b) Cui et al. [10]

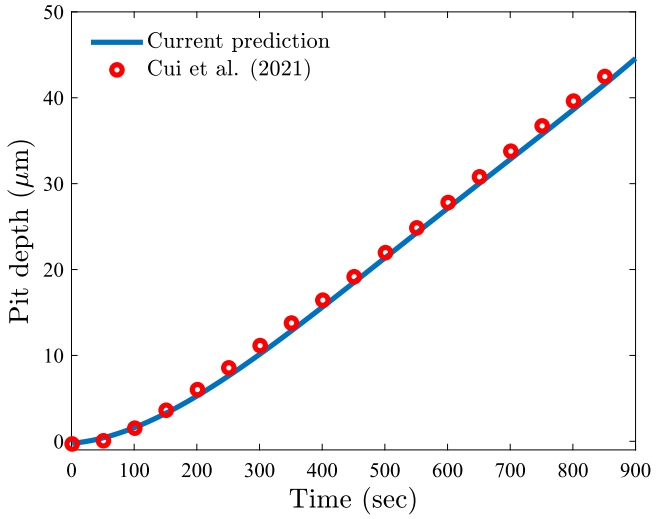

(c)

Fig. 18. Stress-assisted corrosion from a semi-elliptical pit. Phase field contours at a time of $t = 900$ s for: (a) the present implementation, and (b) as obtained with the UEL code by Cui et al. [10]. A quantitative comparison of pit depth versus time is given in (c).

pressure and fluid injection-driven cracks in porous media, the growth of cracks assisted by hydrogen in metallic materials, and the corrosion of metals and their interplay with mechanical fields.

CRediT authorship contribution statement

Yousef Navidtehrani: Writing – review & editing, Writing – original draft, Visualization, Validation, Software, Methodology, Investigation, Formal analysis, Data curation, Conceptualization. **Covadonga Betegón:** Writing – review & editing, Supervision, Resources, Project administration, Funding acquisition, Conceptualization. **Emilio Martínez-Pañeda:** Writing – review & editing, Supervision, Software, Resources, Project administration, Methodology, Investigation, Funding acquisition, Conceptualization.

Declaration of competing interest

The authors declare that they have no known competing financial interests or personal relationships that could have appeared to influence the work reported in this paper.

Acknowledgments

Y. Navidtehrani and C. Betegón acknowledge financial support from the Ministry of Science, Innovation, and Universities of Spain through grant MCINN-22-TED2021-130306B-100. Additionally, C. Betegón acknowledges financial support from the Ministry of Science, Innovation, and Universities of Spain under grant MCINN-23-PID2022-1420150B-100. E. Martínez-Pañeda was supported by a UKRI Future Leaders Fellowship (grant MR/V024124/1).

Table A.5
Unified table of quantities to be defined in a UMATHT subroutine for various equations and their thermal analogies.

Equation	U	DUDT	DUDG	FLUX	DFDT	DFDG
General heat transfer Eq. (65)	$U_t + \dot{U}\delta t$	$\frac{\partial U}{\partial T}$	$\frac{\partial U}{\partial(\nabla T)}$	$\mathbf{f}$	$\frac{\partial \mathbf{f}}{\partial T}$	$\frac{\partial \mathbf{f}}{\partial(\nabla T)}$
General phase field Eq. (66)	$U_t - \eta\delta\phi - w'(\phi)\delta t - g'(\phi)(f_{b1}(\beta) - f_{b2}(\beta))\delta t$	$-\eta - w''(\phi)\delta t - g''(\phi)(f_{b1}(\beta) - f_{b2}(\beta))\delta t$	0	$\kappa\nabla\phi$	0	$\kappa \boldsymbol{I}$
Phase field fracture Eq. (67)	$U_t + \left(\frac{\phi}{\ell^2} + g'(\phi)\frac{\mathcal{H}}{G_c\ell}\right)\delta t$	$\left(\frac{1}{\ell^2} + g''(\phi)\frac{\mathcal{H}}{G_c\ell}\right)\delta t$	0	$-\nabla\phi$	0	$-\boldsymbol{I}$
Metal ion transport Eq. (68)	$U_t + \delta c$	1	0	$-D_m\nabla c + D_m\nabla(h(\phi)(c_{\mathrm{Se}} - c_{\mathrm{Le}}) - c_{\mathrm{Le}})$	0	$-D_m\boldsymbol{I}$
Phase field corrosion Eq. (69)	$U_t - \frac{1}{L}\delta\phi - \frac{\partial\psi^{\mathrm{ch}}}{\partial\phi}\delta t$	$-\frac{1}{L} - \frac{\partial^2\psi^{\mathrm{ch}}}{\partial\phi^2}\delta t$	0	$\kappa\nabla\phi$	0	$\kappa\boldsymbol{I}$
Fluid flow Eq. (70)	$U_t + \left(S\delta p + \alpha_b\chi_{\mathrm{r}}\delta\varepsilon_{\mathrm{vol}}\right)$	S	0	$-\rho_{\mathrm{f1}}\frac{\boldsymbol{K}_{\mathrm{fl}}}{\mu_{\mathrm{fl}}}\nabla p$	0	$-\rho_{\mathrm{f1}}\frac{\boldsymbol{K}_{\mathrm{fl}}}{\mu_{\mathrm{fl}}}\boldsymbol{I}$
Hydrogen transport Eq. (71)	$U_t + \delta c_{\mathrm{H}}$	1	0	$-D_{\mathrm{H}}\nabla c_{\mathrm{H}} + \frac{D_{\mathrm{H}}}{RT_{\mathrm{k}}}c_{\mathrm{H}}V_{\mathrm{H}}\nabla\sigma_h$	$\frac{D_{\mathrm{H}}}{RT_{\mathrm{k}}}V_{\mathrm{H}}\nabla\sigma_h$	$-D_{\mathrm{H}}\boldsymbol{I}$
Heat transfer Eq. (72)	$U_t + c_T\delta T$	c_T	0	$-k_T\nabla T$	0	$-k_T\boldsymbol{I}$

Appendix A. Using a UMATHT subroutine to implement diffusion-type equations

Diffusion-type equations can be readily implemented into commercial finite element packages exploiting the analogy with heat transfer, as discussed in Section 4. In Abaqus, this is achieved through a user-defined thermal material behaviour subroutine (UMATHT). One must define relevant variables, including the internal thermal energy per unit mass U, the variation of internal thermal energy per unit mass with respect to temperature $\partial U/\partial T$, the variation of internal thermal energy per unit mass with respect to the spatial gradients of temperature $\partial U/\partial(\nabla T)$, the heat flux vector $\mathbf{f}$, the variation of the heat flux vector with respect to temperature $\partial\mathbf{f}/\partial T$, and the variation of the heat flux vector with respect to the spatial gradients of temperature $\partial\mathbf{f}/\partial(\nabla T)$. Table A.5 provides the mapping of those variables to the relevant variables of each of the governing equations considered in this work (heat transfer, hydrogen transport, fluid flow, corrosion, transport of metallic ions, phase field corrosion, phase field fracture).

Appendix B. Finite element discretisation of multiphysics phase field models

While in this work the numerical implementation is conducted at the integration point level, details of a more general implementation are also provided for completeness. In a three-field problem involving mechanical deformation, phase transformations and a diffusion-type equation one typically solves for the displacement vector $\mathbf{u}$, the phase field order parameter ϕ and the diffusion field ξ as primary (nodal) variables. Their associated balance equations are provided in Eqs. (28)–(30). Then, using test functions $\delta\mathbf{u}$, $\delta\phi$, and $\delta\xi$, the integral form can be written as:

$$\begin{aligned}
&\int_\Omega \left[\nabla\cdot\boldsymbol{\sigma} + \mathbf{b}\right]\delta\mathbf{u}\,\mathrm{d}V = 0,\\
&\int_\Omega \left[\kappa\nabla^2\phi - w'(\phi) - g'(\phi)\left(f_{\mathrm{b1}} - f_{\mathrm{b2}}\right) - \eta\dot{\phi}\right]\delta\phi\,\mathrm{d}V = 0,\\
&\int_\Omega \left[\rho\dot{U}_\xi + \nabla\cdot\mathbf{f}_\xi - q_\xi\right]\delta\xi\,\mathrm{d}V = 0.
\end{aligned} \tag{B.1}$$

Using the divergence theorem, the weak form of each equation becomes:

$$\begin{aligned}
&\int_\Omega \left[-\boldsymbol{\sigma} : \nabla^{\mathrm{sym}}\delta\mathbf{u} + \mathbf{b}\delta\mathbf{u}\right]\,\mathrm{d}V + \int_{\partial\Omega}\delta\mathbf{u}\boldsymbol{\sigma}\cdot\mathbf{n}\,\mathrm{d}S = 0,\\
&\int_\Omega \left[\left(w'(\phi) + g'(\phi)\left(f_{\mathrm{b1}} + f_{\mathrm{b2}}\right) + \eta\dot{\phi}\right)\delta\phi + \kappa\nabla\phi\cdot\nabla\delta\phi\right]\,\mathrm{d}V - \int_{\partial\Omega}\delta\phi\kappa\nabla\phi\cdot\mathbf{n}\,\mathrm{d}S = 0,\\
&\int_\Omega \left[\left(\rho\dot{U}_\xi - q_\xi\right)\delta\xi - \mathbf{f}_\xi\cdot\nabla\delta\xi\right]\,\mathrm{d}V + \int_{\partial\Omega}\delta\xi\mathbf{f}\cdot\mathbf{n}\,\mathrm{d}S = 0.
\end{aligned} \tag{B.2}$$

With the following boundary conditions applying on $\partial\Omega$:

$$\begin{aligned}
&\mathbf{T} = \boldsymbol{\sigma}\cdot\mathbf{n},\\
&\nabla\phi\cdot\mathbf{n} = 0,\\
&f_\xi = \mathbf{f}_\xi\cdot\mathbf{n},
\end{aligned} \tag{B.3}$$

where $\mathbf{T}$ is the surface traction, f_ξ the diffusion field flux.

To derive the finite element discretised form, we approximate the variables $\mathbf{u}$, ϕ, and ξ using shape functions N_i (shape function of node i) and nodal values of each field as follows:

$$\mathbf{u} = \sum_i^n \boldsymbol{N}_i\mathbf{u}_i, \quad \phi = \sum_i^n N_i\phi_i, \quad \xi = \sum_i^n N_i\xi_i. \tag{B.4}$$

The gradients of each field are found by taking derivatives of the shape functions with respect to space, creating the $\boldsymbol{B}$-matrices:

$$\boldsymbol{\varepsilon} = \sum_i^n \boldsymbol{B}_i^u \boldsymbol{u}_i, \quad \nabla\phi = \sum_i^n \boldsymbol{B}_i \phi_i, \quad \nabla\xi = \sum_i^n \boldsymbol{B}_i \xi_i. \tag{B.5}$$

Using Eqs. (B.4) and (B.5), the residual for each equation becomes:

$$\begin{aligned}
\mathbf{R}_i^{\mathbf{u}} &= \int_\Omega \left[(\boldsymbol{B}_i^{\mathbf{u}})^T \boldsymbol{\sigma} - (\boldsymbol{N}_i)^T \mathbf{b}\right] \mathrm{d}V - \int_{\partial\Omega} (\boldsymbol{N}_i)^T \mathbf{T}\, \mathrm{d}S, \\
R_i^{\phi} &= \int_\Omega \left[\left(\eta \frac{\phi^{t+\delta t} - \phi^t}{\delta t} + w'(\phi) + g'(\phi)\big(f_{\mathrm{b1}} + f_{\mathrm{b2}}\big)\right) N_i - \kappa \boldsymbol{B}_i^T \nabla\phi\right] \mathrm{d}V, \\
R_i^{\xi} &= \int_\Omega \left[\left(\rho \frac{U_\xi^{t+\delta t} - U_\xi^t}{\delta t} - q_\xi\right) N_i - \boldsymbol{B}_i^T \mathbf{f}_\xi\right] \mathrm{d}V - \int_{\partial\Omega} N_i f_\xi \,\mathrm{d}S.
\end{aligned} \tag{B.6}$$

Finally, by taking the variation of each residual with respect to the field variable, we obtain the stiffness matrix:

$$\begin{aligned}
\boldsymbol{K}_{ij}^{\mathbf{u}} &= \frac{\partial \mathbf{R}_i^{\mathbf{u}}}{\partial \mathbf{u}_j} = \int_\Omega (\boldsymbol{B}_i^{\mathbf{u}})^T \boldsymbol{C} \boldsymbol{B}_j^{\mathbf{u}} \,\mathrm{d}V, \\
\boldsymbol{K}_{ij}^{\phi} &= \frac{\partial R_i^{\phi}}{\partial \phi_j} = \int_\Omega \big(\eta + w''(\phi) + g''(\phi)(f_{\mathrm{b1}} + f_{\mathrm{b2}})\big) N_i N_j \,\mathrm{d}V - \int_\Omega (\boldsymbol{B}_i)^T \kappa \boldsymbol{B}_j \,\mathrm{d}V, \\
\boldsymbol{K}_{ij}^{\xi} &= \frac{\partial R_i^{\xi}}{\partial \xi_j} = \frac{1}{\delta t} \int_\Omega N_i \rho \frac{\partial U_\xi}{\partial \xi} N_j \,\mathrm{d}V + \frac{1}{\delta t} \int_\Omega N_i \rho \frac{\partial U_\xi}{\partial \nabla\xi} \cdot \boldsymbol{B}_j \,\mathrm{d}V \\
&\quad - \int_\Omega (\boldsymbol{B}_i)^T \cdot \frac{\partial \mathbf{f}_\xi}{\partial \xi} N_j \,\mathrm{d}V - \int_\Omega (\boldsymbol{B}_i)^T \cdot \frac{\partial \mathbf{f}_\xi}{\partial \nabla\xi} \cdot \boldsymbol{B}_j \,\mathrm{d}V \\
&\quad - \int_\Omega N_i \frac{\partial q_\xi}{\partial \xi} N_j \,\mathrm{d}V - \int_{\partial\Omega} N_i \frac{\partial f_\xi}{\partial \xi} N_j \,\mathrm{d}S.
\end{aligned} \tag{B.7}$$

The off-diagonal stiffness matrices are considered zero to reduce computational effort, allowing the inversion process to handle lower-dimensional stiffness matrices more efficiently.

Appendix C. On the arrangement of the phase field equation

We show here how the arrangement of the strong form of the phase field equation (or any type of diffusion equation) can lead to different weak forms (and thus results) if the mobility coefficient varies in space ($L(\mathbf{x})$). This is for example the case when the mobility coefficient is enhanced to capture the role of mechanics in corrosion, as shown in Eq. (64). We consider three distinct cases, which should be equivalent for a constant (homogeneous) mobility coefficient L:

$$\begin{aligned}
&\frac{1}{L(\mathbf{x})}\dot{\phi} + \nabla\cdot\nabla\phi = 0, \\
&\dot{\phi} + L(\mathbf{x})\nabla\cdot\nabla\phi = 0, \\
&\dot{\phi} + \nabla\cdot(L(\mathbf{x})\cdot\nabla\phi) = 0,
\end{aligned} \tag{C.1}$$

The weak form of each equation can be readily obtained by introducing the test function $\delta\phi$,

$$\begin{aligned}
&\int_\Omega \left(\frac{1}{L(x)}\dot{\phi} + \nabla\cdot\nabla\phi\right)\delta\phi \,\mathrm{d}V = 0, \\
&\int_\Omega \big(\dot{\phi} + L(x)\nabla\cdot\nabla\phi\big)\,\delta\phi \,\mathrm{d}V = 0, \\
&\int_\Omega \big(\dot{\phi} + \nabla\cdot(L(x)\cdot\nabla\phi)\big)\,\delta\phi \,\mathrm{d}V = 0.
\end{aligned} \tag{C.2}$$

Utilising the divergence theorem, the weak forms can also be formulated as,

$$\begin{aligned}
&\int_\Omega \left(\frac{1}{L(x)}\dot{\phi}\delta\phi - \nabla\delta\phi\cdot\nabla\phi\right) \mathrm{d}V + \int_{\partial\Omega} \nabla\phi\cdot\mathbf{n}\,\delta\phi \,\mathrm{d}S = 0, \\
&\int_\Omega \big(\dot{\phi}\delta\phi - L(x)\nabla\delta\phi\cdot\nabla\phi - \nabla L(x)\cdot\nabla\phi\,\delta\phi\big) \,\mathrm{d}V + \int_{\partial\Omega} \nabla\phi\cdot\mathbf{n}\,\delta\phi \,\mathrm{d}S = 0, \\
&\int_\Omega \big(\dot{\phi}\delta\phi - L(x)\nabla\delta\phi\cdot\nabla\phi\big) \,\mathrm{d}V + \int_{\partial\Omega} L(x)\nabla\phi\cdot\mathbf{n}\,\delta\phi \,\mathrm{d}S = 0.
\end{aligned} \tag{C.3}$$

These derived weak forms yield distinct results. In the first equation, the parameter $L(\mathbf{x})$ acts as a regularisation parameter influencing the system's equilibrium. The second equation incorporates the gradient of this parameter into its weak form, while in the third equation, $L(\mathbf{x})$ is a parameter for the gradient term of the field variable. Eq. (C.1)a is the approach typically adopted [41]. Both Eq. (C.1)a and Eq. (C.1)c can be implemented using a `UMATHT` subroutine.

Appendix D. Tangential stiffness matrix for the no-tension split

In the hydraulic fracture analyses, we chose to adopt the no-tension strain energy decomposition [46,71] for both the phase field and the balance of linear momentum equations (i.e., not using the hybrid approach but retaining variational consistency). This requires defining a suitable tangential stiffness tensor, which is the aim of this Appendix. Let us begin by defining the total strain energy density as:

$$\psi(\boldsymbol{\varepsilon},\phi) = g(\phi)\,\psi_1^{\mathrm{M}}(\boldsymbol{\varepsilon}) + (1-g(\phi))\,\psi_2^{\mathrm{M}}(\boldsymbol{\varepsilon})\,, \tag{D.1}$$

with the tangential stiffness tensor being defined as:

$$\boldsymbol{C} = g(\phi)\,\frac{\partial^2\psi_1^{\mathrm{M}}}{\partial\boldsymbol{\varepsilon}^2} + (1-g(\phi))\,\frac{\partial^2\psi_2^{\mathrm{M}}}{\partial\boldsymbol{\varepsilon}^2} = g(\phi)\,\boldsymbol{C}_1^{\mathrm{M}} + (1-g(\phi))\,\boldsymbol{C}_2^{\mathrm{M}}\,. \tag{D.2}$$

Here, $\boldsymbol{C}_1^{\mathrm{M}}$ and $\boldsymbol{C}_2^{\mathrm{M}}$ are the tangential moduli of the first and second materials, respectively.

For the no-tension model, the strain energy can be expressed as:

$$\begin{aligned}\psi =& \frac{E\nu}{2(1+\nu)(1-2\nu)}\left\{\left[\epsilon_1-(1-\sqrt{g})\epsilon_1^t\right]+\left[\epsilon_2-(1-\sqrt{g})\epsilon_2^t\right]+\left[\epsilon_3-(1-\sqrt{g})\epsilon_3^t\right]\right\}^2\\ &+\frac{E}{2(1+\nu)}\left\{\left[\epsilon_1-(1-\sqrt{g})\epsilon_1^t\right]^2+\left[\epsilon_2-(1-\sqrt{g})\epsilon_2^t\right]^2+\left[\epsilon_3-(1-\sqrt{g})\epsilon_3^t\right]^2\right\}\,,\end{aligned} \tag{D.3}$$

where ϵ_i and ϵ_i^t are the principal strain and the principal tensile strain, respectively, with i indexing from the minimum to the maximum principal strain ($\epsilon_3 \geq \epsilon_2 \geq \epsilon_1$). The principal tensile strains are defined based on the strain state:

$$\begin{aligned}&\text{if}\quad \epsilon_1>0 && \Rightarrow\quad \epsilon_1^t=\epsilon_1,\quad \epsilon_2^t=\epsilon_2,\quad \epsilon_3^t=\epsilon_3,\\ &\text{elseif}\quad \epsilon_2+\nu\epsilon_1>0 && \Rightarrow\quad \epsilon_1^t=0,\quad \epsilon_2^t=\epsilon_2+\nu\epsilon_1,\quad \epsilon_3^t=\epsilon_3+\nu\epsilon_1,\\ &\text{elseif}\quad (1-\nu)\epsilon_3+\nu(\epsilon_1+\epsilon_2)>0 && \Rightarrow\quad \epsilon_1^t=0,\quad \epsilon_2^t=0,\quad \epsilon_3^t=\epsilon_3+\frac{\nu}{1-\nu}(\epsilon_1+\epsilon_2),\\ &&&\text{else}\quad \Rightarrow\quad \epsilon_1^t=0,\quad \epsilon_2^t=0,\quad \epsilon_3^t=0.\end{aligned} \tag{D.4}$$

Based on this definition, the strain energy of the second phase can be expressed as:

$$\psi_2^{\mathrm{M}}(\boldsymbol{\varepsilon}) = \begin{cases} 0 & \epsilon_1>0\\ \frac{E}{2}\epsilon_1^2 & \epsilon_2+\nu\epsilon_1>0\\ \frac{E}{2(1-\nu^2)}\left(\epsilon_1^2+\epsilon_2^2+2\nu\epsilon_1\epsilon_2\right) & (1-\nu)\epsilon_3+\nu(\epsilon_1+\epsilon_2)>0\\ \frac{E\nu}{2(1+\nu)(1-2\nu)}\left(\epsilon_1+\epsilon_2+\epsilon_3\right)^2+\frac{E}{2(1+\nu)}\left(\epsilon_1^2+\epsilon_2^2+\epsilon_3^2\right) & \text{else}\end{cases} \tag{D.5}$$

For a fully damaged material, the material Jacobian in the principal direction, $(\boldsymbol{C}_2^{\mathrm{M}})'$, is defined as:

$$(C_2^{\mathrm{M}})'_{ijkl} = \frac{\partial\psi_s}{\partial\epsilon_{ij}\partial\epsilon_{kl}} = \begin{cases} 0 & \epsilon_1>0,\\ \delta_{i1}\delta_{j1}\delta_{k1}\delta_{l1}\,E & \epsilon_2+\nu\epsilon_1>0,\\ \delta_{ij}\delta_{kl}(1-\delta_{i3})\left(\delta_{ik}+(1-\delta_{k3})\,\nu\right)\frac{E}{1-\nu^2} & (1-\nu)\epsilon_3+\nu(\epsilon_1+\epsilon_2)>0,\\ \boldsymbol{C}_0, & \end{cases} \tag{D.6}$$

where δ_{ij} is the Kronecker delta. The tangential matrix of the first phase is equal to the elastic stiffness matrix so $\boldsymbol{C}_1^{\mathrm{M}} = \boldsymbol{C}_0$. The tangential stiffness matrix in the principal direction, $\boldsymbol{C}'$, can be written as:

$$\boldsymbol{C}' = g(\phi)\,(\boldsymbol{C}_0) + (1-g(\phi))\,(\boldsymbol{C}_2^{\mathrm{M}})'. \tag{D.7}$$

The Jacobian matrix in the original direction, $\boldsymbol{C}$, is obtained by rotating $\boldsymbol{C}'$ to the original orientation using:

$$C_{qrst} = a_{qi}a_{rj}a_{sk}a_{tl}C'_{ijkl}\,, \tag{D.8}$$

where $\boldsymbol{a}$ is the transpose of the direction cosines matrix for the principal directions, defined as:

$$\boldsymbol{a}' = [\boldsymbol{v}_1,\boldsymbol{v}_2,\boldsymbol{v}_3]\,, \tag{D.9}$$

where $\boldsymbol{v}_1$, $\boldsymbol{v}_2$, and $\boldsymbol{v}_3$ are the principal vectors of the strain tensor, satisfying:

$$(\boldsymbol{\varepsilon}-\epsilon_{ii}\boldsymbol{I})\cdot\boldsymbol{v}_i = 0, \tag{D.10}$$

with $i=1,2,3$ and $\boldsymbol{I}$ being the identity matrix.

Data availability

Data will be made available on request.

References

[1] Cahn JW, Hilliard JE. Free energy of a nonuniform system i. interfacial free energy. J Chem Phys 1958;28(2):258–67.
[2] Wheeler AA, Boettinger WJ, McFadden GB. Phase-field model for isothermal phase transitions in binary alloys. Phys Rev A 1992;45(10):7424.
[3] Chen LQ. Phase-field models for microstructure evolution. Annu Rev Mater Sci 2002;32:113–40.
[4] Zhao Y, Wang R, Martínez-Pañeda E. A phase field electro-chemo-mechanical formulation for predicting void evolution at the li–electrolyte interface in all-solid-state batteries. J Mech Phys Solids 2022;167:104999.
[5] Mokbel D, Abels H, Aland S. A phase-field model for fluid–structure interaction. J Comput Phys 2018;372:823–40.
[6] Bourdin B, Francfort GA, Marigo J-J. Numerical experiments in revisited brittle fracture. J Mech Phys Solids 2000;48(4):797–826.
[7] Bourdin B, Francfort GA, Marigo JJ. The variational approach to fracture. Springer Netherlands; 2008.
[8] Karma A, Kessler DA, Levine H. Phase-field model of mode III dynamic fracture. Phys Rev Lett 2001;87(4):45501-1–45501-4.
[9] Mai W, Soghrati S, Buchheit RG. A phase field model for simulating the pitting corrosion. Corros Sci 2016;110:157–66.
[10] Cui C, Ma R, Martínez-Pañeda E. A phase field formulation for dissolution-driven stress corrosion cracking. J Mech Phys Solids 2021;147:104254.
[11] Quintanas-Corominas A, Reinoso J, Casoni E, Turon A, Mayugo JA. A phase field approach to simulate intralaminar and translaminar fracture in long fiber composite materials. Compos Struct 2019;220:899–911.
[12] Tan W, Martínez-Pañeda E. Phase field predictions of microscopic fracture and R-curve behaviour of fibre-reinforced composites. Compos Sci Technol 2021;202:108539.
[13] Simoes M, Martínez-Pañeda E. Phase field modelling of fracture and fatigue in shape memory alloys. Comput Methods Appl Mech Engrg 2021;373:113504.
[14] Lotfolahpour A, Huber W, Zaeem MA. A phase-field model for interactive evolution of phase transformation and cracking in superelastic shape memory ceramics. Comput Mater Sci 2023;216:111844.
[15] Wu J-Y, Huang Y, Nguyen VP. Three-dimensional phase-field modeling of mode I + II / III failure in solids. Comput Methods Appl Mech Engrg 2021;373:113537.
[16] Shishvan SS, Assadpour-asl S, Martinez-Paneda E. A mechanism-based gradient damage model for metallic fracture. Eng Fract Mech 2021;255:107927.
[17] Sun X, Duddu R, Hirshikesh. A poro-damage phase field model for hydrofracturing of glacier crevasses. Extrem Mech Lett 2021;45:101277.
[18] Clayton T, Duddu R, Siegert M, Martínez-Pañeda E. A stress-based poro-damage phase field model for hydrofracturing of creeping glaciers and ice shelves. Eng Fract Mech 2022;272:108693.
[19] Schuler L, Ilgen AG, Newell P. Chemo-mechanical phase-field modeling of dissolution-assisted fracture. Comput Methods Appl Mech Engrg 2020;362:112838.
[20] Navidtehrani Y, Duddu R, Martínez-Pañeda E. Damage mechanics challenge: Predictions based on the phase field fracture model. Eng Fract Mech 2024;301:110046.
[21] Ahmadian H, Mehraban MR, Ayatollahi MR, Navidtehrani Y, Bahrami B. Phase-field approach for fracture prediction of brittle cracked components. Eng Fract Mech 2024;309:110417.
[22] Narayan S, Anand L. A gradient-damage theory for fracture of quasi-brittle materials. J Mech Phys Solids 2019;129:119–46.
[23] Korec E, Mingazzi L, Freddi F, Martínez-Pañeda E. Predicting the impact of water transport on carbonation-induced corrosion in variably saturated reinforced concrete. Mater Struct 2024;57(4):91.
[24] Hirshikesh S Natarajan, Annabattula RK, Martínez-Pañeda E. Phase field modelling of crack propagation in functionally graded materials. Compos Part B: Eng 2019;169:239–48.
[25] Kumar PKAV, Dean A, Reinoso J, Lenarda P, Paggi M. Phase field modeling of fracture in functionally graded materials: G -convergence and mechanical insight on the effect of grading. Thin-Walled Struct 2021;159:107234.
[26] Bourdin B, Chukwudozie C, Yoshioka K. A variational approach to the numerical simulation of hydraulic fracturing. Proc - SPE Annu Tech Conf Exhib 2012;2:1442–52.
[27] Heider Y. A review on phase-field modeling of hydraulic fracturing. Eng Fract Mech 2021;253:107881.
[28] Boyce AM, Martínez-Pañeda E, Wade A, Zhang YS, Bailey JJ, Heenan TM, et al. Shearing, cracking predictions of lithium-ion battery electrodes by X-ray computed tomography and modelling. J Power Sources 2022;526:231119.
[29] Ai W, Wu B, Martínez-Pañeda E. A multi-physics phase field formulation for modelling fatigue cracking in lithium-ion battery electrode particles. J Power Sources 2022;544:231805.
[30] Zhang G, Guo TF, Zhou Z, Tang S, Guo X. A phase-field model for fracture in water-containing soft solids. Eng Fract Mech 2019;212:180–96.
[31] Zheng S, Huang R, Lin R, Liu Z. A phase field solution for modelling hyperelastic material and hydrogel fracture in abaqus. Eng Fract Mech 2022;276:108894.
[32] Korec E, Jirásek M, Wong HS, Martínez-Pañeda E. A phase-field chemo-mechanical model for corrosion-induced cracking in reinforced concrete. Constr Build Mater 2023;393:131964.
[33] Fang X, Pan Z, Ma R, et al. A multi-phase-field framework for non-uniform corrosion and corrosion-induced concrete cracking. Comput Methods Appl Mech Engrg 2023;414:116196.
[34] Bourdin B, Marigo JJ, Maurini C, Sicsic P. Morphogenesis and propagation of complex cracks induced by thermal shocks. Phys Rev Lett 2014;112(1):1–5.
[35] Miehe C, Schänzel LM, Ulmer H. Phase field modeling of fracture in multi-physics problems. Part I. Balance of crack surface and failure criteria for brittle crack propagation in thermo-elastic solids. Comput Methods Appl Mech Engrg 2015;294:449–85.
[36] Martínez-Pañeda E, Golahmar A, Niordson CF. A phase field formulation for hydrogen assisted cracking. Comput Methods Appl Mech Engrg 2018;342:742–61.
[37] Cui C, Bortot P, Ortolani M, Martínez-Pañeda E. Computational predictions of hydrogen-assisted fatigue crack growth. Int J Hydrog Energy 2024;72:315–25.
[38] Abdollahi A, Arias I. Phase-field modeling of fracture in ferroelectric materials. Arch Comput Methods Eng 2015;22:153–81.
[39] Quinteros L, García-Macías E, Martínez-Pañeda E. Electromechanical phase-field fracture modelling of piezoresistive cnt-based composites. Comput Methods Appl Mech Engrg 2023;407:115941.
[40] Martínez-Pañeda E. Phase-field simulations opening new horizons in corrosion research. MRS Bull 2024;49:603–12.
[41] Cui C, Ma R, Martínez-Pañeda E. A generalised, multi-phase-field theory for dissolution-driven stress corrosion cracking and hydrogen embrittlement. J Mech Phys Solids 2022;166:104951.
[42] Allen SM, Cahn JW. A microscopic theory for antiphase boundary motion and its application to antiphase domain coarsening. Acta Metall 1979;27(6):1085–95.
[43] Goldenfeld N. Lectures on phase transitions and the renormalization group. CRC Press; 2018.
[44] Amor H, Marigo JJ, Maurini C. Regularized formulation of the variational brittle fracture with unilateral contact: Numerical experiments. J Mech Phys Solids 2009;57(8):1209–29.
[45] Miehe C, Hofacker M, Welschinger F. A phase field model for rate-independent crack propagation: Robust algorithmic implementation based on operator splits. Comput Methods Appl Mech Engrg 2010;199(45–48):2765–78.
[46] Freddi F, Royer-Carfagni G. Regularized variational theories of fracture: A unified approach. J Mech Phys Solids 2010;58(8):1154–74.
[47] De Lorenzis L, Maurini C. Nucleation under multi-axial loading in variational phase-field models of brittle fracture. Int J Fract 2022;237(1–2):61–81.

[48] Navidtehrani Y, Betegón C, Martínez-Pañeda E. A general framework for decomposing the phase field fracture driving force, particularised to a Drucker–Prager failure surface. Theor Appl Fract Mech 2022;121:103555.
[49] Cui C, Ma R, Martínez-Pañeda E. Electro-chemo-mechanical phase field modeling of localized corrosion: theory and comsol implementation. Eng Comput 2023;39(6):3877–94.
[50] Petrova V, Schmauder S. A theoretical model for the study of thermal fracture of functionally graded thermal barrier coatings with a system of edge and internal cracks. Theor Appl Fract Mech 2020;108:102605.
[51] Li W, Shirvan K. Multiphysics phase-field modeling of quasi-static cracking in urania ceramic nuclear fuel. Ceram Int 2021;47(1):793–810.
[52] Ruan H, Peng X-L, Yang Y, Gross D, Xu B-X. Phase-field ductile fracture simulations of thermal cracking in additive manufacturing. J Mech Phys Solids 2024;191:105756.
[53] Mendelsohn DA. A review of hydraulic fracture modeling—part i: General concepts, 2d models, motivation for 3d modeling. J Energy Resour Technol 1984;106(3):369–76.
[54] Chen B, Barboza BR, Sun Y, Bai J, Thomas HR, Dutko M, et al. A review of hydraulic fracturing simulation. Arch Comput Methods Eng 2021;1–58.
[55] Lee S, Wheeler MF, Wick T. Pressure and fluid-driven fracture propagation in porous media using an adaptive finite element phase field model. Comput Methods Appl Mech Engrg 2016;305:111–32.
[56] Gangloff RP, Somerday BP. Gaseous hydrogen embrittlement of materials in energy technologies. Cambridge: Woodhead Publishing Limited; 2012.
[57] Chen Y-S, Huang C, Liu P-Y, Yen H-W, Niu R, Burr P, et al. Hydrogen trapping and embrittlement in metals – a review. Int J Hydrog Energy 2024.
[58] Martínez-Pañeda E, Golahmar A, Niordson CF. A phase field formulation for hydrogen assisted cracking. Comput Methods Appl Mech Engrg 2018;342:742–61.
[59] Kristensen PK, Niordson CF, Martínez-Pañeda E. A phase field model for elastic-gradient-plastic solids undergoing hydrogen embrittlement. J Mech Phys Solids 2020;143:104093.
[60] Cupertino-Malheiros L, Mandal TK, Thébault F, Martínez-Pañeda E. On the suitability of single-edge notch tension (sent) testing for assessing hydrogen-assisted cracking susceptibility. Eng Fail Anal 2024;162:108360.
[61] Parkins RN. Factors influencing stress corrosion crack growth kinetics.. Corrosion 1987;43(3):130–9.
[62] Navidtehrani Y, Betegón C, Martínez-Pañeda E. A unified abaqus implementation of the phase field fracture method using only a user material subroutine. Materials 2021;14:1913.
[63] Navidtehrani Y, Betegón C, Martínez-Pañeda E. A simple and robust abaqus implementation of the phase field fracture method. Appl Eng Sci 2021;6:100050.
[64] Kristensen PK, Martínez-Pañeda E. Phase field fracture modelling using quasi-Newton methods and a new adaptive step scheme. Theor Appl Fract Mech 2020;107:102446.
[65] Jiang CP, Wu XF, Li J, Song F, Shao YF, Xu XH, et al. A study of the mechanism of formation and numerical simulations of crack patterns in ceramics subjected to thermal shock. Acta Mater 2012;60(11):4540–50.
[66] Sicsic P, Marigo JJ, Maurini C. Initiation of a periodic array of cracks in the thermal shock problem: A gradient damage modeling. J Mech Phys Solids 2014;63(1):256–84.
[67] Ruan H, Rezaei S, Yang Y, Gross D, Xu B-X. A thermo-mechanical phase-field fracture model: Application to hot cracking simulations in additive manufacturing. J Mech Phys Solids 2023;172:105169.
[68] Tang SB, Zhang H, Tang CA, Liu HY. Numerical model for the cracking behavior of heterogeneous brittle solids subjected to thermal shock. Int J Solids Struct 2016;80:520–31.
[69] Chu D, Li X, Liu Z. Study the dynamic crack path in brittle material under thermal shock loading by phase field modeling. Int J Fract 2017;208(1–2):115–30.
[70] Mandal TK, Nguyen VP, Wu J-Y, Nguyen-Thanh C, de Vaucorbeil A. Fracture of thermo-elastic solids: Phase-field modeling and new results with an efficient monolithic solver. Comput Methods Appl Mech Engrg 2021;376:113648.
[71] Del Piero G. Constitutive equation and compatibility of the external loads for linear elastic masonry-like materials. Meccanica 1989;24(3):150–62.
[72] Yoshioka K, Bourdin B. A variational hydraulic fracturing model coupled to a reservoir simulator. Int J Rock Mech Min Sci 2016;88:137–50.
[73] Zhou S, Zhuang X, Rabczuk T. A phase-field modeling approach of fracture propagation in poroelastic media. Eng Geol 2018;240:189–203.
[74] Isfandbod M, Martínez-Pañeda E. A mechanism-based multi-trap phase field model for hydrogen assisted fracture. Int J Plast 2021;144:103044.
[75] Mandal TK, Parker J, Gagliano M, Martínez-Pañeda E. Computational predictions of weld structural integrity in hydrogen transport pipelines. Int J Hydrog Energy 2024.
[76] Duddu R. Numerical modeling of corrosion pit propagation using the combined extended finite element and level set method. Comput Mech 2014;54(3):613–27.
[77] Gao H, Ju L, Duddu R, Li H. An efficient second-order linear scheme for the phase field model of corrosive dissolution. J Comput Appl Math 2020;367:112472.
[78] Ernst P, Newman RC. Pit growth studies in stainless steel foils. I. Introduction and pit growth kinetics. Corros Sci 2002;44(5):927–41.

G | Paper 7

A phase field model for hydraulic fracture: Drucker–Prager driving force and a hybrid coupling strategy

Authors:

Yousef Navidtehrani, Covadonga Betegón, Javier Vallejos, Emilio Martínez-Pañeda

Journal:

Computer Methods in Applied Mechanics and Engineering

Year of Publication:

2025

Impact Factor:

6.9 - Q1

Computer Methods in Applied Mechanics and Engineering 444 (2025) 118155

Contents lists available at ScienceDirect

Comput. Methods Appl. Mech. Engrg.

journal homepage: www.elsevier.com/locate/cma

A phase field model for hydraulic fracture: Drucker–Prager driving force and a hybrid coupling strategy

Yousef Navidtehrani [a], Covadonga Betegón [a], Javier Vallejos [b], Emilio Martínez-Pañeda [c,*]

[a] Department of Construction and Manufacturing Engineering, University of Oviedo, Gijón 33203, Spain
[b] Advanced Mining Technology Center, Mining Engineering Department, University of Chile, Chile
[c] Department of Engineering Science, University of Oxford, Oxford OX1 3PJ, UK

ARTICLE INFO

Keywords:
Phase field fracture
Hydraulic fracture
Finite element analysis
Drucker–Prager based split
Hybrid fracture-fluid flow coupling

ABSTRACT

Recent years have seen a significant interest in using phase field approaches to model hydraulic fracture, so as to optimise a process that is key to industries such as petroleum engineering, mining and geothermal energy extraction. Here, we present a novel theoretical and computational phase field framework to simulate hydraulic fracture. The framework is general and versatile, in that it allows for improved treatments of the coupling between fluid flow and the phase field, and encompasses a universal description of the fracture driving force. Among others, this allows us to bring two innovations to the phase field hydraulic fracture community: (i) a new hybrid coupling approach to handle the fracture-fluid flow interplay, offering enhanced accuracy and flexibility; and (ii) a Drucker–Prager-based strain energy decomposition, extending the simulation of hydraulic fracture to materials exhibiting asymmetric tension–compression fracture behaviour (such as shale rocks) and enabling the prediction of geomechanical phenomena such as fault reactivation and stick–slip behaviour. Four case studies are addressed to illustrate these additional modelling capabilities and bring insight into permeability coupling, cracking behaviour, and multiaxial conditions in hydraulic fracturing simulations. The codes developed are made freely available to the community and can be downloaded from https://mechmat.web.ox.ac.uk/.

1. Introduction

Hydraulic fracturing plays a pivotal role in industries such as petroleum engineering [1], mining [2], geothermal energy extraction [3], and various subsurface operations. Due to the necessity of accurately predicting fracture behaviour, extensive research has been dedicated to hydraulic fracturing using theoretical [4], numerical [5], and experimental approaches [6,7]. Among the various numerical methods used to simulate hydraulic fracture, the phase field approach has become particularly popular due to its ability to simulate complex fracture phenomena in a mesh-objective and robust fashion, for arbitrary geometries and dimensions, and without requiring explicit crack tracking [8].

Phase field models for hydraulic fracture were pioneered by Bourdin et al. [9], laying a robust foundation that has been further developed in numerous subsequent works [10–13]. While discrete methods allow for explicit computation of the displacement jump (crack opening), continuum-based approaches such as the phase field fracture method require specialised treatment [14]. Bourdin et al. [9] introduced an integration method that approximates crack opening by integrating the displacement field and weighting

* Corresponding author.
E-mail address: emilio.martinez-paneda@eng.ox.ac.uk (E. Martínez-Pañeda).

https://doi.org/10.1016/j.cma.2025.118155
Received 1 February 2025; Received in revised form 23 May 2025; Accepted 10 June 2025
Available online 24 June 2025

it by the phase field gradient. Building on this framework, Miehe et al. [15,16] incorporated a modified Darcy's law to model fluid flow between crack surfaces as a Poiseuille-type flow. Their approach estimates fluid flux by solving laminar flow equations between parallel surfaces, deriving an anisotropic permeability tensor from crack opening computations, which account for element size and phase field gradient direction. Wilson and Landis [17] addressed element size effects on crack opening by introducing a viscosity-scaling factor. Ehlers and Luo [18] proposed a crack-opening indicator to address the challenges associated with the phase field modelling of closed fractures or fractures that reclose after formation, where fluid flow transitions between Darcy-type and Navier–Stokes-type regimes. Heider and Markert [19] integrated phase field fracture models with the Theory of Porous Media (TPM) to simulate the multiphase behaviour of saturated porous media. Alternatively, Lee et al. [20] employed auxiliary fields to segment the domain into reservoir, transient, and fracture regions, estimating material properties via linear interpolation across these regions, eliminating the need for explicit crack opening computations. This methodology has been widely adopted in subsequent research [21–24]. Additionally, Lee et al. [25] introduced a level-set method for calculating crack opening. Later, Yoshioka et al. [26] compared the line integral method and the level-set method for computing crack opening within the phase field framework. While the line integral method is theoretically robust, its implementation poses challenges. In contrast, the level-set method is more practical, albeit requiring parameter adjustments to achieve acceptable results. Santillán et al. [27] developed a phase field approach to simulate fluid-driven fractures in elastic materials, employing an immersed-fracture formulation to accurately capture fracture propagation. Formulations able to capture the role of inertia were developed by Zhou et al. [28] and Shahoveisi et al. [29]. Efforts have also been directed towards reducing the computational cost. For example, Lusheng et al. [30] used the length-scale insensitive degradation function developed by Lo et al. [31] to tackle large-scale hydraulic fracture problems, while Aldakheel and co-workers [32] proposed a global–local approach, confining fracture computations to a local domain linked to the global domain via a Robin-type interface condition. Additionally, phase field fracture has been employed to model the initiation and propagation of desiccation fractures in porous media [33,34]. For a comprehensive review of phase field hydraulic fracture the reader is referred to Refs. [35,36].

While these recent developments have brought significant progress, establishing phase field modelling as the leading technique in simulating hydraulic fractures, there are aspects of the formulation that need further development to enable accurate and versatile predictions, as needed to capture real site behaviour [37,38]. In this work, we present a formulation that encompasses relevant developments of hydraulic phase field fracture in a single framework, and adds two novel and important contributions. First, we present a new hybrid coupling approach to link the phase field evolution equation with pore pressure more effectively. As demonstrated in the numerical experiments conducted, this approach enhances both flexibility and accuracy in capturing the interactions between fracture and fluid flow in complex environments. Second, building upon our recent work [39], we enrich existing models with a general decomposition of the phase field fracture driving force. This is of key importance and a popular topic in the phase field fracture community as there is a need to enrich models with arbitrary failure surfaces to capture the nucleation and growth of cracks exhibiting asymmetrical tension–compression fracture behaviour [40–42]. Rocks and other quasi-brittle materials exhibit failure criteria that are well-described by Drucker–Prager or Mohr–Coulomb type of failure surfaces and thus a general treatment of hydraulic fractures in shale rocks requires this development to capture both tensile and shear-dominated failures. Accordingly, we particularise our generalised model to a Drucker–Prager-based decomposition of the strain energy density, the fracture driving force, which allows us to simulate geomechanical phenomena like stick–slip behaviour and fault activation. Insight is also gained on the role of the fracture driving force on the crack trajectory and the peak pore pressure in problems involving interactions between multiple cracks. The manuscript is organised as follows. First, in Section 2, we present our phase field-based formulation for hydraulic fracture. We begin by discussing the phase field description of crack evolution, through appropriate constitutive choices and various approaches to decompose the strain energy density. Then, we discuss fluid flow theory in porous media, including Darcy's law and Biot's poroelasticity. Three distinct coupling methods for phase field fracture and fluid flow are introduced and evaluated. The numerical implementation, which takes advantage of the analogy between the heat transfer and the fluid flow and phase field equations, is given in Section 3. In Section 4, four case studies are presented, demonstrating the practical application of the proposed framework and highlighting the importance of the novel ingredients of the model. Hence, the numerical experiments encompass permeability coupling, stick–slip behaviour, crack interaction issues, and multiaxial stress conditions. These case studies illustrate the robustness and adaptability of our generalised framework in modelling hydraulic fractures across diverse geomechanical scenarios. Finally, concluding remarks are given in Section 5.

2. A phase field-based model for hydraulic fracture

The coupled equations of phase field hydraulic fracture are presented in this section. Consider an elastic body occupying an arbitrary domain $\Omega \subset \mathbb{R}^n$ ($n \in [1,2,3]$), with an external boundary $\partial\Omega$, where the outward unit normal is denoted by $\mathbf{n}$. The primary variables considered are the displacement vector field $\mathbf{u}$, the phase field variable ϕ, and the pore pressure of the fluid p. Assuming small strain and isothermal conditions, the strain tensor is defined as $\boldsymbol{\varepsilon} = \left(\nabla\mathbf{u}^T + \nabla\mathbf{u}\right)/2$.

The damage process is described by a smooth scalar field $\phi \in [0,1]$, referred to as the phase field. In this model, $\phi = 0$ represents the undamaged material, while $\phi = 1$ corresponds to a fully cracked state. The phase field value transitions smoothly between these two extremes, representing intermediate states of damage. The length scale parameter ℓ controls the extent of crack regularisation, allowing for a diffuse approximation of cracks. The phase field formulation introduces a crack density function $\gamma(\phi, \nabla\phi)$, approximating the fracture energy as:

$$\boldsymbol{\Phi} = \int_{\Gamma} G_c \, \mathrm{d}S \approx \int_{\Omega} G_c \gamma(\phi, \nabla\phi) \, \mathrm{d}V, \qquad \text{for } \ell \to 0, \tag{1}$$

Table 1
Geometric crack function $w(\phi)$, and scaling constant c_w for the AT2, and AT1 models.

Model	$w(\phi)$	c_w
AT2	ϕ^2	1/2
AT1	ϕ	2/3

where G_c denotes the critical energy release rate for fracture, as established in classical fracture mechanics [43,44]. Using the principle of virtual work, the equations governing the coupled deformation–fracture–pore system are expressed as:

$$\int_\Omega \left\{ \boldsymbol{\sigma} : \delta\boldsymbol{\varepsilon} - \mathbf{b}\cdot\delta\mathbf{u} + \omega\delta\phi + \boldsymbol{\xi}\cdot\delta\nabla\phi + \dot{\zeta}\delta p - \mathbf{q}\cdot\delta\nabla p - q_m\delta p \right\} \mathrm{d}V = \int_{\partial\Omega} (\mathbf{T}\cdot\delta\mathbf{u} + q\delta p)\ \mathrm{d}S, \tag{2}$$

where δ represents a virtual quantity, $\boldsymbol{\sigma}$ is the Cauchy stress tensor, $\mathbf{b}$ is the body force, and $\mathbf{T}$ denotes the traction on the boundary $\partial\Omega$. Also, the term ω refers to the micro-stress conjugate to the phase field ϕ, while $\boldsymbol{\xi}$ is the micro-stress vector conjugate to the gradient of the phase field $\nabla\phi$. In addition, $\dot{\zeta}$ denotes the rate of fluid mass content, corresponding to the mass of fluid per unit bulk volume during a unit of time, $\mathbf{q}$ is the fluid flux vector, q_m is the fluid source, and q is fluid flux per unit area applying on the boundary. Applying the Gauss divergence theorem to Eq. (2) delivers the balance equations describing the coupled deformation–fracture–pore system:

$$\begin{aligned} &\nabla\cdot\boldsymbol{\sigma} + \mathbf{b} = 0 \\ &\nabla\cdot\boldsymbol{\xi} - \omega = 0 \qquad\qquad \text{in } \ \Omega, \\ &\nabla\cdot\mathbf{q} + \dot{\zeta} = q_m \end{aligned} \tag{3}$$

along with appropriate boundary conditions,

$$\begin{aligned} &\boldsymbol{\sigma}\mathbf{n} = \mathbf{T} \\ &\boldsymbol{\xi}\cdot\mathbf{n} = 0 \qquad\qquad \text{on } \ \partial\Omega. \\ &\mathbf{q}\cdot\mathbf{n} = -q \end{aligned} \tag{4}$$

These equations represent the balance of linear momentum for the deformation field, the balance of microforces for the phase field, and mass conservation for fluid, respectively.

2.1. Constitutive theory for phase field fracture

The total potential energy density of the system for the coupled deformation–fracture–pore system is expressed as the sum of the elastic strain energy density ψ, fluid energy density ψ_{fl},[1] and the energy dissipated in creating new crack surfaces φ:

$$W(\boldsymbol{\varepsilon}(\mathbf{u}), \phi, \nabla\phi) = \psi(\boldsymbol{\varepsilon}(\mathbf{u}), g(\phi)) + \psi_{fl}(\boldsymbol{\varepsilon}(\mathbf{u}), p) + \varphi(\phi, \nabla\phi). \tag{5}$$

The effect of the phase field on material stiffness is incorporated via the degradation function $g(\phi) = (1-\phi)^2 + \kappa$ with the conditions:

$$g(0) = 1, \qquad g(1) = 0, \qquad g'(\phi) \le 0 \ \text{ for } \ 0 \le \phi \le 1. \tag{6}$$

A small parameter κ is included to prevent ill-conditioning as $\phi \to 1$. The fracture energy is approximated through the crack density function $\gamma(\phi, \nabla\phi)$:

$$\varphi(\phi, \nabla\phi) = G_c\gamma(\phi, \nabla\phi) = G_c \frac{1}{4c_w\ell} \left(w(\phi) + \ell^2 |\nabla\phi|^2 \right), \tag{7}$$

where ℓ is the phase field length scale, c_w is a scaling constant, and $w(\phi)$ is the geometric crack function. These variables are defined in Table 1 for the commonly used AT2 and AT1 models. See [45] for details.

In the evolution of the phase field order, the strain energy of the undamaged configuration ψ_0, drives fracture. For asymmetric stiffness degradation, the strain energy is split into a dissipative part ψ_d, and a stored part ψ_s, yielding the undamaged and damaged configurations:

$$\psi_0(\boldsymbol{\varepsilon}) = \psi_d(\boldsymbol{\varepsilon}) + \psi_s(\boldsymbol{\varepsilon}), \quad \text{and} \quad \psi(\boldsymbol{\varepsilon}, \phi) = g(\phi)\psi_d(\boldsymbol{\varepsilon}) + \psi_s(\boldsymbol{\varepsilon}), \tag{8}$$

Thus, the total potential energy of the solid Eq. (5), is expressed as:

$$W = g(\phi)\psi_d(\boldsymbol{\varepsilon}) + \psi_s(\boldsymbol{\varepsilon}) + \psi_{fl}(\boldsymbol{\varepsilon}(\mathbf{u}), p) + \frac{G_c}{4c_w} \left(\frac{1}{\ell} w(\phi) + \ell |\nabla\phi|^2 \right). \tag{9}$$

[1] The fluid energy term accounts for the pressure p and fluid volume fraction inside the domain, and can be expressed based on the storage coefficient S, defined in Section 2.2, as follows: $\psi_{fl} = Sp^2/2$.

Hence, by considering the variation of energy with respect to the phase field variable, one can derive the fracture micro-stress variables ω and $\boldsymbol{\xi}$ as [45],

$$\omega = \frac{\partial W}{\partial \phi} = g'(\phi)\psi_d(\boldsymbol{\varepsilon}) + \frac{G_c}{4c_w \ell} w'(\phi), \tag{10}$$

$$\boldsymbol{\xi} = \frac{\partial W}{\partial \nabla \phi} = \frac{\ell}{2c_w} G_c \nabla \phi. \tag{11}$$

Substituting these into Eq. (3)b, the phase field evolution equation reads:

$$\frac{G_c}{2c_w}\left(\frac{w'(\phi)}{2\ell} - \ell \nabla^2 \phi\right) + g'(\phi)\psi_d(\boldsymbol{\varepsilon}) = 0. \tag{12}$$

Finally, damage irreversibility is here enforced by defining a history variable: $\mathcal{H} = \max_{t\in[0,\tau]} \psi_d(t)$.

2.1.1. Strain energy decomposition as fracture driving force

The strain energy split as a fracture driving force was developed to prevent damage evolution under compression. Various phase field fracture driving forces can be found in the literature. In this study, we focus on the most widely used formulations and our novel generalised approach, particularised to the Drucker–Prager case. Alternative strain energy split approaches are discussed in [46–48]. Amor et al. [49] introduced the volumetric-deviatoric split to exclude energy associated with volumetric compaction. This split can be expressed in terms of the first invariant of the strain tensor $I_1(\boldsymbol{\varepsilon})$ and the second invariant of the deviatoric part of the strain tensor $J_2(\boldsymbol{\varepsilon})$ as follows:

$$\psi_d(\boldsymbol{\varepsilon}) = \frac{1}{2}K\langle I_1(\boldsymbol{\varepsilon})\rangle_+^2 + 2\mu J_2(\boldsymbol{\varepsilon}) \tag{13}$$

$$\psi_s(\boldsymbol{\varepsilon}) = \frac{1}{2}K\langle I_1(\boldsymbol{\varepsilon})\rangle_-^2, \tag{14}$$

where K is the bulk modulus, μ is the shear modulus, and the Macaulay brackets are defined as $\langle a\rangle_\pm = (a \pm |a|)/2$. In this model, if the first invariant of strain tensor is negative ($I_1(\boldsymbol{\varepsilon}) < 0$), the fracture is driven by the distortion energy $\psi_d(\boldsymbol{\varepsilon}) = 2\mu J_2(\boldsymbol{\varepsilon})$.

Miehe et al. [50] propose a split based on the decomposition of the principal strain tensor into positive and negative parts, defined as $\boldsymbol{\epsilon}_\pm = \langle \boldsymbol{\epsilon}\rangle_\pm$. This spectral decomposition is given by

$$\psi_d(\boldsymbol{\varepsilon}) = \frac{1}{2}\lambda\left(\langle I_1(\boldsymbol{\epsilon})\rangle_+\right)^2 + \mu\left(\left(I_1(\boldsymbol{\epsilon}_+)\right)^2 - 2I_2(\boldsymbol{\epsilon}_+)\right) \tag{15}$$

$$\psi_s(\boldsymbol{\varepsilon}) = \frac{1}{2}\lambda\left(\langle I_1(\boldsymbol{\epsilon})\rangle_-\right)^2 + \mu\left(\left(I_1(\boldsymbol{\epsilon}_-)\right)^2 - 2I_2(\boldsymbol{\epsilon}_-)\right), \tag{16}$$

where λ is the first Lamé constant and $I_2(\boldsymbol{\epsilon})$ is the second invariant of the strain tensor.

Later, Freddy and Royer-Carfagni [51] developed a decomposition approach known as the no-tension split, which was based on the work of Del Piero [52] and aimed at masonry-like materials. This method can be expressed based on the principal strains ($\epsilon_3 \geq \epsilon_2 \geq \epsilon_1$) as follows:

$$\psi_d(\boldsymbol{\varepsilon}) = \begin{cases} \frac{Ev}{2(1+v)(1-2v)}\left(\epsilon_1+\epsilon_2+\epsilon_3\right)^2 + \frac{E}{2(1+v)}\left(\epsilon_1^2+\epsilon_2^2+\epsilon_3^2\right) & \epsilon_1 > 0 \\ \frac{Ev}{2(1+v)(1-2v)}\left(\epsilon_3+\epsilon_2+2v\epsilon_1\right)^2 + \frac{E}{2(1+v)}\left[\left(\epsilon_3+v\epsilon_1\right)^2+\left(\epsilon_2+v\epsilon_1\right)^2\right] & \epsilon_2+v\epsilon_1 > 0 \\ \frac{E}{2(1-v^2)(1-2v)}\left[(1-v)\epsilon_3+v\epsilon_1+v\epsilon_2\right]^2 & (1-v)\epsilon_3+v(\epsilon_1+\epsilon_2) > 0 \\ 0 & \text{else} \end{cases} \tag{17}$$

$$\psi_s(\boldsymbol{\varepsilon}) = \begin{cases} 0 & \epsilon_1 > 0 \\ \frac{E}{2}\epsilon_1^2 & \epsilon_2+v\epsilon_1 > 0 \\ \frac{E}{2(1-v^2)}\left(\epsilon_1^2+\epsilon_2^2+2v\epsilon_1\epsilon_2\right) & (1-v)\epsilon_3+v(\epsilon_1+\epsilon_2) > 0 \\ \frac{Ev}{2(1+v)(1-2v)}\left(\epsilon_1+\epsilon_2+\epsilon_3\right)^2 + \frac{E}{2(1+v)}\left(\epsilon_1^2+\epsilon_2^2+\epsilon_3^2\right) & \text{else} \end{cases} \tag{18}$$

where E is Young's modulus and v is Poisson's ratio. In this model, only positive principal stresses are considered for computing the fracture driving force.

However, there is growing interest in expanding the capabilities of phase field fracture models to incorporate arbitrary failure surfaces for crack nucleation and growth, so as to better represent the failure behaviour of rock-like materials [40–42]. This is of relevance in hydraulic fracture as shale rocks do not exhibit symmetric tension–compression fracture behaviour. While the injected fluid results in tractions normal to the crack surface, the stress state is often complex due to crack interaction, body forces and other boundary conditions. Therefore, an accurate simulation of hydraulic fracture under complex conditions necessitates a generalised phase field formulation capable of incorporating suitable failure surfaces. Recently, Navidtehrani et al. [39] developed a generalised approach to incorporate arbitrary failure surfaces into the phase field fracture driving force. The approach was demonstrated with the Drucker–Prager failure surface, which is relevant to shale rock and hence will be adopted here. Navidtehrani et al. [39] defined

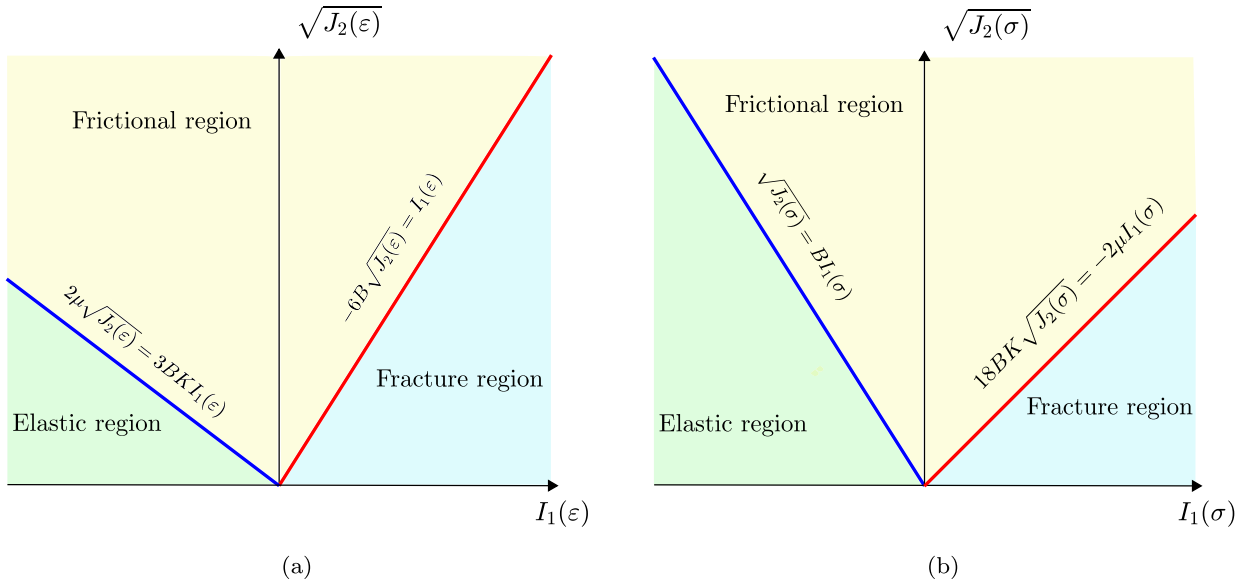

Fig. 1. Elastic, frictional, and fracture regions of Drucker–Prager based model in: (a) the strain space $(I_1(\varepsilon), \sqrt{J_2(\varepsilon)})$, and (b) the stress space $(I_1(\sigma), \sqrt{J_2(\sigma)})$.

the material cohesion c_f to be degraded by the phase field but a constant friction parameter β_f. Then, the strain energy split based on the Drucker–Prager model can be expressed as follows [39]:

$$\psi_d = \begin{cases} \frac{1}{2}KI_1^2(\boldsymbol{\varepsilon}) + 2\mu J_2(\boldsymbol{\varepsilon}) & \text{for} \quad -6B\sqrt{J_2(\boldsymbol{\varepsilon})} < I_1(\boldsymbol{\varepsilon}) \\ \frac{1}{18B^2K+2\mu}\left(-3BKI_1(\boldsymbol{\varepsilon}) + 2\mu\sqrt{J_2(\boldsymbol{\varepsilon})}\right)^2 & \text{for} \quad -6B\sqrt{J_2(\boldsymbol{\varepsilon})} \geq I_1(\boldsymbol{\varepsilon}) \;\&\; 2\mu\sqrt{J_2(\boldsymbol{\varepsilon})} \geq 3BKI_1(\boldsymbol{\varepsilon}) \\ 0 & \text{for} \quad 2\mu\sqrt{J_2(\boldsymbol{\varepsilon})} < 3BKI_1(\boldsymbol{\varepsilon}) \end{cases} \tag{19}$$

$$\psi_s = \begin{cases} 0 & \text{for} \quad -6B\sqrt{J_2(\boldsymbol{\varepsilon})} < I_1(\boldsymbol{\varepsilon}) \\ \frac{K\mu}{18B^2K+2\mu}\left(I_1(\boldsymbol{\varepsilon}) + 6B\sqrt{J_2(\boldsymbol{\varepsilon})}\right)^2 & \text{for} \quad -6B\sqrt{J_2(\boldsymbol{\varepsilon})} \geq I_1(\boldsymbol{\varepsilon}) \;\&\; 2\mu\sqrt{J_2(\boldsymbol{\varepsilon})} \geq 3BKI_1(\boldsymbol{\varepsilon}) \\ \frac{1}{2}KI_1^2(\boldsymbol{\varepsilon}) + 2\mu J_2(\boldsymbol{\varepsilon}) & \text{for} \quad 2\mu\sqrt{J_2(\boldsymbol{\varepsilon})} < 3BKI_1(\boldsymbol{\varepsilon}), \end{cases} \tag{20}$$

where B is a material constant that is a function of the internal friction coefficient β_f, e.g. for Drucker–Prager failure surface middle circumscribes the Mohr–Coulomb surface:

$$B = \frac{2\sin\beta_f}{\sqrt{3}(3+\sin\beta_f)}. \tag{21}$$

Navidtehrani et al. [39] showed that with a Drucker–Prager based fracture driving force, different material behaviours, including confinement, frictional behaviour, and the dilatancy effect, can be captured. The strain and stress spaces in the Drucker–Prager model are illustrated in Fig. 1. Both stress and strain spaces are divided into three different regions. In the elastic region, regardless of the value of the phase field variable ϕ, the material behaviour is completely elastic, with no loss of stiffness. On the opposite side, the fracture region, the entire stress and stiffness are degraded by the phase field, meaning that when $\phi = 1$ there is a traction-free crack. The material stiffness in the frictional region is anisotropic, indicating that only part of the stress and stiffness are degraded by the evolution of the phase field. Due to the frictional behaviour, applying more pressure results in higher shear stress. Finally, when $\phi = 1$, the stress lies on the failure line $\sqrt{J_2(\boldsymbol{\sigma})} = BI_1(\boldsymbol{\sigma})$.

2.2. Fluid flow equation through porous media

To characterise the distribution of pore pressure p within a porous medium, a differential equation governing pore pressure must be defined. This can be achieved by examining the conservation of mass for the fluid, Eq. (3)c, in conjunction with a constitutive equation that relates fluid flux $\mathbf{q}$ and fluid mass ζ to pore pressure. This is typically achieved by considering mass conservation and Darcy's law, whose principles are outlined here.

Darcy's law, developed by Henry Darcy [53], describes the relationship between pore pressure p and the flux vector $\mathbf{q}$ under conditions of low flow rates, providing insights into fluid behaviour in porous media. For anisotropic cases, Darcy's law is expressed as:

$$\mathbf{q} = -\rho_{fl}\frac{\boldsymbol{K}_{fl}}{\mu_{fl}}\nabla p, \tag{22}$$

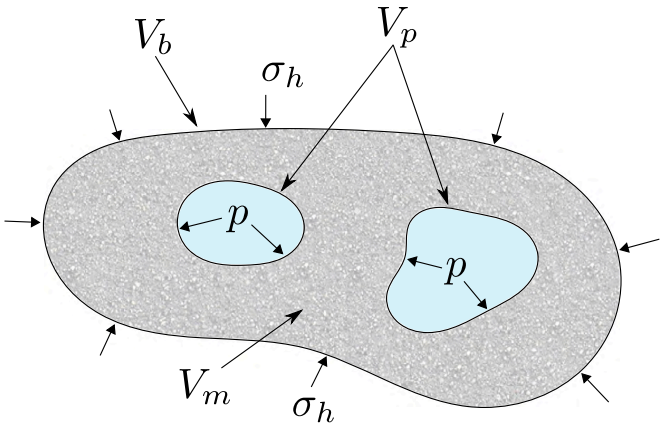

Fig. 2. Porous material illustrating hydrostatic stress σ_h, pore pressure p, pore volume (V_p), bulk volume (V_b), and solid phase volume (V_m).

where gravity has been neglected, $\boldsymbol{K}_{fl}$ is the permeability tensor, and μ_{fl} represents the fluid dynamic viscosity.

The fluid mass content can be expressed using porosity n_p and fluid density ρ_{fl} as:

$$\zeta_{fl} = \rho_{fl} n_p, \tag{23}$$

where porosity is defined as the ratio of pore volume (V_p) to the bulk volume (V_b), i.e., $n_p = V_p/V_b$, as illustrated in Fig. 2. Changes in mass fluid content arise from alterations in porosity due to variations in pore pressure and the compression or expansion of fluid within the pores. This can be expressed as:

$$\mathrm{d}\zeta_{fl} = \rho_{fl}\mathrm{d}n_p + n_p\mathrm{d}\rho_{fl}, \tag{24}$$

Here, fluid density changes due solely to pore pressure variations, while porosity changes result from both pore pressure p and hydrostatic stress σ_h variations. Consequently, Eq. (24) can be reformulated considering differential changes as:

$$\mathrm{d}\zeta_{fl} = \rho_{fl}\left(\frac{\partial n_p}{\partial \sigma_h}\mathrm{d}\sigma_h + \frac{\partial n_p}{\partial p}\mathrm{d}p\right) + n_p\frac{\partial \rho_{fl}}{\partial p}\mathrm{d}p. \tag{25}$$

To expand Eq. (25), we briefly review the hydrostatic theory of poroelasticity. Consider a bulk volume of porous media containing voids and saturated with fluid subjected to hydrostatic stress σ_h and pore pressure p, as shown in Fig. 2. Under static conditions, pore pressure is unable to sustain shear stress, and pore walls cannot transmit any shear traction. The solid is then subjected to two independent stresses, namely σ_h and p, as well as two independent volumes (V_b and V_p). Therefore, four compressibilities can be defined:

$$C_{b\sigma_h} = \frac{1}{V_b}\frac{\partial V_b}{\partial \sigma_h}, \quad C_{bp} = \frac{1}{V_b}\frac{\partial V_b}{\partial p}, \quad C_{p\sigma_h} = \frac{1}{V_p}\frac{\partial V_p}{\partial \sigma_h}, \quad C_{pp} = \frac{1}{V_p}\frac{\partial V_p}{\partial p}. \tag{26}$$

Relationships between these compressibilities were established in Ref. [54], and are as follows:

$$C_{bp} = C_{b\sigma_h} - C_m, \quad C_{p\sigma_h} = \frac{C_{b\sigma_h} - C_m}{n_p}, \quad C_{pp} = \frac{C_{b\sigma_h} - (1+n_p)C_m}{n_p}, \tag{27}$$

where C_m is the compressibility of the solid. Using Eq. (27), we can determine changes in bulk modulus strain ε_b (volumetric strain (ε_{vol})) for a volume control V_b:

$$\mathrm{d}\varepsilon_b = \mathrm{d}\varepsilon_{vol} = \frac{\mathrm{d}V_b}{V_b} = \frac{1}{V_b}\left(\frac{\partial V_b}{\partial \sigma_h}\mathrm{d}\sigma_h + \frac{\partial V_b}{\partial p}\mathrm{d}p\right) = C_{b\sigma_h}\mathrm{d}\sigma_h + C_{bp}\mathrm{d}p. \tag{28}$$

This equation holds generally and does not assume a fixed bulk volume. Biot's coefficient (α) is defined as:

$$\alpha = 1 - \frac{C_m}{C_{b\sigma_h}} = 1 - \frac{K_{b\sigma_h}}{K_m}, \tag{29}$$

where $K_{b\sigma_h}$ and K_m represent the bulk moduli of the saturated porous media and solid phase, respectively. Then, Eq. (28) can be rewritten as:

$$\mathrm{d}\varepsilon_{vol} = C_{b\sigma_h}(\mathrm{d}\sigma_h + \alpha\mathrm{d}p). \tag{30}$$

Now, the variation of porosity n_p with respect to pore pressure and hydrostatic stress σ_h is given by:

$$\frac{\partial n_p}{\partial p} = \frac{1}{V_b}\frac{\partial V_p}{\partial p} - \frac{n_p}{V_b}\frac{\partial V_b}{\partial p}. \tag{31}$$

While for the volume control (V_b), we find:

$$\frac{\partial n_p}{\partial p} = n_p C_{pp} = C_{b\sigma_h} - (1+n_p)C_m = (\alpha - n_p + n_p\alpha)C_{b\sigma_h}. \tag{32}$$

Similarly,

$$\frac{\partial n_p}{\partial \sigma_h} = n_p C_{p\sigma_h} = C_{b\sigma_h} - C_m = \alpha C_{b\sigma_h}. \tag{33}$$

One can then reformulate Eq. (25) considering Eqs. (32)–(33), such that:

$$\mathrm{d}\zeta_{fl} = \rho_{fl}\left((\alpha - n_p + n_p\alpha)C_{b\sigma_h}\mathrm{d}p + \alpha C_{b\sigma_h}\left(\frac{1}{C_{b\sigma_h}}\mathrm{d}\varepsilon_{vol} - \alpha \mathrm{d}p\right)\right) + n_p\frac{\partial \rho_{fl}}{\partial p}\mathrm{d}p. \tag{34}$$

Rearranging yields:

$$\mathrm{d}\zeta_{fl} = \rho_{fl}\left((1-\alpha)(\alpha - n_p)C_{b\sigma_h} + n_p\frac{1}{\rho_{fl}}\frac{\partial \rho_{fl}}{\partial p}\right)\mathrm{d}p + \rho_{fl}\alpha\mathrm{d}\varepsilon_{vol} = \rho_{fl}S\mathrm{d}p + \rho_{fl}\alpha\mathrm{d}\varepsilon_{vol}, \tag{35}$$

where S is the storage coefficient, defined as:

$$S = (1-\alpha)(\alpha - n_p)C_{b\sigma_h} + n_p C_{fl} = \frac{(1-\alpha)(\alpha - n_p)}{K_{b\sigma_h}} + n_p C_{fl}, \tag{36}$$

where fluid compressibility is defined as $C_{fl} = \frac{1}{\rho_{fl}}\frac{\partial \rho_{fl}}{\partial p}$.

As the volumetric strain ε_{vol} and pore pressure p vary over time, the rate of change of fluid mass content can be expressed using Eq. (35) as:

$$\dot{\zeta}_{fl} = \rho_{fl}S\,\dot{p} + \rho_{fl}\alpha\,\dot{\varepsilon}_{vol}, \tag{37}$$

Finally, substituting Eq. (37) into the fluid mass conservation equation, Eq. (3)c, yields:

$$\rho_{fl}\left(S\dot{p} + \alpha\dot{\varepsilon}_{vol}\right) + \nabla\cdot\left(-\rho_{fl}\frac{\boldsymbol{K}_{fl}}{\mu_{fl}}\nabla p\right) = q_m. \tag{38}$$

2.3. Constitutive equations of poroelasticity

The strain–stress relationship for a material in the absence of pore pressure is given by:

$$\boldsymbol{\varepsilon} = \boldsymbol{C}^{-1} : \boldsymbol{\sigma}, \tag{39}$$

where $\boldsymbol{C}^{-1}$ denotes the compliance tensor of elasticity. Since the static pore pressure of fluid flow does not transmit shear stress to the solid structure and is negligible at low flow speeds, its effect is limited to volume changes within the domain, which can be modelled as follows:

$$\boldsymbol{\varepsilon} = \boldsymbol{C}^{-1} : \boldsymbol{\sigma} + \frac{1}{3}C_{bp}p\boldsymbol{I} = \boldsymbol{C}^{-1} : \boldsymbol{\sigma} + \frac{\alpha}{3K_{b\sigma_h}}p\boldsymbol{I}. \tag{40}$$

Using Biot's coefficient, as defined in Eq. (29) and considering an effective stress $\boldsymbol{\sigma}^{eff}$, which represents the stress carried by the solid skeleton, the total stress can be expressed as:

$$\boldsymbol{\sigma} = \boldsymbol{C} : \boldsymbol{\varepsilon} - \alpha p\boldsymbol{I} = \boldsymbol{\sigma}^{eff} - \alpha p\boldsymbol{I}. \tag{41}$$

2.4. Coupling phase field and fluid equation

The microstructure of the solid comprises a porous matrix interspersed with microcracks. The fluid-filled pores constitute the material's intrinsic porosity, with the fluid pressure being governed by Biot's theory of poroelasticity through the principle of effective stress. These pores reside within the intact material and are incorporated into the continuum-scale balance equations. Microcracks can initiate or grow due to damage evolution, potentially coalescing into macroscopic fractures and serving as conduits for fluid transport. Their behaviour is captured by the phase field variable, which represents crack initiation and propagation. Physically, this scale separation assumes that microcracks are significantly smaller than the representative volume element (RVE) and interact with the surrounding pore network primarily by altering porosity, permeability, and fluid pressure distribution. The impact of microcracks on these properties may be negligible at low levels of damage (low ϕ values) but becomes more significant as the material approaches full fracture ($\phi \to 1$). This assumption is prevalent in phase field models of hydraulic fracture, where the phase field impacts permeability and may also influence the effective stress and porosity. While more detailed models could explicitly resolve interactions between individual microcracks and pores at a finer scale based on micromechanics [55–57], such approaches can be more complex in terms of implementation. Instead, our model adopts a homogenised approach, balancing physical accuracy with computational efficiency. In this section, we discuss three different methods for incorporating the effects of phase field evolution into the fluid equations.

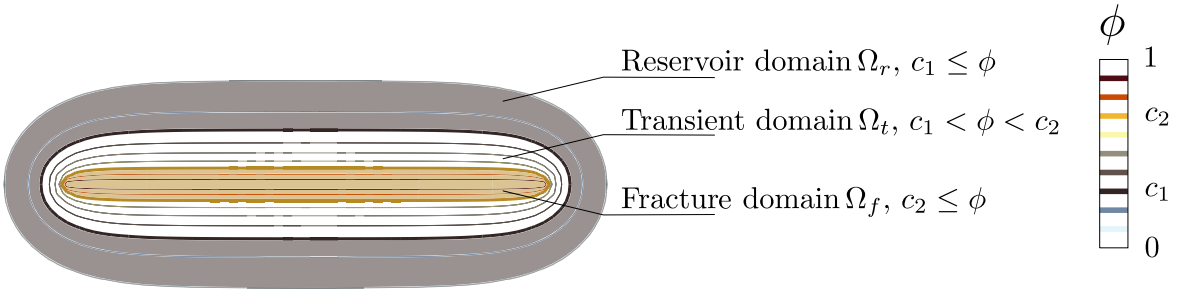

Fig. 3. Reservoir (Ω_r), transient (Ω_t), and fracture (Ω_f) domains identified by phase field variable ϕ.

The poroelastic theory can be combined with the phase field fracture framework by applying Biot's theory of effective stress. Using Eq. (8), the effective stress is defined as:

$$\boldsymbol{\sigma}^{eff} = g(\phi)\frac{\partial \psi_d(\boldsymbol{\varepsilon})}{\partial \boldsymbol{\varepsilon}} + \frac{\partial \psi_s(\boldsymbol{\varepsilon})}{\partial \boldsymbol{\varepsilon}}. \tag{42}$$

Substituting Eqs. (41) and (42) into the linear momentum equation ((3)a), we obtain:

$$\nabla \cdot \left(\boldsymbol{\sigma}^{eff} - \alpha p \boldsymbol{I}\right) + \mathbf{b} = 0. \tag{43}$$

There are several methods to couple fluid effects and the phase field equation. One approach, based on the work by Lee et al. [20], is referred to as the domain decomposition method and has been utilised in other studies [21,58]. This method involves dividing the domain into three distinct regions: the reservoir (Ω_r), fracture (Ω_f), and transient (Ω_t) domains, as illustrated in Fig. 3. These zones are identified using linear indicator functions χ_r and χ_f, which depend on the phase field variable ϕ and material constants c_1 and c_2:

$$\chi_r(\phi) = \begin{cases} 1 & \phi \leq c_1 \\ \frac{c_2-\phi}{c_2-c_1} & c_1 < \phi < c_2 \\ 0 & c_2 \leq \phi, \end{cases} \quad \chi_f(\phi) = \begin{cases} 0 & \phi \leq c_1 \\ \frac{\phi-c_1}{c_2-c_1} & c_1 < \phi < c_2 \\ 1 & c_2 \leq \phi, \end{cases} \tag{44}$$

where the material constants c_1 and c_2 determine whether a given point in the domain belongs to the reservoir, fracture, or transient zones. The continuity equation (Eq. (38)) describes the fluid flow in the reservoir domain. This equation can also be applied to the fracture domain by setting $S = C_{fl}$ and neglecting the volumetric strain rate term, $\dot{\varepsilon}_{vol}$. In the transient zone, the fluid equation is formulated to ensure mass conservation is continuous across all domains and at their boundaries. This approach can be interpreted as an implicit method for capturing the influence of microcracks on fluid behaviour. Thus, fluid and solid parameters between the reservoir and fracture domains are then interpolated as follows:

$$\alpha = \chi_r \alpha_r + \chi_f \tag{45}$$

$$n_p = \chi_r n_{pr} + \chi_f \tag{46}$$

$$\boldsymbol{K}_{fl} = \chi_r \boldsymbol{K}_r + \chi_f \boldsymbol{K}_f, \tag{47}$$

where α_r and n_{pr} are Biot's coefficient and porosity of the reservoir. In the fracture domain, $\alpha = 1$ and $n_p = 1$, while $\boldsymbol{K}_r$ and $\boldsymbol{K}_f$ represent the permeability tensors of the reservoir and fracture domains, respectively. The assumption of linear interpolation of properties between the reservoir and the fracture zone is arguably the simplest one but dedicated experiments are needed to establish more physically-based interpolation functions, with particular attention to complex scenarios, such as highly confined states where grain crushing and compaction can occur.

An alternative method, proposed by Miehe et al. [15], considers Poiseuille-type flow within the crack by modifying Darcy's law to define fracture permeability as follows:

$$K_{\mathrm{f}} = \frac{w_h^2}{12}\left(\boldsymbol{I} - \mathbf{n}_\phi \otimes \mathbf{n}_\phi\right), \tag{48}$$

where $\mathbf{n}_\phi$ is the crack normal vector defined by the phase field gradient ($\mathbf{n}_\phi = \nabla\phi/|\nabla\phi|$), and w_h is the crack opening calculated using the element size h_e:

$$w_h = \langle \left\| h_e \left(1 + \mathbf{n}_\phi \cdot \boldsymbol{\varepsilon} \cdot \mathbf{n}_\phi\right) \right\| \rangle_+. \tag{49}$$

The permeability tensor for the modified Darcy approach is then:

$$\boldsymbol{K}_{fl} = \boldsymbol{K}_r + \phi^b \boldsymbol{K}_f, \tag{50}$$

where b is a permeability transient indicator.

We here propose a third method, combining these two approaches, which is henceforth referred to as the *hybrid permeability method*. In this hybrid method, we use the domain decomposition approach but adopt the definition of $\boldsymbol{K}_f$ from Eq. (48) as follows:

$$\boldsymbol{K}_{fl} = \chi_r \boldsymbol{K}_r + \phi^b \chi_f \boldsymbol{K}_f. \tag{51}$$

The hybrid method leverages the advantages of both the domain decomposition and modified Darcy methods while addressing their respective limitations. As demonstrated in Section 4.1, the domain decomposition method does not account for the effect of crack opening on permeability. Additionally, it assumes a uniform permeability raise across the fracture region in all directions, whereas, in reality, permeability enhancement occurs primarily along the crack direction. In contrast, the modified Darcy method incorporates an anisotropic permeability tensor, effectively capturing directional permeability changes. However, this effect becomes significant at an unrealistic distance from the crack region. To mitigate this issue, the characteristic length scale must be chosen sufficiently small, but this, in turn, increases computational costs by constraining the element size. The proposed hybrid method addresses these limitations by combining the strengths of both approaches. A hybrid approach offers greater flexibility in calibrating parameters with experimental data. Additionally, by leveraging the advantages of the domain decomposition method, the influence of microcracks can be accounted for through the phase field value while also enabling a more precise representation of permeability through cracks. Microcracks can significantly influence permeability and other material properties, such as Biot's coefficient and porosity. Their effects, along with their evolution, can be captured through the phase field variable by appropriately selecting the parameters c_1 and c_2. These parameters can be calibrated experimentally, for example, through permeability testing of fractured rock samples. In such laboratory core tests, specimens are subjected to controlled fluid flow while measuring the resulting pressure drop and flow rate. These measurements are then used to estimate the effective permeability and infer suitable values for c_1 and c_2 through numerical modelling.

The general form of the fluid flow equation, applicable to all methods discussed, is as follows:

$$\rho_{fl} \left(S(\alpha(\phi), n_p(\phi)) \dot{p} + \alpha(\phi) \chi_r(\phi) \dot{\varepsilon}_{vol} \right) + \nabla \cdot \left(-\rho_{fl} \frac{\boldsymbol{K}_{fl}(\phi)}{\mu_{fl}} \nabla p \right) = q_m. \tag{52}$$

where the permeability can be defined based on mentioned method as follows:

$$\boldsymbol{K}_{fl} = \begin{cases} \chi_r K_r \boldsymbol{I} + \chi_f K_f \boldsymbol{I} & \text{Domain decomposition method (Lee et al. [20])} \\ K_r \boldsymbol{I} + \phi^b \underbrace{\left[\frac{w_h^2}{12} \left(\boldsymbol{I} - \mathbf{n}_\phi \otimes \mathbf{n}_\phi \right) \right]}_{\boldsymbol{K}_f} & \text{Modified Darcy method (Miehe et al. [15])} \\ \chi_r K_r \boldsymbol{I} + \chi_f \phi^b \underbrace{\left[\frac{w_h^2}{12} \left(\boldsymbol{I} - \mathbf{n}_\phi \otimes \mathbf{n}_\phi \right) \right]}_{\boldsymbol{K}_f} & \text{Hybrid method (Present work)} \end{cases}. \tag{53}$$

A challenging aspect common to the modified Darcy method and our hybrid formulation is the complexity of estimating $\mathbf{n}_\phi$ accurately [59], particularly at points near the crack tip or where the phase field gradient vanishes. Various approaches have been presented to overcome this (see, e.g., Refs. [60,61]). Here, a new protocol is established, whereby $\mathbf{n}_\phi$ is estimated in those complicated regions using the phase field gradient of a neighbouring integration point. The detailed procedure is presented in Algorithm 1. The first step is to determine, for each integration point, whether we are near a crack ($\phi > 0.5$) or if the phase field gradient is zero. If one of these conditions is met, the second step involves identifying the closest neighbouring Gauss point where $\phi = 1$ and $|\nabla\phi| \neq 0$. In the third step, the cosine of the angle between the phase field gradient vectors of the current point and the neighbouring integration point is computed. If the cosine exceeds 0.866 (i.e., the angle between the vectors is less than 30°, implying that the point is near to the crack, but not close to the crack tip), the gradient direction at the current point is considered reliable

and used for computing $\mathbf{n}_\phi$. Otherwise, if the cosine is below this threshold, indicating proximity to the crack tip, the gradient at the neighbouring Gauss point is adopted for the current point.

Algorithm 1 Determination of crack direction near the crack tip or at points with zero phase field gradient

Check if $\phi > 0.5$ or $|\nabla\phi| = 0$ at the current integration point.
if then $\phi > 0.5$ or $|\nabla\phi| = 0$
  Identify the nearest neighboring point with $\phi_{\text{neighbour}} = 1$ and $|\nabla\phi_{\text{neighbour}}| \neq 0$.
  Compute $\cos\theta = \dfrac{\nabla\phi \cdot \nabla\phi_{\text{neighbour}}}{|\nabla\phi||\nabla\phi_{\text{neighbour}}|}$.
  if then $\cos\theta < 0.866$
    $\mathbf{n}_\phi = \nabla\phi_{\text{neighbour}}/|\nabla\phi_{\text{neighbour}}|$.
  else
    $\mathbf{n}_\phi = \nabla\phi/|\nabla\phi|$.
  end if
end if

3. Numerical implementation

We proceed to describe a general implementation of our model, considering the weak and discretised versions of the balance equations (Section 3.1), the computation of the material Jacobian (Section 3.2) and the solution scheme (Section 3.3).

3.1. Weak formulation and finite element implementation

To implement the formulation presented in Section 2 within a finite element framework, the weak form of the coupled governing equations in Eq. (3) is constructed, using the test functions $\delta\mathbf{u}$, $\delta\phi$, and δp:

$$\int_\Omega \left\{ \left(\boldsymbol{\sigma}^{eff} - \alpha p \boldsymbol{I}\right) : \delta\boldsymbol{\varepsilon} - \mathbf{b}\cdot\delta\mathbf{u} \right\} \mathrm{d}V = \int_{\partial\Omega} (\mathbf{T}\cdot\delta\mathbf{u})\, \mathrm{d}S, \tag{54}$$

$$\int_\Omega \left\{ g'(\phi)\delta\phi\, \mathcal{H} + \frac{1}{2c_w} G_c \left[\frac{1}{2\ell} w'(\phi)\delta\phi - \ell \nabla\phi\cdot\nabla\delta\phi \right] \right\} \mathrm{d}V = 0, \tag{55}$$

$$\int_\Omega \left\{ \left(\rho_{fl}\left(S\dot{p} + \alpha\chi_r\dot{\varepsilon}_{vol}\right) - q_m\right)\delta p + \frac{\rho_{fl}}{\mu_{fl}}(\boldsymbol{K}_{fl}\nabla p)\cdot\nabla\delta p \right\} \mathrm{d}V + \int_{\partial\Omega} \delta p \mathbf{q}\cdot\mathbf{n}\, \mathrm{d}S = 0, \tag{56}$$

The primary variables $\mathbf{u}$, ϕ, and p are approximated using the shape functions N_i corresponding to node i as follows:

$$\mathbf{u} = \sum_i^n \mathbf{N}_i\mathbf{u}_i, \quad \phi = \sum_i^n N_i\phi_i, \quad p = \sum_i^n N_i p_i. \tag{57}$$

The gradients of these variables are computed by differentiating the shape functions with respect to the spatial coordinates, resulting in the following $\boldsymbol{B}$-matrices:

$$\boldsymbol{\varepsilon} = \sum_i^n \boldsymbol{B}_i^u\mathbf{u}_i, \quad \nabla\phi = \sum_i^n \boldsymbol{B}_i\phi_i, \quad \nabla p = \sum_i^n \boldsymbol{B}_i p_i. \tag{58}$$

Using the approximations in Eqs. (57) and (58), the nodal residuals are expressed as:

$$\mathbf{R}_i^{\mathbf{u}} = \int_\Omega \left\{ \left(\boldsymbol{B}_i^{\mathbf{u}}\right)^T \left(\boldsymbol{\sigma}^{eff} - \alpha p\boldsymbol{I}\right) - \mathbf{N}_i^T\mathbf{b} - \mathbf{N}_i^T\mathbf{T} \right\} \mathrm{d}V, \tag{59}$$

$$R_i^\phi = \int_\Omega \left\{ g'(\phi)N_i\mathcal{H} + \frac{G_c}{2c_w\ell} \left[\frac{w'(\phi)}{2} N_i + \ell^2 \left(\boldsymbol{B}_i\right)^T \nabla\phi \right] \right\} \mathrm{d}V, \tag{60}$$

$$R_i^p = \int_\Omega \left[\left(\rho_{fl}\left(S\dot{p} + \alpha\chi_r\dot{\varepsilon}_{vol}\right) - q_m\right) N_i + \boldsymbol{B}_i^T \left(\rho_{fl}\frac{\boldsymbol{K}_{fl}}{\mu_{fl}}\nabla p \right) \right] \mathrm{d}V - \int_{\partial\Omega} N_i q\, \mathrm{d}S. \tag{61}$$

The stiffness matrix is obtained by taking the variation of the residual with respect to each relevant primary variable:

$$\boldsymbol{K}_{ij}^{\mathbf{u}} = \frac{\partial\mathbf{R}_i^{\boldsymbol{u}}}{\partial\boldsymbol{u}_j} = \int_\Omega \left\{ (\boldsymbol{B}_i^{\mathbf{u}})^T \boldsymbol{C}\, \boldsymbol{B}_j^{\mathbf{u}} \right\} \mathrm{d}V, \tag{62}$$

$$\boldsymbol{K}_{ij}^{\phi} = \frac{\partial R_i^\phi}{\partial\phi_j} = \int_\Omega \left\{ \left(g''(\phi)\mathcal{H} + \frac{G_c}{4c_w\ell} w''(\phi) \right) N_i N_j + \frac{G_c\ell}{2c_w} \boldsymbol{B}_i^T \boldsymbol{B}_j \right\} \mathrm{d}V, \tag{63}$$

$$\boldsymbol{K}_{ij}^{p} = \frac{\partial R_i^p}{\partial p_j} = \int_\Omega \left\{ \frac{1}{\delta t} N_i \left(\rho_{fl} S\right) N_j + (\boldsymbol{B}_i)^T \cdot \left(\rho_{fl}\frac{\boldsymbol{K}_{fl}}{\mu_{fl}} \right) \cdot \boldsymbol{B}_j - N_i \frac{\partial q_m}{\partial p} N_j \right\} \mathrm{d}V - \int_{\partial\Omega} N_i \frac{\partial q}{\partial p} N_j\, \mathrm{d}S, \tag{64}$$

where $\boldsymbol{C}$ represents the Jacobian, obtained by taking the second variation of the strain energy with respect to the strain tensor.

3.2. Computation of the material Jacobian

The computation of the material Jacobian is intrinsically linked to the choice of strain energy decomposition. Let us start by expressing the strain energy density as a function of the undamaged strain energy $\psi_0(\boldsymbol{\varepsilon})$ and the stored strain energy $\psi_s(\boldsymbol{\varepsilon})$, such that

$$\psi(\boldsymbol{\varepsilon},\phi) = g(\phi)\,\psi_0(\boldsymbol{\varepsilon}) + (1-g(\phi))\,\psi_s(\boldsymbol{\varepsilon}), \tag{65}$$

where the tangential stiffness tensor is given by:

$$\boldsymbol{C} = g(\phi)\,\frac{\partial^2\psi_0}{\partial\boldsymbol{\varepsilon}^2} + (1-g(\phi))\,\frac{\partial^2\psi_s}{\partial\boldsymbol{\varepsilon}^2} = g(\phi)\,\boldsymbol{C}_0 + (1-g(\phi))\,\boldsymbol{C}_s, \tag{66}$$

Here, $\boldsymbol{C}_0$ and $\boldsymbol{C}_s$ are the tangential stiffness tensors for the undamaged and fully cracked configurations, respectively. Calculating $\boldsymbol{C}_s$ provides the anisotropic tangential stiffness tensor $\boldsymbol{C}$.

The strain energy splits defined in Section 2.1.1 can be divided into two main groups. The first group includes those based on the strain tensor in its original form (i.e., without rotations), such as the volumetric-deviatoric split [49] and the Drucker–Prager model [39,41]. The second group is based on principal strains, such as spectral decomposition [50] and the no-tension model [51]. The first group can be directly obtained by differentiation with respect to the strain tensor, whereas for the second group, the Jacobian is first determined for the principal directions and subsequently rotated to the original coordinate system.

For the first group, it can be shown that the volumetric-deviatoric split is a special case of the Drucker–Prager model when $B = 0$. Hence, let us derive $\boldsymbol{C}_s$ for the Drucker–Prager model and particularise later. Thus,

$$\boldsymbol{C}_s = \frac{\partial^2\psi_s}{\partial\boldsymbol{\varepsilon}^2} = \begin{cases} 0 & \text{if} \quad -6B\sqrt{J_2(\boldsymbol{\varepsilon})} < I_1(\boldsymbol{\varepsilon}), \\ \boldsymbol{C}_s^{DP} & \text{if} \quad -6B\sqrt{J_2(\boldsymbol{\varepsilon})} \geq I_1(\boldsymbol{\varepsilon}) \;\&\; 2\mu\sqrt{J_2(\boldsymbol{\varepsilon})} \geq 3BKI_1(\boldsymbol{\varepsilon}), \\ \boldsymbol{C}_0 & \text{if} \quad 2\mu\sqrt{J_2(\boldsymbol{\varepsilon})} < 3BKI_1(\boldsymbol{\varepsilon}). \end{cases} \tag{67}$$

where $\boldsymbol{C}_s^{DP}$ is defined as:

$$\begin{aligned} (C_s^{DP})_{ijkl} = {} & \frac{K\mu}{9B^2K+\mu}\left(\frac{\partial I_1}{\partial\varepsilon_{ij}} + \frac{3B}{\sqrt{J_2}}\frac{\partial J_2}{\partial\varepsilon_{ij}}\right)\left(\frac{\partial I_1}{\partial\varepsilon_{kl}} + \frac{3B}{\sqrt{J_2}}\frac{\partial J_2}{\partial\varepsilon_{kl}}\right) + \\ & \left(\frac{6Ba_1\left(I_1 + 6B\sqrt{J_2}\right)}{\sqrt{J_2}}\right)\left(\frac{\partial^2 J_2}{\partial\varepsilon_{ij}\partial\varepsilon_{kl}} - \frac{1}{2J_2}\frac{\partial J_2}{\partial\varepsilon_{ij}}\frac{\partial J_2}{\partial\varepsilon_{kl}}\right). \end{aligned} \tag{68}$$

Considering $B = 0$ in Eqs. (67)–(68), renders the material Jacobian for the volumetric-deviatoric split.

For the second group, the Jacobian in the principal direction $\boldsymbol{C}_s'$ is calculated. For the spectral decomposition, the fully cracked stiffness tensor in the principal direction is given by:

$$(C_s')_{ijkl} = \frac{1-\operatorname{sgn}\left(I_1(\epsilon)\right)}{2}\delta_{ij}\delta_{kl}\lambda + 2\mu\left(\delta_{ij}\delta_{kl} - \frac{\partial^2 I_2(\epsilon_-)}{\partial\epsilon_{\mathrm{ij}}^-\partial\epsilon_{\mathrm{kl}}^-}\right)\frac{\partial\epsilon_{ij}^-}{\partial\epsilon_{\mathrm{ij}}}\frac{\partial\epsilon_{kl}^-}{\partial\epsilon_{\mathrm{kl}}}, \tag{69}$$

where δ_{ij} is the Kronecker delta. The variation $\partial\epsilon_{ij}^-/\partial\epsilon_{\mathrm{ij}}$ is defined as:

$$\frac{\partial\epsilon_{ij}^-}{\partial\epsilon_{\mathrm{ij}}} = \begin{cases} 0 & \epsilon_{ij} > 0, \\ \frac{1}{2} & \epsilon_{ij} = 0, \\ 1 & \epsilon_{ij} < 0. \end{cases}, \quad \operatorname{sgn}(x) = \begin{cases} 1 & x > 0, \\ 0 & x = 0, \\ -1 & x < 0. \end{cases} \tag{70}$$

For the no-tension model, the material Jacobian in the principal direction is:

$$(C_s')_{ijkl} = \frac{\partial\psi_s}{\partial\epsilon_{ij}\partial\epsilon_{kl}} = \begin{cases} 0 & \epsilon_1 > 0, \\ \delta_{i1}\delta_{j1}\delta_{k1}\delta_{l1}\,E & \epsilon_2 + \nu\epsilon_1 > 0, \\ \delta_{ij}\delta_{kl}(1-\delta_{i3})\left(\delta_{ik} + (1-\delta_{k3})\,\nu\right)\frac{E}{1-\nu^2} & (1-\nu)\epsilon_3 + \nu(\epsilon_1+\epsilon_2) > 0, \\ \boldsymbol{C}_0 & \text{else} \end{cases} \tag{71}$$

The tangential stiffness matrix in the original direction $\boldsymbol{C}$ is obtained by rotating $\boldsymbol{C}'$ using:

$$C_{qrst} = a_{qi}a_{rj}a_{sk}a_{tl}C'_{ijkl}, \tag{72}$$

where $\boldsymbol{a}$ is the transpose of the direction cosines matrix for the principal directions, $\boldsymbol{a}' = [\boldsymbol{v}_1, \boldsymbol{v}_2, \boldsymbol{v}_3]$, with $\boldsymbol{v}_1$, $\boldsymbol{v}_2$, and $\boldsymbol{v}_3$ as the principal vectors of the strain tensor, satisfying:

$$(\boldsymbol{\varepsilon} - \epsilon_{ii}\boldsymbol{I})\cdot\boldsymbol{v}_i = 0, \tag{73}$$

for $i = 1, 2, 3$, and $\boldsymbol{I}$ as the identity matrix.

Table 2
Selection of variables for steps 4 to 6 of Algorithm 2 based on the solution scheme. In f^i_n, the subscript n represents the time increment number, while the superscript i denotes the iteration number.

Solution scheme	Step 4			Step 5		Step 6		
	u	ϕ	p	$\mathcal{H}$	ϕ	$\dot{\varepsilon}_{vol}$	ϕ	p
Monolithic	$\mathbf{u}^i_{n+1}$	ϕ^i_{n+1}	p^i_{n+1}	$\mathcal{H}^i_{n+1}$	ϕ^i_{n+1}	$(\dot{\varepsilon}_{vol})^i_{n+1}$	ϕ^i_{n+1}	p^i_{n+1}
Single-pass staggered	$\mathbf{u}^i_{n+1}$	ϕ_n	p_n	$\mathcal{H}_n$	ϕ^i_{n+1}	$(\dot{\varepsilon}_{vol})_n$	ϕ_n	p^i_{n+1}
Multi-pass staggered	$\mathbf{u}^i_{n+1}$	ϕ^{i-1}_{n+1}	p^{i-1}_{n+1}	$\mathcal{H}^{i-1}_{n+1}$	ϕ^i_{n+1}	$(\dot{\varepsilon}_{vol})^{i-1}_{n+1}$	ϕ^{i-1}_{n+1}	p^i_{n+1}
Mixed monolithic	$\mathbf{u}^i_{n+1}$	ϕ^i_{n+1}	p^{i-1}_{n+1}	$\mathcal{H}^i_{n+1}$	ϕ^i_{n+1}	$(\dot{\varepsilon}_{vol})^i_{n+1}$	ϕ^i_{n+1}	p^i_{n+1}
Mixed staggered	$\mathbf{u}^i_{n+1}$	ϕ^i_{n+1}	p^{i-1}_{n+1}	$\mathcal{H}_n$	ϕ^i_{n+1}	$(\dot{\varepsilon}_{vol})^i_{n+1}$	ϕ^i_{n+1}	p^i_{n+1}

3.3. Solution scheme

After computing all necessary components of residual and stiffness matrices, we can solve the nonlinear coupled equations using an iterative procedure based on the Newton–Raphson method. The algorithm is detailed in Algorithm 2. As shown, the coupled stiffness matrices are omitted ($\boldsymbol{K}^{\mathbf{u},\phi} = 0$, $\boldsymbol{K}^{\mathbf{u},p} = 0$, $\boldsymbol{K}^{\phi,p} = 0$). While these stiffness matrices can enhance the convergence rate for strongly coupled equations, solving the equations separately reduces the size of subproblem, thereby saving computational time and storage per iteration, resulting in less computational effort overall.

Algorithm 2 Solution algorithm for phase field hydraulic fracture in $[t_n, t_{n+1}]$

Input: Displacement field $\mathbf{u}_n$, phase field ϕ_n, history field $\mathcal{H}_n$, and fluid pressure field p_n at time t_n.
Initialization: Set the initial guess for Newton-Raphson iterations at t_{n+1}: $\mathbf{u}^0_{n+1}$, ϕ^0_{n+1}, p^0_{n+1}. Initialize the iteration counter $i = 0$.
repeat
  Compute $\mathbf{R}^{\mathbf{u}}$ and $\boldsymbol{K}^{\mathbf{u}}$ for the variables $\mathbf{u}$, ϕ, p^*.
  Compute $\mathbf{R}^{\phi}$ and $\boldsymbol{K}^{\phi}$ for the variables $\mathcal{H}$, ϕ^*.
  Compute $\mathbf{R}^{p}$ and $\boldsymbol{K}^{p}$ for the variables $\dot{\varepsilon}_{vol}$, ϕ, p^*.
  Solve the coupled system of equations for $\mathbf{u}^{i+1}_{n+1}$, ϕ^{i+1}_{n+1}, p^{i+1}_{n+1} using:

$$\begin{bmatrix} \mathbf{u}^{i+1} \\ \phi^{i+1} \\ p^{i+1} \end{bmatrix}_{t_{n+1}} = \begin{bmatrix} \mathbf{u}^{i} \\ \phi^{i} \\ p^{i} \end{bmatrix}_{t_{n+1}} - \begin{bmatrix} \boldsymbol{K}^{\mathbf{u}} & 0 & 0 \\ 0 & \boldsymbol{K}^{\phi} & 0 \\ 0 & 0 & \boldsymbol{K}^{p} \end{bmatrix}^{-1}_{t} \begin{bmatrix} \mathbf{R}^{\mathbf{u}} \\ \mathbf{R}^{\phi} \\ \mathbf{R}^{p} \end{bmatrix}_{t}. \tag{74}$$

  Compute the norm of the residual for the updated variables, $||\mathbf{R}(\mathbf{u}^{i+1}_{n+1}, \phi^{i+1}_{n+1}, p^{i+1}_{n+1})||$.
  if $||\mathbf{R}|| < \text{TOL}$ **then**
    Converged. Proceed to the next time increment t_{n+2}.
  else
    Increment the iteration counter $i \leftarrow i + 1$.
  end if
until Convergence is achieved.

* The variables are selected based on the solution scheme described in Table 2.

Various solution schemes exist for coupled equations, such as the monolithic and staggered schemes [62,63]. In the monolithic scheme, all equations are solved simultaneously, updating all variables in each equation. In contrast, the staggered method updates only the primary variable of an equation while using variables of other equations from the previous increment (single-pass staggered) or the last iteration (multi-pass staggered). The monolithic scheme is unconditionally stable, allowing for larger time increments, but it often requires more iterations to achieve convergence due to the highly nonlinear behaviour. On the other hand, the staggered scheme converges with fewer iterations but requires smaller time increments for accurate results.

The required variables in steps 4 to 6 of Algorithm 2 for different solution schemes are shown in Table 2. A combination of monolithic and staggered approaches can be used for systems with more than two coupled equations. For example in the mixed monolithic scheme, the linear momentum equation and phase field evolution equation are solved using the monolithic scheme, while the fluid equation is solved with the other two in a multi-pass staggered manner. In the mixed staggered scheme, the linear momentum and phase field evolution equations are solved using a single-pass staggered scheme, while the fluid equation is solved with a multi-pass staggered approach.

As described in Appendix, we implement this framework, and the solution schemes provided in Table 2, within the commercial finite element package Abaqus. A novel procedure is exploited to carry out the numerical implementation at the integration point level, without the need to define residuals and stiffness matrices, which are here provided for the sake of generality.

Table 3
Material and model parameters for the first case study, aimed at investigating the permeability-phase field coupling.

Parameter	Symbol	Value	Unit
Young's modulus	E	50	GPa
Poisson's ratio	ν	0.3	–
Characteristic length scale	ℓ	0.5	m
Critical fracture energy	G_c	10^6	J/m^2
Biot's coefficient of reservoir domain	α_r	0.002	–
Porosity of reservoir domain	ε_{pr}	0.002	–
Density of the fluid	ρ_{fl}	1000	kg/m^3
Dynamic viscosity of the fluid	μ_{fl}	0.001	Pa s
Compressibility of fluid	c_{fl}	10^{-8}	Pa^{-1}
Permeability of reservoir domain	K_r	0	m^2
Permeability of fracture domain	K_f	1	m^2

4. Numerical experiments

Four case studies are extensively investigated to evaluate the proposed methods and highlight the relevance of the two novel ingredients proposed: the Drucker–Prager-based split and the hybrid permeability approach. In the first case study (Section 4.1), we analysed a rectangular domain with a central vertical crack to examine the coupling effects between the phase field variable and the permeability tensor. This configuration allowed us to assess how the phase field influences permeability in fractured regions, demonstrating the efficacy of the hybrid permeability approach presented. The second case study, presented in Section 4.2, focused on a stick–slip problem, illustrating the capability of the Drucker–Prager-based split method to model stick–slip behaviour accurately. This example highlights the suitability of the Drucker–Prager-based split in simulating stress redistribution and frictional resistance in geotechnical applications. The third case study (Section 4.3) investigated the influence of different fracture-fluid coupling methods and strain energy decompositions as the driving force for fracture propagation in a crack interaction problem. By considering different decomposition approaches, we evaluated how different fracture-driving mechanisms affect crack growth and interaction. Finally, the fourth case study, presented in Section 4.4 involved modelling an axisymmetric domain with initial stress, subjected to fluid injection to simulate multiaxial conditions. This scenario allowed us to assess the applicability of the proposed framework under complex loading conditions, relevant to subsurface applications involving fluid-driven fracture under multiaxial stress states. Unless otherwise stated, the AT2 model is employed.

4.1. Influence of the approach adopted to model the coupling between permeability and phase field

We begin by investigating the impact of various coupling methods between permeability and phase field. This study examines three distinct coupling strategies, as discussed in Section 2.4. The problem setup involves a rectangular domain with a vertical crack located at the centre, see Fig. 4. The focus of this analysis is on fluid behaviour within the crack rather than crack propagation. To this end, a pre-existing vertical fracture is introduced at the centre of the domain. Fluid pressure is applied with the following boundary conditions: (i) a $p = 0$ Pa pressure at the top, maintained constant throughout the analysis, and (ii) a linearly increasing pressure going from 0 to $p = 5$ Pa over 100 s. Both lateral boundaries are considered impermeable. Following the application of pressure, a horizontal displacement of $u_x = 0.1$ m is imposed on the left boundary over an additional 100 s to investigate the effect of crack opening under the different coupling methods. The material parameters, as outlined in Table 3, are chosen for illustrative purposes and are not intended to represent realistic values. For example, the critical fracture energy release rate, G_c, is set to a very high value (10^6 J/m^2) to prevent crack propagation during the pressure loading phase. The domain is discretised using a uniform mesh of bilinear quadrilateral elements, each with a size of 10 cm. This analysis primarily focuses on the phase field fracture AT2 model. However, for the sake of completeness, the effect of the coupling method on the AT1 model is also investigated.

Before analysing the effects of different coupling methods on fluid flux, we first examine their impact on pressure distribution within the domain. Fig. 5 compares the pressure distribution for the three coupling methods considered to simulate the interplay between permeability and phase field. In Fig. 5a, the pressure distribution is shown for the domain decomposition and hybrid methods. With reservoir permeability $K_r = 0$, the pressure in that region is zero and is only distributed across the transient and fracture domains. In contrast, Fig. 5b displays a uniform pressure distribution for the modified Darcy method due to element size contributions to crack width ($w_h = \langle |h_e(1 + \mathbf{n}_\phi \cdot \boldsymbol{\varepsilon} \cdot \mathbf{n}_\phi)| \rangle_+$), influencing permeability in such a way that there is no region in the domain with zero permeability. Thus, the modified Darcy method introduces artificial permeability in the undamaged region, which does not accurately reflect physical behaviour. In contrast, the domain decomposition method and the proposed hybrid method preserve the physical permeability of the undamaged region.

Additional, quantitative insight can be gained by plotting the flux distribution, as shown in Fig. 6 for the case of the domain decomposition method [20]. The results are obtained using domain indicator variables, see Eq. (44), with three material constant sets, $S_n = \{c_1, c_2\}$: $S_1 = \{0.5, 0.8\}$, $S_2 = \{0.5, 1\}$, and $S_3 = \{0.8, 1\}$. With no phase field evolution (constant ϕ), the permeability tensor $\boldsymbol{K}_{fl}$ is constant across the domain and time. The fluid flux for each set is shown in Fig. 6a–c, with a comparison of all sets being given in Fig. 6d. The division of the domain into three regions based on ϕ values and material constants c_1 and c_2 is illustrated in Fig. 6a–c. Reservoir permeability is equal where $\phi < c_1$, while fracture domain permeability, K_f, applies where $\phi > c_2$. The transient domain's permeability varies linearly, affecting fluid flux along the x-direction (Fig. 6a–c).

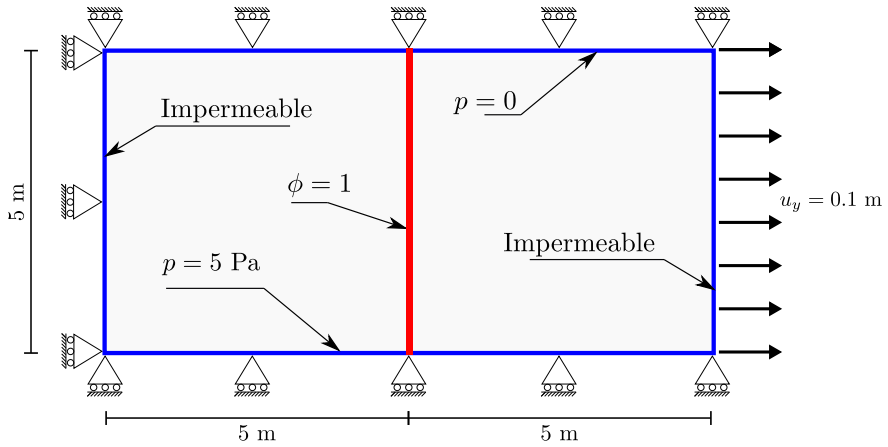

Fig. 4. Geometry, dimensions, and boundary conditions of a rectangular domain with a central vertical fracture subjected to pressure at the bottom.

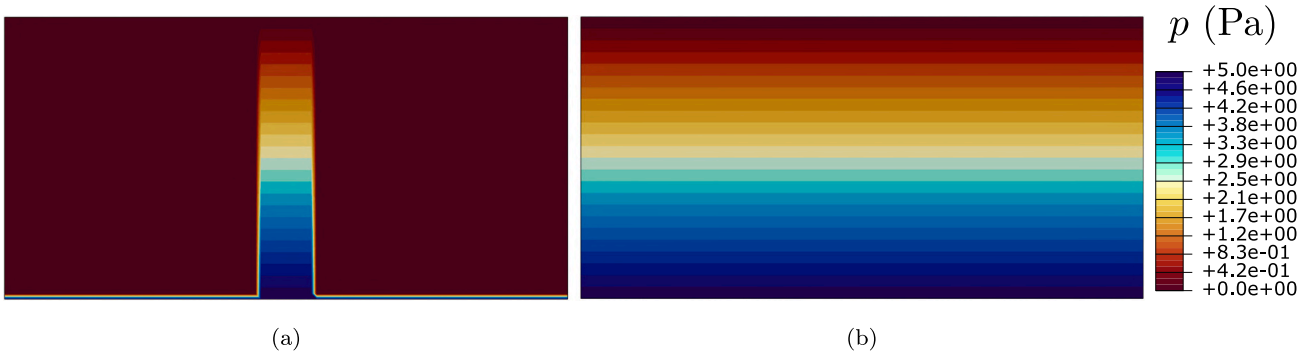

Fig. 5. Fluid pressure contours for the rectangular domain with a centred crack: (a) Permeability determined using the domain decomposition and hybrid methods, (b) Permeability determined using the modified Darcy method.

The effect of the three constant sets on fluid flux is compared in Fig. 6d, showing equal flux in the fracture domain due to consistent permeability. The transient zone width varies with the selected c_1 and c_2 values, impacting mass flow rate Q, which takes values of $Q = 550$ tons/s for S_1, $Q = 450$ tons/s for S_2, and $Q = 225$ tons/s for S_3. This emphasises the importance of carefully calibrating the values of c_1 and c_2 for accurate modelling.

For the modified Darcy method [15], permeability is modelled as an anisotropic tensor to represent Poiseuille-type flow in cracks. Three values of the transition parameter $b = \{0, 1, 2\}$ were considered. Fig. 7a–c shows fluid flux for each b value at times $t = 100$ s, $t = 150$ s, and $t = 200$ s. For $b = 0$ (no transition), flux remains uniform across regions with $\phi < 1$, though permeability in zero-ϕ areas is non-zero due to element size contributions. This changes with linear ($b = 1$) and quadratic ($b = 2$) transitions, where permeability in low-ϕ regions decreases as b increases, see Fig. 7d. Employing a large transient parameter b results in a narrower flux profile.

The hybrid method combines the domain decomposition and modified Darcy methods. The results obtained for material constants $c_1 = 0.5$, $c_2 = 1$, and $b = \{0, 1, 2\}$ are shown in Fig. 8a–c, where the fluid flux is plotted at $t = 100$ s, $t = 150$ s, and $t = 200$ s, for each b value. As observed, fluid flux is zero for $\phi < c_1$, given the zero permeability of the reservoir domain. Comparison of flux profiles in the transient zone ($c_1 < \phi < c_2$) in Fig. 8d reveals minimal effect from b due to domain indicator variables χ_r and χ_f varying linearly in the transition zone.

We proceed to assess the influence of the specific phase field model adopted (AT2 vs. AT1), as the AT2 model produces a broader damage zone, relative to the AT1 model. Consequently, less sensitivity to the coupling method is expected for the latter case. Their comparison is shown in Fig. 9, where both the phase field profile and the fluid flux distribution are shown. For the domain decomposition method, the difference is not significant if c_1 is selected to be sufficiently large (e.g., $c_1 \geq 0.5$), as depicted in Fig. 9a. This is because the difference in the phase field profiles of the AT1 and AT2 models becomes negligible for values of $\phi \geq 0.5$. In the case of the modified Darcy method, if the transient parameter b is sufficiently large ($b \geq 2$), the difference becomes negligible, as shown in Fig. 9b. Finally, as shown in Fig. 9c, the hybrid method is largely insensitive to the choice of phase field model for the aforementioned choices of parameters. It must be noted that, since the history field method does not yield an optimal phase field fracture profile for the AT1 model, the penalty method is here employed to enforce the irreversibility condition. For further details, see Ref. [62].

The comparison of Fig. 9a and b shows that the fluid flux obtained from the modified Darcy method approaches that of the hybrid method when the transient parameter b is sufficiently large. However, this conclusion is intrinsic to the benchmark considered here,

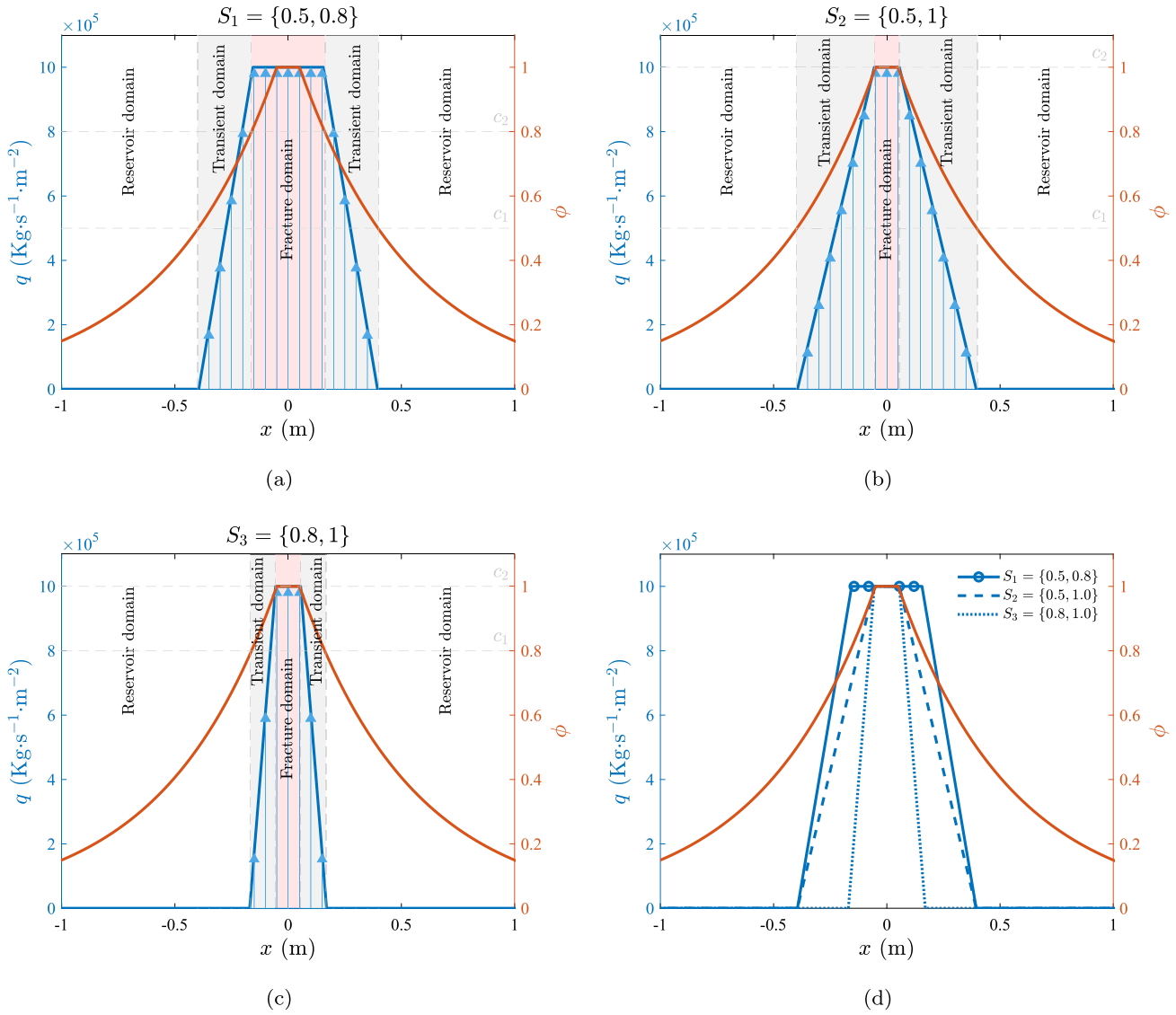

Fig. 6. Phase field profile and fluid flux distribution along the x-direction at the top of the domain for the domain decomposition method [20] and: (a) $S_1 = \{0.5, 0.8\}$, (b) $S_2 = \{0.5, 1\}$, (c) $S_3 = \{0.8, 1\}$, while (d) shows the comparison of fluid flux distribution for all sets.

where a constant phase field is assumed. In cases involving phase field evolution (i.e., crack propagation) the results of these two methods can differ significantly. This is because in the modified Darcy method only the permeability is a function of the phase field variable, while Biot's coefficient and porosity remain constant. In contrast, the hybrid method accounts for variations in permeability, Biot coefficient, and porosity due to phase field evolution.

In summary, this study highlights the importance of appropriate parameter selection for accurate results. The domain decomposition method benefits from isotropic permeability but lacks sensitivity to crack opening changes. The modified Darcy method, which models anisotropic permeability and Poiseuille-type flow, suggests $b \geq 2$ for an effective transition. The hybrid method combines the strengths of both, providing distinct permeability domains while accounting for crack opening effects.

4.2. Stick–slip modelling using a Drucker–Prager-based split

In this case study, we demonstrate the capability of the proposed Drucker–Prager-based split of the strain energy density to model stick–slip within hydraulic fracturing. As shown in Fig. 10, a rectangular domain with a central horizontal crack is considered. To comprehensively investigate different regions of the strain space within the Drucker–Prager-based split (discussed in Section 2.1.1), we consider two loading configurations that result in a path in the strain space that begins either in the elastic region or in the frictional region. Each boundary condition configuration is named according to the stress state at the end of the first step. The boundary conditions are applied in three steps, each lasting 10^6 s.

The first configuration is referred to as *biaxial initial state* (Fig. 10a) and involves fixing the lower half of the domain. Both domain sides are impermeable. A traction $(t_n)_{s1} = 8.86$ MPa is applied linearly over time to the top boundary during the first step. As the

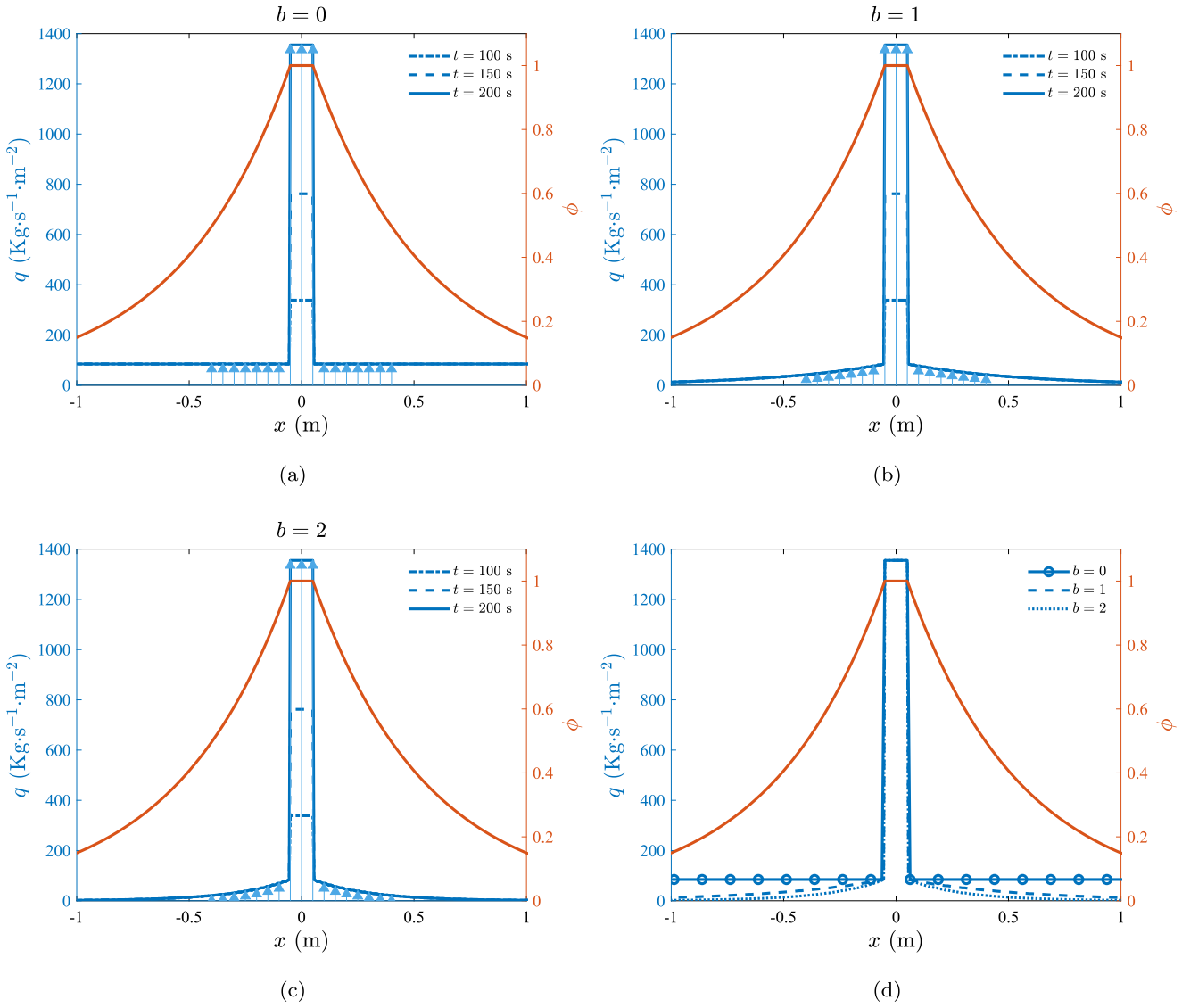

Fig. 7. Phase field profile and fluid flux distribution along the x-direction at the top of the domain for the modified Darcy method [15] and: (a) $b = 0$, (b) $b = 1$, (c) $b = 2$, while (d) shows the comparison of fluid flux distribution for all b values.

plane strain is adopted, the model experiences biaxial stress in this step. In the second step, a traction $(t_n)_{s2} = 5$ MPa is applied to the upper half of the left side, ramped over time. In the third step, the fluid pressure p is increased linearly over time to reach $p = 15.55$ MPa at the domain's bottom.

The second configuration, referred to as the *triaxial initial state*, is designed to ensure that the strain invariant path includes the elastic region (see Fig. 1). In this setup, the left bottom corner has its displacements constrained in both directions, while the right bottom corner restricts only vertical displacement. As in the first configuration, both domain sides are impermeable. A uniform traction $(t_n)_{s1} = 8.86$ MPa is applied to the entire boundary during the first step, which leads to a triaxial stress state. In the second step, a traction $(t_n)_{s2} = 5$ MPa is applied linearly to the upper half of the left side. Finally, in the third step, fluid pressure is applied to the bottom side until it reaches $p = 15.55$ MPa.

In both configurations, a horizontal crack is introduced by setting $\phi = 1$. A uniform mesh of bilinear quadrilateral elements is used, with a characteristic finite element length of 10 cm. The material properties adopted correspond to those employed in the previous case study (see Table 3), unless specified otherwise. Poisson's ratio equals $\nu = 0.2$, the characteristic length scale is $\ell = 0.2$ m, the permeability of the reservoir domain is assumed to be $K_r = 10^{-15}$ m^2, and the permeability of the fracture domain equals $K_f = 1.333 \times 10^{-6}$ m^2. A high value of the material toughness G_c is set to prevent crack propagation. The domain decomposition method with constants $c_1 = 0.5$ and $c_2 = 1$ is used for the permeability coupling, and a monolithic solution scheme is employed.

To analyse the results, we first examine the displacement at the top of the domain for each problem. Fig. 11a compares the horizontal displacement u_x for both configurations. Initially, u_x remains nearly zero during the first step but increases when traction $(t_n)_{s2}$ is applied. After reaching equilibrium at the end of the second step, fluid pressure increases during the third step. Initially, there is no displacement change, but as the fluid pressure rises, the displacement increases until elements along the horizontal

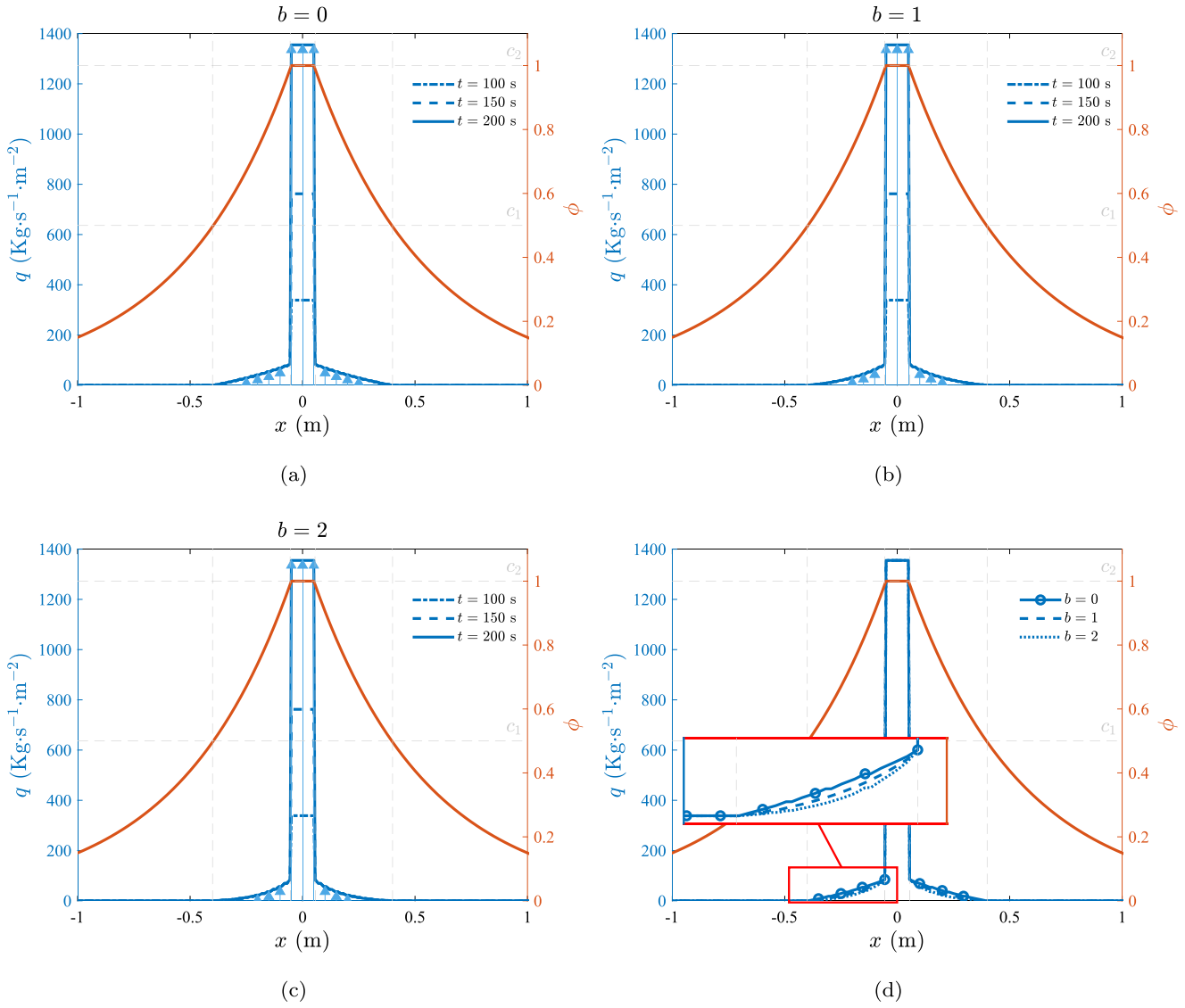

Fig. 8. Phase field profile and fluid flux distribution along the x-direction at the top of the domain for the proposed hybrid method for the following choices of parameters: $c_1 = 0.5$, $c_2 = 1$ and: (a) $b = 0$, (b) $b = 1$, (c) $b = 2$, while (d) shows the comparison of fluid flux distribution for all b values.

crack lose stiffness, causing the displacement solution to diverge. The horizontal displacement u_x at the top provides insight into the stress and strain paths. We examine the strain space $(I_1(\boldsymbol{\varepsilon}), \sqrt{J_2(\boldsymbol{\varepsilon})})$ (Fig. 11b) and the stress space $(I_1(\boldsymbol{\sigma}), \sqrt{J_2(\boldsymbol{\sigma})})$ (Fig. 11c,d) for an element along the crack line in each problem, analysing both the total stress $\boldsymbol{\sigma}$ and the effective stress $\boldsymbol{\sigma}^{\text{eff}}$.

Let us start with the biaxial initial state, where the strain is in the frictional region (see Fig. 1a). Since $\phi = 1$ at this integration point, the material follows the Drucker–Prager failure criterion, as seen in Fig. 11c. Applying traction $(t_n)_{s1}$ initiates the effective stress from $(I_1(\boldsymbol{\sigma}^{\text{eff}}) = 0, \sqrt{J_2(\boldsymbol{\sigma}^{\text{eff}})} = 0)$ along the criterion line $\sqrt{J_2(\boldsymbol{\sigma})} = BI_1(\boldsymbol{\sigma})$. In the second step, traction $(t_n)_{s2}$ increases $J_2(\boldsymbol{\sigma}^{\text{eff}})$ while $I_1(\boldsymbol{\sigma}^{\text{eff}})$ also increases due to frictional behaviour. $I_1(\boldsymbol{\sigma})$ decreases with fluid pressure p until reaching zero stress, as indicated by the strain line intersecting the line $-6B\sqrt{J_2(\boldsymbol{\varepsilon})} = I_1(\boldsymbol{\varepsilon})$. Consequently, the total stress loses its deviatoric part, transitioning to a hydrostatic state.

The triaxial initial state, shown in Fig. 11b and d, starts in the elastic region, meaning that the material remains elastic without phase field influence. In the first step, the application of a traction $(t_n)_{s1}$ increases strains and stresses elastically. In the second step, the application of a traction $(t_n)_{s2}$ changes the stress and strain paths, which still lie within the elastic region. With fluid pressure being applied in the third step, $I_1(\boldsymbol{\sigma}^{\text{eff}})$ decreases, intersecting the failure criterion $\sqrt{J_2(\boldsymbol{\sigma})} = BI_1(\boldsymbol{\sigma})$. Here, the material behaviour follows the Drucker–Prager criterion, and with $\phi = 1$, the effective stress lies on the failure line $\sqrt{J_2(\boldsymbol{\sigma})} = BI_1(\boldsymbol{\sigma})$. A continued rise in fluid pressure causes the effective stress to return towards the origin, with the strain path intersecting the line $-6B\sqrt{J_2(\boldsymbol{\varepsilon})} = I_1(\boldsymbol{\varepsilon})$, indicating zero effective stress and complete stiffness loss, leading to a hydrostatic stress state.

This case study demonstrates that the stick–slip behaviour of rock joints can be effectively modelled by incorporating pore pressure variations using a Drucker–Prager-based split model. Stick–slip behaviour refers to the alternating phases of sticking and sudden slipping along a rock joint, driven by the accumulation and abrupt release of effective stress. As illustrated in Fig. 11c,d,

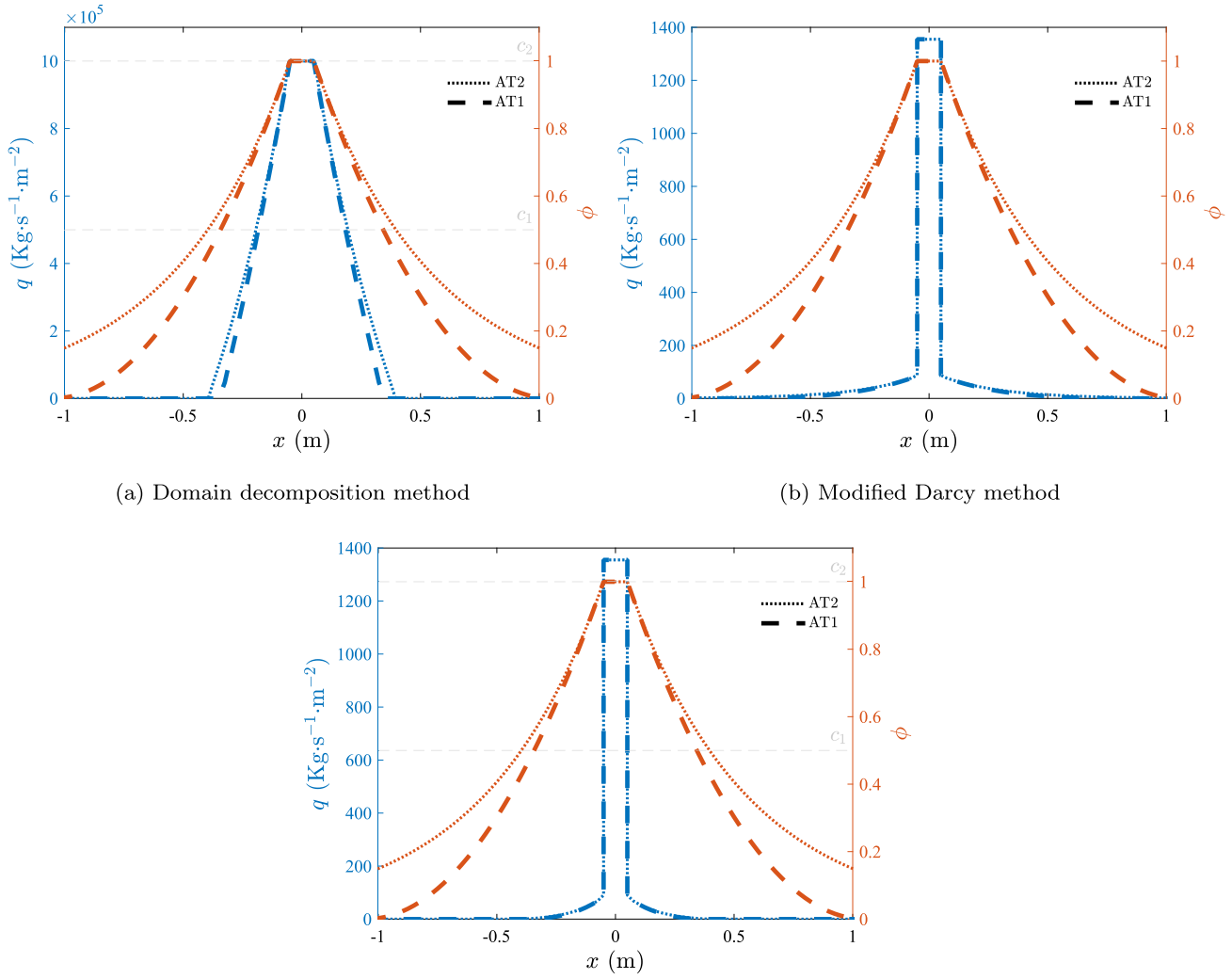

(a) Domain decomposition method

(b) Modified Darcy method

(c) Hybrid method

Fig. 9. Phase field profile and fluid flux distribution along the x-direction at the top of the domain for AT2 and AT1 models, (a) domain decomposition method with parameter $c_1 = 0.5$ and $c_2 = 1$, (b) modified Darcy method with transient parameter $b = 2$, and (c) hybrid methods for selecting parameters $c_1 = 0.5$, $c_2 = 1$, and $b = 2$.

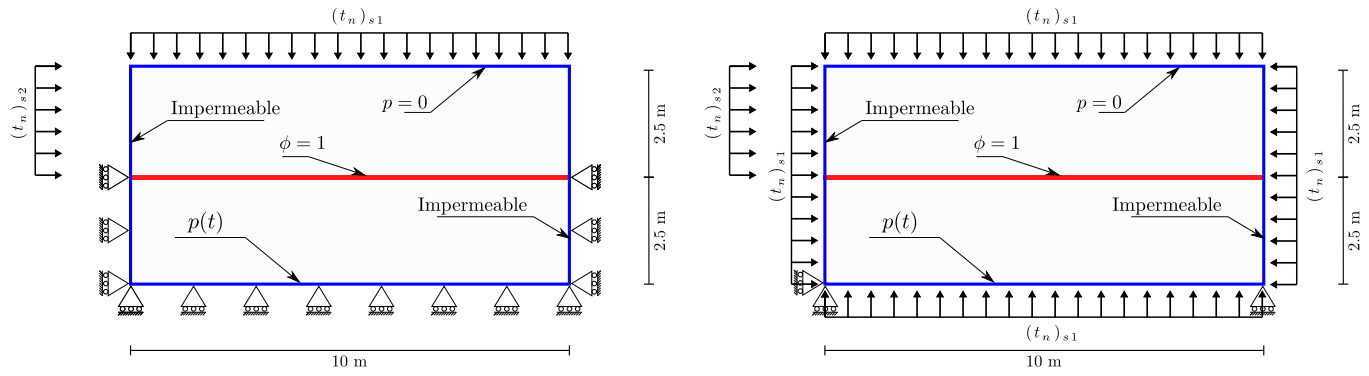

(a) Biaxial initial state

(b) Triaxial initial state

Fig. 10. Geometry and boundary conditions of stick–slip problems: (a) Biaxial initial state, and (b) Triaxial initial state.

the stress path captures these transitions. This modelling approach accounts for variable field conditions, including in-situ stress, and elucidates how pore pressure fluctuations influence the frictional behaviour of rock joints, determining whether they remain stationary (stick) or undergo slip, as relevant to many applications such as reducing seismic hazard during mining process [64].

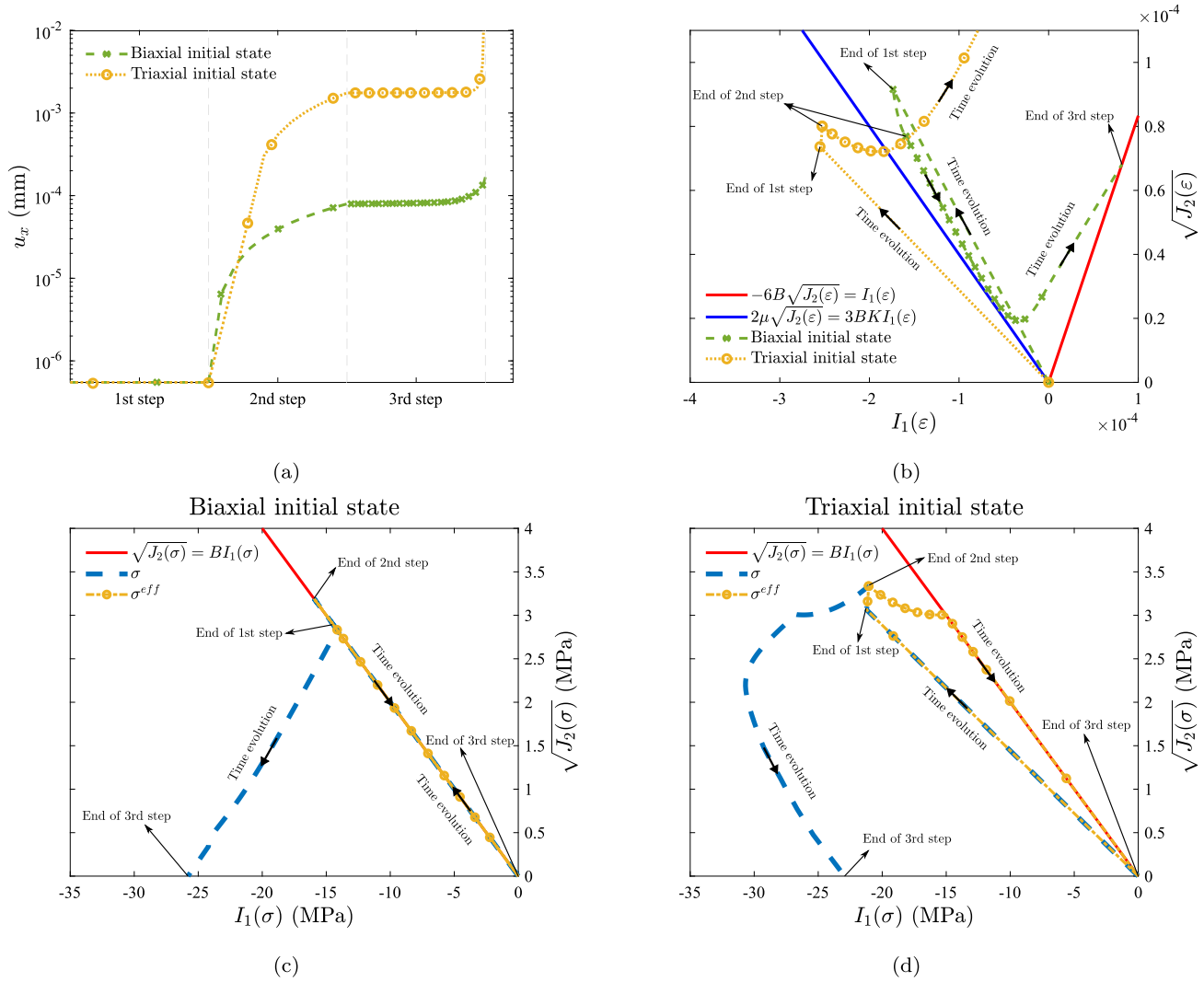

Fig. 11. Stick–slip problem: (a) Horizontal displacement u_x of top side at different steps, and (b) comparison of the strain path for biaxial and triaxial initial states. The bottom half of the figure shows the total ($\boldsymbol{\sigma}$) and effective ($\boldsymbol{\sigma}^{\text{eff}}$) stress paths of integration point with $\phi = 1$ for (c) the biaxial initial state, and (d) the triaxial initial state.

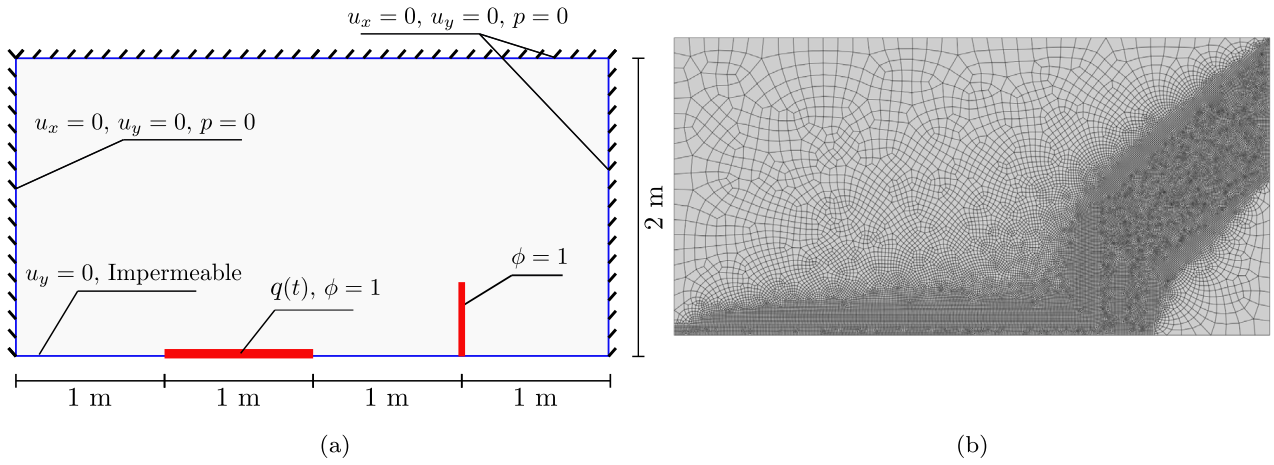

Fig. 12. Crack-interaction problem: (a) Geometry and boundary conditions, and (b) finite element mesh discretisation.

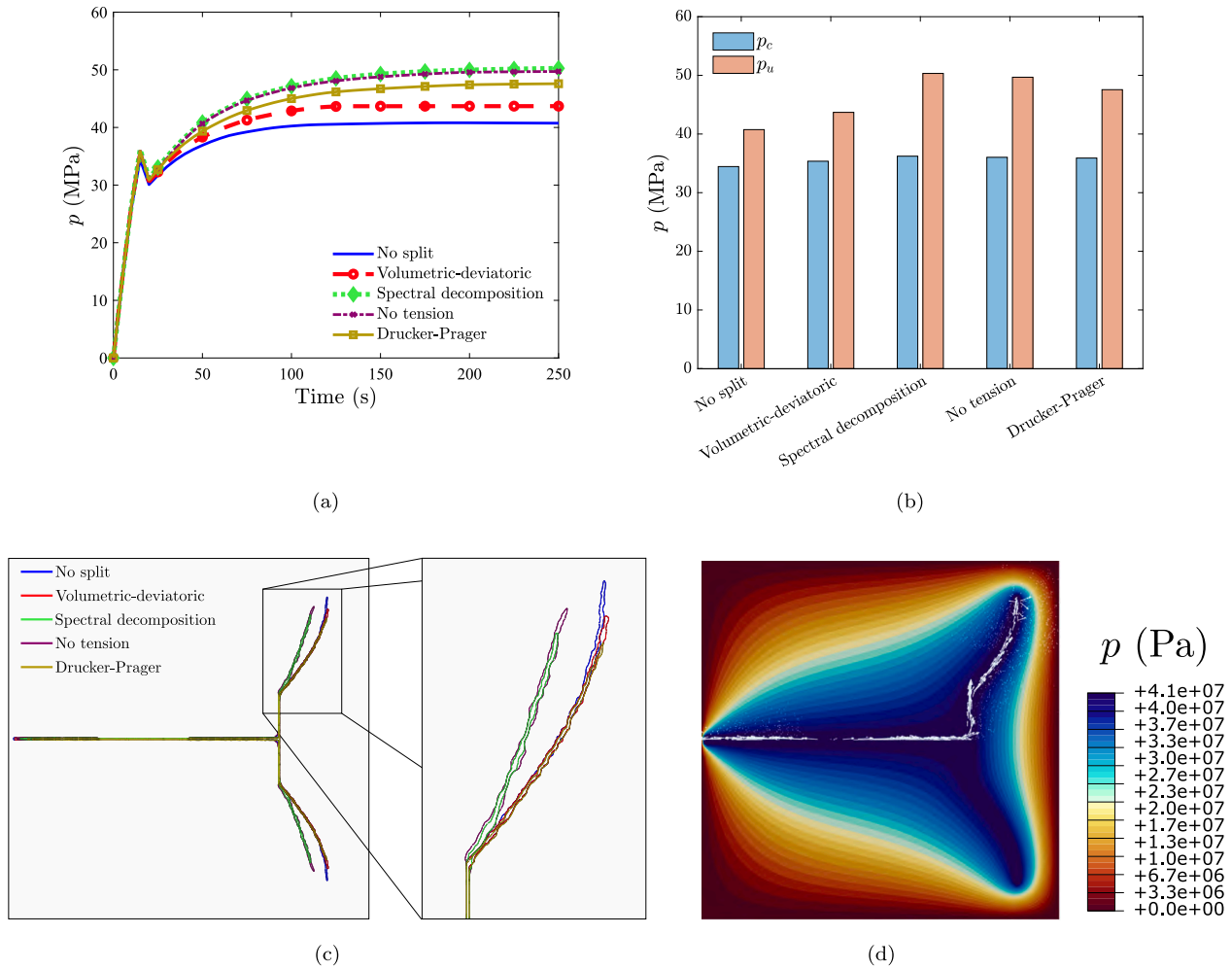

Fig. 13. Crack-interaction problem: (a) Evolution of fluid pressure p versus time at a point on the horizontal crack for different strain energy decompositions, (b) critical p_c and ultimate p_u fluid pressures, (c) crack paths for different fracture driving forces, and (d) fluid pressure p contour and fluid flux vector at the steady state for the case without strain energy decomposition.

4.3. Influence of the fracture driving force on fluid-driven crack interactions

In this case study, we investigate the influence of the adopted strain energy decomposition and of the fracture-fluid coupling method (discussed in Section 2.4) on the crack propagation behaviour of hydraulic fractures. A square domain with two pre-existing cracks is considered, arranged is such a way so as to examine both tensile and shear contributions of the strain energy density in crack propagation (Fig. 12a). Due to symmetry, only half of the boundary value problem is simulated. The displacement and pressure at the domain perimeter are fixed, and each crack has a width of 1 cm ($\phi = 1$ prescribed over a row of elements). A fluid flux of $q_m = 80$ kg s^{-1} m^{-2} is applied to the horizontal crack at $t = 0$ and held constant throughout the analysis. Material properties follow those used in the second case study, but considering a Young's modulus of $E = 210$ GPa, a Poisson's ratio equal to $\nu = 0.3$, a characteristic length scale of $\ell = 0.02$ m, and a critical fracture energy release rate of $G_c = 2700$ J/m^2. The domain decomposition method is used for permeability coupling with constants $c_1 = 0.4$ and $c_2 = 1$. The model is discretised using bilinear quadrilateral elements. A total of 31,277 elements are used, with the mesh being refined along the anticipated crack propagation region, giving a minimum element size of 0.01 m (Fig. 12b). The mixed staggered method is used, with a time increment of 0.05 s over a total duration of 500 s.

As described in Section 2.1.1, the present phase field framework for hydraulic fracture includes five different treatments of the fracture driving force: no split, volumetric-deviatoric, spectral, no tension and Drucker–Prager. All five are considered in this case study. For the Drucker–Prager-based split, the parameter $B = -0.2$ is used.

The results obtained are shown in Fig. 13. In all cases, applying volumetric fluid flux to the horizontal crack causes fluid pressure to increase until it reaches a critical value p_c, as shown in Fig. 13a. When the fluid pressure reaches p_c, crack propagation initiates. The critical pressure varies only slightly depending on the strain energy split, as the fracture of the initial crack is primarily driven by tensile stresses. The highest critical pressure p_c is attained with the spectral decomposition. The fluid pressure p decreases with crack propagation until the two cracks merge, causing the pressure in the second crack to rise. The fluid pressure then continues

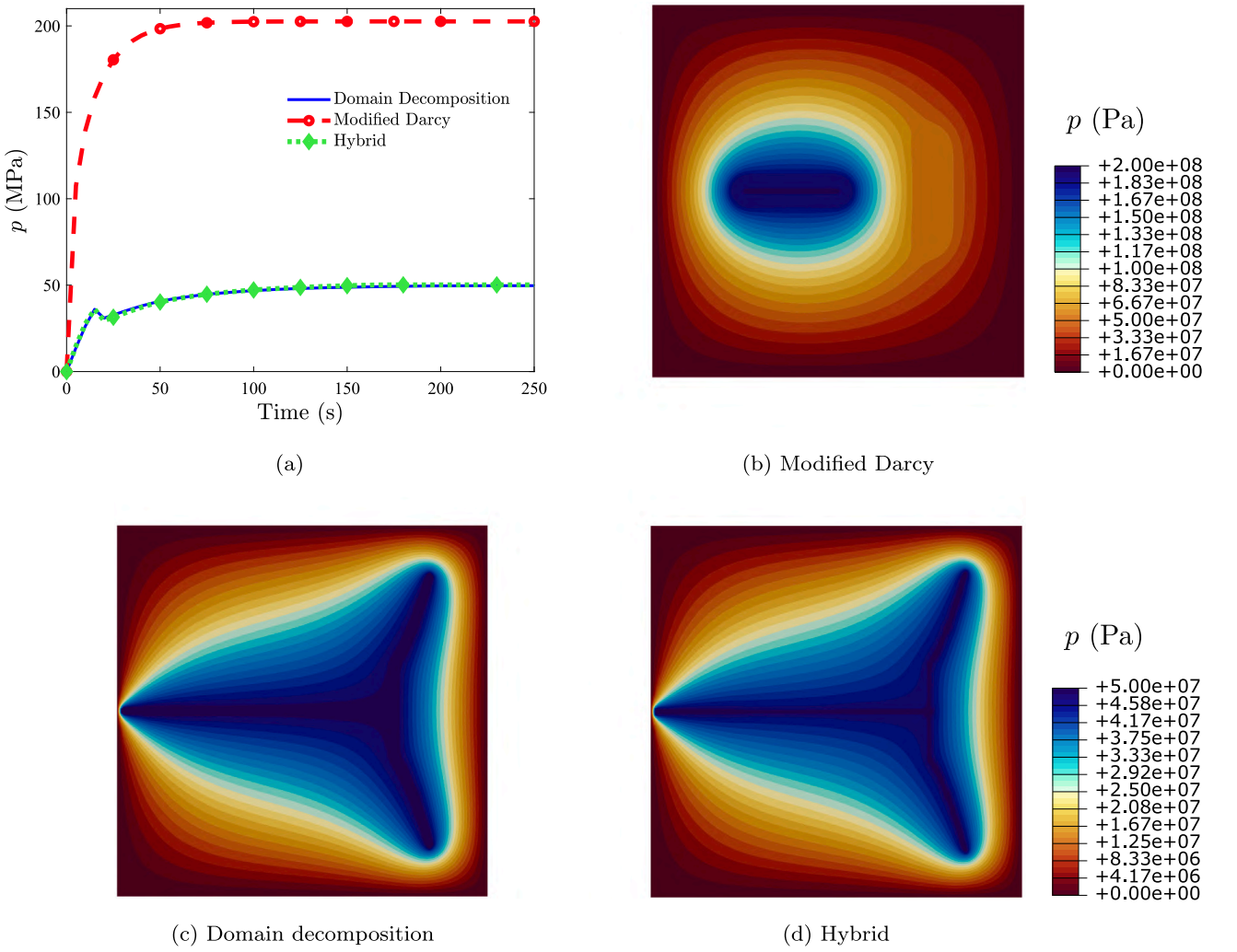

Fig. 14. Crack interaction analysis under various coupling strategies employing a no-tension model for a fluid flux of $q_m = 80$ kg s^{-1} m^{-2}. (a) Temporal evolution of fluid pressure p, and fluid pressure p contour distributions at $t = 150$ s for: (b) the modified Darcy method, (c) the domain decomposition method, and (d) the present hybrid method.

to increase, with subsequent crack propagation being gradual and influenced by shear stresses. Eventually, a steady state in crack growth is reached, indicated by the lack of further pressure increases after Time = 200 s in Fig. 13a.

The critical pressure p_c and ultimate pressure p_u (steady-state pressure) are reported in Fig. 13b. The highest ultimate pressure is attained with the spectral decomposition, where the material is weaker in shear compared to tension. Conversely, the lowest ultimate pressure corresponds to the no split case, where all the strain energy drives fracture. The impact of the shear contributions of the strain energy density to the crack trajectory is shown in Fig. 13c: decompositions incorporating shear strain energy contributions (no split, volumetric-deviatoric, and Drucker–Prager) exhibit a higher degree of deflection from the vertical crack tip, while tensile-based decompositions (spectral and no tension models) show straighter paths. Fig. 13d shows the fluid pressure contour and flux vectors, where the pressure in the fractured area is uniform due to low permeability. These results are qualitatively the same for all the fracture driving forces. The fluid flux begins at the horizontal crack and follows the crack path, facilitating propagation towards the vertical crack.

The influence of the property coupling method was extensively assessed in Section 4.1 for the case of a uniform phase field (stationary crack), with a focus on permeability. The analysis is extended here to consider their effect on crack growth. To this end, the crack-interaction boundary value problem illustrated Fig. 12 is evaluated, with the no tension strain energy decomposition approach and the three different coupling models: modified Darcy (power-law), domain decomposition and the presently proposed hybrid one. In the modified Darcy method, only the permeability tensor is dependent on the phase field variable. In contrast, the domain decomposition and hybrid methods incorporate the phase field dependency into the permeability tensor, Biot's coefficient, and porosity. As a result, during fracture propagation, the critical pressure is expected to be higher in the modified Darcy method due to the insensitivity of Biot's coefficient to phase field evolution. Conversely, in the domain decomposition and hybrid methods, Biot's coefficient approaches unity in the crack region and at the crack tip, thereby enhancing the influence of pore pressure on the deformation process.

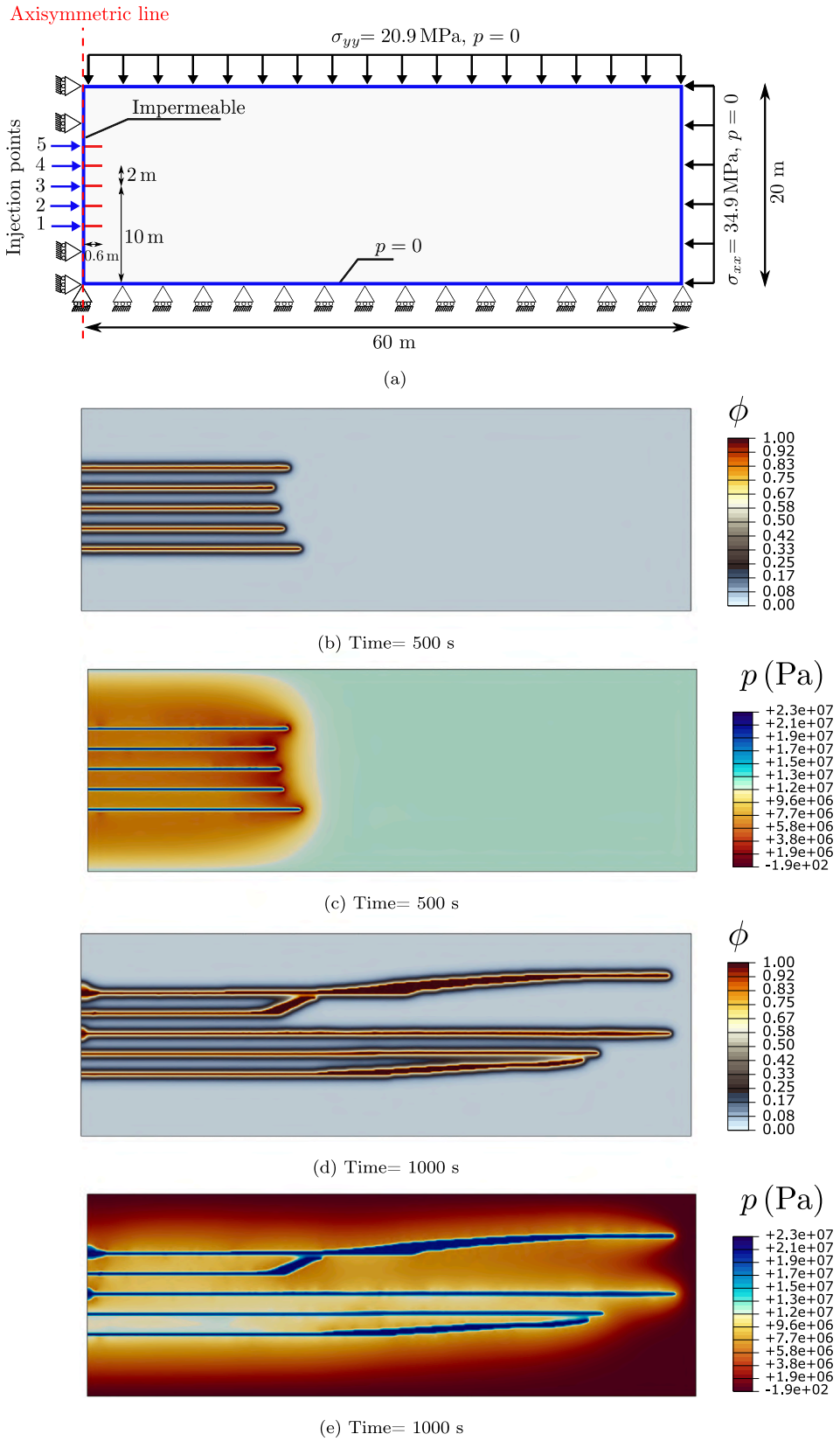

Fig. 15. Injection into an axisymmetric boundary: (a) Geometry and boundary conditions, (b) contour of phase field at time t = 500 s, (c) contour of pore pressure at t = 500 s, (d) contour of phase field at t = 1000 s, and (e) contour of pore pressure at t = 1000 s.

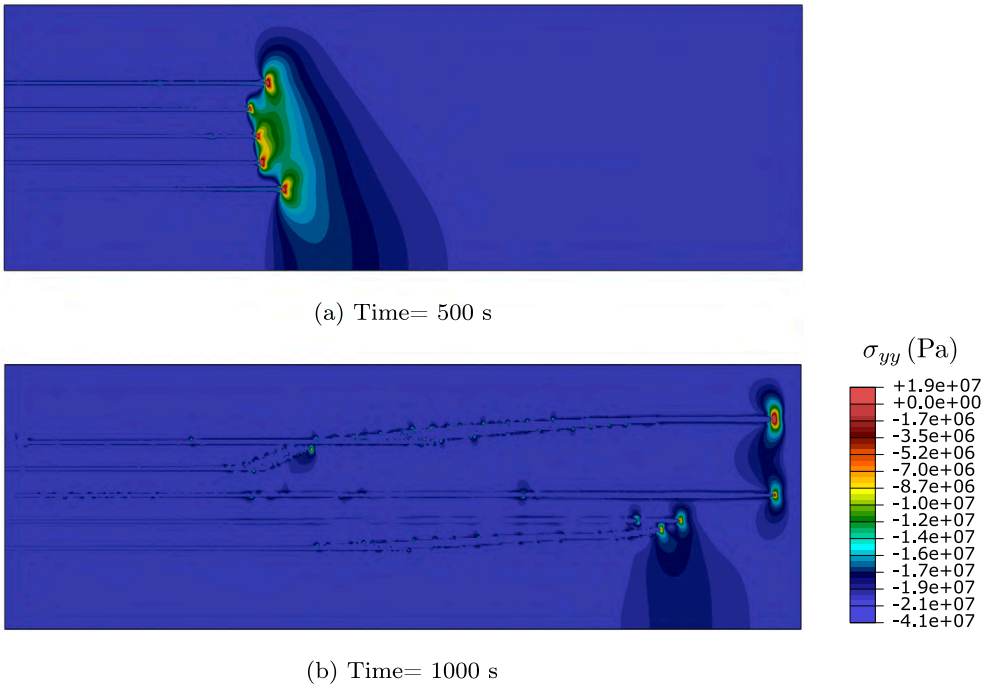

Fig. 16. Vertical stress σ_{yy} contour at: (a) Time = 500 s, and (b) Time = 1000 s.

The results obtained are shown in Fig. 14 for a fluid flux $q_m = 80$ kg s^{-1} m^{-2} and a transient parameter of $b = 2$. In the modified Darcy method, these conditions do not result in crack growth. The fluid pressure rises to 200 MPa, and the system reaches steady state without crack propagation, as shown in the pressure contours provided in Fig. 14b. This result aligns with the assumption that Biot's coefficient remains constant and is not influenced by the phase field. To determine the critical pressure, a significantly higher fluid flux of $q_m = 70{,}000$ kg s^{-1} m^{-2} is applied, leading to crack propagation at a pressure of $p = 12{,}350$ MPa. Conversely, in the hybrid method the evolution of Biot's coefficient and porosity with ϕ promotes crack propagation at a lower pressure. The observed critical pore pressure is comparable to that of the domain decomposition method, approximately $p = 37.3$ MPa. As depicted in Fig. 14a, the time evolution of pore pressure in the hybrid method closely follows that of the domain decomposition method. However, a comparison of the fluid pressure distributions for the domain decomposition (Fig. 14c) and hybrid (Fig. 14d) approaches reveals that, due to the consideration of anisotropic permeability in the hybrid method, the pressure is more concentrated near the crack in the hybrid model compared to the domain decomposition method, which employs an isotropic permeability tensor.

In this case study, we observe that the choice of fracture driving force significantly affects both the pressure field and the crack path. However, this effect can be negligible if the fracture is driven primarily by tensile stress. On the other hand, shear stress can play a significant role in determining the crack trajectory and pressure distribution. Fracture driving forces that mainly consider tensile stresses, such as the spectral decomposition and no tension models, result in higher pressures for crack propagation. In contrast, methods like the volumetric-deviatoric and Drucker–Prager-based splits incorporate shear stress effects, influencing both crack path and pressure distribution. The lowest pressure is observed in the original formulation (no split), where the entire strain energy density contributes to fracture propagation. Moreover, this crack-interaction boundary value problem is used to assess the influence of the coupling strategy under crack growth conditions, extending the analysis in Section 4.1. While in Section 4.1, focused on permeability and considering a uniform and stationary phase field, the hybrid approach was closer to the modified Darcy model, under crack growth conditions our hybrid approach aligns better with the domain decomposition method. This is primarily because in the domain decomposition and hybrid methods, the Biot coefficient evolves with the phase field. The consideration of anisotropic permeability in the hybrid method shows a more concentrated distribution of pressure near the crack relative to the domain decomposition method, showcasing its greater modelling flexibility, as it allows for the evolution of material behaviour via the phase field while also leveraging an anisotropic permeability tensor based on computed crack openings.

4.4. Simultaneous injection into an axisymmetric boundary with initial stress

To demonstrate the robustness of the current implementation, we analyse a complex problem involving multiple injections along an axisymmetric boundary, as depicted in Fig. 15(a). The material properties are identical to those used in the second case study, with the following exceptions: Young's modulus $E = 53$ GPa, Poisson's ratio $\nu = 0.19$, critical fracture energy release rate $G_c = 500$ N/m, and characteristic length scale $\ell = 0.29$ m. The geometry is discretised with over 55,000 bilinear quadrilateral elements, and the mixed staggered scheme is applied with a time increment of 1 s over a total injection period of 2400 s. The hybrid permeability method is used, with initial stresses applied in both horizontal and vertical directions. Specifically, a horizontal stress

of $\sigma_{xx} = 34.9$ MPa and a vertical stress of $\sigma_{yy} = 20.9$ MPa are applied in the first step to establish the initial stress state. In the second step, five pre-existing cracks are introduced, followed by five simultaneous injections at a rate of $q = 126$ kg s^{-1} m^{-2} over 2400 s in the third step. The top, bottom, and right edges of the domain are considered to be pore-pressure-free boundaries ($p = 0$).

Crack growth is observed at each of the five injection points. Figs. 15(b) and 15(c) show the initial propagation of cracks horizontally up to 500 s. Beyond this point, the crack originating from injection point 4 begins to approach the crack from injection point 5. At this stage, the crack originating from injection point 4 is coalescing with the crack from injection point 5 through crack interactions, leading to increased fluid flux within the crack at injection point 5 and further propagation through other cracks. Crack propagation from injection points 2 and 3 remains horizontal throughout the injection, while the crack from injection point 1 deviates after 610 s. Figs. 15(d) and 15(e) illustrate the phase field and pressure contours at 1000 s, highlighting continued propagation and interaction between cracks.

Finally, vertical stress σ_{yy} contours at 500 s and 1000 s are shown in Fig. 16. Throughout the domain, compressive vertical stress increases, except at the crack tip, where tensile stress drives further crack propagation.

5. Conclusions

We have presented a novel, theoretical and computational framework to simulate hydraulic fractures based on the phase field method. The model encompasses a number of relevant features, from constitutive choices to solution schemes, and introduces two key innovations that enhance the accuracy and adaptability of hydraulic fracture simulations. First, a novel hybrid coupling approach is introduced to link the phase field evolution equation with the pore pressure equation. This approach offers refined control over permeability transitions, making it especially effective in capturing fluid flow and fracture propagation interactions in complex geomechanical problems. Second, we incorporate a Drucker–Prager-based strain energy split to model stick–slip behaviour accurately, a critical aspect in hydraulic fracturing and fault activation scenarios.

Through a series of representative case studies, we demonstrated the robustness and versatility of our proposed formulation. The results highlighted the significant impact of different coupling strategies on fluid behaviour within fractures and underscored the influence of strain energy decomposition on fracture propagation paths and crack interactions. Our hybrid permeability approach effectively addressed the limitations of existing methods, providing a more flexible solution for hydraulic fracturing scenarios characterised by complex geometries and evolving fracture patterns. Additionally, the Drucker–Prager-based split effectively modelled the transition between elastic, frictional, and fully fractured states, yielding new insights into the role of shear stress in hydraulic fracture propagation.

The phase field framework developed in this work not only extends the current capabilities of hydraulic fracture modelling but also serves as a valuable tool for a wide range of geomechanical applications, including reservoir engineering, fault activation, and fracture interaction under multiaxial stress conditions.

CRediT authorship contribution statement

Yousef Navidtehrani: Writing – review & editing, Writing – original draft, Visualization, Validation, Software, Methodology, Investigation, Formal analysis, Data curation, Conceptualization. **Covadonga Betegón:** Writing – review & editing, Supervision, Project administration, Funding acquisition, Conceptualization. **Javier Vallejos:** Writing – review & editing, Project administration, Funding acquisition. **Emilio Martínez-Pañeda:** Writing – review & editing, Supervision, Software, Resources, Project administration, Methodology, Investigation, Funding acquisition, Conceptualization.

Declaration of competing interest

The authors declare that they have no known competing financial interests or personal relationships that could have appeared to influence the work reported in this paper.

Acknowledgements

Y. Navidtehrani and C. Betegón acknowledge financial support from the FUO contract 22-364 and from the Ministry of Science, Innovation and Universities of Spain through grant PGC2018-099695-B-I00. C. Betegón acknowledges financial support from the Ministry of Science, Innovation, and Universities of Spain under grant MCINN-23-PID2022-1420150B-100. J. Vallejos acknowledges the financial suport from CONICYT, Chile (Project AFB230001). E. Martínez-Pañeda was supported by an UKRI Future Leaders Fellowship, UK (grant MR/V024124/1).

Table A.4
Analogy of variables between heat transfer, phase field, and fluid flow equations.

Heat transfer equation	Phase field evolution equation	Fluid flow equation
$\rho\dot{U} + \nabla \cdot \mathbf{f} = r$	$\left(\frac{g'(\phi)\mathcal{H}2c_w}{\ell G_c} + \frac{w'(\phi)}{2\ell^2}\right) - \nabla \cdot (\nabla\phi) = 0$	$\rho_{fl}\left(S\dot{p} + \alpha\chi_r\dot{\varepsilon}_{vol}\right) - \nabla \cdot \left(\rho_{fl}\frac{\boldsymbol{K}_{fl}}{\mu_{fl}}\nabla p\right) = q_m$
T	ϕ	p
$\mathbf{f}$	$-\nabla\phi$	$-\rho_{fl}\frac{\boldsymbol{K}_{fl}}{\mu_{fl}}\nabla p$
ρ	1	1
$\dot{U}$	$\frac{g'(\phi)\mathcal{H}2c_w}{\ell G_c} + \frac{w'(\phi)}{2\ell^2}$	$\rho_{fl}\left(S\dot{p} + \alpha\chi_r\dot{\varepsilon}_{vol}\right)$
r	0	q_m

Table A.5
Variables that must be defined in a UMATHT subroutine and their associated expressions for the heat transfer, phase field and fluid flow problems.

UMATHT variable	Heat transfer	Phase field	Fluid flow
U	$U_t + \dot{U}\Delta t$	$U_t + \left(\frac{g'(\phi)\mathcal{H}2c_w}{\ell G_c} + \frac{w'(\phi)}{2\ell^2}\right)\Delta t$	$U_t + \rho_{fl}\left(S\dot{p} + \alpha\chi_r\dot{\varepsilon}_{vol}\right)\Delta t$
DUDT	$\frac{\partial U}{\partial T}$	$\left(\frac{g''(\phi)\mathcal{H}2c_w}{\ell G_c} + \frac{w''(\phi)}{2\ell^2}\right)\Delta t$	$\rho_{fl}S\Delta t$
DUDG	$\frac{\partial U}{\partial(\nabla T)}$	0	0
FLUX	$\mathbf{f}$	$-\nabla\phi$	$-\rho_{fl}\frac{\boldsymbol{K}_{fl}}{\mu_{fl}}\nabla p$
DFDT	$\dot{\mathbf{f}}$	0	0
DFDG	$\frac{\partial \mathbf{f}}{\partial(\nabla T)}$	$-\boldsymbol{I}$	$-\rho_{fl}\frac{\boldsymbol{K}_{fl}}{\mu_{fl}}$

Appendix. Abaqus implementation

The generalised phase field model for hydraulic fracture presented is implemented in the commercial finite element package Abaqus in a very straightforward way, without the need for user element subroutines (i.e., at the integration point level). This is achieved by exploiting the analogy between the heat transfer balance equation and the fluid flow and phase field balance equations. The idea is similar to that exploited in Refs. [45,65] to implement phase field fracture by means of (solely) a user material (UMAT) subroutine. However, on this occasion, the approach is extended to encompass an additional balance equation, as explained below.

First, consider the heat transfer equation in its general form,

$$\rho\dot{U} + \nabla \cdot \mathbf{f} = r, \tag{A.1}$$

where U is the internal thermal energy, $\mathbf{f}$ is the heat flux vector, and r is the heat source. Rearranging the phase field evolution (12) and fluid flow (38) equations,

$$\left(\frac{g'(\phi)\mathcal{H}2c_w}{\ell G_c} + \frac{w'(\phi)}{2\ell^2}\right) - \nabla \cdot (\nabla\phi) = 0 \tag{A.2}$$

$$\rho_{fl}\left(S\dot{p} + \alpha\chi_r\dot{\varepsilon}_{vol}\right) - \nabla \cdot \left(\rho_{fl}\frac{\boldsymbol{K}_{fl}}{\mu_{fl}}\nabla p\right) = q_m. \tag{A.3}$$

By comparing Eqs. (A.2)–(A.3) with Eq. (A.1), we observe an analogy between these diffusion-like equations. Table A.4 summarises the analogous variables across the heat transfer, phase field, and fluid flow equations.

The numerical implementation is carried out in Abaqus using a UMATHT subroutine, where several variables must be defined to establish equivalence with heat transfer and mass diffusion variables. Table A.5 outlines the required quantities and their corresponding expressions for the heat transfer, phase field, and fluid flow equations.

By exploiting this analogy, the temperature variable T becomes equivalent to the phase field variable ϕ, which varies between 0 and 1, or to the pore pressure variable p. To account for these analogies, a user material (UMAT) subroutine is employed to degrade both the material stiffness and the stress tensor with respect to the phase field variable, while incorporating as well the effect of pore pressure on the total stress using Biot's coefficient α. The evolution equation for the phase field and the fluid flow equation are subsequently addressed using the UMATHT subroutine, which defines the internal heat energy U and the heat flux vector $\mathbf{f}$ along with their respective variations concerning temperature T and the temperature gradient ∇T, as shown in Table A.5.

Different to Refs. [45,65], the temperature field is now used to describe two fields: phase field ϕ and pore pressure p. This can be accomplished by defining two identical Abaqus Parts with the same geometry and mesh. Since only one temperature can be defined per integration point, this approach enables effective data transfer between the two parts. Local numbering for elements and nodes remains consistent across both parts if the same meshing algorithm is used.

The proposed procedure is as follows: for a given element, Abaqus provides the UMAT integration point-level subroutine with values of strain and phase field (temperature) in the first part, interpolated from the nodal solutions. The pore pressure, represented as the temperature field in the second part, is stored in a FORTRAN module and transferred to the UMAT subroutine using local element numbering. Within each integration point and loop, the UMAT is first called. Inside the UMAT, the material Jacobian $\boldsymbol{C}$ and effective stress $\boldsymbol{\sigma}^{eff}$ are computed from the strain tensor. The current phase field value ϕ (temperature in the first part) is then used to account for the degradation of these quantities, while the pore pressure value p (temperature in the second part) is used

to compute the total stress $\boldsymbol{\sigma}$. The dissipation part of the strain energy density ψ_d is stored in solution-dependent state variables (SDVs), enabling enforcement of the irreversibility condition. The rate of volumetric strain $\dot{\varepsilon}_{vol}$ is stored within a FORTRAN module and transferred to the UMATHT subroutine to solve the fluid flow equation. In the UMATHT subroutine, definitions of internal heat energy U, heat flux vector $\mathbf{f}$, and their variations ($\partial U/\partial T$, $\partial U/\partial \nabla T$, $\partial \mathbf{f}/\partial T$, $\partial \mathbf{f}/\partial \nabla T$) are performed for the phase field equation in the first part and for the fluid flow equation in the second part. The UMATHT subroutine distinguishes between parts based on the material name, where MATERIAL-1 denotes the first part (deformation and phase field problems) and MATERIAL-2 denotes the second part (fluid flow equation).

The updated SDVs are transferred to the UMATHT subroutine to carry the current value of the history field $\mathcal{H}$ without requiring external FORTRAN modules. Additionally, the values of volumetric strain rate and the phase field variable are transferred from the UMAT subroutine to the UMATHT subroutine, which manages the fluid flow equation, via a FORTRAN module. This process is repeated for each integration point, allowing Abaqus to assemble the element stiffness matrices and residuals externally and subsequently form the global system of equations, as per the procedure outlined in Algorithm 2. The coupled problem can be approached using either a *monolithic* or *staggered* scheme. In the monolithic scheme, all variables are updated simultaneously, resulting in unconditional stability. In contrast, the staggered scheme updates variables sequentially, with some equations utilising variables from the previous increment or iteration instead of the current one, as described in Section 3.3.

This implementation offers two types of schemes: the Mixed monolithic scheme and the mixed staggered scheme. In the mixed monolithic scheme, equilibrium and phase field evolution equations are solved using a monolithic approach, while the pore pressure is derived from the previous iteration. In the mixed staggered scheme, the history field $\mathcal{H}$ is not updated within an increment for the phase field evolution equation; instead, the previous increment's history field $\mathcal{H}$ is applied. However, as in the mixed monolithic scheme, pore pressure is updated based on the solution of the previous iteration.

Data availability

Data will be made available on request.

References

[1] R. Barati, J.-T. Liang, A review of fracturing fluid systems used for hydraulic fracturing of oil and gas wells, J. Appl. Polym. Sci. 131 (16) (2014).
[2] E. Rojas, P. Landeros, Hydraulic fracturing applied to tunnel development at el teniente mine, in: Proceedings of the Ninth Rockburst and Seismicity in Mines Conference, 2017, pp. 251–257.
[3] Z. Lei, Y. Zhang, S. Zhang, Y. Shi, Numerical study of hydraulic fracturing treatments and geothermal energy extraction from a naturally fractured granitic formation, Geothermics 111 (2023) 102692.
[4] K. Sampath, M. Perera, P. Ranjith, Theoretical overview of hydraulic fracturing break-down pressure, J. Nat. Gas Sci. Eng. 58 (2018) 251–265.
[5] B. Lecampion, A. Bunger, X. Zhang, Numerical methods for hydraulic fracture propagation: A review of recent trends, J. Nat. Gas Sci. Eng. 49 (2018) 66–83.
[6] R. Navarrete, C. Soto, F. Henriquez, H. Godoy, Hydraulic fracturing in the construction of andes norte project, in: Caving 2022: Proceedings of the Fifth International Conference on Block and Sublevel Caving, Australian Centre for Geomechanics, pp. 1227–1240.
[7] G. Amorer, S. Duffield, J. De Ross, G. Viegas, Surface hydraulic fracturing trial at cadia east, in: Caving 2022: Proceedings of the Fifth International Conference on Block and Sublevel Caving, Australian Centre for Geomechanics, pp. 1173–1188.
[8] L.-P. Yi, H. Waisman, Z.-Z. Yang, X.-G. Li, A consistent phase field model for hydraulic fracture propagation in poroelastic media, Comput. Methods Appl. Mech. Engrg. 372 (2020) 113396.
[9] B. Bourdin, C. Chukwudozie, K. Yoshioka, A variational approach to the numerical simulation of hydraulic fracturing, Proc.-SPE Annu. Tech. Conf. Exhib. 2 (2012) 1442–1452.
[10] M.F. Wheeler, T. Wick, W. Wollner, An augmented-Lagrangian method for the phase-field approach for pressurized fractures, Comput. Methods Appl. Mech. Engrg. 271 (2014) 69–85.
[11] A. Mikelić, M.F. Wheeler, T. Wick, Phase-field modeling of a fluid-driven fracture in a poroelastic medium, Comput. Geosci. 19 (2015) 1171–1195.
[12] A. Mikelic, M. Wheeler, T. Wick, A phase-field method for propagating fluid-filled fractures coupled to a surrounding porous medium, Multiscale Model. Simullation 13 (2015) 367–398.
[13] A. Mikelić, M.F. Wheeler, T. Wick, A quasi-static phase-field approach to pressurized fractures, Nonlinearity 28 (5) (2015) 1371.
[14] T. Hageman, E. Martínez-Pañeda, A phase field-based framework for electro-chemo-mechanical fracture: Crack-contained electrolytes, chemical reactions and stabilisation, Comput. Methods Appl. Mech. Engrg. 415 (2023) 116235.
[15] C. Miehe, S. Mauthe, S. Teichtmeister, Minimization principles for the coupled problem of darcy–biot-type fluid transport in porous media linked to phase field modeling of fracture, J. Mech. Phys. Solids 82 (2015) 186–217.
[16] C. Miehe, S. Mauthe, Phase field modeling of fracture in multi-physics problems. Part III. Crack driving forces in hydro-poro-elasticity and hydraulic fracturing of fluid-saturated porous media, Comput. Methods Appl. Mech. Engrg. 304 (2016) 619–655.
[17] Z.A. Wilson, C.M. Landis, Phase-field modeling of hydraulic fracture, J. Mech. Phys. Solids 96 (2016) 264–290.
[18] W. Ehlers, C. Luo, A phase-field approach embedded in the theory of porous media for the description of dynamic hydraulic fracturing, part ii: The crack-opening indicator, Comput. Methods Appl. Mech. Engrg. 341 (2018) 429–442.
[19] Y. Heider, B. Markert, A phase-field modeling approach of hydraulic fracture in saturated porous media, Mech. Res. Commun. 80 (2017) 38–46.
[20] S. Lee, M.F. Wheeler, T. Wick, Pressure and fluid-driven fracture propagation in porous media using an adaptive finite element phase field model, Comput. Methods Appl. Mech. Engrg. 305 (2016) 111–132.
[21] S. Zhou, X. Zhuang, T. Rabczuk, A phase-field modeling approach of fracture propagation in poroelastic media, Eng. Geol. 240 (2018) 189–203.
[22] P. Li, D. Li, Q. Wang, K. Zhou, Phase-field modeling of hydro-thermally induced fracture in thermo-poroelastic media, Eng. Fract. Mech. 254 (2021) 107887.
[23] S. Lee, M.F. Wheeler, T. Wick, A phase-field diffraction model for thermo-hydro-mechanical propagating fractures, Int. J. Heat Mass Transfer 239 (2025) 126487.
[24] X. Wang, P. Li, D. Lu, Phase-field hydraulic fracturing operator network based on en-deeponet with integrated physics-informed mechanisms, Comput. Methods Appl. Mech. Engrg. 437 (2025) 117750.

[25] S. Lee, M.F. Wheeler, T. Wick, Iterative coupling of flow, geomechanics and adaptive phase-field fracture including level-set crack width approaches, J. Comput. Appl. Math. 314 (2017) 40–60.
[26] K. Yoshioka, D. Naumov, O. Kolditz, On crack opening computation in variational phase-field models for fracture, Comput. Methods Appl. Mech. Engrg. 369 (2020) 113210.
[27] D. Santillán, R. Juanes, L. Cueto-Felgueroso, Phase field model of fluid-driven fracture in elastic media: Immersed-fracture formulation and validation with analytical solutions, J. Geophys. Res.: Solid Earth 122 (4) (2017) 2565–2589.
[28] S. Zhou, X. Zhuang, T. Rabczuk, Phase-field modeling of fluid-driven dynamic cracking in porous media, Comput. Methods Appl. Mech. Engrg. 350 (8) (2019) 169–198.
[29] S. Shahoveisi, M. Vahab, B. Shahbodagh, S. Eisenträger, N. Khalili, Phase-field modelling of dynamic hydraulic fracturing in porous media using a strain-based crack width formulation, Comput. Methods Appl. Mech. Engrg. 429 (2024) 117113.
[30] L. Yang, Y. Ma, G. Yang, Z. Liu, K. Kang, M. Zhang, Z. Wang, Phase field modeling of hydraulic fracturing with length-scale insensitive degradation functions, Energies 17 (20) (2024) 5210.
[31] Y.-S. Lo, T.J. Hughes, C.M. Landis, Phase-field fracture modeling for large structures, J. Mech. Phys. Solids 171 (2023) 105118.
[32] F. Aldakheel, N. Noii, T. Wick, P. Wriggers, A global–local approach for hydraulic phase-field fracture in poroelastic media, Comput. Math. Appl. 91 (2021) 99–121.
[33] C. Maurini, B. Bourdin, G. Gauthier, V. Lazarus, Crack patterns obtained by unidirectional drying of a colloidal suspension in a capillary tube: experiments and numerical simulations using a two-dimensional variational approach, in: Fracture Phenomena in Nature and Technology: Proceedings of the IUTAM Symposium on Fracture Phenomena in Nature and Technology Held in Brescia, Italy, 1-5 July 2012, Springer, 2014, pp. 75–91.
[34] C. Luo, L. Sanavia, L. De Lorenzis, Phase-field modeling of drying-induced cracks: Choice of coupling and study of homogeneous and localized damage, Comput. Methods Appl. Mech. Engrg. 410 (2023) 115962.
[35] Y. Heider, A review on phase-field modeling of hydraulic fracturing, Eng. Fract. Mech. 253 (June) (2021) 1–24.
[36] B. Chen, B.R. Barboza, Y. Sun, J. Bai, H.R. Thomas, M. Dutko, M. Cottrell, C. Li, A review of hydraulic fracturing simulation, Arch. Comput. Methods Eng. (2022) 1–58.
[37] R. Rimmelin, G. Chitombo, E. Rojas, Hydraulic fracturing in cave mining: Opportunities for improvement, in: MassMin 2020: Proceedings of the Eighth International Conference & Exhibition on Mass Mining, University of Chile, pp. 275–288.
[38] C. Pardo, E. Rojas, Selection of exploitation method based on the experience of hydraulic fracture techniques at the el teniente mine, in: Proceedings of the Seventh International Conference and Exhibition on Mass Mining, Massmin 2016, The Australasian Institute of Mining and Metallurgy, pp. 97–103.
[39] Y. Navidtehrani, C. Betegón, E. Martínez-Pañeda, A general framework for decomposing the phase field fracture driving force, particularised to a Drucker–Prager failure surface, Theor. Appl. Fract. Mech. 121 (2022) 103555.
[40] G. Molnár, A. Doitrand, R. Estevez, A. Gravouil, Toughness or strength? regularization in phase-field fracture explained by the coupled criterion, Theor. Appl. Fract. Mech. 109 (2020) 102736.
[41] L. De Lorenzis, C. Maurini, Nucleation under multi-axial loading in variational phase-field models of brittle fracture, Int. J. Fract. 237 (1) (2022) 61–81.
[42] O. Lopez-Pamies, J.E. Dolbow, G.A. Francfort, C.J. Larsen, Classical variational phase-field models cannot predict fracture nucleation, Comput. Methods Appl. Mech. Engrg. 433 (2025) 117520.
[43] A.A. Griffith, The phenomena of rupture and flow in solids, Philos. Trans. A 221 (1920) 163–198.
[44] P.K. Kristensen, C.F. Niordson, E. Martínez-Pañeda, An assessment of phase field fracture: crack initiation and growth, Phil. Trans. R. Soc. A 379 (2203) (2021) 20210021.
[45] Y. Navidtehrani, C. Betegón, E. Martinez-Paneda, A unified abaqus implementation of the phase field fracture method using only a user material subroutine, Mater. 14 (8) (2021) 1913.
[46] E. Haghighat, D. Santillán, An efficient phase-field model of shear fractures using deviatoric stress split, Comput. Mech. 72 (6) (2023) 1263–1278.
[47] P. Hesammokri, H. Yu, P. Isaksson, An extended hydrostatic–deviatoric strain energy density decomposition for phase-field fracture theories, Int. J. Solids Struct. 262-263 (2023) 112080.
[48] F. Vicentini, C. Zolesi, P. Carrara, C. Maurini, L. De Lorenzis, On the energy decomposition in variational phase-field models for brittle fracture under multi-axial stress states, Int. J. Fract. 247 (3) (2024) 291–317.
[49] H. Amor, J.J. Marigo, C. Maurini, Regularized formulation of the variational brittle fracture with unilateral contact: Numerical experiments, J. Mech. Phys. Solids 57 (8) (2009) 1209–1229.
[50] C. Miehe, M. Hofacker, F. Welschinger, A phase field model for rate-independent crack propagation: Robust algorithmic implementation based on operator splits, Comput. Methods Appl. Mech. Engrg. 199 (45–48) (2010) 2765–2778.
[51] F. Freddi, G. Royer-Carfagni, Regularized variational theories of fracture: A unified approach, J. Mech. Phys. Solids 58 (8) (2010) 1154–1174.
[52] G. Del Piero, Constitutive equation and compatibility of the external loads for linear elastic masonry-like materials, Meccanica 24 (3) (1989) 150–162.
[53] H. Darcy, Les Fontaines Publiques De La Ville De Dijon, Dalmont, paris, 1856.
[54] J. Jaeger, N. Cook, R. Zimmerman, Fundamentals of Rock Mechanics, Blackwell Publishing, Oxford, UK, 2009.
[55] N. Xie, Q.-Z. Zhu, J.-F. Shao, L.-H. Xu, Micromechanical analysis of damage in saturated quasi brittle materials, Int. J. Solids Struct. 49 (6) (2012) 919–928.
[56] C. Jia, S. Zhang, W. Xu, Experimental investigation and numerical modeling of coupled elastoplastic damage and permeability of saturated hard rock, Rock Mech. Rock Eng. 54 (2021) 1151–1169.
[57] J. Ulloa, N. Noii, R. Alessi, F. Aldakheel, G. Degrande, S. François, Variational modeling of hydromechanical fracture in saturated porous media: A micromechanics-based phase-field approach, Comput. Methods Appl. Mech. Engrg. 396 (2022) 115084.
[58] S. Zhou, X. Zhuang, H. Zhu, T. Rabczuk, Phase field modelling of crack propagation, branching and coalescence in rocks, Theor. Appl. Fract. Mech. 96 (2018) 174–192.
[59] C. Chukwudozie, B. Bourdin, K. Yoshioka, A variational phase-field model for hydraulic fracturing in porous media, Comput. Methods Appl. Mech. Engrg. 347 (2019) 957–982.
[60] E.C. Bryant, W.C. Sun, A mixed-mode phase field fracture model in anisotropic rocks with consistent kinematics, Comput. Methods Appl. Mech. Engrg. 342 (2018) 561–584.
[61] V. Ziaei-Rad, L. Shen, J. Jiang, Y. Shen, Identifying the crack path for the phase field approach to fracture with non-maximum suppression, Comput. Methods Appl. Mech. Engrg. 312 (2016) 304–321, phase Field Approaches to Fracture.
[62] T. Gerasimov, L. De Lorenzis, On penalization in variational phase-field models of brittle fracture, Comput. Methods Appl. Mech. Engrg. 354 (2019) 990–1026.
[63] P.K. Kristensen, E. Martínez-Pañeda, Phase field fracture modelling using quasi-newton methods and a new adaptive step scheme, Theor. Appl. Fract. Mech. 107 (2020) 102446.
[64] F. Gonzalez, J. Vallejos, E. Rojas, P. Landeros, Evaluation of the seismic rock mass response to mining and the impact of preconditioning using an epidemic-type aftershock model, Int. J. Rock Mech. Min. Sci. 150 (2022) 104975.
[65] Y. Navidtehrani, C. Betegón, E. Martínez-Pañeda, A simple and robust abaqus implementation of the phase field fracture method, Appl. Eng. Sci. 6 (2021) 100050.

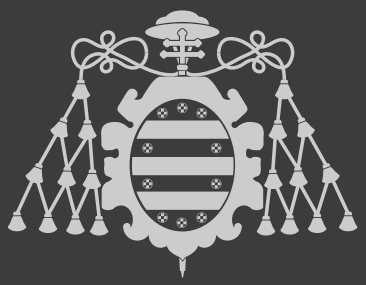

Universidad de Oviedo

PhD Thesis in Computational Mechanics of Materials

Yousef Navidtehrani